ANNUAL REPORT 1993

CENTRAL LASER FACILITY

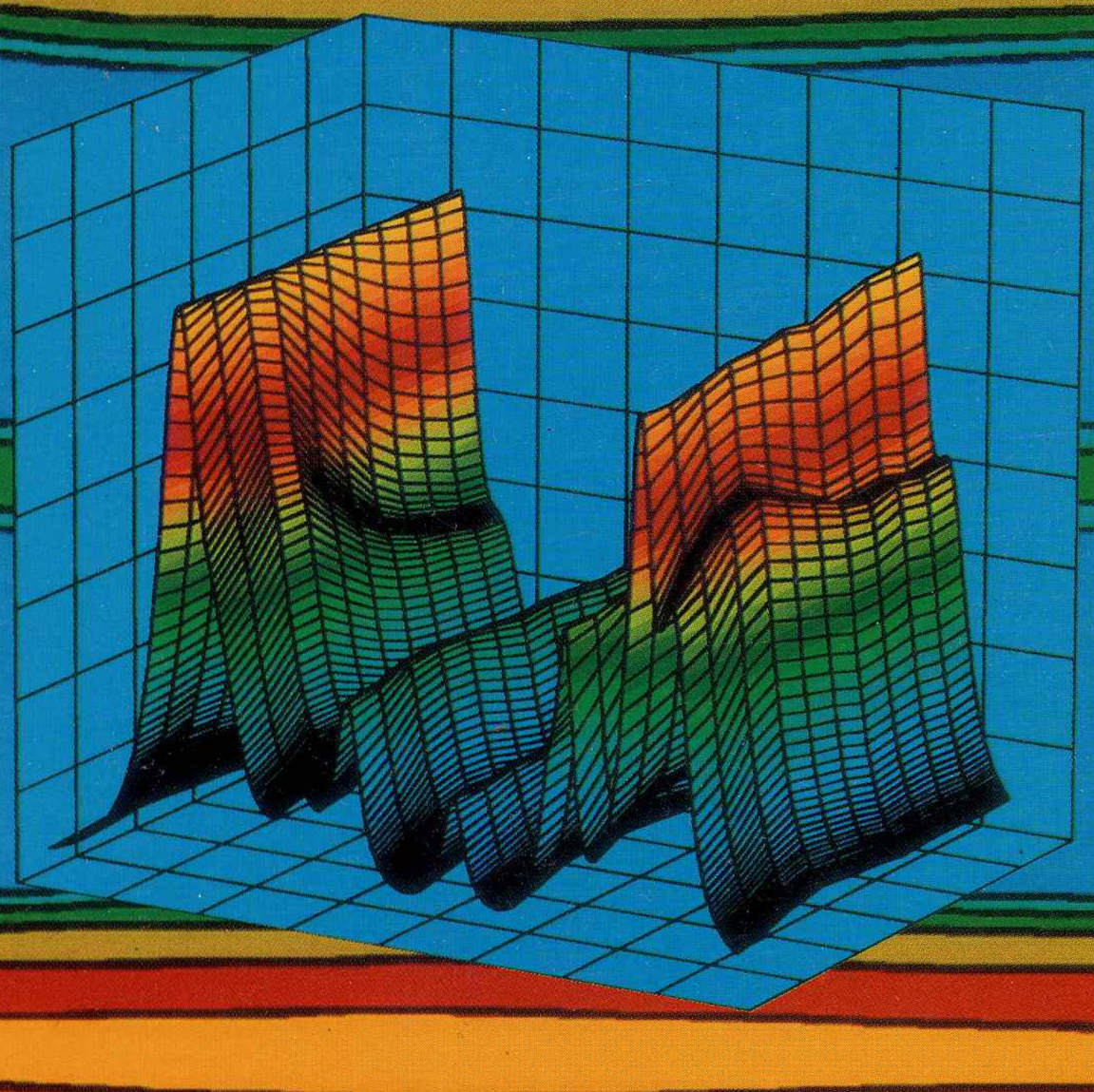

SERC

RUTHERFORD APPLETON LABORATORY

ANNUAL REPORT TO THE LASER FACILITY COMMITTEE 1993

5 April 1992 to 4 April 1993

SERC CENTRAL LASER FACILITY
RUTHERFORD APPLETON LABORATORY
CHILTON
DIDCOT
OXON
OX11 0QX

Telephone **0235 821900**
Telefax **0235 445888**

Rutherford Appleton Laboratory Report RAL-93-031

The cover design features time resolved resonance Raman spectra of a photo-excited molecule showing structural changes on a picosecond timescale (see P 147).

ACKNOWLEDGEMENTS

M H Key

This report is the product of a team effort, and, I would like to acknowledge the contributions of all those who have brought it to fruition.

The production was organised by Nic Allen, Chris Naboulsi and Katharine Higgs with Chris Reason overseeing the technical specifications.

The Chapter Editors were Peter Norreys, Mick Shaw and Bill Toner. Sections Editors were Abdes Djaoui, Phil Taday, Edmond Turcu, Steve Rose, Chris Edwards, Colin Danson, Chris Hooker, Dave Pepler, Graeme Hirst, Tony Parker, Sue Tavender, Mike Towrie and Andrew Langley. The important task of collecting publications was overseen by Ian Ross with the help of Abdes Djaoui, Sue Tavender and Andy Kidd.

Most of the text has been provided in camera-ready format by the facility users and they deserve particular thanks for supplying their contributions to our production deadline.

The document has been produced by the RAL Reprographics Service . The winners of the cover design competition this year were Mike Towrie, Pavel Matousek and Tony Parker with the assistance of Kate Crennell and the ISIS VAX image processing system.

PREFACE

M H Key

In introducing this Annual Report it is a pleasure for me to highlight a year's work (to 31 April 1993) which has produced both a record level of scientific achievement by facility users and significant developments of the facilities.

Striking progress has been made in the first year of a two year project carried out jointly by University groups and facility staff to develop ultra-short pulse and ultra-bright beam operation of the high power lasers. Already users have gained access to new levels of focused intensity in compressed pulses from both the Nd glass laser, Vulcan and the KrF laser, Sprite. The project is on course to meet all its goals.

Underpinned by this development programme, the users' research work with the high power lasers has been extremely productive. Scientific results of strategic importance for laser fusion were obtained in a series of experiments by Imperial College researchers who have developed new ways to minimise non-uniformity of pressure in laser driven implosions. X-ray laser research by an inter-university consortium of research groups also advanced significantly with the successful development of a unique injector-amplifier laser giving improved coherence. The new bright beams have stimulated interest in high intensity interaction phenomena and novel results have been obtained for example in the study of multiphoton ionised gases and production of near solid density plasmas by Oxford University and Imperial College teams. Vigorous activity in theory and computational modelling has also been a feature of the year's work.

A similarly buoyant atmosphere has pervaded the work of the users of the smaller lasers in the Laser Support Facility. An improved femtosecond source was provided last year. Equipment for picosecond resonance Raman spectroscopy was brought into full operation and the high repetition rate laser-plasma X-ray source was upgraded to a record output. A notably diverse scientific programme was accomplished using the full range of LSF equipment. Among many achievements, pioneering work has shown that the Vitamin E radical is located at the cell membrane - water interface so that it can be recycled by Vitamin C to enhance its role in cancer prevention. In the field of gas phase chemistry, studies at low temperature have been extended down to 14K in a European collaboration involving use of LSF equipment in a laboratory in France.

The productivity of the scientific programmes of both the High Power Laser and Laser Support Facility users has been extremely high in terms of publications in the scientific literature and it's pleasing to note that the record number of publications (167) listed in this report is 20% up on last year and continues a trend of sustained increase in productivity.

Rapid progress has been made this year in constructing a new high energy KrF laser amplifier for incorporation into an upgraded KrF laser facility named Titania which will come into operation in 1995/96. The Titania laser will give users new opportunities to develop their research programmes with unique capabilities at their disposal and is the basis of the mid-term plan for the high power laser work.

A welcome event at the close of this year was the pre-selection by the CEC of the CLF's high power lasers as one of the European Large Facilities to be opened for access by European researchers. This is a significant step in the internationalisation of the work of the CLF and taken together with this substantial role which will be played by its users in several of the new CEC funded research networks, will bring an enhanced European dimension to our work.

The high levels of scientific achievement, productivity and cost effectiveness of the work of the CLF have proved a strong defence in recent financial scenario studies, some of which have included options for drastic cuts in funding of the CLF as part of options for ~ 5% savings in SERC's overall budget. Although such excercises are unsettling for both users and staff of the facility they are a necessary part of the management of science and continued high performance in the scientific work of the facility is clearly the only way to ensure the security of future funding.

It is my pleasure to record my thanks to both users and staff of the facility, whose dedication has made the past year so scientifically stimulating and productive.

INTRODUCTION TO THE CENTRAL LASER FACILITY

C B Edwards

Foreword

The mission of the SERC Central Laser Facility is to enable pure and applied research by UK University scientists, and their overseas collaborators, whose requirements for advanced lasers, diagnostic hardware, and specialist technical and theoretical support cannot be met within the Universities.

By pooling resources at the CLF, the research community gains access both to state of the art facilities, and the technological infra-structure necessary for sophisticated experiments. This enables users to contribute to science and technology in areas of strategic importance, eg, inertial confinement fusion, X-ray lasers etc.

The training of post-graduate researchers features prominently in the work of the CLF. Responsibility for organising experiments on a day-to-day basis, data gathering, and subsequent analysis is often taken by experienced graduate students working under the direction of a university group leader. In the past year, 51 such students have obtained data from experiments using CLF facilities for incorporation in theses for higher degrees.

The partnership which has developed between academia and the staff at the CLF since its formation in 1976, makes an extremely cost-effective contribution to science and technology at the highest international level. The success of the CLF scientific programme may be judged from the large number of publications in the most respected scientific journals, the many invited presentations at International conferences, and the key role played by its scientists in international collaborations based at prestigious research centres. (see Facts & Figures)

Facilities available

Vulcan is a large, highly versatile Nd glass laser, delivering up to 3 kJ of 1μ laser irradiation in eight main beams in spherical, cluster, or line focus geometry. In ultra-short pulse mode, (2 ps) up to 10 TW is available in a single beam producing focused intensities approaching 10^{18} Wcm^{-2}.

SPRITE, a UV Raman laser pumped by KrF excimer laser radiation, is capable of producing intensities on target up to 10^{19} Wcm^{-2}. It delivers 1 TW in a pre-pulse free Raman-shifted beam of 10 ps duration at a repetition rate of 12 shots per hour. Recent development of the system enables 1 TW to be generated in pulses as short as 300 fs.

The Laser Support Facility (LSF) makes a wide range of high repetition rate lasers available to users for experiments in chemistry, biology, and photo-physics. Pulse durations down to 100fs are available, and the wavelength coverage spans the infrared to the ultra-violet. The LSF also provides equipment on loan for use in university laboratories.

In addition to the laser facilities, users have access to a specialist target fabrication service, electrical and mechanical engineering support, and numerical modelling services. Figure 1 shows the divisional and group structure of the CLF in the reporting year.

Facility access

The programme at the CLF is managed by the Laser Facility Committee (LFC), currently chaired by Prof W Sibbett of St Andrews University (see Committee Membership).

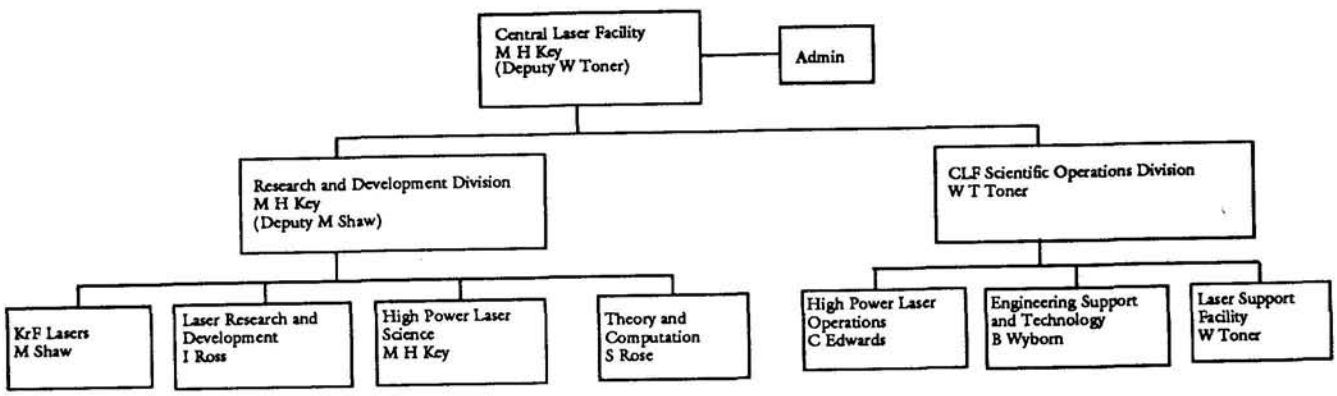

Fig.1 Divisional and Group Structure of the Central Laser Facility

Two specialist panels with representation from the user community (see Committee Membership) monitor the High Power Laser and Laser Support Facility programmes, and report to the LFC. The committees and panels meet three times per year.

Proposals for work, submitted by potential users, are considered by the specialist panels and are awarded a scheduling priority. Applicants are normally expected to have secured SERC approval and funding for their programmes before submitting applications to the panels. However, there is some flexibility, particularly for LSF applicants, for small scale preliminary investigations pending submission of a full grant proposal. The requests for facility time typically exceed the time available by a factor between two and three. A schedule of experiments is arranged by CLF staff via two scheduling committees.

EC access to CLF facilities

Historically, the CLF programme has benefited greatly from the scientific contribution made by International colleagues of the British university researchers. Until recently, however, experimental time was only allocated to scientific teams led by members of British universities.

Starting in early 1994 the CLF expects to be able to make beam time available to scientists throughout the EC. This will be funded through the Access to Large Facilities Programme of the CEC. A highly successful pilot experiment has already been conducted by a team from the University of Pisa in Italy.

Facts and figures

In the past year, the total funding of the CLF was £4.38M, including the costs of 53.2 years of staff effort, and users' travel and subsistence costs incurred while undertaking experiments at the CLF. The distribution of the financial resources between the main programmes of the CLF is shown in Figure 2.

Figure 3 shows the sustained growth of the scientific output of the CLF user programme measured in terms of the total number of refereed publications and published conference proceedings recorded in these annual reports over the last 8 years. Over this period the total budget allocation and staff usage after indexation have remained largely constant. Comparing the number of publications in the year ended 1993 (167) with the corresponding figure for 1985 (70) it will be seen that both productivity and the cost effectiveness of the CLF show a substantial increase over the period.

During the year covered by this report, 124 weeks of experimental time were scheduled on the high power lasers involving 25 experiments. At the Laser Support Facility, there were a total of 41 user experiments using the in-house facilities and 15 user experiments using the loan lasers. The CLF was also host to 15 researchers from Japan, China, Italy, France, America and Canada.

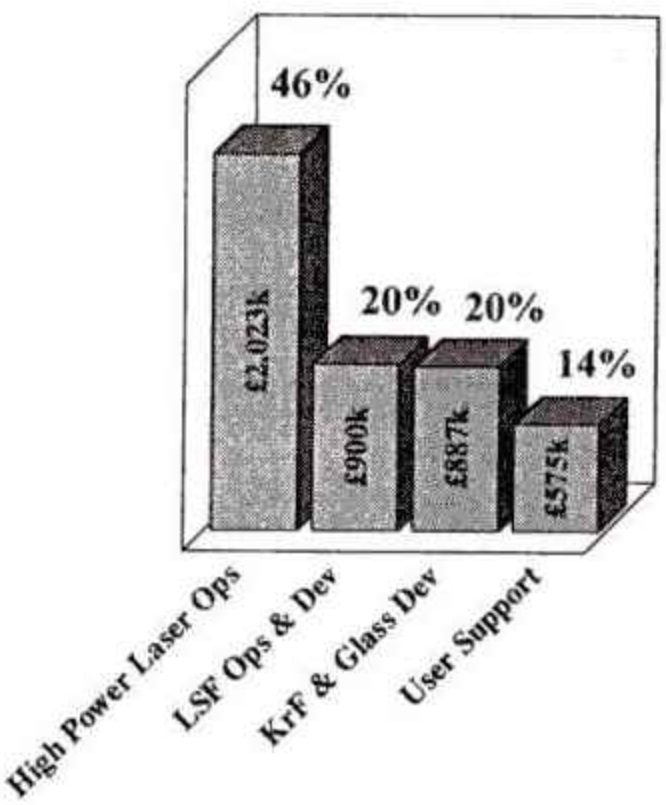

Fig 2: Distribution of CLF Resources 92/93

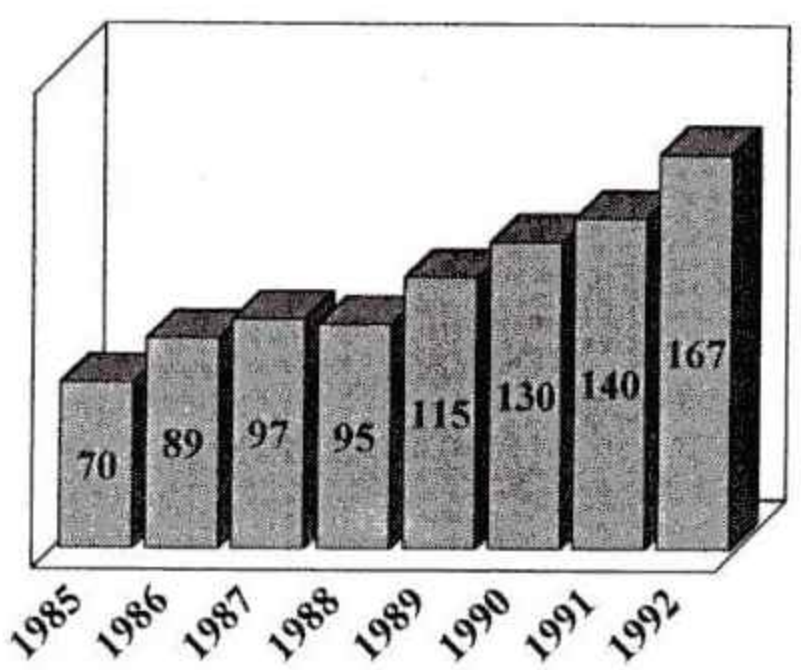

Fig 3: Refereed publications & published conference proceedings

SOFT X-RAY LASER COUPLING WITH AN XRM IN A SEQUENTIALLY PUMPED AMPLIFIER GEOMETRY

D. Neely[1], C. L. S. Lewis[1], G. Cairns[1], A. G. MacPhee[1], M. Holden[2], J. Krishnan[2], G. J. Tallents[2], M. H. Key[3], P. N. Norreys[3], C. G. Smith[4], J. Zhang[4], M. T. Browne[5], R. E. Burge[5], G. E. Slark[5], P. B. Holden[6], G. J. Pert[6], J. Ploues[6] and S. A. Ramsden[6].

[1]Dept. of Pure & Applied Physics, Queens University of Belfast, N. Ireland, BT7 1NN
[2]Department of Physics, University of Essex, Colchester, England C04 3SQ
[3]Central Laser Facility, Rutherford-Appleton Lab, Chilton, Oxon, OQ11 0QX
[4]Clarendon Laboratory, University of Oxford, Oxford OX1 3PU
[5]Wheatstone Physics Laboratory, King's College, London WC2R 2LS
[6]Department of Computational Physics, University of York, York YO1 5DD

INTRODUCTION

Many of our previous experimental studies of soft X-ray laser schemes have concentrated in detail on either studying the conditions required to achieve gain in a plasma or enhancing the gain production efficiency. This experiment was designed to investigate and modify the characteristic properties i.e. spatial coherence and brightness of a Ne-like Ge soft X-ray laser output beam. To manipulate these properties of the output beam, an apertured concave mirror was used to image relay the laser beam from an injector target in the standard TAE six beam chamber into a variety of amplifier target geometries situated in the new add-on chamber. This run was also successfully used to experimentally commission the new X-ray laser add-on chamber and associated alignment and line focus optics[1].

EXPERIMENTAL

A schematic diagram of the experimental geometry is shown in figure 1 of reference 1. Six 110 mm 1.05 μm Vulcan glass laser beams were used in the Target Area East standard chamber in an off-axis illumination geometry to drive a Ge 18+18 mm double slab target[2]. A Gaussian shaped pulse of FWHM 1.1 ns was used to drive 160 μm wide targets at an average irradiance of $1x10^{13}$ Wcm^{-2}. The North propagating soft X-ray laser beam from this double target which will be referred to as the 'injector' (see figure 1) was image relayed and injected into an amplifier target situated in the new chamber. Two 150 mm beams were used in the new chamber either in a staggered mode from opposite sides to drive 14+14 mm 160 μm wide double slab targets at an average irradiance of $1x10^{13}$ Wcm^{-2} or, for exploding foil shots the beams were superimposed from opposite sides onto a single target. Plasma uniformity along the axial direction of both the injector and amplifier plasmas was monitored using space resolving crystal spectrometers observing the resonance line emission in the 8↔10 Å region. A streaked crystal spectrometer was also used to monitor the time varying emission from Ne and F-like lines under different drive and target conditions (see figure 5). Soft X-ray lasing signal levels from the injector and amplifier targets when they were operated without any coupling were initially monitored using a flat-field spectrometer with either Q-plates or 10402 film as the recording medium. The spectrometer was operated with a wide entrance slit of 140 μm which combined with a 1200 lines per mm aperiodically ruled flat-field grating gave a resolving power of ≈1000 at 234 Å. With this instrument at the South end of the chamber coupling from the injector target into a single 14 mm slab target via a normal incidence soft X-ray mirror[3] (XRM) was observed. Using the flat-field spectrometer it was only possible to sample a 1D slice through the output beam. To obtain 2D information a 56 degree glancing angle multi-layer mirror was inserted 600 mm from the amplifier target. The reflected beam from this mirror was directed onto a 10402 film back with a 0.8 μm thick Al filter to provide light rejection. Due to the lower resolving power of this system (≈ 7) it was not possible to observe (above background) the self ASE signal from a double 14+14 mm target in the amplifier position. Spatial coherence of the laser beam was studied using a spectrally resolving Young's double slit geometry and preliminary results are reported in a separate section[4].

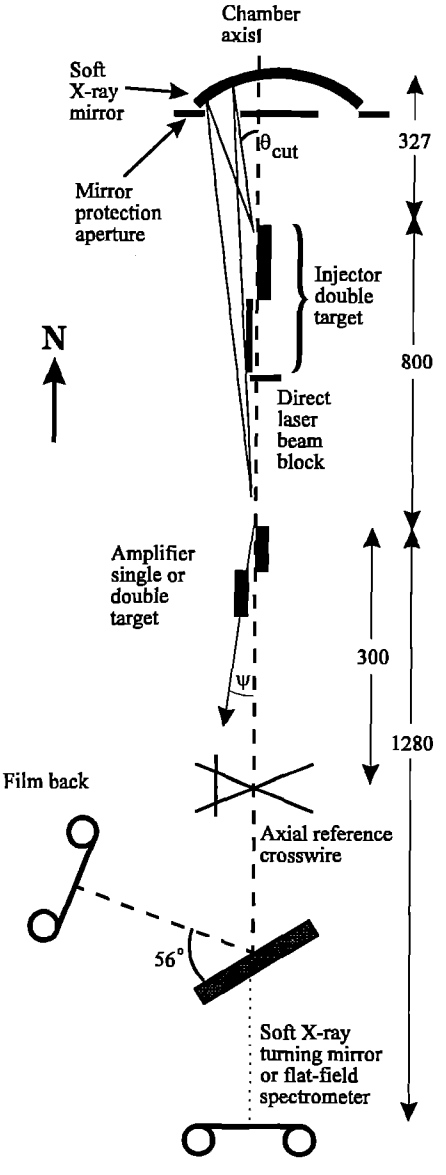

Figure 1 Schematic diagram showing the X-ray laser coupling geometry used.

The standard coupling geometry used throughout the experiment was with a 250 mm focal length normal incidence XRM placed at a distance d_m = 327 mm from the exit plane of the injector target. To prevent exposure of the entire XRM surface during each laser shot to scattered laser light and plasma debris/emission, an 8 mm (horizontal) x 11 mm (vertical) mask was placed 10 mm in front of

the XRM. The centre of the mask was positioned on the horizontal plane at 12 mrad from the chamber axis to intercept the beam maximum. In this geometry the image plane of the injector target is situated ≈ 62 mm in front of the entrance plane of the amplifier target at a magnification of x3.3. The XRM was initially aligned optically using a dummy target with a fibre optic source situated at the exit plane of the injector target. Light from the fibre was imaged onto a graticule placed at the entrance plane of the amplifier target. The graticule was viewed using a x10 microscope objective coupled to a TV system. The focal position of the mirror was set to an accuracy of ±1.5 mm along the chamber axis and to ±25 μm transverse to the axis. To test the soft X-ray mirror alignment, a reference 150 μm cross wire was placed at the input amplifier plane and an 18+18 mm injector target shot fired. With the image plane of the injector target set at 62 mm upstream of the crosswires a ≈x20 shadow of the crosswires is obtained on the film back. Since the lasing region is displaced a distance X_{off}, from the target surface then during the optical alignment of the XRM it is necessary to displace the alignment spot at the amplifier plane by an amount MX_{off}, where M the magnification of the system. From a number of alignment shots it was found that to centralise the relayed image onto the amplifier plane required $65 < X_{off} < 80$ μm. A second set of cross wires with its bars rotated through 45 degrees with respect to the first was placed a further 300 mm downstream from the amplifier to provide a fixed reference for both alignment and full coupling shots. A test alignment shot showing the centre of the beam is shown in figure 3(iv). On this image a sharp cut off to the left hand side is also observed. This is caused by the beam clipping the back of the south end of the injector target as shown on figure 1. To reduce the amount of beam clipped the south injector target substrate was reduced in thickness from the standard 1.5 mm thick glass plates to a 0.5 mm thick plate. This corresponds to all emission from the injector plasma travelling at less than a critical angle θ_{cut} = 3.5 mrad not being imaged onto the amplifier plane. Since the centre of the beam was typically at 10 mrad from the axis then only the weaker wing to one side of the beam was chopped off.

If we define a coupling factor C as the fraction of the injector beam which intersects the gain region at the amplifier entrance plane then C can be used to compare the coupling efficiency of different geometries. The direct geometrical coupling factor C_d between two identical plasmas separated a distance L is given by

$$C_d \approx \frac{vh}{(v+L\phi_v)(h+L\phi_h)} \approx \frac{vh}{L^2\phi_v\phi_h} \qquad (1)$$

where, a gain region of rectangular cross section of dimensions v and h in the vertical and horizontal planes is assumed and ϕ_v and ϕ_h are the beam divergences in the vertical and horizontal planes respectively. In our geometry the distance between the south end of the injector plasma and the north end of the amplifier plasma is 764 mm. Inserting the gain region sizes and beam divergences into equation 1 we would expect a geometrical coupling factor of $C_d \approx 10^{-4}$. The coupling factor C_m using a relay mirror of reflectance R is given by

$$C_m \approx \frac{RC_d}{M^2} \qquad (2)$$

Where L in equation 1 is replaced by d_p which is the distance between the exit face of the injector target to the object plane which is imaged onto the amplifier plane. An added advantage of operating the relay mirror at high magnification M is that the relayed beam solid angle is reduced by a factor M^2 compared to the emitted beam. In our case with the XRM situated at d_m = 327 mm, d_p = 5.4 mm and M = 3.5. Evaluating equation 2 we obtain $C_m \approx 3R \times 10^{-2}$ indicating that even with an XRM reflectivity of ≈ 4%, $C_m \approx 10^{-3}$ which is an order of magnitude greater than for the direct coupling case. The limit maximum value for image relayed coupling is $C_m \approx RM^{-2}$.

SOFT X-RAY MIRRORS

During the experiment the bandwidth and spectral position of peak reflectivity for two XRM's was measured. Spectral lines in the 15-30 nm region from a brass / Al target were recorded directly on one shot and then on a subsequent shot after reflection from the mirror under test. The normalised intensity ratio R_n of the recorded lines is shown on figures 2(i) and 2(ii). The 250 mm focal length concave mirror was found to have a peak reflectivity at 240 ± 10 Å with a bandwidth of 30 ± 5 Å. It was also observed that the mirror had a second narrower ≈15 Å bandwidth centred at 160 ± 5 Å. The R_n curve measured at a glancing angle of 45 degrees for the second flat mirror is shown on figure 2(ii). The mirror had a bandwidth of 30 ± 5 Å centred at 200 ± 10 Å. Using a calculated 2d spacing of 282 Å the mirror was rotated and used at a glancing angle of 56° to reflect the dominant J=2-1 232 and 236 Å Ne-like Ge lasing lines. Absolute reflectivities of the soft X-ray mirrors are not known. However, we estimate that at 234 Å the reflectivity of the normal incidence mirror after being used for roughly twenty shots on the same surface area probably did not exceed ≈ 5 %.

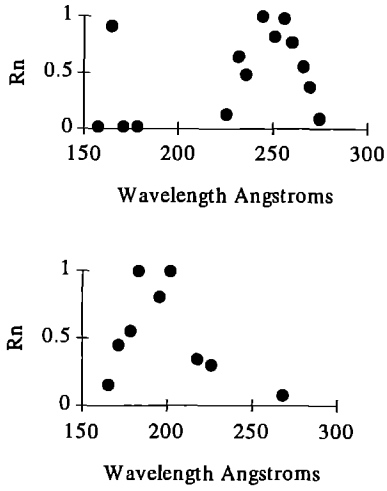

Figure. 2(i) and 2(ii) Graphs showing the measured normalised reflectivity for (i) a normal incidence and (ii) a 45 degree glancing angle soft X-ray multi-layer mirror.

RESULTS

INJECTOR BEAM PROFILES

All of our earlier studies of the soft X-ray laser beam cross section have only been possible in the far field due to diagnostic limitations. Although this can give us accurate information on the beam divergence it provides little information on the uniformity, size and distribution of the beam as it exits the plasma. Such near-field information is useful for additional comparison with code predictions and was obtained here by imaging planes near the injector exit face onto film. Using the 250 mm focal length concave XRM situated at a distance d_m from the north end of the injector target, images of planes at different distances d_p from the exit face of the injector target were recorded on 10402 film at a magnification M. A thick 0.8 ↔ 3.0 μm thick Al filter placed 15 mm in front of the film provided rejection of optical emission. The concave mirror was used in three set-ups as shown in table 1. A fourth set-up using the flat multi-layer turning mirror where the total path length from the plasma to the film was 1170 mm was also used to obtain a far field distribution from the plasma. Due to experimental constraints the angular acceptance range of emission from the plasma which was recorded at the detector plane was slightly different for each set-up and is shown on table 1. The lower two images of figure 3 show the intensity distribution at the end of an 18+18 mm injector target for stripe widths of 115 and 160 μm. The 115 μm stripe has a horizontal and vertical FWHM

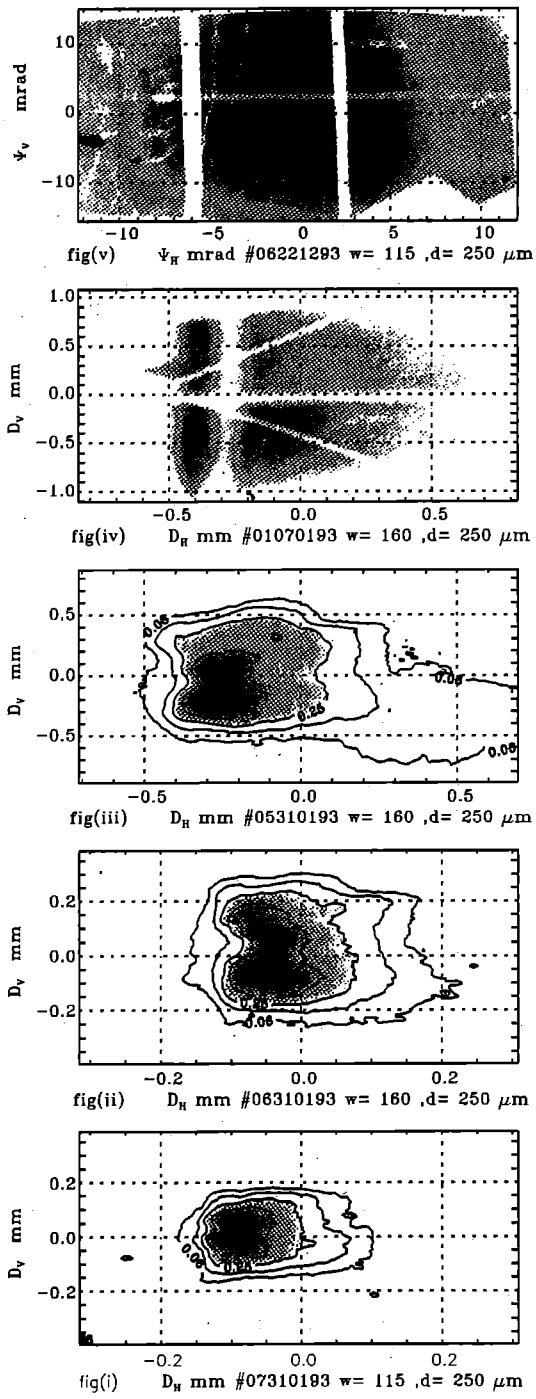

Figures 3 (i)↔(v) Images showing the intensity distribution of the J=2-1 Ne-like Ge lasing beam at different distances of (i) 0 mm, (ii) 0 mm, (iii) 18 mm, (iv) 48 mm and (v) 1170 mm from the exit face of the injector target. Details of the target conditions present during an individual shot are listed under each image.

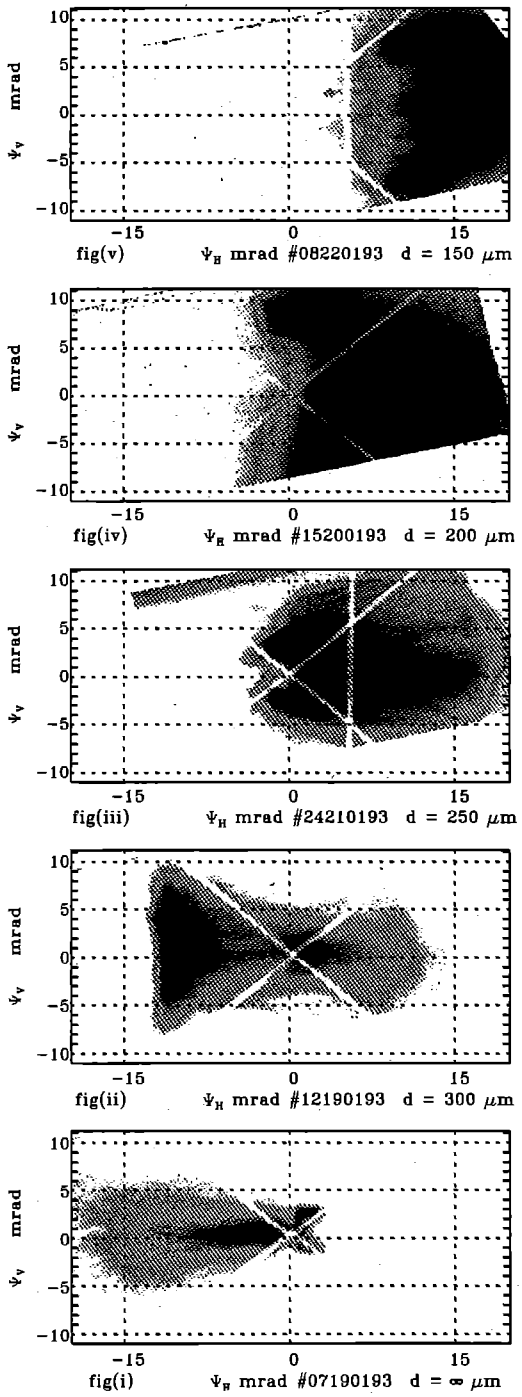

Figures 4 (i)↔(v) Cross sections taken at a distance of 1.26 m from the exit face of a pumped amplifier target. The angular intensity distribution of the amplified beam observed using a single target amplifier is display in figure (i) and those obtained using double target amplifiers are shown on figures (ii)↔(v).

of 120 and 190 μm respectively. The vertical section shows a reasonably symmetrical profile, whilst the horizontal section shows a steep rise and a more gradual decay with distance away from the target surface. The FWHM for the vertical section is much larger than the initial stripe width. This may be attributable to significant amounts of lasing emission leaving the gain region before reaching the exit face of the target. A 3D ray tracing code and a wave code are presently being developed at York University which will be able to examine this aspect of imaging emission from planes close to the source plasma in more detail. Semi-analytic ray tracing codes are also being developed at QUB to describe coupling involving multiple target elements and mirrors. Figure 3(ii) shows the image from shot 06310193, an 18+18 mm 160 μm wide injector target. The image has a horizontal and vertical FWHM of 120 and 355 μm respectively. The horizontal section is similar in profile to that recorded on shot 07310193. However, the vertical profile is markedly different displaying a central 15% intensity dip of about 100 μm width. Evidence for the central dip is also shown

on figure 3(iii) which is an image taken under similar target conditions but with the object plane now located 18 mm away from the face of the target. This image has a horizontal and vertical FWHM of 250 and 570 μm respectively. From this we can estimate a vertical and horizontal beam divergence of 20± 5 and 8±3 mrad. This result is consistent with other estimates for beam divergence taken from figures 3(iv) and 3(v) which give horizontal and vertical divergences of 10± 3 and 25± 5 mrad respectively. Measurements of the beam size at 10% of the maximum would suggest that the weaker wings of the beam are spreading much more rapidly at ≈ 40±5 mrad in both directions. Figure 3(iv) shows the image obtained with the object plane set at 48 mm from the exit face of the target. This image was recorded during alignment testing of the relayed beam. Unfortunately, due to crosswire shadows and cut-offs it is not possible to accurately measure the beam divergence. However, after examining a number of theses shots no evidence for an observable central dip in the vertical direction was obtained. It was noted that on average one half (in the vertical direction) of the laser beam seemed to be brightest. Figure 3(v) shows a far-field laser distribution similar to shot 01070193 in that no central dip is observable. However, one half of the image contains about 15% more energy than the other. This energy asymmetry in the beam is associated with the lobe like structure observed in the near field images which may reflect asymmetries in the pump beam radiation geometry.

	d_m (mm)	d_p (mm)	M	Ψ_{HT} (mrad)	Ψ_{VT} (mrad)
Set-up					
1	280	0	8.44	0↔39	-25↔25
2	297	18	8.51	0↔37	-23↔23
3	327	48	8.63	3.5↔33	-21↔21
4		1170		-25↔25	-10↔10

Table 1 List showing the position of the object planes for imaging modes 1-3. For mode 4 where no imaging optics were used the distance from the source to the film plane is indicated. Ψ_{HL} and Ψ_{VL} are the limiting apertures in the horizontal and vertical planes of the imaging system, where $\Psi_H = 0$ represents a ray emitted along the axis.

COUPLING INTO SINGLE TARGET AMPLIFIERS

With the amplifier target aligned parallel to the chamber axis the relayed X-ray laser beam is at an angle Ψ_N/M to the chamber axis where Ψ_N is the angle that the north going injector beam makes with the axis. In our case Ψ_N/M was typically 2 to 4 mrad. Since for a single 14 mm target the peak of its ASE beam is located at ≈ 10 mrads from the axis then it was decided to rotate the amplifier target to bring the injection angle w.r.t it's surface close to this angle. We rotated the amplifier target by 5 mrads which increased the injection angle to 8±1 mrad. Operating at an injection angle of 8±1 mrad slightly increased the energy of the amplified beam but did not appear to significantly alter its angular distribution compared to the 3±1 mrad injection angle case.

With the imaged injector beam set to come to a focus before the amplifier plasma then during coupling into single target amplifiers we routinely obtained shadowgraphs of the amplifier plasma. Although we would expect the plasma cross section to be much larger than the gain region cross section we can use the measured missing energy which is significantly refracted by the amplifier plasma to estimate what the maximum coupling using the mirror was. Typically 2↔3% of the relayed injector beam was refracted through large angles by the single target amplifier plasma. This figure compares well with the estimated 2.7% from geometrical considerations. By integrating under the missing portion of the relayed injector beam which is refracted by the amplifier plasma and comparing this with the total energy recorded on film due to the amplification of the injected beam in a single 14 mm target then typically the observed energy ratio was between x20-70. Assuming that the output energy is given by the input energy times the exponential of the gain length product of the lines of interest in the plasma then this corresponds to a gain coefficient of 2.5±0.5 cm^{-1} which is consistent with our earlier measurements of gain at these intensities.

The drive beams for the injector and amplifier targets were set such that photons leaving the injector plasma at the peak of its driving pulse arrived at the amplifier target at the peak of its driving pulse. This corresponded to the drive beams arriving at the amplifier target 4.85 ns after the injector target was hit. Two shots were taken where the drive beams hitting the amplifier target were moved by -ve 300 and +ve 300 ps respectively. With the amplifier drive beam arriving 300 ps earlier than normal no amplified signal could be detected. When the amplifier drive beam was delay by 300 ps the output beam had lower energy than normal, however it also had a reduced divergence. Theses results are consistent with the density gradients across the gain region in the plasma reducing later in time and the gain coefficient peaking near the centre of the drive pulse.

Two 14 mm double-sided illumination exploding foil single target amplifier shots were taken. The shadowgraphs obtained showed expansion of the plasma to approximately twice the size of that obtained for slab targets. The amplified output beam displayed similar divergence but lower energy than that routinely obtained for slab target amplifiers. Optimisation of exploding foil design in terms of obtaining high gain and low density gradients will require additional effort.

Evidence for the beneficial effect of compensating for refraction by bending the target substrate has already been demonstrated at

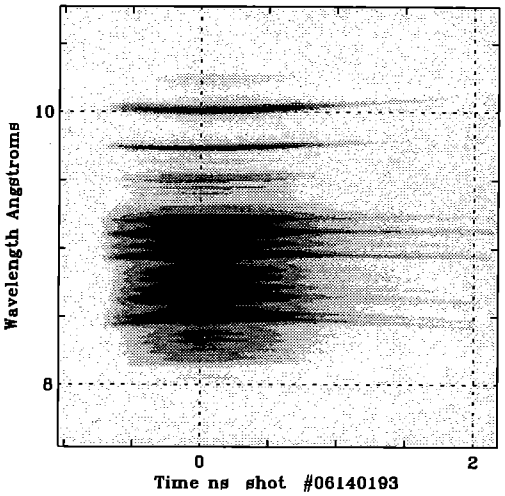

Figure 5 Streaked spectrum showing resonance lines from a Ge slab target. This will aid in our understanding of the ionisation balance kinetics during the drive pulse.

Osaka in a recent collaborative experiment[5]. Following these results we tested the effect on the amplifier target by bending it through a range of angles of ≈ 0.5↔1 mrad per mm of target length. No significant effects on the amplified beam divergence or output energy were observed for the 232/236 Å lines. In future with 196 Å XRM optics we expect a beneficial effect.

COUPLING INTO DOUBLE TARGET SLAB AMPLIFIERS

A series of four shots showing the output beam cross section from a double target amplifier as a function of the target plane separation d is shown in figure 4. Also shown is the output from a single target amplifier which corresponds to the case of two targets placed at infinite separation. The total energy E, maximum intensity I and angular direction of the peak θ for the five shots displayed in figure 4 are shown in Table 2. When an additional 14 mm slab amplifier is added in a double target configuration to a single amplifier then at small d the beam from the first target interacts with the high density and density gradient regions of the second plasma and thus suffers high refraction (figure 4(v)). As d

increases the beam from the first plasma enters the second plasma at greater distances from its surface where the density gradients are smaller and thus refraction is lower (figures 4(iii) and 4(iv)). Eventually, at a sufficiently large target plane separations only the outer edge of the emission from the first amplifier interacts with the second plasma (figure 4(ii)) and in this case it is possible to get the peak of the beam situated further off axis than for a single target case (figure 4(i)). Another interesting feature of the images displayed in figure 4 is the wispy like intensity structures present. We believe that these are associated with inhomogeneities in the gain region and our intentions are to study these features in more detail in a future experiment. Comparing single and double slab target amplifiers the average increase in energy due to the second amplifier is ≈x8 and the maximum intensity on film increases by ≈ x2.5. A comparison of the beam divergences and peak intensities of the output beam (scaled to a plane at 1 m distance from the nearest plasma amplifier) for four typical shots is shown in table 3.

d μm	θ mrad	E a.u.	I a.u.
∞	2	1	1.0
300	12	5	2.5
250	-3	6	2.0
200	-5	12	2.4
150	-15	9	2.0

Table 2 Amplified beam energy, intensity and pointing measurements as a function of the target plane separation d.

shot	Number of amplifier targets	θ_H mrad	θ_V mrad	I a.u.
injector	0	10	25	2.5
07190193	1	11	2.7	1.0
12190193	2	19	14	2.5
24210193	2	17	14	2.0

Table 3 Beam divergence and relative peak intensity for shots displayed in figures 3 and 4. For the injector shot the quoted intensity is for the pump beam before reflection from the XRM. For the amplifier shots the measured intensity can be expected to increase by an order of magnitude for a good quality (maximum reflectivity) XRM.

One of our primary aims during this experiment was to increase the spatial coherence of the output laser beam. A rough estimate of the benefits of injecting the beam into single and double slab target amplifiers can be obtained from a measurement of the central Fresnel fringe visibility in the geometrical shadow region of the axial reference crosswires. An intensity distribution obtained from one of the 180 μm crosswires which were situated at ≈300 mm from the plasma and at 920 from the film pack is shown in figure 6.

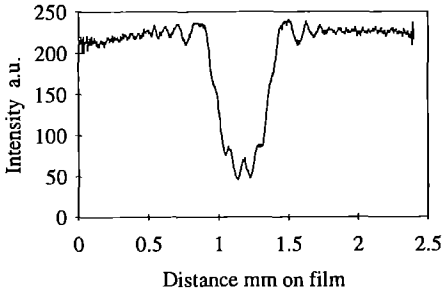

Figure 6 Plot showing soft X-ray fringes observed in the shadow region of a wire.

A number of shots were analysed and the resulting visibilities are shown in figure 7. The large error bars present are associated with the difficulty in accurately measuring the fog level. However, clearly the visibility increases as additional amplifier targets are inserted, which suggests that the spatial coherence is improving. These observations (which are complementary to the Young's slit measurements[4]) are being further analysed. Another interesting observation was that on a few shots the fringe visibility varied considerably depending on the position along the wire sampled. This would suggest that at least in some cases the beam coherence is not constant at different locations across it.

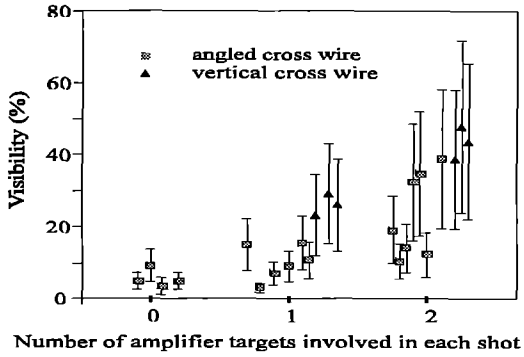

Figure 7 Graph showing the measured fringe visibility under different amplifier conditions.

To reduce the number of modes being injected into the amplifier the relay mirror aperture was reduced from 100 to 4 mm^2 in size. Coherence measurements from this parameter scan are presently being analysed. However, from earlier measurements we estimate that to illuminate the amplifier with a coherent wave front would require an aperture of ≈0.2 mm^2, which is over an order of magnitude smaller again than was tested.

CONCLUSION

We have successfully demonstrated coupling using a relaying concave soft X-ray mirror in a sequentially pumped amplifier geometry. This mirror was situated sufficiently far away from the plasma that multiple use of the same surface elements did not appear to significantly degrade mirror performance. However, a change of appearance of the mirror surface can be observed by eye and the significance of this with regard to X-ray properties is being investigated. Preliminary results indicate that the output beam coherence was significantly higher that the input pumping beam. Near field imaging showing features reminiscent of two lobes from 160 μm wide double targets has been observed. This indicates a horizontal plane of symmetry within the gain zone with refracting beamlets propagating outwards on either side of it. This is in addition to an overall refraction effect sending both beamlets away from the vertical plane containing the target surface. We hope in the near future that by using a higher reflectivity XRM and smaller apertures combined with optimised amplifier designs that it will be possible to achieve a fully coherent saturated output beam.

---

1 G. F. Cairns, D. M. O'Neill, C. L. S. Lewis, D. Neely, A. G. MacPhee, C. Danson, A. Damerell, M. H. Key, D. Rodkiss and R. Wyatt. New X-ray laser atregt geometry, This report

2 C. L. S. Lewis, D. Neely, D. M. O'Neill, J. O. Uhomoibhi, M. H. Key, Y. AlHadithi, G. J. Tallents and S. A. Ramsden. An injector amplifier double target configuration for the Ne-like Ge X-ray laser scheme. Optics. Comm. 91 (1992) p71-76.

3 A 30 mm diameter W-Si multi-layer mirror of 30 periods Ref. No. 2011192 supplied by A. V. Vinagradov

4 R. E. Burge, M. T. Browne, P. Charalambous and G. E. Slark. Development of a coherence Diagnostic for use on the neon like Ge X-ray laser. This report.

5 D. Neely et al. This report.

DEVELOPMENT OF A COHERENCE DIAGNOSTIC FOR USE ON THE NEON LIKE Ge X-RAY LASER

R E Burge, M T Browne, P Charalambous and G E Slark

Physics Research, King's College, Strand, London WC2R 2LS

INTRODUCTION

There have been many theoretical studies of the expected output beam characteristics of X-ray lasers, particularly with a view to calculating intensity profiles and coherence (see Sec 5 to 6 in (1)). Experimentally, the spatial coherence of an X-ray laser, or indeed any source, can be found by a Young's slit type experiment. The fringe visibility is directly related to the transverse spatial coherence function at the slit position. If the laser is characterised by an effective source size then the relationship between the spatial coherence function and the source intensity profile is given by the van Cittert-Zernike theorem (2).

The first attempt to measure the coherence of the RAL X-ray laser made use of a know diffracting structure which had previously been used on the NOVA laser at Lawrence Livermore Laboratory, USA. This method employs an Al filter and multilayer mirror to select the lasing wavelengths and requires that the fringe pattern be deconvoluted to yield the coherence function (3).

A novel coherence diagnostic which has recently been developed by the King's College X-ray microscopy group obviates the need for filters and mirrors and allows the coherence function to be determined by straightforward visibility measurements on Young's slits type interference fringes. Furthermore, this diagnostic allows the coherence of each of the lasing lines to be determined independently. It consists of a group of Young's slit pairs with different separations in which each slit is itself a narrow diffraction grating.

The spectral dispersion occurs at right angles to the interference fringes, Figure 1. Preliminary results were obtained at the RAL X-ray laser in January 1993 as part of an experiment develop a new target chamber and beam amplifier system. The slits separations range from 75 to 400 microns, enough to span a large part of the visibility envelope at the slit position. The grating pitch was chosen to be 3.3 microns with an equal mark-space ratio and each grating consisted of 30 slits which was sufficient to resolve the two lasing lines at 23.2 and 23.6 nm in third order. It was found that the ratings were efficient enough to allow visibility information to be obtained under a wide range of shot conditions, in fact visible fringes were obtained for one shot to the 9th diffraction order. A great advantage of this diagnostic is its tolerance to variations in beam intensity; for weaker shots the visibility information can be obtained from the 1st order diffraction pattern, for more intense shots, where first order saturation may occur, higher orders can be used.

DIAGNOSTIC FABRICATION

During the course of the experiment two basic types of diagnostic were used. The basic fabrication process started with a typically 50 nm thick silicon nitride membrane. On to this was evaporated a 100 nm layer of gold which was

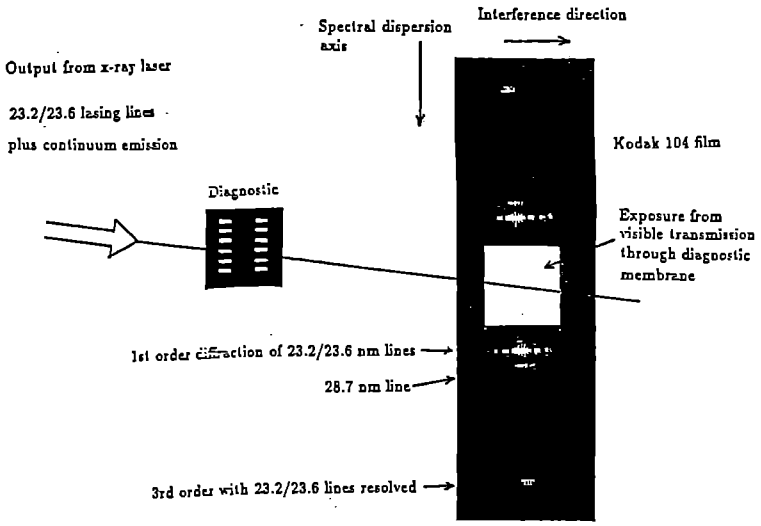

Figure 1 Diffractive Young's slits coherence diagnostic

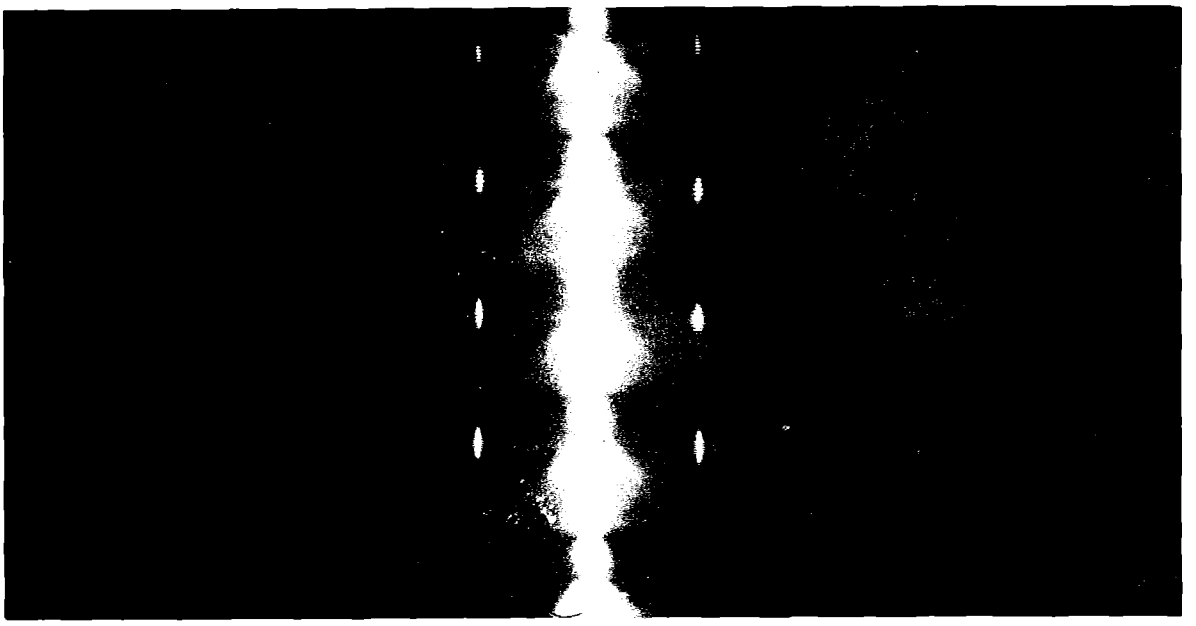

then coated with the photoresist PMMA. An electron beam then exposed the required slit pattern. After development the remaining undeveloped PMMA resist acted as a mask during an argon milling process which transferred the slit pattern in to the gold. The resultant structure consists of a

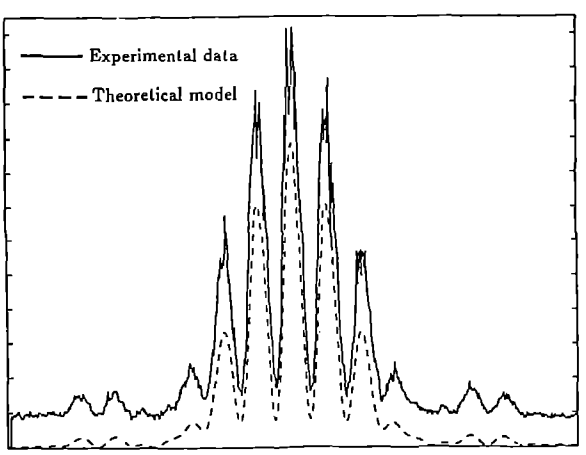

Figure 3 Diffraction intensity distribution

gold grating on a silicon nitride substrate. Another type of grating was obtained by leaving out the gold and simply writing the required slit pattern in the PMMA. Model calculations suggested that a 170 nm thickness of PMMA should produce a phase lag in the incident X-ray beam sufficient to lead to an efficiency greater than that of a purely amplitude grating of the gold type. The actual relative efficiencies of these different types of grating us currently under investigation.

EXPERIMENT

During the course of the experiment slit separations ranging from 75 to 400 microns were used. Figure 2 shows an enlargement of an image obtained with a range of slit separations, fringes can be seen to the 5th order and the 23.2 and 23.6 lines are clearly resolved in the 3rd order. Analysis of the data is currently being carried out on the basis of a scalar Fresnel-Kirchoff diffraction formalism which does not assume far field conditions. The purpose of this analysis is to establish the transverse spatial coherence at the slit position and to relate this to be source parameters. Figure 3 shows the comparison of the experimentally obtained fringe pattern for the 1st order diffraction pattern produced by the 75 micron slit separation with the result theoretically predicted by diffraction theory. The source-to-slits and slits-to-film distances were 0.5 m. For this calculation a Gaussian source intensity profile was assumed and the best fit was obtained with a Gaussian FWHM of 30 microns.

REFERENCES

1. X-ray Lasers 1992, IOP Conference Series 125, (1992).

2. J W Goodman, Statistical Optics, Wiley, (1985).

3. J E Trebes, X-ray Lasers IOP Conference Series 125, p 265, (1992).

SCALING OF NE-LIKE COLLISONAL EXCITATION X-UV LASING TO 15.5 NM

J. Krishnan,[1] G. Cairns,[2] L. Dwivedi,[1] M. H. Key,[3,4] C. L. S. Lewis,[2] A. MacPhee,[2] D. Neely,[2] P. A. Norreys,[3] G. J. Pert,[5] A. Ramsden,[5] C. G. Smith,[4] G. J.Tallents[1] and J. Zhang[4]

[1]Department of Physics, University of Essex, Colchester CO4 3SQ, UK.
[2]Department of Pure and Applied Physics, Queens University of Belfast, Belfast BT7 1NN, UK.
[3]Central Laser Facility, SERC Rutherford Appleton Laboratory, Didcot OX11 0QX, UK.
[4]Clarendon Laboratory, University of Oxford, Oxford OX1 3PU, UK.
[5]Department of Computational Physics, University of York, York Y01 5DD, UK.

INTRODUCTION

Since the first demonstration of a collisionally excited X-ray laser in 1984 much progress has been made. Important objectives in the development of X-ray lasers now are to maximise their brightness and coherence, to produce shorter wavelength lasers and to narrow the band width of laser output in order to produce sources suitable for applications in fields such as biological microscopy and holography.

We report here lasing at 15.5 nm observed from plasmas produced by irradiating 100μm wide Yttrium stripes at 6 x 10^{13} W/cm^2 with 1.06 μm, 650 ps pulses from the VULCAN laser. Time-integrated gain and other measurements are presented for the 3p-3s transition in Ne-like Yttrium. Exponential growth was observed with a gain coefficient of 3±1 per cm. To compare the efficiency of the massive slab targets, a limited number of thin exploding foil targets have also been studied. The shorter wavelength J = 2-1 transition at 15.5 nm is about 70 times brighter than the lasing line at 15.7 nm. Single wavelength lasing appears to be a unique property of Ne-like Yttrium amoung the Ne-like X-ray lasers. The monochromatic output from Yttrium is well-suited for applications requiring high temporal coherence.

EXPERIMENTAL SETUP

Targets were irradiated by the six beam Nd-glass VULCAN laser at the Rutherford Appleton Laboratory. The laser delivered ~ 1KJ energy in 650 picoseconds. A double target geometry was employed with two separate targets irradiated from opposite directions in such a way that ASE from one plasma can couple into the second plasma and amplify further[1]. This configuration helps to reduce the refraction effects, which in a single plasma column limit the useful amplifier length and enables more beams of the VULCAN laser to be used for X-ray laser pumping. The 'injection plasma' length was 9mm long and the target nearer to the spectrometer was varied from 3 to 9mm. The double targets were pre-aligned relative to each other in a single mount using an alignment jig. This allowed the two target surface planes to be accurately set parallel to each other, with the stripes in the same horizontal plane, at a fixed separation along the plasma length of 0.58mm and a variable lateral displacement. The Y stripe targets were massive (1 μm thick) and were 100 μm wide. The stripes were deposited onto 1500 μm thick glass substrates overcoated by a very thin layer of CH. Some data were obtained for exploding foil targets consisting of a 0.1 micron thick Y stripe supported on 0.1 micron thick formvar.

A standard flat-field grazing incidence spectrometer with a double flat mirror grazing incidence reflection filter[2] and a 0.25 μm thick Si transmission filter was employed to record the X-ray laser output. The concave (5 meter radius of curvature) aperiodic grating had an average ruling of 1200 lines/mm.[3] The spectrometer viewed the Y stripes axially and was operated in time-integrated mode. A 75 μm wide slit was placed parallel to the target normal. The spectra were recorded on Kodak 104-02 film, which was absolutely calibrated[4] to enable conversion of optical density to photons/μm^2.

Uniformity of the plasma was monitored using a 2-D spatial imaging camera consisting of two orthogonally crossed, spacially displaced slits to give differential magnification along and across the line focus with 25 micron resolution. In addition, a double KAP crystal spectrometer[5] was used to record the Ne-like and F-like resonance lines.

RESULTS AND DISCUSSION

A spectrum obtained with the axial spectrometer is shown in fig. 1. The silicon filter gives an absorption edge at 12.3nm which provides a wavelength marker for determining the wavelength scale. The data were digitised using a MK6 Joyce Loeble microdensitometer.

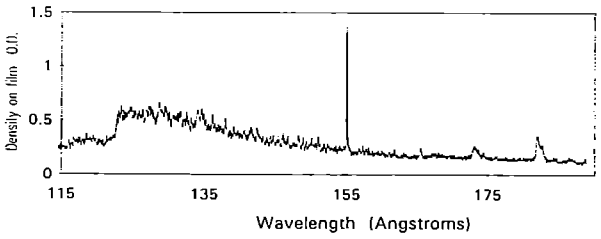

Fig. 1 - A spectrum obtained with the axial flat-field spectrometer.

Peak intensities (I) were measured for different lengths (l) and were fitted to the following formula[6]

$$I = \frac{\varepsilon}{g}\frac{(\exp gl - 1)^{3/2}}{(gl\exp gl)^{1/2}}$$

which describes the output of a Doppler-broadened, homogeneous source of ASE of gain-length product, gl and emissivity per unit length ε. These results obtained under the optimal coupling conditions are shown in fig. 2. We observed exponential growth of the J = 2-1 transiton at 15.5nm with a gain coefficient of 3 ± 1 cm^{-1}. Maximum coupling is observed when the lateral displacement of the target is at 150 ± 25 microns (fig. 3). The angular intensity distribution of the Y laser output (fig. 4) is similar to that found[7] for Germanium.

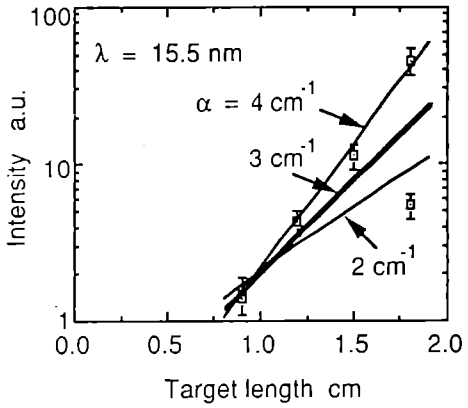

Fig. 2. - Gain fits for Y 15.5 nm line.

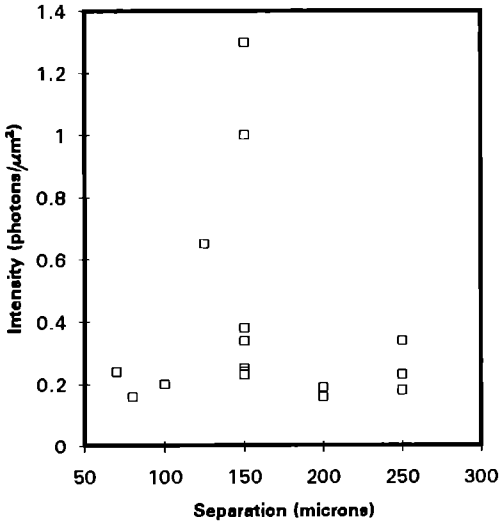

Fig. 3 - Intensity versus double target lateral displacement for Y at 15.5nm.

During the experiments, we had technical difficulties in reproducing Y coatings of constant quality. Coatings irradiated ranged in appearance from black to clear with shiny, brown 'metallic-looking' targets giving better apparent gains. We analysed the targets with a Scanning Electron Microscope(SEM) and it was found that the Y coatings were flaking. Therefore we were irradiating the Si substrate in places rather than the Yttrium. Fig. 5 shows the difference between a Yttrium target and a Ge target under the same magnification using a SEM. In contrast to the Y target, the Ge target appears very smooth.

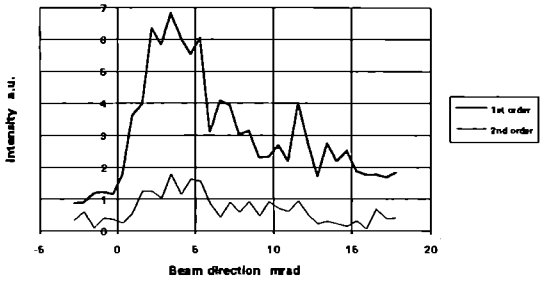

Fig. 4 - Angular intensity distribution of Y line intensity from a 9+9 mm foil target with a lateral separation of 150 μm.

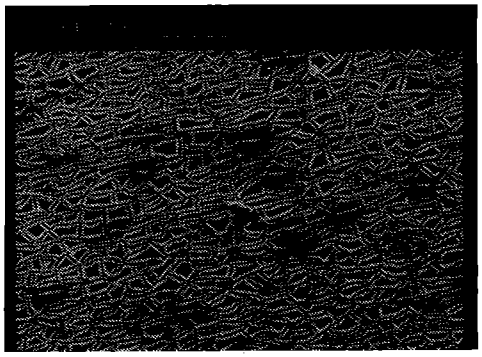

Y target

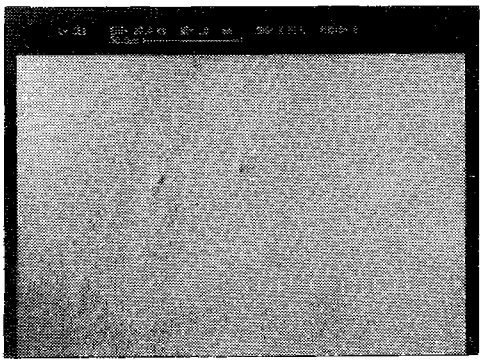

Ge target

Fig. 5 - Pictures taken for Y and Ge targets using the Scanning Electron Microcope (SEM) at the same magnification.

The collisional X-ray lasers which have demonstrated so far have utilised either exploding foil or solid target amplifiers.[8,9] The foil targets should refract less radiation out of the gain region as they expand during the initial heating phase to produce a relatively uniform temperature and density plasma.[10,11] However, the foil targets and the slab targets gave the same intensity as a function of separation (fig. 3) variation. The slab targets also seem to give slightly higher gain.

For one shot, the incident laser mode beated producing two pulses (of duration ~ 340±30 ps with a separation of 275 ps) and the 15.5 nm line nearly saturated the film through a 0.8 μ m thick Al filter (fig. 1). This result suggests that double pulsing the pump laser energy increases the X-ray laser output, but further investigation of this single observation is, of course, needed.

REFERENCES

1. C. L. S. Lewis, D. Neely, D. M. O'Neill, J. O. Uhomoibhi, M. H. Key, Y. Al-Hadithi, G. J. Tallents and S. A. Ramsden, Optics Comm., 91 p71 1991.
2. D. Neely, Ph.D thesis, Queens University of Belfast (1992), sec. 5.3.
3. Toshiaki Kita, Tatsuo Harada, N. Nakana and H. Kuroda. Appl. Optics., 22 p512 1983.
4. J. Krishnan, G. J. Tallents, L. Dwivedi, D. Neely, C. L. S. Lewis and C. Danson, to be submitted to Journal of X-ray Science and Technology.
5. Y. Al-Hadithi, D. Neely and G. J. Tallents, Proceedings of the 2nd International Colloquium on X-ray Lasers (York 1990) edited by G. J. Tallents (Bristol: IOP Publishing Ltd.) p169.
6. G. J. Linford, E. R. Peressini, W. R. Soy and M. L. Speath, Appl. Optics, 13 p379 1974.
7. R. Kodama et al. Optics Comm., 90 p95 1992.
8. G. M. Shimkaveg, M. R. Carter, R. S. Walling, J. M. Ticehurst, R. A. London and R. E. Stewart. Proceedings of 3rd Internationall Colloquium on X-ray Lasers (Schliersee 1992) edited by E. E. Fill (Bristol:IOP Publishing Ltd.) p61.
9. D. M. O'Neill, C. L. S. Lewis, D. Neely, J. Uhomoibhi, M. H. Key, A. MacPhee, G. J. Tallents, S. A. Ramsden, A. Rogoyski, E. A. McLean and G. J. Pert, Optics Comm.,75 p406 1990.
10. M. D. Rosen et al. Phys. Rev. Letts., 54 p106 1985.
11. R. A. London. Phys. Fluids, 31 p184 1988.

MINIMUM EFFECTIVE LINE FOCUS WIDTH DUE TO LATERAL TRANSPORT OF ENERGY FOR THE GERMANIUM XXIII XUV LASER.

Craig Smith,[1] M H Key[1,2], G Cairns [3], L Dwivedi [4] , J Krishnan[4], C Lewis[3], A Macphee[3], D Neely[3], P Norreys[2], G Tallents [4]
1 Clarendon Laboratory, Oxford University
2 Rutherford-Appleton Laboratory
3 Dept of Pure and Applied Physics, Queen's University Belfast
4 University of Essex

INTRODUCTION

The energy required to drive the GeXXIII laser is proportional to the width of line focus and to the intensity in the line focus. More efficient laser operation is obtained with narrower line focus provided that the intensity required to excite the GeXXIII ions remains constant. There is a minimum line width below which lateral transport of energy from the line focus reduces the heating requiring a higher intensity for a given level of excitation of the laser ions. In this paper experimental data giving evidence of the minimum useful line width are discussed.

DATA

During an experiment in June-July '92 a KAP crystal spectrometer was used to record the GeXXIII (Ne-like) and GeXXIV (F-like) X-ray resonance spectra, on Industrex CX film. The targets were single 18mm stripes of Germanium of width 50μm and 100μm, and the laser line focus widths were matched to the stripe widths. The laser irradiation was at λ=1.05μm in 0.6 ns at intensities upto $3x10^{13}Wcm^{-2}$. The spectra were microdensitometered to obtain he intensities of the 3-2 lines for Ne-like ions (at 9.76Å) and for F-like ions (at 9.48Å), shown as figure 1.[1]

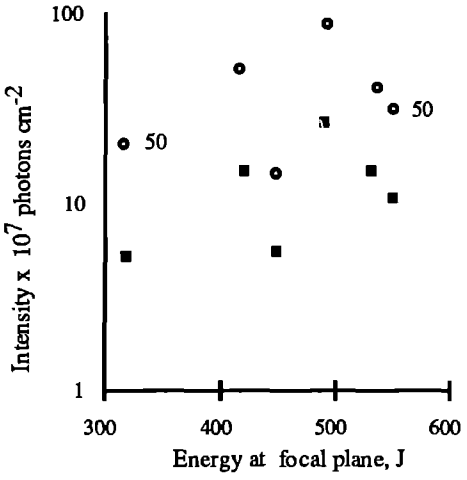

Figure 1. A graph of the relative emissions for the Ne-like (squares) and F-like lines (circles) against energy at the focal plane. Targets were 18mm long and 100 μm wide, except were labelled 50 μm wide, and were illuminated by three superimposed 22mm line foci.

Some scattered low values of data observed in figure 1 can probably be attributed to poor alignment of the line focus onto the Ge stripe giving only partial irradiation of the full area of the stripe.

The ratio of the two intensities was then determined, as plotted in figure 2, which shows a monotonically decreasing ratio.

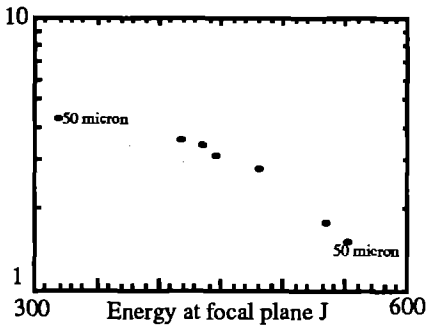

Figure 2. The ratio of Ne-like line intensities to F-like .

A monotonic reduction of the ratio of Ne-like intensity to F-like is expected as the intensity and energy density on the target increases and the fraction of F like ions increases. A difference in ratio for 100μm and 50 μm targets would be expected in the absence of lateral transport of energy.

Yet the results show a different behaviour. Since all the data in Figure 2 lie on the same line there are no apparent differences in effective intensity on target for a given total energy of the driver laser whether the line width is 100μm or 50μm.

CALCULATED BEHAVIOUR

For very low electron densities a coronal model is applicable. This suggests that the fraction n^{z+1}/n^z is S/α where S is the temperature dependant collisional ionisation coefficient and α the radiative recombination coefficient. Suitable expressions for S and α are[2]

$$S = \frac{1.1x10^{-5}}{\chi_i^{3/2}}\left(\frac{kT_e}{\chi_i}\right)^{1/2}\frac{1}{\left(6+kT_e/\chi_i\right)}\exp\left(\frac{-\chi_i}{kT_e}\right) \qquad (1)$$

$$\alpha = 5.2\times10^{-14}\left(\frac{\chi_i}{kT_e}\right)^{1/2} Z\left(0.43+1/2\ln\left(\frac{\chi_i}{kT_e}\right)\right)$$
$$+0.47Z/\left(\frac{\chi_i}{kT_e}\right)^2 \times 5.2\times10^{-14}\left(\frac{\chi_i}{kT_e}\right)^{1/2} \qquad (2)$$

A theoretical model for self-regulating bremsstrahlung absorption in an ablation wave gives [3]

$$T_e = 2.3\times10^{23}\left(\frac{I}{10^{13}Wcm^{-3}}\right)^{4/7}\left(Z\frac{r}{100\mu m}\right)^{-1/7} / kN_e \qquad (3)$$

For the present arrangement with I varying from $3.8x10^{13}Wcm^{-2}$ to $4.5\ x10^{13}Wcm^{-2}$ the range of predicted temperature is from 463 eV to 538eV. The values of S/α are predicted to change over this range by a factor of 1.1, whilst the data in figure 2 show a change in ratio 1.2 which is reasonably consistent..

LATERAL TRANSPORT OF ENERGY

We attribute this to lateral transport of the incident energy. Consider the development of the of the plasma in time. Looking at a transient treatment [3] at a time t the absorption front in plasma is at a distance z_a from ablation front of

$$z_a = 3.6\times10^{6} I_{13}\lambda_\mu^{3/4} t \qquad (4)$$

This treatment would suggest a distance of 6μm at 0.25ns in the 100 μm line focus width case.

A steady state treatment[3] becomes applicable at sufficiently great times. The value of r_c/r is

$$r/r_c = 1.3\lambda^{0.38} I_a^{0.17} (Zr_c)^{-0.05} \qquad (5)$$

Thus the final value of r_c-r for a 100 μm spot is 12 μm and for 50 μm is 6 μm, and so at a time 0.25 ns steady-state has not been achieved. This is illustrated below for the 100 μm case.

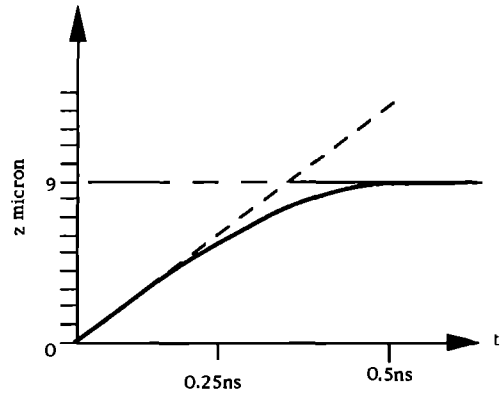

Figure 3. A diagram of absorption front displacement from the ablation front with time.

We estimate the range of line widths over which lateral transport is important as follows, with reference to figure 4.

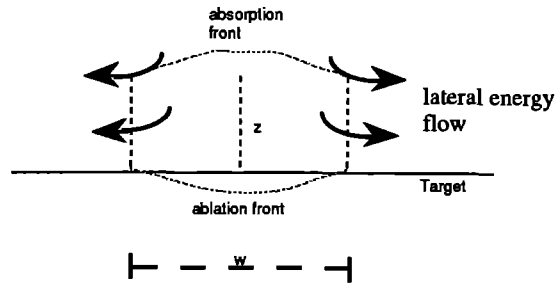

Figure 4. A schematic of the deposition of energy into the target.

The area ratio for lateral transport against forward transport is 2z/w. Lateral transport has been shown to be negligible[3] if this ratio is much less than about 20%. In this case the calculated value is 18% and thus at a level where lateral transport is clearly significant.

We conclude that the effective width on target is independent of the focal line width for widths less than 100μm for the conditions of Ge XXIII laser operation.

CONCLUSION

Experimental evidence shows that reduction of focal line width below 100μm does not increase the efficiency of producing irradiance for a slab target GeXXIII XUV laser driven at 1.05μm. The experimental result is basically consistent with lateral transport broadening of the energy deposition on the target.

---

[1]Measurements of the response of Kodak "Industrex" CX Film made at the Excalibur Facility- AWE Aldermaston- May 88.

[2]McWhirter-Plasma Diagnostic Techniques-Ed. Huddlestone, 1965

3 M H Key, Energy transport in laser produced plasmas, Handbook of Plasma Physics, Eds Rosenbluth and Sagdeev.

FURTHER COLLABORATIVE STUDIES OF THE NE-LIKE GE SOFT X-RAY LASER CARRIED OUT AT THE INSTITUTE OF LASER ENGINEERING

H. Daido[1], T. Honda[2], H. Iwasaki[4], Y. Kato[1], R. Kodama[1], I. Kodama[2], C. L. S. Lewis[3], A. G. MacPhee[3], K. Murai[1], S. Nakai[1], D. Neely[3], M. S. Schulz[1], K. Shinohara[6], G. Slark[7], M. Takagi[1], H. Tsunemi[5], T. Yoshinobu[4] and G. Yuan[1].

[1]Institute of Laser Engineering, Osaka University, Suita, Osaka, 565 Japan.
[2]Tokyo Institute of Technology, Japan.
[3]Dept. of Pure & Applied Physics, Queens University of Belfast, N. Ireland, BT7 1NN
[4]The Institute of Scientific and Industrial Research, Osaka University, Ibaraki, Osaka, 567 Japan.
[5]Dept. of Physics, Faculty of Science, Osaka University, Tayonaka, Osaka, 560 Japan
[6]The Tokyo Metropolitan Institute of Medical science, Japan.
[7]Wheatstone Physics Laboratory, King's College, London WC2R 2LS.

INTRODUCTION

During October and November 1992 we participated in a highly productive collaborative experiment using the GEKKO X11 glass laser facility at the Institute of Laser Engineering, Japan. The primary aims of the experiment were to study and optimise double pass coupling using normal incidence soft X-ray mirrors, optimise the target geometry to enhance lasing output, attempt to produce a dominant single line output from a Ne-like Ge plasma on the J=0-1 19.6 nm line, characterise in detail the output lasing beam properties and use the soft X-ray laser beam to produce holograms. Some observations based on a preliminary survey of the results is presented below.

EXPERIMENTAL

Two 1.053μm opposing beams from the GEKKO X11 glass laser were used to irradiate Ge stripe targets deposited onto glass substrates. Each beam was able to deliver 1-1kJ of energy in a 1ns Gaussian shaped pulse onto the target plane. The focusing optics were set to generate a 60 mm long line focus length, with only the central high intensity 45 mm portion of the line focus being routinely used to avoid the formation of cold plasma at the ends. Plasma uniformity was monitored using a crossed slit camera, a 1D space resolving soft X-ray (30-300Å) spectrometer and a 1D space resolving crystal spectrometer (7-10·1Å) with an inverted mode CCD detector[1]. A typical set of data from two of these instruments is shown in figure 1. Two spectrometers were used to examine the soft X-ray lasing emission from either end of the plasma. A high resolution Hettrick XUV 5·5m spectrometer was used to examine spectral lasing widths and positions. This instrument was operated throughout the early part of the experiment and then replaced by an applications beam line set-up for holography and coherence measurements. A flat-field spectrometer was used on the other side of the chamber either in a spectral /angular resolving mode (with a q-plate as the recording media), or in a temporal /angular mode with a streak camera set to examine an individual lasing line's emission during each shot.

RESULTS

During the early phase of the experiment the gain coefficients of the main Ne-like Ge lasing lines from a flat slab target were measured and found to be similar to previous results[2]; ≈ 3±1 cm^{-1} for the dominant J=2-1 lines. The shorter wavelength J=0-1 19.6 nm line was observed as before to be weaker than the J=2-1 lines. Double passing the lasing emission using either mirrors suited for the dominant J=2-1 lines or the weaker J=0-1 19.6 nm line was demonstrated. The coupling efficiencies for three mirror curvatures (r=80 mm convex, planar, r=80 mm concave) was measured. Apparent signs of mirror damage during the drive pulse were recorded when the mirror was moved to within 3 cm of the end of the plasma. The effect of compensating for refraction away from the target surface by bending the target substrate was studied and strong enhancement of the J=0-1 19.6 nm line observed. Examination of the soft X-ray holograms taken showed that higher fringe visibility was observed using the 19.6 nm line illumination compared to 23.2 / 23.6 nm illumination.

CONCLUSION

The major objectives of the experiment, namely obtaining a 'monochromatic' beam, recording holograms, mirror coupling/damage testing, laser spectroscopy and beam refraction/compensation studies were all achieved during the run. Data from the experiment is presently being analysis by the various groups involved and a more comprehensive and detailed review of all the results will be presented in next year's report.

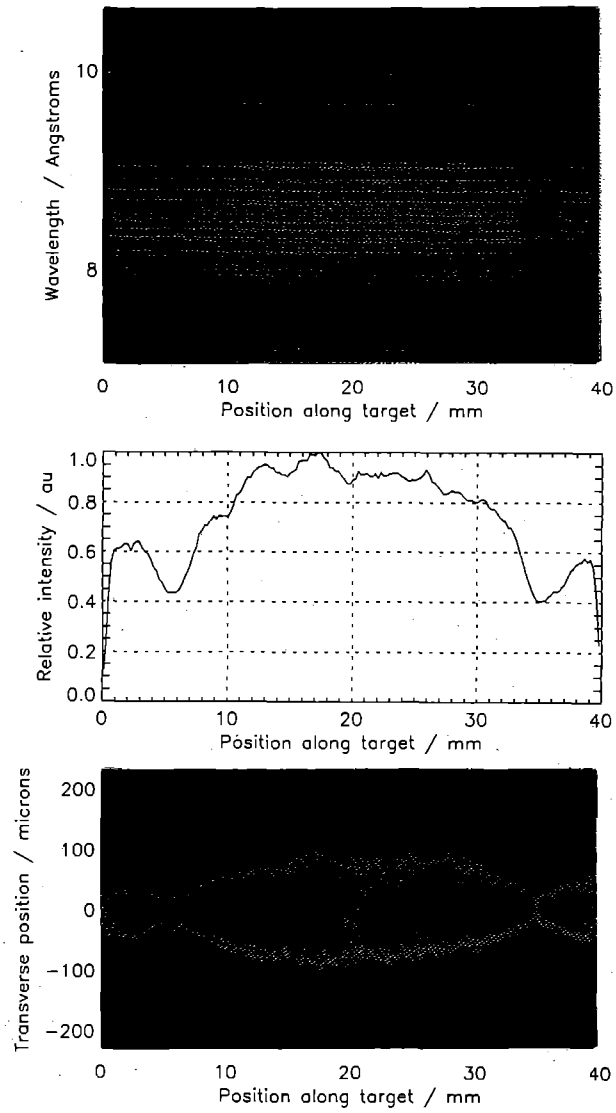

Figures 1(i)-(iii) (i) space resolved crystal spectrometer image, (ii) graph showing the relative Ne-like 3s-2p emission intensity as a function of position on target and (iii) Image from a 2D space resolving crossed slit camera.

REFERENCES

[1] A.G. MacPhee and C.L.S. Lewis. SERC annual report to The Central Laser Facility (1993)
[2] Y. Kato et al, Inst. Phys. Conf. Ser. No 125 (1992) p9-16

ABSORPTION OF HIGH CONTRAST 12PS UV LASER PULSES BY SOLID TARGETS

D. Riley, L.A. Gizzi, A.J. Mackinnon, S.M. Viana and O. Willi

The Blackett Laboratory
Imperial College of Science, Technology and Medicine
Prince Consort Road, London SW7 2BZ

The primary controlling factor in laser plasma experiments is the level and mechanisms of laser light absorption. We have carried out absorption measurements in a different regime to those used previously, by using the SPRITE laser at Rutherford Appleton Laboratory, which produces pre-pulse free Raman amplified KrF pulses of 12ps duration at 268nm wavelength [1]. The laser has low divergence (2x diffraction limit) and produces up to 6J of energy (about 3.5J on target). Although 12ps is long enough for significant hydrodynamic motion to occur, the high incident irradiances possible (in excess of 10^{17} Wcm^{-2}) and short wavelength allows hot plasma to be produced at high density.

The laser was directed on to solid aluminium targets with an off-axis paraboloid with approximately f/4.7 focussing. The targets were mounted on a translatable rotating stage. The axis of rotation was changed to alternate from P to S polarisation. The position of the target was controlled to 10 microns by a high magnification T.V. alignment system. Because the focal depth was approximately 25 microns the variation in spot size was kept small. Overall shot to shot variation including energy fluctuation was about 15%. An angled plate was used to direct a portion of the directly backscattered light onto a fluorescent sample which converted the UV light to optical radiation which was detected by a calibrated photodiode. This system was carefully checked to have a linear response for light levels used in the experiment. The light not directly backscattered was collected by an Ulbricht sphere around the target. A diagnostic hole was used to monitor the X-ray focal spot via a pinhole camera fitted with a 5 μm diameter pinhole which was filtered with 25 μm Beryllium. The area open for target insertion, alignment and diagnostics was about 3.6% of the total surface area of the sphere. The energy incident on the surface was measured by a surface absorbing calorimeter. The calorimeter was calibrated and tested to be linear in the region used experimentally. By firing laser shots into the sphere with no target present the sphere/calorimeter system was calibrated and tested to be linear up to about $1Jcm^{-2}$ incident on the sphere surface. During the experiment the energy density incident on the sphere was kept below this level, this was helped by the fact that the specularly reflected light was found to be dispersed into an approximately f/1.5 cone due to refraction effects in the focal region, with a maximum of about 15% of incident energy being backscattered in the focussing cone at normal incidence. The targets were polished aluminium, although not of optical quality.

The absorption as a function of angle is shown in figure 1 for both S and P polarised light. The average irradiance used was $5x10^{16}$ Wcm^{-2}, corresponding to a spot size of around 20 microns.

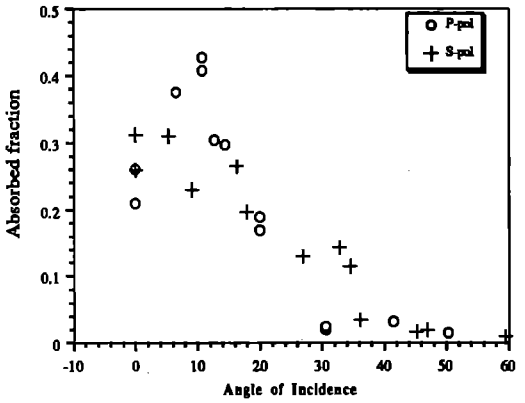

Figure 1. The absorbed fraction for S(crosses) and P(circles) as a function of incident angle at $I=5x10^{16}Wcm^{-2}$

For the P-polarised light we see that there is a peak absorption at around $10^{o}\pm 1^{o}$. Using the standard resonance absorption model [2], this corresponds to the condition $(K_oL)^{1/3}\sin(\theta_{max}) \approx 0.8$, giving a scalelength between 3.1 and 5.7μm (4.2μm for 10^{o}). The S-polarised data shows no such peak, supporting the hypothesis of resonance absorption, being important in the P-polarised case. The small angle for peak absorption tells us that the focussing of the laser beam is likely to be an important consideration as the half angle for the f/4.7 cone is about 6^{o}. This implies that resonance absorption may be important even for nominally S-polarised light. For the moderate values of $I\lambda^2$ in our experiment we might also expect collisional absorption to play a role in both cases. In order to try and get an idea of their relative importance we have carried out modelling for the normal incidence case with the 1-D hydrocode MEDUSA [3]. The code includes collisional absorption with a correction for the reduced absorption due to high electric field. This turns out in our case not to be very important because absorption is efficient enough to provide a high electron thermal velocity at critical density, keeping Vosc/Vth less than 1. The treatment does not include ray tracing or interference effects, but a simple 1-D transmission of the beam through each cell up to critical and out again.

Resonance absorption is included in a simple way by calculating the density scalelength at critical density and using the standard Denisov function for the absorbed fraction of energy reaching critical density. The effective angle assumed

was either a simple average of 3^{o} or a weighted average over the fairly flat topped near field of 3.8^{o}.

The modelling was compared to experimental data taken in a separate run where the irradiance was varied for normal incidence. Figure 2 shows the results compared to modelling. We can see that the code reproduces the experimental data reasonably well at lower irradiances. The principal absorption mechanism below 10^{16} Wcm^{-2} was collisional absorption in the modelling with some contribution from resonance absorption amounting always to less than 10% of the incident light.

However, for $5x10^{16}$ Wcm^{-2}, the agreement is not so good, although for absorptions of about 40% the scalelength is very similar to the experimentally inferred value (4.3 μm for 37% absorption in the simulation). This may be accounted for to some extent by the wide variation in data for normal incidence at high irradiance, with absorptions between about 10% and 25%. We estimated our scattered light measurement to be accurate to better that 10%, but of course for low

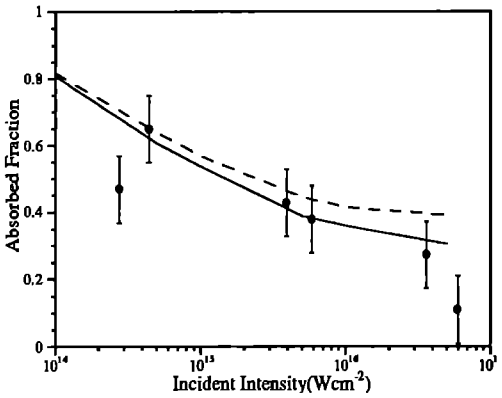

Figure 2. Experimental data compared to modelling from MEDUSA. The solid curve is a simulation assuming average angle of 3°. Broken line is for 3.8°.

absorption this gives a large error in the absorbed fraction. There are several important other points that must be considered further. Firstly, the focal spot is about 20μm compared to about 4 μm for the scalelength. This suggests that 2-D effects [4] may be important in determining the temperature of the coronal plasma and thus the collisional absorption levels. On the other hand, we also expect in this situation that strong magnetic fields will be generated by the $\nabla N x \nabla T$ mechanism. Assuming the temperature in the corona from the 1-D simulation and the measured density scalelength we estimate from the B- field generation rate as;

$$\frac{\partial B}{\partial t} \approx \frac{k}{e} \nabla T_e \times \nabla \ln N_e$$

For our conditions this gives approximately 0.7MG/ps, resulting in a several MG field at the pulse peak. This may confine the plasma [5] and keep the temperature high. A justification for assuming the 1-D temeprature in the above estimate is simply that the modelling gives a scalelength consistent with the experimentaly inferred value. A much lower temperature, due to lateral expansion, it might be argued would lead to slower expansion and a reduced density scalelength. The B-field can affect the plasma in other ways. The strong field can lead to inhibition of the the thermal transport. For instance if we take the field to be approximately the puse length times the rate above we get 8MG field. This means that the Larmour radius for thermal electrons at 6.5keV is 0.4μm. This compares to a mean free path at the critical density of about 9μm (with lnΛ =7), showing that transport of electrons can be severely restricted. Also, Kruer et al [6] have pointed out that resonance absorption, driven by the vxB force on electrons oscillating in the laser field can be quite effective even for S-polarisation at normal incidence. For our conditions their estimates suggest around 25% of incident energy could be absorbed at normal incidence for S-polarised light by damping of the plasma waves generated. A complete self-consistent modelling of this experiment is therefore not at all trivial and is beyond the scope of this paper.

We can get some idea of the temperature in the corona from using X-ray spectroscopy. Streak camera data from an aluminium target irradiated at around $10^{17}Wcm^{-2}$ with a focal spot of about 10μm was used to infer an electron temperature of over 700ev at a peak electron density for both Heβ and Lyβ lines in excess of 10^{23} cm^{-3}. This is likely to be a lower estimate of temperature because of the rapidity of laser heating. With this information, the temperature of around 6.5keV at critical predicted by the 1-D model does not seem unreasonable. This result suggests that there may not be the degree of lateral expansion in the corona expected

In conclusion, we have measured the absorption of relatively short uv laser pulses. A high level of absorption is found even at high irradiance. This is due to both resonance and collisional absorption. For our experimental conditions resonance absorption is probably quite important even for S polarised light because of the low peak angle combined with the focal cone. Collisional absorption remains an important mechanism due to the high electron density at which energy is directly deposited. The importance of B-field generation on absorption might be manifested in several ways, firstly the field can confine the plasma, thus keeping the temperature high which increases the scalelength but reduces the collisional absorption coefficient. Secondly, the transport is affected by the electrons having a small Larmour radius. Thirdly, the vxB force acting on electrons oscillating in the laser field can lead to enhanced resonance absorption.

1. E.C. Harvey et al laser Facility Ann. rep. 1991 p77
2. G.J. Pert, Plasma Physics **20** p175 (1978)
3. J.P. Christiansen et al Computer Phys Comm **7** p271 (1974)
4. G.J. Tallents et al SPIE Conf. Proc 1413, 1991
5. M.D.J. Burgess et al Phys. Fluids **28**(7) p2286 (1985)
6. W.L Kruer and K. Estabrook Phys. Fluids **20** p1688 (1977)

EXPERIMENTAL OBSERVATION OF THE CREATION AND EXPANSION OF AN OPTICAL-FIELD-INDUCED IONIZATION CHANNEL IN A GAS JET TARGET

M. Dunne, T. Afshar-rad, J. Edwards, A. J. MacKinnon and O. Willi

Blackett Laboratory, Imperial College, London. SW7 2BZ.

This report details the first experimental measurements on the creation and evolution of an optical field ionized channel by a high intensity, short wavelength picosecond laser pulse. For the first time the crucial issue of how the cylindrical plasma channel expands after the heating pulse is addressed. In this experiment, the formation of the plasma channel resulted in a highly anisotropic electron distribution function throughout the laser pulse. An initial 1D transverse electron temperature of approximately 90eV has been inferred from a hydrodynamic model fitted to the channel expansion characteristics, whereas a simultaneous longitudinal temperature of less than 1eV was obtained from spectral details of stimulated Raman backscatter signals.

An understanding of the lateral expansion of these plasma columns is of fundamental interest in the study of non-equilibrium high temperature explosions, but is also invaluable in many topical applications, as detailed by Sprangle and Esarey[1]. In particular, the possibility of producing a cold, highly ionized, low density plasma channel has led to the suggestion of a number of recombination x-ray laser schemes.

The experiments were performed on the SPRITE KrF gas laser using a 3.5ps, 248nm, 1.5J, linearly polarised pulse. The beam was focused by an f/5 off-axis parabaloid mirror to a FWHM spot size of approximately 30μm, achieving intensities on target of around $2x10^{16}$ Wcm^{-2}. The short pulse was superimposed upon a low intensity 20ns pedestal with a focused intensity of less than $5x10^{9}$ Wcm^{-2}. This pedestal was shown to have a negligible effect on the plasma production in the low density gas and has therefore been ignored. A small fraction of the beam was split off in order to provide a temporally independent probe beam, perpendicular to the heating beam, for the Moiré deflectometry system, which supplied snapshot information on the electron density gradients and absolute electron densities for discrete times up to 1ns after the heating pulse. The magnification of the system was 100x with a spatial resolution of 1μm at the target plane. The timing of the probe beam relative to the heating beam was accurate to within 5ps. The target consisted of a pulsed supersonic gas jet which delivered Nitrogen through a simple DeLaval nozzle. This jet formed a cylindrical gas column perpendicular to the axis of laser irradiation with a diameter of about 1mm, yielding a particle density of approximately 10^{17} atoms cm^{-3} at the point of interaction. The light backscattered during the heating pulse was monitored with a time-integrating grating spectrometer with 2.5Å resolution. In addition, a time integrating XUV toroidal grating spectrometer was used to record the K-Shell emission from the heated channel, providing information on the peak ionization stage.

Information on the initial laser created plasma channel was obtained with the Moiré deflectometer and through Stimulated Raman Scattering (SRS). This channel was formed through a tunnel ionization process in which the intense electric field of the laser directly induced nonresonant ionization of the nitrogen gas.

By employing a simple Coulomb-barrier model, the threshold intensity required to reach each of the different ionization stages can be calculated; it was found that intensities of $2.3x10^{15}$, $9x10^{15}$, $1.4x10^{16}$ and $1x10^{19}$ Wcm^{-2} were required for the Be-, Li-, He- and H-like stages respectively. Collisional ionization can be neglected at these low densities. The plasma therefore reaches a He-like peak ionization stage, as confirmed by the toroidal grating XUV spectrometer. Figure 1 shows a Moiré deflectogram taken immediately after the turn-off of the heating pulse, in which the fringe shifts are directly proportional to the local spatial density gradients. Only the central section (approximately 120μm in length) of the laser focus is shown. A strong discontinuity can be observed in the fringe pattern, indicating the radial extent of the ionizing laser profile. Abel inversion of these shifts yields the absolute electron densities at each time frame. Probe measurements taken before the arrival of the main pulse, with only the low intensity laser pedestal incident on target, produced no observable fringe shift.

The light backscattered from the laser - gas jet interaction was used to infer the initial longitudinal electron temperature in the target. The backscattered signal was red-shifted relative to the fundamental and was split into three separate spectral features, with the long wavelength spike shifted by approximately 15Å. These features correspond to SRS from three different ionization stages present in the plasma, with the strong, central spectral feature corresponding to the dominant Li-like stage. Note that Stimulated Brillouin Scattering or Compton Scattering effects cannot explain the shifts observed. For the dominant plasma conditions the growth rate for SRS from a finite pump is calculated to be of the order of 0.15ps, significantly shorter than the 3.5ps heating pulse length. These three discrete tunnel-ionized stages are produced either at different times in the laser-gas interaction, or in different spatial regions of the target as a result of hot spots in the beam or the fall-off of the laser profile.

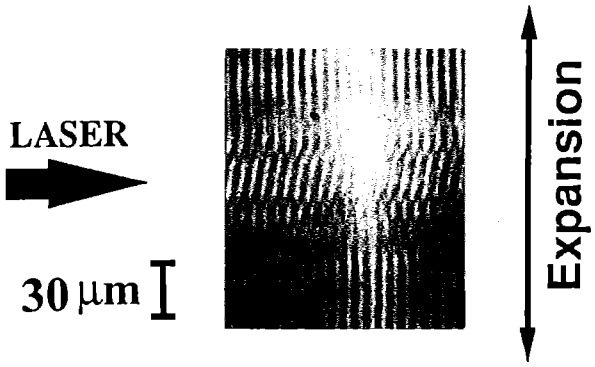

Figure 1 Moiré deflectometer fringe pattern at the end of the heating pulse. The well defined plasma channel seen at this time propagates rapidly outwards, cooling the central plasma.

On less intense shots the longest wavelength spike was not observed, indicating that the laser intensity was not sufficient to ionize the plasma to a He-like state, thus confirming the simple intensity threshold estimate.

The density dependence of Raman backscatter fits the observed spectral shifts remarkably well. This indicates that the longitudinal electron temperature during the heating pulse must be low. By using the peak electron density known from the Moiré data, the longitudinal electron temperature can be determined from the wavelength shift of the He-like feature. The Raman backscatter instability is in the non-relativistic, weakly coupled regime and so the temperature required to produce the observed frequency shift at the measured density can be calculated by using phase matching conditions and the Bohm-Gross dispersion equation. For each of the discrete electron densities corresponding to the three tunnel-ionized stages, the calculated temperature was less than 1eV. The small uncertainties in the calculation of the peak electron density do not alter this temperature constraint.

The temporal evolution of the hot, central channel was also studied with the Moiré deflectometer by delaying the probe beam with respect to the heating beam. The rapid expansion of the laser-created channel is demonstrated in Figure 2. A strong discontinuity was observed throughout the expansion, corresponding to a large electron density gradient at the position of the wavefront. It is this strong front which defines the spatial extent of the ionized channel and which propagates into the gas with an initial velocity of 4×10^6 cm/s.

The behaviour of the expansion was modelled by MEDUSA in cylindrical geometry and with a modified absorption routine which deposited a stated fraction of the incident energy on-axis in a channel of 30μm diameter. Both the spatial and temporal profiles of the laser were taken to be Gaussian. The absorbed energy was used to ionize and heat the ambient gas, with the peak ionization reaching a He-like charge state in line with observations. The fraction of absorbed energy acted as a free parameter and was altered until the radius of the expanded channel at 1ns after the heating pulse matched the observed radius. This is equivalent to varying the initial isotropic temperature of the cylindrical explosion. The evolution of the electron density profile was then predicted through the use of a time-dependent, non-LTE, screened-hydrogenic, average-atom ionization code similar to XSN which post-processed the results from the hydrocode. This was necessary in order to model the transient ionization occurring in the underdense gas, where extremely low collisional ionization rates produced a plasma far removed from the steady-state.

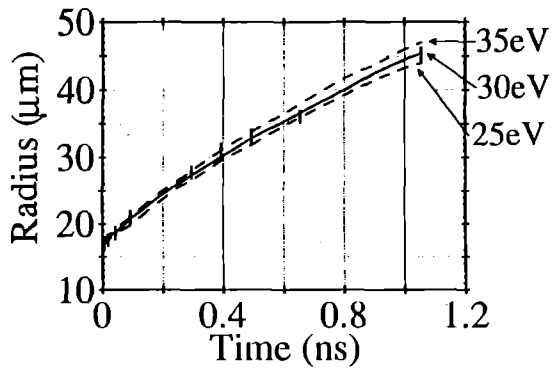

Figure 2 Simulations of the expansion of the channel, with measured data points (vertical bars). Best agreement was 30eV.

The properties of the simulated expansion at all times earlier than the 1ns fixed point were directly compared with the data (see Figure 2). The simulations can be seen to be in very good agreement with the observed radial extent of the channel. The hydrocode modelled expansion characteristics which varied on timescales far longer than the temperature isotropization times for the conditions present in the initial plasma channel, as detailed below. The expansion is thus accurately described by an isotropic temperature driving the cylindrical explosion. The rate of expansion provides an accurate indication of the isotropic temperature in the initial channel, with a change in energy absorption sufficient to produce a 5eV change in initial plasma temperature leading to a noticeably different expansion profile. The best fit to the data was obtained with an initial isotropic temperature of 30±5 eV.

The rapid, expansion-induced cooling of the central channel was determined from the hydrocode simulations, with the temperature predicted to drop from 30eV to 15eV in 200ps.

The isotropic temperature predicted by the hydrocode is in reasonable agreement with estimates of the relative heating contributions from the various absorption mechanisms. Inverse Bremsstrahlung (IB) absorption was found to be the dominant source of heating. The resulting temperature has been estimated from a 1D propagation-ionization model[2]. It was found that ATI heating contributed less than 5eV to the final plasma temperature in these simulations, whereas IB was predicted to heat the gas to up to 35eV once the 50% reduction due to the Langdon effect was taken into account. This level of IB heating was also confirmed by analytical estimates of the absorption, which predicted temperatures of between 25 and 35eV. Consequently, the 30eV temperature required by the hydrocode to match the channel expansion is not unreasonable. Note, however, that due to the low density of the gas target and hence the low electron-ion collision frequency for the quivering electrons (approximately 1.1×10^{10} sec^{-1}), the IB heating will be largely one dimensional, along the axis of the E-field. Any ATI heating will also be along this transverse direction, resulting in a high initial 1D transverse temperature in the experiment. From the predicted isotropic temperature of 30eV, the 1D temperature could be as high as 90eV during the laser pulse. In contrast, the longitudinal temperature should remain low during the laser pulse since the thermal isotropization times for the initial plasma conditions are of the order of 30ps, far longer than the laser pulse. This is confirmed by the low longitudinal temperature obtained from the Raman backscatter spectra.

In summary, the formation and subsequent temporal evolution of an optical-field-induced ionization channel have been observed and the global features of the expansion accurately reproduced by a 1D cylindrical-geometry hydrocode. Gross temperature anisotropy in the initial channel was inferred from the expansion characteristics and details of Raman backscatter spectra. A precursor to the main ionization front was also detected in the expansion profile which may be due to non-local heat flow effects.

1. P. Sprangle and E. Esarey.
Interaction of ultrahigh laser fields with beams and plasmas.
Phys. Fluids B4, 2241 (1992).
2. S. C. Rae and K. Burnett.
Possible production of cold plasmas through optical-field-induced ionization.
Phys. Rev. A46, 2077 (1992).

OBSERVATION OF PLASMA CONFINEMENT IN PICOSECOND LASER-PLASMA INTERACTIONS.

F.N.Beg[1], A.R.Bell[1], Z.Chang[2], A.E.Dangor[1], C.N.Danson[2], C.B.Edwards[2], A.P.Fews[3], M.H.R.Hutchinson[1], S.Luan[1], P.Lee[1], P.A.Norreys[2], R.A.Smith[1], P.F.Taday[2], F.Zhou[1]

1. Imperial College of Science and Technology, Prince Consort Rd., London SW7 2AZ, United Kingdom.
2. SERC Rutherford Appleton Laboratory, Chilton, Didcot, Oxon OX11 0QX, United Kingdom.
3. H.H.Wills Physics Laboratory, University of Bristol, Royal Fort, Tyndall Avenue, Bristol, BS8 1TL, United Kingdom.

Energetic ion emission has been observed under conditions where the laser pulse length is long enough to allow the hydrodynamic flow of the plasma to approach a steady state and where heating occurs at densities close to the critical density, especially at high irradiance[1]. However, few studies have been performed under conditions where the laser pulse is short compared with the hydrodynamic response time of the plasma and where heating occurs close to solid density. The intrinsic interest in the response of the plasma to laser intensities as high as 10^{18} Wcm^{-2} under short (picosecond) pulse conditions led us to conduct an experiment on the Nd-glass laser VULCAN at the Central Laser Facility of the Rutherford Appleton Laboratory.

Laser pulses were generated using the Nd glass laser VULCAN which was equipped a chirped pulse amplification (CPA) system. This consisted of an additive pulse mode-locked oscillator that provided pulses of 2.1 picoseconds of 3 nJ energy and wavelength 1.053 μm. This pulse was then temporally expanded in a grating pair stretcher to 80 psec and amplified in the laser chain. The pulse was then recompressed by a second pair of diffraction gratings (1700 grooves/mm and dimensions 150 x 300 mm). The second diffraction grating of this pair was located inside the target chamber under vacuum. The recompressed beam of diameter 140 x 88 mm was then incident onto a partially reflecting turning mirror which allowed 5% of the recompressed pulse through for measurements of the laser pulse length, pre-pulse, spectral distribution and focal spot aberations. An off-axis parabolic mirror located 44 cm from the target then focused the laser beam onto target. A diagram of the compression chamber and the focusing arrangement is shown in Figure 1. Approximately half of the laser energy was incident onto target in a focal spot of 15 μm by 50 μm (as measured by the equivalent plane monitor).

A full description of the laser system has been given elsewhere[2]. The important parameters of the laser system are: up to 30 J of laser energy was incident on target; the pulse length ranged from 2.1 psec to 7.5 psec; 90% of the laser energy was focused by the off-axis paraboloid mirror through a 100 μm pinhole; the incident irradiance on target varied from 1.0 - 12.0 x 10^{17} Wcm^{-2}; the beam was p-polarised and was incident on the target at an angle of 30° to the target normal. The pre-pulse was measured by both a cross correlator and an auto-correlator to be less than 10^{-6} of the main pulse intensity[2].

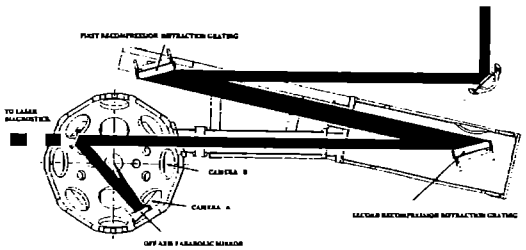

Figure 1. Schematic outline of the target chamber and focusing optics.

A variety of different targets were irradiated. These were plastic (mylar), carbon (graphite) copper and gold. They consisted either of solid slabs of material or small 'lollipop' disks 270 μm in diameter and 10 μm thickness for gold and copper, and 50 μm for mylar. The laser beam was at 30° to the traget normal. This was for two reasons, firstly to eliminate as much as possible back-scattered radiation from the target to protect the laser chain and secondly to ensure that there was some resonance absorption.

Four diagnostics were employed to measure the plasma parameters. The first was a pair of pinhole cameras to image the plasma that was created. Both cameras were situated 37 degrees in the vertical direction from the horizontal plane and at 11 and 35 degrees to the target normal (called cameras A and B for brevity). The positions of theses cameras are shown in figure 1. Both cameras had 10 μm pinholes in 100 μm platinum substrates. The magnifications were x16 and x11 giving spatial resolutions of 11 μm and 12 μm for cameras A and B respectively. They were filtered differently from shot-to-shot depending on the target material that was being irradiated. All images were recorded on Kodak DEF film. The gamma curves for the different x-ray wavelengths were taken from [3].

Two diagnostics were used to monitor the ion velocity from the plasma. CR39 nuclear plastic track detectors [4] of

dimensions 2.5cm^2 were used to monitor particles with energies > 75 keV/nucleon. These detectors also gave quantitative information on the ion species, energy distribution, total number of particles incident on the detector and the angular distribution of the particles around the axis normal to the target. In all shots one piece of CR39 were placed at normal incidence (at a distance of 3.0m from the target), and two pieces were placed in the horizontal plane at 45° and 75° to the target normal on the chamber wall at a distance of 46 cm. A mylar filter array consisting of eight steps of 2 μm of mylar was placed in front of each detector. On some shots, two additional detectors were placed at 20° and 60° to the target normal.

Finally, two NaI scintillators coupled to photo-multiplier detectors were used to detect and measure the hard x-ray emission. The detectors were placed outside the target chamber at a distance of 60 cm from the target behind an entrance port fitted with 15mm of aluminium plate. Some information about the energy distribution was obtained by using a lead filter (which varied from 2 to 4 mm thick) in front of one of the detectors; the other detector was not filtered.

The pinhole cameras show clearly that in nearly all high energy laser shots there is a collimated plume of plasma flowing from the target in the direction normal to the target

E_{laser}=13.5J
τ_{laser}=7.7psec
Mylar target
1 μm Ni filter
Camera A

E_{laser}=15.0J
τ_{laser}=3.5 psec(estimate)
Cu target
5 μm Ta filter
Camera A

E_{laser}= 13.2J
τ_{laser}=2.1 psec
Au target
5 μm Ta filter
Camera A

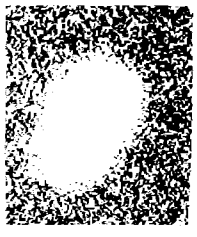

E_{laser}=19.0J
τ_{laser}=2.4psec
Cu target
5 μm Ta filter
Camera A

E_{laser}=15.3J
τ_{laser}=5.0psec(estimate)
Cu target
5 μm Ta filter
Camera B

E_{laser}=15.0J
τ_{laser}=3.5psec(estimate)
Cu target
5 μm Ta filter
Camera B

E_{laser}=15.0J
τ_{laser}=2.5psec
Cu target
5 μm Ta filter
Camera B

Fig 2. X-ray images of laser irradiated targets.

The second diagnostic to monitor the ions was an array of Faraday cups. These cups were of a conventional design with a honeycomb collecting electrode to reduce secondary electron emission and were biased at about 150 V to seperate the neutralising electron from the collecting ions. This sets the upper detectable ion energy at 300 keV/nucleon with decreasing sensitivity above 100 keV/nucleon. The cups were positioned at the chamber wall at a distance of 41 cm from the plasma. The signal were detected on a multichannel Hewlett-Packard digitising oscilloscope with a time resolution of 5 nsec.

surface. This can be seen in figure 2 which shows x-ray images obtained in a number of different shots (except the 15J/3.5 psec on copper images which are the same shot but viewed from different directions). The laser parameters for each shot are listed under each image as is the filtering used.

The pulse length quoted was that obtained from the single shot auto-correlator. In those cases where only an estimate of the pulse length is given in figure 2, the pulse length was taken from shots fired under similar conditions (ie similar energy and B-integral). Two x-ray filters were used 1 μm of nickel for mylar targets 5 μm of tantalum for copper and gold targets. The plasma plumes can clearly been seen in all

the shots. The longest plume length was 240μm for a gold target for a 15 J shot.

Figure 3 shows the energy spectrum for ions >100keV for a CR39 detector placed at zero angle to the target normal when a laser pulse of energy 17.3J and pulse length 3.0psec was incident onto a mylar 'lollipop' target. The spectrum in the 100-700 keV region was found by counting the particle tracks in the different mylar layers (as the track density was too high for detailed spectroscopy). The spectrum in the 0.7-1.5 MeV range was measured of the analysis of individual particles. The count is per 20 keV energy bin. The number of tracks in both regimes was counted over a solid angle of 10^{-7} steradians.

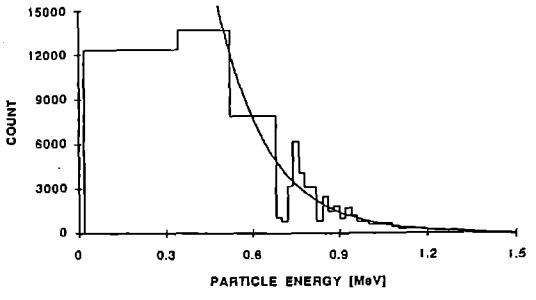

Figure 3. Ion count plotted against energy for 10^{-7} steradians solid angle to the CR-39 detector. A best fit exp (-E/kT) temperature curve of 200 keV is shown.

Where detailed spectroscopy was possible, it was found that on all shots of whatever target material the particles were protons. This observation that the fastest ions are protons, even for non-hydrogenic targets, is consistent with previous experiments [1] where they are presumed to be associated with hydrocarbon contamination of the target surface and with theory [5] which shows that lighter ions are accelerated to higher speeds.

Clearly, figure 3 suggests that there is a peak in the spectrum at 300-400 keV after which there is an exponentially decaying tail. Particles up to 1.5 MeV were detected. The broad peak and exponential tail was observed in all shots. By fitting an exp(-E/kT) curve to the exponentially decaying tail, a best fit ion temperature of 200 keV was fitted for this particular shot. The measured ion temperatures were in the range 100-200 keV.

The hard x-ray NaI - photomultiplier detectors indicated the existance of fast electrons. Assuming that the emission is bremstrahlung from the fast electrons and can be described by a exp(-E/kT) profile, then the measured intensities of the two hard x-ray detectors are consistent with an electron temperature of around 300 keV.

The Faraday cups were not calibrated, so it is not possible to gain any information from them about collimation. The main information that they give is about the ion velocity spectrum. They show that most of the energy comes off in ions with energy/nucleon ~100keV, even though the sensitivity of Faraday cups is falling at this energy due to biasing voltage. These graphs show that the Faraday cups do not detect a significant amount of energy in a lower energy 'thermal' component.

The angular flux of 100-300 keV ions detected by the CR-39 is shown in figure 4a. It is clear that these ions are collimated into a half angle cone of ~10°. Figure 4b shows the total flux of ions incident on the CR-39 detectors with angle. It shows that the integrated fast ion emission is rather broader and occupies a ~20° half angle cone. Clearly, these results confirm that the plasma blow-off is collimated about the target normal.

By knowing the number of ions, the solid angle of the detector and the energy of the particles it is now possible to estimate the absorbed laser energy. Assuming that there is symmetry about the target normal in the ion emission, and that all ion making tracks in the detectors were protons. The energy absorption in the >100 keV range averaged ~2% of the incident energy and was never greater than ~5%. This absorption fraction in the fast ions did not appear to vary with target material and remained fairly constant over the range1.0- 12.0 x 10^{17} Wcm^{-2} incident irradiance.

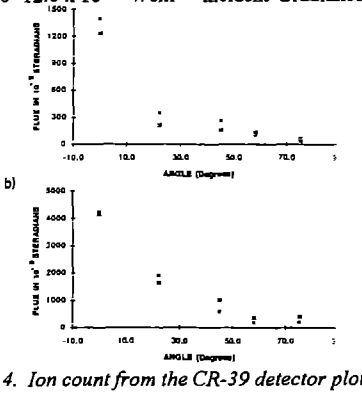

Figure 4. Ion count from the CR-39 detector plotted against angle to the target normal for two 20 J shots onto Cu targets for an energy range of a) 100-300 keV and b) >100 keV incident on the detector

Numerical investigations that we have performed suggest that the plasma is confined to a collimated flow by a large azimuthal magnetic field pinching the plasma due to the large crossed density and temperature gradients. Further details of this numerical investiagtion will be presented for future publication.

[1] S.J.Gitomer, R.D.Jones, F.Begay, A.W.Ehler, J.F.Kephart, R.Kristal *Phys Fluids* **29**, 2679 (1986).

[2] C.N.Danson et al *Ann Rep to LFC* Section B1 (1993)

[3] S.L.Niffikeer, PhD thesis, University of London (1991).

[4] A.P.Fews, D.L.Henshaw *Nucl. Instr. Meth.* **197**, 517 (1982); A.P.Fews *Nucl. Instr. Meth.* **B71**, 465 (1992); A.P.Fews *Nucl. Instr. Meth.* **B72**, 91 (1992).

[5] L.M.Wickens, J.E.Allen *Phys Fluids* **24**, 1894 (1981).

THOMSON SCATTERING MEASUREMENTS OF OPTICALLY IONISED PLASMAS

W.J.Blyth[1], S.G.Preston[1], A.A.Offenberger[2],
Z.Najmudin[3], M.H.Key[4], J.S.Wark[1], A.E.Dangor[3]

[1] Department of Physics, Clarendon Laboratory, University of Oxford, Parks Road, Oxford OX1 3PU
[2] University of Alberta, Edmonton, Alberta, T6G 2G7, Canada
[3] Department of Physics, Imperial College, London
[4] Rutherford Appleton Laboratory, Chilton, Didcot, Oxon, OX11 OQX

INTRODUCTION

Optically ionised plasmas have been proposed as a medium for recombination X-ray lasers[1-4]. Using a short pulse UV laser, with intensities above 10^{17} W/cm^2, a gas target can be highly ionised by optical ionisation, while being left relatively cool, if the pulse-length is shorter than the timescale for collisional heating[5,6]. This creates a plasma in a state far from thermal equilibrium. After the laser pulse has left the plasma, the electrons recombine rapidly into upper states of the ions and population inversion between the upper states and the ground states of the ions can be established. This could be a method of producing an X-ray laser for which the total energy required is relatively small.

Work has been carried out to measure the temperature and density of the plasma, and to investigate the heating mechanisms using the Raman amplified KrF beam on SPRITE[7]. The main diagnostics used were Thomson scattering, and stimulated back-scattering including Stimulated Raman Scattering (SRS), Stimulated Compton Scattering (SCS) and Stimulated Brillioun Scattering (SBS).

THE EXPERIMENT

The 268nm Raman amplified beam of SPRITE KrF laser was used with an average energy per shot of about 2 J, and a pulse length of 9 ps. The beam was focused using an off-axis paraboloid mirror to a spot of about 3 μm radius to give an intensity on target of about 4 x 10^{17} W/cm^2. Two types of gas target were used. At low pressures static fill gas was used, at higher pressures (above 400 torr) a gas-jet target was used to relieve the laser propagation problems through the gas. In both cases the gases used were He, Ne, Kr, and H_2 was used in the gas-jet. The gas-jet was capable of operating at a backing pressure of up to 1500 psig. The closest working distance between the nozzle and the focus of the laser was 0.7 mm. At this distance the gas pressure was several atmospheres. Thus pressures from 1 torr to several thousand torr were investigated.

THOMSON SCATTERING

Thomson scattering was measured at 90° to the incident laser direction and to the polarization direction. The light was collected through an f/5 achromatic lens and was relayed to a spectrometer with either a 600 or 1200 lines per mm grating.. The source was magnified by 10 times at the entrance slit of the spectrometer. The entrance slit width was 200 μm, so that light was collected from a 20 μm region at the source. The slit in the other (axial) direction was over 1 cm long. The length of plasma imaged in this direction was limited by the detector to about 1mm. The detector at the back of the spectrometer was a UV streak camera. This was operated at speeds no greater than 50 ps / mm. Thus the signal was not time resolved but the streak mode was used to separate the signal from light scattered from the walls of the chamber. The signal from the back of the streak camera was recorded using a 2-dimensional CCD. The image was spatially resolved in the axial direction (with a resolution of about 40 μm) and spectrally dispersed in the other direction with a resolution of about 1.5 nm.

The spectrum of Thomson scattering depends on $\alpha = 1/k\lambda_D$ where k is the magnitude of the k-vector of the plasma wave, and λ_D is the Debye length. For values of $\alpha \ll 1$ the electrons are uncorrelated. The Gaussian spectral profile can then be related to a thermal velocity, and the temperature can be deduced. At higher pressures, collective effects in the plasma become important. In the limit that $\alpha \gg 1$, the spectrum has very distinct side-bands at $\omega_0 \pm \omega_p$ where ω_p is the plasma frequency. At intermediate values of the α-parameter theoretical curves can be fitted to deduce both temperature and density.

STIMULATED BACK-SCATTER

The back-scattered light was collected by the same off-axis paraboloid as was used for focusing the beam initially. Approximately 8% of the back-scattered light was split off using a quartz beam-splitter. The light was then split and focused into two separate spectrometers. The first was a high resolution 0.75 m spectrometer with a 2400 lines per mm grating lens coupled to a streak camera with approximately 3 X magnification. The spectral resolution was about 0.5 Å. This was used to measure the spectrum of SBS near to the laser wavelength. The second spectrometer was a lower resolution 0.3 m spectrometer with a 1200 lines per mm grating. The output was lens coupled to another streak camera with approximately one to one imaging. The spectral resolution of this channel was about 1 nm, and the wavelength range that could be measured on a single shot was about 40 nm. This channel was used to measure the SRS or SCS spectra. These channels were calibrated so that the absolute reflectivity of the signals could be measured. This was done by reflecting a known fraction of the beam from the oscillator into the detection channels, so that the signals could be compared to the experimental data.

SBS is stimulated scattering from ion acoustic waves in the plasma. The Doppler shifted spectrum of this scattered light can be used to determine the electron temperature in the plasma since the ion acoustic wave speed depends on the electron temperature.

SRS and SCS are the same scattering process but in different plasma regimes. In this case it is electron plasma waves that cause the scattering. SRS occurs in the case when $\alpha \gg 1$ when Landau damping of the plasma wave is weak. In this case, plasma oscillations have a well defined resonance frequency ω_1 given by the Bohm-Gross dispersion relation. The scattered wave is red-shifted by the Bohm-Gross frequency. When $\alpha \ll 1$ Landau damping of the waves is strong. In this case the plasma waves do not have a well defined resonance and are strongly driven by the laser field producing SCS. The spectrum of SCS is broader than for SRS, and the growth rates are smaller.

RESULTS

The Thomson scattering results are shown in Figure 1. The results presented here are for He. In He, the static fill pressures we used ranged from 2 torr to 400 torr. At full ionisation, this corresponds to an electron density range of 1.3 x 10^{17} cm^{-3} to 2.6 x 10^{19} cm^{-3}. In Ne, static pressures ranged from 1 torr to

100 torr (corresponding for 8x ionisation to an electron density range of 2.6 x 10^{17} cm^{-3} to 2.6 x 10^{19} cm^{-3}). At 2 torr, the spectrum shows no sign of a resonant electron feature which suggests that the electrons are uncorrelated. Thus Gaussian fits to the data can be made. The width of these Gaussians then determines the temperature. At 20 torr He, an enhanced feature near the laser frequency starts to appear. This is scattering at the ion resonance. At 100 torr, there are distinct peaks displaced from the laser frequency which are caused by the collective effects in the plasma. At 200 torr, these electron features are more well defined.

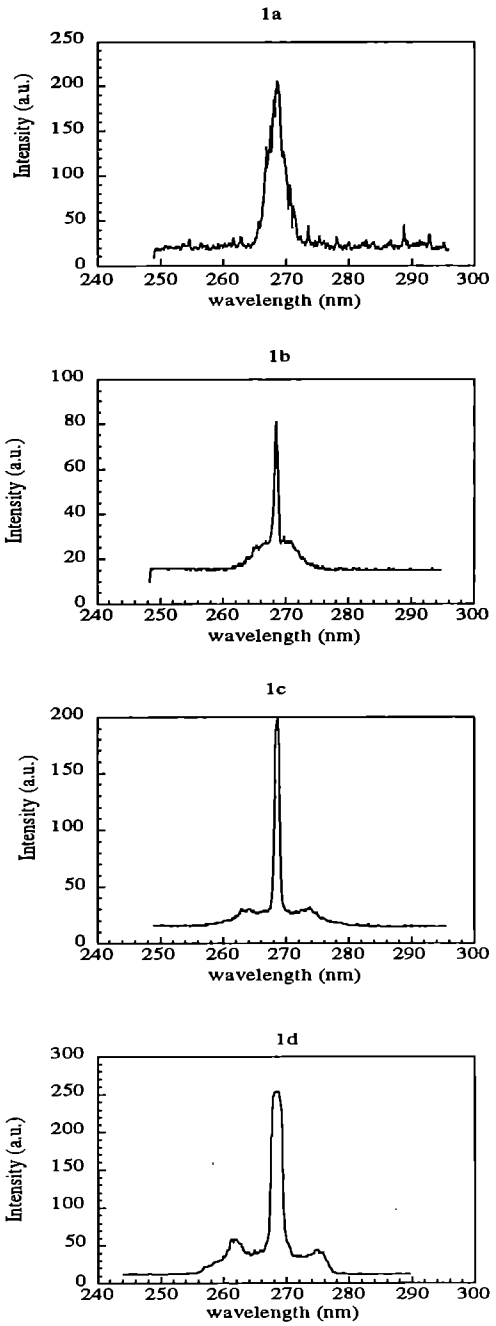

Figure 1 Thomson Scattering plots from static fill He.
a) 2 torr b) 20 torr c) 100 torr d) 200 torr (the spectrum in this case is slightly cut off by the edge of the detector causing the asymmetry)

The back-scatter signals from the lower dispersion spectrometer are shown in figure 2. The spectrum can be seen to evolve from a distribution that is symmetrical about λ_0 to a well-defined Raman scattering spectrum in the gas-jet shots. The scattering at λ_0 increases as the pressure increases due to SBS. At the lowest pressures, the backscatter spectrum has the form of unstimulated Thomson scattering from uncorrelated electrons. This confirms the low value of α deduced from the Thomson scattered data for these low pressures.

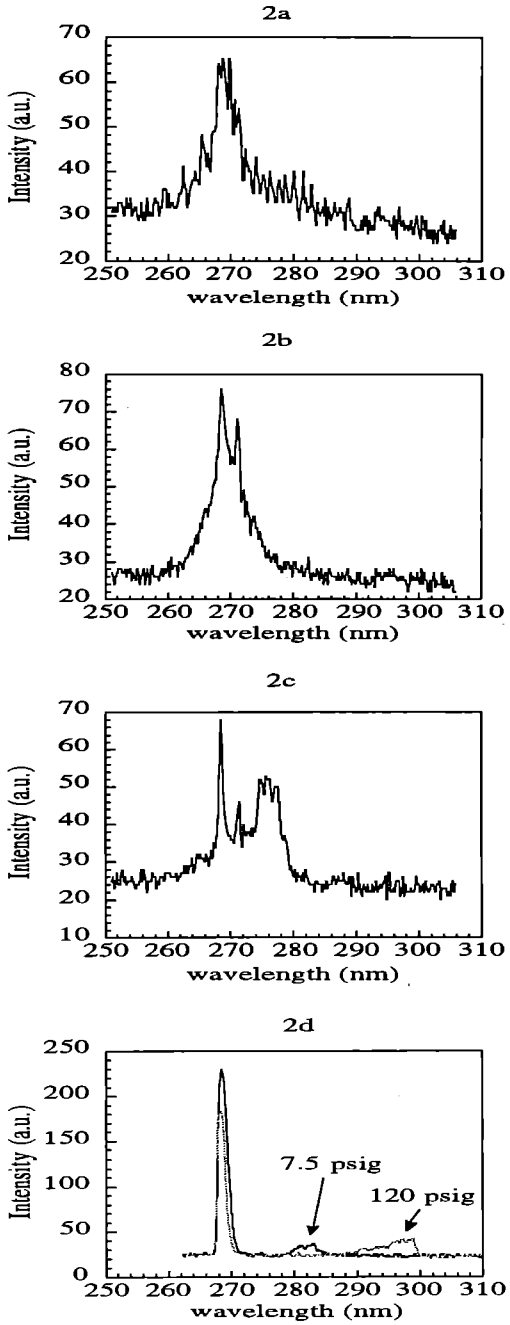

Figure 2 Backscattered spectra collected from the low dispersion spectrometer. a) 1 torr Ne b) 10 torr Ne c) 30 torr Ne d) gas-jet Ne at 7.5 psig and 120 psig.

The fraction of light backscattered was calculated by taking a known percentage of the KrF oscillator beam incident on the SBS and SRS measurement channels and using a calorimeter to determine the mean beam energy. From this it is possible to calculate absolute values for reflectivities.

The conclusion that the scattering becomes stimulated at higher pressures is confirmed by the measurements of the reflectivities. The reflectivities of the SRS and SBS backscatter for varying pressures is shown in fig 3. For 1 torr Ne, it can be seen that the SRS reflectivity is down to levels which would be expected for non-enhanced Thomson scattering. This is consistent with the fact that the spectrum is symmetrical, since any convective gain would enhance only the red wing of the spectra. The SRS reflectivity at higher pressures appears to saturate at 10^{-2}% whereas the SBS reflectivity reaches values of the order of 10%. This highlights the much faster growth rate of SBS backscatter, compared to SRS, once it has started.

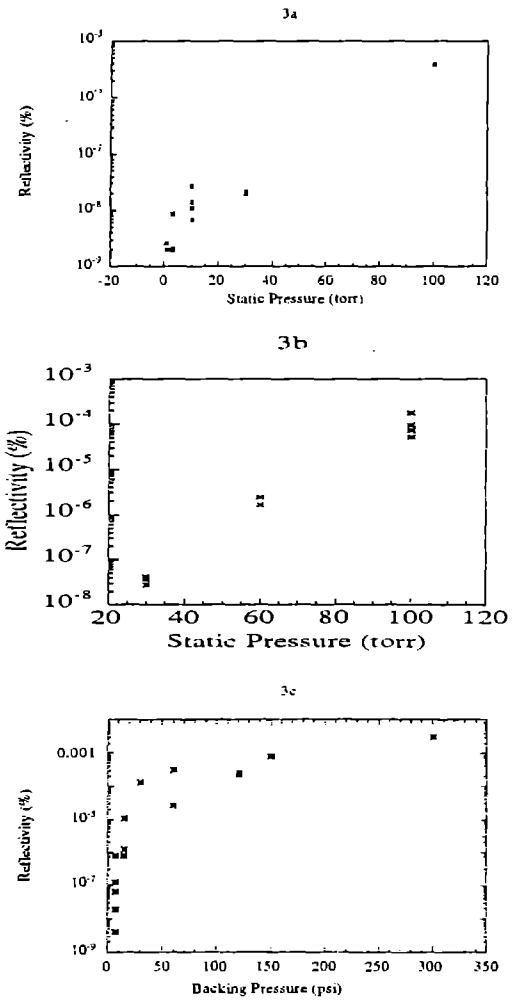

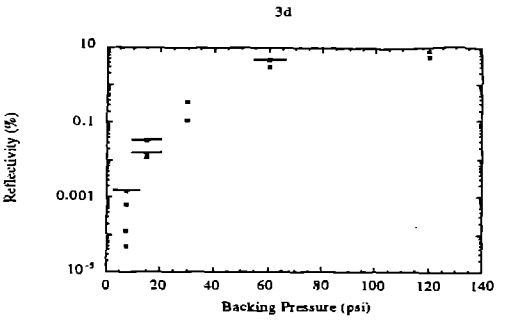

Figure 3 Backscatter reflectivity as a function of pressure for Neon static gas fill for SRS (a), for SBS (b); and Neon gas jet at 0.7mm separation from focus for SRS (c), for SBS (d). Horizontal bars through data points indicate that the image was saturated.

REFERENCES

1. J. Peyraud and N. Peyraud, J. Appl. Phys. **43** 2993 (1972).
2. M. V. Ammosov, N. B. Delone and V. P. Krainov, Zh. Eksp . Teor. Fiz. **91** 2008 (1986) [Sov.Phys. _JETP **64** 1191 (1986)].
3. N. H. Burnett and G. D. Enright, IEEE J. Quant. Electron. **26** 1797 (1990)
4. D. C. Eder, P. Amendt and S. C. Wilks, Phys. Rev. A **45** 6761 (1992)
5. B. M. Penetrante and J. N. Bardsley, Phys. Rev. A **43** 3100 (1991)
6. C. B. Darrow, C. Coverdale, M. D. Perry, W. B. Mori, C . Clayton, K. Marsh and C. Joshi, Phys. Rev. Lett. **69** 442 (1992)
7. A. A. Offenberger, W. J. Blyth, M. H. Key, J. Wark, Z.Najmudin and A. E. Dangor, Proc SPIE Jan1993

X-RAY PRODUCTION MEASUREMENT USING PULSES FROM THE HIGH BRIGHTNES KrF-PUMPED RAMAN LASER SPRITE.

R. Evans, T. A. Hall, J. Ellison and A. Ridgeley*
University of Essex, Colchester, Essex.
*RAL Space Science Division

Plasmas produced by short pulses (i.e. ones of a few picoseconds or less) and high intensities (i.e. in excess of 10^{14} Wcm^{-2}) constitute a novel form of hot, dense matter. Since the plasma has little time to expand during the laser pulse, the extension of the plasma can be characterised by a scale length which is smaller than the laser wavelength, these plasmas are fundamentally different from those produced by long pulses for inertial confinement fusion. The observation of x-rays emitted from these plasmas have led to some interesting results, for example the spontaneous emission of x-rays up to energies of 1MeV have been reported[1]. Short pulse laser produced plasmas also show considerable promise as sources for time-resolved x-ray probing and backlighting (e.g for microscopy and EXAFS) and as active media for x-ray gain and lasing.

Initially experimental results for plasmas generated by short pulses in the intensity range of 10^{15} Wcm^{-2} suggested that the dominant laser absorption process was inverse bremsstrahlung[2]. Recently, however, new evidence based on x-ray emission at 10^{16}-10^{18} Wcm^{-2} and second harmonic generation has suggested that other absorption processes such as resonance absorption into an electron plasma wave could play an important role. If this is the case, the x-ray yield from the plasma could be increased by optimising the total absorption (both collisional and resonance) at the target. Investigation of the x-ray emission from the plasma as a function of laser irradiation etc. can provide useful information about the laser-plasma interaction process and the plasma conditions.

The 12ps (FWHM) SPRITE (268nm) laser pulse was focused onto the target via f10 CaF_2 transmission optics, defocusing the system allowed a wide range of focal spots to be obtained, 50μm to 500μm were used which meant that incident laser irradiances were between 10^{14} and $10^{17}Wcm^{-2}$. By using the Raman shifted frequency it was possible to eliminate the amplified spontaneous emission (ASE) and the contrast ration I_0/I_{ASE} has been measured to be ~10^{10}, consequently no preformed plasma was formed by the ASE. The targets were thin (2000Å) coatings of Al, Ge, Cu or U on a glass microscope slide, both smooth and rough surfaces were explored.

Characterisation of the plasma conditions was carried out using time integrated and time resolved x-ray spectroscopy, the focal spot area was imaged using an x-ray pin-hole camera and the total x-ray yield was measured with two filtered (25μm and 125μm of Be) x-ray photodiodes. The time integrated spectra were recorded by dispersing the x-rays with both a TlAP and an ADP crystal onto two CCD arrays. A UV sensitive photodiode placed in the back-scatter channel was used the monitor the target reflectivity on a shot to shot basis.

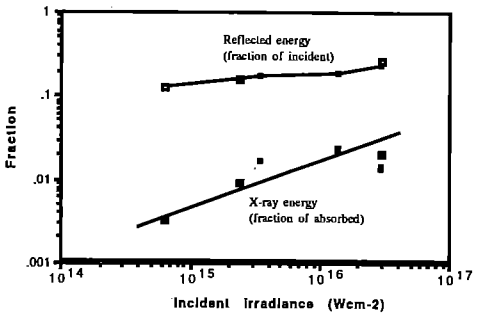

Figure 1.

Figure 1 shows preliminary data for the Al targets only, the upper curve shows the variation with incident laser irradiance of the fraction of the incident laser energy which is reflected and detected by the backscatter monitor. The lower curve shows what fraction of the absorbed laser energy (~1-reflected fraction) is converted into x-ray emission (>1keV) again for various values of the incident irradiance. The data is in good agreement with the results from a study by Teubner et al, who used lower laser energies but much shorter pulses (~400fs). The data for other target materials has not yet been analysed fully but the general trend is for higher Z materials to generate more x-rays at a given irradiance, but for the reflected fraction to remain constant with irradiance at a similar value to that of Al.

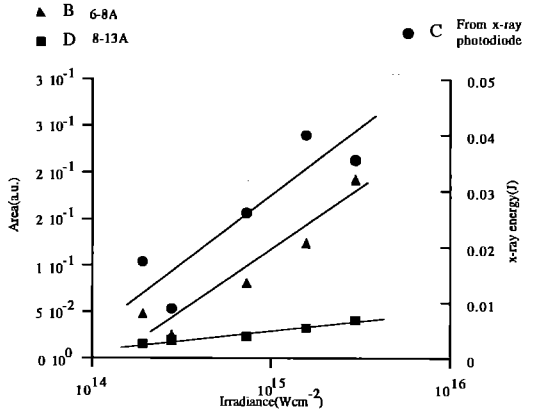

Figure 2.

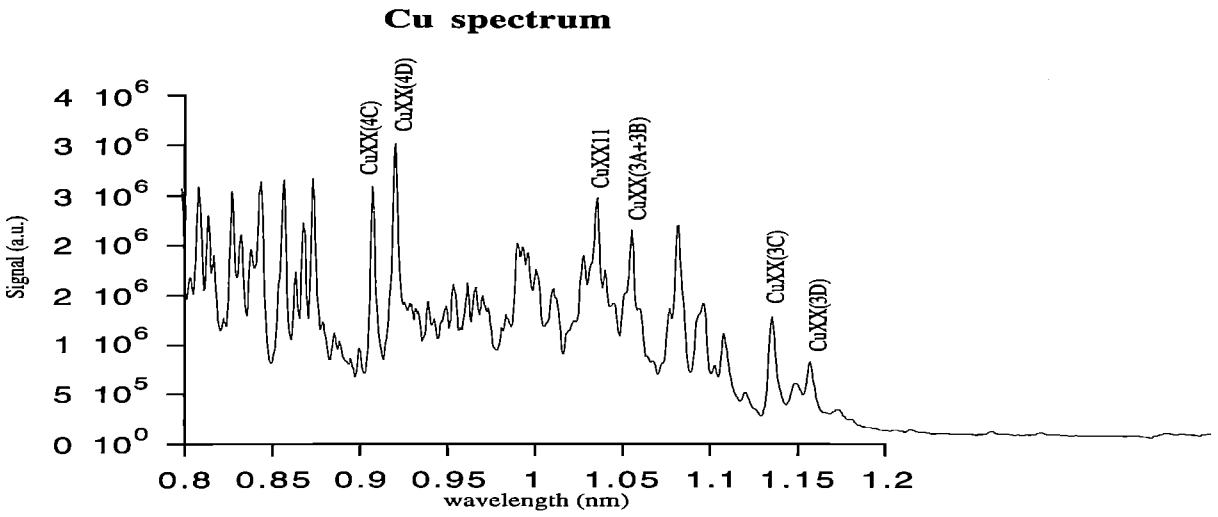

Figure 3.

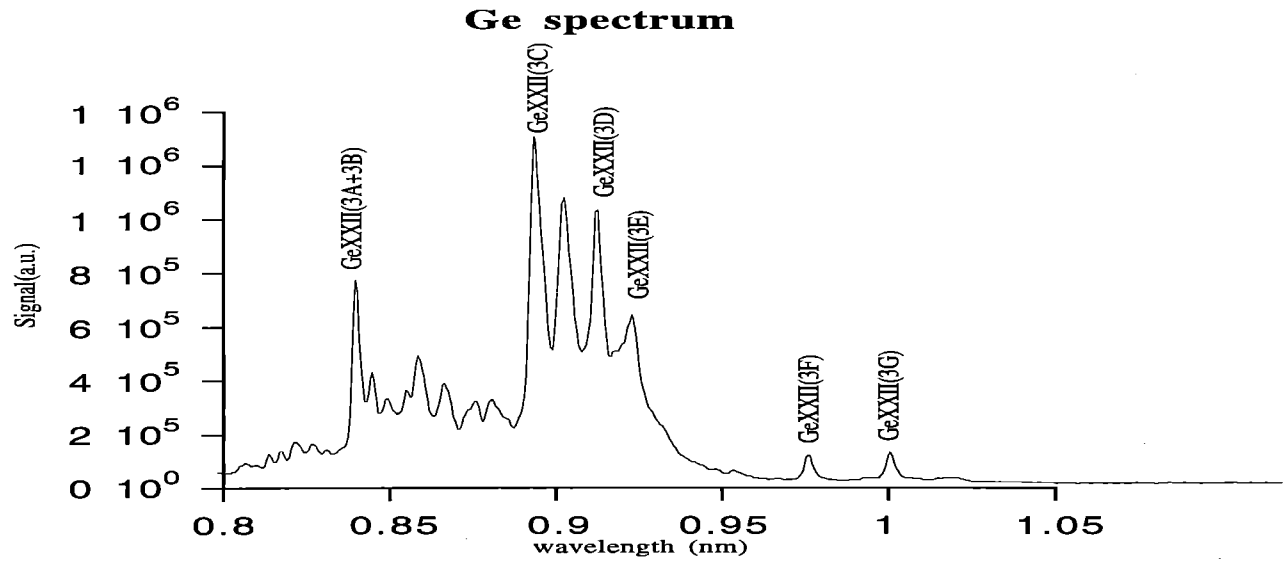

Figure 4.

Figure 2 shows the x-ray energy in Joules recorded on an x-ray photodiode (with a 125μm Be filter) along with the integrated area from the two CCD arrays one measuring between 6 and 8Å and the other betwen 8 and 13Å, as a function of incident irradiance. The harder x-ray component increases more rapidly with irradiance than the softer component as expected.

A typical Copper spectrum obtained at a low irradiance (~$5*10^{15}$ Wcm^{-2}) is shown in Figure 3. As the irradiance is increased the spectral lines increase in brightness but the level of the background continuum rises relative to the resonance lines, this phenomena occurred for all target materials. A Germanium spectrum generated by a similar irradiance shot is presented in Figure 4.

1. J. D. Kmetec et al Phys. Rev. Lett. **68**, 1527 (1992).
2. H. M. Milchberg et al Phys. Rev. Lett. **61**, 2364 (1988).
3. U. Teubner et al Phys. Rev. Lett. **70**, 794 (1993).

DECOUPLING OF AN INTENSE SOFT X-RAY PULSE FROM THE ABLATION SURFACE

M. Desselberger, J. Edwards, R. Taylor and O. Willi

Imperial College of Science, Technology and Medicine, London.

High-power lasers are considered to be favourable candidates for the driving power source to achieve inertial confinement fusion. Currently, two different approaches are pursued. Intense laser beams can be focussed directly onto the shell of a spherical fuel capsule causing ablation of the surface and subsequent implosion of the target which compresses the fuel mixture to the required density and temperature. Alternatively, the laser light can first be converted into intense soft x-rays which can then be used to drive the implosion. In the former, the energy to sustain the ablation is derived from that laser energy which is deposited near the critical surface and carried into the target by electron conduction. In the latter, the energy is supplied directly by those x-rays which are transported into the high density target material through the plasma blow-off. Therefore, experimental measurements of the interaction, heating and dynamics of low Z targets irradiated with intense, approximately Planckian, soft x-ray pulses are essential, both to help assess the relative merits of either system and to test modelling capabilities. The first measurements of the dynamics of thin foil targets of different thicknesses were made, which were irradiated with intense, approximately Planckian soft x-ray pulses. The soft x-ray pulses were generated from separate laser irradiated converters consisting of 1 μm thick CH which was overcoated with 750 Å of gold. The foil targets were driven either with shaped soft x-ray or optical pulses or a combination of both and diagnosed with a high magnification (80x) time-resolving (100ps) XUV imaging system. The timing of the backlighter emission was such that it began to probe the stripe target 250ps before the main soft x-ray pulse was incident so that the initial position of the target was recorded.

Figure 1 shows streak records in the (t,z) plane (t=time, z=position measured perpendicular to the target surface) obtained at a probe wavelength of 50 Å for x-ray heated 12 μm thick plastic foil targets. The image on the left was obtained of a target which was irradiated with a gaussian pulse whereas a shaped soft x-ray pulse was used in the second case. At first, the foil appears as a dark shadow because it is initially opaque to the probe radiation. As the target is heated, temperature and density gradients are generated when the plasma expands.

The soft x-ray interaction was simulated using the 1D Lagrangian hydrodynamic code, MEDUSA, coupled to a 1D multi-group radiation transport code. The simulation results were compared with the experimental data by generating probe transmission contours ($\exp(-\rho\kappa L)$, for pathlength L, along which the opacity is κ and the density ρ) in the (t,z) plane from the predicted plasma density and temperature profiles for thr rear side of the target. It was observed that the efficiency of the soft x-ray drive was significantly reduced later in the shaped pulse due to absorption of radiation in the plasma blow-off. Figure 2 shows hydrodynamic simulations for a gaussian and shaped soft x-ray pulse. Both the actual experimental pulses shapes (used in the simulations) and the prediced ablation pressure are plotted as a function of time.

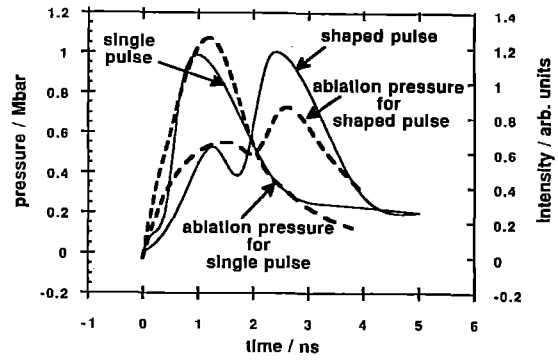

Figure 2. Radiation hydrodynamic simulations showing x-ray pulse shapes and predicted ablation pressure histories demonstrating that the ablation pressure strongly depends on the shape of the soft x-ray pulse.

The data is very striking showing that the efficiency of the x-ray drive is reduced by around a factor of two with the shaped pulse compared to the predrive free case. This is because as more material is ablated by the soft x-ray drive, the attenuation of the drive radiation in the plasma blow-off increases. As a result, a decreasing fraction of the drive radiation is available to drive the ablation. These results are in distinct contrast to similar data taken on targets which were driven by shaped optical laser pulses where no such reduction in the ablation pressure was observed.

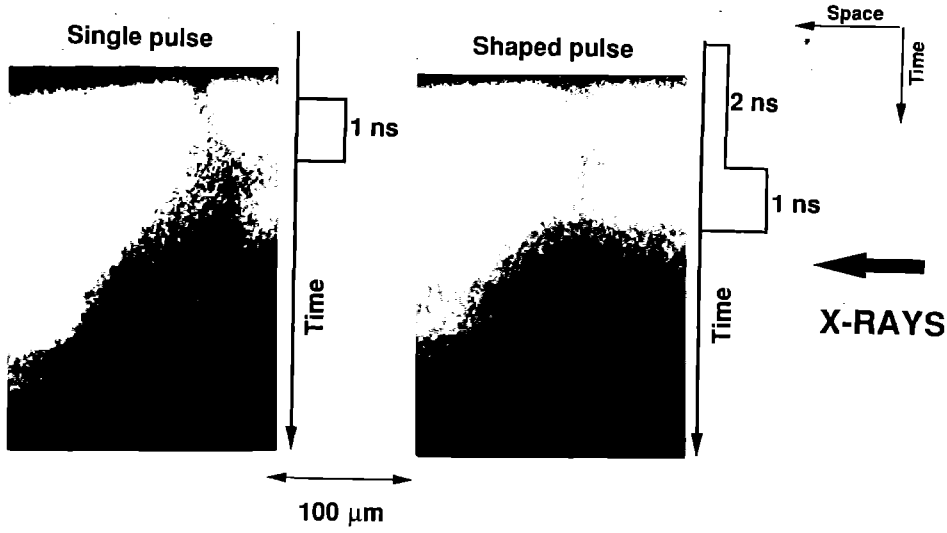

Figure 1. Streaked XUV radiograms of 12 μm thick plastic foil targets irradiated by soft x-rays.

SUPERSONIC PROPAGATION OF AN IONIZATION FRONT IN A LOW DENSITY FOAM TARGET DRIVEN BY THERMAL RADIATION

T. Afshar-rad[1], M. Dunne[1], J. Edwards[1], J. M. Foster[2], S. J. Rose[3], P. A. Rosen[2], R. Taylor[1] and O. Willi[1].

1) Blackett Laboratory, Imperial College, London.
2) Atomic Weapons Establishment, Aldermaston.
3) Rutherford Appleton Laboratory, Chilton.

Several studies have recently been carried out to investigate the interaction and heating of thin solid targets with intense quasi-Planckian soft x-ray pulses. These experimental observations measured the global radiation transport [1-3], the opacities [4-7], the propagation of Marshak waves [8] and the acceleration dynamics of thin foil targets [9]. In these measurements the initial propagation of the heat wave is supersonic but is rapidly overtaken by the hydrodynamic motion and the flow soon becomes ablative [10]. A supersonic heat wave can, however, be maintained by lowering the target density such as in low density foams. The investigation of supersonic heat wave propagation in matter driven by thermal radiation is not only of fundamental interest in the study of radiation hydrodynamics, but may also have important applications in Inertial Confinement Fusion (ICF). In particular, it has been proposed to have a low density foam layer surrounding the fusion pellet to overcome the severe initial imprint of nonuniformities in laser driven targets [11]. The initial x-ray irradiation of the foam layer produces a smooth plasma in which the critical surface of the main drive laser is separated by many tens of microns from the ablation surface, thus allowing the dominant laser nonuniformities to be thermally smoothed. A spatially uniform drive pressure can therefore be produced at the ablation surface. Since the supersonic radiation front propagates ahead of the shock front, the preforming of the foam layer can be achieved without preheating the fuel capsule. This is extremely important if the implosion is to proceed along a low adiabat. Direct radiative preheating from the preforming x-rays may also be avoided by simply tailoring the x-ray pulse to penetrate only as far as the ablation surface. Supersonic heat wave propagation may also be important in ion beam driven inertial confinement fusion where the ion beam energy is deposited in a region which is separated from the fusion capulse. So far low density foam targets have only been irradiated with laser radiation for shock propagation studies[12].

This report details the first direct measurements of the sustained propagation of a supersonic, radiation driven heat wave. An intense pulse of thermal x-ray radiation originating from a laser produced gold plasma was used to irradiate a low density foam target. The position of the ionizing heat front was observed with a high resolution soft-ray imaging system. The experimental results were modelled with 1D and 2D Lagrangian radiation hydrodynamics code and good agreement was observed.

Four frequency-doubled (λ=0.53 μm) beams from the VULCAN glass laser system were used in a cluster arrangement to irradiate a thin gold layer, 750 Å thick, supported on a 1 μm plastic substrate. The laser beams were focussed to focal spot of approximately 250 μm diameter. The laser pulse length had a full-width-half-maximum (FWHM) duration of typically 800 ps. Laser irradiances of up to 5×10^{14} Wcm^{-2} were used. The soft x-ray pulse transmitted through the rear of the converter foil was used to irradiate a low density plastic foam target separated from the foil by 125 μm. The foam sample consisted of a triacrylate foam ($C_{15}H_{20}O_6$), 160 μm in diameter, 200 μm in length and at a density of 30 mg/cm^3 (approx 1/50th solid density) [13]. The time behaviour and the absolute flux levels of the soft x-ray pulse were measured by using an absolutely calibrated, time resolved, flat response vacuum x-ray diode. The incident soft x-ray flux on the foam target was measured to be about 5×10^{12} Wcm^{-2}.

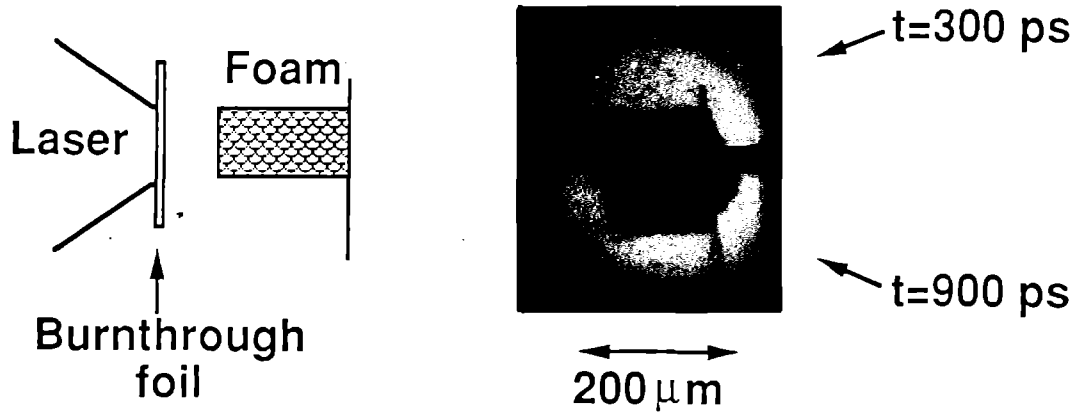

Figure 1 Soft x-ray gated radiograms of a 30mg/cc foam target showing the propagation of a supersonic, radiatively driven ionization front. A schematic of the experimental set up is shown on the left of the figure, with a multilayered XUV mirror (not shown) used to image the backlit target. In the print of the data, the x-ray drive is incident from the left, as in the schematic. The light circle in the print is the unattenuated probe radiation, while the dark areas in the centre are what remains of the foam at the two different probe times.

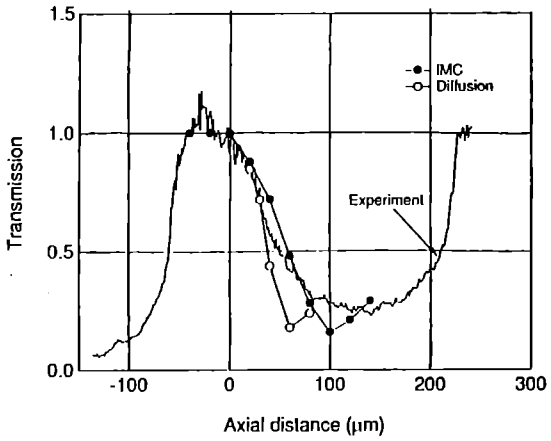

Figure 2 Comparison of 2D NYM simulations of the foam transmission with experimental data at 900ps. The x-ray drive is incident from the left.

The foam target was imaged perpendicularly to the soft x-ray drive with a spherical multilayered mirror, reflecting with a 3Å bandwidth at a central wavelength of 55Å. The foam sample was backlit by a thermal x-ray source [14]. The source for the x-ray probe was generated by irradiating a separate gold target, 250 μm in diameter, with a green backlighter pulse 800 ps (FWHM) in duration.

The 50 times magnified image of the cylindrical target was recorded on a two frame gated microchannel plate (MCP) intensifier with the target image placed across the two frames. The framing times were set at 0.3ns and 0.9ns after the beginning of the soft x-ray heating pulse. The gating time has been measured to be approximately 120ps. The spatial resolution of the imaging system was found to be 2 μm by the use of a ray tracing program, in good agreement with past experimental measurements.

Radiograms of the heated foam at two times in the evolution of the ionization wave are shown in Figure 1, along with a schematic of the experimental arrangement. In the upper frame the foam is almost entirely intact. This is because the drive pulse is weak at this time and still rising. In the lower frame, however, the front part (approximately 50 μm) of the foam has become transparent. This results from the propagation of the radiation wave into the target which heats and ionizes the foam, thus lowering its opacity to the soft x-ray probe.

The radiation is transported into the undisturbed foam target through a volumetric heating process rather than a diffusive transport process. That is, the x-rays can be thought of as penetrating a mean-free-path into the foam target, which is consequently heated and ionized. The resulting drop in opacity allows the thermal x-rays to penetrate deeper into the target, which is then heated. The evolution of this bulk heating process in the target is what constitutes the propagation of the x-ray heating wave. That is, the wave is driven almost entirely by the externally applied radiation field, with little or no contribution from the re-emission of the target. It is the low density of the target which allows this radiation-driven wave to propagate at velocities greater than the sound speed. In higher density material, the hydrodynamic response of the target rapidly catches up with the initially supersonic 'radiation wave', resulting in a radiatively driven ablation wave [10]. Indeed, we have measurements taken with foams at densities of only 50 mg/cc which exhibit ablative flow.

The velocity of the wave can be approximated from the experimental data since it has travelled approximately 50 μm in no more than 600ps. This gives a lower limit for the front velocity of 8.5×10^6 cm s^{-1}. The maximum sound speed in the heated material is around 5.5×10^6 cm s^{-1}. Consequently, at this stage of its evolution the ionization front propagates supersonically with respect to both the unionized and ionized material with a Mach number of at least 1.5.

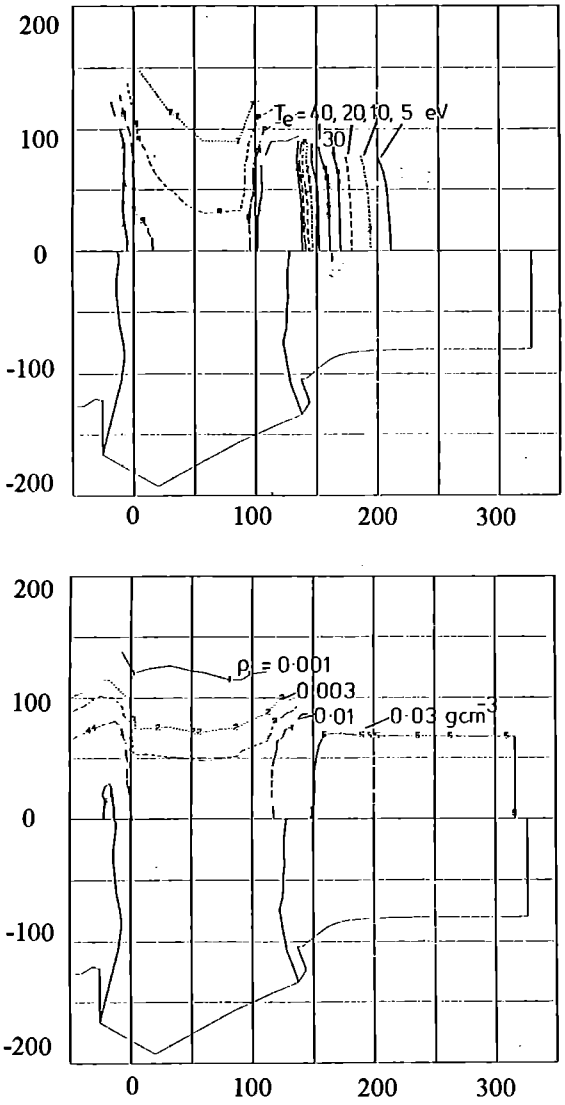

Figure 3 2D NYM simulations of the temperature and density contours existing in the foam at 900ps. The burnthrough foil and intervening vacuum are also included in the mesh. The bottom half of each plot shows the 2D expansion of the foil and foam. Comparison of the two plots shows that the temperature contours penetrate well into the undisturbed 30mg/cc foam. The initial foam extended from 125 to 315 μm.

Simulations were performed using a two-dimensional Lagrangian hydrodynamics code NYM [16]. Radiation transport is modelled using either a multi-group diffusion approximation using Kershaw's diffusion algorithm or multigroup implicit Monte-Carlo (IMC) transport. Opacities are generated using a screened hydrogenic atom model. Figure 2 shows a comparison of NYM simulations with the experimental data at 0.9 ns. The drive is incident from the left of the figure, with the initial undisturbed foam extending between 0 and 190 μm. The calculated foam transmission curves were obtained by post-processing the output of the hydro simulations with opacities generated from the detailed opacity code, IMP [15]. The heated foam becomes transparent to the probing x-rays (defined as the point where the transmission falls to 50% of the unattenuated signal) at a plasma temperature of 40eV for the initial target density of 30 mg/cm^3. Good agreement on the extent of propagation of the x-ray heating wave can be observed.

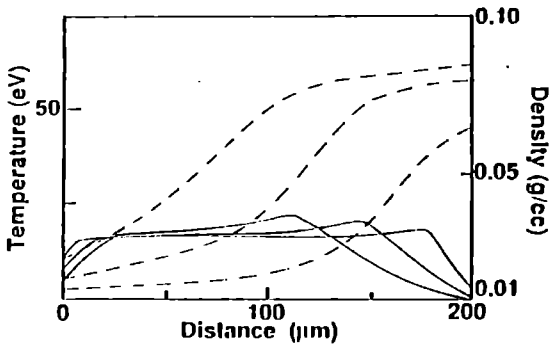

Figure 4 Predicted temperature and density profiles as the radiatively driven wave propagates through the foam. At all three times the temperature contour can be seen to be well ahead of the density disturbance.

The density and temperature contours predicted by NYM at this time are shown in Figure 3, where it can clearly be seen that the temperature front has penetrated far into the undisturbed foam. Indeed, the 2D NYM simulations indicate that the x-ray driven heating wave remains supersonic until approximately 1400ps after the start of the x-ray pulse.

A time sequence of predicted temperature and density profiles throughout the foam target is shown in Figure 4. This demonstrates the heat wave extending beyond the hydrodynamic motion which takes the form of a weak compression wave propagating behind the radiation heat front. The 1D and 2D radiation hydrocode simulations indicate that the supersonic front moves at a velocity of between 9.0×10^6 and 1.5×10^7 cm s^{-1}, corresponding to a minimum Mach number of 1.5 to 2.5.

In summary, we have observed the propagation of a supersonic ionization wave driven by thermal radiation for the first time. The production of a preformed, long scale length plasma by a supersonic heating wave may prove to be the ideal solution to eliminate laser nonuniformity imprint in the initial start-up phase of laser driven implosions. Previous measurements [11] of the interaction of nonuniform laser profiles with preformed plasmas have demonstrated that the scheme is highly successful in eliminating plasma jetting and can result in uniform ablative acceleration of planar targets. The drive scheme detailed in this report should provide not only the same thermal smoothing capabilities as the previous scheme, but should eliminate the fuel shock-preheat problem and will, in addition, be easily adaptable to spherical geometry.

A number of questions remain to be experimentally answered regarding the proposed drive scheme. In particular, quantitative measurements need to be made concerning the degree of laser beam non-uniformity which can be tolerated, the hydrodynamic efficiency with which the hybrid targets can be accelerated, and also observations on the levels of Rayleigh-Taylor growth as the low density foam layer accelerates the high density pusher.

Future measurements should also concentrate on regimes in which the transition from a supersonic to subsonic radiatively driven wave occurs and also on the regime in which target re-emission starts to dominate the transport. Such a diffusive regime is of great fundamental interest and will also provide valuable benchmarking data for radiation transfer codes.

The authors would like to acknowledge the technical support of the CLF staff, Dr. B. Evans (University of Reading) for supplying the multilayered mirrors, C. Horsefield (AWE) and Dr J. Falconer (Dundee University) for supplying the foam targets.

REFERENCES

[1] J. Edwards, V. Barrow, O. Willi and S. Rose, Europhys. Lett. **11**, 631 (1990).
[2] J. Edwards, M. Dunne, D. Riley, R. Taylor, O. Willi and S. Rose, Phys. Rev. Lett. **67**, 3780 (1991)
[3] W. Schwanda and K Eidmann, Phys. Rev. Lett. **69**, 3507 (1992).
[4] S. J. Davidson *et al.*, Appl. Phys. Lett. **52**, 847 (1988)
[5] P. Springer *et al.*, Phys. Rev. Lett. **69**, 3735 (1992)
[6]L. Da Silva *et al.*, Phys. Rev. Lett. **69**, 438 (1992).
[7] J. Foster *et al.*, Phys. Rev. Lett. **67**, 3255 (1991).
[8] R. Sigel *et al.*, Phys. Rev. Lett. **65**, 587 (1990).
[9] J. Edwards, M. Dunne, O. Willi, C. A. Back and S. Rose, submitted to Phys. Rev. Lett.
[10] N.Kaiser, J. Meyer-teh-Vehn and R. Sigel, Phys. Fluids **B1**, 1747 (1989).
[11] M. Desselberger, T. Afshar-rad, F. Khattak, S. Viana, and O. Willi, Phys. Rev. Lett. **68**, 1539 (1992).
[12] R. Kodama *et al.*, Phys. Fluids B **3**, 735 (1991).
[13] J. Falconer, W. Golnazarians, M. Baker and D. Sutton, J. Vac. Sci. Technol. **A8**, 968 (1990).
[14] M. Desselberger, T. Afshar-rad, F. Khattak, S. Viana and O. Willi, Appl. Optics **30**, 2285 (1991); O. Willi, T. Afshar-rad, M. Desselberger, M. Dunne, J. Edwards, F. Khattak and R. Taylor, Rev. Scientific Instrum. **63**, 4818 (1992).
[15] S. Rose, J. Phys. B: **25**, 1667 (1992).
[16] P. D. Roberts, AWE report (unpublished, 1980).

STUDY OF THE RAYLEIGH-TAYLOR INSTABILITY IN LASER AND SOFT X-RAY DRIVEN TARGETS

T. Afshar-rad, M. Desselberger, M. Dunne, J. Edwards, R. Taylor and O. Willi

Imperial College of Science, Technology and Medicine, London.

The Rayleigh-Taylor hydrodynamic instability occurs in any accelerating fluid system in which the density and pressure gradients are of opposite sign. In the case of inertial confinement fusion experiments the hot, low density ablating plasma accelerates a cooler, more dense part of the target and thus this region is susceptible to the RT instability. In an ICF implosion, small imperfections in the target surface or intensity nonuniformities present in the laser irradiation may initiate the RT instability. At present the intensity nonuniformities in the laser beam focal spot profiles are the dominant sources as seed perturbations of the RT instability. The laser beam nonuniformities arise due to imperfections in the laser system and nonlinear processes occurring during amplification which cause the beam to incur phase and intensity nonuniformities. To combat this problem, a number of laser beam optical smoothing techniques have recently been proposed and implemented including induced spatial incoherence, Random Phase Plate Arrays and Smoothing by Spectral Dispersion.

The effects on the Rayleigh-Taylor instability and the secular target break-up were studied by using different illumination schemes including coherent, ISI/RPP smoothed green and soft X-ray radiation. The accelerated targets were diagnosed side-on using a high resolution XUV probing technique[1]. Side-on images with a probe wavelength of about 50 Å were obtained for various targets with modulation wavelengths between 20 and 50 μm. Figure 1 shows a series of images of targets which were irradiated with the three different illumination schemes.

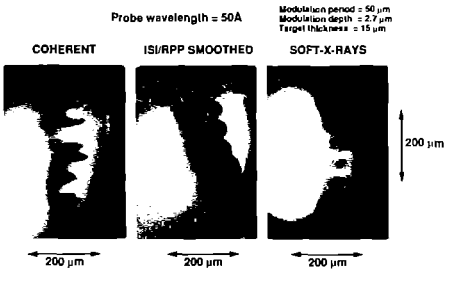

Figure 1. Side-on soft X-ray radiograms of premodulated CH foil targets driven by coherent, ISI/RPP smoothed laser beams and soft X-ray radiation. In each case, the frames were recorded 3ns after the start of the driving 1ns pulse.

Targets with a 50 μm periodicity were used for this study. As can be seen the target driven with coherent laser beams shows both RT growth and break-up caused by nonuniformities in the laser illumination. The target driven by RPP/ISI smoothed irradiation was accelerated more uniformly and clearly shows the bubble-and spike formations characteristic of the weakly nonlinear regime. It moved furthest at the centre of the beam where the laser intensity was highest. The third image taken of a target driven entirely uniformly by an intense soft X-ray pulse clearly shows target break-up caused solely by the RT instability. Again, bubble-and-spike formation is observed. Figure 2 shows a time-sequence of images taken of a target which had a modulation periodicity of 20 μm and a modulation depth of 1 μm. The target was driven by coherent laser radiation.

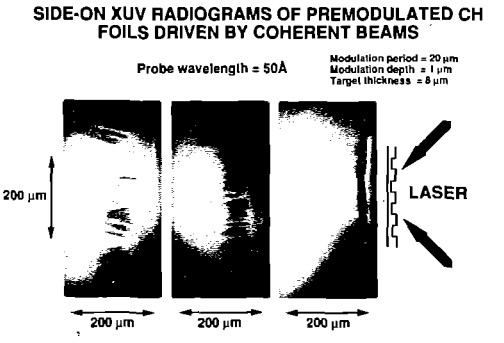

Figure 2. A time sequence of side-on soft X-ray radiograms of premodulated CH foil targets driven by coherent laser beams recorded at 1, 1.2 and 2ns after the laser pulse.

Again, a fascinating target break-up is seen after 3 ns which has never previously been observed. These measurements clearly show that break-up seen in targets driven by coherent laser beams may not only be due to the RT instability, but also due to laser-related effects.

Initial experimental results have also been obtained for thin foil targets with a modulation periodicity of 2.7 μm and with an initial amplitude of 0.2 μm The target was driven by ISI/RPP irradiation. Side-on images recorded 3ns after the start of a 2ns laser pulse show that the target is broken up into a jet-like stricture with wavelengths between 5 and 50 μm. The longer wavelengths are seen on the part of the target which is driven furthest caused by the most intense part of the laser beam (which had a gaussian spatial profile). Figure 3 shows a typical result.

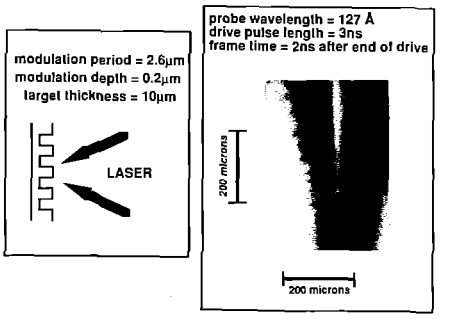

Figure 3. A side-on image of a target premodulated with a period of 2.6 μm, showing clearly a decrease in the scale of nonuniformities across the accelerated target.

Initial simulations were carried out with a 2D hydrodynamic code to interpret the experimental data. CH targets 10 μm in thickness were used in the simulations. A modulation periodicity of 10 μm with an amplitude of 1μm was imposed on the target surface. The targets was irradiated with a 2ns pulse at an irradiance of $5x10^{13}$ Wcm^{-2}. A nonuniform laser beam was used in the simulations with a modulation wavelength of 40 μm and an intensity variation of 3:1. Figure 4 shows two simulation results demonstrating the target break-up at two different times.

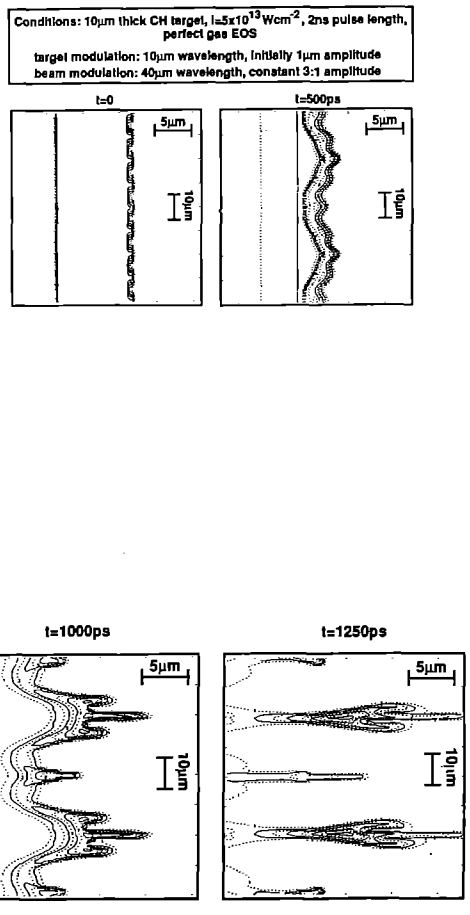

Figure 4. 2D hydrodynamic code simulations of a modulated target driven with a nonuniform laser beam.

REFERENCES

[1] M. Desselberger, T. Afshar-rad, F. Khattak, S. Viana and O. Willi, Appl. Optics 30, 2285 (1991); O. Willi, T. Afshar-rad, M. Desselberger, F. Khattak, and R. Taylor, Review of Scientific Instrum. 63, 4818 (1992).

PRODUCTION AND CHARACTERIZATION OF LONG-SCALE-LENGTH EXPANDING PLASMAS FOR ICF CORONAL STUDIES

L.A.Gizzi, T.Afshar-Rad[1], V.Biancalana, P.Chessa, C.Danson [2], A.Giulietti, D.Giulietti[3]
E.Schifano [4], S.M.Viana[1], O.Willi [1].

Istituto di Fisica Atomica e Molecolare via del Giardino, 7 - 56127 Pisa, Italy.

[1] The Blackett Laboratory, Imperial College of Science, Technology and Medicine, London, UK.
[2] Central Laser Facility, Rutherford Appleton Laboratory, Chilton, Didcot, UK.
[3]Dipartimento di Fisica, Università di Pisa
[4] Laboratoire pour l'Utilization des Lasers Intenses, Ecole Polytechnique, Palaiseau, France.

INTRODUCTION

Interaction of high power laser light with long scale-length preformed plasmas offers the possibility of study under controlled conditions the physics involved in Inertial Confinement Fusion (ICF) experiments as well as in other fields of laser-plasma interaction. However very recently more attention is being devoted to the problem of characterization of test plasmas used in this studies. In fact an incomplete knowledge of background plasma conditions is regarded as a strongly limiting factor in the study of interaction phenomena.

EXPERIMENTAL SET-UP

The long-scale-length plasma experiment described here was performed at the SERC Central Laser Facility. The main features of the experimental set-up are shown in the layout of Fig.1. Four 600 ps, 1.053 μm beams of the Vulcan laser were used to preform the plasma.

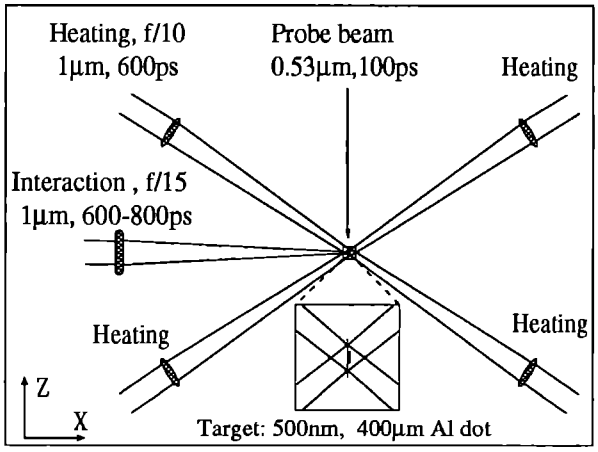

Fig.1 Schematic of the experimental set-up showing laser beams configuration with respect to the target. The interaction beam was delayed by typically 2.5ns with respect to the four heating beams.

These heating beams were focused f/10 in two opposite pairs and superimposed on target in a 600 μm spot providing a total irradiance of typically 6×10^{13}W/cm^2. Targets consisted of 400 μm diameter Aluminium dots coated onto 1000Å plastic stripes. A fifth interaction beam was delayed typically by 2.5ns and focused f/15 onto the underdense preformed plasma along the target symmetry axis at an irradiance ranging from 10^{13} to 5×10^{14} W/cm^2 This beam was either unsmoothed or smoothed with three different devices, namely random phase plates (RPP), induced spatial incoherence (ISI) , spectral dispersion (SSD).

Both narrow-band (0.5 Å) and broad-band (13Å) laser regimes were tested. Specially designed controlled phase plates (CPP) were used on the interaction beam in order to induce controlled intensity modulations in the focal region of the interaction beam. A sixth 100 ps beam was frequency doubled, delayed and used as a probe for interferometric measurements. A seventh 600 ps beam was also frequency doubled and used as a wavelength fiducial for second harmonic time resolved spectroscopy.

Time-resolved X-ray spectroscopy of K-shell Al emission was employed in order to characterize the plasma in terms of electron temperature evolution before and during the interaction. Electron density was measured by means of a polarization interferometer. Abel inversion of the pattern allowed the transverse scale-length of the plasma to be measured, while the longitudinal scale-length was estimated from the pattern directly. Results obtained by the study of second harmonic emission and stimulated Brillouin scattering data will be reported elsewhere[1]

HYDRODYNAMIC MODELLING

A preliminary design of the experiment was done on the basis of a 1-D self-similar model of plasma expansion from laser irradiated foil targets[2]. The density profile predicted for a 0.5 μm thick Al foil heated at 6×10^{13}W/cm^2, 3ns after heating, has a maximum of 1.4×10^{20}cm^{-3}. The longitudinal density scale-length is about 1mm, suggesting that the initial 1-D expansion suffers 2-D effects. The expected electron temperature is approximately 1KeV.

Plasma production and heating has also been studied numerically by means of the 1-D Lagrangian hydro-code MEDUSA[3]. Thermal conductivity is modelled in terms of the classical Spitzer conductivity with the electron thermal flux limited for high temperature gradients to a given fraction of the free-streeming limit. Laser light is absorbed by the plasma via inverse Bremsstrahlung absorption and resonance absorption. If we neglect the thin plastic substrate of our targets, the heating scheme is symmetric respect to the Al layer which is irradiated by both sides. Simulation has been performed using a single side irradiating scheme, fixing the target boundary opposite to the laser and scaling target thickness and laser intensity by a factor of two.

TEMPERATURE MEASUREMENTS

X-ray time resolved spectroscopy of K-shell Al emission was used as diagnostic tool for measurements of plasma electron temperature during heating and interaction. An X-ray spectrometer, consisting of a flat TlAP crystal ($2d$ = 25.9Å) was set in a first order Bragg configuration in order to spectrally resolve X-ray radiation emitted from the plasma. An intensified low-magnification X-ray streak-camera, fitted with a CsI photocathode, was coupled to the spectrometer. A spectral region from approximately 5.5Å to 6.8Å was selected in order to study resonance line emission from He-like and H-like Aluminium. The analysis of such spectra relies on the dependence of line intensity ratios between H-like lines and He-like lines on

electron temperature. The comparison of measured line ratios with predictions of a steady state atomic physics numerical code RATION[4], for a given temperature and density, allows electron temperature to be estimated.

Fig.2(a) shows a typical time-resolved spectrum obtained in standard heating conditions. Fig.2(b) shows a 1D trace taken 500ps after the peak of emission of the spectrum of Fig2(a) and integrated over approximately 100ps, which is the temporal resolution of the spectrum.

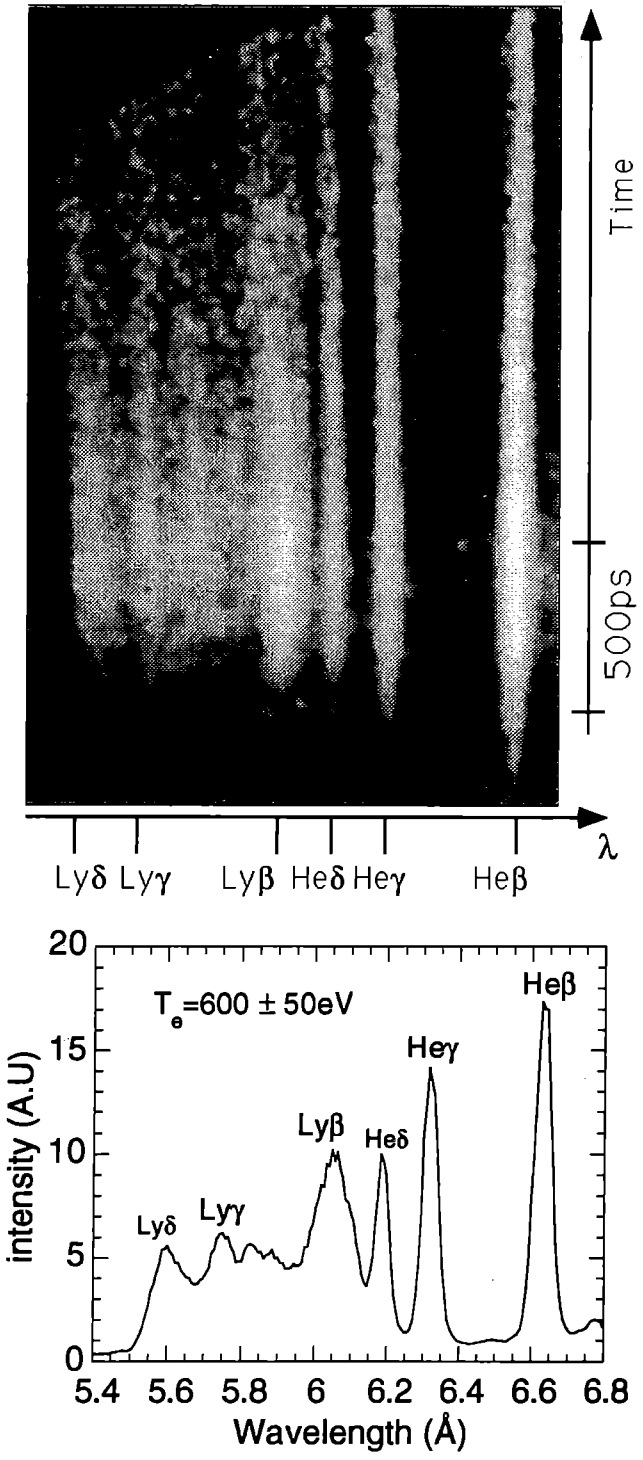

Fig.2(a) Time resolved X-ray spectrum of K-shell Al emission from plasma heated at an irradiance of $6 \times 10^{13} W/cm^2$. **(b)** Lineout of spectrum of Fig.2(a) taken 500ps after the peak of heating pulse.

Emission lines from Heβ to Lyδ are clearly visible with Lyγ and Lyδ emerging from the He-like continuum; Heε is just visible as a shoulder-like feature on the long wavelength side of the Lyβ line. Since no slit was used on the spectrometer the spectral resolution is basically due to the size of the emitting region. Line intensity profiles were found to be well fitted using gaussian profiles with 30mÅ±10% FWHM.

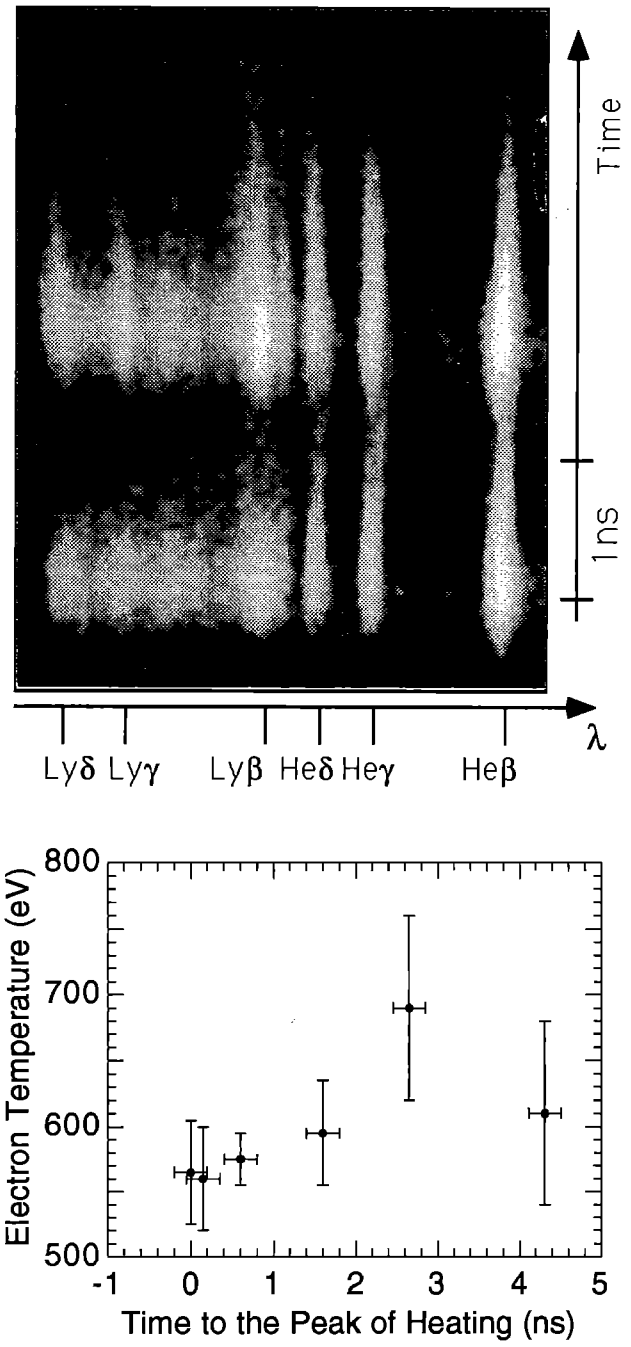

Fig.3(a) X-ray time-resolved spectrum of K-shell Al emission. The interaction beam reached the plasma approximately 2.5ns after the heating pulse. **(b)** Temporal history of plasma electron temperature obtained from the X-ray spectrum of Fig.3(a).

Except Heε and Lyβ, all remaining lines are well resolved and it is therefore relatively easy to determine line background level. With the available spectral resolution

Heε and Lyβ line are found to be merged with higher quantum number He-like lines and with the He-like continuum edge. Intensity ratios of γ and δ lines of Fig.2(b) consistently give an electron temperature of 600eV, while Lyβ to Heβ intensity ratio tends to give slightly higher temperature, as Lyβ intensity is likely to be overestimated. In the shot of Fig.3(a) both heating and interaction were on. The effect of the interaction beam on the X-ray emission is clearly visible as an increase of emission intensity after the initial peak due to heating pulses. Fig.3(b) reports the temperature vs time obtained from the spectrum of Fig.3(a).

DENSITY MEASUREMENTS

A number of interferograms were obtained with the green probe beam crossing the plasma perpendicularly to the plane where heating and interaction beams are located.

A polarization interferometry[5] was employed to measure electron density. Such device gives two partially overlapped interferential patterns, corresponding to two orthogonal polarization components of the probe beam. The imaging system of the interferometer also produces two time integrated images of the interaction region at the same wavelength as the probe beam.

Fig4(a) shows a typical interferogram of the preformed plasma taken 3ns after the peak of the heating pulses. Plasma shape is quite regular and shows symmetry around the interaction axis. The interaction beam was switched off in this case. The original position of the target is marked by the two dark lines. A minor fraction of energy in the tail of the focal spot distribution of the heating beams hits the edges of the target holder producing a tenuous plasma which affects fringe position in the region away from the denser Al plasma. Consequently plasma density in this central region may result underestimated.

Fig.4(b) gives the electron density profile at 220μm from the target on the side of the interaction beam as function of distance from the x axis described above. It can be seen that at this distance transverse plasma size slightly exceeds the original target diameter.

Abel inversion was used in order to deconvolve phase information given by interferometric pattern. Fig.4(c) shows the electron density profile along the symmetry axis, namely the x axis, versus the distance from the original target plane. We observe that the denser plasma region extends along the x axis over a distance of the order of the original Al dot diameter while a lower density plasma (10^{18} cm^{-3}) fills a millimetre sized region.

Fringe visibility in Fig.4(a) goes to zero for distances from the target less than 220μm due to hydrodynamic plasma expansion during the probe pulse. In order to estimate density profile along the interaction axis up to the original target plane we considered interferograms taken at a later time when hydrodynamic velocity and density of the plasma are smaller and fringes are less perturbed. The interferogram of Fig.5(a) was taken 4.3ns after the peak of heating pulses and the resulting electron density longitudinal profile is plotted in Fig.5(b).

Assuming a 1-D plasma behaviour for distances from the target smaller than the transverse plasma size, 1-D simulation can be employed to extend the electron density profile of Fig.4(c) to distances smaller that 220μm. We find that the peak electron density relative to 3ns (Fig.4(c)) is approximately 10^{20} cm^{-3}.

Let's now briefly consider the effect of interaction beam on the preformed plasma as observed by the same interferometric channel. In Fig.6(a) the interaction pulse

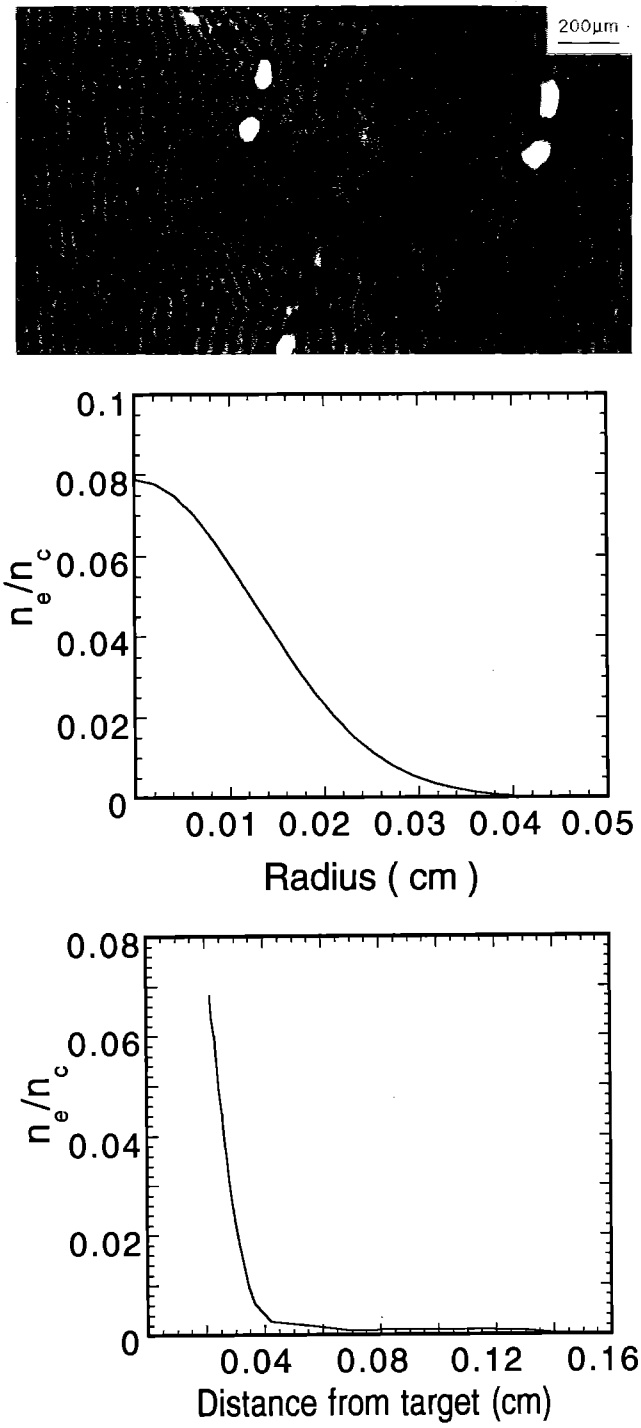

Fig.4(a) Interferogram of preformed plasma (top) taken 3ns after the peak of the heating pulses. Original target position is shown by the two dark lines. **(b)** Radial electron density profile (middle) at 220μm away from the target and **(c)** longitudinal electron density profile (bottom) along the plasma symmetry axis.

and the green probe pulse were timed to reach the plasma respectively 2.5ns and 3ns after the peak of the heating pulses. Bright 2ω emission is clearly visible at a distance of approximately 150μm from the original position of the target, on both sides, were plasma density gradients are expected to be important.

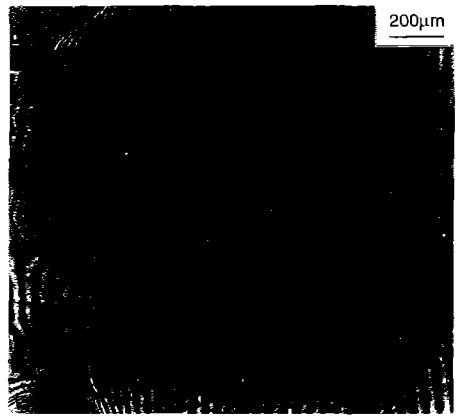

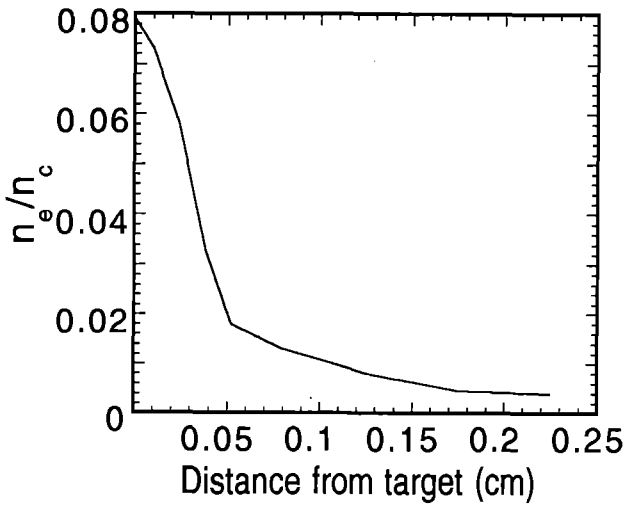

Fig.5(a) Interferogram of preformed plasma (top) taken 4.3ns after the peak of heating pulses. **(b)** Longitudinal electron density profile along the plasma symmetry axis.

The transverse size of the 2ω emitting regions is approximately 100μm, which is the diameter of the interaction beam focal spot. Emission of 2ω light on the interaction beam input side is much more intense than emission on the output side. This can be attributed to absorption of laser energy by inverse bremsstrahlung, which leads to depletion of interaction beam energy and consequent reduction of 2ω emission. We notice that one of the two twin images of the 2ω emission is much more intense than the other. Taking in account that the interferometer gives two orthogonally polarized images this result could be explained assuming that the observed 2ω emission at 90° is partially polarized. Also visible outside the higher density region on the rear side of the target there is a perturbation in the fringe position which extends up to the limit of the observed region and is typical of a channel-like density depletion.

Finally Fig.6(b) shows an interferogram obtained in similar conditions as that of Fig.6(a), except that the interaction beam focusing lens was tilted in order to obtain a focal spot elongated along the line of sight of the interferometer imaging system.

In this case filament-like structures of ≈10μm diameter can be clearly distinguished in the 2ω emitting region. The ring-like region of fringe perturbation, which surrounds the central higher density region, is still under investigation. However we believe it is due to interaction of the main expanding Al plasma with the tenuous plasma originating from marginal heating of target support.

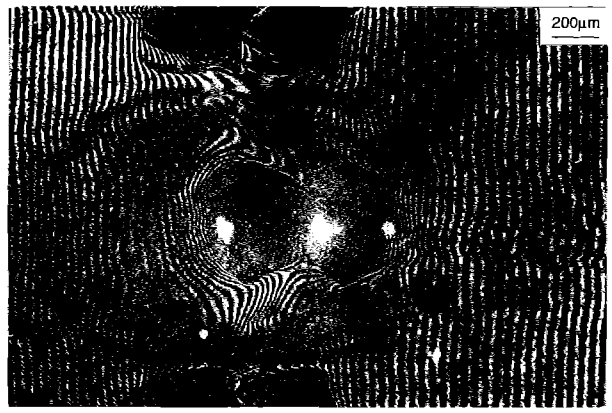

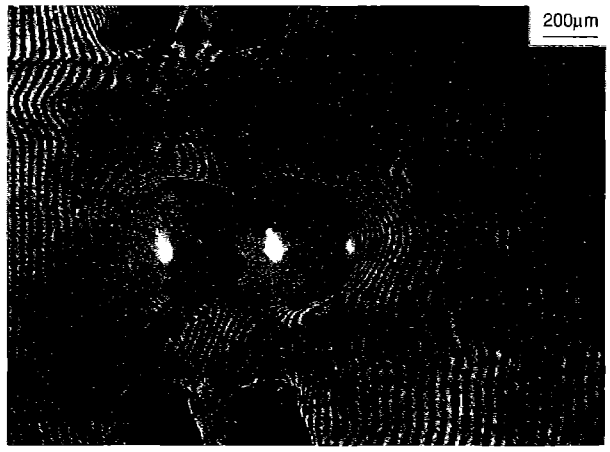

Fig.6 (a) Interferogram of the plasma (top) with interaction and probe pulses delayed respectively by 2.5ns and 3ns respect to the heating pulses; (b) same as Fig.6(a) but with interaction and probe pulses delayed respectively by 2ns and 2.5ns. The interaction beam focusing lens was tilted in order to obtain an elongated focal spot in the line of sight of the interferometer imaging system.

REFERENCES

[1] A. Giulietti, T.Afshar-Rad, V.Biancalana, P.Chessa, C.Danson, D.Giulietti, L.A.Gizzi, E.Schifano, S.M.Viana, O.Willi, this report.

[2] R. A. London, M. D. Rosen, Phys. Fluids, **29**, 3813 (1986).

[3] J. P. Christiansen, D. E. Ashby, K. V. Roberts, Computer Phys. Comm. **7**, 271 (1974); P. A. Rodgers, A. M. Rogoyski, S. J. Rose, RAL Report,RAL-89-127 (1989)

[4] R. W. Lee, L. Whitten, R. E. Stout II, J. Quant. Spectr. Rad. Transfer **32**, 91 (1984).

[5] O. Willi, in Laser-Plasma Interaction 4, Proceedings of XXXV SUSSP, St. Andrews, 1988.

PLASMA INTERACTION WITH SMOOTHED OR MODULATED LASER BEAMS DIAGNOSED BY 2ω EMISSION AND BACKSCATTERING

A Giulietti, T Afshar-rad, V Biancalana, P Chessa, C Danson[1], D Giulietti[2], L A Gizzi, E Schifano[3], S M Viana[4] and O Willi[4]

Istituto di Fisica Atomica e Molecolare, Via del Giardino,7 Pisa, Italy
[1] SERC Central Laser Facility
[2] also at Dipartimento di Fisica, Università di Pisa
[3] also at LULI, Ecole Polytechnique, Palaiseau, France.
[4] The Blackett Laboratory, Imperial College, London.

INTRODUCTION

Laser interaction with preformed plasmas is a powerful technique to investigate coronal instabilities of interest for laser fusion. A series of experiments has been performed at CLF since 1986 using line-focused beams to preform homogeneous plasmas with negligible motion along the interaction axis[1].

This new experiment was designed to study interaction with an expanding plasma whose transverse scalelength is larger than the interaction beam spot in order to avoid refractive effects. We succeeded in characterize the plasma both in density profile and temperature[2], thus providing a reliable background to interpret the interaction data. Most of the diagnostic means were based on second harmonic (SH) detected both forward and sidewards, extending methods already experienced at IFAM at lower irradiance[3]. A further diagnostic was supplied by time resolved spectroscopy of backscattered light. In this configuration we tested the effect on interaction of phase plates designed using an original code[4] and made at CLF. Both controlled and random phase plates have been used to modulate or smooth the interaction beam respectively. Other smoothing techniques have been also tested in a limited number of shots, including broad band operation with ISI or SSD devices.

Some two hundred laser shots were successfully fired on target. In this paper we partially report on data obtained from interaction and shortly discuss some of them.

SET-UP

The experiment was performed in TAE using two pairs of opposite beams (heating beams) from Vulcan, 600 ps, 1.053μm. They were focused in a 600 μm spot at a total irradiance of typically 6 10^{13} W/cm^2 to produce the plasma. Typical target consisted of 400 μm diameter, 500 nm Al dot coated on 100 nm plastic stripe, unless differently specified in the text. A fifth (interaction) beam was delayed by 2.5 ns and focused f/5 in a spot of 120 μm at an irradiance from 10^{13} W/cm^2 to 5 10^{14} W/cm^2. Further details on beam configuration and probe optics for interferometric measurements can be found in another paper[2] of this Report. Beside X-ray diagnostics and interferometry, three other detection channels were activated. A forward channel provided alternatively time resolved spectra of SH or time resolved images of SH sources. A sidewards channel provided time resolved spectra of SH emitted at 90°. Time integrated 2ω images were also obtained sidewards by the probe optics. Finally a backward channel provided time resolved spectra of laser backscattered light.

STUDY OF SECOND HARMONIC EMISSION

The probe channel supplied very important information on location and distribution of 2ω sources. We obtained time integrated images, some superimposed to the probe fringe pattern allowing to locate exactly the source of emission in the density profile, some other with probe off giving maximum contrast. The right portion of Fig 1 shows the sidewards SH emission from the triple spot obtained by a stripe phase plate[5]. In this case the interaction beam was focused directly on Al thick target. The 2ω image is compared with both simulation of the spot by FT code[4] and equivalent plane imaging of the phase modulated laser spot at fundamental frequency. The overall agreement is quite good. The 2ω image shows also details due to the interaction with the plasma and the mechanism of harmonic generation. In particular this kind of images generally showed that each source has maximum emissivity at its boundary where gradients are located, as expected from theory.

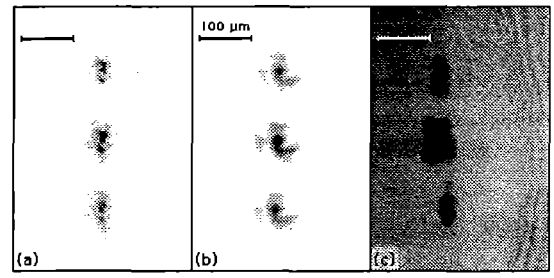

Fig 1 Effects of stripe phase plate on the focal spot of the interaction beam. From left to right: simulation of the intensity distribution in the focal plane by FT code; equivalent focal plane imaging of the same beam at laser frequency; side image of SH sources from interaction of the phase modulated beam with Al thick target.

In the case of interaction with preformed plasmas it is very important to know the location of 2ω sources. This information was provided by probe pictures with both source images and fringe pattern as reproduced in another paper[2] of this Report (Figs 6a and 6b of that paper). The fringe pattern evidences that the SH is mostly generated in a well confined spot located at the crossing between the boundary of the high density region and a channel of lower plasma density produced by the interaction beam. This is the place where both longitudinal and transverse gradients are maxima. An intense spot of 2ω is always visible at the laser side of the dense region with dimension comparable with the interaction beam spot. The spot is very often structured in filaments as shown in Fig 6b of that paper[2] where filaments of few microns diameter and less than 100 microns length are clearly visible. No SH is visible from the bulk of the dense region, while a weaker 2ω spot is sometime visible at the exit boundary of the dense region. No SH was visible sidewards from heating beams.

Time resolved spectra of side emitted SH have been obtained with an optical streak camera coupled with a 1/2 m spectrometer. Two typical results obtained by interaction with preformed plasma are shown in Fig 2. Some features showed clear reproducibility, namely the signal duration which is generally shorter than the interaction pulse, the spectral shift which is toward the red increasing in time up to some 4Å, the spectral width also resulted to increase to comparable values. Bi targets gave generally more structured spectra, with both spectral and temporal modulations, if compared to the Al targets. Similar spectra have previously been observed[2,6] and a model[7] have been proposed for the emission mechanism, tak-

ing into account non-linear coupling of forward and backward propagating radiation. In this experiment no clear evidence was shown for such a mechanism. This is not surprising because we know from images discussed above that SH is emitted from well definite regions at the boundary of the dense region. On the contrary there are indications that SBS originates in the low density tail of the expanding plasma (see below).

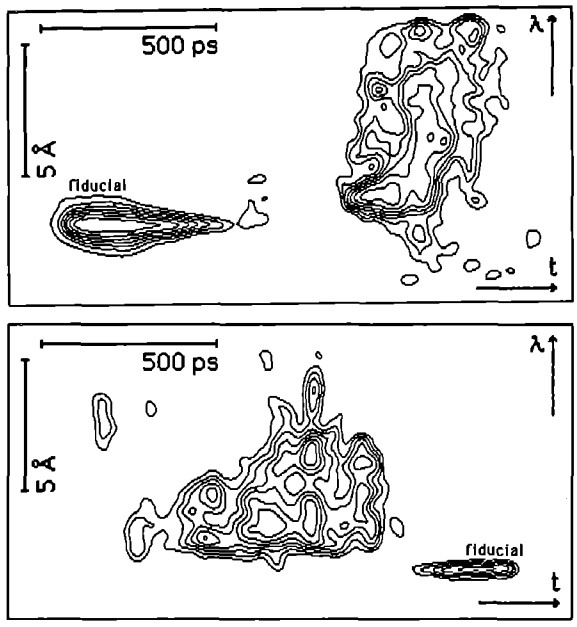

Fig 2 Time resolved spectra of SH emitted sidewards during interaction.
Top: 500nm Al dot target, heating irradiance 6 10^{13} W/cm^2, interaction 5 10^{14} W/cm^2.
Bottom: 120nm Bi dot target, heating irradiance 6 10^{13} W/cm^2, interaction 5 10^{14} W/cm^2.
In both cases the interaction pulse was delayed 2.5 ns.

Time resolved spectra of forward emitted SH were also obtained with preformed plasmas. The duration of emission was considerably shorter than the laser pulse duration. Red shift of few Å, lower than for side-emitted SH, was observed. One of those spectra is shown in Fig 3. In the second part of the experiment the forward SH channel was used to take time resolved images. Among a number of interesting pictures, Fig 4 shows two cases: left hand pictures refers to the beam modulated as in Fig 1 and interacting with the preformed plasma. The SH emission is earlier and stronger at the plasma boundary, later on SH "burns through" the plasma bulk where the central spot is located. Right hand picture was obtained in the same interaction condition but with broadband beam smoothed with RPP. It is relevant that in this case SH is produced by small sources with very short bursts.

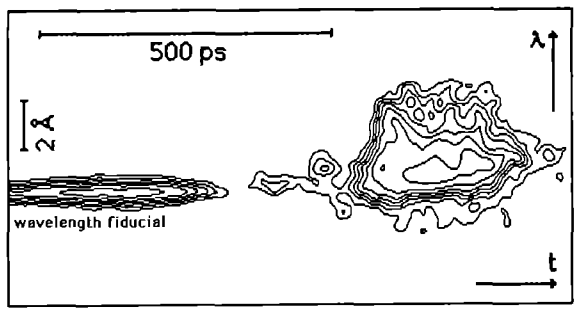

Fig 3 Time resolved spectrum of SH emitted forward during interaction. 500nm Al dot target, heating irradiance 6 10^{13} W/cm^2, interaction 5 10^{14}W/cm^2. Interaction pulse was delayed by 2.5 ns.

STUDY OF BACKSCATTERED LIGHT

Time resolved spectra of backscattered light were obtained with a 1m spectrometer coupled with an S1 streak-camera. Some reference spectra were taken by directly irradiating targets with the interaction beam only (Fig 5 left). They typically spread over some 20 Å moving in time from the blue to the red side with respect to the laser wavelength. There is some similarity with spectra recently obtained[8] and it is possible that dense region including $n_c/4$ layer could play an important role in exciting ion-acoustic waves.

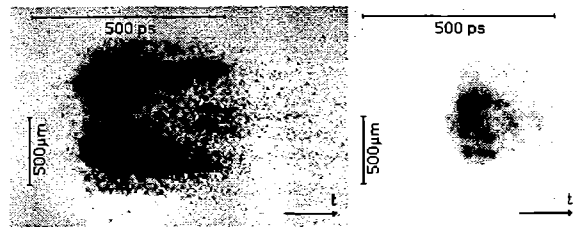

Fig 4 Time resolved images of SH emitted forward during interaction.
Left: 500 nm Al dot target, heating irradiance 9 10^{13} W/cm^2, interaction 10^{14} W/cm^2;
the interaction beam was modulated in three spots as in Fig 1 and delayed 2.5 ns.
Right: 500 nm Al dot target, heating irradiance 7 10^{13} w/cm^2, interaction 10^{14} W/cm^2;
the interaction beam was 150 mm apodized, broad band, RPP smoothed.

With preformed plasma, we obtained 25 spectra showing interesting features very reproducible shot-by-shot. A typical spectrum is shown in Fig 5 right. Two temporally separated phases with different spectral behaviour can be noticed. First, a short flash is emitted in a broad band of more than 30 Å, more extended in the blue side than in the red one. A second emission follows in time: it is narrow-band and shifts quite regularly from the red to the blue side of the spectrum. A possible explanation of these novel spectra can be given in terms of the ordinary theory of Stimulated Brillouin Scattering. The background of the interpretative model is shown in Fig 6.

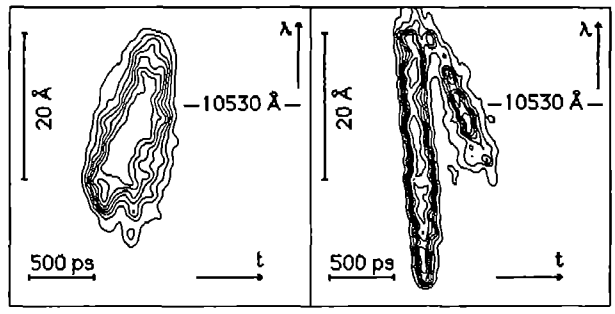

Fig 5 Time resolved spectra of light backscattered during interaction.
Left: 500nm Al dot target, no preformed plasma, interaction 4 10^{14} W/cm^2.
Right: 500nm Al dot target, heating irradiance 5 10^{13} W/cm^2, interaction 4 10^{14} W/cm^2; the interaction pulse was delayed 2.5 ns.

The relative red shift of the backscattered light is expected to be $(2/c)(v_s + v_f)$ where v_s is the ion-sound velocity and v_f is the flow velocity which is positive in the direction of propagation of the laser beam. The absolute value of v_f is expected to increase, along the laser beam, about linearly with distance from the original target position, i.e. the maximum plasma density position. In a plasma or plasma region where

$v_s >> v_f$, the red shift is simply proportional to v_s. In an expanding plasma as we have, three regions can be identified in terms of shift: the subsonic region where $v_f < 0$ and $v_s > v_f$ and the region beyond the target plane where $v_f > 0$ both give red shift increasing with distance from the first sonic layer (from where unshifted back-scattering originates); on the contrary, the supersonic region where $v_f < -v_s$ gives blue shifted backscattered light.

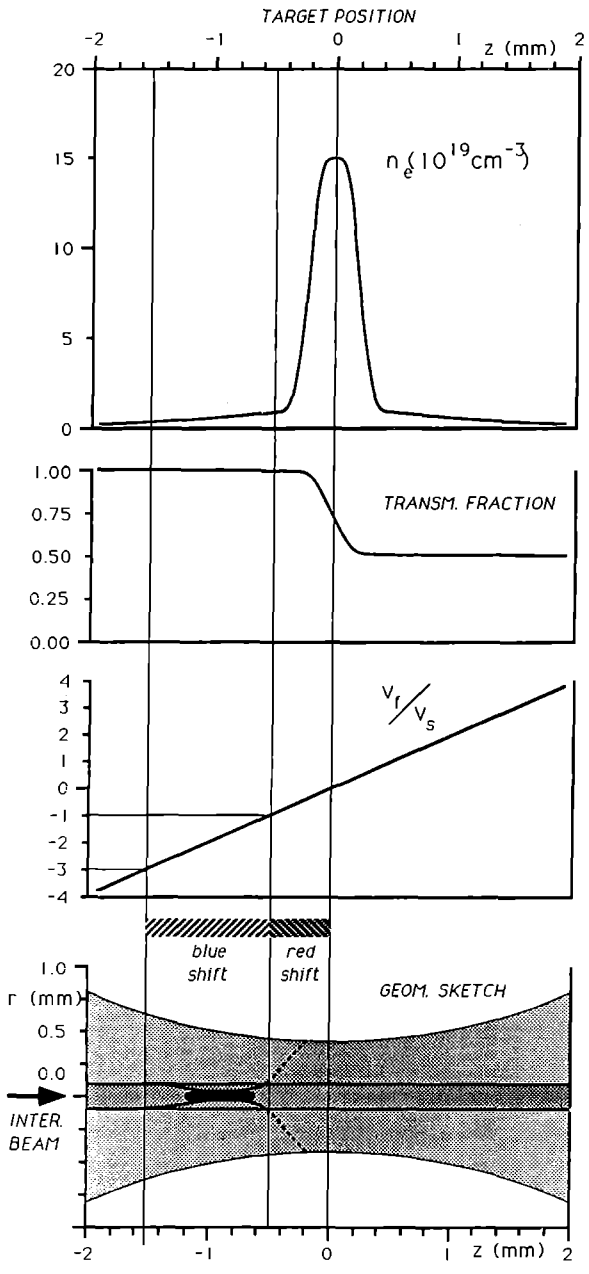

Fig 6 Elements for an explanation of SBS spectra from expanding preformed plasma (as in Fig 5 right). From top to bottom: plasma density profile at the beginning of interaction (2 ns after heating pulse peak) extrapolated from interferometric data; transmitted fraction of laser light at 2 ns; ratio between flow and sound velocities at 2 ns (T_e= 600 eV; configuration of the interaction region with the unperturbed laser beam penetrating the plasma and possible self-focusing effect.

Following this simple scheme and considering the electron temperature measured at the beginning of interaction and later on[2], we found that the initial broad-band flash (Fig 5 right) originates between the layer with $v_f \approx 0$ and a layer with $v_f \approx -3\ v_s$. In the second phase of scattering the involved plasma region is much narrower and moves regularly from the $v_f \approx 0$ layer to the $v_f \approx -1.5\ v_s$ layer. In terms of length it means that more than 1 mm of plasma is involved in the backscattering process initially. In terms of density, because of the strong deviation from the 1-D expansion observed at distance >0.5 mm from the target[2], it means that the region involved in the backscattering process is mostly at very low density, down to few units of 10^{18} cm^{-3}.

The physical meaning of this interpretation is that the interaction beam initially stimulates Brillouin scattering in a large region of the plasma up to the the high density peak where the short scalelength inhibits the parametric coupling and do not allow the beam to penetrate uniformly the region beyond, due to both absorption (estimated of about 50%, see Fig 6) and refraction. Suddenly, as a consequence of the local heating of the plasma, the beam suffers a self-focusing process with a growth-time of the order of 100 ps. This process decouples the beam from the whole plasma region and restricts the scattering region to the reduced beam waist which moves backward from the original lens focus due to the effect of the increasing optical power of the perturbed density profile. At the same time this "additional variable lens" just allowed the backscattered light coming from the moving waist to be collected in the backward channel of the experiment.

In conclusion we obtained a great number of data on interaction of powerful laser beams with coronal plasmas in a variety of conditions providing a coherent set of information on the physics involved.

We are very grateful to all the CLF staff members for their invaluable and enthusiastic support. This work was possible thanks to the European Community funding (under Contract GE1*-CT91 - 0034).

REFERENCES

1. O.Willi, T.Afshar-rad, S.Coe and A.Giulietti; Phys.Fluids B **2**, 1318 (1990)
2. L.A.Gizzi, T.Afshar-rad, V.Biancalana, P.Chessa, C.Danson, A.Giulietti, D.Giulietti, E.Schifano, S.M.Viana and O.Willi; "Production and characterization of long-scalelength expanding plasmas for ICF coronal studies" in this Report (1993)
3. A.Giulietti, D.Giulietti, D.Batani, V.Biancalana, L.A.Gizzi, L.Nocera and E.Schifano; Phys.Rev.Lett. **63**, 524 (1989)
4. V.Biancalana and P.Chessa; to be published in Applied Optics (1993)
5. V.Biancalana, P.Chessa, C.Danson, D.Pepler; in this Report (1993)
6. E.Schifano, S.Baton, C.Labaune, T.Jalinaud, V.Biancalana and D.Giulietti; Rapp.Scient. LULI-Ec.Pol. (Palaiseau France 1991)
7. J.A.Stamper, R.H.Lehmberg, A.Schmitt, M.J.Herbst, F.C.Young, J.H.Gardner, S.P.Obenschain; Phys. of Fluids **28**, 2563 (1985)
8. P E Young, H A Baldis and K G Estabrook, Phys.Fluids B **3**, 1245 (1991)

MEASUREMENTS OF MOTIONAL DOPPLER SHIFTS IN X-RAYS EMITTED BY LASER-PRODUCED-PLASMAS

J.S. Wark,[1] H. He,[1] O.Renner,[2] M. Kopecky´,[2] E. Förster,[3] T. Mißalla[3]

[1]Department of Physics, Clarendon Laboratory, University of Oxford, Oxford OX1 3PU, UK

[2]Institute of Physics, Czech Academy of Sciences, 18040 Prague, Czechoslovakia

[3]X-ray Optics Group of Max-Planck-Gesellschaft at Friedrich-Schiller-University, D-O-6900-Jena, FRG

INTRODUCTION

A knowledge of the degree of the motional Doppler shift of x-rays emitted by laser-produced-plasmas is useful for estimating the degree of radiation trapping in x-ray lasers, as well as being of import in simple photopumping studies and fundamental aspects of radiation transport. Although the velocity of the emitting ions has been studied in the past, most of these previous experiments have hitherto been limited to the XUV regime.[1,2] This restriction to relatively long wavelengths has largely been due to the poor resolution of Bragg crystal spectrometers compared to grating instruments, and associated difficulties in wavelength calibration. The ultimate spectral resolution given by the diffractive properties of the crystals used is reasonably high, however the real resolution of the spectrometers is limited by purely geometrical factors. Thus an extension of these Doppler shift measurements to shorter wavelength would complement existing studies of laser-plasma interactions. We present here measurements of Doppler shifts in laser-produced-plasmas in the x-ray regime obtained by use of a novel high resolution, high dispersion x-ray spectrometer.[3-5]

THE DOUBLE CRYSTAL SPECTROMETER

Typical ion velocities in the corona of a laser-produced plasma easily reach several times 10^7 cm s^{-1}. Thus for accurate Doppler shift measurements we may need to resolve velocities of order 5 x 10^6 cm s^{-1}. This in turn means that we need spectral resolutions of 6000, along with a reference wavelength. Such resolutions are high by the normal standard of Bragg crystal spectrometers used in laser-plasma experiments.

The measurements described here were obtained by use of a novel vertical dispersion variant of the double crystal spectrometer (DCS). The DCS, described in detail elsewhere,[3-5] is a two crystal instrument with extremely high spectral resolution and dispersion, similar to that of a conventional single crystal instrument operating extremely close to a Bragg angle of $\pi/2$.

To illustrate the resolution possible using such a high dispersion instrument, we have performed ray tracing calculations to determine the spectral resolutions available for a variety of source sizes, and compared these results with the resolution that would be achieved using a single-crystal spectrometer. In all the calculations, both for single-crystal and DCS, we have used Ammonium Dihydrogen Phosphate (ADP) (101) crystals ($2d$ = 10.64 Å), and assumed an x-ray wavelength, for illustrative purposes, of 7.17 Å (the Ly-α line of hydrogenic aluminum). The ultimate resolution that can be achieved with a single crystal at this wavelength, as determined by the rocking curve limit, is 11,600. For the DCS calculations we assumed a total source-to-detector distance of 10 cm, as used in the experiments described below. The results are shown in Fig. 1. We have plotted the resolution as a function of distance on the film and wavelength for three source sizes. For a 50 µm source it can be seen that theDCS resolution exceeds the ultimate resolution possible using a single crystal instrument. This is because, for such a small source the DCS is approaching its own ultimate resolution limit, which is determined by the convolution of the two rocking curves of the two separate diffracting crystals. It is this convolution that results in the composite rocking curve of the DCS being narrower than that of one crystal alone, and thus an increased resolution above the single-crystal limit.

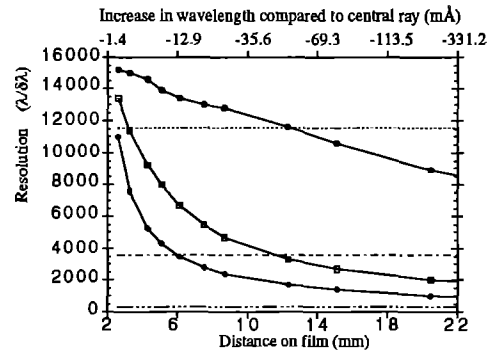

Fig. 1. Resolution of the double crystal spectrometer as a function of distance on film from the centre of symmetry. Also shown is the corresponding deviation in wavelength from that of the central ray. Open circles - 50 µm x 50 µm source, open squares - 250 µm x 250 µm source, open diamonds - 500 µm x 500 µm source. Dashed line - single crystal rocking-curve limit. Dot-dashed line - single crystal 1 m from the 250 µm x 250 µm source. Triple-dot-dashed line - single crystal 10 cm from the 250 µm x 250 µm source.

For larger source sizes the degradation of resolution due to source broadening starts to become apparent as the angle φ increases (and thus the dispersion starts to fall). However, for a 250 µm source the resolution still exceeds 3000 upto 65 mÅ away from the central wavelength λ_0. This spectral range is usually more than sufficient to record a single line (which is the mode in which this instrument is usually operated, due to the extreme dispersion). This performance should be compared with that of a single-crystal spectrometer. In this case, for a 250 µm source, a resolution of a mere 300 is achieved if the source-to-detector distance is kept at 10 cm as in the DCS case. Indeed, the instrument must be removed by a large distance (~1 m) to obtain resolutions comparable to the DCS. In addition, a reference point in the spectrum is not easily available in the single crystal case, whereas for the DCS any shift in wavelength is readily observable, as the central point in the spectrum, λ_0, is defined by the angle between the two crystals.

The DCS also affords a degree of spatial resolution in a direction perpendicular to the dispersion plane of approximately the double-crystal rocking-curve width multiplied by the distance from the source to the detector, i.e 6 µm for the above specified experimental parameters. More detailed information about the

theory and performance of the instrument can be found in the work of Renner.[4,5]

EXPERIMENT

Previous preliminary experiments using the instrument showed that spectra could be recorded by integrating approximately 20 3 J, 1 ns (FWHM), 1.05 μm laser shots.[6] We thus expected to be able to record single shot spectra with laser energies of order 100 J. A single beam containing 80 J of 0.53 μm light in a pulse of 1.2 ns (FWHM) was incident normally onto a 10 μm thick 500 μm diameter aluminum foil. The focal spot diameter on target was varied between 350 and 75 μm, giving a range of incident intensities of 7×10^{13} to 1.5×10^{15} W cm^{-2}.

The DCS was fitted with two ADP crystals ($2d$ = 10.64 Å). The angle between the two crystals was set so that the x-ray line of interest would be recorded on film. The DCS was mounted on a rotation stage whose axis of rotation was aligned with the centre of the aluminum foil. The axis of rotation of the DCS and the target were measured to be coincident within ± 30 μm using a helium-neon alignment system. The line shifts were measured in the following way. A series of laser shots were taken with a given laser energy and focal spot size. For each shot in the series, the angle between the DCS and the incident laser was varied by rotating the instrument around the axis containing the target. For each shot the x-ray film holder of the DCS was moved transversely by approximately 2 mm, keeping the total target to film distance constant. The data were recorded on Kodak Industrex-C x-ray film.

RESULTS

In Fig. 2 we show the spectra recorded from Al Ly-α ($1s\ ^2S$ - $2p\ ^2P$) for various angles of observation with respect to the target normal. For all six shots recorded here the spot size was kept constant at a diameter of 160 μm, and the incident energy of 0.53 μm light was 80 J, giving rise to an incident irradiance of 3×10^{14} W cm^{-2}. The variation in laser energy over the shot series was measured to be less than ± 10 %. It can be seen that as the emission is viewed from larger angles with respect to the target normal there is an increase in the wavelength of the peak of the emission consistent with Doppler motion away from the target. For the two spectra recorded at 150° and 180° to the target normal (the latter corresponding to the instrument viewing directly through the target towards the laser beam), the 10 μm Al foils were replaced by 15 μm thick plastic (CH) foils coated with 1 μm of Al to prevent significant attenuation of the x-rays. Even so, it can be seen that these spectra are weaker than those from the front side as they are viewing the emission through the foil. As the DCS affords a degree of one dimensional spatial resolution (at unit magnification) in the direction perpendicular to the spectral direction, the width of the spectra in this direction gives information about the size of the emitting region. The spatial resolution of the instrument is a function of the effective rocking curve width and the source to film distance; for the conditions used here it has been measured to be better than approximately 30 μm.

From Fig. 2 it can be seen that the line profiles are significantly assymmetric. The emission is almost independent of angle on the red side of the line, and on the blue side the emission increases in intensity as the angle of observation with respect to the laser beam decreases (i.e. as we observe closer to the target normal). A full analysis of this data for an explanation of this effect will require extensive simulations incorporating the kinetics as well as the hydrodynamics. Such simulations will especially need to take into account the effect of the velocity gradient on the opacity of the plasmas. Indeed, previous work by Lee et al has shown that for conditions not dissimilar to those produced here the velocity gradient can reduce the opacity in the centre of the line by up to a factor of 5.[7]

For the Ly-α radiation a velocity of 1×10^7 cm s^{-1} gives rise to a shift of 2.4 mÅ. Thus if we translate the shift in the peak of the radiation from observing side-on to the target to that at an angle of 30° to the laser beam, we would infer an ion velocity of 2×10^7 cm s^{-1} normal to the target surface. Note however, as stated above, due to the high opacity of the line and the wide range in densites, temperatures, and velocities over which emission is taking place, it is not possible to assign a single velocity in a meaningful way to such a resonance line. However the data do show the effects of velocity on the line profile, and conclusively demonstrate that the DCS has the capability to record such effects - this being the main point to which we wish to draw attention in this paper.

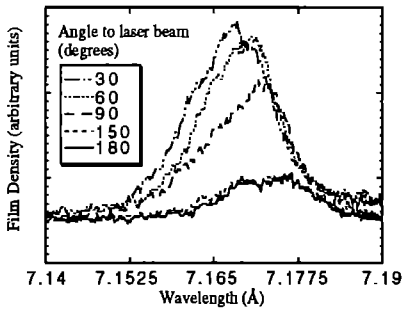

Fig. 2. Film density lineout of the spectrum of the Ly-α line of hydrogenic aluminum recorded as a function of angle to incident laser beam.

CONCLUSION

We have used a novel high resolution, high dispersion, double crystal x-ray spectrometer to view the x radiation emitted from a laser-produced-plasma. The high resolution of the instrument, in conjunction with a reference wavelength defined by the angle between the two separate diffracting crystals, has enabled us to accurately observe the variation in x-ray line profiles as a function of angle around the target. Future work will concentrate on a detailed analysis of the lineshapes of the resonance lines, taking into account the effect of the velocity gradient on the opacity,.

REFERENCES

1. F.E. Irons, R.W. McWhirter, and N.J. Peacock, J. Phys. **B, 5,** 1975 (1972).
2. P. Nicolosi, G. Tondello, and E. Jannitti, Phys. Rev. A, **20,** 2574 (1979).
3. J. Hrdý, Czech. J. Phys. B, **18,** 532 (1968).
4. O. Renner and M. Kopecký, Czech. J. Phys., **40,** 1107 (1980).
5. O. Renner and M. Kopecky, Laser and Particle Beams (to be published).
6. H. He, J.S. Wark, E. Foerster, I. Uschmann, O.Renner, M. Kopecky, and W. Blyth, Rev. Sci. Instr. **64,** 26 (1993).
7. Yim T. Lee, Richard A. London, and George B. Zimmerman, Phys. Fluids B **2,** 2731 (1990).

STUDIES OF LASER-PRODUCED-PLASMAS IN CONFINED GEOMETRY

G R Bennett,[1] J S Wark,[1] H He,[1] N.C. Woolsey,[1] R. Cauble,[2] R.W. Lee,[2] and P. Young[2]

[1]Department of Physics, Clarendon Laboratory, University of Oxford, Oxford, OX1 3PU, UK
[2]Lawrence Livermore National Laboratory, Livermore, CA 94550, USA

INTRODUCTION

The production of low-temperature high-density plasmas is of great interest to astro and plasma physicists alike; such plasmas are generally strongly-coupled in character and may be created in ion or electron beams, self-pinching discharges, laser fusion, electrically-driven foils, laser-produced plasmas, etc. The work presented here reports on a new method for plasma production, where the plasmas created have potentially good temperature and density uniformity in comparison to previous methods, as well as a relatively long lifetime.

Several workers have investigated a somewhat similar laser-produced plasma source - namely confined ablation where an absorbing metallic layer is sandwiched between two confining substrates (normally glass or quartz), which are transparent to the chosen laser light.[1-2] These workers measured the pressure history and the energy absorbed. The results from the work suggests energy balance can only explained if the plasma has an unusually high ionisation. However, their method for plasma production introduces difficulties in calculating the plasma volume, causing an error in the energy per unit volume value. We aim to overcome such problems by producing the confined plasma in a well-defined gap.

We present here the results of two experiments performed at the RAL that used this plasma source in order to make comparisons with previous work on confined ablation.

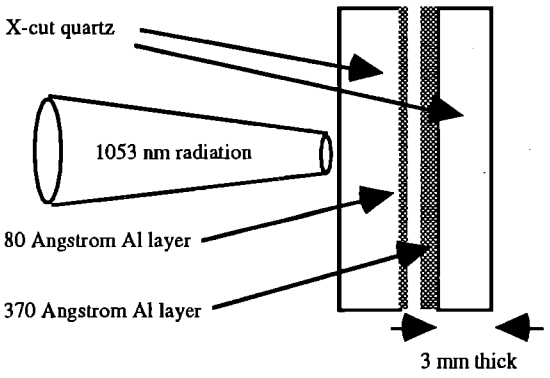

Fig 1 Confined-geometry target

PLASMA PRODUCTION

A target consists of two x-cut quartz disks polished to $\lambda/10$, and separated by 4 microns. Aluminium is vacuum-deposited onto the inside surfaces to the thicknesses shown, and when the surfaces are truly parallel a single colour (part of a Newton ring) can be viewed through the left hand disk, the gap is then measured to high accuracy using an interference method with 543.5 nm He-Ne laser radiation. The x-cut quartz is transparent to the 1053 nm laser radiation, and for intensities around ~ 10 GW/cm^2 (600 psec FWHM) about 90 % of the laser energy is absorbed - with inverse Bremsstrahlung being the main heating mechanism. The Aluminium plasma becomes uniform and fills up the gap on a nsec time-scale. The gap increases with time of course, and the speed of each surface is proportional to the plasma pressure and inversely proportional to the acoustic impedance of x-cut quartz. For pressures around 10 Kbar and a gap of 4 micron, the fractional change in volume is less than 3 % over 1 nsec. During the nsec time-scale a few eV temperature plasma loses only a tiny amount of its energy by T^4 black body radiation, and so this energy loss is negligible, although at higher temperatures (> 10 eV) the loss will start to become comparable with the input power from the laser. The confining surfaces are directly heated by the plasma and a several nm depth of quartz will melt, however, the thermal conductivity of molten quartz is very low - therefore energy is effectively trapped in the plasma, and so energy losses by conduction should in principle be negligible.

X-cut quartz is an ideal confining wall material for the following reasons:- it has a very high acoustic impedance, low thermal conductivity, is transparent to 1 micron light, can be polished to great flatness, and has a piezoelectric response to applied pressure. This piezoelectric response has been thoroughly investigated,[3] and the main conclusions from this work are:- when a disk of x-cut quartz has a diameter to thickness ratio ≥ 5, and only the surfaces are coated with metal, the short-circuit current produced is proportional to the difference in pressures applied to the two surfaces. This linear effect can be observed for a pressure of up to 25 Kbar, and this pressure range is ideal for the plasmas of interest.

EXPERIMENTS

The TA2 facility was used to make simultaneous measurements of the pressure P, energy per unit volume U and density ρ of the confined plasma. Laser radiation of $\lambda = 1053$ nm and 800 psec FWHM was focused to a 15 mm spot onto the double-crystal target. In this experiment a separate disk of x-cut quartz was brought into contact with the outside surface of the confining wall. This disk was 7 mm in diameter and 0.7 mm thick, the surfaces were vacuum-deposited with Chrome and Gold, and the flatness of the disks was quoted as being $\lambda/4$; the piezoelectric current produced was measured using a 1 GHz Tektronix 7104 oscilloscope, and the wave forms were recorded on Polaroid film. The energy absorbed by the plasma was calculated by measuring the incident, reflected and transmitted laser light from the plasma, and these energies were measured using three Scientech beam calorimeters.

RESULTS

The plot below compares the experimental results with pressures predicted by the equation of state package 'Occipital'. This EOS is a set of tabulated data (similar to the well known SESAME) produced at Lawrence Livermore National Laboratory, and is based on results from a variety of models for the EOS in this regime. The results show that the pressure is rather low in comparison to theory.

In a subsequent experiment in the TA4 facility the absorbed energy was re-measured accurately using an integrating sphere - and only slightly altered the previous (below) data points. The fraction of laser-light absorbed in the x-cut quartz was measured to be $1 \rightarrow 2$ % for the maximum fluence used in the first experiment. The $1/e$ depth for attenuation of a pressure pulse in the x-cut quartz was measured to be > 80 mm, hence attenuation through 3 mm is negligible, and cannot account for the low pressures measured.

A Hewlett Packard HP54510A 1 GSa/s 2 channel digital oscilloscope was used to record the piezoelectric response from the rear confining wall itself and 7 mm transducer simultaneously. Now that it was known that attenuation and temporal dispersion were negligible, the two wave forms should therefore be identical. It turned out that the confining wall wave form was much more physically meaningful than that of the transducer, see figure 3 below.

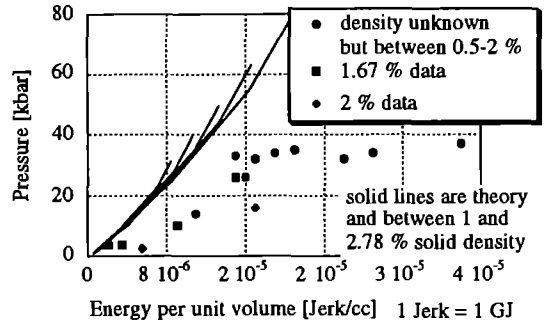

Figure 2 Data comparison with 'Occipital'

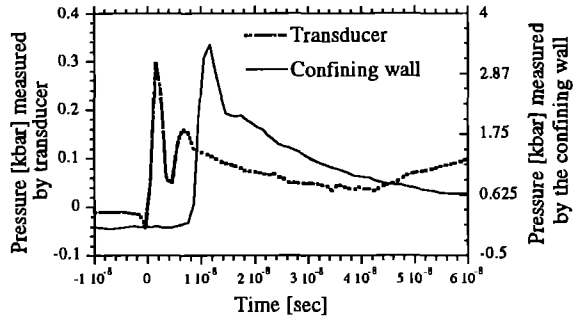

Figure 3 Simultaneous pressure measurements using confining wall and transducer

The two peaks are slightly separated so that the reader can easily compare the temporal responses. Notice that the wall gives a peak pressure reading of ~ 10 times that of the transducer. This result implies that there could be problems in measuring the pressure response with the separate transducer.

During this second experiment some P, U, ρ data shots were also taken - although at a much reduced energy per unit volume to that of the first experiment; the confining wall responses were used to measure the peak pressures and the values recorded were still rather low in comparison to those predicted. In the future we will investigate whether the poor contact between the transducer and target was also a significant effect at higher irradiances.

ENERGY BALANCE

Using a Q-switched Ruby laser of 15 nsec pulse length, Yang measured peak pressure as a function of laser fluence and layer thickness for many metals, including Aluminium.[1] Yang assumed that the plasma pressure increased linearly to its peak at the laser switch off. This allows one to calculate the plasma volume and the Pdv work done on the confining walls. If one assumes the plasma is an ideal gas, then its energy is $1.5PV$ where P is the peak pressure and V is the calculated volume. Adding this *thermal* energy to the work done, Yang found that the result is much less than the energy absorbed. Neglecting energy loss by black-body radiation and conduction to the walls, the missing energy must be used for ionisation: a smaller amount will be used for latent heats of fusion and vapourisation.

Fabbro used a similar experimental arrangement, but with a range of pulse lengths - he also uses a similar analytical model to Yang: that is, no conduction or black-body losses and zero width plasma at $t = 0$.[2] One important difference however, is that a top hat (in time) laser pulse is assumed. One result from the model is that pressure is predicted to be constant throughout the laser pulse, also the pressure is predicted to only be a function of intensity and a variable α where

$$\alpha = \frac{3PV}{2E}$$

and E is the energy absorbed by the plasma. α is predicted to be independent of pulse length and intensity; however, Fabbro's experimental results show that it is actually a function of both. Despite this limitation in the model the results do show very small values of α at intensities around of 1 GW/cm^2, i.e. very high ionisation. Yang came to the same conclusion, and our results are some what similar. It is interesting to note that the appropriate numerical integration of the confining wall pressure response shown in Fig. 3, yields a work done value negligible in comparison to the absorbed energy.

Assuming 'Occipital' is correct, it appears that, contrary to our initial assumptions, some energy may be lost by heat conduction to the x-cut quartz walls; though this is difficult to reconcile with the $1/e$ falloff in pressure of several tens of nanoseconds that can be seen in Fig. 3. We are currently simulating this problem using the hydrocode 'Medusa' incorporating the SESAME equations of state and values for thermal conductivity.

SUMMARY, CONCLUSIONS & FUTURE WORK

The thermodynamic variables P, U, ρ of a strongly-coupled plasma were measured using a confined ablation approach. The results showed that for a given energy per unit volume, the pressure was low in comparison to theory. A later experiment showed that the wall/transducer interface is a large source of pressure loss in the above measurements. During this experiment some data was obtained using an improved pressure diagnostic - although at much lower energy per unit volume values; It appears that the pressure is still rather low, and this result is similar to the results of confined ablation experiments by previous workers.

Future work will include more P, U, ρ measurements. It will be interesting to use a longer pulse length - say 6 nsec - and to dump in the same energy per unit volume and to then compare the pressure with that from an 800 psec pulse. If heat conduction is an important energy loss then one would expect a difference in peak pressure. Also planned are simultaneous measurements of P, U, ρ, temperature, electron density, plasma spectroscopy/lineshapes and visible/UV opacity.

REFERENCES

1. L.C.Yang, J. Appl. Phys. **45**, 2601 (1974).
2. R.Fabbro *et al*, J.Appl. Phys. **68**, 775 (1990).
3. R.A.Graham *et al*, J. Appl. Phys. **36**, 1775 (1965).

ACKNOWLEDGEMENTS

We are happy to acknowledge the assistance of Chris Goodwin and Bella Lake, at the Oxford Physics Department. Thanks are also due to R.W.W.Wyatt and D.Rodkiss, and the target preparation group at RAL for help in preparing the experiments. Thanks to Ray Reed (Sandia Labs, New Mexico, USA) for his very helpful discussions on x-cut quartz pressure transducers.

SUB-PICOSECOND X-RAY DIFFRACTION

H. He and J.S. Wark

Department of Physics, Clarendon Laboratory, University of Oxford, Oxford OX1, 3PU, UK

INTRODUCTION

Interest in the interaction of intense, subpicosecond laser pulses with solid targets has grown considerably over recent years. The motivation behind such interest is the study of high-density plasmas and the production of ultra-short-pulse x-ray sources. At present the precise length of the x-ray pulse generated is often not known accurately; recent work by Murnane et al showed that when a 160-fsec pulse was focused onto a solid target x-rays of energies up to 1 keV were produced in a pulse length of 2±2 psec, hinting that the x-ray pulse could be closely following the laser-pulse.[1] Numerical modeling has also shown that mixtures of light and heavy elements may be used as targets for femtosecond time-scale x-ray line radiators.[2] Such short x-ray pulses are believed to produced due to the laser energy being absorbed by the electrons within an optical skin depth, leading to rapid ionisation before significant ablation can occur; rapid cooling of the electrons upon expansion into the vacuum and heat conduction into the surrounding material is expected to quench the x-ray emission.

With the advent of these extremely short x-ray pulses it seems timely to investigate the effect of x-ray pulse length on Bragg crystal reflectivity. We shall show below that the response of a crystal (in terms of rocking curve width and integrated reflectivity) to ultra-short x-ray pulses is itself time-dependent. The temporal response of the crystal may then be one of the limiting factors determining the ultimate temporal resolution achievable in flash x-ray absorption or emission spectroscopy.

TIME-DEPENDENT DIFFRACTION (DYNAMICAL)

There are two descriptions of the diffraction of x-rays by crystals - dynamical and kinematic diffraction theory. Dynamical theory is applicable in the limit of perfect crystals, where the attenuation of the incident beam due to strong diffraction is important; whereas kinematic theory describes the diffraction process for so-called perfectly-imperfect crystals (i.e. those which are highly mosaic) where the main contribution to the attenuation of the incident beam is photoelectric absorption. We first turn our attention to the dynamical case.

The integrated reflectivity of a crystal to x-rays is a function of crystal thickness. At thicknesses very much greater than an extinction depth the reflectivity takes on the infinite crystal value. However, at crystal thicknesses close to and less than an extinction depth the reflectivity falls almost linearly. Thus we expect that if an x-ray pulse of pulse length τ is incident on a crystal of extinction depth A, then if $c\tau < A$, then the *instantaneous* reflectivity will be reduced from the infinite crystal value (note that, as the system is linear, the reflectivity integrated over both angle and time will be the same as in the time-indepenent case, although the shape of the rocking curve will alter). The exact value of the reflectivity at any given time will be a function of the pulse shape, and therefore for a full analysis time dependence must be introduced into the diffraction equations. Now typical extinction depths for strongly diffracting planes are of order 1 - 30 μm, corresponding to extremely short x-ray pulses of 3 - 100 fs duration.

There are several different approaches to finding the temporal response of the crystal. For the dynamical case, the angle-integrated but time-dependent reflectivity can be found simply by taking the fourier transform of the the time-independent reflectivity (in amplitude) as a function of frequency of the crystal - i.e. we simply convert from frequency space to time. As crystal rocking curves are approximately Lorentzian, we expect an exponential temporal response of the crystal to an input x-ray pulse which is a delta-function in time. This response can then be convolved with a realistic time-dependent input pulse to find the x-ray output as a function in time. Alternatively, of course, we could simply take a time-dependent input pulse, take the fourier transform into frequency space, multiply each frequency component by the complex reflectivity of the crystal (i.e. take into account reflection and phase shift) and fourier transform once more to find the time-dependence of the output pulse.

Results from such a process are shown in Fig. 1. It is obvious that weaker reflections, with narrower rocking curve widths (and thus longer extinction depths), have the longest temporal response.

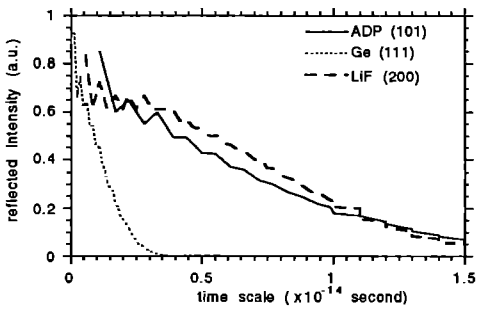

Figure 1 Fourier transform of several rocking curves. The corresponding x-ray wavelength used is 2.6 Å for LiF, 3.2 Å for Ge and 7.7565 Å for ADP crystals.

Although a simple fourier transform of the rocking curve gives us an overview of the temporal response of the crystal, as it stands it gives no information about the amplitude of the electric field within the crystal, or about the instantaneous reflectivity as a function of angle. This detailed information can be obtained using the Green's function approach (as has been used to calculate the mutual coherence function),[3] or by explicitly including time-dependence in the fundamental dynamical diffraction equations. For illustrative purposes we take the second approach here.

The form given to the incident wave in the vacuum is

$$\mathbf{D}(\mathbf{r},t) = \mathbf{D_0}(\mathbf{r},t)\exp[i(\omega_0 t - \mathbf{k_0}\cdot\mathbf{r})] \qquad (1)$$

where ω_0 remains constant in the vacuum and in the crystal. In the vacuum $\mathbf{D_0}(\mathbf{r},t)$ is taken to be real but time and space dependent; within the crystal the incident wave is also given by (1), in this case $\mathbf{k_0}$ is kept constant and the perturbations to the incident wave introduced by the crystal are introduced into $\mathbf{D_0}(\mathbf{r},t)$ and thus it becomes complex. The wave is reflected from the H planes, H ≡ (h,k,l), where h, k, l are the Miller indices. The reflected wave within the crystal is given by:

$$\mathbf{D}(\mathbf{r},t) = \Sigma_H\, \mathbf{D_H}(\mathbf{r},t)\exp[i(\omega_0 t - (\mathbf{k_0}+\mathbf{G_H})\cdot\mathbf{r})] \qquad (2)$$

This expression can be generalised to include the incident as well as the reflected rays by allowing H to take the value (0,0,0) with the convention $\mathbf{G_0 \cdot r} \equiv 0$. For x-rays the susceptibility $\psi << 1$; the wave equation can then be written

$$\text{Curl Curl}\,[(1-\psi)\mathbf{D}] = -\frac{1}{c^2}\frac{\delta^2 \mathbf{D}}{\delta t^2} \qquad (3)$$

where the susceptiblity ψ, of the crystal, is taken to be complex and periodic

$$\psi = \Sigma_H \psi_H \exp(-i\mathbf{G}.\mathbf{r}) \quad , \qquad (4)$$

Equating terms in the incident and diffracted direction, and taking the first order approximation we obtain

$$i\frac{\lambda}{\pi}\frac{\delta D_0}{\delta x_0} = \psi_0 D_0 + \psi_H D_H - \frac{i\omega_0}{c^2 k^2}\frac{\delta D_0}{\delta t} \qquad (5)$$

$$i\frac{\lambda}{\pi}\frac{\delta D_H}{\delta x_H} = \psi_0 D_H + \psi_H D_0 - \alpha_H D_H - \frac{i\omega_0}{c^2 k^2}\frac{\delta D_H}{\delta t} \qquad (6)$$

where α_H is a quantity that represents the deviation from the Bragg angle and is given by:

$$\alpha_H = [\,\mathbf{G_H}^2 + 2\,\mathbf{G_H} \cdot \mathbf{k_0}]/k_0^2 \equiv 2\,\Delta\theta \sin(2\,\theta_b) \qquad (7)$$

If time dependence is ignored, (5) and (6) become the well known Tagaki-Taupin equations.[4,5]

In practice we solve equations (5)-(7) in dimensionless units, similar to those introduced by Zachariasen.[6] The unit of dimensionless angle for symmetrical Bragg diffraction is given by

$$y = \alpha_H / 2\psi'_H \qquad (8)$$

and that of time by

$$T = c\pi\psi'_H t/\lambda \qquad (9)$$

where t is the time in seconds for the x-ray pulse to enter and emerge from crystal.

These equations are solved using a simple upwind differencing scheme. For pulse lengths τ such that $c\tau >> A$ we expect this time dependent solution of the reflectivity $|D_H/D_0|^2$ to approach the steady state solution. As an example we show the crystal response to an x-ray pulse suddenly switched on at time t = 0. The results are shown in Fig. 2. It can be seen that the rocking curve approches the steady state value after T ≈ 2.5, i.e. after the front of the x-ray pulse has travelled a few extinction depths into the crystal. As a check we have compared the full diffraction equations with the results obtained by a simple fourier transform, and found the results to be identical for the angle-integrated time-dependent reflectivity as expected.

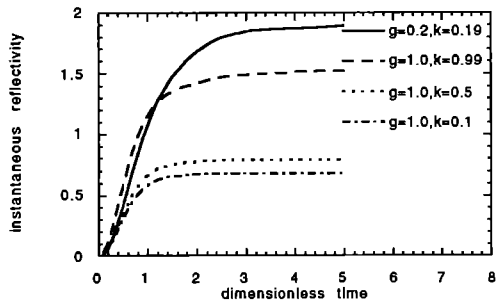

Figure 2 Instantaneous crystal reflectivity integrated over dimensioness angle y.

TIME-DEPENDENT DIFFRACTION (KINEMATIC)

Diffraction from imperfect crystals can be described by kinematic diffraction. The reflectivity of an imperfect crystal is greater than its dynamical counterpart, so that such crystals are often used in spectroscopy if high diffracting efficiency is required. The reflectivity as a function of angle in this case is determined by the angular distribution of the mosaic crystallites, and is unrelated to the temporal response of the crystal to an ultra-short pulse. In this case the reduction in intensity of the incident beam is dominated by photoelectric absorption. We have written a simple code, neglecting extinction effects, to model the temporal response of such crystals to a delta function input pulse. It is those crystals with low absorption coefficients (such as graphite and LiF) which will have the longest temporal response.

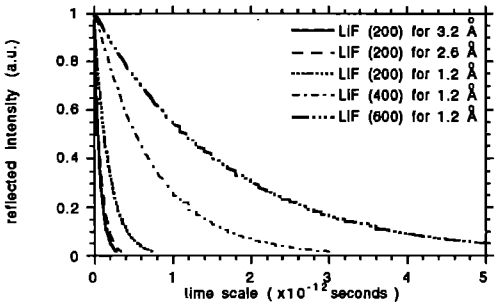

Figure 3 temporal response of kinematic LiF crystal to different x-ray wavelengths.

REFERENCES

1) M.M. Murnane, H.C. Kapteyn, and R.W. Falcone, Phys. Rev. Lett. **62**, 155 (1989).
2) S.E. Harris and J.D. Kmetec, Phys. Rev. Lett. **61**, 62 (1988).
3) V. Holy', Phys. Stat. Sol. B **101**, 575 (1980)
4) S. Takagi, Acta Cryatallogr. **15**, 1311 (1962)
5) J. Burgeat and D. Taupin, Acta Crystallogr. **A24**, 99 (1968)
6) W.H. Zachariasen, *Theory of X-Ray Diffraction in Crystals* (Wiley, New York) (1945).

THE EFFECT OF HIGH X-RAY FLUXES ON LASER-PLASMA X-RAY SPECTROMETERS

J. S. Wark

Department of Physics, Clarendon Laboratory, University of Oxford, Parks Road,Oxford OX1 3PU, UK

R. R. Whitlock

Naval Research Laboratory, Washington, DC 20375, USA

INTRODUCTION

In last years annual report we presented calculations showing that the x-ray reflectivity of Bragg crystal x-ray spectrometers can change during the nanosecond timescale of the data collection time in a laser-plasma experiment.[1] This rapid change in the integrated reflectivity is due to a change from dynamical to more kinematic diffraction caused by an x-ray induced thermal strain gradient in the surface layer of the crystal. We present here results of an experiment designed to observe the effect of x-ray heating on the integrated reflectivity of Lif (200) crystals, and to gain some rudimentary data as to the magnitude of the effect. The results are compared with calculations based on a simple x-ray absorption model used in conjunction with the dynamical diffraction equations as applied to strained crystals.

EXPERIMENT

A laser pulse containing approximately 30 J of 0.35 μm light in a pulse of 0.6 ns duration was incident normally on a 25 μm thick foil of titanium coated with 500 Å of gold. The laser was focussed to a spot of approximately 50 μm diameter, thus producing an average incident irradiance of 2.5×10^{15} W cm^{-2}. The diffracting crystal was freshly cleaved LiF (200), and the centre of the crystal was positioned coplanar with the target normal and the axis of the laser beam (the horizontal plane) at an angle of 45^0 to the target normal. The crystal surface was placed at an angle of 40^0 to the horizontal, and the distance along the horizontal from the target to the centre of the crystal was 19 mm.

The rationale behind the design of the x-ray emitting target is as follows. At the beginning of the laser pulse the gold is ablated from the surface of the target. High Z targets such as gold emit x-rays in a broad band of radiation around their M band, which in the case of gold occurs around 5.0 Å. The conversion efficiency of laser energy to x-ray energy is relatively high (of order a few percent for the M band). This x-ray flux was incident on the LiF crystal, and caused the heating of the crystal surface. Once the laser has ablated away the gold layer, the underlying titanium is heated, and emits strongly at the resonance, intercombination, and dielectronic satellite lines of the helium-like ion. The conversion efficiency of laser light to this K-shell emission is far lower than that to the gold M-band, and thus the titanium helium-like x-radiation does not heat the crystal significantly compared to the radiation from the gold. Thus any change in the integrated reflectivity of the crystal caused by prior heating from the gold x-rays manifests itself as a change in the intensity of the recorded titanium x-rays.

The $2d$ spacing of LiF (200) is 4.027 Å; thus the helium-like titanium x-rays are short enough to be diffracted from the crystal, but the emission from the gold M-band is of too great a wavelength to be recorded. Therefore a separate (002) pentaerythritol (PET) crystal was used to monitor the radiation from the gold layer. In addition a (111) germanium crystal ($2d$ = 6.532 Å) was used to monitor the titanium helium-alpha radiation. These crystals were placed at a distance of 220 mm along the horizontal from the target, and thus were not subject to significant x-ray heating. They recorded x-rays emitted at an angle of 45^0 to the target normal. The PET was set at an angle of 35^0 to the horizontal, and the Ge at 23.5^0 to the horizontal.

In order to observe the effects of x-ray heating on the integrated reflectivity of the LiF crystal, it is necessary to have part of the crystal x-ray heated, whilst keeping another portion of the crystal relatively unperturbed by the x-rays. A set of x-ray filters was arranged such that there were two possible paths by which x-rays could be diffracted from the crystal and be recorded on the Kodak DEF x-ray film. For the first path, an x-ray filter was placed just above and parallel to the surface of the crystal. Thus x-rays passed twice through this filter at an angle of $(\pi/2 - \theta_b)$ to the normal to its surface, and were then incident upon the film. For the second path, the x-rays were first incident upon the crystal, and then passed through two filters (identical to the filter used in the first path) which were again placed parallel to the surface of the crystal. Thus the total filter thickness through which the x-rays passed was identical for both paths. However, in the first case the filter protected the crystal from x-ray heating by the gold x-rays, whereas in the second case the crystal was exposed to heating by this radiation. Thus a measure of the relative intensity of the helium-like titanium x-rays following these two different paths onto the film gives a measure of the change of the integrated reflectivity of the crystal due to the x-ray heating. The filters were 5 μm thick titanium. Titanium is relatively transparent to its own helium-alpha radiation. The x-rays incident on the LiF crystal at the Bragg angle of 40.5^0 pass through a total of 15.4 μm titanium before reaching the x-ray film, and the resultant transmission is approximately 51 %. For the gold x-rays incident on the crystal at 40.5^0 the transmission through a single thickness of the titanium filter is 15 % for 5.0 Å radiation. Thus there is a significant difference (at least a factor of 6.7) in the M-band x-ray heating of the unfiltered and filtered portions of the crystal.

In addition, a further filter of 6 μm aluminised mylar was placed in front of the whole crystal and filter assembly. The transmission of this extra filter was 98 % to the helium-like titanium radiation, and 86 % at 5.0 Å. The purpose of this filter was to prevent significant heating of the crystal by much softer x-rays (10's of Å) emitted from the gold plasma (the transmission at 10 Å was 34 %, and obviously is reduced even further at longer wavelengths). LiF (200) was chosen as the diffracting crystal as previous calculations had shown that its reflectivity could increase by almost an order of magnitude when x-ray heated.[1]

RESULTS

Laser shots were taken with filter conditions described above, i.e. with the 6μm aluminised mylar covering the whole of the crystal assembly. The films were digitised on a Perkin-Elmer PDS system. The film densities were converted to intensities

using the calibration given by Henke.[2] Although Henke does not give explicit film calibrations at the wavelengths of titanium helium-alpha and the gold M-band, his results were scaled to these wavelengths by calculating the appropriate absorption coefficients of the emulsion and silver bromide using tabulated values of the mass absorption coefficients of the elements,[3] and then utilising the constants *a* and *b* of reference (2).

From the gold spectra recorded with the PET (002) crystal we calculate a total energy of 0.36 J was produced in the spectral range from 2.3 to 2.6 keV, i.e. a conversion of approximately 1 % of the laser energy into this spectral band. Note that the M-band of gold actually extends over a greater spectral range than that monitored here, and by comparison with Fig.1(b) of reference (4) we would estimate a total energy of order 0.75 J in the spectral range from 1.6 to 3.6 keV.

The effect of the x-ray pulse on the LiF crystal can be seen in Fig.1, where we show the titanium spectrum reflected from the x-ray heated and unheated portions of the crystal. It can be seen that the intensity of the x-rays diffracted from the x-ray heated part of the crystal is greater than that of the heated part. An integration of the two curves shows that the reflectivity of the heated crystal is 36 % greater than the unheated crystal.[5] Note that the magnitude of the differences in the intensities of the helim-like titanium x-rays cannot be explained by misalignment of the x-ray filters. We estimate that the filters covering the two portions of the crystal were parallel to better than 5^0, which in turn would only produce a difference of order 8 % in the intensities of the titanium lines.

As stated above this increase in reflectivity is due to the x-ray-induced thermal strain gradient in the surface of the crystal. The magnitude of the increase can be compared with previous calculations. In reference (2) we calculated the change in integrated reflectivity of LiF(200) when subjected to an x-ray flux produced by irradiating a gold foil with 5 kJ of 0.35 μm light. The increase in the integrated reflectivity was calculated as a function of the distance between the x-ray source and the crystal. For the gold spectrum of Fig.(2) of ref(2) approximately 250 J of x-rays lie in the M-band, compared to the 0.75 J in this experiment. Thus we would expect similar increases in reflectivity in ref(2) at distances of order $\sqrt{(333)}$ times the source to crystal distance used in the experiment described here, i.e. at 35 cm from the target. However, we can see from Fig.(9) of ref.(2) that at this distance we predict an increase in integrated reflectivity of a factor of 2, i.e. a 100 % increase compared to the 36 % observed here One possible reason for this discrepancy is that in the calculations of the increase in reflectivity given in ref.(2) it has been assumed that the x-ray heating of the crystal is instantaneously converted to an x-ray strain. Of course, in practice this is not the case - if a certain thickness of the surface of the crystal is rapidly heated, then for that part of the crystal lattice to expand will take a time of order the thickness divided by the sound speed. For the conditions described here the 1/*e* depth of the heated region (assuming 5 Å heating radiation) is approximately 5.4 μm, and at a sound speed of 5 μm ns^{-1} it will take over 1 ns for the strain profile to be set up within the crystal. This time should be compared with the time in the experiment between x-ray heating of the crystal by the gold radiation and the diffraction of the titanium radiation. We estimate that it takes less than 200 ps for the laser pulse to burn through the 500 Å gold layer to the underlying titanium, and thus the titanium x-rays are being diffracted from the LiF crystal significantly before the strain profile is fully set up.

Despite these differences in the calculated and observed increase in integrated reflectivity, it is can be seen that the increase in reflectivity is at least of a similar magnitude to that predicted, and thus should be a factor to be taken into account when performing laser-plasma experiments where high x-ray fluxes are produced.

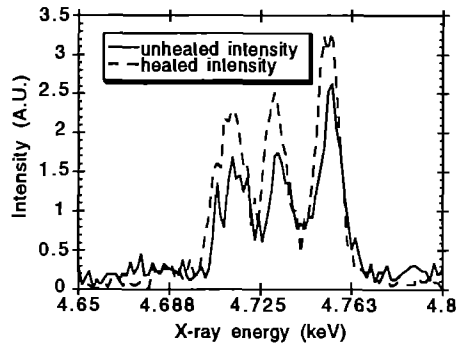

Fig.1 The titanium x-ray spectrum recorded from both the heated and unheated portions of the LiF (200) crystal placed 19mm from the x-ray source.

The simplest solution to the problem of x-ray induced thermal strain is to filter the crystal more heavily. However, in our experience, spectroscopists sometimes place more importance on filtering the detector rather than the crystal. This most often occurs in time-resolved x-ray spectroscopy where the crystal is usually mounted off a streak-camera up to tens of centimetres from the entrance slit of the streak camera. The main purpose of this paper is to point out that this is not good practice, especially if large x-ray fluxes are being produced, and as much care should be taken in filtering the crystal as in filtering the detector.

REFERENCES

1 J.S. Wark, Laser and Particle Beams, **9**, 569 (1991).
2. B.L. Henke, J.Y. Uejio, G.F. Stone, C.H. Dittmore, and F.G. Fujiwara, J. Opt. Soc. Am. B **11**, 1540 (1986).
3. B.L. Henke, P. Lee, T.J. Tanaka, R.L. Shimabukuro, and B.K. Fujikawa, Atomic Data and Nuclear Data Tables, **27**, 1 (1982).
4. D.L. Matthews, E.M. Campbell, N.M. Ceglio, G. Hermes, R. Kaufmann, L. Koppel, R. Lee, K. Manes, V. Rupert, V.W. Slivinsky, R. Turner, and F. Ze, J. Appl. Phys. **54**, 4260 (1983).
5. J.S. Wark and R.R. Whitlock, Rev. Sci. Inst. (to be published).

X-RAY SOURCE CHARACTERISTICS FOR X-RAY CONTACT MICROSCOPY IN TA4

R.A. Cotton, A.D.Stead & T.W.Ford

Department of Biology, Royal Holloway, University of London,
Egham, Surrey, TW20 0EX

INTRODUCTION

Soft X-ray contact microscopy (SXCM) is now well established in Target Area 4 ("TA4") of the Vulcan laser. A wide variety of hydrated biological specimens have been imaged over the last year with a much greater throughput of samples and with ever increasing success. A selection of recent images are presented in this volume[1]. For SXCM to play a significant role in microscopy for the life sciences, we believe that untreated, hydrated biological material must be imaged at a resolution of approximately 50nm on a routine basis. Although we have successfully imaged 50nm gold particles[2] and dry diatom frustules[3] at a resolution considerably better than 50nm, these are ideal, high contrast specimens and structure on a 50nm scale has only been observed in a few hydrated biological specimens. Tomie reports to have observed periodic structure in hydrated biological specimens with a resolution of 40nm[4]. Therefore, although the reality of sub-50nm resolution has been achieved, it is far from routine operation. To achieve this goal, in parallel to our imaging program, we are investigating the factors which currently limit the resolution of the technique, of which the X-ray source is of paramount importance.

SPECTRAL EMISSION

The ability to image the ultrastructure of biological specimens in an aqueous environment relies on the large difference in absorption coefficients between carbon and oxygen in the region between the carbon and oxygen K-shell absorption edges known as the water window (4.4-2.3nm). The transmission of a 1μm thickness of protein and a 1μm thickness of water are shown in figure 1.

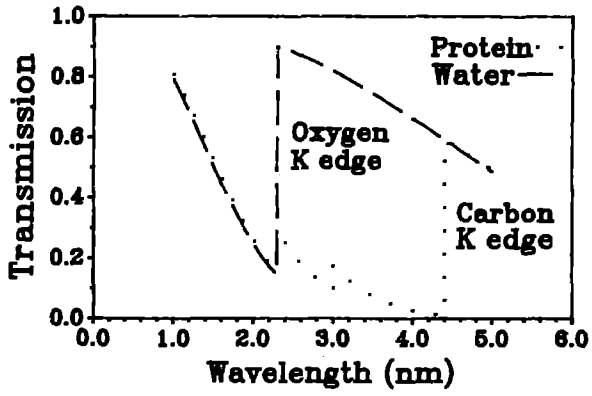

Figure 1. The transmission of a 1μm thickness of protein and a 1μm thickness of water showing the water window region.

The radiation emitted from an laser generated plasma (LGP) consists of a broad band continuum on which line emission is superimposed. The line emission arises from inner shell excitation from constituent atoms or ions followed by de-excitation of one or more higher state electrons. Consequently, there occur a set of line spectra corresponding to each inner shell for a particular element and the energy associated with each transition will be dependent on the elements atomic number Z. It is therefore possible to 'tune' the line emission to some extent by choosing Z, whilst at the same time adjusting laser irradiance on target to obtain a suitable plasma temperature to excite the ion species of interest.

For optimum conditions for SXCM we require that strong line emission lie in the water window and that radiation outside the water window (hard X-ray emission with a wavelength less than 2.3nm and UV/XUV radiation) be minimized. The target materials we have predominantly used are titanium (Z=22), molybdenum (Z=42) and tungsten (Z=74) which have been reported to have line emission (arising from the L, M and (N and O) shells respectively) that lie wholly or partly in the water window[5].

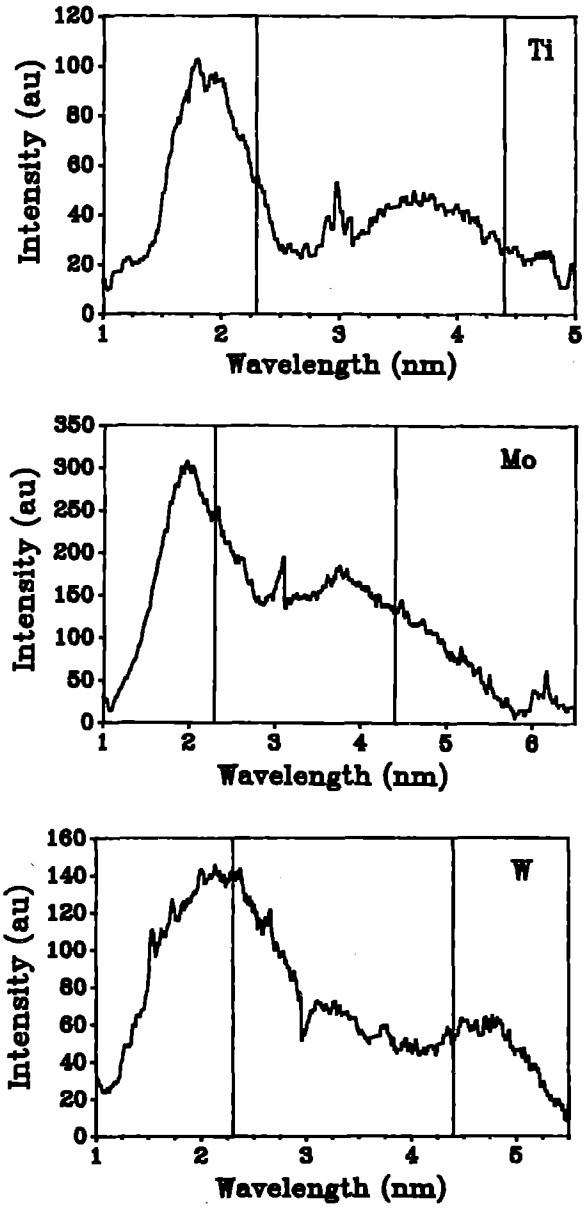

Figure 2. Plasma emission spectra for titanium, molybdenum and tungsten target material taken with a transmission grating with a line period of 185nm. An identical filter to that used in imaging experiments was used to reproduce the emission as seen by the specimen. The water window region is shown in each case.

We have measured the spectral emission from plasma from these elements using a transmission grating, averaged over 10 shots using approximately 5J of energy on target per shot in a 1ns pulse at a wavelength of 1.06μm and a focal spot of approximately 150μm in diameter. The grating consisted of gold shadowed lines with a period of approximately 185nm supported on silicon nitride substrate of thickness 100nm. The grating efficiency was approximately constant from 2-6nm. The spectra were recorded on Kodak 104-02 X-ray film and read out using an autodensitometer with step size 5μm. A supplementary filter of a Si_3N_4 substrate of thickness 120nm with a 50nm coating of aluminium was used to reduce the amount of UV radiation reaching the film and to reproduce the filtering conditions under which imaging is performed. The emission spectra were taken at an angle of 60° to the laser, identical to that used for imaging experiments.

The wavelength scale was calculated from the grating line spacing and the geometry of the arrangement and was cross-calibrated against known emission lines from carbon emission spectra (Lyman-α at 3.37nm and Helium-α at 4.03nm) taken with the same system. The emission spectra for titanium, molybdenum and tungsten material are shown in figure 2.

It is clear that in each case there is a component of radiation on the long wavelength side of the water window, which will have an adverse effect on image quality and resolution to some extent. Whether this makes a significant contribution to image formation has been investigated by measuring the rates of dissolution of PMMA resist, exposed by plasma radiation under various filtering conditions and is discussed below. It is also clear that for all three materials (Ti and Mo especially) the peak line emission lies just outside the water window, on the short wavelength side. Therefore, target materials with slightly lower atomic numbers may in fact be more suitable and produce images of higher resolution and contrast. For example calcium (Z=20) or scandium (Z=21) to replace titanium, niobium (Z=41) or Zirconium (Z=40) to replace molybdenum and tantalum (Z=73) to replace tungsten.

Another crucial factor in choosing the correct target material is the absolute value of X-ray flux emitted in the water window. It is well known that the total X-ray emission generally increases with increasing atomic number[5]. The conversion efficiencies from laser energy on target to water window X-rays were measured using X-ray PIN diodes (125 PIN diode from Alrad Instruments Ltd) filtered with a 500nm thickness of vanadium to isolate the water window region and is described in detail elsewhere[6]. Typical values for conversion efficiencies for the materials used in the present experiments were; titanium 4-5%, molybdenum 6-7% and tungsten 7-8%.

DISSOLUTION RATE MEASUREMENTS

Silicon nitride windows of thickness 120nm are used as the entrance window of the specimen holder to protect the specimen from vacuum. The average transmission in the water window is approximately 56% and decreases for longer wavelength radiation, known to be present in plasma emission. An aluminium coating may be applied to the Si_3N_4 window to provide additional filtering of UV/XUV radiation.

To investigate the effectiveness of particular filtering, the rates of dissolution of PMMA resist in methyl isobutyl ketone (MIBK) were measured following exposure to plasma radiation from titanium, molybdenum and tungsten material. The dissolution rate was measured with unfiltered emission and emission filtered with Si_3N_4 (120nm) and Si_3N_4 (120nm) + aluminium (50nm). The transmission of the two filters is shown in figure 3. The plasma-resist distance was varied so that in each case the water window X-ray fluence on the resist surface was approximately equal.

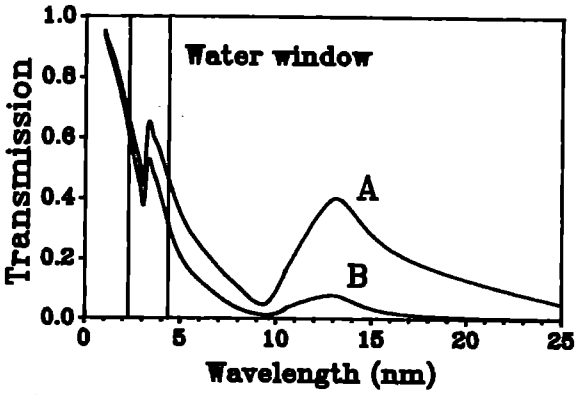

Figure 3. The transmission of A. Si_3N_4 (120nm) and B. Si_3N_4 (120nm) + aluminium (50nm).

Therefore differences in dissolution rates are due to radiation outside the water window, and in particular due to radiation on the long wavelength side.

The depth of development was measured using a Leitz MPV-SP thickness measurement system which can determine the thickness of photoresist on a silicon wafer to within $\pm$5nm. Figure 4 shows the rate of dissolution for plasma emission from tungsten target material with no filtering, with a Si_3N_4 (120nm) window and a Si_3N_4 (120nm) coated with a layer of aluminium (50nm). In each case the water window X-ray fluence on the resist surface was approximately 30mJcm^{-2}.

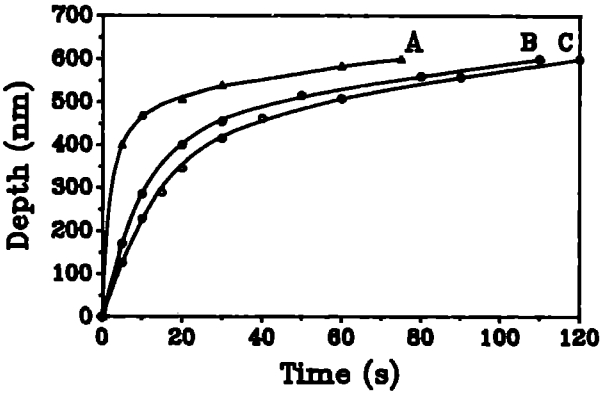

Figure 4. The rate of dissolution of PMMA resist in 100% MIBK when exposed to plasma radiation from tungsten target material with various degrees of filtering. In each case the X-ray fluence in the water window was approximately 30mJcm^{-2} on the resist surface. A. No filtering, B. Si_3N_4 (120nm) and C. Si_3N_4 (120nm) + Al (50nm)

It is clear that in the case of unfiltered radiation there is a large contribution to the dissolution of the resist from UV/XUV radiation which is responsible for a large initial dissolution rate. The absorption coefficient for PMMA increases steadily from a wavelength from 4.4nm upwards, towards the UV region of the spectrum and is therefore strongly absorbed in the top layer of resist. There is a small difference in the dissolution rate when a 50nm thick aluminium coating is applied to the Si_3N_4 window, showing a small amount of UV/XUV is transmitted by the Si_3N_4 window alone. However, it should be noted that water, present when imaging biological specimens, is a good filter of radiation outside the water window region. It is therefore concluded that when imaging wet specimens the Si_3N_4 window alone is sufficient to ensure that image formation is very largely due to water window X-ray flux.

DETERMINATION OF WATER THICKNESS

The biological specimens are imaged in an aqueous environment and are held in an environmental holder. The specimens are protected from vacuum by either a Si_3N_4 window or a Si_3N_4 window coated with a layer of aluminium. When the specimen is loaded in the holder, the liquid present can be seen to cause the window to bulge. The subsequent development of the exposed resist often reveals that images first appear at the edge of the exposed area, again indicating that the thickness of water is least at the edge of the window, increasing to a maximum at the centre.

It is of paramount importance to be able to determine and control the thickness of liquid present for several reasons. Firstly, if this thickness is too great it will absorb too high a fraction of the X-ray flux (1/e transmission is approximately 5μm for λ = 3nm). Secondly, if the thickness is considerably greater than the specimen thickness, the specimen may not be in close contact with the resist, which would result in a loss of resolution due to penumbral blurring and Fresnel diffraction. If there is insufficient water present the specimen may dehydrate causing structural damage.

By measuring the depth of the exposed area after a given development time, the attenuation of the X-ray flux by the liquid can be calculated from the dissolution rate measurements. Figure 5 shows a corner of an imaged area showing SXCM images of isolated chloroplasts in one particular imaging experiment[1], together with a height profile across part of the imaged area. The water window X-ray fluence on the surface of the Si_3N_4 window was 95mJcm^{-2} from tungsten target material. The resist was developed in 100% MIBK for 2 minutes and the image and height profile were taken using an atomic force microscope. It can be seen that at the edge of the exposed area the depth of development is approximately 300nm. From the dissolution rate measurements using tungsten target material, this depth would be predicted from an exposure of approximately 28mJcm^{-2}, implying that the liquid present transmitted approximately 30% of the X-ray flux. From this it is estimated that the thickness of water at the edge of the imaged area was approximately 5μm, similar to the diameter of a single chloroplast. However the thickness of liquid increases rapidly towards the centre. The images can be seen to become fainter towards the centre until no images can be observed at about 80μm from the edge after 2 minutes of development.

It is clear that there is a necessity to be able to accurately control the thickness of liquid present between the window and the resist surface. To help achieve this aim, Si_3N_4 windows are being made which have a grid structure of a known thickness. The thickness of the grid can be made to match the thickness of the particular specimen to be imaged (eg 5μm in the case of isolated chloroplasts) so that the specimen can sit in a well of known depth, in intimate contact with the resist surface. In addition, the grid structure will greatly strengthen the window and reduce the tendency for the window to bulge, helping to maintain a uniformity of water thickness across the imaged area.

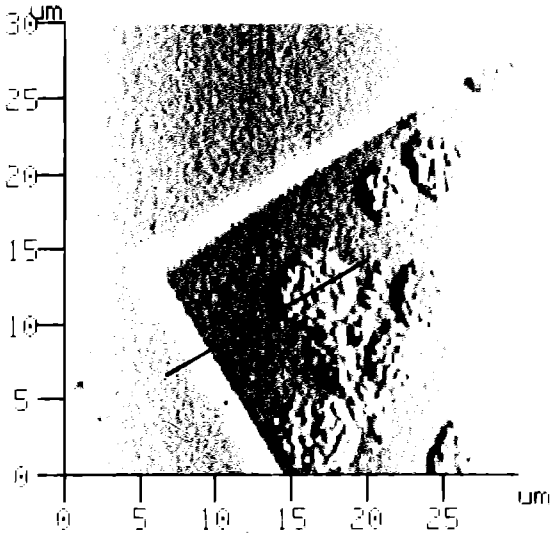

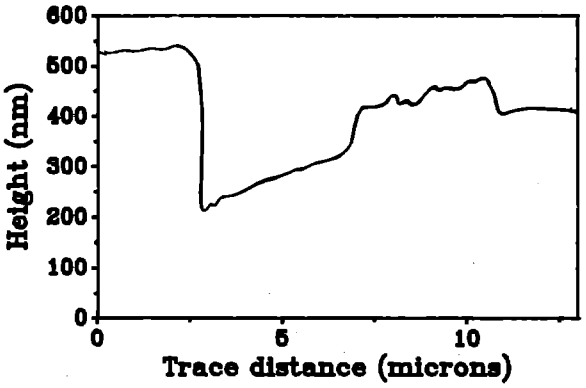

Figure 5. A corner of an exposed area of resist after 2 minutes of development (100% MIBK) showing SXCM images of isolated chloroplasts, together with the height profile across part of the resist. The resist was viewed using an atomic force microscope.

ACKNOWLEDGEMENTS

The work reported has been financed by grants from the UK Science and Engineering Research Council GR/F 81514 and GR/H 72441. We would like to thank the support staff on the "Vulcan" laser at RAL for their help with this work. We would also like to thank P. Charalambous for the manufacture of the transmission grating and Pete Anastasi for the manufacture of silicon nitride windows (both at Kings College) and to Lalit Dwivedi (Essex University) for reading out the recorded spectra using an autodensitometer. We are also grateful to Oxford University for access to AFM facilities.

REFERENCES

1. Ford, T.W., Cotton, R.A., Page, A.M. & Stead A.D.- this volume

2. Stead, A.D., Cotton, R.A., Jackson, A.J., Ridgeley, A. & Ford T.W., Annual Report to the Laser Facility Committee, Rutherford Appleton Laboratory 1991. pp34-35.

3. Ford, T.W., Stead, A.D., Hills, C.P., Rosser, R.J. & Rizvi, N., *J.Vac.Sci.Tech*, 1, pp207-210, 1989

4. Tomie, T., Shimizu, H., Majima, T., Kanayama, T., Yamada, Y. & Miura, E., *Proc.SPIE Conf.* 1741, pp118-129, 1992

5. Mochizuki, T. & Yamanaka, C., *Proc.SPIE Conf.* 733, p23, 1986

6. Cotton, R.A., Jackson, A.J., Ridgeley, A., Stead, A.D. & Ford, T.W., Annual Report to the Laser Facility Committee, Rutherford Appleton Laboratory 1991. pp32-33.

ULTRASTRUCTURAL STUDIES OF HYDRATED BIOLOGICAL SPECIMENS USING SOFT X-RAY CONTACT MICROSCOPY

T.W. Ford, R.A. Cotton, A.M. Page and A.D. Stead

Department of Biology, Royal Holloway, University of London,
Egham, Surrey, UK. TW20 0EX.

INTRODUCTION

It is now possible to examine the fine structure of a range of biological specimens using the technique of soft X-ray contact microscopy (SXCM). A well-characterized soft X-ray-rich plasma is generated in a target chamber situated in area TA4 using the VULCAN laser and a variety of target materials. The development and characterization of this system is described elsewhere[1]. Whilst the imaging of such specimens is now routine, the examination of the image in the chemically developed resist is still under review. The use of interference light microscopy (LM) is valuable for monitoring the early stages of the development process but has too low a resolution limit to reveal fine structure. Scanning electron microscopy (SEM) has a superior potential resolution but also several drawbacks. Beam damage to the resist is common and the necessity of sputter coating the resist surface reduces the resolution and prevents further chemical development of the resist. We now routinely use atomic force microscopy (AFM) for examining resists at various stages in the development process and for producing the final high resolution image. We report here the results of several studies using SXCM to investigate biological problems, with AFM being used for readout of the resist image.

BIOLOGICAL IMAGING

A. Comparison of SEM and AFM to study SXCM images of fresh tomato epidermal hairs.

For transmission electron microscopy (TEM) it is normal to chemically fix the tissue prior to dehydration, embedding in resin and sectioning. It has already been shown by LM[2] that the commonly used fixative glutaraldehyde, can cause alterations in the appearance of the cytoplasmic contents. More recently these findings have been confirmed by SXCM[3,4], however, whilst the resolution of these X-ray images was superior to that of LM, it was limited by the use of SEM to examine the photoresists. These photoresists have now been reevaluated using AFM.

Using SEM to study chemically developed photoresists of fresh tomato hairs it is possible to distinguish many linearly arranged ridges which correspond to the denser carbon-containing cytoplasmic strands. However, no internal structure can be discerned in any of these strands or associated organelles (Fig. 1). This is due, in part at least, to the of use low accelerating voltages and in consequence the quality and resolution of these micrographs is reduced. The use of AFM has, however, allowed images of the photoresists to be obtained with a greatly improved resolution (Figs. 2 & 3). In the case of the fresh tomato epidermal hair cell shown in Fig. 1 the use of AFM produces images with much greater clarity (Fig. 2). Furthermore, at higher magnification images of single organelles can be obtained (Fig. 3). In this case the cytoplasm surrounding the organelle is less carbon dense than the organelle itself but the vacuole beyond the ensheathing membrane is even less carbon dense, this can be clearly seen by recording the height profile across the imaged area (Fig. 4). The ability to resolve the cytoplasm surrounding the organelle in such a cytoplasmic strand is well beyond the capability of LM and, in this particular case, the image resolution is equal, or better than, 100nm.

B. Examination of abscission cells in the moss *Bryum tenuisetum.*

The filamentous protonema of many mosses can fragment by the formation of abscission, or tmema, cells[5]. In some species (eg *Funaria* and *Calympere*s) new cell wall material is laid internal to the old wall, which will eventually rupture, during the formation of these abscission cells. This new cell wall material can be detected by fluorescence under the LM using the cellulose-specific stain calcofluor white and is also easily visible under TEM[5,6]

Examination of *Bryum tenuisetum* protonema by incident UV light microscopy after staining with calcofluor white shows considerable fluorescence associated with the short cell following intercalary cell division, such images would normally be taken to suggest that new cellulosic wall material is being laid down in these cells. However, TEM images of similar material fails to show any evidence of new cell material[7]. The use of SXCM has now been used to explain this apparent anomaly.

SXCM images of the abscission cells of *B. tenuisetum,* using AFM, show that rather than the very discrete breakage in the cell wall that is apparent when examined by TEM, the cell wall appears to be extensively degraded (Fig. 5). If this is normally the case then it could explain why these cells fluoresce when stained with calcofluor; since the extensive degradation would result in a large number of free cellulosic fibres to which calcofluor would bind. The explanation as to why such extensive degradation is not seen by TEM probably relates to the methods of preparation. For both LM and SXCM the tissue is grown on cellophane overlays and is transferred with the minimal of disturbance. For TEM however, the tissue is transferred from a series of solutions and therefore receives considerable physical pressures, during which we believe that abscission cells rupture at the point where cell wall weakening commences. Normally it is anticipated that cell wall rupturing only occurs much later, when wall degradation is more extensive.

At high magnification the cellulosic fibrils appear, in the AFM images of the resist, to continue into the adjacent cells; certainly such continuity is not contary to existing theories on the methods for cell wall deposition. Other features associated with these fibrils may represent carbon-dense cytoplasmic structures which are internal to the cellulosic wall. Furthermore, TEM studies have shown that, compared to the adjacent chloronemal cells, the abscission cells have few cytoplasmic contents[7] and it would therefore be expected that the SXCM images would show detail of the abscission cells long before any detail in the adjacent cells was visible.

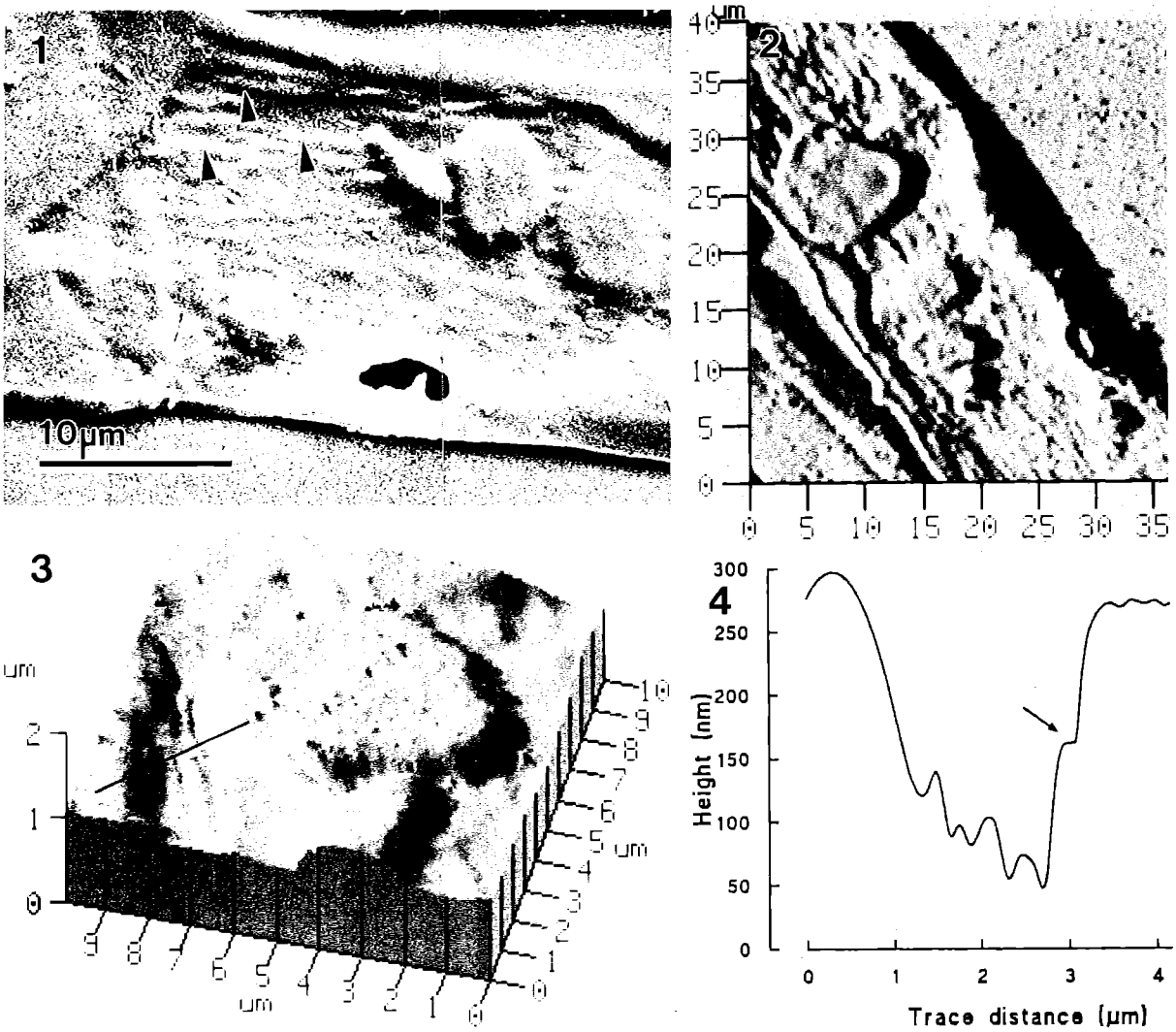

Fig. 1 SEM image of the chemically developed photoresist of a fresh tomato hair. Several intracellular organelles are visible and numerous small cytoplasmic strands are apparent (arrowed).
Fig. 2 Similar field of view as in Fig. 1 but obtained by AFM.
Fig. 3 Higher magnification, using AFM, of one of the organelles from Fig. 2. The carbon-dense organelle is clearly surrounded a less dense region of carbon. The height profile of the transect indicated with the solid line is given in Fig. 4.
Fig. 4 Height profile across the part of the organelle in Fig. 3 indicated with a solid line.

C. Cell ultrastructure of *Chlamydomonas*

Chlamydomonas is a unicellular green alga which can move rapidly by means of two equal length flagella inserted in the anterior end of the cell. It's basic structure can be seen by LM, though its rapid movement must be slowed considerably by using viscous mounting media or by loss of the flagella. Even when its rate of movement is reduced, photography is virtually impossible. The ultrastructure of *Chlamydomonas* has been examined by conventional TEM. By using SXCM we have been able to obtain high resolution images of living *Chlamydomonas* cells with the nanosecond duration of exposure effectively 'freezing' the cells in motion. When the developed resists are examined by AFM the individual cells can be clearly seen, each with two flagella (Figs. 7 & 8). The interior of the cells has a granular appearance with several small spherical inclusions. Although these are a regular feature of SXCM images of these cells, it has not yet been possible to relate them to any structure seen in thin sections under TEM. For this latter technique, the cells have to be chemically fixed and processed before embedding and thin sectioning which may introduce structural artefacts and hence complicate comparison of SXCM results from living cells with TEM results from chemically processed material. Another feature which has not been reported previously is the outer rim of relatively dilute carbon material (Fig. 7). This is too small to be easily seen by LM and is not a regular feature of TEM sections. It is particularly prominent at the anterior of the cell where the flagella are inserted (Fig. 8). It is hoped that future images of these cells, possibly after histochemical treatment, may provide more information on the identity of this structure.

D. Other imaging

In addition to the results reported above, a range of biological material has been examined by SXCM but space does not permit inclusion of more figures. Material imaged this past year has included :

i) *Microthamnion* - this small, filamentous green alga is a useful organism for the study of structural organization of vacuolate plant cells. Images obtained so far of living filaments show details of the arrangement of chloroplasts and nuclei for comparison with TEM thin section studies.

ii) Chloroplasts - isolation of chloroplasts from pea leaves is a routine method for biochemical studies on these organelles. Providing the extraction is carried out carefully, a high proportion of the organelles remain intact and provide a source of material for studying the internal membrane organization of these organelles by SXCM in a way that is not possible in the intact leaf. Images obtained so far show clearly the arrangement of the granal stacks within the chloroplast.

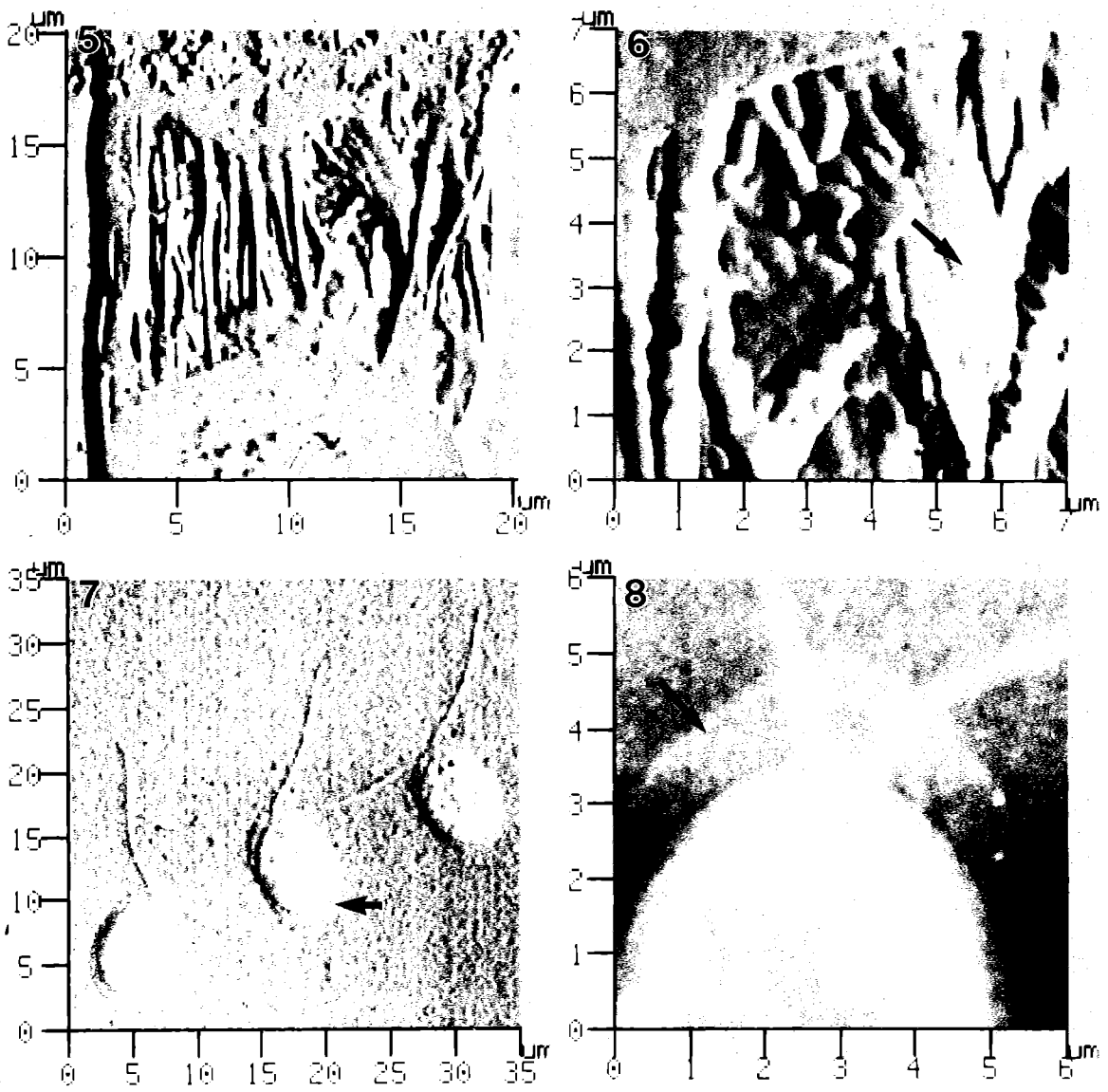

Fig. 5 AFM image of an abscission cell from *Bryum tenuisetum*. The cells adjacent to the abscission cell are very carbon dense and no detail of their structure can be discerned. The fibrillar structure of the abscission cell wall has been imaged because of the lack of cytoplasmic contents (and hence carbon) within the abscission cell.
Fig. 6 High power AFM of part of the abscission cell. Structures, possibly representing underlying cytoplasmic structures can be identified (arrow).
Fig. 7 *Chlamydomonas* cells showing two equal flagella and outer rim of carbon-dilute material (arrow).
Fig. 8 Anterior end of a *Chlamydomonas* cell showing outer rim of thin material (arrow) and insertion of the flagella.

iii) Fibroblasts - cells cultured directly on the photoresist have enabled high resolution images of living animal cells to be produced. This work has been carried out in co-operation with Dr. Chris Wharton from Birmingham University.

iv) Bacteria - a range of bacteria have been imaged by SXCM both for structural studies (comparison of wild type and mutant *Escherichia coli* cells - Bruce Maguire, Oxford) and to follow the germination sequence of bacterial spores (Unilever PLC).

ACKNOWLEDGMENTS

The work reported has been financed by grants from the UK Science and Engineering Research Council, most notably GR/F 81514 and GR/H 72441. At the Rutherford Appleton Laboratory assistance was given by several students. We are also grateful to Pete Anastasi (Kings College) for the manufacture of silicon nitride windows; the staff of the Electron Microscope Unit at Royal Holloway for provision of the electron microscopy facilities and Park Scientific and Oxford University for access to AFM facilities.

REFERENCES

1. Cotton , R.A. , Stead, A.D. & Ford, T.W. - this volume
2. Mersey, B. & McCully, M.E. J. Microsc. 114, 49-76. 1978.3.
3. Cotton, R.A., Dooley, M.D., Page, A.M, Stead, A.D. & Ford, T.W. Annual Report to the Laser Facility Committee, Rutherford Appleton Laboratory. 1992. pp 50-53.
4. Stead, A.D., Cotton, R.A., Page, A., Dooley, M. & Ford, T.W. . SPIE Proceedings (Eds. C.J. Jacobsen & J.E. Trebes) 1741, 351-362. 1993.
5. Bopp, M., Quader, H., Thoni, C., Sawadis, T. & Schnepf, E. F. J. Pl. Physiol. 13, 273-284. 1991.
6. Duckett, J.G. & Ligrone, R. Crypt. Bot. 2/3, 219-228. 1991.
7. Goode, J.A., Alfano, F., Stead, A.D. & Duckett, J.G. Protoplasma, in press.

FOKKER-PLANCK SIMULATIONS OF SHORT PULSE LASER PLASMA EXPERIMENTS

R P J Town[1], S J Rose[2] and A R Bell[1]

[1]Imperial College of Science, Technology and Medicine

[2]Rutherford Appleton Laboratory

The recent development of short pulse high intensity lasers has opened up an exciting new regime in the study of laser produced plasmas. These lasers typically have intensities greater than 10^{15} Wcm^{-2} and pulse duration less than 1 psec. Due to the short timescales the normal long scalelength plasma corona does not have time to develop. The density scalelengths are therefore typically submicron. The energy from the laser is absorbed in a narrow skin layer. This region is rapidly heated to the order of 1 keV. Again due to the short timescales the heat front has little time to penetrate into the target. The temperature scalelength is therefore typically submicron.

The electron mean free path at solid density and a temperature of 1 keV is approximately 0.1 micron. Hence the temperature scalelength and the mean free path of the heat carrying electrons are of the same order. It will be recalled that the Spitzer-Harm approximation [1] for heat transport is valid when the temperature scalelength is approximately a hundred times the electron mean free path. We therefore expect the heat flow to be strongly non-Spitzer and the electron distribution function to be strongly non-Maxwellian.

In order to model the non-local heat flow which is present in short pulse experiments we have written a one dimensional Fokker-Planck code. We have employed the diffusive approximation for the distribution function. This approximation has been successfully used in previous calculations [2-5]. In order that the scheme is unconditionally stable the ADI [6] time splitting scheme is used. The heat transport is coupled to a standard ion hydro equation in Lagrangian form.

Our initial simulations employed classical Inverse Bremsstrahlung absorption. At early times considerable energy was absorbed. This led to a rapid increase in the temperature of the absorbing region. The inverse Bremsstrahlung absorption

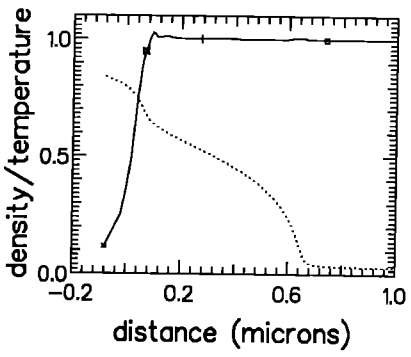

Figure 1: The density (solid line) and temperature (dotted line) profiles at the peak of the pulse.

Figure 2: The temperature profile (dotted line), Fokker-Planck (sold line), Spitzer flux limited to 0.1 (solid squares) and Spitzer flux limited to 0.3 (open triangles) heat flow at the peak of the pulse.

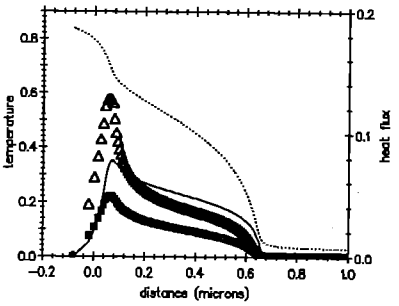

mechanism is directly proportional to the density, but inversely proportional to the temperature. As the density decreased and the temperature increased during the simulation, so the energy absorbed rapidly decreased. For example, less than 10% of the energy was absorbed at an intensity of 10^{15} Wcm^{-2}. In order to achieve realistic absorption levels we use a simple energy dump in a skin layer. This skin depth is calculated from the density of the outermost Lagrangian cell if a critical surface has not formed, or the critical density if the cell has gone underdense. This absorption mechanism assumes that the energy is taken up by the relatively low velocity collisional electrons. Recent PIC simulations [7] have shown that the energy absorption can be explained in terms of both resonance absorption and vacuum heating (the so called Brunel effect [8]). These absorption mechanisms are collisionless effects. The energy is therefore taken up by the higher energy collisionless electrons leading to the creation of fast electrons. In the simulations reported here the effect of these fast electrons has been ignored.

We have modelled the interaction of a 5.10^{15} Wcm^{-2}, 0.5 psec Gaussian KrF laser pulse on a micron thick solid carbon target. The target was initially at solid density and fully ionised. The initial temperature of the target was 15eV. A very fine zoning was employed to accurately model the hydrodynamic response. A step function between the solid target and vacuum was used, i.e. the laser pulse was considered to be pre-pulse free. A 70 zone velocity mesh was employed.

Figure 1 shows the density profile (solid line) and temperature profile (dotted line) at the peak of the pulse. We can clearly see that the target has expanded into the vacuum forming an underdense corona. It is worth noting that even with a cell size of 0.002 microns the region of energy deposition is poorly resolved. Figure 2 shows the temperature profile (dotted line), Fokker-Planck heat flow (solid line), Spitzer heat flow with a

flux limit of 0.1 (open triangles) and Spitzer heat flow with a flux limit of 0.3 (solid squares). The Spitzer heat flow has been calculated from the Fokker-Planck temperature profile with the appropriate limiter applied. In long pulse experiments a flux limiter of 0.1 has been found to reduce the heat flow sufficiently to model the Fokker-Planck results. However this limiter appears to be too severe for short pulse experiments. The limiter has reduced the flux substantially throughout the target. A flux limit of 0.3 gives a much better agreement throughout the target. As the flux limiter is increased beyond 0.3 the Spitzer heat flow substantially overestimates the heat flow near the region of energy deposition.

An important physical process which has been ignored in these simulations is ionisation. Ionisation requires energy to be supplied to the atoms, thus reducing the temperature of the target and therefore reducing the penetration of the heat front into the target. If ionisation took place rapidly then our approximation of a fully ionised target would be reasonable. We have employed the NIMP (Non-LTE Ionisation Material Package) code [9] to model the ionisation state. This is a stand-alone package to post process particular Lagrangian cells. The code takes as its inputs the nuclear charge, atomic weight and the time histories of the temperature, density and radiation temperature (which was set to zero in our case). Collisional and radiative rates for excitation, de-excitation, ionisation and recombination are included in the model. Figure 3 shows the average charge (z*) as a function of time for four Lagrangian cells (these cells are marked on the density plot in figure 1 with the appropriate symbol). As can be seen ionisation takes a considerable time. For example the outermost cell requires 0.3 psec to reach full ionisation. Further into the target the Carbon never reaches the fully ionised state. It should be noted that NIMP post processes the data, hence the energy necessary to perform the ionisation has not be accounted for. Thus the ionisation states probably represent the maximum possible states.

The inclusion of atomic processes in the Fokker-Planck equation has been performed by Marchand and Matte [10]. They have taken account of the same processes as NIMP. Our

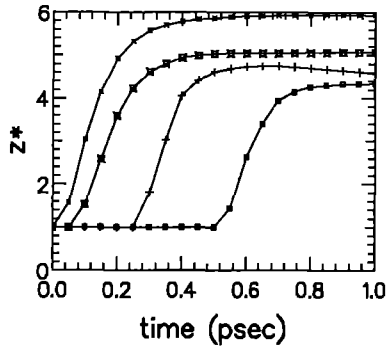

Figure 3: The time evolution of the average ionisation state for 4 Lagrangian cells in the Carbon target. The cell positions correspond to the appropriate symbol marked on the density profile in figure 1.

aim is to produce a code which can be used to model experiments in a reasonable computational time. We feel that it is prohibitive to take account of all the atomic processes. In order to see if it is possible to neglect any atomic processes we modified NIMP to calculate the ionisation state by switching off the effects of (a) radiative process, (b) collisional excitation and de-excitation and (c) three body recombination. Radiative processes gave no difference in the ionisation state. This is reasonable since for the most part the plasma is dense and relatively cold, i.e. it is a collisionally dominated plasma. The absence of collisional excitation and de-excitation led to a difference in the ionisation state. In the outermost cell the final ionisation state was approximately 20% smaller than when all terms were considered. Further into the target the ionisation state was reduced by approximately 10%. Given the level of approximation in the code the difference in the ionisation state is acceptable. When three body recombination was ignored a substantial departure from the exact solution was found. For example the 40th cell reached full ionisation when three body recombination was ignored, but had an ionisation state of only 4.0 when all terms were considered. This error is to be expected. Three body recombination is the opposite of collisional ionisation and, through the law of detail balance, brings the ions to the correct ionisation state. Hence we can model the effect of ionisation by the inclusion of collisional ionisation and three body recombination.

We are currently adding the effects of collisional ionisation and three body recombination into the Fokker-Planck code. As a first step we have post processed the distribution function by multiplying by the cross section for collisional ionisation. Preliminary results indicate that the non-Maxwellian distribution alters the rates by less than 10%.

REFERENCES

1. L. Spitzer Jr. and R. Harm, Phys. Rev. 89, 977 (1953).
2. J. R. Albritton, Phys. Rev. Lett. 50, 2078 (1983).
3. A. R. Bell, Phys. Fluids 28, 2007 (1985).
4. T. H. Kho and M. G. Haines, Phys. Rev. Lett. 55, 825 (1985).
5. E. M. Epperlein, G. J. Rickard and A. R. Bell, Comput. Phys. Commun. 52, 7 (1988).
6. J. Douglas, Num. Math. 4, 61 (1962).
7. P. Gibbon and A. R. Bell, Phys. Rev. Lett. 68, 1535 (1992).
8. F. Brunel, Phys. Rev. Lett. 59, 52 (1987).
9. A. Djaoui and S.J.Rose, J. Phys. B: At. Mol. Opt. Phys. 25, 2745 appendix A (1992).
10. R. Marchand and J. P. Matte, J. Comput. Phys. 97, 352 (1991).

A SATURATION MODEL OF THE RAYLEIGH-TAYLOR INSTABILITY

J D Findlay and A R Bell

Imperial College of Science, Technology and Medicine

Full fluid code simulation of a Rayleigh-Taylor (RT) unstable interface with a large set of sustainable modes is computationally very expensive. Furthermore, simulation of a broad band spectrum covering many decades of k-space, is almost impossible given current computing resources. There are many applications where information about non-linear mode amplitudes is needed without the expense of full simulations. One such example is a one dimensional fluid code being used at Rochester (Deletrez 1990) to study aspects of ICF target implosions. A knowledge of the net perturbation on a RT unstable interface is needed for the 1D code to be realistic, but the computational overhead imposed by calculating spectra using a fluid code would negate the advantage of using a 1D code. It is for this reason that models are needed that can generate spectra by calculating the saturation amplitude of each mode and then assuming the way in which these modes will grow after saturation.

The idea behind this saturation model is that a mode will saturate when the 3rd order component of a mode's amplitude satisfies some given condition with respect to the 1st order component. It was initially envisaged that this condition would be the simple rule that a mode saturates when the magnitude of the 3rd order component reached some detectable fraction of the 1st order component. As will be explain further on, this proved not to be the case. Instead, the ratio of the first to third order components, satisfies a more complex condition at saturation.

Haan's non-linear mode coupling model (Haan 1991) gives the amplitude of a mode k given the amplitude of any other two modes k_1 and k_2, where $k = k_1 \pm k_2$. This can be used to yield the amplitude of low k modes stimulated by the larger amplitude, faster growing high k modes. The amplitude of the low k modes is completely dominated by the coupling of higher k modes and so their amplitudes are second order with respect to the high k modes. At this point, Haan's coupling model can be used again to couple the second order, low k modes back to the high k modes to give a third order contribution to the growth of the high k modes. E.g. $(k_1-k_2)+k_2$ yields a third order contribution to the amplitude of mode k_1. This process is expressed analytically for all possible combinations of couplings between high and low k modes yielding an expression for the third order contribution to the growth of any given mode.

A fluid code was run with a set of 11 perturbed modes from m=15 to m=25, where m=1 is the longest wavelength supportable mode on a periodic mesh. The saturation amplitudes of these modes were measured manually from graphical output and a graph was plotted of kA at saturation against the ratio, ε ,of the third to first order components of each mode's amplitude. It was expected that for any given saturation amplitude, ε, would be a constant. I.e. if ε=0.05 then modes saturate when the third order component is 5% of the first order component. In reality though, a relationship between ε and kA at saturation was found that satisfied the equation,

$$kA_s = 0.2 \pm \sqrt{(2\varepsilon + 0.016)}$$

The next stage is to include this saturation criterion in a code that 'grows' modes from some initially specified amplitude at the classical growth rate. At each timestep ε is calculated for all modes. If the above equation is satisfied for a given mode, or if the equation was satisfied at some point during the last timestep, then the exponential growth of that mode is replaced with ηgt^2 growth with initial amplitude, velocity and acceleration of A_s, γA_s and $\gamma^2 A_s$ respectively. The model yields a spectrum that can be compared with spectra generated by other methods such as fluids codes.

The system being modelled involved a set of 21 dominant modes from m=5 to m=25. The initial amplitudes were calculated using the equation, $A_0(m)$=0.0016-0.00004m. The computational box was 3 units wide with a heavy fluid of density 1 unit, supported by a light fluid of density 0.5 units in a gravitational field of acceleration 1/6 units. Figure (1) shows a comparison of spectra generated by three different methods. First, there are the set of bars representing the spectrum taken from a fluid code run, next there is a line showing the spectrum calculated by another saturation model, namely the saturation model of Haan (Haan 1989). Finally, the spectrum generated by this new saturation model is included. As can be seen, the new saturation model gives good agreement with the fluid code spectrum even when the interface has become very non-linear (Figure 2).

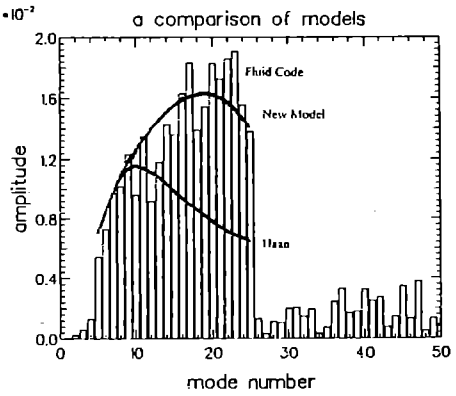

Figure 1: A graph showing a comparison of three spectra.

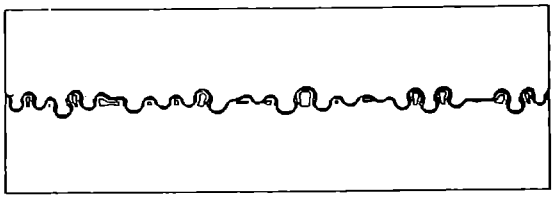

Figure 2: A density contour plot of the interface at a time corresponding to figure (1).

References :

Deletrez, J. Private communication, 1990

Haan, S. W. Phys. Rev. A 39, 5812 (1989)

Haan, S. W. Phys. Fluids B 3, 8, 2349 (1991)

AVERAGE ATOM AND DETAILED MODEL CALCULATIONS OF IONISATION IN GERMANIUM

A Djaoui[1], SJ Rose[1], PB Holden[2] and SB Healy[2]

[1]Rutherford Appleton Laboratory
[2]Department of Physics, University of York, Heslington, York YO1 5DD, UK.

INTRODUCTION

Following the successful demonstration in many laboratories[1-5] of soft X-ray laser based on Ne-like ions, a large number of theoretical simulations for such experiments [6-9] have been reported. The modelling is complicated by the number of physics issues which have to be taken into account. These include heating of the target by the driving optical laser, time dependent atomic physics and finally x-ray laser propagation optics. For many situations it is possible to model the hydrodynamics as well as the x-ray beam propagation with the help of simple models. The kinetics of ionisation and population inversion however, require extensive data sets for hundreds of energy levels, radiative and collisional rate coefficients as well the solution a large number of coupled rate equations. Such large models when incorporated in hydrodynamic codes are usually too complex and simpler and faster models such as the average atom model can be of great help. One advantage of the use of the average atom model is its general applicability to all elements and the ease of its implementation in complex time-dependent coupled atomic physics and hydrodynamics. The simplicity of the model is achieved at the expense of reduced details and it is not always clear how reliable the model is. In this paper the average atom model is compared with more detailed models for the case of germanium under soft X-ray laser operating conditions. A detailed account of the ionisation kinetics is given since this is the most relevant issue in this case and we willl not touch on the issue of population inversion here.

DESCRIPTION OF THE MODELS

The detailed model calculations were performed at York University using a detailled collisional radiative model (COLRAD) for the Ne-like ion coupled with a two level mechanistic model (MGM) for the other ion species. 124 levels were used in the COLRAD calculation, collision rates between n=2 and n=3 levels are calculated using the R-matrix approximation[10]while rates for optically allowed transitions between other levels are calculated according to Van Regemorter[11]. Calculations which include COLRAD for the Ne-like stage are referred to as COLRAD and those without it as MGM.
In the average atom model[8,12], the different ion species present in the plasma are replaced by a single fictitious average ion. This average ion is described by a screened hydrogenic model which calculates average populations for the bound electron shells defined by the principal quantum number n and having degeneracy $2n^2$. The model is therefore unable to describe $\Delta n=0$ transitions or metastable levels. The energy levels are calculated using screening constants and hydrogenic formulae are used for the radiative and collisional rates. The average population are obtained from the solution of n rate equations only. Another useful by-product from the average atom model is that one can use the average population to find the ionic occupations to good accuracy by use of a binomial distribution[8] . This gives the probability of having an ion with a given number of electrons in a given level regardless of the occupation of the other lelvels and reduces to Poisson distribution for the highest levels.

APPLICATION TO GERMANIUM

In the experiment a germanium slab is irradiated with 125 J of the neodymium glass laser in a line focus geometry. The pulse duration is about 500ps and the irradiance 2.5 10^{13} W/cm^2. The slab is heated to a few hundred eV on a timescale of the order of the driving pulse duration. The plasma region where gain occurs starts

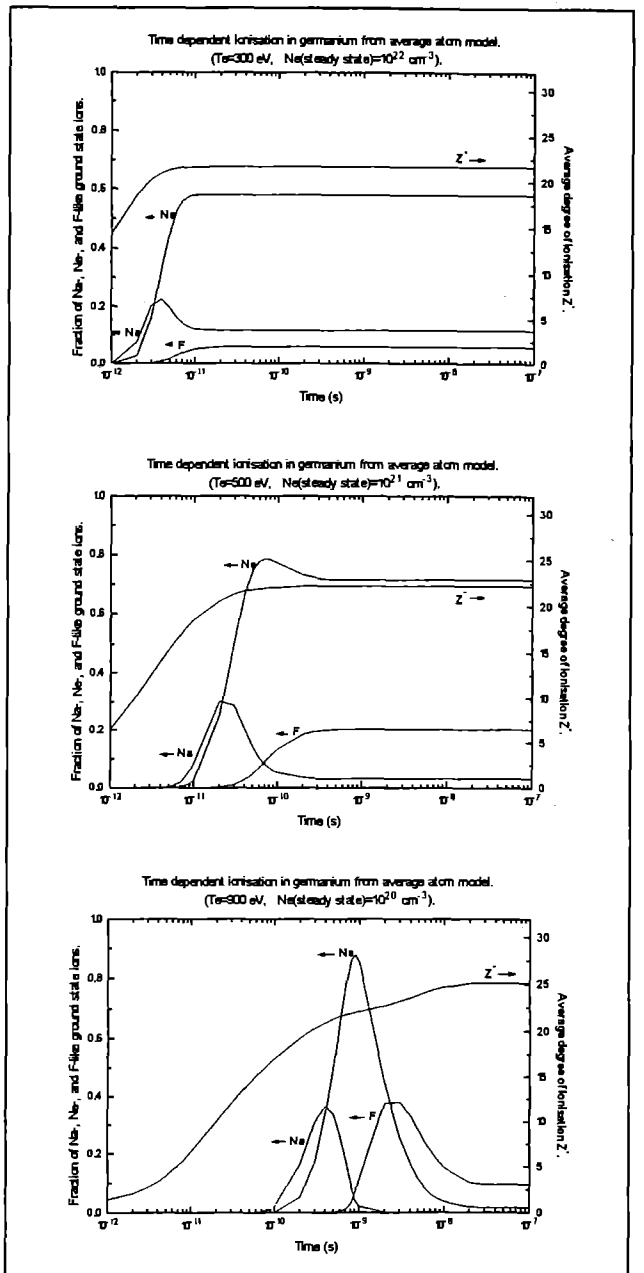

Figure 1: Time dependent ionisation in germanium under different conditions as calculated by the average atom model. A sharp temperature step is imposed at t=0.

off at a high density and low temperature and as it is heated up it expands before reaching optimum gain conditions. The development of ionisation in the plasma follows the local changes in electron density and temperature. The time it takes the ionisation to reach steady state equilibrium is of the order of $10^{12}Te^{3/2}/Ne$ seconds, where Te is in keV and Ne in cm^{-3}. This time is of the order of 10 ps for Ne $=10^{22}$ cm^{-3} and Te=300eV and rises to 10 ns for Ne $=10^{20}$ cm^{-3} and Te=900eV This can be better seen in Figure 1 where the time development of ionisation as well as the fraction of Na-, Ne- and F-like fraction of ground state ions are

shown for different conditions. In these calculations a step in temperature (instantaneous heating) is used. This is not realistic for the modelling of the experiment (since heating occurs over a few hundred ps) but is instructive in showing that initially the conditions in the plasma are very close to steady state since the density is

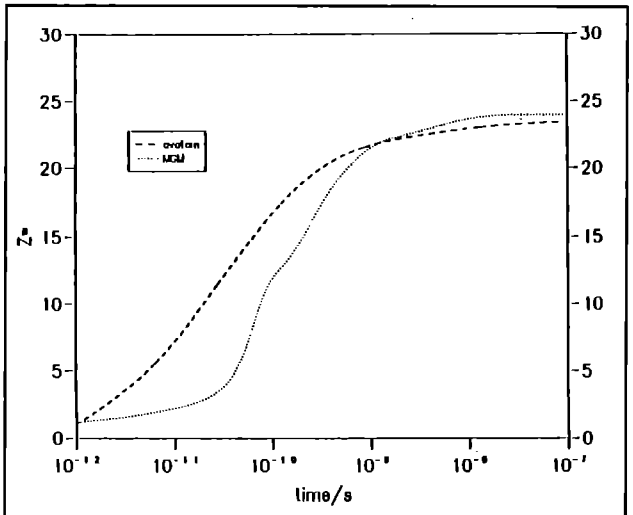

Figure 2: Time development of average degree of ionisation as calculated by different model at Ne=10^{20} cm^{-3} and Te=700 eV.

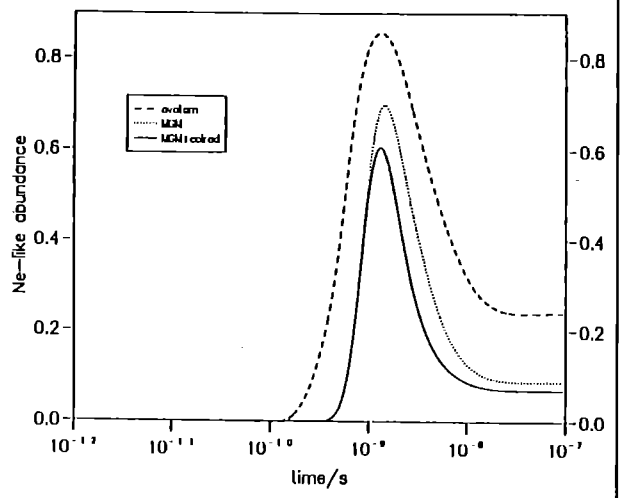

Figure 3: Time development of Ne-like abundances as calculated by different model at Ne=10^{20} cm^{-3} and Te=700 eV.

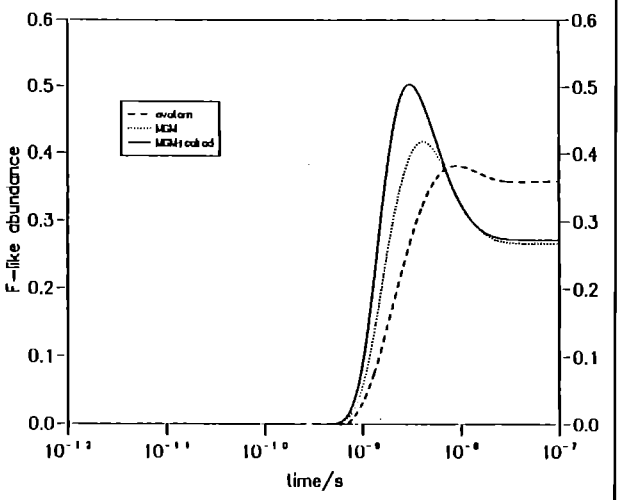

Figure 4: Time development of F-like abundances as calculated by different model at Ne=10^{20} cm^{-3} and Te=700 eV.

high and the relaxation times short. As the plasma heats and expands to optimum conditions, the relaxation time for ionisation becomes much larger than the time scales for changes in the system. The modelling of the x-ray laser gain is then sensitive to the method used for the calculation of ionisation kinetics. Figure 2 shows the average degree of ionisation as calculated by the average atom model and MGM. The steady state values are in good agreement. This was verified over a wide range of temperature and densities. The discrepancy at early times is the result of the use of a temperature step. The use of a gradual temperature ramp results in a better agreement at early times. The agreement gets better as the duration of the ramp is increased from 10 ps to 1ns. Figure 3 and 4 show the time development of the Ne-like and the F-like ground state ion fractions respectively. Clear discrepancies appear between the average atom and the detailed models. The average atom model consistently over-estimates the Ne-like fraction and underestimates the F-like fraction on time scales of relevance to the x-ray laser experiment despite the fact that the average degrees of ionisation are very similar (Figure 2). This a consequence of the use of the binomial distribution for the calculation of the fraction of ions. Such assumed distribution is simply unable to treat strong ionisation from Ne-like to F-like ions correctly. Any depletion of the n=2 population is implicitly assumed to result in a distribution of ions around the average ionisation stage. The average atom model, although predicting the correct ionisation degree results in a broader ionic distribution. The calculation from COLRAD shows a higher ionisation from Ne- to F-like ions as compared to MGM. This the consequence of ionisation from excited states which is modelled correctly in COLRAD but not in MGM. The discrepancy between COLRAD and MGM is also as large as the discrepancy between MGM and the average atom model. This shows that in order to model the kinetics of ionisation correctly a detailed model is necessary. When such model is not available the average atom model provides the best second choice. The extra effort invested in an intermediate model in not always justifiable.

CONCLUSION

We have compared calculations of ionisation in germanium using three different models. There is good agreement in the calculated average degree of ionisation. Time dependent ionic abundances show some discrepancies from model to model. Accurate results in this case can only be obtained with a detailed collisional radiative model which is able to account for the details of the kinetics between different ionisation stages and different excited states. For near steady state situations however, the results from the average atom model are within a factor of two from the results of the detailed models. If some loss of accuracy can be tolerated, the use of the average atom model is recommended.

REFERENCES

1. D L Matthews *et al*, Phys. Rev. Lett. **54**, 110 (1985).
2. T N Lee *et al* Phys. Rev. Lett. **59**, 1185 (1987).
3. D M O'Neill *et al*, Optics Communications, **75**, 5, 406-412, (1990).
4. D Naccache *et al*, Phys Rev. A., 42, 5, 3027, (1990).
5. H Daido *et al*, OSA Topical Meeting on Short Wavelength Coherent Radiation: Generation and Applications., Monterey, CA., April 8-10, (1991).
6. B L Witten *et al*, J. Opt. Soc. Am. **5**, 2537, (1988).
7. R A London *et al* J. Phys. B: At. Mol. Opt. Phys. 22, 3363-3376, (1989).
8. A Djaoui and S J Rose, J. Phys. B: At. Mol. Opt. Phys. **25**, 2745-2762, (1992).
9. P B Holden *et al*, to be published.
10. E Robertson et al, Annual Report of the Central Laser Facility, **RAL-92-020**, 72, (1992).
11. H Van Regemorter, *Ap. J.*, **136**, 906, (1962).
12. W A Lokke and W H Grasberger, *XSNQ-U: A non-LTE emission and absorption subroutine*, UCRL-52276, LLNL, Livermore CA 94550, (1977).

MHD CALCULATIONS OF THE EFFECT OF MAGNETIC FIELD IN SHORT PULSE EXPERIMENTS

A R Bell

Imperial College of Science, Technology and Medicine

Recent short pulse experiments with the new CPA system at the CLF have shown that the ablating plasma is collimated into a jet. The experiment is described elsewhere in this report (Beg et al). Collimation of the very fastest ions may be explicible in terms of uniform acceleration by an electrostatic field at the surface of the target while it is still relatively flat at the start of the expansion[1], but the collimation of the majority of ions cannot be explained in this way since their dynamics are more correctly described as a bulk expansion away from a point origin (the laser spot). Fluid simulations of the experiment which neglect magnetic field predict nearly isotropic expansion.

We suggest that collimation is caused by magnetic pinching. Order of magnitude estimates indicate that the pressure-driven source of magnetic field[2] might generate fields of 10's of MegaGauss with a magnetic pressure comparable with the thermal pressure and hence capable of influencing the target dynamics. We investigated this possibility with a computer code (MH2D) which solves the MHD equations in cylindrical (r,z) geometry. The code includes the presssure-driven source term, resistive diffusion of magnetic field, and Spitzer thermal conduction with magnetic inhibition. The plasma is treated as a single temperature, fully ionised perfect gas. Laser energy is absorbed by a 20% dump at the critical surface into the thermal plasma. Electric currents are limited so that the electron drift velocity does not exceed the electron thermal velocity. Additional transport effects such as the Righi-Leduc and Nernst terms are ignored. Transport by ions or suprathermal electrons is not included. Thus the code ignores many undeniably important effects, but in practice, it appears that the most serious uncertainty lies in the effect of the magnetic field on transport. A particle code[1], although more appropriate to the experiment, would be too slow to model the full experiment.

The code was run for a plastic foil irradiated by a 4 psec laser pulse at an irradiance of 3×10^{17} W cm^{-2} focussed to a 50 micron diameter spot. The density profile was initialised with an exponential ramp with a 2 micron e-folding length. Magnetic inhibition of heat flow was imposed by reducing the Spitzer conductivity by $(\omega\tau)^{-3/2}$, which is the geometric mean of Braginskii and Bohm inhibition. Before the laser intensity reaches its peak, transport is unmagnetised, and energy spreads easily along the target surface beyond the edge of the laser spot. But as the magnetic field grows, $\omega\tau$ reaches a critical magnitude at which transport becomes inhibited, energy cannot escape from the laser spot, the peak temperature rises, the temperature gradient increases and magnetic field is produced more rapidly. This positive feedback causes a rapid rise in temperature and magnetic field[3]. The magnetic field field reaches a peak value of 30 MG. The magnetic pressure of 40 Mbar plays an important part in driving the ablation [4]. Figure 1 presents logarithmic contour plots of calculated density, temperature and magnetic field 28 psec after the peak of the laser pulse. The surface plasma is ablating freely away from the target, and is clearly collimated into a jet. The length of the jet is approximately 100 micron. Its temperature is 10 keV.

The calculations were repeated with the transport reduced by $(\omega\tau)^{-1}$ (Bohm-like) and $(\omega\tau)^{-2}$ (Braginskii). In neither case was substantial collimation observed. However, both of these inhibition laws produced temperatures in clear disagreement with the experiment: 10 keV in the Bohm-like case, 1 MeV in the Braginskii case. Our chosen $(\omega\tau)^{-3/2}$ inhibition gives a peak temperature around 100 keV, which seems large but agrees with experiment. As an indication that our results are not extreme, we note that Wilks et al[5] using a particle code, albeit at an irradiance 10x larger, find magnetic fields of 250 MG and magnetic pressures of 2500 Mbar.

Our calculations are very sensitive to the treatment of transport, but they show that the observed collimation can be reproduced in numerical calculations which include magnetic pinching.

References:

1. DW Forslund and JU Brackbill.
Phys. Rev. Lett., 48, 1614 (1982).
2. JA Stamper.
Lasers & Particle Beams, 9, 841 (1992).
3. T Yabe and M Hasegawa.
Phys. Rev. Lett., 57, 2667 (1986).
4. RS Craxton and MG Haines.
Plasma Phys., 20, 487 (1978).
5. SC Wilks, WL Kruer, M Tabak and AB Langdon.
Phys. Rev. Lett., 69, 1383 (1992).

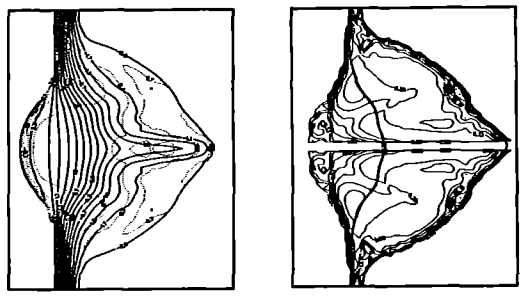

Figure 1. Logarithmic contours of a) density (full lines in units of 10^{21} cm^{-3}) and temperature (dotted lines in keV) and b) magnetic field (MG) 28 psec after the peak of the laser pulse. The thick contour lines on b) give the positions of the critical surface and the plasma-vacuum interface. The computational box is 283x212 micron.

THREE DIMENSIONAL SIMULATIONS OF THE RAYLEIGH-TAYLOR INSTABILITY DURING THE DECELERATION PHASE

B. J. Jones, R. P. J. Town and A. R. Bell

Imperial College of Science, Technology and Medicine

A major obstacle to the attainment of fusion conditions in Inertial Confinement Fusion (ICF) is the problem of achieving implosion symmetry. In a typical ICF implosion there are 2 distinct periods during which the shell is vulnerable to Rayleigh-Tayler (RT) growth. The majority of the work done on the ICF related RT instability has been concerned with the acceleration phase. We present here results of simulations modelling the deceleration phase using the three dimensional spherical hydrocode PLATO. Details of the code and typical simulation initial conditions have been given elsewhere [1].

We have recently performed simulations to improve the quality of our estimates for the reduction of RT growth from the classical value. Instead of averaged quantities we now use instantaneous values of interface acceleration and perturbation wavenumber to calculate the theoretical growth rate. We also remove the effect of a Richtmeyer-Meshkov growth contribution caused by a reflected shock passing through the shell just before maximum compression.
We find that for modes 6, 10 and 12 there is a constant reduction to approximately 85% of the classical value. The possible effects leading to RT growth rate reduction in the deceleration phase are i) spherical geometry effects, ii) the presence of finite density gradient scalelengths and iii) finite shell thickness. We have estimated the size of these three effects [2,3,4] and found the thin shell effect to be of negligable importance. It seems that the observed reduction can be attributed to a combination of spherical geometry and a density gradient with a scalelength of ~1.0μm. Note that the density gradient effect becomes stronger with increasing mode number whereas the spherical effect has the opposite mode dependance explaining the observed uniform reduction across a range of modes.

In order to examine the saturation of linear growth we have compared simulations which remain in the linear regime to large amplitude simulations which saturate. We overlay plots of amplitude against time normalised to have the same initial scaled amplitude. The point at which the curves deviate is an indication of the time at which saturation has occured. We have found that modes 6, 10 and 12 all saturate when the perturbation amplitude is ~10% of the wavelength.

We have previously attempted to quantify RT instability growth in the non-linear regime by fitting an $\eta g t^2$ law to the evolution of the total mixing region thickness. This is, however, a crude approximation to the non-linear development. For this reason the seperate effects of the spike and bubble have been examined. The bubble amplitude is defined as the distance from the unperturbed interfacial position to the maximum radial position of the shell inner surface. The spike amplitude is defined as the distance from the unperturbed interfacial position to the minimum radial position of the inner surface.
The unperturbed position of the interface is calculated from a 1-D code, equivalent to performing an unperturbed 3-D simulation. The spikes should be in approximate free-fall with an amplitude, δ_s, given by

$$\delta_s = \delta_{s_0} + \tfrac{1}{2}\sigma\alpha g(t - t_0)^2$$

where σ is constant and α is the Atwood number. The bubbles of height δ_b are predicted to grow with a velocity [5] of

$$\dot{\delta}_b = \varepsilon\sqrt{g\lambda}$$

where g is the system acceleration, λ is the perturbation wavelength and ε is the Froude number. The value of ε depends on the geometry of the system. Theoretical and experimental values for ε have clustered around 0.16 for 2-D planar systems and 0.24 for 3-D axisymmetric bubbles. For simulations of modes 6, 10 and 12 we have found that the spikes fall as predicted with σ~0.75-0.85. Our simulations of mode 6 bubbles have given values of ε dependant upon the perturbation configuration. The bubble-ridge configuration gives a value of 0.26 whereas the valley-spike configuration gives a value of 0.17. This form of growth is observed until just before maximum compression when a reflected shock passes across the fuel-shell interface and causes an increase in $\dot{\delta}_b$ by the Richtmeyer-Meshkov effect. Examination of the shapes of the two different perturbation configurations [1] shows that the bubble-ridge case has bubbles similar in shape to Layzer's 3-D axisymmetric bubbles while the valley-spike case has bubbles which are much more 2-D in form. It is interesting to note, then, that the values of ε observed are very close to those predicted for 3-D and 2-D bubbles respectively. Modes 10 and 12 seem to grow similarly to mode 6 but we have observed the presence of different sized bubbles leading us to expect some bubble competition effects.

We are currently extending the code to model electron thermal transport. We are also planning to use a radially sliding mesh so that we can investigate perturbation growth during implosions with a high compression ratio.

References:

1. RPJ Town and AR Bell, Phys. Rev. Lett. 67, 1863 (1991).
2. MS Plesset, J. Appl. Phys. 25, 96 (1954).
3. KO Mikaelian, Phys. Rev. A 40, 4801 (1989).
4. LD Landau and EM Lifshitz, Fluid Mechanics 2nd edition, section 12, 36.
5. D Layzer, Astrophys. J. 122, 1 (1955).

X-RAY ROCKING CURVE CALCULATION FROM SHOCKED SINGLE CRYSTALS

N C Woolsey and J S Wark

Clarendon Laboratory, Department of Physics,
Oxford University

INTRODUCTION

Laser driven shock compression of crystalline materials has been performed using the VULCAN laser[1-3]. The shocked state of the crystal is observed by time resolved *in-situ* X-ray diffraction. This technique allows the material behaviour under ultra-high rates of strain to be diagnosed at the lattice level, a facility unique in the field of shock wave physics. The hydrodynamics of laser shock compressed solid state materials can be modelled using a modified Med101[11] code. The modifications incorporate a Mie-Grüneisen equation of state to allow accurate modelling of the solid material. To aid comparison between experiment and numerical modelling it is necessary to extract X-ray rocking curves from the strain profiles provided by simulation. The theory of X-ray diffraction for strained media was developed 20 years ago by Takagi[4] and independently by Taupin[5]. The Tagaki-Taupin formulation extends the dynamical theory of X-ray diffraction to a strained infinite crystal by allowing the Fourier coefficients of the periodic dielectric constant to slowly vary as a function of position instead of being constants. The dynamical theory, a first order theory[7], takes account of absorption (photoelectric effect and Compton scattering) and extinction (coherent scattering) of the wave fields within a crystal. This theory provides excellent descriptions of diffracted intensities and directions.

THEORY

For the case when the crystal is close to the Bragg condition only the incident and one diffracted wave exist, assuming the crystal is centro-symmetric the Tagaki-Taupin equations can be written,

$$i\frac{\lambda}{\pi}\frac{\partial D_H}{\partial x_H} = \psi_0 D_H + \psi_H D_0 - \alpha_H D_H - \frac{i\lambda^2}{2\pi} D_H(\nabla\phi_H), \qquad (1a)$$

$$i\frac{\lambda}{\pi}\frac{\partial D_0}{\partial x_0} = \psi_0 D_0 + \psi_H D_H - \frac{i\lambda^2}{2\pi} D_0(\nabla\phi_0). \qquad (1b)$$

Where D_0 and D_H are the incident and diffracted (from the lattice planes (h,k,l)) wave fields, λ the X-ray wavelength and $\phi_{0,H}$ a phase parameter. The Lapacians in Equations (1) can be shown to be negligible for X-rays[5], α_H is the deviation from the Bragg angle due to strain at each point in the crystal. For 1-dimension distortion, such as the depth dependent strain found in planar shock waves, Equations (1) reduce to[7];

$$i\frac{dX}{dA} = X^2(1+ik) - 2X(y+ig) + (1+ik). \qquad (2)$$

Where the complex variable X is introduced and

$$X(A) = \frac{D_H(A)\sqrt{|\gamma_H|}}{D_0(A)\sqrt{|\gamma_0|}}. \qquad (3)$$

The Zachariasen[6] definitions have been used

$$x_{0,H} = -\frac{\lambda A_{0,H}}{\pi\psi_H'}, \qquad (4a)$$

$$\psi_{0,H} = \psi_{0,H}' + \psi_{0,H}''; \qquad \psi_H = \psi_H'(1+ik), \qquad (4b)$$

$$b = \frac{\gamma_0}{\gamma_H}; \qquad \gamma_{0,H} \text{ are the direction cosines}, \qquad (4c)$$

$$A = -\frac{\gamma_H A_H + \gamma_0 A_H}{\sqrt{|\gamma_0\gamma_H|}}, \qquad (4d)$$

$$g = -\frac{(1-b)\psi_0''}{2\psi_H'\sqrt{|b|}}, \qquad (4e)$$

$$y = -\frac{(1-b)\psi_0' + b\alpha_H}{2\psi_H'\sqrt{|b|}}. \qquad (4f)$$

Using Equation (2) Larson and Barhorst[8] obtained strain depth profiles for ion bombarded and laser annealed silicon single crystals. They used Runge-Kutta numerical integration to interate towards a satisfactory solution to the equation. Wie, Tombrello and Vreeland[9] improved on this computationally expensive procedure by integrating Equation (2) to obtain

$$X(A) = \frac{sX_0 + i(B+CX_0)\tan[s(A-A_0)]}{s - i(C+BX)\tan[s(A-A_0)]}. \qquad (5)$$

with the definitions;

$$X(A_0) = X_0, \qquad B = -(1+ik), \qquad (6)$$

$$C = y + ig, \qquad s = \sqrt{C^2 - B^2}.$$

Equation (5) is evaluated by a layer approximation. The crystal is divided into a number of parallel laminae of constant strain, the solution is obtained by solving (5) for each layer working from the inner-most to the surface. The number of laminae is determined by ensuring the shift in the Bragg angle as a result of the strained lattice is smaller than the rocking curve width for each laminae. In shock wave simulations considered here, tensile and compressive states upto 8% of the initial density are generated, for such large shifts a large number of laminae are needed for an accurate evaluation of the rocking curve. Post-processing hydrodynamic output in this fashion is CPU intensive.

Kinematic theory offers a considerable reduction in computational time and a simplification of the mathematics. Recent data analysis has shown the integrated reflectivity from a shocked crystals reaches the kinematic limit as the shock-wave breaks out the rear surface[10]. If the integrated reflectivity approaches the kinematic limit then each layer within the crystal must be kinematic, kinematic theory can be applied in such cases. The dynamical theory of Tagaki and Taupin can be applied to the kinematic extreme by neglecting dynamical interactions and extinction. The diffracted intensity is extracted by summing the coherently interfering reflections accounting for phase lags and ordinary absorption. This procedure offers little computational improvement over a full dynamical calculation.

Another approach is taken here. We assume the X-ray beam enters the crystal and is reflected by a layer at depth T, the

absorption within the layer is ignored. The integrated reflectivity of the layer is[6]

$$\delta P = \left(\frac{4w_s}{3\sqrt{|b|}} \right) \tanh[A]. \qquad (7)$$

Where w_s is the dynamical width of the laminas' rocking curve. The incident and reflected beams are attenuated by ordinary absorption μ (this is essentially the kinematic approximation; extinction is ignored). The reflective power of a laminae of thickness A at depth T is[6]

$$R(A,T) = \tanh[A] \exp\left(\frac{-\mu T}{\frac{1}{\gamma_0} - \frac{1}{\gamma_H}} \right). \qquad (8)$$

The reflecting power is assumed constant over the angular range w_s centred on the Bragg angle of the strained layer. The hydrodynamic output is re-zoned into a large number of layers to ensure the angular change in Bragg angle from one strained laminae to the next is the same as the dynamical width.

RESULTS

A typical strain profile calculated with the modified Med101 code on a 150 cell grid is shown in Figure 1. The simulation shows the shock wave during shock breakout, a rarefaction is travelling back into the bulk of the target, the material close to the surface is in tension whilst material deeper in the target is still compressed. The kinematic theory can be safely used on materials with strain profiles similar to Figure 1 as the material is perfectly kinematic. Figure 2a shows the rocking curve calculated from Figure 1 using the dynamical theory of X-ray diffraction. Figure 2b shows the same calculation using the approximation expressed by Equation (8). The curves in Figures 2a and 2b are in excellent agreement, with integrated intensities in agreement to better than 3%. The calculation for Figure 2b (approximation) was 60-100 times faster than the calculation for Figure 2a. The small scale differences between Figures 2a and 2b are of little significance since the rocking curves are convolved with the line emission from a laser-plasma (e.g. helium-like). After convolution the small scale structure is lost.

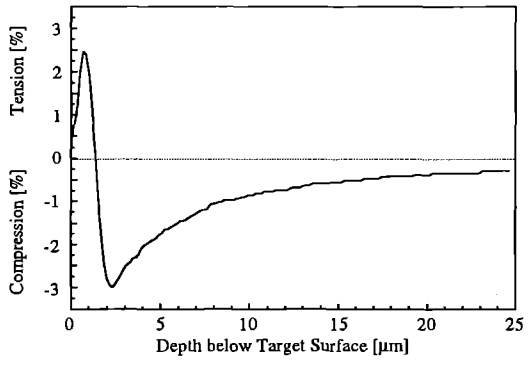

Figure 1 Output from Medusa, 150 cell simulation of a shock wave breaking out from the rear surface of a crystal.

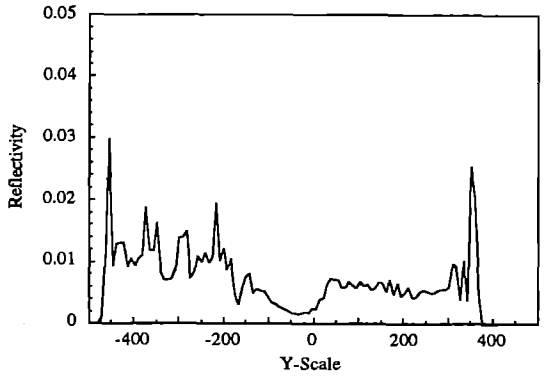

Figure 2a Rocking curve calculated from the strain profile shown in Figure 1. This calculation used the dynamical theory.

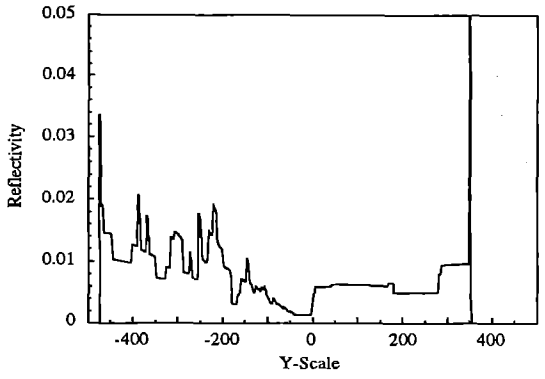

Figure 2b Rocking curve calculated using the approximate theory of Equation (8).

REFERENCES

1. J S Wark, R R Whitlock, A A Hauer, J E Swain and P J Solone Phys. Rev. B35, 9391 (1987).
2. J S Wark, R R Whitlock, A A Hauer, J E Swain and P J Solone. Phys. Rev.. B40, 5705 (1989).
3. J S Wark, G Klein, R R Whitlock, D Riley and N C Woolsey. J. Appl. Phys., 68, 4531 (1990).
4. S Tagaki. Acta Crystallog. 15, 1311 (1962).
5. D Taupin. Bull. Soc. Franç. Minér. Crist. 87, 469 (1964).
6. W H Zachariasen. *Theory of X-ray Diffraction in Crystals*, New York (1945).
7. The deviation of refractive index is taken to first order and the variation in complex amplitudes over one X-ray wavelength are taken to first order (see ref. 6)
8. B C Larson and J F Barhorst. J. Appl. Phys., 51, 3181 (1980).
9. C R Wie, T A Tombrello and T Vreeland. J. Appl. Phys. 59, 3743 (1986).
10. The crystal appears to behave kinematically when the shock occupies a region from the crystal surface to a depth of 2-3 extinction depths.
11. P A Rodgers, A M Rogoyski and S J Rose. RAL Report, RAL 89-127, (1987).

OPTIMISATION OF BRIGHTNESS AND COHERENCE IN XUV LASER AMPLIFIERS

M H Key [1,2] and C G Smith [2]
[1] SERC Rutherford Appleton Laboratory
[2] Oxford University Dept of Atomic and Laser Physics

INTRODUCTION

Optimisation of brightness and coherence in XUV lasers which operate by amplification of spontaneous emission (ASE) requires diffraction limited output divergence and saturation of gain. The necessary conditions can be obtained with two similar but axially separated laser elements in injector-amplifier configuration.

If the width of the two gain elements is w and their separation is L, then, $w/L=\lambda/w$ gives a diffraction limited beam (provided the amplifier does not distort the wavefront by more than a small fraction of λ).

Saturation is obtained for laser elements of length l and gain coefficient g when

$$\frac{\exp gl}{\sqrt{gl}} = 4\pi\left(\frac{L}{W}\right)^2\left(\frac{1}{\tau A_l}\right)\left(1-\frac{n_l g_u}{n_u g_l}\right) \qquad (1)$$

where A_{ul} is the radiative lifetime, τ the gain recovery time, g the gain and $(1-n_l g_u/n_u g_l)$ the population inversion fraction.
The brightness of the saturated and fully spatially coherent output is then.

$$B_s = \frac{8\pi h\upsilon^5}{c^4}\left(\frac{1}{\tau A_{ul}}\right)\Delta\upsilon W^2 \quad Wcm^{-2}sterad^{-1} \qquad (2)$$

There has already been significant experimental progress towards these ideal conditions, with saturation demonstrated[1] and divergence reduced to as low as 5 times the diffraction limit[1].

Further progress can be anticipated with the full exploitation of separated laser elements. New facilities for injector -amplifier XUV lasers have been developed and tested in a preliminary way as described elsewhere in this Annual Report . The optical characteristics of the amplifier are a crucial limiting factor . The purpose of the present discussion is to assess this limitation, with particular reference to the λ=23.6 nm Ge XXIII laser.

INJECTOR CHARACTERISTICS

An injector element with half the gain length gl required for saturation will have a length to width ratio l/w giving a lower bound geometrically limited divergence w/l, which is n times diffraction limited with $n= w^2/l >>1$. For the example of Ge XXIII, with w= 100 microns, g=4/cm and l=2.5 cm we have n=17 (divergence 4 mrad) . Refraction effects typically increase the divergence to 10 mrad.

BRIGHTNESS GAIN IN AN AMPLIFIER

The separation L of the injector and amplifier elements specified earlier ensures that the injected wavefront at the amplifier element is fully coherent and planar over the aperture w .The injected intensity I is then approximately I_0/n^2.The amplifier has in general a spatially varying refractive index across its aperture the effect of which can be characterised as creating at its exit a beam divergence βl. This assumes that the lateral deviation of rays in the amplifier is smaller than the width w of the gain region, requiring $l\leq (2w/\beta)^{1/2}$,and that angular deviation of rays is due to a transverse variation of refractive index which is constant along the length of the amplifier.(Scattering by random fluctuations of index would give divergence increasing as $l^{1/2}$).The convolution of diffraction limited and refraction induced divergence is then,

$$d\theta = ((\lambda/w)^2+(\beta l)^2)^{1/2} \qquad (3)$$

The output brightness for an injected intensity I is given by,

$$B = I\exp(gl)/d\theta^2 \qquad (4)$$

and the gain in brightness can be expressed as,

$$G = (\lambda/w)^2\exp(gl)/(\beta l)^2 \qquad (5)$$

This assumes that the divergence is due to uncorrectable deformations of the wavefront. The possibility of a correctable component of the divergence is discussed later.

The ratio g/β is then a significant figure of merit for an amplifier and a typical value for the slab GeXXIII laser estimated from numerical modelling is 1000. (gain 4/cm and $\beta = 4$ milliradians/cm). Figure 1 illustrates how the gain in brightness varies with gl and with the figure of merit and shows that there is a minimum gl required to obtain any increase in output brightness.

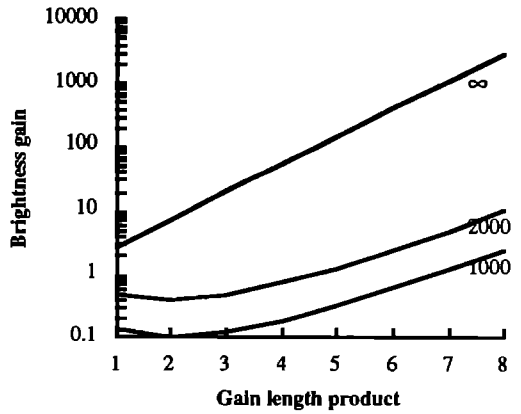

Figure 1.Ordinate shows gain in brightness ; abscissa shows gain length product. Plots are for g/β values 1000, 2000 and ∞.

It also follows that, since reaching saturation requires each element to have $gl\geq 10$, he divergence of the saturated output will be approximately $10\beta/g$ which relative to the diffraction limit is $10(\beta/g)(w/\lambda)$. For the example quoted this is 42 x diffraction limited, (10mrad).

CORRECTABLE WAVEFRONT DISTORTION

For the quoted example the injector- amplifier appears to fail to give diffraction limited performance, but the estimate ignores the important difference between uncorrectable and correctable wavefront distortions.

The previous discussion of the injector noted the geometrical limit to divergence. The source of ASE can be regarded as an incoherent disc of aperture w and the Van Cittert Zernike theorem shows this to create random phase variations on a transverse coherence length $l_c=\lambda l/w$ at the injectors exit aperture, (w/17 for the quoted example). This coherence length is directly related to the geometrical divergence, $(\lambda/l_c=w/l)$. There is no way to correct this basically random imperfection of the wavefront.

By contrast the source of radiation in the amplifier is from a small part of the injector output beam which is diffraction limited and coherent over the aperture of the amplifier . It is easy to show that this injected radiation dominates strongly over the spontaneous emission in the amplifier. The exit wave front from the amplifier has systematic aberration rather than random phase variation and part of this aberration is correctable.

PERPENDICULAR TO THE TARGET SURFACE

Figure 2 shows as an example the numerically calculated variation of electron number density and gain in a GeXXIII laser in the direction perpendicular to the surface of a foil target.[3]

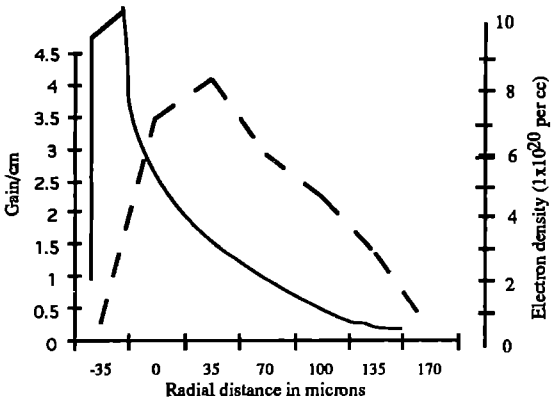

Figure 2 Ordinate plots gain (dashed) and electron number density and abscissa the distance perpendicular to the target surface computed numerically for $I=2x10^{13}Wcm^{-3}$ 600 ps after the 0.6ns pulse peak[2].

This can be used to compute the phase retardation per unit length of the amplifier at the laser wavelength, $d\phi=\pi\ N/\lambda N_c$ where N is the density of electrons and N_c is the critical density at the laser wavelength. The spatial profile of phase can be represented as a power series expansion centred at a chosen transverse location so that $\phi= a+by+cy^2+$ ..... The first term gives a spatially uniform retardation and is of no concern. The second term represents the prismatic component of the aberration. It does not affect the divergence but does limit the length over which rays remain within the gain region as noted earlier For the example quoted its magnitude is 20 mrad/cm, limiting the validity of our approximation to length of 1cm . It is however fully correctable by bending the target and experiments to study this have already been carried out as reported in another section of this report. The third term represents a spherical lens in the paraxial limit. Its effect on the wavefront for the example quoted introduces a positive focusing of the beam which deflects the marginal rays at 50% of peak gain by plus or minus 5mrad/cm. This would be observed in the exit beam as a divergence of 10 mrad/cm but is fully correctable with a spherical mirror and does not degrade the brightness or coherence of the beam . An interesting corollary is that with a bent target compensating the prismatic deviation ,the lens effect gives a trapped mode as in an optical fibre., if the length exceeds the previously quoted criterion for lateral deviation equal to the dimensions of the gain region. Higher order terms are not simply correctable and the divergence which they contribute will in general diminish the brightness and coherence of the beam. The higher order effects can be considered as residual phase aberrations after subtraction of the first three terms. A criterion for an ideal amplifier which sets a limit on the length is that these residual effects should give less than $\lambda/2$ aberration. Figure 3 shows an estimate from the numerically modelled example suggesting in the best 50 μm aperture a 1cm amplifier has reasonably good optical characteristics.

PARALLEL TO THE TARGET SURFACE

Effects parallel to the target surface can be analysed similarly. The main difference is that the profiles of electron number density and of gain are symmetrical peaks of width similar to the width of the line focus producing the plasma. For the example of interest this is typically 100 microns. There is therefore no prismatic component and the lens effect is negative, in contrast to the positive lensing perpendicular to the target. The magnitude of the lensing can be estimated from the experiments described elsehwere in this report to be 5 mrad/cm for the rays undergoing half peak gain. The higher order residual effects depend on the detailed shapes of the density and gain profiles, which require 2D numerical modelling, and have not been estimated here.

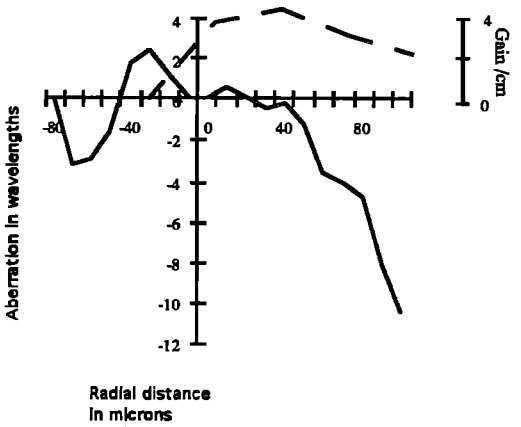

Figure 3 Ordinate shows gain (dashed) and residual retardation in wavelengths of the XUV laser . The abscissa is distance from the target surface. The data are computed for the conditions of figure 2 for a 1cm length.

MEASUREMENT OF BRIGHTNESS AND COHERENCE

The effects discussed limit the brightness and coherence attainable in injector- amplifier systems. Experimental measurement is probably most easily accomplished by recording the laser beam pattern obtained by focusing with a spherical mirror. For the previous example the ideal injector amplifier separation is 42cm. If the output beam were focused by a mirror of for example focal length 50cm located 100cm from the amplifier, the waist of the focused beam would be located at 98cm from the mirror in the plane of the target surface and at 102 cm in the perpendicular plane for the lens effects of the previous example. The astigmatism in the 4cm separation of the foci would make the foci up to 200 microns long in the aberrated direction. In the optimally focused direction the diffraction limited width would be 5 microns , and proportionally wider if the higher order effects aberrations were significant. Such measurements would therefore test directly the quality of the XUV laser beam.

TEMPORAL AND SPATIAL VARIATIONS

The profiles of density and gain perpendicular to the target surface vary significantly with time during the laser pulse as shown by numerical modelling . This means that a curved target can fully compensate prismatic effects only at one instant in time and that the location of the astigmatic focus in the plane perpendicular to the target surface will change with time. Streak camera measurements could reveal the magnitude of this change, which can also be estimated from numerical modelling. In the plane of the target the profiles of density and gain expand slightly with distance from the target so that the strength of the negative lensing is not constant across the gain aperture perpendicular to the surface. This effect would broaden the astigmatic line focus perpendicular to the target surface. In general observation of the minimum width of the astigmatic line foci can show the approach to fully coherent and therefore diffraction limited output. Streak camera time resolution can show the temporal variation of the lensing, though any application of the time integrated beam involving optical correction of the astigmatism will be limited to the time averaged quality.

The discussion here suggests that significant increases in brightness and coherence will be obtainable by optically correcting the beam from two element injector- amplifier lasers.

REFERENCES

1 A Carillon,H Z Chen, P Dhez, L Dwivedi, J Jacoby, P Jaegle, G Jamelot, J Zhang, M H Key, A K kidd, A Klisnick, R Kodama, J Krishnan, CLS Lewis, D Neely, P Norreys, D O'Neill, GJ Pert, S A Ramsden, J P Raucourt, G J Tallents, J Uhomoibhi, Phys Rev Lett 68, 2917 (1992)

2 P Holden, S Healy, M Lightbody, G J Pert, A Kingston, E Robertson, C L S Lewis, D Neely, (to be published)

ESTIMATING DENSE PLASMA TEMPERATURES FROM EXAFS.

F.I. GORDON, Physics Department, Essex University, Colchester, C04 3SQ, Essex, U.K.

INTRODUCTION.

The first direct experimental observation of ion correlation used EXAFS as a diagnostic[1] on a plasma source to infer the density, and temperature (T) effects were approximated through the Debye-Waller factor σ^2. A full account of EXAFS theory and notation can be found in reference(5). The ion correlation parameter $\Gamma = Z_*^2/R_0T$ and is roughly the ratio between potential and kinetic enregies of a typical ion with charge Z_* and ion-sphere radius R_0. The results for the estimate of ion correlation parameter Γ in reference(1) however were inconclusive to the extent that only relative values of Γ were determined, normalised to one particular initial measurement. The EXAFS Debye-Waller factor gives the mean square relative displacement of atoms in a given shell from the central absorbing atom. At low T, there is a linear relation between σ^2 and T where the displacements are small, but beyond T_{melt} (933K for Al) this is expected to be inadequate, and the interatomic potential is increasingly anharmonic. Naive extrapolation of the low-T results[4] (e.g. the correlated Debye model) yields unreasonably large values for σ^2 at temperatures in the range of interest, which can be estimated independently from MEDUSA simulations of the colliding-shock experiments[1].

THEORY.

We instead adopt the model of Laughlin[3] for the T-dependence of interatomic forces, based on Thomas-Fermi theory. Laughlin showed, how these forces could be modelled by displacing the ions a distance r_0 away from the centres of spherical cells, radius R_0, allowing us to treat the ions of net charge Z_* as if they are attached to springs with a spring constant γ which is given by $\gamma = 3\, Z_*^2/R_0^3$. We use atomic units such that e=m=h=1. He showed how the interatomic forces were substantially stiffened for temperatures between the Fermi level and that for complete ionization, so that ions start to behave like hard spheres.

Laughlin gave definitions and expressions for the expectation value of the mean and mean-square particle displacement, $\bar{r}_0$ and $\overline{r_0^2}$ respectively.

It has been shown[2] that the effects of screening (in a very dense electron gas) of the free electrons is to reduce the values of Z_* and Γ by factors $\exp(-r_s/2)$ and $\exp(-r_s)$ respectively, where r_s is the usual electron Wigner-Seitz radius. We take this approximate relation to apply in our case, so the effective values become Z_*' and Γ' ;

$$Z_*' = Z_* \exp(-r_s/2)\ ;\ \Gamma' = \Gamma \exp(-r_s) \qquad (1)$$

The mean square displacement σ_0^2 for a single atom is

$$\overline{r_0^2} - \bar{r}_0^2 = \sigma_0^2 \qquad (2)$$

To get the EXAFS Debye-Waller factor requires the relative mean squared displacement for a given shell, σ_1^2, and this is related to σ_0 dependent on the degree of correlation. A completely uncorrelated and perfectly correlated case will have respectively-

$$\sigma_1^2 = 2\sigma_0^2 \qquad (3)$$

$$\sigma_1^2 = 0. \qquad (4)$$

As the degree of such correlation is unknown we assume

$$\sigma_1^2 = \sigma_0^2 \qquad (5)$$

with its known temperature dependence. Using equation (3) gives upper limits for Γ, and from (5) a proposed improvement on the previous estimates.

APPLICATION TO RESULTS.

From the data[1] we match the values of σ^2 to temperature. The More formula[3] gives an ionization state, and hence an effective Z_*' and Γ'. The results are shown in Figure 1, giving the values of correlation parameter from using both equations (3) and (5). We see that the maximum values of Γ are not unreasonable compared to those in reference(1). It should be noted as a crude benchmark figure that the one-component plasma values for freezing to a lattice[6] are approximately Γ=178 (bcc) and Γ=192 (fcc). The uncertainties in these estimates are similar to those in reference(1) namely an error of 20-25% in the size of Γ.

It should be pointed out that Laughlin's theory[3] is controversial in some of its predictions but the temperature regime of relevance here is below that where his results may be called into question.

A full account of this work can be found in a paper to appear in Plasma Physics and Controlled Fusion.

The author would like to thank A. Djaoui for many helpful discussions.

REFERENCES.

1. DJAOUI, A., HALL, T.A., EASON, R., JACKSON, C. and ROSE, S.J.,(1989) Plasma Physics and Controlled Fusion, **31**, No.1, 111
2. DJAOUI, A., HALL, T.A. and ROSE, S.J. (1988) Annual Rep. to the Laser Fac. Ctee.,RAL,**88**,042,A4.1
3. LAUGHLIN, R.B. (1986) Phys. Rev. A.,**33**, No. 1,510
4. SEVILLANO, E., MEUTH, H. and REHR, J. J. (1979) Phys. Rev.B **20**, No.12, 4908
5. LEE, P.A., CITRIN, P.H. , EISENBERGER, P. and KINCAID, B.M.(1981) Rev. Mod. Phys.,**53**,4,1
6. DEWITT, H.E. , SLATTERY, W.L. and STRINGFELLOW, G.S. (1990) in Proceedings of the Yamada 1989 conference on 'Strongly coupled plasma physics', Ed. S. Ichimaru (Elsevier).

Figure 1 - Correlation parameter versus shot delay time.

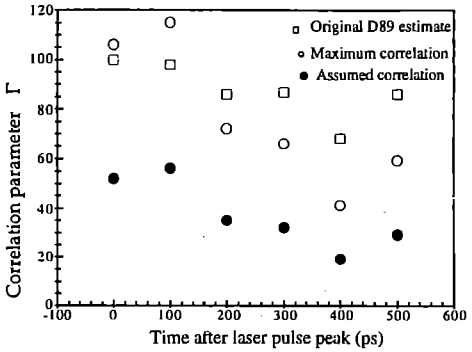

MODELLING EXAFS SPECTRA USING RADIAL DISTRIBUTION FUNCTIONS

F.I. GORDON, PHYSICS DEPT., ESSEX UNIVERSITY, COLCHESTER CO4 3SQ, ESSEX, U.K.

We present a demonstrative prediction of Xray absorption fine structure (EXAFS) using radial distribution functions (rdfs) obtained for the one-component plasma. The normal EXAFS formulae have a sum over shells of atoms replaced by an integral over the rdf. This approach will in general be necessary for a correct treatment of the effects of high temperature, replacing the use of the Debye-Waller factor, and is more suitable for modelling highly correlated plasma sources, similar to those observed in recent experiments. Significant differences between the plane wave and spherical wave treatments are found, and that the mean free path term is more critical. We show that, in principle, the information available from such spectra cannot be reliably obtained through the usual EXAFS processing. Fully correct EXAFS theory includes treatment of spherical wavefronts in the Muller and Schaich[6] prescription, but a more transparent formulation, and one which is asymptotically correct at high energies, is the plane-wave single scattering approximation, (1)

$\chi(k)=-\Sigma_j N_j \sin(2kR_j+\varphi)\exp(-2R_j/\lambda)\exp(-2\sigma_j^2k^2)f(k,\pi)k^{-1}R_j^{-2}$

in usual notation, see eg. reference(5). Inelastic losses are accounted for by a meanfree path λ and temperature effects can be approximated by the Debye-Waller factor σ_j^2. The use of this factor essentially assumes that the thermal vibrations of atoms about their mean position are of small displacements. However for plasmas it is no longer adequate to consider discrete fixed shells of atoms but more correct to approach the problem via the radial distribution function g(r). Thus the EXAFS equation is adapted to an integral over g(r) not a sum over shells;

$\chi(k) = 4\pi n_0 k^{-1} f(k,\pi) \int_0^\infty g(r)\sin(2kR_j+\varphi)\exp(-2R_j/\lambda)dr$ (2)

and $g(r) \rightarrow 1$ as $r \rightarrow \infty$, with n_0 is the mean number density.

A problem in plasma EXAFS work is the limited range of energy data available- the consequences for the Fourier transform (FT) analyses are severe. The Fourier transform into r-space[5] peaks at distances corresponding to the atomic shells, allowing the density to be found. Curve-fitting the EXAFS to match the experiment is the basis of the EXCURV92 codes at the Daresbury Lab, see ref(1). This is limited in use for Fourier-filtered data, as the required number of fitting parameters is quite large, leading to poor determinacy. The important restriction for our purposes is the implicit assumption of discrete gaussian shells with simple parameters equivalent to N_j, R_j and σ_j in our notation. The crucial aspect is that the rdf shape can no longer be asssumed to be a sum of gaussian shells, thus unless we know how to parameterise the essentially unknown rdf, the best one could do would be to find the closest gaussian fit, which may not provide physically meaningful information.

The rdf g(r) of a typical liquid shows peaks at the positions most likely to be occupied by neighbouring atoms and a sharp fall for distances less than about 80% of the first peak distance. Obtaining a plasma rdf is problematic- the best studied case is the 'ideal' one-component plasma (OCP). The properties, including the rdf, of the classical OCP turns out to depend on the correlation parameter Γ. Tables of g(r) data and other properties for various Γ have been published[7]. Although we do not expect these to resemble in detail the rdf of Al, the qualitative features should not be too different.

Our avenue of approach to EXAFS with rdfs is to use the OCP data for the rdf, and apply the Al data for phaseshifts and scattering amplitudes. The different Γ effectively represent different temperatures. The calculation is made for both plane wave (PW) and spherical wave(SW) (reference 2) versions of the EXAFS formula. For a normal EXAFS calculation, the two give very similar results for E > 2.5 Ryd, only differing substantially below that point.

We first perform both the PW and SW calculations. The mean free path is essential in the presence of an rdf, as it allows the integral to converge. It is easiest to split the calculation into two parts by writing g(r)= 1.0 + h(r) and utilising the known analytic form when g=1. The calculation is done for various Γ = 40,80,110,160, the results shown for Γ=160 in Fig. 1.

The mean free path plays an important role. It can be seen easily that for a given Γ, the PW and SW do not match very well, e.g. the position of the first minimum near 2.5 Ryd. is significantly moved- the lower this is in energy, the lower the density one might infer from converntional methods, although both represent the same density. This is qualitatively different from the standard sum-over-shells approach and indicates the PW results cannot be taken as a realistic EXAFS spectrum. By comparing the EXAFS thus obtained at different Γ, we see the problem that a standard analysis would face. These spectra all come from the same density of material, but from different (efffective) temperatures, yet the amplitude of the EXAFS does not just decay in energy as expected from a Debye-Waller factor but the peak positions as well as their amplitudes are changed. Processing of such curves with the Daresbury EXCURV92 package through Fourier filtering/curve fitting normally gives the density and temperature. For these OCP curves, it can be seen that spurious parameters may be derived. There is also the question of parameter correlations to be considered. This has been tested for Γ=160, and on the best-fit rdf χ(E) to see to what extent the best fit parameters will tally.

We therefore, in view of the discussion above, fit directly the EXAFS curves to the theory in EXCURV92, as if they were experimental data, with a weighting of k. A larger weighting factor would overemphasise the spectrum at high values of k, where the 'signal' is small. The object is to determine the extent to which this can reproduce the 'known' rdf parameters found from a best-fit to the OCP rdf. Since the mean-free path is treated via a complex potential (the vpi parameter) this must be assigned a value for our fitting, as it is the same for all values of Γ. A conventional figure is vpi=-5eV. Thus the for parameters to vary are R_1, N_1, σ_1 and E_0 in our notation, i.e. the first shell parameters and E_0. We note that a more correct treatment of the mean free path is that of reference(3), as the use of an imaginary potential is a poor representation of inelastic losses at low energies- this is especially relevant for this work. The fitting of the EXAFS curves yields best-fits with gaussian parameters significantly different from those of a gaussian-sum best-fit to the OCP rdf data -this emphasises the difficulty in extracting worthwhile structural information from the EXAFS of a correlated plasma source.

A full account of this work can be found in a paper to be submitted to Plasma Physics and Controlled Fusion(1993). The author is grateful to A. Djaoui for many helpful discussions.

REFERENCES.

1. BINSTED, N. , CAMPBELL,J.W., GURMAN, S.J. AND STEPHENSON, P.C. (1990) [SERC Daresbury Laboratory EXCURV90 program]

2. DJAOUI, A., HALL, T.A., ALBERS, R.C. , REHR,J.J. and MUSTRE, L. (1990) Laser and Particle. Beams,**8**, 1-2,319

3. GORDON, F.I. and DJAOUI, A. (1992) Physics of Fluids B, **4**,12,3985

4. GORDON, F.I. (1993) Plasma Physics and Controlled Fusion (in press)

5. LEE, P.A., CITRIN, P. H., EISENBERGER, P. and KINCAID, B.M. (1981) Rev. Mod. Phys. , **53**, No.4,1

6. MULLER, J.E. and SCHAICH, W.L. (1975) Phys. Rev. B, **27**, No. 10,6489

7. SLATTERY, W.L., DOOLEN, G.D. and DEWITT, H.E. (1980) Phys.Rev.A,**21**,No.6,2087

FIGURE 1 Γ=160 χ(E) for OCP rdf

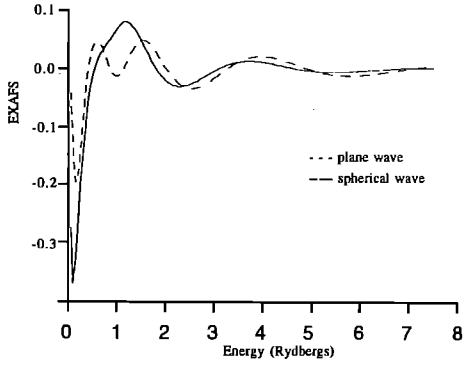

NON-LTE SOURCE PHOTO-PUMPED Fe XVII XUV LASER

J. Zhang[1] and E.E. Fill[2]

[1]Department of Atomic and Laser Physics, University of Oxford, UK

[2]Max-Planck-Institut fuer Quantenoptik, Garching, Germany

In radiation-pump schemes, pump plasmas is always assumed to be LTE plasmas[1-3]. For a thermal plasma (Maxwellian particle distribution) the maximum attainable pumping flux at a frequency υ is given by the Planck function. To actually obtain such pumping flux from a plasma of kinetic temperature Te requires that the plasma be in local thermodynamic equilibrium (LTE) and be optically thick in the frequency. To reach LTE requires either very high density, very high optical depth, or sufficient combination of high density and high optical depth[4]. In practical situations, an LTE plasma produced by laser irradiation is very hard to achieve. Pump plasmas are usually not LTE plasmas. In this paper, we will show that it may be not necessary to use LTE plasmas as pump plasmas and an appropriate non-LTE plasma could be better than an LTE pump plasma with a similar pump temperature.

In the resonantly photo-pumped Ne-like scheme, all excited levels of manifolds of 2p - 3s, 2p - 3d, 2p - 4s and 2p - 4d main absorption transitions in the lasant plasma are photo-pumped by the same Ne-like ion in the pump plasma, populating all of these excited levels. These levels then decay to the 3p levels. Because of the quasimetastablility of 3p levels, lasing occurs between the 3p and 3s levels. The lower lasing levels 3s then decay rapidly back to the ground state. To determine the pump temperatures of the different pump lines from the pump plasma, an experiment was carried out using the high-power iodine laser system ASTERIX IV[5]. The laser supplied an energy of 120 J to a Fe slab target. The pulse duration was 300 psec. Most of the measurements were done at the fundamental wavelength of the iodine laser (λ = 1.315 μm). The pump strengths and the corresponding pump temperatures obtained in the experiment are shown in the table.

Table I Experimental values of pump strengths and pump temperatures from the laser produced plasma

Transition	2p - 3s		2p - 3d		2p 4d	
Upper levels	$(3/2,1/2)_1$	$(1/2,1/2)_1$	$(3/2,5/2)_1$	$(1/2,3/2)_1$	$(3/2,5/2)_1$	$(1/2,3/2)_1$
Wavelength (nm)	1.705	1.678	1.526	1.502	1.226	1.212
Pump strength (10^{-3})	1.3	1.4	5.2	5.6	1.0	0.9
Pump temperature (eV)	112	109	154	159	146	146

As seen from the Table I, the pump temperature of the line emissions form the pump plasma are quite different. It appears that the line emissions form the pump plasma are correlated to the spontaneous radiative rates. This implies that the pump plasma generated in the experiment deviated from the LTE condition. Compared with the emissions from an LTE plasma with a pump temperature of 146 eV, the pump strengths of 2p - 3s line emissions decreased by about 80%, and those of 2p - 3d lines increased by about 40% to 60%. Both these variations of the pump strengths are favourable for population inversion between 3p and 3s levels.

A set of calculations using the experimental pump strengths were made to estimate effects of the non-LTE plasma. A collisonal-radiative plasma model with the automatic line-match scheme[3] was adopted.

Figure 1 presents the time history of the expected lasing gains calculated with the experimental pump strengths from the non-LTE pump plasma. The simulation yields maximum gains of 5.6 cm^{-1}, 2.8 cm^{-1} and 1.9 cm^{-1} on the dominant lasing transitions at 38.74 nm, 25.47 nm and 20.46 nm. It is found that the lasing gain at 38.74 nm increased by about 1.5 cm^{-1} using the pump strengths from the non-LTE pump plasma over that photo-pumped by an LTE plasma with a pump temperature of 146 eV, owing to the decreased pumping rate of 2p - 3s. The other lasing gains behave in like manner.

In summary, practical pump plasmas are usually not LTE plasmas. Our results indicate that it may be not necessary to use LTE plasmas as pump plasmas and an appropriate non-LTE pump plasma could be better that an LTE pump plasma with a similar pump temperature.

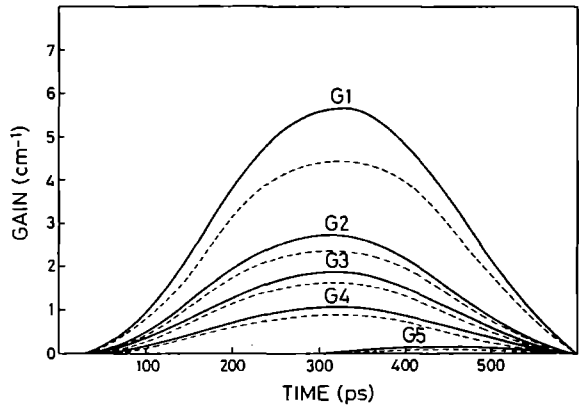

Figure 1. Evolution of expected lasing gains calculated with the experimental pump strengths from a non-LTE pump plasma (solid lines). Bashed lines are those of corresponding lasing gains pumped by an LTE plasma with a pump temperature of 146 eV for comparison. G1 = $(2p_{1/2}3p_{1/2})_1$ - $(2p_{1/2}3s_{1/2})_1$ at 38.74 nm. G2 = $(2p_{1/2}3p_{1/2})_0$ - $(2p_{1/2}3s_{1/2})_1$ at 25.47 nm, G3 = $(2p_{1/2}3p_{1/2})_0$ - $(2p_{3/2}3s_{1/2})_1$ at 20.46 nm, G4 = $(2p_{3/2}3p_{3/2})_0$ - $(2p_{1/2}3s_{1/2})_1$ at 41.43 nm, G5 = $(2p_{3/2}3p_{3/2})_1$ - $(2p_{3/2}3s_{1/2})_1$ at 35.83 nm.

REFERENCES

1. P.L. Hagelstein, Plasma Physics, **25**, 1345 (1983).

2. R.H. Dixon and R.C. Elton, J. Opt. Soc. Am., **B1**, 232 (1984).

3. B.N. Chichkov and E.E. Fill, Opt. Commun., **74**, 202 (1989).

4. J.P. apruzese and J. Davis, Phys. Rev., **A5**, 2976 (1985).

5. E.E. Fill, Th. Schlegel, J. Steingruber and J. Zhang, *X-Ray Lasers 1990*, G.J. Tallents ed., Bristol, IOP pulisher, 115 (1991).

ISOELECTRONIC STUDY OF H-LIKE RECOMBINATION X-RAY LASERS USING A PSEC PULSE DRIVER

J. Zhang and M. H. Key

Department of Atomic and Laser Physics, University of Oxford

Central Laser Facility, Rutherford Appleton Laboratory

INTRODUCTION

The optimum recombination laser operation relies on production of maximum inversion density when LTE conditions prevail for levels above n = 3, and n = 2 is depopulated mainly by radiative decay. The condition is reached at a density scaling with atomic number as Z^7 at the time when lasing gain appears. This scaling can be understood by considering the ratio of radiative decay of the upper lasing level (n = 3), which is proportional to Z^4, to the collisional mixing rate of the lasing levels, which is proportional to N_eZ^{-3}. This ratio scales as Z^7N_e. Consequently, optimum operation of recombination lasers ideally require a rapid Z^7 increase of the initial electron density to match the Z^7 scaling of the density at laser time. But the electron density in initial formation of the plasma in laser-driven ablation scales only as Z^1 or Z^0, therefore the initial density needs to be greatly increased to achieve the optimum operation mode of recombination lasers[1,2].

The initial density of the plasma can be enhanced by irradiating targets with shorter pulses[3]. When the laser pulse duration is less than the hydrodynamic response time, hydrodynamic motion of the plasma can be insignificant and electron thermal conduction heats targets at close to solid density in contrast to steady state ablation where the main heating occurs at densities close to the critical density. Consequently, the initial density can be two or three orders of magnitude higher and corresponds to near solid density. The new CPA beam on the Vulcan laser facility has the capability of providing up to 30 J energy in 2 psec pulses. The high contrast ratio of 10^6 allows the psec pulse to interact directly with the target rather than with underdense preformed plasma and offers the possibility of high gain recombination laser operation using this scheme.

For high gain recombination laser operation, the mass of the expanding plasma must be small, because smaller plasmas expand more rapidly and produce less recombination to the ground state of the H-like ions. This small size also reduces trapping of Lyman α radiation. The end result is that lower temperature can be used giving higher population in the n = 3 upper state of the laser transition. Thin fibre targets irradiated in line focus geometry have proven to be the most successful for generating recombination lasers with high gains.

MODELLING STUDY

A one-dimensional Lagrangian Hydrocode MEDUSA is used to simulate the formation of plasmas from the surface of fibre targets under irradiation[4,5]. The Sobelev trapping factor is used[6]. Simulations have been made along the isoelectronic sequence of H-like C, N, F and Na recombination lasers from 7 μm diameter fibre targets irradiated with 2 psec, 1.05 μm pulses. The dependence of the Balmer α gain coefficient in the sequence on the absorbed energy is studied to find the optimum conditions for the recombination lasers. Elements with Z < 12 have been chosen because the practical limit of driver energy of the CPA beam. It is found in simulations that the absorption through inverse bremsstrahlung is highly inefficient and resonance absorption is the main absorption process, as expected for interaction of plasma and psec pulse driver. Around 10% energy of the resonance absorption

Table I. Optimised Plasma Parameters at X-ray Laser Time

	H-like C	H-like N	H-like O	H-like F	H-like Na
λ_{laser} (nm)	18.2	13.4	10.2	8.09	5.41
$G_{peak}(cm^{-1})$	62	98	119	83	35
$G_{eff}(cm^{-1})$	51	88	109	74	24
E_{abs} (J/cm)	0.570	1.423	3.083	5.105	15.13
N_e (cm^{-3})	$1.04x10^{19}$	$3.46x10^{19}$	$8.79x10^{19}$	$1.86x10^{20}$	$8.34x10^{20}$
T_e (eV)	9.242	16.00	22.01	40.39	112.3
N_0 (cm^{-3})	$1.25x10^{18}$	$4.19x10^{18}$	$5.94x10^{18}$	$1.01x10^{19}$	$4.01x10^{19}$
N_H (cm^{-3})	$3.92x10^{17}$	$1.8x10^{18}$	$3.49x10^{18}$	$7.17x10^{18}$	$2.67x10^{19}$

is assumed to go into hot electrons.

In the recombination laser scheme presented here, the 2 psec CPA pulse heats the fibre surface and ionises the atoms in the fibre to bare nuclei. In the heating phase plasma is ablated from the surface of the fibre[7]. During the subsequent adiabatic expansion, recombination into H-like ions leads to population inversion and gain. Simulations show that plasmas have been formed by the incomplete burn of 7 μm diameter fibres. A layer typically less than 1 μm thick is ablated from the surface of the fibre. Energy transport is dominated by thermal conduction. The optimised conditions under which the recombination lasers in the H-like isoelectronic sequence achieve their maximum gain respectively at x-ray laser time are summarised in the table I.

In the table, G_{peak} is the computed peak gain coefficient for time-resolved and space-resolved measurements, G_{eff} stands for the effective gain coefficient for a 5 mm long fibre, deduced from the non-linear increase from 2.5 mm length of the spatially integrated axial intensity using the Linford formula[8]. The effective gain is what is measured experimentally by spatially integrated and temporally resolved spectroscopy along the axis of the fibre target[9,10]. E_{abs} is the absorbed energy by the fibre under a cylindrically symmetric irradiation circumstance. N_0 represents the density of stripped nuclei, N_H is the density of H-like ions. T_e and N_e are the electron temperature and electron density in plasmas respectively. The other parameters are used in the conventional sense.

It is found that the optimised electron density in the table is given by $N_e = 4.2 \times 10^{13} Z^7$ cm^{-3}. The optimum electron temperature scales roughly as $T_e = 7.0 \times 10^{-3} Z^4$ eV.

The simulations show that the initial density is increased by two to three orders of magnitude by using the 2 psec pulse driver than using long pulse drivers. The increased initial density intersects the ideal Z^7 line at about Z = 8. The H-like oxygen recombination laser therefore acquires the highest gain coefficient in the sequence. The corresponding H-like oxygen recombination Balmer α laser is the optimum operation in this scheme. For the H-like sodium recombination laser at 5.41 nm, the predicted gain is still quite significant. With scaling to shorter wavelength, the gain coefficient starts to decrease seriously because the initial density departs far from the ideal scaling. The initial density ($\sim Z^0$) and the density at laser time ($\sim Z^7$) tend to convergence at higher Z. One of the solutions for getting high gain operation for H-like Mg, Al ions in water window spectral region may be further decreasing duration of the driver.

Practically, pure oxygen fibre targets are not available. In a coming experiment we will irradiate 7 μm diameter SiO_2 fibres with the 2 psec CPA beam. Simulations show that including silicon will reduce gain by a factor of 2. Alternatively, polymer fibre targets consisting of C, N and O are ideal for the experimental purpose. The use of these targets allows the Balmer α transitions in C, N, and O to be simultaneously examined and enables isoelectronic scaling of the potential laser transition to be investigated. For F and Na ions, NaF coated carbon fibre will be used for investigation.

CONCLUSION

In conclusion, we have presented an optimisation design for high gain recombination x-ray lasers for Balmer α transitions driven by 2 psec VULCAN CPA beam. Significant improvement in gain performance of the H-like recombination lasers has been shown due to the enhanced initial density with psec driver pulse, which might be a way towards saturated recombination x-ray lasers. The H-like oxygen recombination Balmer α laser at 10.2 nm is the optimum operation in this scheme. The validity of the hydrocode in predicting the gain coefficient is not however fully proven. The most recent experiment on SPRITE indicated that the gain length product achieved was less by a factor of 2 than predicted by the code[10]. Nevertheless, if the same relation of practical performance and code prediction were attained for the fibre targets driven by the CPA beam, it would still appear that a very significant gain length might be achieved by using this scheme. Further scaling to high gain operation in the water window spectral region needs to increase further the initial density, because of the different Z dependence of the initial electron density and the electron density at laser time. It is hoped that this new scheme will be demonstrated in the near future.

ACKNOWLEDGEMENTS

We gratefully acknowledge S.J. Rose, A. Djaoui, G.J. Pert and P. Holden for discussions on simulations and P.A. Norreys and S.A. Ramsden for many useful suggestions.

REFERENCES

1. M.H. Key, *Central Laser Facility Annual Report*, RAL-89-045, Rutherford Appleton Laboratory, Chilton, UK, 119 (1989); RAL-87-041, Rutherford Appleton Laboratory, Chilton, UK, 100 (1987).

2. G.J. Pert, Plasma Physics and Controlled Fusion, **27**, 1427 (1985).

3. R.A. Smith, V. Barrow, J. Edwards, G. Kiehn, and O. Willi, Appl. Phys. B, **50**, 187 (1990); J.C. Kieffer, P. Audebert, M. Chaker, J.P. Matte, H. Pepin, T.W. Johnston, P. Maine, D. Meyerhofer, J. Delettrez, D. Strickland, P. Bado, and G. Mourou, Phys. Rev. Lett., **62**, 760 (1989).

4. M.H. Key, N. Tragin, and S.J. Rose, *X-Ray Lasers 1990*, G.J. Tallents ed., Bristol, IOP Publisher, 163 (1991).

5. J.P. Christiansen, D.E.T.F. Ashby, and K.V. Roberts, Comput. Phys. Commun., **7**, 271 (1974).

6. V.V. Sobolev, *Theoretical Astrophysics*, V.A. Ambartsumyan ed., London, Pergamon, 478 (1958).

7. G.J. Pert, J. Phys. B., **9**, 3301 (1976); J. Phys. B. **12**, 2067 (1979).

8. G.J. Linford, E.R. Peressini, W.R. Sooy, and M.L. Spaeth, Appl. Opt., **13**, 379 (1974).

9. G.J. Tallents, L. Dwivedi, Y. Kato, M.H. Key, R. Kodama, J. Krishnan, C.L.S. Lewis, K. Murai, P.A. Norreys, G.J. Pert, S.A. Ramsden, H. Shiraga, C. Smith, J. Uhomoibhi, G. Yuan, and J. Zhang, *Third International Colloquium on X-Ray Lasers*, Schliersee, Germany, 1992.

10. J. Zhang, M.H. Key, P. Norreys, and G.J. Tallents, Opt. Commun., **95**, 53 (1993).

SIMULATION OF A LASER-PLASMA ENERGY TRANSPORT EXPERIMENT ON THE SPRITE LASER FACILITY

J. Zhang[1,2], M.H. Key[1,2], P. Norreys[2] and G.J. Tallents[3]

[1]Department of Atomic and Laser Physics, University of Oxford

[2]Central Laser Facility, Rutherford Appleton Laboratory

[3]Department of Physics, University of Essex

INTRODUCTION

The study of energy transport in laser-plasmas is of great interest because it develops understanding of laser-plasma interactions including laser fusion, the production of intense x-ray sources and x-ray lasers[1]. When the laser pulse duration is less than the hydrodynamic response time, the energy transport process is quite different from that in steady state ablation. The hydrodynamic motion of the plasma can be insignificant during the pulse and electron thermal conduction heats targets at close to solid density in contrast to steady state ablation where the main heating occurs at densities close to the critical density.

EXPERIMENT

An experiment was carried out[2] with 12 psec pulses from the Raman shifted KrF SPRITE laser facility at 0.268 μm wavelength to investigate the energy transport process in plasmas produced by laser pulses with shorter duration than the hydrodynamic response time. 3J energy was focused to line foci of 10x330 μm^2 or 10x660 μm^2 giving irradiances of (1.5 - 3.0)x10^{15} W/cm^2 taking account of transmission loss through the focusing optics. The energy transport was recorded using layered targets designed to show the penetration of heating into the solid evidenced by the emission spectrum of the Na or F in the NaF layer buried below the CH plastic overlay or Al overlay with variable thickness. From the target surface to inner layers, the target layer composition was CH plastic overlay (Al overlay) of thickness 0 to 0.5 μm; NaF buried layer of thickness 0.25 μm ; with a 10 μm CH plastic substrate.

SIMULATIONS

In order to analyse and understand the experimental data, a 1-D hydrocode MEDUSA[3] was used to simulate the experiment. In the code, the heat flow is given by the smaller of the Spitzer value and a flux limited free streaming limit. For the simulations presented here, a flux limit of 0.1 is chosen[4]. The energy is absorbed by inverse bremsstrahlung and resonance absorption. The resonance absorption fraction is set at each time step by calculating the scale length at critical density. Some resonantly absorbed energy is dumped at critical density. The rest is put into hot electrons which are transported in ten energy groups with an initial temperature at critical density. The non-local-thermodynamic-equilibrium (non-LTE) rate calculation describes radiation transport with an escape factor for the resonance lines, accounting for Doppler decoupling using the Sobelev approximation[5]. The Sobelev formula is applied separately to each Lagrangian cell with the average velocity gradient taken from the hydrodynamic simulation.

In simulations, planer geometry was set. 70 Lagrangian cells were used to specify the plasmas produced from the layered target. The Lagrangian cell boundaries were allowed to move with the fluid. 20 cells of them were assigned to specify the plasma from the CH (Al) overlay. 40 cells were used to represent the plasma from the buried NaF layer. 10 cells were assigned to specify the plasma from the substrate. Laser pulses were assumed to be incident on the CH (Al) overlay. The emission of the H-like F 1s - 3p (Ly β) and He-like F $1s^2$ - 1s3p lines from the plasma of the buried NaF layer was calculated by assuming that their upper levels were in LTE with the bare nuclei and hydrogenic ground states respectively[6]. Line widths were Doppler. The intensities of the line transitions were calculated by summing the emission from the 40 cells in the buried layer. Some typical simulated intensities of Ly β transition of H-like F and $1s^2$ - 1s3p transition of He-like F are shown in figures 1 - 4 for different thickness of CH and Al overlay.

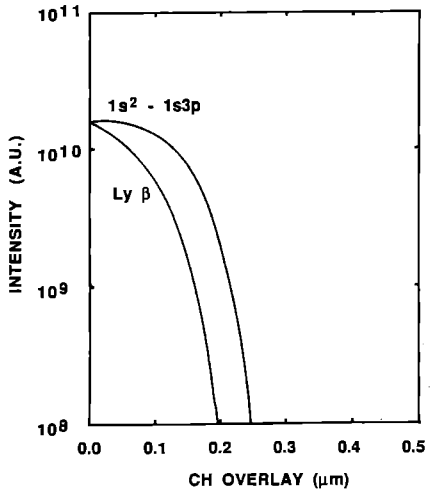

Figure 1. Intensities of the Ly β transition of H-like F ions and $1s^2$ - 1s3p transition of He-like F ions as a function of CH plastic overlay thickness for laser irradiance of 5.0x10^{14} W/cm^2.

It is known[6] that in a dense recombining plasma with LTE in its excited states the intensity of the hydrogenic resonance line Ly β is proportional to the concentration of bare nuclei and the intensity of the resonance line $1s^2$ - 1s3p of He-like ions is proportional to the ground state population density of the H-like ions. The ratio of the resonance line intensities therefore gives the ratio of the concentration of bare nuclei to that of the ground state population of the H-like ions in the plasma produced from the buried layer. The intensities of the H-like Ly β line and the He-like $1s^2$ - 1s3p line can be regarded as sensitive indicators of the penetration of energy through the overlay to the NaF buried layer. When a laser pulse irradiates the overlay, the overlay will or will not be burned through depending on amount of the laser irradiance. The buried NaF layer is then heated at its outer surface by the energy transported through the overlay and the plasma is formed from the overlay and the NaF layer. If the energy remaining after burn through the overlay is high enough, a fraction of plasma will be ionised to bare nuclei, consequently H-like Ly β emission occurs. As the overlay thickness increases, decreasing intensity of H-like Ly β is produced. The emission of the H-like Ly β transition disappears when the temperature is too low to ionise the H-like ions. The emission of the $1s^2$ - 1s3p transition of He-like ions also disappears as the overlay thickness further increases to a level in which most of the laser irradiance is absorbed by the overlay, and thus at the end of the

laser irradiation there is a body of hot expanding plasma from the overlay surrounding a layer of cold residual overlay material. On the other hand, if the energy on the buried layer is too large, the LTE population of the higher excited states will be reduced by the increased temperature, which results in reduced intensities of the resonance lines[6]. This explains the lower intensities of the resonance lines in figures 3 - 4 for no overlay and smaller thickness of the overlay under high laser irradiances.

Compared with the experimental data using variable laser irradiances on NaF layer without overlay, the fraction of the energy absorbed by the overlay and the depth of penetration can be estimated. It is shown in the simulations that about 2.7 times thicker CH overlay can be burned through for the same absorbed energy than the Al overlay because that the density of Al overlay is higher than that of CH overlay by a factor of 2.7. This is expectable since the mass burned through by laser irradiation is linearly dependent on the absorbed energy for short pulses[7].

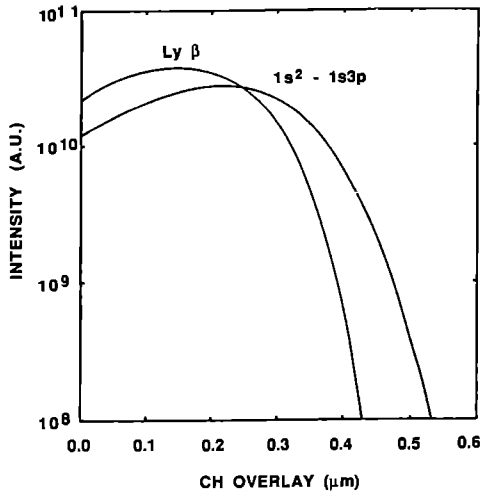

Figure 2. Intensities of Ly β transition of H-like F ions and $1s^2$ - 1s3p transition of He-like F ions as a function of CH plastic overlay thickness for laser irradiance of $1.5x10^{15}$ W/cm^2.

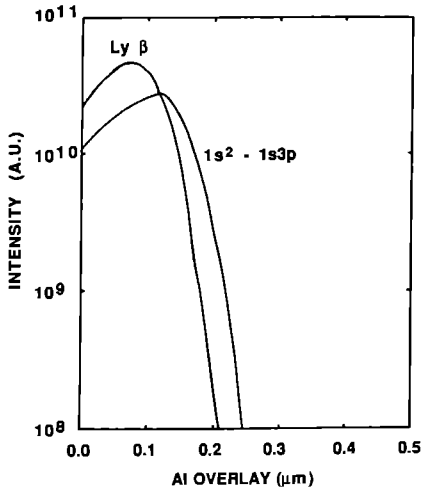

Figure 3. Intensities of Ly β transition of H-like F ions and $1s^2$ - 1s3p transition of He-like F ions as a function of Al overlay thickness for laser irradiance of $3.0x10^{15}$ W/cm^2.

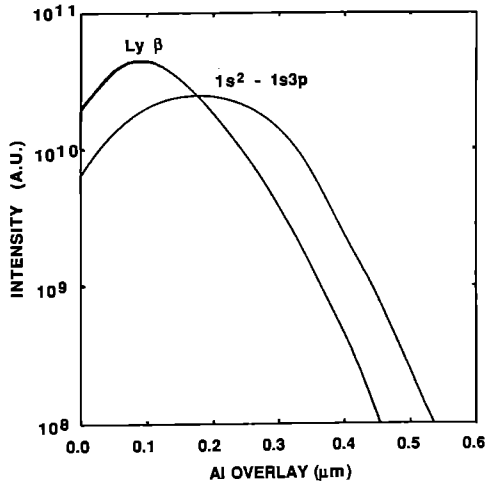

Figure 4. Intensities of Ly β transition of H-like F ions and $1s^2$ - 1s3p transition of He-like F ions as a function of Al overlay thickness for laser irradiance of $5.0x10^{15}$ W/cm^2.

CONCLUSION

In conclusion, a 1-D hydrodynamic code MEDUSA are used to simulate the laser-plasma energy transport experiment carried out on the SPRITE facility. Preliminary analysis suggests that the intensities of resonance lines of Ly β in H-like ions and $1s^2$ - 1s3p in He-like ions calculated by the code for variable thickness of overlays agree roughly with the experimental data. The dependence of the depth of penetration of heating on the laser irradiance can be given by numerical simulations. The simulations can provide information about temperature, density, pressure and energy balance in different layers, which will help analysis and explanation of the experimental data and understanding of the transport process. Detailed comparisons between simulation results and experimental data are in progress.

ACKNOWLEDGEMENTS

The authors would like to thank S.J. Rose and A. Djaoui for discussions on simulations.

REFERENCES

1. M.H. Key, E.T. Toner, T.J. Goldsack, J.D. Kilkenney, S.A. Veats, P.F. Cunningham, and C.L.S. Lewis, Phys. Fluids **26**, 2011 (1983); G.J. Tallents, M.H. Key, P. Norreys, D. Brown, J. Dunn, and H. Baldis, Phys. Rev., A**40**, 2857 (1989).

2. Y. Al-Hadithi and G.J. Tallents, Personal Communication.

3. J.P. Christiansen, D.E.T.F. Ashby, and K.V. Roberts, Comput. Phys. Commun., **7**, 271 (1974).

4. G.J. Rickard, A.R. Bell, and E.M. Epperlein, Phys. Rev. Lett., **62**, 268 (1989).

5. M.H. Key, N. Tragin, and S.J. Rose, *X-Ray Lasers 1990*, ed. G.J. Tallents, IOP Publisher, Bristol, 163 (1991).

6. J. Zhang, M.H. Key, P. Norreys, and G.J. Tallents, Opt. Commun., **95**, 51 (1993).

7. G.J. Pert, Plasma Physics and Controlled Fusion, **27**, 1427 (1985).

CPA PULSE DRIVEN H-LIKE OXYGEN RECOMBINATION X-RAY LASER

J. Zhang and M.H. Key

Department of Atomic and Laser Physics, University of Oxford

Central Laser Facility, Rutherford Appleton Laboratory

INTRODUCTION

Major progress has been made in the field of x-ray laser research worldwide since the first soft x-ray amplifier has been demonstrated[1,2]. Amplification has been observed at wavelengths as short as 3.56 nm[3] while gain saturation has been reached at about 20 nm[3,4] using the collisional excitation scheme. However, current collisionally excited x-ray lasers require about 10 kJ driver energy for saturated and diffraction limited operation in the water window spectral region. Recombination x-ray lasers operating with adiabatic cooling are of continuing interest because of their future potential for the development of x-ray lasers requiring much lower driver energy[5-7] but are still unproved to be able to obtain sufficient gain length product for saturated laser action. There is thus very strong motivation of demonstrating high gain length product for recombination x-ray lasers. In the present paper we provide a theoretical investigation of a high gain H-like oxygen recombination laser at 10.2 nm driven by a 2 psec chirped pulse amplification (CPA) beam, which is now available on the VULCAN Nd glass laser facility, and show the potential advantages for recombination x-ray lasers by using picosecond pulse driver.

PHYSICAL BACKGROUND

In the recombination x-ray laser scheme, a fully stripped plasma is rapidly cooled by adiabatic expansion, and electrons preferentially recombine via three-body collisions into the upper levels, which radiatively cascade to the ground state levels of the H-like ions. If the expansion is sufficiently rapid, the adiabatic cooling of the plasma may induce population inversion between the n = 3 and n = 2 levels of the H-like ions during the recombination cascade. Higher initial density gives greater adiabatic cooling in the expansion to the density below which population in the n = 3 and n = 2 levels is not thermalised by collisions. A cooler plasma with more recombination when inversion develops therefore gives higher gain.

The initial density of the plasma can be enhanced by irradiating targets with shorter pulses, since the hydrodynamic motion of the plasma is insignificant during the laser pulse(~ picosecond) and the absorbed laser energy is transported to near solid density by electron thermal conduction[8].

The CPA beam on Vulcan laser facility has the capability of providing up to 30 J energy in 2 psec pulses, with a contrast ratio of 10^6 which prevents the formation of a pre-plasma and offers the possibility of high gain recombination laser operation using this scheme.

Oxygen was chosen as an element for study because the driver energy required for optimum performance of an H-like oxygen recombination laser could be supplied by the VULCAN CPA beam.

NUMERICAL SIMULATIONS

In order to estimate the gain that may be expected for the plasmas from targets irradiated by the CPA beam, a series of numerical simulations have been carried out. A one-dimensional Lagrangian hydrodynamic code MEDUSA coupled to an atomic physics code NIMP are used[9] to simulate the heating and exploding of the targets under irradiation.

The performances of the H-like oxygen recombination laser for 7 μm diameter fibre targets and slab targets can be compared. Figure 1 illustrates the computed peak gain coefficient and the effective gain coefficient for a 5 mm long plasma, deduced from the non-linear increase from 2.5 mm length of the spatially integrated axial intensity using the Linford formula[10]. This effective gain is what is measured experimentally by spatially integrated and time-resolved spectroscopy along the axis of the target[11,12].

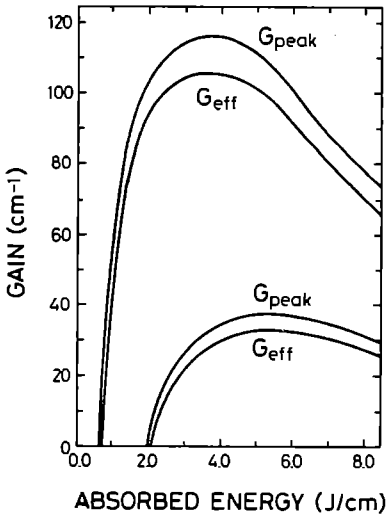

Figure 1. The peak gain coefficient and effective gain coefficient for time-resolved and spatially integrated measurements as functions of absorbed energy. The upper two curves represent the performance of H-like oxygen recombination laser action of a 7 μm diameter fibre uniformly irradiated by the CPA beam. The lower two curves are the corresponding performance for a slab target irradiated by a 20 μm wide line focus CPA beam.

For a 7 μm fibre target assuming symmetric irradiation there is very high (100 cm^{-1}) effective gain coefficient. By contrast irradiation of a solid slab with consequent one dimensional rather than two dimensional expansion gives a much reduced effective gain coefficient (~30cm^{-1}). The focal width of the optical driver is taken to be 20 μm corresponding to the best focus on the VULCAN laser facility. The production of a 20 μm wide focus on a slab target is straightforward. The irradiation of a fibre target can be readily accomplished by placing the 7 μm fibre in the 20 μm wide focus. In this case the target would be irradiated from one side rather than in a cylindrically symmetric fashion, but it is expected that the behaviour of the plasma on that part of the target surface directly facing the beam would be similar to that for a uniformly irradiated fibre at the same intensity.

Note in figure 1 that the threshold of lasing gain for the fibre target is much lower than that for slab target because a fibre target yields comparable electron temperature and ionisation for a reducedabsorbed energy. The maximum gain operation needs less

absorbed energy for the fibre target than that needed for the slab target.

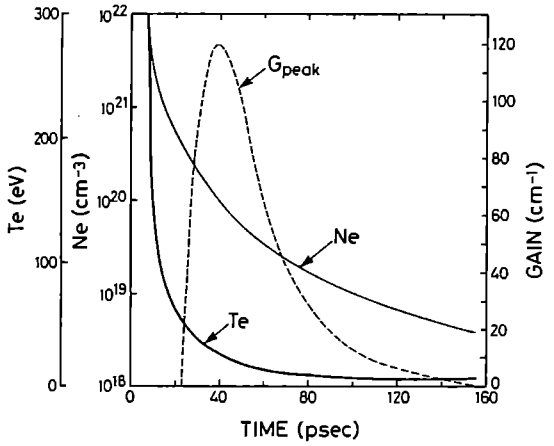

Figure 2. Time evolution of Te, Ne and 10.2 nm H-like oxygen recombination peak gain coefficient in the Lagrangian cell which gives maximum peak gain for a 7 μm diameter fibre target irradiated by a 20 μm wide focus CPA beam with an absorbed energy of 3.08 J/cm.

Figure 2 shows the results for an optimised simulation of the time evolution of electron temperature (T_e), electron density (N_e) and peak gain for the O VIII recombination laser at 10.2 nm in the Lagrangian cell, which gives maximum peak gain (time and spatially resolved) for a 7 μm diameter fibre target irradiated by the 2 psec CPA beam with the optimised absorbed energy of 3.08 J/cm in the plasma. During the 2 psec interaction, there is a rapid rise in temperature and very steep density gradients are produced. The temperature increases abruptly to a peak of 2.0 keV and after the interaction, the plasma expands quite quickly and the temperature drops rapidly. The gain reaches the maximum when $N_e = 8.8 \times 10^{19}$ cm^{-3} and $T_e = 22$ eV. The FWHM time duration of the gain is about 40 psec, relatively long compared to the 2 psec driving pulse. The maximum value occurs at 40 psec. Note in Fig. 2 that the rapid cooling rate and expansion rate, which consequently induce high gains.

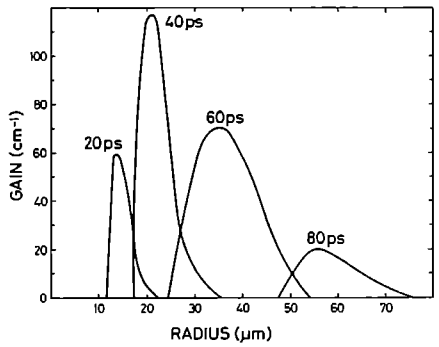

Figure 3. Spatial gain profile of H-like oxygen recombination laser calculated at 20, 40, 60 and 80 psec after the start of the laser pulse with the same conditions as in figure 2..

Theoretical simulation predicts, illustrated in figure 3, an annular gain region. The spatial gain profiles are shown in figure 3 at 20, 40, 60 and 80 psec after the start of the laser pulse with the same conditions as in figure 2. Gain onset occurs at $T_e = 108$ eV after approximately 13 psec with very narrow spatial FWHM. The maximum peak gain coefficient is generated for Ne ~ 8.8×10^{19} cm^{-3} at a temperature 22 eV after 40 psec. The ground state ionic abundances are 54% stripped nuclei and 26% H-like. The time dependence of the maximum peak gain coefficient for the single zone of the plasma is shown in Fig. 2. Spatial FWHM of the peak gain coefficient is 7 μm at 40 psec. As the plasma expands further, the peak gain coefficient decreases with increasing spatial FWHM. After 60 psec of the start of the laser, the gain coefficient is reduced to 70 cm^{-1} for Ne ~ 2.7×10^{19} cm^{-3} at a temperature of 13 eV. The spatial FWHM then increases to 17 μm. As the absorbed energy in plasma is increased further over the optimal value, the peak gain decreases (Fig. 1) with increasing electron temperature and spatial FWHM of the peak gain. For slab targets, the maximum gain of 36 cm^{-1} occurs at about 55 psec when the electron density and temperature are 1.3×10^{20} cm^{-3} and 37 eV respectively with the absorbed energy of 5.5 J/cm.

CONCLUSION

In summary, we have presented a design for a high gain recombination H-like oxygen x-ray laser driven by the 2 psec VULCAN CPA beam. Significant improvement in gain performance of the H-like oxygen recombination laser with a picosecond pulse driver has been shown. An experiment based on this scheme will be carried out in August 1993 aiming at demonstrating high gain length product in the H-like recombination laser by using the CPA beam.

We gratefully acknowledge S.J. Rose for discussions on simulations and C.L.S. Lewis, Y. Kato and P.A. Norreys for many useful suggestions.

REFERENCES

1. D.L. Matthews, P.L. Hagelstein, M.D. Rosen, M.J. Eckart, N.M. Ceglio, A.U. Hazi, H. Medecki, B.J. MacGowan, J.E. Trebes, B.L. Whitten, E.M. Campbell, C.W. Hatcher, A.M. Hawryluk, R.L. Kauffman, L.D. Pleasance, G. Rambach, J.H. Scofield, G. Stone, and T.A. Weaver, Phys. Rev. Lett., **54**, 110 (1985).

2. M.D. Rosen, P.L. Hagelstein, D.L. Matthews, E.M. Campbell, A.U. Hazi, B.L. Whitten, B. MacGowan, R.E. Turner, and R.W. Lee, Phys. Rev. Lett., **54**, 106 (1985).

3. B.J. MacGowan, L.B. Da Silva, C.J. Keane, J.A. Koch, R.A. London, D.L. Matthews, S. Maxon, S. Mrowka, A.L. Pstetheld, J.H. Scofield, G. Shimkaveg, J.E. Trebes, and R.S. Walling, Phys. Fluids, B **4**, 2326 (1992); J.A. Koch, B.J. MacGowan, L.B. Da Silva, D.L. Matthews, J.H. Underwood, P.J. Batson, and S. Mrowka, Phys. Rev. Lett., **68**, 3291 (1992).

4. A. Carillon, H.Z. Chen, P. Dhez, L. Dwivedi, J. Jacoby, P. Jaegle, G. Jamelot, J. Zhang, M.H. Key, A. Kidd, A. Krisnick, R. Kodama, J. Krishnan, C.L.S. Lewis, D. Neely, P. Norreys, D. O'Neill, G.J. Pert, S.A. Ramsden, J.P. Raucourt, G.J. Tallents, and J. Uhomoibhi, Phys. Rev. Lett., **68**, 2917 (1992).

5. C. Chenais-Popovics, R. Corbett, C.J. Hooker, M.H. Key, G.P. Kiehn, C.L.S. Lewis, G.J. Pert, C. Regan, S.J. Rose, S. Sadaat, R. Smith, T. Tomie, and O. Willi, Phys. Rev. Lett., **59**, 2161 (1987).

6. Z.Z Xu, P.Z. Fan, Z.Q. Zhang, S.S. Chen, L.H. Lin, P.X. Lu, L. Sun, X.F. Wang, J.J. Yu, and A.D. Qian, *X-Ray Lasers 1990*, G.J. Tallents ed., Bristol, IOP publisher, 151 (1991); Y. Kato, H. Azuma, K. Murai, K. Yamakawa, H. Shiraga, G.J. Pert, S.A. Ramsden, and M. H. Key, *X-Ray Lasers 1990*, G.J. Tallents ed., Bristol, IOP publisher, 1 (1991).

7. S. Suckwer, C.H. Skinner, D. Kim, E. Valeo, D. Voorhees, and a. Wouters, Phys. Rev. Lett., **57**, 1004 (1986).

8. R.A. Smith, V. Barrow, J. Edwards, G. Kiehn, and O. Willi, Appl. Phys. B, **50**, 187 (1990).

9. M.H. Key, N. Tragin, and S.J. Rose, *X-Ray Lasers 1990*, G.J. Tallents ed., Bristol, IOP Publisher, 163 (1991).

10. G.J. Linford, E.R. Peressini, W.R. Sooy, and M.L. Spaeth, Appl. Opt., **13**, 379 (1974).

11. G.J. Tallents, L. Dwivedi, Y. Kato, M.H. Key, R. Kodama, J. Krishnan, C.L.S. Lewis, K. Murai, P.A. Norreys, G.J. Pert, S.A. Ramsden, H. Shiraga, C. Smith, J. Uhomoibhi, G. Yuan, and J. Zhang, *Third International Colloquium on X-Ray Lasers*, Schliersee, Germany, 1992.

12. J. Zhang, M.H. Key, P. Norreys, and G.J. Tallents, Optics Commun., **95**, 53 (1993).

INCORPORATION OF THE SESAME EQUATIONS OF STATE IN THE MEDUSA CODE

D.J. Heading & J.S. Wark

Clarendon Laboratory, Dept Of Physics, University Of Oxford, Parks Rd., Oxford, OX1 3PU, UK.

INTRODUCTION.

The equations of state of dense, cool plasmas are not easily calculated, nor are the existing calculations Necessarily in agreement with each other at all plasma temperatures and densities. Cool, high density plasmas are known to deviate from the well-known equations of state that are derived for diffuse plasmas, or the Thomas-Fermi equations of state. Thus, the actual equation of state of any high density and low temperature plasma must be carefully modelled to find, for example, the pressure of the plasma at a given internal energy. No universal method exists for calculating the equation of state for all pressures, temperatures and chemical compositions. To test the accuracy of any calculated plasma equation of state, it is necessary to include the calculated equation of state in a hydrodynamic computer code. Only then can comparisons with experimental data be made. The aim of this work was to incorporate the Sesame equation of state library[1] into the Medusa hydrodynamic code[2].

The original Medusa code used Spitzer equations of state, derived from the perfect gas laws for a plasma. This was refined by incorporating Thomas-Fermi and equations of state for the electrons[3], but no such corrections have been made for the ions. This is a reasonable assumption at relatively low densities and high temperatures but not for cool, dense plasmas. In these plasmas, the ion motion becomes correlated, and so the ions no longer behave as a perfect gas. Thus the original and corrected Medusa equations of state for both ions and electrons have been replaced by the Sesame tables. The Sesame tables contain equation of state data calculated in a variety of ways. They cover a wide range of materials and conditions, from solids at room temperature to high temperature under and over dense plasmas.

The Sesame tables give the internal energy and pressure as a function of density and temperature. There are tables for many species, and most of these have a total equation of state table and an ionic equation of state table. The electron equation of state is obtained by subtracting the ion contribution from the total equation of state. The Sesame subroutines contain coding for loading the tables, interpolating from the given points and for calculating the ionic contribution from the Cowan[4] model in the case where no ionic table is available. The tables are called by searching the library for the material identity number, and then loading the data into an array.

RUNNING MEDUSA WITH SESAME

The subroutines which load, search and interpolate the Sesame tables have been added to the end of the MED101 code, and calls to have been inserted at relevant points within the Medusa code itself. Medusa requires three parameters from the Sesame tables. These are the pressure for a given temperature and density, the specific heat capacity (C_v) and the rate of change of internal energy with density (B_v).

Relatively few problems were encountered in incorporating the Sesame equation of state tables into the Medusa code. The version of Medusa (MED101) with the Sesame equations of state is called MEDEOS. The input data file has some changes to allow the correct identification and running of the required equation of state. The equation of state is identified with the parameter LEOS for each layer. If this is zero, then the normal Medusa equations of state are used. If this parameter is 1, then the Sesame table is invoked. A second array, EOSPRM controls the equation of state. This is set to the material identification number (MID) for the material constituting the layer. For example, aluminium has MID=3717. It should be noted that several different tables may exist for each material, covering different ranges of density and temperature. Upon running the MEDEOS code, the tables are loaded in the subroutine Seslib. If two of the layers are the same, then the table will only be loaded once. Some of the information used by Sesame is printed at the beginning of the output file, including the MID for each layer, and the flags reporting successful loading of the table. The code then runs normally, replacing the pressures, C_v and B_v for the ions and electrons for the layers required. The runtime for a simulation using three layers with Sesame equation of states is significantly increased from that of the basic Medusa code. This is due to the time taken to look up and interpolate the equation of state data, as this must happen once per cell per time step. The time for a 200000 time step run of MEDEOS is about 70 minutes.

ACKNOWLEDGEMENTS

We would like to thank Dr A. Djaoui, Mr N. Woolsey and Dr T. Bar-Noy for their work on the early stages of this project.

REFERENCES

1 Cooper, N.G. (ed) Sesame '83. Report on the Los Alamos Equation of State Library, Los Alamos Scientific Laboratory Brochure, LALP-83-4, 1983
Cooper, N.G.(ed), An Invitation to Participate in the LASL Equation of State Library, Los Alamos Scientific Laboratory brochure LASL-79-62, 1980

2 Christiansen, JP., Ashby, D.E.F.T., Roberts, K.,
Comp. Phys. Comm., 7, 271-287, 1974.

3 Rodgers, P.A., Rogoyski, A.M., Rose, S.J.,
RAL-89-125 internal report, 1989.

4 Cranfil, C.W., More, R.,
Los Alamos Scientific Laboratory Report, LA-7313, 1978

THE ROLE OF IMPURITY IONS IN RECOMBINATION LASERS.

SB Healy and GJ Pert
Department of Physics, University of York.

INTRODUCTION

The underlying principles of Hydrogenic Recombination Lasers are well understood (Pert,1976). A small fibre is irradiated by a high powered optical pumping laser, forming a plasma of bare nuclei and free electrons. The plasma is allowed to expand, and consequently the free electrons cool. Recombination of the electrons is dominated by three body recombination into upper bound states of the hydrogenic ion, which become preferentially filled. A population inversion is formed between the n = 3 and n = 2, as the upper level is populated by a collisional cascade, whilst the lower is depopulated by rapid radiative decay. In order to optimise gain on the transition it is necessary that:

1. the free electrons cool rapidly, ensuring fast recombination;
2. the plasma expands sufficiently to minimise collisional transitions between the lasing levels;
3. re-absorption, or trapping, of the Lyman Alpha photon does not destroy the population inversion.

The purpose of this work has been primarily to assess the effect of seeding heavy ion impurities into the plasma. The intention was to investigate the possibility of increasing the cooling rate of the free electrons by enhanced radiative losses from the impurity. Additionally, we have looked at possible benefits of seeding impurities lighter than the lasant species

DETAILS OF MODEL

The simulations have been performed for a hydrogenic aluminium laser. The code assumes a self similar expansion of a mixture of lasant and impurity ions. The atomic physics of the lasant has been modelled using existing routines based on Griem's Model (Davé, 1984) and the Collisional Radiative Model. The impurity is described using a time dependent Average Atom Model. Both the total number of ions and the initial fibre radius (1.0×10^{-4} cm) were constant for all runs. The impurity was seeded as a percentage of the total number of ions.

RESULTS AND DISCUSSION

The effect of the impurities has been assessed by comparing the peak gain of the mixtures, optimised with respect to energy absorbed and the lasant/ impurity ratio, with the peak gain of a pure aluminium run ($\sim 10.0 cm^{-1}$).

Simulations were performed seeding a number of heavy ion impurities into the lasant, the heaviest being Gold. It was hoped that the free electron cooling rate would increase through collisional excitation of the partially stripped impurity, followed by radiative decay. However, a series of problems were encountered. Firstly, the energy required to sufficiently ionise the lasant was significantly increased. This was due to radiative cooling by the impurity during the heating of the plasma. In addition, cooling due to expansion of the plasma was less efficient because of the increased mass. Finally, it was found during the recombination phase that the impurity could reheat the free electrons because of the dominant recombination and de-excitation transitions into the lower energy states.

Following on from earlier work by Davé and Pert (Davé and Pert,1984) seeding light impurities into the lasant was found to give more encouraging results. In fact, with a carbon impurity we were able to more than double the gain calculated for the pure aluminium case. As the impurities were fully stripped at the end at the pumping pulse, this was not due to radiative cooling. Similarly to Eder's (Eder et al 1990) calculations for gain in magnesium and magnesium fluoride targets, the presence of the impurity was found to reduce the trapping of the Lyman Alpha photon from the lower lasing level. Additionally, because of the lower number of electrons, less expansion was necessary to minimise transitions between the lasing levels. Although in comparison with hydrogenic carbon schemes, the electron densities required in the aluminium were high, some expansion from the solid density was required. As the electron densities scale with atomic number, z, of the lasant as z , this can clearly be seen by scaling the electron density quoted by Pert (Pert,1990) for a carbon fibre at peak gain, $n_{e,C} = 2.17 \times 10^{19} cm^{-3}$. For aluminium this scaled to $n_{e,Al} = 4.86 \times 10^{21} cm^{-3}$. In comparison a fully stripped aluminium plasma at solid density would give $n_{e,sol} = 7.8 \times 10^{23} cm^{-3}$. Therefore a population inversion was formed at higher lasant ion densities, despite dilution by the impurity. The optimum lasant/impurity ratio was found consistently to be ~ 1/3.

To summarise briefly, the results indicate heavy ion impurities have no apparent benefits, whereas light impurities result in higher calculated gain values.

REFERENCES

Davé AK 1984, PhD Thesis, University of Hull
Davé AK and Pert GJ 1984, J. Phys. B. 17 4953
Eder DC, Rosen MD, Shepard R, Staffin R, Nash JK and Keane CJ 1990, X RAY Lasers, IOP Conference No.116 p. 309
Pert GJ 1976, J. Phys B. 9 18 3301
Pert GJ 1990, X RAY Lasers, IOP Conference No. 116 p. 143

COLLISIONALLY PUMPED NE-LIKE LASERS

PB Holden[1], A Kingston[2], MTM Lightbody[1], GJ Pert[1] and E Robertson[2]
[1]Department of Physics, University of York
[2]Department of Mathematics, Queen's University, Belfast

The complex problem of the collisionally pumped Ne-like Ge laser is examined through several models. The central model is EHYBRID, a 1½D code which self consistently treats the plasma expansion with the atomic physics of the Ne-like ion for 124 excited levels through a collisional radiative treatment, other ion stages being approximated through the Modified Griem's Model (Daveé 1984. The atomic data required has been calculated at Belfast, accurate collision rates calculated using the R-matrix approximation being used for all transitions from ground and for all transitions between p-hole $n = 3$ levels. The inversion is generated under suitable plasma conditions - typically $T_e \sim 800$eV and $n_e \sim 5 \times 10^{20}$cm^{-3} - between the 3p and 3s levels, the former of which are metastable but are populated by strong monopole collisions from the 2p ground state in addition to other mechanisms such as collisions with higher excited states and dielectronic recombination from F-like ions. The output of EHYBRID is used as data for ray-tracing and saturation codes which generate experimental observables. The former of these is necessitated by the high electron densities required for the generation of gain which typically results in high refractive index gradients. All aspects of this work are discussed in detail in Holden *et al* (1993).

The steady state ionisation balance under suitable conditions for gain is significantly higher than Ne-like, and the dominance of Ne-like ions arises only as a consequence of long relaxation times; Ne-like ions are created in the relatively cold dense plasma near the ablation front and further ionisation is inhibited as the plasma is heated and the density falls. As such, the accurate calculation of the time dependence of the ionisation balance is crucial to the calculation of gain. We have found that a full collisional radiative treatment of the Ne-like ion stage is necessary for an accurate calculation (whilst a less accurate treatment is required between other ion stages, provided the laser is not operating near threshold intensities when Na-like ions are present) and that dielectronic recombination is a significant process in the determination of the ionisation balance. Some aspects of this modelling and a comparison with average atom calculations are discussed in Djaoui *et al* (1993).

Refraction is examined at present through a 2D raytrace. The plasma is assigned to a mesh of 10 x 100 cells, from each of which 100 rays are emitted over an angular spread of 100mrad. To each of the rays is assigned the appropriate fraction of the spontaneous emission within the cell of origin. The rays are then traced through the mesh as a series of continuous parabolas being amplified as they pass through regions of gain, and collectively they describe the angular dependence of the output intensity at a given time instant. Ray averaged values of saturation intensities and Doppler and Lorentz components to the line shape are calculated and these can be used to calculate the modifying effects of saturation should it occur.

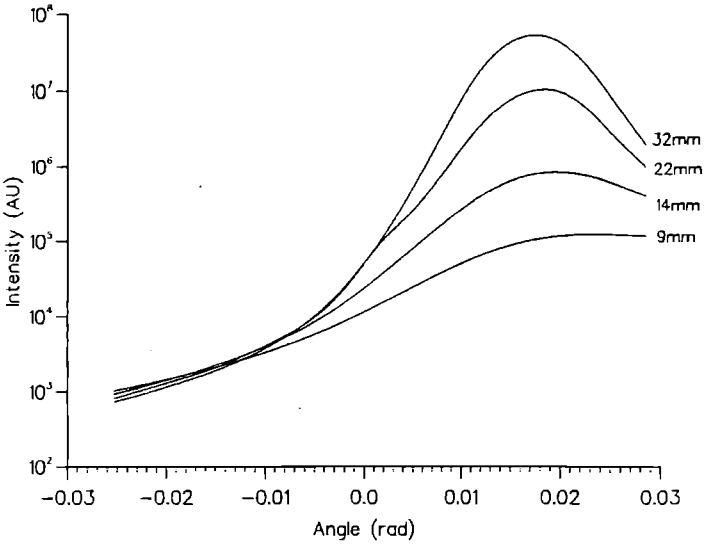

Figure 1 The time integrated intensity output on the 236 Å line as a function of angle for several plasma lengths

The output intensity of the 236Å line is illustrated in figure 1. The progressive narrowing of the beam and reduction in the refracted angle are apparent as the target length is increased. A fit to these peaks gives a time integrated gain coefficient of 3.3cm^{-1}. The dependence of beam divergence on length is found to be in excellent agreement with experiment, although the refracted angle of the beam is significantly overestimated; experimental measurements indicating values of ~10mrad. The discrepancy could be explained by a 30% error in the hydrodynamics, although we expect that analysis by 3D ray-tracing (Plowes 1993) will reduce the angle as refraction in the second dimension will further shorten the paths of rays travelling through high density plasma.

We note that ray-tracing of the 232Å line gives virtually identical output profiles to the 236Å line, yielding equal gain coefficients to within a few percent. The intensity ratio of the lines $I_{236} : I_{232}$ is found to be typically 1.5 as a consequence of partial equilibration between the upper

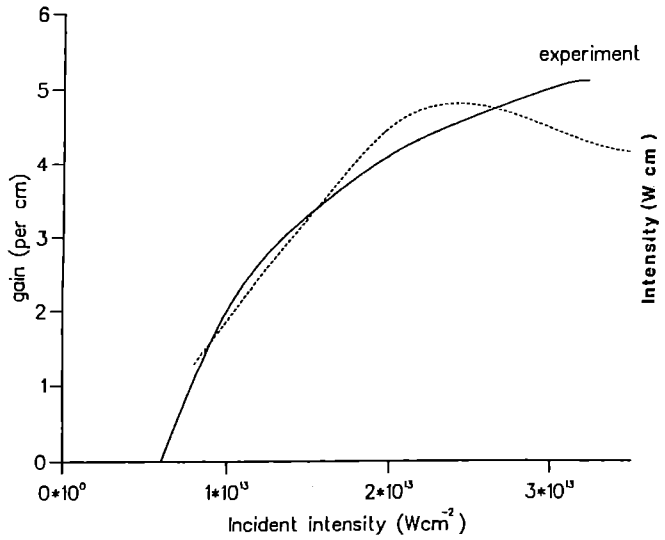

Figure 2: The variation of 236Å gain with intensity, assuming 50% laser losses. Experimental data is that of Nealy *et al* 1992.

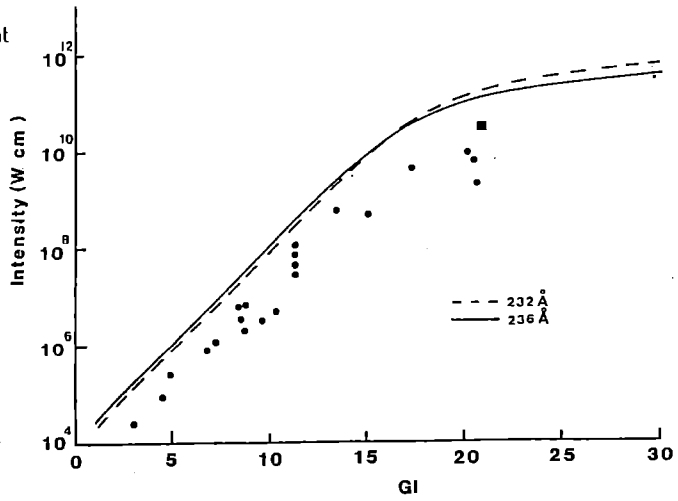

Figure 3: The output intensity of the 232Å and 236Å lines as a function of gain length. The roll over a saturation is apparent for $GL \sim 15$ as is the switch in the $I_{236} : I_{232}$ intensity ratio. The experimental data of Carillon *et al* (1992) are marked, the square point being measured at an intensity of 1.4MW. The experimental data are scaled to absolute units using this value and by assuming an aperture size of $60 \times 100\mu$m.

lasing levels, although the value is intensity dependent.

Figure 2 illustrates a comparison between theory and experiment of the time integrated gain as a function of intensity. The theoretical intensity has been scaled empirically to fit the experimental data (assuming 50% losses through stimulated Brouillon scattering, beam inhomogeneities and other such mechanisms not included in the model). The strength of the output signal is dependent upon the magnitude of gain, the volume of plasma over which significant gain is supported and the refractive index gradient in the region of high gain. As the laser operates below steady state ionisation, the effect of higher incident intensities is reduced Ne-like populations at the resultant higher electron temperatures, especially at late times, and lower gain coefficients result. Conversely, high intensities drive the expansion faster and create larger plasma masses, producing lower refractive index gradients and gain over a larger volume of space. The latter two effects tend to compensate for the reduced gain by allowing the prolonged passage of the laser through the active medium and optimum driving conditions are found at somewhat higher intensities than would be expected from local gain coefficient considerations.

We note that a similar effect is responsible for the reduced gain obtained from irradiation with 2ω light - the shorter wavelength light is absorbed deeper in the plasma resulting in more severe refractive index gradients whilst the more rapid fall off in electron density inhibits the ionisation and results in larger gain coefficients. The net effect is a decrease in the apparent gain.

The effect of saturation at long gain lengths is illustrated in figure 3. The quantities required for these calculations (Doppler and Lorentz widths, saturation intensities and spontaneous emission densities) are ray averaged values. The beam divergence is obtained directly from the ray trace. Saturation is found to occur for gain lengths greater than ~ 15. The intensity ration $I_{236} : I_{232}$ is seen to switch from 1.5 to 0.5 (the ratio of the saturation intensities) at saturation.

We are generally satisfied with these models and are at present continuing the work through the development of a 3D ray-trace and a wave model of the beam propagation. These tools will enable the future modelling of more complex target configurations, utilising multi-targets and mirrors which are the practical issues currently being experimentally addressed.

REFERENCES

Carillon A *et al* 1992, *Phys. Rev. Lett.* **68** 2917

Davé AK 1984, PhD Thesis, University of Hull

Djaoui A, Healy SB, Holden PB, Pert GJ and Rose GJ 1993, in this report

Holden PB, Healy SB, Lightbody MTM, Pert GJ, Kingston A, Robertson E, Lewis CLS and Nealy D 1993, submitted to *J. Phys. B*

Nealy D *et al* 1992, XRAY lasers 1992, IOP Conference No. 125

Plowes JA and Pert GJ 1993, in this report

COMPUTATIONAL STUDIES OF THE EFFECT OF SUPRATHERMAL ELECTRONS ON K-SHELL EMISSION

A. Khan, J. Edwards, D. Riley, O. Willi

Blackett Laboratory, Imperial College of Science Technology and Medicine, London SW7

INTRODUCTION

The interpretation of spectroscopic data is crucial in understanding and diagnosing laser produced plasmas. With the increasing use of high intensity short pulse lasers, the generation of high energy electrons via wave breaking phenomena like resonance absorption, (RA), is inevitable. Given the recent interest in characterizing X-ray emission from high-intensity short-pulse laser-target interactions, there is a need to assess the influence of suprathermal electrons on such emissions. Recent work performed by Teubner and co-workers [1] has highlighted that for the same absorbed intensity, p-polarized light is significantly more efficient in producing X-rays than is s-polarized light. The observed increase in X-ray yield for p-polarization is directly linked to the suprathermal electron population generated by RA with the X-ray continuum emission arising through bremsstrahlung in the solid target, [2]. Since the effect of high energy electrons on the ionization dynamics of the laser-plasma system is still not fully understood the need to quantify the influence of these high energy electrons on the emission spectra and line emission has become of paramount importance. Presented here are studies conducted into analysing the effect of suprathermal electrons on the ionization charateristics of K-shell emission for an aluminium, (Al), plasma. We have considered the effect of pulse length and the presence of a preformed plasma on the hot electron emission spectra. Time dependant simulations have been conducted for solid Al targets, with and without the presence of a prepulse for $\lambda=1\mu m$ with a 1 picosecond, (ps), FWHM pulse of peak intensity 10^{17} W/cm^2 and for a high contrast ratio 12 ps KrF laser pulse of peak intensity 10^{17} W/cm^2.
A general description of the computational model with its assumption will be presented in the theory section followed by some simulations highlighting the influence of hot electron on the Heβ and Lyβ emission

THEORY

To assess the effect of suprathermal electrons on the ionization dynamics of the laser plasma system, MED101 a 1-D lagrangian hydrodynamic code, [3] was post-processed with POPNLT, a time-dependent non-LTE screened-hydrogenic average atom (AA) ionization code, very similar to the XSN code of W. A. Lokke and W. H. Grasberger . In MED101 a set fraction of the laser energy at the critical density is deposited into the plasma by resonance absorption, (RA). Of this, a specific fraction is converted to hot electrons, with the hot electron temperature following ;

$$T=f(I\lambda^2) \qquad (1)$$

where $f(I\lambda^2)$ is the LASL compilations of T verse $I\lambda^2$.
In the 1-D hydrodynamic code, the suprathermal electrons are divided into 10 energy groups with each group being seperately transported through the target. The absorption routine in MED101 is modified to ensure a smooth variation of the hot electron energy as the beam 'burns' through the computational mesh. At each time step the hot electron density is calculated at critical density and used to calculate the hot electron fraction given by equation (2) in each computational cell throughout the target. The results generated from the hydro-code are post-processed with a POPNLT code thus enabling a time-dependent approach to the problem.

$$\text{hot electron density} = 2\alpha I / m v_h^3 \qquad (2)$$

where αI = energy deposited at the critical density surface
m = electron mass
v_h = hot electron velocity

The presence of suprathermal electrons in the AA ionization code is accounted for by adopting a multi-temperature description of the electron velocity distribution. For the results presented, a two temperature approximation was assumed comprising of a 'cold' thermal temperature and a 'hot' suprathermal temperature. The hot and cold temperatures are obtained from the hydro-code as are the electron densities. Since three body recombination requires two incident electrons, one to attach to the ion and the other to carry of the binding energy, the cross-section velocity integral for this rate will contain an electron distribution function for each of the two electrons, rather than the one for one electron processes such as collisional excitation. Thus the multi-temperature approximation is not strictly applicable for the 3 body recombination process. However this form can still be used without introducing a significant error into the collisional rate since the rate per electron pair of electron capture events involving one or two electrons from the hot populations is less than the probability of recombination where both electrons are from the cold populations. The total recombination rate will be no less than the rate due to the cold electrons and no greater than the rate obtained assuming that the hot and cold electrons contribute equally to the total rate. This range of bi-maxwellian rate values will represent a spread of only a few precent if the hot fraction is approximately 1 %. Consequently the error in adopting the multi-temperature approach as an intermediate estimate for the recombination process will have a negligible consequence compared with the order of magnitude effect of the hot electrons on the collisional ionization rate, since the most significant effect of the hot component on the ion population is through the collisional ionization and excitation rates in which the most important temperature dependent factor at threshold of emission is the exponential term

$$\text{rate}(T) \sim e^{(\chi/KT)} \qquad (3)$$

where χ = the relevant excitation or ionization energy

RESULTS

Shown in figure 1 are the results for a 1 μm, 1 ps FWHM laser-pulse, of peak intensity 10 ^{17} W/cm^2 interacting with solid aluminium at the peak of the pulse.

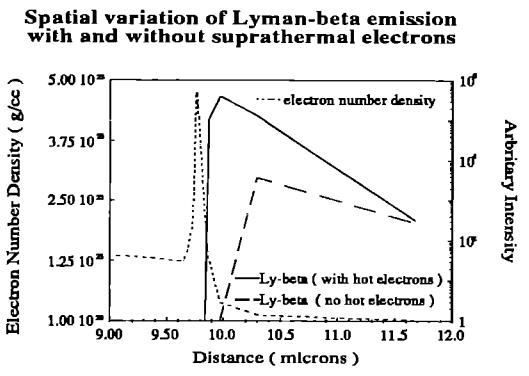

Figure 1

The influence of suprathermal electrons on the K-shell emission is clearly visible with the peak of emission shifting to a higher density. The shift towards high densities is a direct consequence of the hot electrons large mean-free path. This enables the high energy electrons to propagate ahead of the thermal front, ionizing the material. Indeed, at a distance of approximately 10 microns, the inclusion of the hot electrons in the ionization code

causes the Lyβ emission to be enhanced by approximately five orders of magnitude as compared to the results obtained when the hot electrons are unaccounted for. As one moves away from the high density plasma regions towards the hot coronal plasma, the effect of suprathermal electrons in increasing the Lyβ emission is considerably reduced. If one considers the spatial variation of the thermal electron temperature, which increases going out towards the coronal region, such a feature is explainable. With the higher temperature, there are more high energy thermal electrons with the ability to take part in ionization. Thus the influence of the suprathermal electrons is considerably diminished. The highly ionized nature of the plasma effectively diminishes the influence of the hot electron population. Similar results were also obtained for the Heβ emission, figure 2.

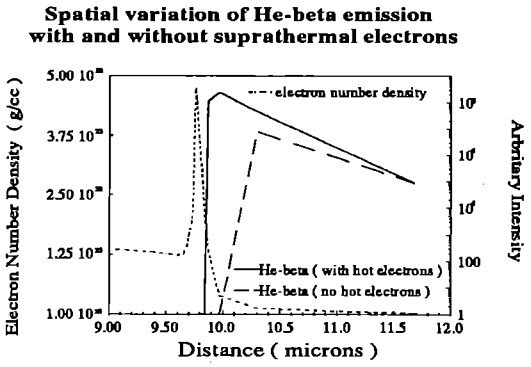

Figure 2

Simulations were also conducted with the presence of a preformed plasma for the intensity-wavelength conditions specified above. The preformed plasma is generated by the interaction of a linearly rising ASE laser pulse peaking at 10^{13} Wcm^{-2} within 25 ps. The main pulse of 1 ps and 10^{17} Wcm^{-2} interacts with the plasma at time 0.0 ps, figure 3. The presence of a hot electron population results in the smoothing of the line ratio. If in the ionization code the suprathermal electrons are unaccounted for, it would appear that the initial decrease in the line ratio is a consequence of the preformed plasma being heated strongly. After some time the heat front is of sufficient strength to heat the high density region, resulting in the increase of Heβ emission before eventually being strong enough to increase the Lyβ emission. When hot electrons are included, the large mean free path of the hot electrons ensure deep propagation into the target where they deposit their energy, heating up the target infront of the thermal front. This effectively smooths the transition from the heating of the preplasma to the higher density regions. With solid Al this effect does not occur.

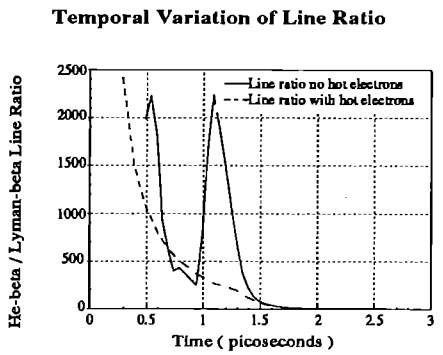

Figure 3

Despite the discrepancies in wavelength and pulse length, it is of interest to compare the above simulations to the experimental work of Teubner, [1]. Our simulations support Teubner's conclusions and in essence, are in broad agreement with the experimental results.

In a recent Rutherford Laboratory experiment of similar intensity and wavelength, [4], but significantly longer pulse-length to that of Teubner's, we found that the hot electron influence was minimal. The disparity between the two results is made clearer if we consider that the most significant effect of the hot electron population on the ion populations will be through the collisional ionization and excitation rates. At the threshold of emission, the most important factor in the rate formalism is the exponential term, equation (3). If we assume a background thermal temperature of 400 eV, where the 1.7 KeV aluminium Lyα is seen, equation (3) yields an exponential factor of 10^{-2} for the needed excitation. If $kT_h > \chi$, where χ is the relevant excitation or ionization energy, this factor is nearly unity so that a 1 % hot population is as effective as the entire cold population in driving the ionization. Thus the suprathermal electron population will make a significant impact in the ionization process of the material provided $kT_c << \chi$. Such conditions can be generated by the action of very short high intensity laser pulses, (400 fs 10^{17} Wcm^{-2}), were the resulting temperature scalelengths are small in stark contrast to longer pulses, (12 ps). For small temperature scalelengths the hot electrons need not travel far in the target before the condition $kT_c << \chi$ is statisfied.

CONCLUSIONS

Preliminary time-dependant simulations have been conducted into monitering the influence of high energy electrons, as generated by resonance absorption, on K-shell emission. We have shown that in the case of moderately ionized plasma, suprathermal electrons can make a significant difference. We have also shown that in the case of a preformed plasma, suprathermal electrons make a definitive impact on the Heβ/Lyβ line ratio results. It is of interest to consider more detailed simulations into the suprathermal electron effects with and without the presence of a preformed plasma for numerous conditions, so we can generalize under what laser intensity-wavelength-pulse length parameters hot electron influences are significant. The main influence of suprathermal electrons is through the collisional and ionization rates, of which the most important term at the threshold of emission is the exponential, $e^{(\chi/kT)}$. As such, the ionization dynamics of the laser-plasma system will be significantly altered by a hot electron population if $kT_c << \chi$ and $kT_h > \chi$. These conditions seem to have been generated in the case of Teubner's work where the action of short high intensity laser pulses results in very steep thermal fronts with sub-micron plasma scalelengths, [1]. In Riley's work the action of the longer 12 ps pulses result in plasma scalelengths of a few microns, supporting our above statements.

REFERENCES

[1] Angle-Dependent X-ray Emission and Resonance Absorption in a Laser-Produced Plasma Generated by a High Intensity Ultrashort Pulse
U. Teubner, J. Bergmann, B. Van Wonterghem, F. P. Schafer and R. Sauerbrey
Phys. Rev. Lett. 70 794 (1993)

[2] MeV X-ray Generation with a Femtosecond Laser
J. D. Kmetec, C. L. Gordon, J. J. Macklin, B. E. Lemoff, S. G. Brown and S. E. Harris
Phys. Rev. Lett. 68 1527 (1992)

[3] MED101 : A laser-plasma simulation code : User guide
P. A. Rodgers, A. M. Rogoyski and S. J. Rose
Rutherford Appleton Laboratory Report No. RAL-89-127, 1989 (unpublished)
MEDUSA, A One-Dimensional Laser Fusion Code
J. P. Christiansen, D. E. T. F. Ashby and K. V. Roberts
Conput. Phys. Commun. 7 271 (1974)

[4] Plasma Conditions Generated by Interaction of a High Brightness, Prepulse Free, Ramman Amplified KrF Laser Pulse with Solid Targets.
D. Riley, L. A. Gizzi, F. Y. Khattak, A. J. Mackinnon, S. M. Viana and O. Willi.
Phys. Rev. Lett. 69 3739 (1992)

THREE DIMENSIONAL RAY TRACING IN COLLISIONALLY PUMPED SYSTEMS

J A Plowes and G J Pert
Department of Physics, University of York

INTRODUCTION

The high electron densities, generated in collisionally pumped X-ray laser systems, which are required for the formation of adequate inversion densities, result in large refractive index gradients in the region of gain. This leads to refraction of the X-ray laser beam. In a computational model, the effects of refraction must be included if the model is to successfully reproduce experimentally observed results.

Currently a two dimensional ray trace is used, as a post processing program for the quasi two dimensional code EHYBRID, which generates the hydrodynamic and atomic parameters used as data for the ray tracing, and produces an output which can be compared to that measured by experiment. The combination of these models has given good agreement with experimentally observed values in most respects, and it is hoped that the extension of the ray trace to three dimensions will provide an even better description of experiment.

THE TWO DIMENSIONAL MODEL

The three dimensional ray trace, upon which work is currently carried out, is essentially an extension of the two dimensional ray tracing program which derives from well tested routines designed to model the absorption of the driving laser by the plasma(1). The plasma variables are defined on a rectangular mesh and each rectangular cell is further divided into two triangular cells for the purposes of ray tracing. The electron density gradients, assumed to be constant within cells, are defined by the densities at the cell corners. In a constant electron density gradient the path of the ray will be parabolic; due to Snell's law. The total ray path is calculated as a series of such parabolic arcs as the ray moves from cell face to cell face across the mesh. Many rays are traced this way and, collectively, this ray pattern describes the angular dependence of the output beam intensity at a given time instant.

THE EXTENSION TO THREE DIMENSIONS

The extension to three dimensions assumes a system with a plasma uniform along the longitudinal axis. The rays are traced in a transverse plane perpendicular to the longitudinal axis and the governing equations are

$$\mu \cos\chi = \mu_0 \qquad (1)$$

$$\mu' \sin\varphi = \mu'_0 \qquad (2)$$

μ is the refractive index, χ is the angle the ray makes with the longitudinal axis, φ is the angle the ray makes in the transverse plane and the quantity, μ', is given by $\mu'^2=\mu^2-\mu_0^2$. The distance the ray has travelled along the longitudinal axis d' is given by

$$d' = \frac{2\mu_0 n_c}{n_g}\sqrt{\mu'^c \mu'^2_0} \qquad (3)$$

n_c and n_g are the critical density and the density gradient respectively. Equation 2 is Snell's law and so, working with μ' instead of μ, the existing 2D ray trace program can be modified to follow the movement of the ray in the transverse plane.

The plasma is assumed to extend a specified distance in the longitudinal direction. This gives a cuboid space in which the rays are traced. Rays are started at one end of the plasma, ray tracing being carried out in the transverse plane and the distance that this relates to in the longitudinal direction being followed, until either the rays exit the end face of leave by one of the side faces.

At the time of writing this report, work on the 3D ray tracing program is still continuing and so no comparison with experiment is possible, although it is hoped that this new work will bring the theoretically calculated values closer to the experimentally measured ones.

REFERENCES

1. D J Toft, PhD Thesis, University of Hull (1979).

A MONTE CARLO TREATMENT OF ELECTRON-ION COLLISIONS IN PIC SIMULATIONS

G J Pert

University of York, Department of Physics, York

The multiphoton ionisation of gases at very high intensity by plane polarised light can in principle lead to an electron-ion system with very low residual energy - above threshold ionisation (ATI). Such a system is in principle an ideal medium for the generation of gains by recombination (Corkum et al, 1989, Eder et al, 1992). However, there are a number of effects which can significantly heat the plasma and mitigate against gain. These include focal spot structure, electron-ion displacement, electron-ion collisions (inverse bremstrahlung), collisional ionisation and Raman scatter.

To investigate the collective plasma effects we reported earlier (Pert et al 1990) on the development of particle (PIC) simulation to account for the gross development and heating. It was found that provided the focal spot was sufficiently wide, electron channelling and the strong heating associated with the collapse of the channel could be avoided, and the electrons remain cold.

However, such conclusions require that collisional heating be small, essentially that the electron-ion collision time be large compared to the laser pulse duration. In fact many experiments are limited by the laser device to pulse lengths comparable to somewhat in excess of this time. It is therefore desirable to explore the possibility of including collisional behaviour into PIC simulations. At this stage we restrict ourselves to considering only electron-ion collisions, as these alone lead to heating. Electron-electron collision drive the relaxation towards a Maxwell-Boltzmann distribution, but do not increase the average energy of the plasma during the laser pulse - at least in the non-relativistic limit.

We therefore consider the scattering of electrons by fixed ions within the PIC framework. Particle-in-cell codes consider a group of electrons as a single particle and calculate the dynamics of the system from the dynamic behaviour of an ensemble of such particles subject to the dynamics of the electron group considered as one entity. Clearly such a description cannot embrace the internal degrees of freedom within the group of electrons, but will allow relaxation amongst the ensemble of particles. It will therefore accurately account for inverse bremstrahlung which is due to scattering of the total (thermal and quiver) electron velocity.

The electron-ion interaction in a PIC model describes the collective forces over distance greater than a cell width Δx, which for an accurate representation should be less than the Debye length λ_D. The collisional scattering model must therefore account for forces over the length range $0-\Delta x$. It is well known that electron-ion interaction over lengths large compared to the Landau length b_0 is due to multiple small angle scattering, and that this dominates over the short range binary large angle deflection. We may therefore regard the scattering as a sequence of small random scatterings occurring continuously in time. Therefore if we consider a small time interval δt, the variance of deflection angle increases linearly with time. More generally it follows from the central limit theorem that the distribution of deflection angles follows a normal (Gaussian) distribution with variance increasing linearly with time. Using the standard Rutherford scattering formula it is easily shown that the variance of the scattering angle increases at a rate given by the momentum transfer cross section σ_d.

$$\frac{d<\theta^2>}{dt} = \int_0^{\pi} n_i \sigma v \theta^2 d\theta \simeq 2 n_i \sigma_d v = \frac{4\pi e^2 n_i}{m^2 v^3} \ln\left[1+\beta_{max}^2\right] \quad (1)$$

where Z is the ion charge, n_i is the ion density e and m the electron charge and mass respectively, and v the electron (total) speed. β_{max} is the interaction field cut-off parameter which should be limited by the cell width Δx, rather than the more usual Debye length

$$\beta_{max} = \Delta x / b_0 = m v^2 \Delta x / Z e^2 \quad (2)$$

Hence the variance increase rate is accurately expressed as:

$$\frac{d}{dt}<\left[2\sin(\theta/2)\right]^2> = 4\pi b_0^2 \ln\left[1+(\Delta x / b_0)^2\right] n_i v \quad (3)$$

We implement this result using a Monte Carlo approach as follows. In a time interval δt the scattering angle is given by a random variable of normal distribution with variance given by (3), whose value is easily obtained by the Box-Müller method. Equation (1) yields strictly $2\sin(\theta/2)$, rather than θ, from which we obtain

$$\cos\theta = 1-2\sin^2(\theta/2)$$
$$\sin\theta = 2\sin(\theta/2)\sqrt{\left[1-\sin^2(\theta/2)\right]} \quad (4)$$

The angle of rotation ϕ, is a uniform deviate in the range $0-2\pi$. The new velocity after scattering is given by

$$\underline{v}' = \left\{\underline{i} v_z v_x / v_r + \underline{j} v_z v_y / v_r - \underline{k} v_r\right\}\sin\theta\cos\phi + \left\{-\underline{i} v_y + \underline{j} v_x\right\} v / v_r \sin\theta\sin\phi + \underline{v}\cos\theta \quad (5)$$

where $v_r^2 = v_x + v_y^2$ and $v^2 = v_r^2 + v_z^2$

This result expresses the rate at which transverse fluctuations in the electron momentum increase with time due to electron collisions with stationary ions. The transformation to the statistical group representing the simulation particle can be performed in two ways. More simply we take all electrons in the group as identical and assign a single (electron) scattering angle to the whole, ie: to the particle. In this case we correctly describe the randomisation of energy through the velocity distribution of the particles. For our purposes this method is satisfactory. However, if the group is allowed to have internal degrees of freedom, then we may note that the transverse momentum gain for the group has a variance N times that of an individual electron, and the angle of scatter 1/N times, where N is the number of electrons in the group. In this case the individual electrons have a distribution about the group mean, ie: internal energy, which accounts for much of the thermalisation. At a statistical level if our samples are sufficiently large both methods must lead to the same results, although the latter will require more complex energy accounting, and in principle involves electron exchange between particle groups.

Clearly since $\sin(\theta/2) < 1$, the time-step δt must be chosen so that $\delta t \le 2 / n_i \sigma_d v$. With an efficient generator for uniform deviates the method does not introduce unacceptable overheads, and takes time comparable to the particle pushing sections of the programme.

Tests show that the energy increase rate calculated in this way is in good agreement with the accurate inverse bremstrahlung rate.

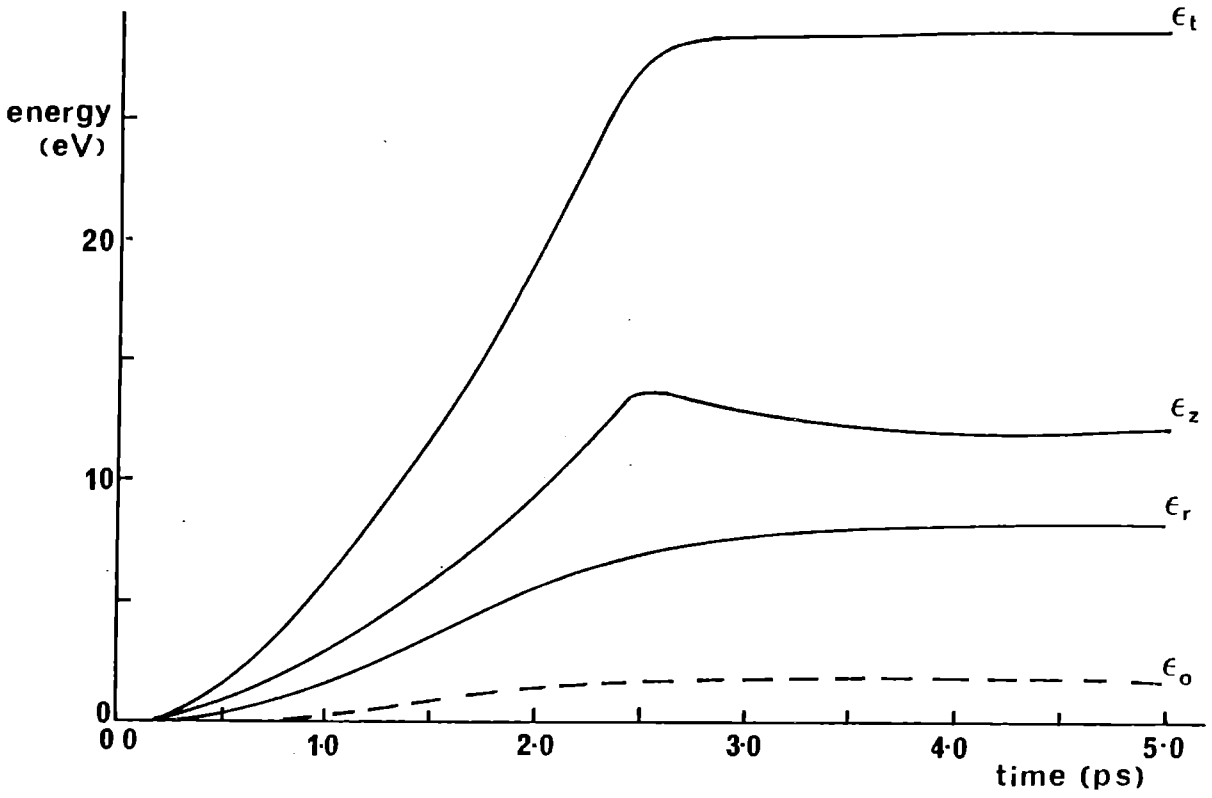

Fig 1 Plots of the electron energy terms as a functions of time during the laser pulse, and subsequent relaxation.

As an illustration of the calculation we investigate the case of the breakdown of nitrogen by 0.248 μm radiative in a pulse 3 ps duration of intensity 2 x 10^{16} W/cm^2 in a focal spot 30μm diameter. At an atomic density 10^{17}/cc in fig 1 we show plots of the total energy with, ε_t, and without, ε_o, collisions, and the growth of energy in the directions parallel, ε_z, and perpendicular, ε_r (ε_x or ε_y) to the incident laser field during and after the pulse. It can be clearly seen that collisional absorption increases the energy by over an order of magnitude due to the long pulse, and relatively high density. It can also be seen that the parallel energy increases more rapidly during the pulse, and there is consequent re-distribution towards isotropy once the pulse is finished. The two components ε_x and ε_y in ε_r are statistically equal.

REFERENCES

1. Corkum P B *et al* 1989 Phys. Ref, Lett. 62 1259
2. Eder D E *et al* 1992 in X-Ray Lasers 1992 ed. E Fill (I o P Conference Series No. 125) p 177.
3. Pert G J *et al* in X-Ray Lasers 1992 ed. E Fill (I of P Conference Series No 125) p 105.

FEASIBILITY STUDY OF NON-LINEAR DIFFERENCE FREQUENCY GENERATION IN A LASER PRODUCED PLASMA WITH A GeXXIII XUV LASER AND A Nd GLASS LASER

M H Key[1] and P L Shkolnikov[2]

[1]Rutherford Appleton Laboratory and University of Oxford
[2] Johns Hopkins University ,Baltimore,USA

INTRODUCTION

Theoretical analysis [1] has suggested the interesting possibility of generating laser radiation at close to the second harmonic frequency of an XUV laser by four wave mixing with optical laser radiation in a plasma, using near resonances with electronic states of highly ionised ions to enhance the non-linear susceptibility . If the optical laser were frequency tunable the process would offer fine scale tunability of the XUV output , thus removing a significant limitation to the usefulness for spectroscopic applications of the typically one part in 10^4 spectral purity of XUV lasers operating on transitions of highly ionised ions.

EXAMPLE

The particular example of a Ge XXIII XUV laser emitting at 23.6/23.2 nm and a Nd glass laser at 1053 nm is considered here. A plasma of Ar VIII ions is chosen as the non-linear medium because of the near- resonances for difference frequency mixing illustrated in figure 1.

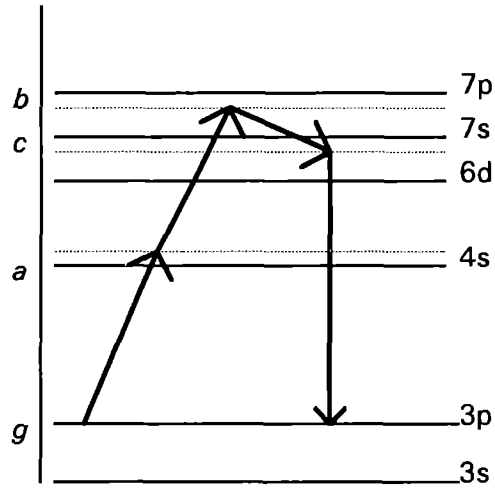

Figure 1
Ar VIII energy levels and virtual levels in difference frequency generation

An expression for the conversion efficiency in focussed Gaussian beams[1] is,

$$C = P/P_1 = KN^2 P_1 P_2 |F_2|^2 \qquad (1)$$

where P_1 and P_2 denote power at the optical and XUV wavelengths, N is the density of ions , $|F_2|^2$ is the phase matching factor and K is derived from the resonant susceptibility of the ion.

$$K = 512\pi^6 c^{-2}(1-\lambda_1/2\lambda_2)\lambda_1^{-3}\lambda_2^{-1}\left(\sum \alpha S\right)^2$$

with the resonant factors contained in S in the form,

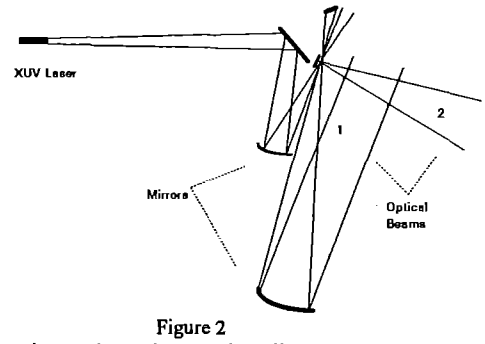

Figure 2
Schematic experimental system for difference frequency generation

$$S^2 = A_{ag}A_{ba}A_{ac}A_{cg}\left[(E_a-E_g)(E_b-E_a)(E_b-E_c)(E_c-E_g)\right]^{-3} \times$$

$$\left[(E_a-E_g-\lambda_1^{-1})(E_b-E_g-\lambda_2^{-1})(E_c-E_g-2\lambda_1^{-1}+\lambda_2^{-1})\right]^{-2}$$

where A's denote the radiative transition probabilities and E's the energy gaps in cm^{-1} .

The phase matching factor is well known for interaction of focused Gaussian beams with equal values of the confocal parameter b. In such a beam the intensity in the focal plane is $I=4P/b\lambda$. The phase factor can be recast in a form due to Bjorklund, viz. $G=[b\Delta kF_2]$ and has a constant maximum value when $b\Delta k=2.5$. Contributing factors to the mismatch are the changes in k due to focusing, to the refractive index of free electrons in the plasma and to any angle θ between the optical and XUV beams, giving an effective k value,

$$k' = k(1-\lambda/\pi b - r_e N\lambda^2/2\pi - \theta^2/2)$$

REALISTIC EXPERIMENTAL CONDITIONS

Figure 2 illustrates how beams available with the Vulcan facility i.e. the Ge XXIII XUV laser at 23.2/23.6 nm and the CPA Nd glass laser at 1053 nm (1) could be combined in a laser produced plasma generated by another Nd glass laser beam (2). The XUV beam, having expanded from 100 microns to 4 mm diameter, is focused at f/12.5 to an intensity of 10^{12} Wcm^{-2} in a 5 micron diameter focal spot with b= 125 micron ,assuming 1MW power for 500 ps and 4 mrad divergence . The CPA Nd glass laser beam with 5TW power in 2 ps and with f/10 focusing gives a 50 micron focal spot of intensity 3 10^{17} W cm^{-2} and b=100 micron. These parameters are chosen to give close to optimal phase mismatch due to the inter-beam angle and strength of focusing. The optimal plasma density is similarly determined to be 6 10^{18} electrons /cc . With these assumed conditions and recasting equation (1) in terms of intensity to use the practical rather than Gaussian beam intensities, the conversion efficiency for generation of radiation at 11.7 nm is estimated to approach 10%, suggesting that experiments with presently available lasers could give significant results.

REFERENCES

1. P Shkolnikov et al . Appl. Phys. Letts. 61 2001 (1992)

SHORT PULSE HIGH INTENSITY LASER INTERACTION WITH GAS TARGETS

A Djaoui

Rutherford Appleton Laboratory

INTRODUCTION

The rapid progress in short pulse high intensity lasers has resulted in the possibility of investigation of new laser-matter interaction physics. The strong electric field associated with these lasers results in highly non-linear phenomena while their short duration results in highly transient behaviour. There are currently two broad areas of experimental physics conducted with these lasers; solid density and gaseous target interactions. Solid target interactions have been used successfully for the generation of intense x-rays[1,2]. Aspects of gas target experiments which are of interest include multiphoton and tunnel ionisation[3], Above Threshold Ionisation (ATI or residual) energy[4], inverse bremsstrahlung[5] (collisional heating), Stimulated Compton and Raman scattering heating[6], relaxation of non-isotropic non-maxwellian distributions and space charge effects associated with the laser ponderomotive force[7]. The above processes are not always important; for very low densities for example, ATI may be the dominant heating mechanism. At higher densities collisional heating is much larger than ATI heating. For longer pulses, parametric heating phenomena relating to stimulated Raman and Compton scattering become important. A possible application of tunnel ionised plasmas is the creation of highly ionised medium with a relatively low electron residual temperature which can be used as amplifying medium for recombination XUV lasers. The achievement of a low temperature is crutial for such a scheme, hence the importance of understanding heating processes in tunnel ionised plasmas. After a brief description of tunnel ionisation, ATI energy and high field correction to collisional absorption, simulations of recent gas target experiments[8,9] conducted on the 12ps beam of the Sprite system are presented. Details of the experiments are given in reference 9.

TUNNEL IONISATION AND ATI ENERGY.

Two regimes of field induced ionisation can be defined depending on the adiabaticity parameter $\gamma = \omega\sqrt{2mU_i}/eE$ where E is the electric field strength, ω the laser frequency and U_i the ionisation potential. For large values γ (low intensities) field ionisation has a multiphoton character with the photoelectron energy spectrum showing peaks separated with the photon energy[4]. For low values of γ (high intensities) the tunneling time for a bound electron through the potential barrier is much smaller than the optical laser period. In this case the electron is ionised in a time less than half the laser period and its energy is determined by the Lorentz force. The photoelectron energy distribution changes into a smooth exponential like distribution[10]. The tunnel ionisation regime can only be obtained using pulses with a very fast rise time, otherwise ionisation occurs during the rising edge of the pulse at intensities which correspond to the multiphoton regime. An intensity threshold for tunnel ionisation can be defined as the intensity for which the electric field depression of the atomic potential barrier is equal to the binding energy of the electron[7]. This is approximately given by

$$I_{th} = \frac{1.4 \times 10^{14}}{Z^2}\left(\frac{U_i}{U_H}\right)^4 \quad W/cm^2 \qquad (1)$$

where Z is the residual charge seen by the photoelectron and U_H the ionisation potential for hydrogen (13.6 eV). This is also the intensity for which the rate of tunnel ionisation is of the order of 10^{13} s^{-1}. Above this threshold the rate of ionisation rises very rapidly. For a fast rising pulse ionisation occurs at approximately this threshold intensity and the average ATI energy can be estimated from figure 1. It is seen that the more tightly bound electrons are ionised at much higher intensity than the loosely bound ones and contribute the largest residual energy to the plasma.

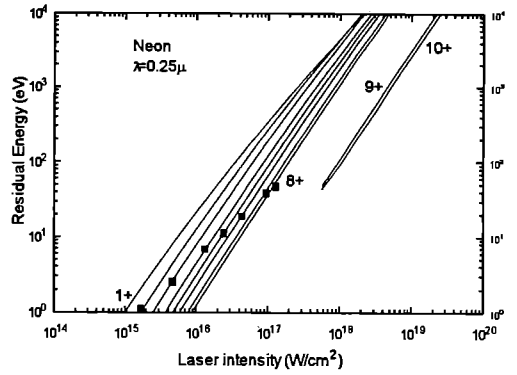

Figure 1: Average ATI energy of photoelectrons in neon as a function of laser intensity (λ=0.25μ). The squares correspond to the threshold intensity as given by equation 1.

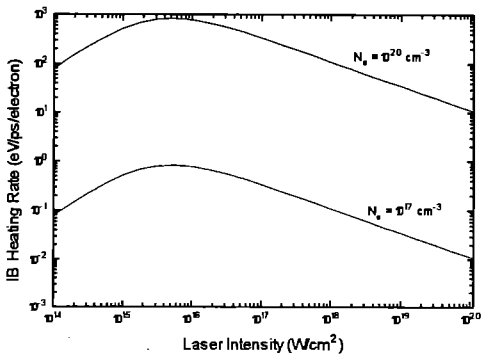

Figure 2: Heating rate of individual electron by inverse bremsstrahlung with the high field correction. The two curves are for He-like neon at 10 eV, λ=0.25μ and two densities.

HIGH FIELD CORRECTION TO INVERSE BREMSSTRAHLUNG.

One of the most important mechanism for heating plasmas with lasers is inverse bremsstrahlung. At low intensities the absorption is proportional to the product of electron ion collision frequency and the laser intensity. At high laser intensity the velocity distribution is severely modified as a result of the quiver energy. Correction to standard absorption rate are then needed[5]. To a laser intensity I corresponds an oscillating electric field with a magnitude $E = \sqrt{2I/\varepsilon_0 c}$. The maximum oscillatory velocity of a free electron in such a field is $v_{osc} = eE/m\omega$. If the thermal velocity is defined as $v_{th} = kT/m$ an approximate correction which interpolates between the low and high field limits is obtained by replacing $3v_{th}^2$ by $3v_{th}^2 + v_{osc}^2$. For low intensities the rate absorption of laser energy is proportional to I. At very high intensity it decreases as $I^{-1/2}$. There is an optimum intensity for absorption by inverse bremsstrahlung when the oscillatory velocity is of the order of the thermal velocity given by

$$I_{opt} = 1.6 \times 10^{13}\, T_{[eV]}/\lambda^2_{[\mu]} \quad W/cm^2 \qquad (2)$$

The high field correction factor used in this work is simply given by[5]

$$F=\left(1+\frac{I}{I_{opt}}\,\frac{1}{(1-\omega_p^2/\omega^2)^{1/2}}\right)^{-3/2} \qquad (3)$$

where ω_p is the plasma frequency. Figure 2 shows the corrected collisional heating rate in He-like neon at 10 eV and two densities of relevance to the experiments. The heating rate per electron is simply proportional to density. Comparing figures 1 and 2 it can be seen that ATI heating is more important for low densities but that inverse bremsstrahlung heating can dominate for high densities and long pulses.

SIMULATION OF EXPERIMENTS

The modelling is based on a hydrodynamic code coupled to a time dependent atomic model. A cylindrical target is irradiated in the axial direction. Hydrodynamic motion and heat conduction are calculated in the radial direction. Tunnel ionisation occurs on the rising edge of the pulse. ATI heating contributes to the heating during ionisation. Inverse bremsstrahlung becomes more important following ionisation as a result of increased electron density. The temperature profile is determined by a balance between heating and flux limited heat conduction in the radial direction. A typical profile is shown in figure 3 where the pulse used is a gaussian with 10μ radius. It is seen that heat conduction is effective at clamping the rise in temperature on axis where the laser intensity peaks. This typical flat temperature profile in the central region is even more pronounced for smaller beam radii as a result of more effective heat conduction. This can be better seen in figure 4 where the temperature at the cylinder axis is plotted as a function of beam radius at constant intensity. At a radius of about 3μ the temperature on axis is reduced by a factor of 2 as a result of heat conduction. At smaller beam radii, the effect is larger. The experiment measures a time and space integrated scattered spectrum which is proportional to the electron density and laser intensity. Such a measurement is heavily weighted spatially by the central region where the density and intensity are highest and temporally by the peak of the laser pulse. Figure 5 shows the temperature on the cylinder axis at the time of the peak of the laser pulse for neon at a range of static pressures. The different curves attempt to simulate the axial behaviour away from the focal point. As the intensity is decreased, the beam radius is increased so as to keep the power constant. Above an intensity of 4×10^{17} W/cm^2 no further increase in temperature is possible, this because the beam radius is small enough for heat conduction to clamp the temperature rise. The curve marked experiment profile was calculated using a measured radial profile which had a peak intensity of 10^{18} W/cm^2.

CONCLUSION

A 1D model for the simulation of short pulse high intensity gas target interactions is presented. It includes tunnel ionisation, ATI heating, inverse bremsstrahlung with high field corrections and classical flux limited heat conduction. Simulations for a 12ps pulse show that the temperature in a neon gas increases rapidly with density as a result of collisional heating. For the purpose of creating a low temperature, highly ionised plasma for XUV lasers it might me necessary to use shaped pulses in order to reduce collisional heating and small filaments which would be rapidly cooled by heat conduction. No space charge effects, ponderomotive force or parametric instability heating processes are taken into account at this stage. Future comparison with experimental results will allow us to determine the magnitude of these effects.

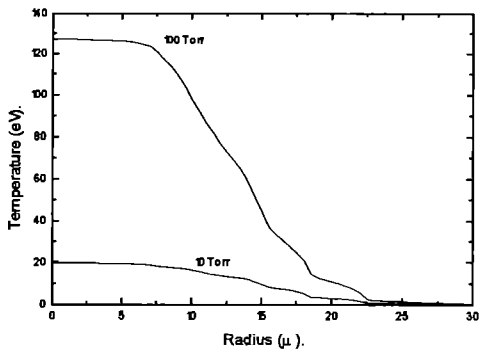

Figure 3: Radial temperature profile in Neon at peak of the 12 ps radially gaussian pulse with Δr=10μ. The intensity is 4 10^{16} W/cm^2.

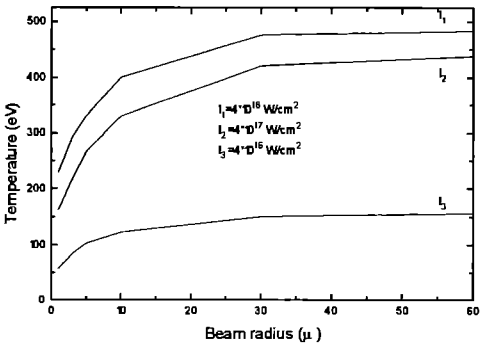

Figure 4: Effect of radial heat conduction on electron temperature at the cylinder axis in neon at 100 Torr. The intensity (KrF laser) is kept constant as the radius is reduced.

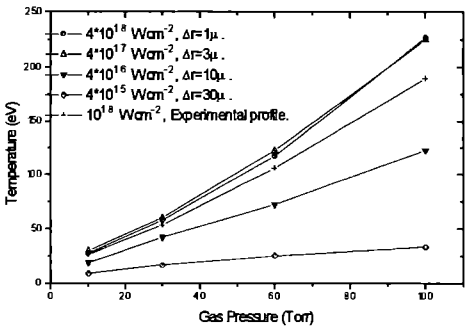

Figure 5: Electron temperature at peak of the 12ps KrF laser pulse at the axis of the cylinder under different irradiation conditions. The power is kept constant as the irradiance is varried.

REFERENCES

1. D Riley *et al*, Phys. Rev. Lett. **69**, No 26, 3739 (1992).
2. R Evans *et al*, *X-ray production measurement using pulses from the high brightness KrF pumped Raman laser system*, this report.
3. E Mevel *et al*, Phys. Rev. Lett., **70**, No 4, 406 (993).
4. K.J Schaffer *et al*, Phys. Rev. Lett, **70**, No 11, 1599 (993).
5. L Schlessinger and J Wright, Phys. Rev. A **20**, No 5, 1934 (1979).
6. C B Darrow *et al*, Phys. Rev. Lett., **69**, No 3, 442 (1992)
7. B M Penetrante and J N Bardsley, Phys. Rev. A., 43, No 6, 3100 (1991).
8. A Offenberger *et al*, *Thomson scattering measurements in optically ionised gases produced by high intensity KrF radiation*, SPIE meeting on laser sensors and applications, Los Angeles, Jan 1993, to be published by SPIE.
9. W.J. Blyth *et al*, *Thomson scattering measurements of optically ionised plasmas.* this report.
10. N. B. Delone and V. P. Krainov, J. Opt. Soc. Am. B, 8, No 6, 1207 (1991).

HIGH POWER LASER DEVELOPMENT AND OPERATIONS

M J Shaw

INTRODUCTION

This year has seen major developments in the performance of the high power lasers VULCAN and SPRITE. The highlight has been the successful implementation of the chirped pulse amplification (CPA) technique to produce a significant reduction in pulse duration and a large increase in peak power on both systems.

These developments have been brought about by Joint Development Projects between RAL, Imperial College and Southampton University on the VULCAN system and between RAL and St Andrews University on SPRITE.

On VULCAN, a peak power of 10 TW at 1.05 μm has been achieved in a pulse duration of 2.5 ps and used for target experiments for the first time. An important parameter of a CPA system is the contrast ratio between the main pulse and any long pulse background. A novel third order autocorrelator developed at Imperial College was used to show that the background level was less than 10^{-6} of the main peak.

On SPRITE, 1 TW peak power has been achieved on target at a pulse duration of 300 fs. The focal spot achieved was 3 μm, giving a focal intensity of $>10^{19}W/cm^2$. Target runs to exploit this exceedingly bright source are in preparation.

The SPRITE Raman Enhancement, which is a Joint Project with Imperial College, has demonstrated the compression of pulses in a lightguide and investigated the cause of second Stokes emission from the final Raman amplifier. Hardware for the upgrade has been designed and is due to be installed later this year.

The TITANIA programme, which is SPRITE's successor, is underway with a new 42 cm dia final amplifier being assembled for tests scheduled in November 1993. Earlier experiments on a prototype e-beam diode are reported here.

The numerous innovations in phase plate technology for the tailoring of the distribution of on-target irradiance are the highlight of Other Developments. Considerable interest is being shown from other laboratories in the techniques developed here.

The operation of both high powered lasers this year has been very smooth especially considering the major changes required for CPA operation. With SPRITE now fully scheduled, its high repetition rate capability is being exploited by users with 500+ shots per target run becoming commonplace. VULCAN continues to support the bulk of experiments and the new X-ray target chamber produced the world's first X-ray laser injector/amplifier system as a crowning achievement for this year.

VULCAN CPA JOINT DEVELOPMENT PROGRAMME

CB Edwards and CN Danson

Rutherford Appleton Laboratory

The joint development programme between RAL, Imperial College, London and the Optoelectronics Research Centre, Southampton University has successfully completed a number of important goals during the past year. These include:

- First target experiments using the new CPA chamber (see figure 1)
- ~180 CPA shots fired to target
- Reliable operation of the 2-3ps diode pumped Nd:YLF APM oscillator
- Highest power to target in excess of 8 TW
- Maximum energy to target of 39 J
- Contrast ratio measurements of the system output, on full energy shots, using a third-order cross-correlator
- Demonstration of sub picosecond pulses using Nd:LMA as the active medium

Other in-house developments associated with the CPA programme have concentrated on providing flexible operational options for the user community. These have included:

- Synchronised long pulse Q-switched oscillator with the Additive Pulse Mode-locked oscillator
- Parallel operations of an experiment in the CPA area and in an additional target area
- Synchronised CPA pulses with an 80 ps stretched high energy probe
- Design of line focus options for X-ray laser experiments using the CPA beam

Future developments on the CPA programme will concentrate on:

- Regenerative amplifier pre-amp development
- Second harmonic generation of the sub-picosecond pulse
- Synchronisation of the CPA beam with a standard actively mode-locked AML oscillator

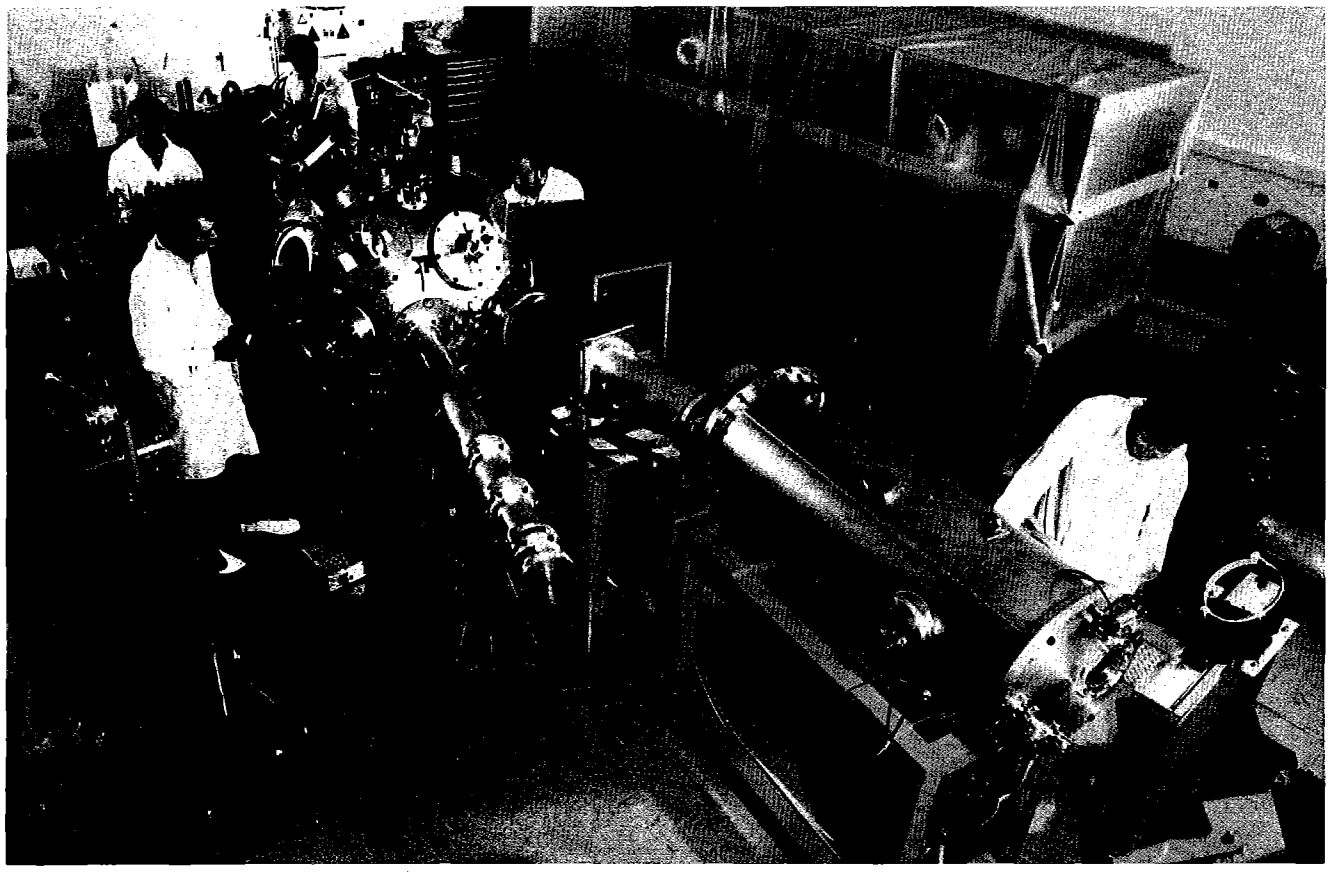

Figure 1. The CPA experimental interaction chamber showing the chamber extension for the second grating in the right foreground and the spherical target vessel

ULTRA-SHORT PULSE AMPLIFICATION EXPERIMENTS ON VULCAN

C Danson, L Barzanti, Z Chang[1], A Damerell, M Dooley, C Edwards, S Hancock, M Key, R Mahadeo, M Miller, P Norreys, C Ollman, D Pepler, D Rodkiss, I Ross, M Smith, P Taday, W Toner, K Wigmore, T Winstone, R Wyatt
Central Laser Facility, Rutherford Appleton Laboratory, Chilton, Didcot, Oxon, UK.
[1] Visiting scientist from Xian Inst. of Optics and Precision Mechanics, People's Republic of China

S Luan, M Hutchinson, I Mercer, R Smith, F Zhou
Blackett Laboratory, Imperial College, Prince Consort Road, London, UK.

INTRODUCTION

Chirped pulse amplification (CPA) is now installed on the VULCAN high power glass laser facility, giving access to single beam powers at the 10 TW level in ~2.5 ps pulse duration. CPA operations are now possible in parallel with the existing long/short pulse mode, increasing the flexibility of the system. This section describes the CPA facility development.

HIGH POWER PULSE GENERATION

An Additive Pulse Modelocked[1,2] oscillator was used to generate a bandwidth limited pulse of ~2 ps duration, which was stretched to ~ 80ps using a double passed grating pair. The gratings introduce a frequency dependent time delay, producing a pulse with a linear frequency sweep (chirp). The stretched pulse was then amplified in one beam line of the VULCAN laser. The amplified pulse was propagated to target area west and re-compressed using a single pass of a pair of large aperture (300 x 150 mm) diffraction gratings.

Propagation of ultra high intensity pulses through optical components and long air paths leads to pulse distortion due to self phase modulation. This was avoided by mounting the second grating in vacuum, and by the use of reflective focusing optics in the target chamber In this configuration, the fully compressed pulse has a direct vacuum path to target. The vacuum/air chamber window is also situated in the non-compressed region of the beam.

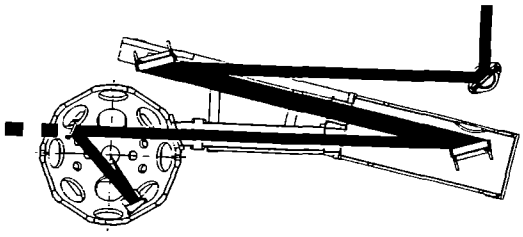

Figure 1 The CPA target interaction chamber

The beam was focused by an off-axis parabola with a clear aperture of 165 mm, a focal length of 448 mm and an off-axis distance of 110 mm. It was coated with a multi-layer dielectric to give > 99% reflectivity at 1053 nm. The residual beam passing through the 95% reflective steering mirror was used to provide the diagnostics with a sample of a pulse. An engineering drawing of the CPA chamber is shown in figure 1.

CONTRAST RATIO MEASUREMENTS

For many experiments involving short pulse irradiation it is essential to minimise prepulse to avoid pre-heating of the target. This requires high contrast between the mode-locked pulses and the interpulse background in the output of the oscillator, measured using a third-order cross-correlator. The results of these measurements are shown in figure 2. A small pre-pulse is present at the 10^{-6} level. This is believed to be due to an intra-cavity reflection from one end of the optical fibre. Improved index matching to the fibre is expected to reduce the pre-pulse level, but the 10^{-6} ratio was acceptable for the preliminary experiments reported here. The limit of the measurement of the contrast was 10^{-7}, determined by the power available from the APM oscillator.

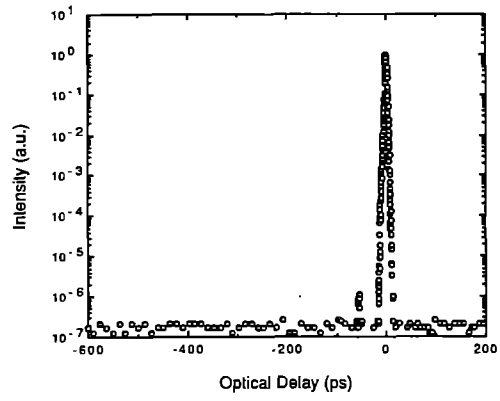

Figure 2 Contrast ratio measurements of the oscillator

The cross-correlator was also used to measure the peak to pedestal contrast ratio of the pulse at the output of the system. The contrast of the output was measured with the amplifier chain operating in different configurations; i) with the pre-amplifiers alone; ii) using only pre-amplifiers and rod amplifiers; and iii) with the full system.

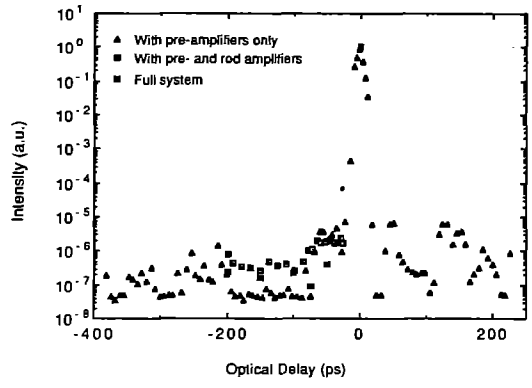

Figure 3 Contrast ratio measurements of the compressed pulse

The results of these measurements are shown in figure 3. A background contrast level of between 10^{-6} and 10^{-7} was observed with a small pre-pulse with an intensity of ~4×10^{-6} that of the peak.

B-INTEGRAL EFFECTS

It was found that as the energy in the pulse increased, above 10 J, the re-compressed pulse-width also increased. This is believed to be due to self-phase modulation (SPM) effects[4].

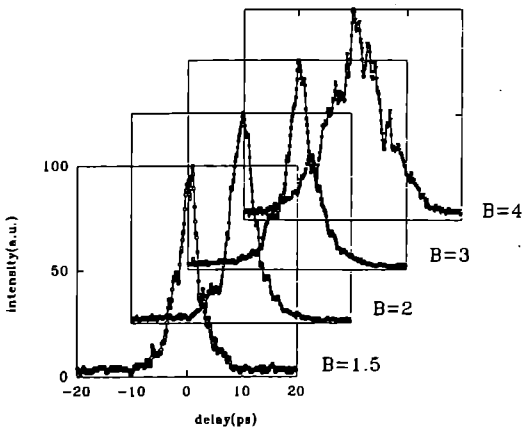

Figure 4 Pulse length variation with B-integral

Figure 4 shows the pulse length variation with the total system B-integral. Having optimised the grating separation for a particular configuration at low energies, the extra SPM at higher energies causes a further chirp on the pulse, detuning the system and giving the longer pulse-widths. However, by optimising the system to operate at the lowest B-integral during the experiment, it was possible to increase the threshold for the onset of pulse broadening to ~ 20 J. A measurement of the dependence of the time-bandwidth product on the B-integral is shown in figure 5.

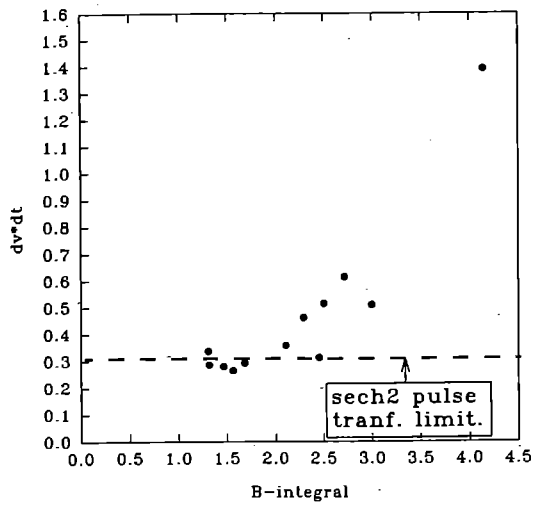

Figure 5 Time-bandwidth product as a function of B-integral

BEAM FOCUSING

An equivalent-plane monitor was used to measure the far-field intensity distribution of the re-compressed pulse. The beam was focused through a 4.3 m lens, then passed through an etalon to produce an array of foci. Figure 6 shows the beam at best focus to be between 5 and 10 times the diffraction limit.

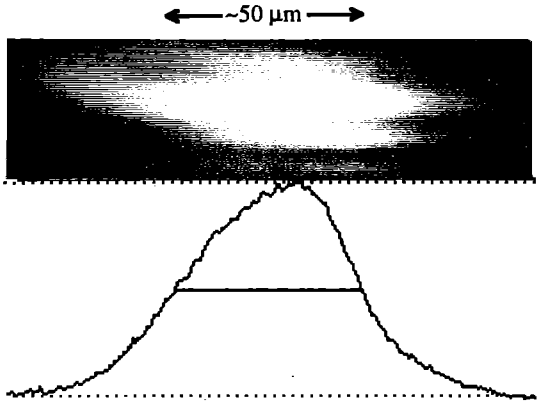

Figure 6 Equivalent plane image of the focal plane

To measure the energy contained within the focal spot a series of shots were taken, focusing the beam through a 100 µm pinhole in a 100 µm thick platinum substrate. The transmitted energy was measured with a calorimeter. The energy was varied from 6 J to 23 J to confirm that there was no significant beam degradation with increased energy. Each shot gave a pinhole transmission of 89%. If a gaussian profile is assumed, this corresponds to ~50 µm FWHM, consistent with X-ray pinhole data, and the equivalent plane monitor results.

PERFORMANCE

We have demonstrated VULCAN CPA operations, with a maximum power on target of 8 TW, generated from a ~2.4 ps pulse with an energy of 19 J. This produces focused intensities onto target of ~ 4 x 10^{17} Wcm^{-2}. A third order cross-correlator was developed for these experiments measuring contrast ratios in the compressed pulse at full output power of ~10^{-6}.

In future experiments it is planned to increase the output power from the facility by using shorter pulses (< 1 ps)[6] and increasing the energy to target to ~ 40 J.

ACKNOWLEDGEMENTS

The authors are pleased to acknowledge the valuable assistance of the Optoelectronics Research Centre at Southampton University in the construction of the oscillator.

REFERENCES

1. J M Liu and J K Chee, *Optics Letters*, Vol. 15, No. 12, pp 685-687 (1990)
2. G P A Malcolm, P F Curley and A I Ferguson, *Optics Letters*, Vol. 15, No. 22,(1990)
3. S Luan et al., in press
4. Y-H Chuang et al., "Suppression of the pedestal in a chirped-pulse amplification laser", *J Opt Soc Am B*, Vol 8, No 6, pp 1226-1235 (1991)
5. P.A. Norreys et al., to be published.
6. M W Phillips et al., "Self-starting additive-pulse mode-locking of a Nd:LMA laser", *Optics letters*, Vol 17, No20 (1992)

PERTURBATIONS IN CHIRPED PULSE AMPLIFICATION (C.P.A.) ARISING FROM THE KERR EFFECT

I.P. Mercer, M.H.R. Hutchinson
Blackett Laboratory, Imperial College, Prince Consort Road, London,UK.

INTRODUCTION

In striving to reach higher laser peak powers, the ability to produce the shortest pulses possible at high energy becomes more critical. In C.P.A. a short pulse is stretched by a grating expander, amplified and re-compressed by a grating compressor. If no perturbations exist during amplification, the compressor can be configured to impart an equal and opposite phase profile across the pulse spectrum thus reforming the original pulse precisely. Unfortunately perturbations do exist mainly in the form of bandwidth narrowing and the optical Kerr effect[1]. For the Vulcan laser system operating with a 2 ps seed pulse, the latter effect proves to be the most significant.

The optical Kerr effect (self phase modulation) occurs at high intensities where the refractive index of a medium is linearly dependant on the intensity that is incident upon it. On traversing a medium such as glass, the high intensity portion of a pulse in time and space is delayed in phase relative to the wings. The maximum relative phase delay measured in radians is generally called the 'B-integral'[1]. Such phase perturbations cause spatial self focusing, the effects of which are straight forward to remove with the use of spatial filters, at the cost of increased losses. However, it is not straight forward to remove the temporal B-integral which accumulates through the amplifier chain. This added phase profile cannot be completely compensated for by a grating compressor, resulting in imperfect pulse reconstruction.

MODELLING OF PULSE PROPAGATION IN C.P.A.

AN ANALYTIC APPROACH

An analytic model has been developed utilising a quadratic approximation for phase imparted across the pulse spectrum for expansion, the optical Kerr effect and compression[1]. For the case of a flat spatial intensity profile with the grating expander and compressor matched, it can be shown that:

$$\frac{\tau_f}{\tau_0} = \sqrt{1+B^2} \qquad (1)$$

where τ_f is the final pulse width, τ_0 is the initial pulse width and B is the B-integral acquired during amplification.

In reality: the beam does not have a flat spatial intensity profile, it is conceivable that spatial filtering will preferentially modify the high B-integral parts of the radiation in time as well as space and the grating expander and compressor are likely to be arranged for a finite value of B-integral. This can lead to the full width half maximum (F.W.H.M.) of the resultant pulse being less than that of the initial pulse and an offset to the value of B. Taking such considerations into account, this result correlates sufficiently well with experimental data[2] to conclude that self phase modulation effects are the major cause of pulse perturbation in C.P.A. on Vulcan.

In the approximation taken, it has been assumed that the temporal envelope of the compressed pulse can be fitted to a quadratic profile, thus yielding no information about higher order pulse modulation and wing formation. As a result of pulse modulation, the re-compressed pulse F.W.H.M. can deviate considerably from that given by a full analysis. In order to gain insight into higher order effects, a full computational approach is required.

A COMPUTATIONAL APPROACH

A computational model has been developed to analyse the effects of perturbations in C.P.A. to low background levels (less than 10^{-7} is of interest experimentally). The model accounts for: an arbitrary seed pulse, grating expander/compressor, phase additions to all orders, an expansion ratio greater than 10^4, self phase modulation, gain bandwidth narrowing with an arbitrary gain profile and homogeneous gain saturation. Note that the Vulcan C.P.A. system is operated well below saturation, and for a 2 ps seed pulse the bandwidth is nearly one order of magnitude less than the effective gain bandwidth. In this regime, gain saturation and bandwidth narrowing may be ignored.

If the grating expander and compressor are set to give the minimum re-compressed pulse width for zero amplifier B-integral, the model shows that the re-compressed pulse exhibits strong temporal envelope modulation[3] for B-integrals greater than approximately 2.5. This matched case is mathematically identical to the well documented observation of spectral modulation being imparted to a pulse on traversing a short length of fibre[4,5,8].

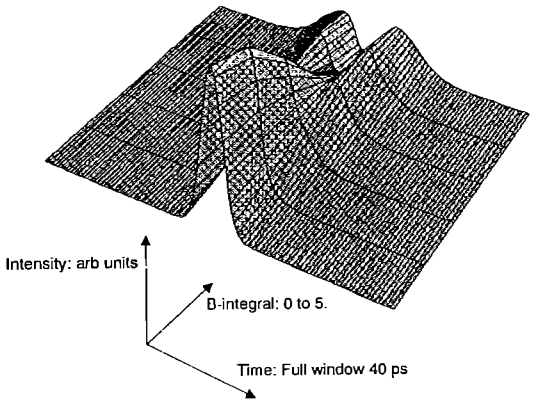

Figure 1: The output pulse in time, shown for increasing B-integral acquired within the amplifier chain for the case of matched expander and compressor

PHYSICAL EXPLANATION OF THE ENVELOPE MODULATION

For a narrow bandwidth and a large expansion ratio where the grating expander operator acting on the spectral amplitude function is taken to be[7]:

$$\exp\left(ik\beta^2\omega^2 z\right) \qquad (2)$$

the temporal intensity function of the stretched pulse is[6]:

$$I_t(t) \propto I_\omega\left(t/2k\beta^2 z\right) \qquad (3)$$

The Vulcan C.P.A. laser system conforms sufficiently well to the case described above to conclude that self phase modulation, in where k is the wave number, β is a measure of the angular dispersion of the diffraction grating[7], z is the effective separation of the gratings in the expander for a double pass configuration, I_t is the temporal intensity of the stretched pulse and I_ω is the spectral intensity distribution. Equation 3 shows that the temporal intensity profile of the stretched pulse is linearly related to the spectral intensity distribution[3].

The Vulcan C.P.A. laser system conforms sufficiently well to the case described above to conclude that self phase modulation, in adding phase proportionally to the temporal intensity of the stretched pulse will simultaneously add a phase profile across the spectrum of the pulse, proportional to the spectral intensity. The compressor system removes the phase imparted by the expander to all orders leaving for a Gaussian transform limited seed pulse, a Gaussian phase profile across the frequency spectrum.

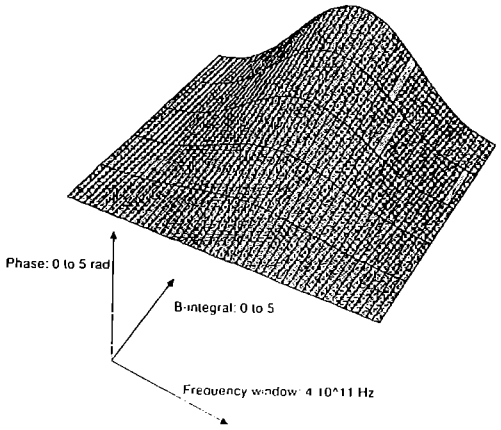

Figure 2: Phase profile in frequency space for increasing B-integral in a C.P.A. amplifier chain

If the frequency spectrum is broken down into small frequency groups, each group can be thought of as having a linear phase change with frequency. The application of standard Fourier theory shows that:

$$T_{shift} = \frac{d\phi(\omega)}{d\omega} \quad (4)$$

where T_{shift} is the position in time of a frequency group and $\phi(\omega)$ is the spectral phase profile. The same phase gradients exist at the centre of the spectrum as at the edges but there is a relative phase shift between the two. If the phase shift is 1.5 pi, interferometric addition of these regions results in a dip at the temporal re-compressed pulse centre. A series of dips in time can be formed for larger phase shifts between the centre and the wings of the spectrum i.e. larger B-integrals. Note that the form of the modulation profile that is created, is independent of the initial pulse width.

REMOVAL OF PULSE PERTURBATIONS

There are schemes that permit the removal of the accumulated phase shifts during amplification[6], but none are as effective as simply reducing the B-integral acting on the stretched pulse. The B-integral depends on the peak intensity of the stretched pulse and can be reduced while maintaining pulse energy by either further stretching the pulse or increasing the aperture for amplification.

It is possible to avoid the formation of temporal envelope modulation at the centre of the compressed pulse by slightly mismatching the effective grating separation in the expander with that in the compressor. If B-integral effects are ignored, the ideal effective separation of the gratings in the compressor is equal to that in the expander. When B-integral is included, the separation of the gratings in the compressor required to give the minimum temporal width near pulse centre, is reduced. The resultant pulse F.W.H.M. can be less than that of the original seed pulse, however shoulders are produced (see fig. 3) making this approach unsuitable where low background intensity levels are required.

CONCLUSION

Some aspects of the modifications of the recompressed pulse profiles produced by the Vulcan C.P.A. laser system have been numerically investigated. Under the appropriate conditions of narrow bandwidth and no saturation, the Kerr effect acting on the pulse throughout the amplification chain is the main source of pulse distortion. In C.P.A. the Kerr effect is effectively acting on the intensity spectrum. If the intensity is a slowly varying function of frequency (as is the case for the Vulcan C.P.A. system) the added phase will also be slowly varying and its Fourier complement is only effected around pulse centre. If the grating expander and compressor are mismatched in order to minimise the pulse F.W.H.M., shoulders are produced. However, a significant prepulse is not expected to result from the Kerr effect where the spectral profile is slowly varying.

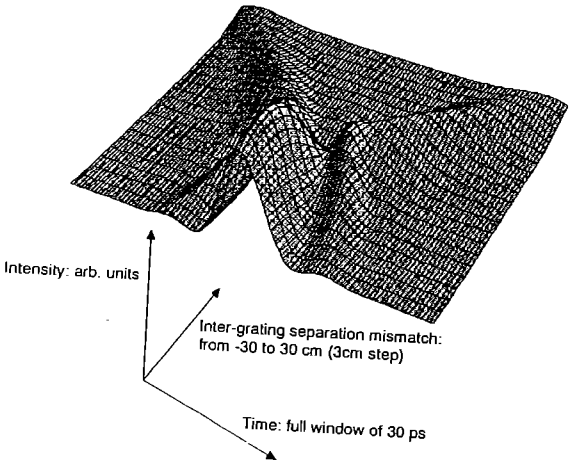

Figure 3: Simulation of the temporal output of the Vulcan C.P.A. laser system vs. inter-grating mismatch between expander and compressor for an amplifier B-integral of 5. The near side of the 3-D plots is for the compressor system arranged to have a shorter effective grating separation than the expander. Note the formation of shoulders.

REFERENCES

1.A.E.Siegman, Lasers, Oxford University Press
2. C.Danson et.al., Vulcan Laser Development Run, R.A.L. Annual report '92
3. Y.H.Chuang, L.Zhang, D.D.Meyerhofer, I.E.E.E. J.Quan.Elec. p.270 (Jan '93)
4. R.H.Stolen and Chinlon Lin, Phys. Rev. A Vol.17 no.4, p. 1448 (1978)
5. G.P.Agrawal, Nonlinear Fibre Optics, Academic Press
6. I.P.Mercer, PhD Thesis to be sub. 1993
7. O.E.Martinez, J.Opt.Soc.Am. B, Vol.3, No.7, p.929 (1986)
8. W.Toner, R.A.L., private communication

THIRD ORDER CORRELATOR FOR THE MEASUREMENT OF PULSE CONTRAST.

S Luan, M H R Hutchinson, R A Smith and F Zhou

Blackett Laboratory, Imperial College, London

INTRODUCTION

An important consideration in the development of a high intensity laser system is the temporal shape of the output pulse. In particular, it is important that there is negligible prepulse which would preionise a target and dramatically change the target conditions prior to the arrival of the high-intensity pulse. In a Chirped Pulse Amplification (CPA) system in which the pulse is stretched, amplified and compressed distortions in the phase of the stretched pulse can produce a long (ns) background pedestal which, even though its intensity is many orders of magnitude lower than that of the main pulse, may be of sufficient intensity to preionise solid and gaseous targets.

The conventional method for measuring pulse duration is (second order) autocorrelation by second harmonic generation (SHG). However they have several disadvantages. Firstly, the scattered light from the SHG crystal limits the dynamic range to ~10^5 which is insufficient for CPA lasers which can generate peak intensities >10^{17} W/cm^2. Secondly, second order correlations are symmetrical and cannot determine pulse shape. In particular, it is not possible to determine whether structure in the wings of the pulse occurs before or after the main pulse.

A system is described which has been used to measure the contrast of *single* pulses from the Vulcan laser system by measuring the third order correlation.

THIRD ORDER CORRELATION

The normalised third order correlation of a pulse I(t) is given by

$$G^3(\tau) = \frac{\int I^2(t)\, I(t-\tau)\, dt}{\int I^3(t)\, dt}$$

where τ is the relative delay between I(t) and I^2 (t). In this case, the I^2(t) pulse is generated by second harmonic generation and is correlated with the fundamental pulse I(t) by sum frequency generation $(\omega + 2\omega = 3\omega)$ in a second crystal.

The experimental layout is shown in figure 1. This correlator is of the Michelson configuration but with an additional arm. In one arm, the fundamental and second harmonic pulses are made to overlap in the mixing crystal with the delay to provide a reference. In the other arm, the delay may be continuously varied to measure the third-order correlation function G^3 . The fundamental pulse is focused into a 2mm second harmonic crystal (KTP) and the output beams are collimated. A fraction of both the fundamental and second harmonic beams are focused into a mixing crystal (BBO) with a variable optical delay at the fundamental frequency to

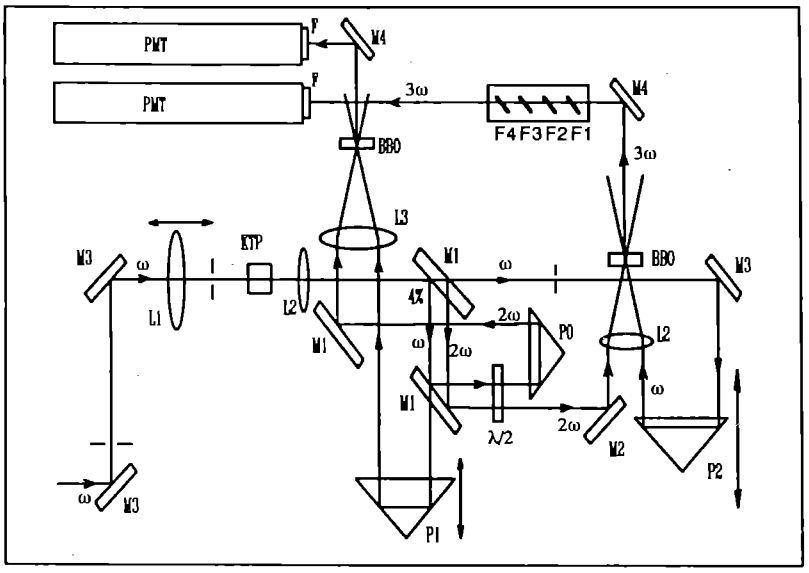

Figure 1. Optical layout of correlator

permit adjustment to $\tau=0$ as a reference. The remainder in passed to the second arm where the delay can be varied from shot to shot. The contrast is obtained from the ratio of the signals from the photomultipliers and a set of calibrated attenuators (F1-F4) are used to extend the dynamic range and consequently the range of measurement of contrast to ~ $1:10^8$. The correlation of the output pulses from the diode-pumped, mode-locked oscillator used as the source of short pulses for the Vulcan CPA system is shown in figure 2. The background was approximately 10^{-7} that of the peak intensity, except for a prepulse with a relative intensity 10^{-5} appearing 55ps before the main pulse.

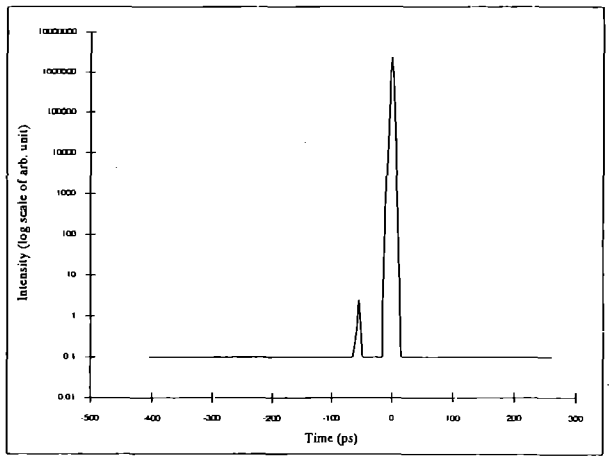

Figure 2. Correlation of oscillator output pulses

This prepulse is believed to be due to a reflection from the end of the fibre in the secondary cavity of the coupled-cavity mode-locked oscillator.

The correlation of the pulse after stretching, amplification and compression was recorded for various degrees of amplification, up to a maximum pulse energy of ~20J. Shot to shot power fluctuations were compensated by use of the reference arm of the instrument and attenuators were used to avoid saturation and damage. The results of these measurements are shown in figure 3.

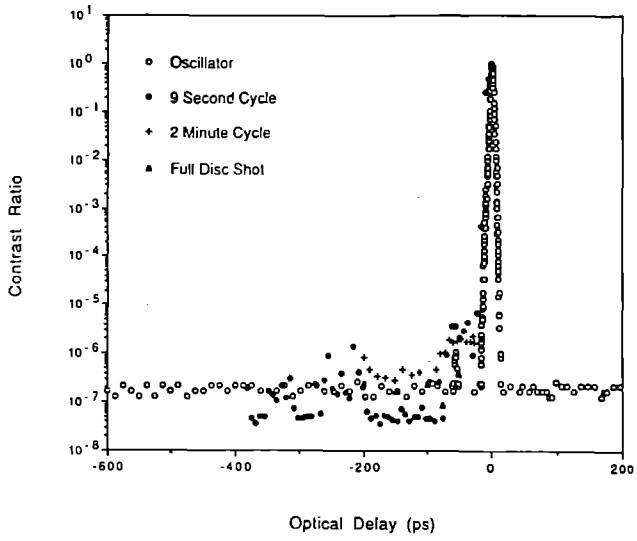

Figure 3. Measured contrast ratio of oscillator output and amplified CPA pulses.

The contrast ratio of the amplified pulses is approximately 10^6 over a wide temporal window and range of experimental conditions. These results confirm that instrument is suitable for the measurement of contrast ratios and will be used to perform routine measurements on high-intensity pulses in future CPA experiments.

SHORT PULSE OSCILLATOR DEVELOPMENT FOR VULCAN

D.W. Hughes, J.R.M. Barr, G.J. Friel, D.C. Hanna, A.A, Majdabadi and M.W. Phillips[1]
Z. Chang, C.N. Danson and C.B. Edwards[2]

[1]University of Southampton
[2]Rutherford Appleton Laboratory

INTRODUCTION

For chirped pulse amplification (CPA) experiments on the VULCAN Nd:glass laser system which require sub-picosecond pulse durations a new oscillator source is required. Currently, a laser-diode-pumped additive-pulse mode-locked (APM) Nd:YLF laser capable of generating pulses between 1 and 2 psec is being used[1]. The new source must meet a range of specifications, including the ability to be laser-diode-pumped, to match the operating wavelength (1054 nm) of the VULCAN system, and to generate pulses of energy greater than 0.5 nJ. Recent work at the Optoelectronics Research Centre at Southampton University has identified the $Nd_xLa_{1-x}MgAl_{11}O_{19}$ (LNA, or Nd:LMA) laser as an excellent candidate to meet these requirements. It has a gain bandwidth of 1.3 THz centred at 1054 nm, indicating the potential for the generation of pulses as short as 350 fsec, and offers a broad absorption peak centred at around 800 nm, making it ideal for pumping with commercially available GaAlAs laser diodes. In this report we will describe the experiments carried out on this laser. Finally, a brief mention will be made of work recently carried out on a laser-diode-pumped Nd:glass laser, which is a very interesting candidate for producing shorter pulses than those obtained from the LNA laser.

THE APM LNA LASER

Ti:SAPPHIRE LASER PUMPED OPERATION

Initial work focused on longitudinally pumping the LNA laser with a Ti:sapphire laser[2]. This was used to simulate laser-diode-pumping, since high power laser diode arrays were not available at the time. The pump laser was operated at a wavelength of 790 nm. The experimental apparatus is shown in figure 1. The active medium was a 10 mm long, 4 mm diameter plane-Brewster LNA rod (made by Crystal Technology) with x = 0.15. This (and the crystal used in the laser-diode-pumped work described later) was cut with the crystal c-axis perpendicular to the plane surface. The plane surface was coated to give high transmission at the pump wavelength and high reflectivity at 1054 nm, to act as the laser cavity rear mirror. The cavity was completed with a 15 cm radius of curvature (ROC) off-axis turning mirror and a 15% transmission output coupler.

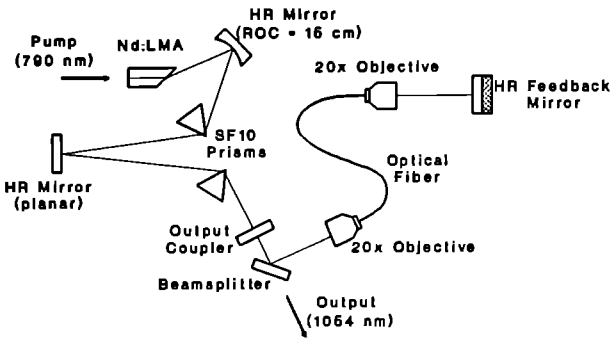

Figure 1. Schematic diagram of the experimental apparatus

A pair of Brewster-angled SF10 prisms separated by 1.4 m was inserted in the cavity to compensate for the net positive dispersion of the coupled cavity scheme. The total cavity length was 1.9 m.

It was found that particular care had to be taken to match the pump laser spot size to the LNA laser mode size. Only when the pump spot size and the laser mode size were approximately equal was it possible to obtain single transverse mode operation. This problem was found to be less critical, although by no means negligible, in the lower doped LNA rod whose use is described later, and has been attributed to thermal lensing. When a good mode overlap was ensured, output powers as high as 350 mW could be obtained for 1.8 W of incident pump power.

The external coupled cavity used is clearly shown in figure 1. A 90% reflectivity mirror was used to direct a portion of the laser output into 80 cm of single mode optical fibre. Coupling in and out of the fibre was carried out using 20x microscope objectives, with typical launch efficiencies of around 45% being obtained. The external cavity was completed using a high reflector mounted on a piezoelectric stack. Mode-locking was achieved when the relative phase mismatch between the two cavities was such that positive interference (between a self-phase-modulated pulse returning from the external cavity and a pulse circulating in the main laser cavity) occurred at the peak of the pulse, and negative interference in the wings, leading to a net pulse shortening. The relative phase mismatch between the two cavities was locked at the correct value for mode-locked operation using the scheme of Mitschke and Mollenauer[3].

Successful APM operation of the LNA laser was achieved when more than 80 mW of laser light was launched into the fibre. At maximum pump power, the useful average laser output power was 50 mW. At a repetition rate of 50 MHz, this corresponded to an energy per pulse of 1 nJ. Mode-locked pulses of duration 600 fsec were obtained from this laser, and a typical interferometric autocorrelation trace is shown in figure 2. The high fringe visibility into the wings of the trace indicates that the pulses are unchirped.

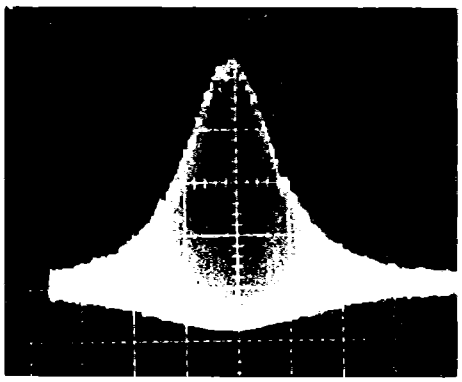

Figure 2. Typical autocorrelation trace from the APM Ti:sapphire pumped LNA laser

This laser exhibited very stable operation, with continuous mode-locking for periods of up to several hours.

LASER-DIODE-PUMPED OPERATION

Having successfully characterized the performance of the APM LNA laser using a Ti:sapphire pump source, work commenced on developing a laser-diode-pumped system[4]. The advantages of laser-diode-pumping over Ti:sapphire laser pumping are well known, and include greater reliability, compactness and reduced running costs[5]. A significant disadvantage, however, is the poor quality of the laser diode output, which means that more care is necessary to achieve a good match between the pump beam and the laser mode.

The laser diode used in these experiments was a 3 W array (SDL 2482). The output from this source was collected and collimated in the diffraction limited plane (the plane perpendicular to the junction) by a compound lens of focal length 6.5 mm. The beam was then collimated in the non-diffraction limited plane (the plane parallel to the junction) using a 15 cm focal length cylindrical lens. All the collimating and focusing optics used in this experiment were antireflection (AR) coated at the pump wavelength. The beam was next split into two before being recombined at a polarizing beam cube, in an attempt to improve the quality of the pump near the focus of the 3.2 cm focal length lens. It was found that this technique yielded a significant improvement (≈40%) in the slope efficiency which could be obtained from the laser. This improvement is shown in figure 3, where the laser performance has been plotted both with the beam split and unsplit. This data was taken using a 10% output coupler, without the prisms in the cavity. Typically, insertion of the prisms yielded a drop in output power of around 10%.

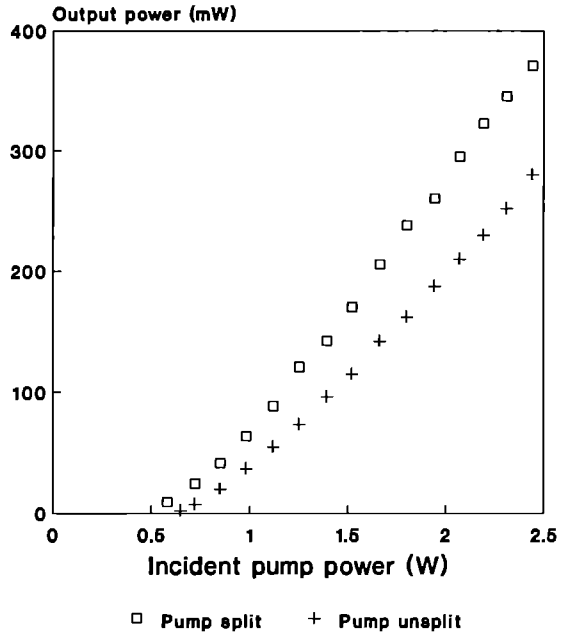

Figure 3. Comparison of the laser performance with the pump beam split and unsplit

The laser cavity was very similar in design to that shown in figure 1. The active medium was a 9 mm length, 5 mm diameter, plane-Brewster LNA rod,with x = 0.09 (supplied by LETI, Grenoble, France). A 30 cm ROC turning mirror was used, and an 85% reflectivity output coupler. Using this output coupler, the average laser output power (before the beam was split) was 300 mW.The prism pair was separated by 92 cm, and the laser cavity length was 1.4 m.

A number of beamsplitters with reflectivities between 85% and 95% were used to direct a portion of the laser output into the external cavity. GRIN lenses were used to couple light in and out of an 82 cm length of single mode optical fibre, with coupling efficiencies of between 60% and 70% being obtained. Finally, the coupled cavity was completed by a high reflector mounted on a piezoelectric stack.

When the prisms were removed from the cavity, the mode-locked pulses were between 1 and 2 psec in duration, and were strongly chirped, indicating the necessity for intracavity dispersion compensation.

Self-starting mode-locking was readily achieved for powers greater than 30 mW launched into the optical fibre. A typical interferometric autocorrelation trace obtained when a 95% reflectivity beamsplitter was used is shown in figure 4. If a hyperbolic secant pulse shape is again assumed, the pulse duration which was obtained was 420 fsec.

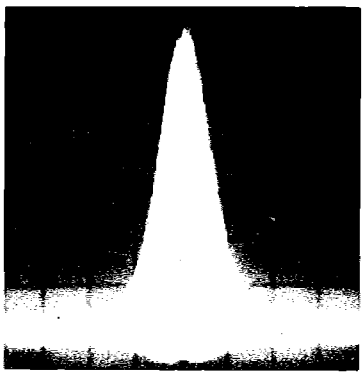

Figure 4. Typical autocorrelation trace from the APM laser-diode-pumped LNA laser

The corresponding optical spectrum had a bandwidth of 750 GHz, indicating that essentially transform-limited pulse durations were obtained. With the 95% beamsplitter, the average laser output power was 18 mW, corresponding to an energy per pulse of 0.19 nJ. The use of the lower reflectivity beamsplitters led to pulse durations in the region 500 to 600 fsec, and pulse energies as high as 0.65 nJ.

HIGH POWER OPERATION OF THE LASER-DIODE-PUMPED LNA LASER

In addition to the work described above, brief experiments have been carried out to investigate the possibility of increasing the output power (and hence the mode-locked pulse energy) by pumping the LNA laser with two 3 W laser diodes polarization coupled. The performance of this laser is shown in figure 5.

As can be seen from figure 5, greater than 1 W of output power could be obtained. However, above pump powers of approximately 3.75 W, it was observed that the laser output began to become unstable, with spontaneous 'jumps' in the transverse mode spatial profile occurring. These problems, which were attributed to thermal effects (in particular thermal lensing), were not catastrophic, and may possibly be overcome by better consideration of cavity design, improved heatsinking of the laser rod and/or use of a lower dopant crystal.

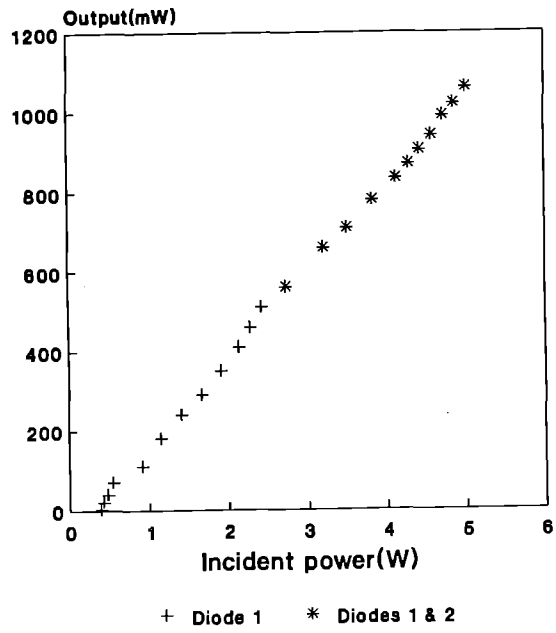

Figure 5. Performance of the LNA laser when pumped with two 3 W laser diodes

DEVELOPMENT OF A LASER-DIODE-PUMPED Nd:GLASS LASER

While the work discussed above on the LNA laser underlines its promise for the application required, its minimum pulse duration is ultimately limited by bandwidth considerations. Another potential seed system is the laser-diode-pumped Nd:glass laser which has a fluorescence linewidth of 5.3 THz (figure quoted for Schott LG760 Nd:phosphate glass), allowing the generation of pulse durations of less than 100 fsec[6]. Work is currently being carried out to develop a high power laser-diode-pumped Nd:glass laser. Previous work on the diode-laser-pumped Nd:glass laser has indicated that its ultimate performance in terms of output power is limited by thermal problems, in particular the low melting point of glass compared to crystal hosts[7]. To try to alleviate this problem, a very low dopant (2% wt.) phosphate glass is being used, which is being pumped by two broad stripe 1.2 W laser diodes. Initial experiments have yielded output powers in excess of 580 mW from this laser, which indicates that it should be a practical source of ultrashort pulses at 1054 nm, using the APM technique.

REFERENCES

1. G P A Malcolm and A I Ferguson.
Opt. Lett.16, 1967 (1991)
2. M W Phillips, Z Chang, J R M Barr, D W Hughes, C N Danson, C B Edwards and D C Hanna.
Opt. Lett.17, 1453 (1992)
3. F M Mitschke and L F Mollenauer.
IEEE J. Quantum Electron.QE-22, 2242 (1986)
4. D W Hughes, A A Majdabadi, J R M Barr and D C Hanna.
Tech Dig, Conf. On Advanced Solid State Lasers (ASSL), New Orleans, USA (1993) Paper ATuC1
5. D W Hughes and J R M Barr.
J. Phys. D.: Appl. Phys.25, 563 (1992)
6. C Spielmann F Krausz T Brabec E Wintner and A J Schmidt.
Appl. Phys. Lett.58, 2470 (1991)
7. D W Hughes, J R M Barr, M W Phillips and D C Hanna.
IEEE J. Quantum Electron.QE-28, 1010 (1992)

1-TERAWATT, 300 FEMTOSECOND PULSES by CHIRPED PULSE AMPLIFICATION IN SPRITE

I N Ross, A R Damerell, E Divall, J M Evans[1], G J Hirst, C J Hooker, J R Houliston, M H Key, Z Najmudin, P Norreys, K Osvay[2] and J M D Lister

Rutherford Appleton Laboratory
1 University of St Andrews
2 On sabbatical from JATE University, Szeged, Hungary.

INTRODUCTION

Chirped pulse amplification (CPA) is an important technique for obtaining high-energy ultra-short pulses for plasma physics experiments, because it overcomes the power limitations imposed by nonlinear optical effects on direct amplification of ultra-short pulses. The large bandwidth of KrF gives it the potential to amplify pulses shorter than 100 fs to multi-joule energies if two-photon absorption and self-phase modulation in the high-power beam can be avoided. In the report which follows we describe the first implementation of a CPA scheme on the Sprite laser system.

OSCILLATOR CONFIGURATION

The experimental arrangement for the generation, preamplification and stretching of 249 nm pulses is shown schematically in Figure 1. Transform-limited 110 fs pulses at 746 nm were generated at a repetition frequency of 82 MHz by a mode-locked Ti:sapphire laser (Spectra Physics Tsunami), pumped by a Spectra Physics 2040 CW argon ion laser (not shown in the diagram). The bandwidth of these pulses was measured at 100 cm^{-1}, corresponding to a time-bandwidth product of 0.32. The 7 nJ pulses were amplified to 20 μJ at a repetition frequency of 8 Hz in two dye amplifiers with a spatial filter between them to limit ASE. The pulses were then amplified in double pass in a Ti:sapphire rod of length 8 mm and diameter 3 mm mounted in a Bethune cell configuration in a sapphire prism. This was pumped by 8 ns pulses of 150 mJ energy from a frequency-doubled Q-switched Nd:YAG laser. The rod was index-matched to the prism using glycerol. The double-pass gain in the Ti:sapphire rod was approximately 10, giving amplified pulse energies of 200 μJ.

The amplified pulses were frequency-tripled to 249 nm in a pair of BBO (Type I) crystals. The beam size through the crystals was 3 mm. The group velocity mis-match between the fundamental (746 nm) and the second harmonic (373 nm) in the doubling crystal was compensated before the mixing crystal by delaying the residual 746 nm beam by a few picoseconds with respect to the harmonic, using a pair of closely-spaced mirrors. The measured bandwidth of the 373 nm pulses was 130 cm^{-1}. The frequency-mixing crystal was made as thin as possible (0.4 mm) to minimise group velocity dispersion (GVD) effects. After a diffraction-limited spatial filter the average 249 nm pulse energy was approximately 2 μJ and the measured bandwidth was 94 cm^{-1}.

The 249 nm beam was expanded to give a collimated beam of 12 mm diameter. Prior to stretching, the beam was amplified to approximately 20 μJ in one pass of a Lambda Physik EMG 103 discharge-pumped KrF laser, which operated in off-axis configuration [1]. The THG crystal was angle-tuned to maximise the bandwidth after the first pass of the amplifier; the largest bandwidth measured was 90 cm^{-1}, which was obtained by shifting the central wavelength of the 249 nm output about 20 cm^{-1} to the short wavelength side of the KrF ASE peak.

The stretcher was operated in a single-pass folded geometry with a 58 mm x 58 mm holographic diffraction grating having 3600 lines per mm. The grating was used in first order at near-Littrow geometry, with an angle of incidence of 29° and an angle of diffraction of 24.6°. A plano-convex fused silica lens of focal length 99 cm focused the dispersed beam from the grating onto a dielectric UV mirror, which reflected the beam back to the grating. A 2° biprism was placed 20 cm from the mirror to separate the input and output beams horizontally. The assembly of lens, mirror and biprism was mounted on a slide allowing it to be moved towards or away from the grating, in order to vary the length of the stretched pulse. The grating diffraction efficiency was 60%, giving stretched pulse energies of approximately 6μJ. The duration of the stretched pulses was calculated using the formula

$$\tau = \frac{2(F-l)(ma)^2 \lambda\Delta\lambda}{c\cos^2\theta_d} \qquad (1)$$

where F is the focal length of the stretcher lens, l is the distance between the grating and the lens, m is the grating diffraction order, a is the grating line density, $\Delta\lambda$ is the input pulse bandwidth and θ_d is the angle of diffraction of the input beam at the grating. The dimensions were chosen to give stretched pulses of around 10-14 picoseconds duration.

The unstretched pulse length was measured after single-pass amplification in the EMG 103 using a single-shot UV

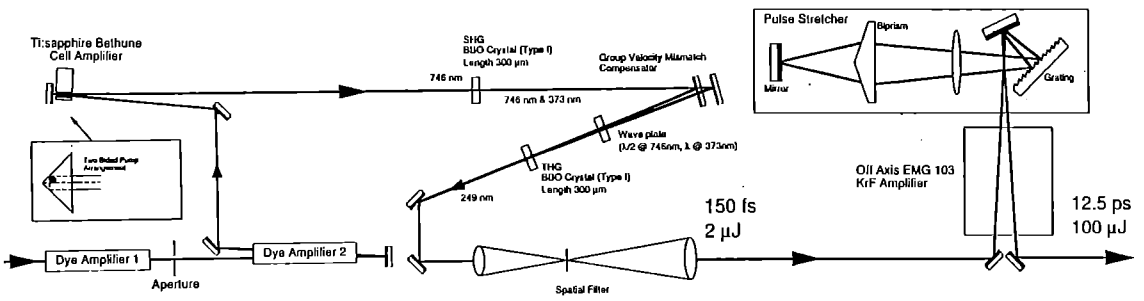

Figure 1. Schematic of the short-pulse generator and stretcher. The source oscillator and its pump laser are not shown.

autocorrelator, which is described in an Appendix. A pair of prisms was used to compensate for the temporal broadening of the pulses due to GVD. Figure 2 shows autocorrelation traces obtained both with and without GVD compensation;

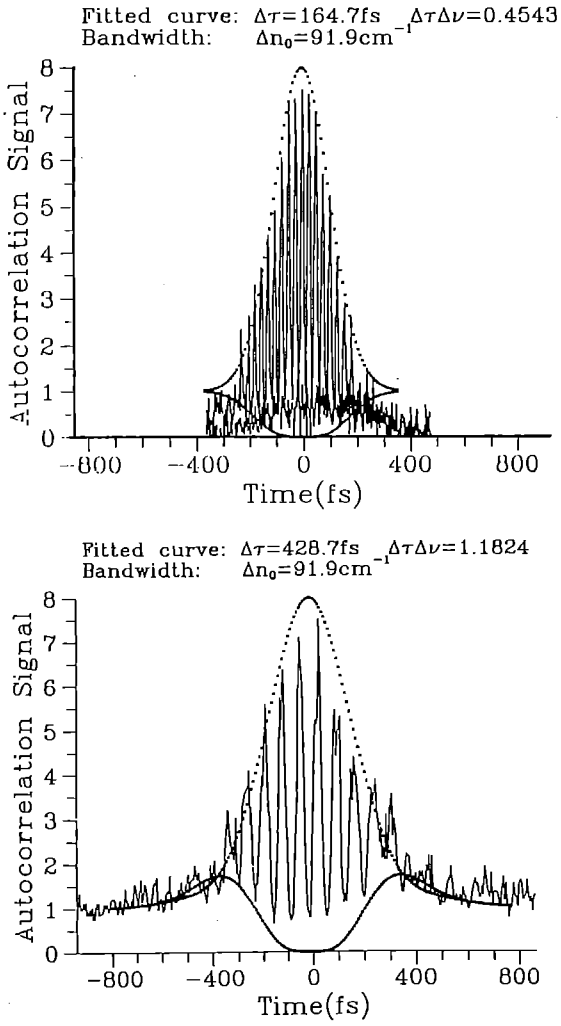

Figure 2. Autocorrelation traces and fitted pulse shapes of the unstretched 249 nm pulses. Upper trace with GVD compensation; lower trace without GVD compensation.

the uncompensated pulse length was 430 fs, while with compensation the shortest pulse length obtained was 165 fs. The data indicate that the pulse shape has changed from a $sech^2$ profile to a gaussian. The measured bandwidth of the pulses at the input to the stretcher was 92 cm^{-1}, which together with the minimum pulse duration gives a time-bandwidth product of 0.45, the expected value for a transform-limited gaussian pulse.

Following the stretcher, the pulses were amplified again in a second pass through the EMG 103, then spatially filtered through a diffraction-limited pinhole, for injection into the KrF amplifier chain, consisting of the two e-beam pumped amplifiers Goblin [2] and Sprite [3].

CONFIGURATION OF THE SPRITE SYSTEM

Various changes were made to the beam path through Sprite and Goblin prior to the start of the experiment. These were aimed at improving the optical quality of the beam, mainly by minimising B integral around the system. This was done by reducing the number of transmissive components and by reducing the laser intensity in the remaining ones as far as possible.

In Goblin, the 15 mm silica window at the laser end of the beam pipe was eliminated by joining the end of the pipe to the end plate of the Goblin cell. The Sprite beam pipe was also modified to allow it to seal onto the end of the Sprite cell. The pressure loading on the window when Sprite is fired is too great to allow operation with the beam pipe evacuated, but by filling it with helium at atmospheric pressure the air was eliminated, reducing the total B integral by approximately 0.4 .

The focusing optics were changed to increase the output beam diameter to 10 cm, the maximum size that could be accommodated on the compressor gratings. This was done by moving the lens plate 50 cm closer to Sprite, and installing a new calcium fluoride collimating lens of -7.5 metres focal length. The optical path from this output lens to the target chamber was kept as short as possible, to minimise the B integral due to the air. The other contributions to this B integral come from the calcium fluoride windows between the multiplexer and target areas and on the target chamber itself. The reflections from the first of these are used for laser diagnostics in the multiplexer room, and the window has a 1.5 degree wedge angle to separate the beams. The pulse front tilt introduced by this wedge would be unacceptably large, causing an apparent increase of 80 fs in the length of the compressed pulse. A second wedge, also of calcium fluoride, was installed so as to cancel out the tilt, at the price of an increased B integral. Assuming a stretched pulse length of 10 ps with 1.5 joules of energy, as expected, the B integral from Sprite to the target would be 1.0 .

SPRITE SYSTEM PERFORMANCE

The average energy of the stretched pulses was 40 μJ at the input to Goblin, and between 5 and 10 mJ after double-pass amplification, corresponding to an extracted fluence of 1.3 mJ cm^{-2}. The 249 nm beam was then further amplified in double pass in Sprite, giving output energies as high as 1.6 joules. This energy corresponds to an output fluence of 6 mJ cm^{-2}, which is three times the saturation fluence for KrF. Measurements of the spectrum, near-field and far-field of the amplified beam were made at this point, and the results are shown in Figures 3, 4 and 5. Figure 3a shows the oscillator

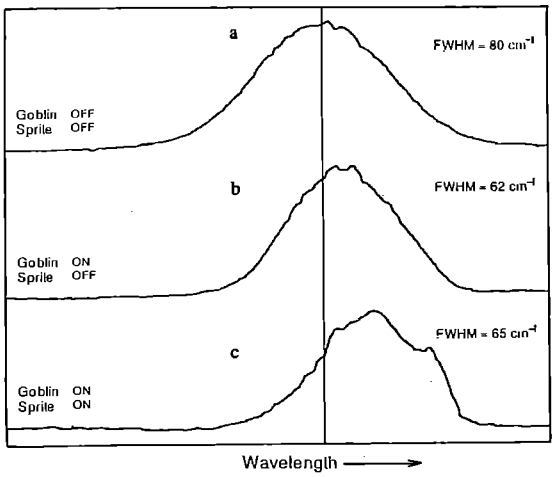

Figure 3. Spectra measured at the output of Sprite. (a) is the oscillator spectrum; (b) and (c) are amplified: see text.

spectrum measured at the output of Sprite. After double-pass amplification in Goblin, the bandwidth of the pulses decreased from 80 cm^{-1} to 62 cm^{-1} and the peak wavelength shifted by about 15 cm^{-1} to the red (Figure 3b). On amplification in Sprite to energies of less than 0.6J, the bandwidth decreased again, from 62 cm^{-1} to 55 cm^{-1}, and the peak shifted a further 5 cm^{-1} to the red. At higher energies, a slight increase in bandwidth from 62 cm^{-1} to 65 cm^{-1} was observed, together with some modulation of the spectrum (Figure 3c). These effects were attributed to self-phase modulation in either the air path or the calcium fluoride wedges.

Figure 4. Near-field distribution after amplification in Goblin and Sprite.

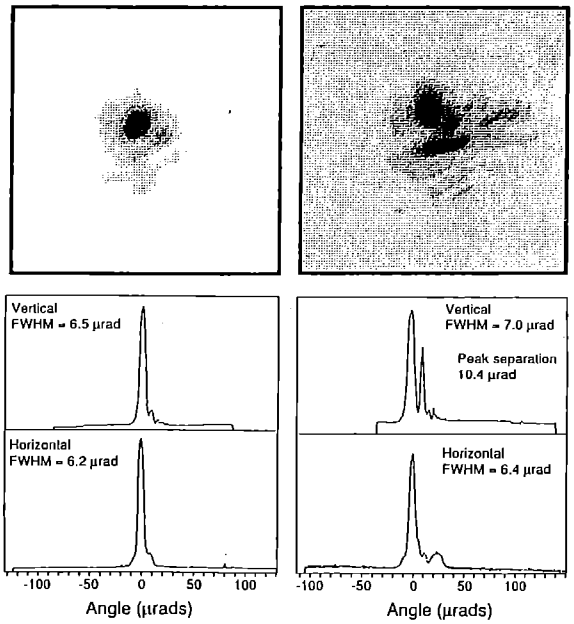

Figure 5. Far-field distributions of (a) the stretched pulse oscillator and (b) the amplified pulse at the output of Sprite.

The far-field distribution of the amplified beam was recorded at the focus of a lens combination with 19m focal length. A CCD camera and frame store were used to record images of the focal spot. The FWHM divergence of the unamplified beam (Figure 5a) was 6.5 µrad, corresponding to 2.3 times the diffraction limit. With amplification in GOBLIN and SPRITE to 1.5 J the FWHM divergence of the central spot was only marginally increased to 7 µrad (Figure 5b), but a significant fraction of the pulse energy lay outside the main peak. The near-field pattern is reasonably uniform, with no severe hot spots, although intensity variations due to the e-beam pumping distribution are visible at the edges of the beam.

PULSE RECOMPRESSION AND MEASUREMENT

The compressor gratings have 3600 lines per mm and are blazed for the first order at 249 nm. They are coated with aluminium, but have no overcoating of any kind and are correspondingly fragile. The substrates are 12 cm square, and at the working angle of 26 degrees they can accommodate a beam of 10 cm diameter. Their reflectivities in first order were measured at 257nm, and found to vary between 60% and 75%. Earlier measurements on damage thresholds of aluminium-coated gratings had suggested that the maximum fluence at which the gratings would survive for at least 100 shots was in the region of 6-7 mJ per cm^2, imposing a limit of around 0.5 joules on the energy incident on the first grating.

The gratings are placed inside the vacuum chamber in the target area, to avoid problems with non-linear effects at the high intensities of the compressed pulse. One grating is mounted in an extension tube on the target chamber, while the other is mounted in the chamber itself. For simplicity of adjustment, it was decided to keep the spacing of the compressor gratings fixed, and to adjust the stretcher spacing until the shortest pulse was obtained after the compressor. The spacing of the compressor can, however, be varied by the use of different lengths of extension tube. A major concern is the parallelism of the gratings, which must be accurate to within 100 microradians for the residual dispersion to have a negligible effect on the length of the compressed pulse. A special technique was developed to ensure that the gratings could be set parallel to this degree of accuracy. A mirror sliding on rails inside the chamber can be moved into the beam paths between the gratings in one of two positions (A and B in Figure 6). If the gratings are parallel, the beams at A and B are also parallel, so by comparing the far-field positions of the retro-reflected beams from the mirror, the gratings can be brought into parallelism.

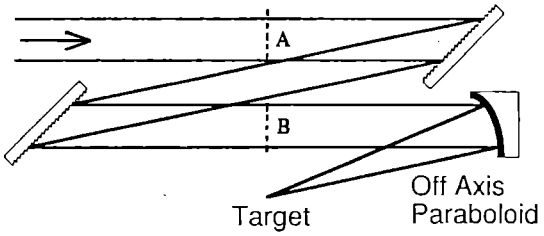

Figure 6. Layout of the grating compressor, showing the positions of the mirror used to adjust them to parallelism.

The far-field monitor set up for this purpose was also used to monitor the changes of the grating alignment when the chamber was evacuated, and to compensate for the effect by making a controlled offset in the angle of the first grating.

The length of the pulse stretcher was set by employing an effect which is usually unwanted in the Sprite system, namely two-photon absorption. A 5mm silica window was mounted close to the focus of the off-axis paraboloid in the target chamber. The transmitted oscillator beam was detected on a photodiode, and compared with a reference signal from another diode monitoring the input beam. Using an oscilloscope in XY mode, the angle of the trace gave a direct measure of the relative sizes of the signals. As the silica was moved into the focus, the change of angle corresponding to the increase in two-photon absorption could easily be seen.

The stretcher was adjusted to obtain the minimum transmission through the silica, corresponding to the shortest compressed pulse. The validity of the technique was later confirmed using the autocorrelator to measure the pulse lengths after the chamber.

An attempt was made to measure the size of the focal spot formed by the off-axis paraboloid, by imaging the fluorescence from a thin glass plate, placed at the focus, onto a CCD camera. It was found, however, that at a magnification sufficient to resolve the spot the laser fluence required for the fluorescence to be detectable caused the glass to damage after only a few shots, and the scatter from the damaged region increased the apparent spot size by a factor of two or three. An indirect measure of the spot size was obtained from far-field distributions measured in the compressed oscillator beam after the chamber. These agreed very well with previous measurements made in the output beam from Sprite (Figure 5), indicating that the beam divergence in the amplified beam would be around 8 microradians. Since the paraboloid is known to be capable of near diffraction-limited performance, this implies that the spot size in the focus would be close to 3 microns FWHM.

The energy of 1.5 joules obtained from Sprite was too large for the gratings, so one of the turning mirrors was replaced with a 50% reflector during subsequent measurements. Difficulties were encountered in measuring the spectrum and autocorrelation of the recompressed pulses, because of self-phase modulation occurring in the air, especially at the spectrometer slit, when the beam was telescoped down. Eventually, by attenuating the beam sufficiently before the diagnostics, a set of measurements was obtained free from distorting effects. The shortest pulse length measured was 260 fs, although 280 to 300 fs was more frequent. A typical autocorrelation trace is shown in Figure 7, and it can be seen

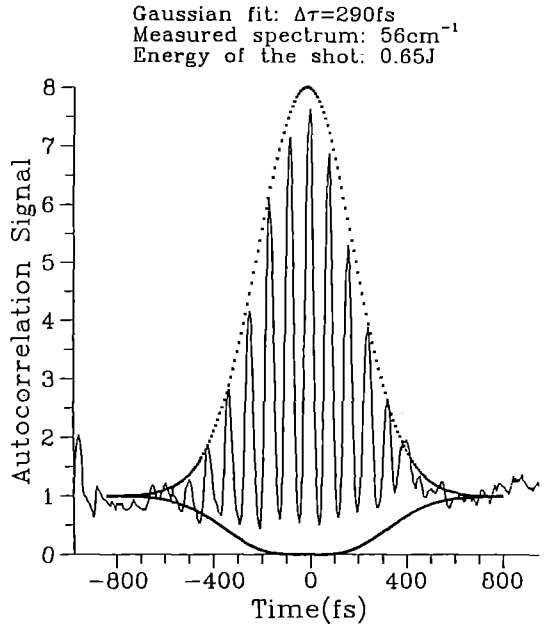

Figure 7. Autocorrelation trace of recompressed pulse measured in the Sprite target area.

that the pulse is essentially chirp-free, indicating that the compression is complete. The recompressed pulse bandwidth was 56 cm^{-1} giving a time-bandwidth product of 0.45, which is still close to the transform limit. However, the reduction in bandwidth caused by the gain narrowing in the main amplifiers has stretched the pulse to the duration measured.

The net transmission of the grating-pair was measured as 45%, which, combined with the energy limit of 0.5 joules on the grating to avoid damage, restricted the compressed pulse energy to 250 mJ. At a pulse duration of 300 fs and a spot size of 3 microns, this gives an intensity in excess of 10^{19} W cm^{-2}. A few shots were fired with energies of 0.6 to 0.7 joules without apparent damage to the gratings. The ASE energy accompanying the amplified recompressed pulse was determined by blocking the input to Goblin, and was typically 1.5% of the total recompressed energy. The ASE pulse duration was not measured, but is believed to be around 50 ns.

CONCLUSIONS

The results of this first CPA experiment may be summarised as follows. Energies of 300 mJ have been delivered to target, in pulses of 260 to 300 fs FWHM in a beam of 8 microradian divergence. These figures are limited by, respectively, the damage threshold of the compressor gratings, the bandwidth of the amplified pulses and the B integral in the optical path. A preliminary experiment has been performed with the compressed pulses, in which more than 50 shots were fired into low-pressure helium in the target chamber, and streaked spectra of scattered light were obtained.

FUTURE DEVELOPMEMT

There are several ways in which the performance of the system could be enhanced. The possibility of overcoating the gratings with a 90% reflecting dielectric coating is under investigation. This would reduce the amount of energy reaching the aluminium layer, thus overcoming the energy limit at present imposed by the grating damage threshold. In addition, the transmission of the grating pair would be enhanced by overcoating. The B integral in the optical path could be reduced further, by changing the diagnostic arrangements, piping the beam in helium to the target chamber, and by stretching the pulse to 20 or 25 ps. The limit on compressed pulse length imposed by gain narrowing might be overcome by simply increasing the bandwidth from the oscillator, or by shaping the spectrum at the pulse stretcher to enhance the wings relative to the centre. Ultimately, it might be possible to deliver 1.5 joules to target in a pulse of 150 fs in a near diffraction-limited beam.

REFERENCES

1. S Szatmári et al, Appl. Phys B 53, 82, (1991)

2. F Kannari, M J Shaw and F O'Neill, J. Appl. Phys. 61, 476 (1987)

3. C B Edwards et al, in Excimer Lasers1983, AIP Conf. Proceedings No. 100, p59 (Eds Rhodes, Egger & Pummer).

APPENDIX 1.

SINGLE SHOT PHASE-SENSITIVE AUTOCORRELATOR

Figure 1 shows the single shot phase sensitive second order autocorrelator used for the pulse length measurements. This device is based on a design by Szabó [1], and is essentially a Michelson interferometer with a wedge in one of the arms, which introduces a spatially-varying time delay into one of the recombined beams by tilting the pulse front. The phase

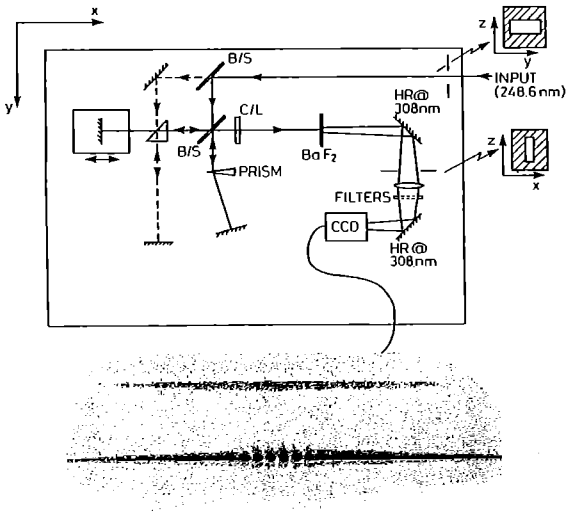

Figure 1. The optical layout of the single-shot phase-sensitive autocorrelator. Sample autocorrelation and reference traces are shown below the schematic.

information, which is necessary for evaluating pulse chirp when CPA techniques are used, is obtained from interference fringes formed when one of the mirrors is tilted to make the beams in the two arms of the interferometer non-parallel. The recombined beam is then focused by a cylindrical lens onto a barium fluoride crystal, which exhibits two-photon-excited exciton fluorescence peaked at around 310nm. The variation of fluorescence intensity with signal was checked experimentally to verify the second-order nature of the process between 280-480nm. Thus, the autocorrelation function in time is transformed into a spatial variation of fluorescence intensity along the line focus in the crystal. The fluorescence is imaged onto a CCD camera and recorded by a frame store. A typical video signal is shown in negative form in Figure 1 below the schematic. By analysing the optical density (or video grey level) distribution in the fringes the autocorrelation function can be obtained.

The main difficulty with this technique is that it requires a beam which is spatially homogeneous. To overcome this problem a reference arm has been built: a portion of the input beam is split off just before the Michelson interferometer, and imaged by the cylindrical lens just above the autocorrelation trace. This is shown by the dashed line in Figure 1. Ensuring the correct horizontal position of the reference trace, one obtains a very accurate picture of the intensity distribution of the input beam, which can be used to normalise the autocorrelation signal.

Another important consideration when measuring very short pulses is the phase front distortion introduced by the cylindrical focusing lens. This effect was noted by Bor [2], and is due to the non-achromatism of the lens. It can be corrected either by using an achromat, or, as in the present device, by restricting the aperture of the lens so that the effect is small by comparison with the pulse length. The input aperture shown in the diagram is designed to do this.

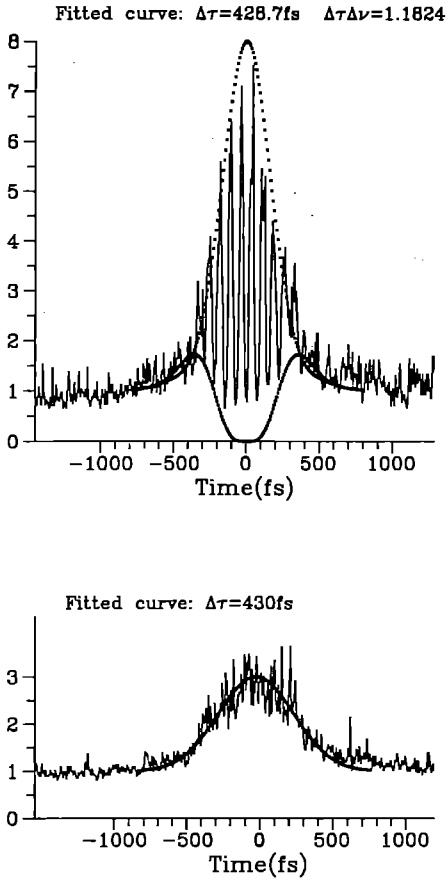

Figure 2. Example autocorrelation traces of a chirped pulse. The upper, interferometric, trace shows the presence of chirp, while the intensity autocorrelation below does not.

The measured and the fitted gaussian phase sensitive autocorrelations of a chirped pulse can be seen in Figure 2 (top). The fringes provide chirp information which would otherwise have been lost. The corresponding intensity autocorrelation is shown in Figure 2 at bottom. This latter can be obtained by further rotating one of the mirrors of the interferometer until the fringes can no longer be resolved by the imaging optics. In this position the fringes are averaged, so that the ordinary intensity autocorrelation trace is obtained.

REFERENCE

1. G Szabó, Z Bor and A Müller, Optics Lett. 13, 746 (1988)

2. Z Bor, J. Modern Optics 35, 1907-1918, (1988)

SATURATED AMPLIFICATION IN CPAC LASERS

J R Houliston, M H Key and I N Ross

Rutherford Appleton Laboratory, Chilton, Didcot, Oxon, OX11 0QX, UK.

In chirped pulse amplification and compression (CPAC) it is important to assess the extent to which saturated amplification of the stretched pulse, as required for efficient energy extraction from the amplifier, leads to temporal distortion of the recompressed pulse. We present a model of CPAC which includes saturated amplification of the stretched pulse and spectral narrowing due to the gain profile of the amplifier.

THEORETICAL MODEL

A physical picture of pulse stretching is that the delay in the stretcher, $\tau_s(\omega)$, is a function of frequency. As a result there is a change in the relative phases of the spectral Fourier components of the input pulse (which have temporally constant amplitudes) which redistributes energy in time producing a stretched pulse. Time varying saturated amplification of the stretched pulse can be treated as introducing a temporally varying amplitude of the Fourier components such that each amplitude becomes modulated in time by the square root of the time-dependent intensity gain. In the compressor the Fourier components are recombined with frequency-dependent time delay and therefore with relative changes in both phase and amplitude consistent with the conjugate nature of the stretcher and compressor. The phase of each spectral component in the perfectly recompressed pulse at time t relative to the central position in time of the recompressed pulse (t=0) is identical to the phase of the same spectral component in the input pulse at the same relative time.

The electric field amplitude of the recompressed pulse at any time t, $E_r(t)$, is expressed as a Fourier summation over frequency (equation 1) where $E_r(\omega,t)$ is the spectral amplitude at frequency ω at time t

$$E_r(t) = \int E_r(\omega,t) e^{i\omega t} d\omega \qquad (1)$$

$E_r(\omega,t)$, in equation 1, is the product of the time-independent spectral amplitude of the input pulse at frequency ω and the square root of the intensity gain at time $t + \tau_s^1(\omega_0)(\omega-\omega_0)$, $\sqrt{G(t+\tau_s^1(\omega_0)(\omega-\omega_0))}$, experienced by the stretched pulse under amplification where t is relative to the central position in time of the unamplified stretched pulse and $\tau_s^1 = \frac{\partial \tau_s}{\partial \omega}$. Moreover, $\sqrt{G(t+\tau_s^1(\omega_0)(\omega-\omega_0))}$ is equal to the amplitude gain experienced by the spectral component at frequency ω present in the recompressed pulse at time t. For a transform-limited gaussian input pulse of FWHM duration τ, the spectral amplitude at frequency ω is given by $e^{\frac{-(\omega-\omega_0)^2}{4a}}$ where $\tau = \sqrt{\frac{2\ln 2}{a}}$ and we write

$$E_r(\omega,t) = e^{\frac{-(\omega-\omega_0)^2}{4a}} \sqrt{G(t+\tau_s^1(\omega_0)(\omega-\omega_0)} \qquad (2)$$

In order to determine the recompressed pulse temporal profile we evaluate the intensity gain, $G(t)$, experienced by the stretched pulse under amplification as a function of time using a rate equation model[1] which includes the amplifier gain profile and then use equations 1 and 2.

NUMERICAL RESULTS

We assume an input 100 fs FWHM transform-limited Gaussian pulse at 249 nm which is stretched to 2.77 ps FWHM and amplified prior to recompression. Recompressed temporal profiles are computed for stretched pulse amplification at different levels of output energy density, F_{out}, in an amplifier with small signal gain equal to 5500, saturation fluence, F_{sat}, equal to 2 mJ/cm^2 and with 4 nm FWHM bandwidth Gaussian gain profile centred at 249 nm which is an approximation of KrF amplifier characteristics.

In Figure 1 we show recompressed pulse temporal profiles for different levels of amplifier saturation where the peak intensity of each curve is normalised to the peak intensity $(1.1x10^{11} W/cm^2)$ of the recompressed pulse under highest amplification, $\frac{F_{out}}{F_{sat}} = 5.55$. Saturated amplification of the stretched pulse leads to smooth temporal broadening of the recompressed pulse at low intensity levels without any intensity pedestal.

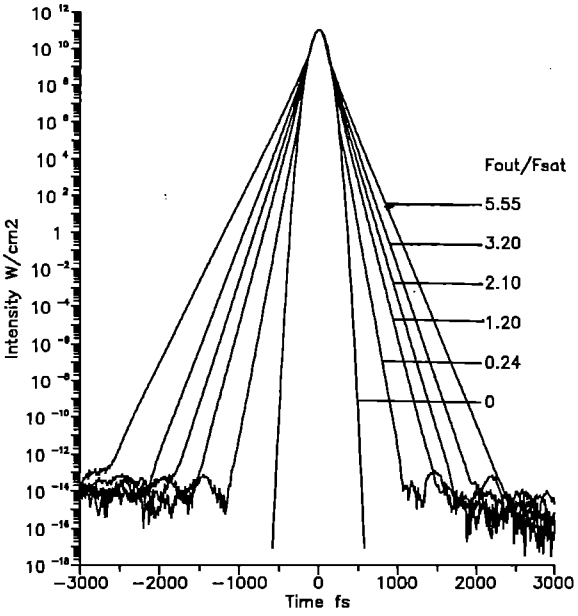

Figure 1 Normalised recompressed pulse temporal profiles for different levels of amplifier (frequency-dependent) saturation $(F_{sat} = 2mJ/cm^2)$.

In Figure 2 we show the normalised recompressed pulse temporal profiles near the peak intensity and we can see that increasing saturation of the stretched pulse leads to slight temporal narrowing at the peak of the recompressed pulse which results from the temporal and hence spectral broadening under saturated amplification of the stretched (chirped) pulse. However, spectral narrowing resulting from the Gaussian amplifier gain profile gives pulses temporally slightly broader than the 100 fs FWHM input pulse.

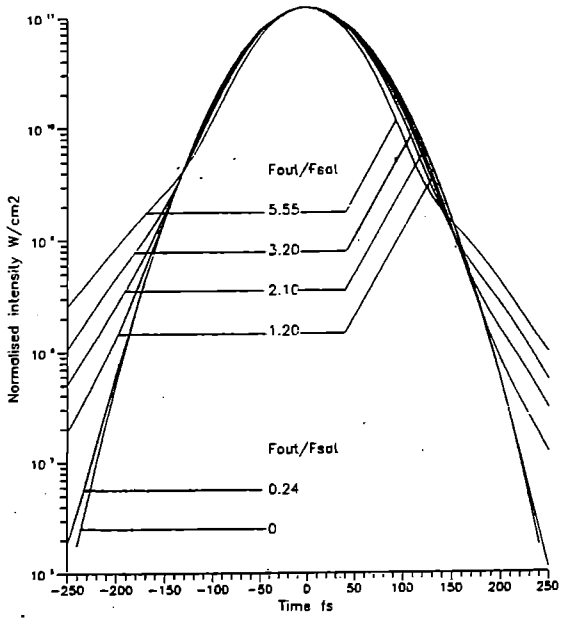

Figure 2 Normalised recompressed pulse temporal profiles near peak intensity (See Graph 1).

The temporal distortion of the recompressed pulse due to saturated amplification of the stretched pulse is independent of the stretch factor for stretch factors > 10 near the peak of the recompressed pulse with some weak dependence in the wings. Thus our result for the changes in recompressed pulse shape are almost generally true for any CPAC system where the stretch ratio is large and the gain saturation is expressed as $\frac{F_{out}}{F_{sat}}$.

The principal conclusion from the modelling is that saturated amplification (in comparison to unsaturated amplification) of the stretched pulse in a CPAC system leads to broadening of the recompressed pulse at low intensity levels without the formation of a distinct intensity pedestal. At the peak of the recompressed pulse saturated amplification leads to temporal narrowing. This conclusion is particularly relevant for the implementation of the CPAC technique for subpicosecond operation of large aperture KrF lasers such as SPRITE[2] where amplifier saturation is required in order to reach high powers in the recompressed pulse.

References

1. H Y Chuan et al, 'Propagation of Light Pulses in a Chirped Pulse Amplification Laser', IEEE Journal of Quantum Electronics, Vol 29, No 1, p270, 1 Jan 1993.

2. I N Ross et al, ibid.

MEASUREMENT OF ULTRAVIOLET LASER DAMAGE THRESHOLDS WITH PICOSECOND AND SUBPICOSECOND PULSES

C J Hooker, J M D Lister and K Osvay*
Rutherford Appleton Laboratory

D T Sheerin and D C Emmony,
Department of Physics, Loughborough University of Technology

R L J Cowell,
Technical Optics Ltd

*Permanent address: Department of Optics and Quantum Electronics, Jozsef A. University, H-6720 Szeged, Hungary.

Over the past year, a programme of UV coating development has been carried out in collaboration with Technical Optics Ltd and Loughborough University. This was motivated by the perceived need for higher-quality optics for the Titania system, and also by the observation of laser damage to mirrors at the output of Sprite. Recent reports [1] of rare-earth fluoride/cryolite multilayers having significantly higher UV damage thresholds than standard multilayers prompted us to try fabricating and characterising similar coatings. Damage tests using 25 nanosecond pulses and scatter measurements made at Loughborough were described in last year's Annual Report [2]. In recent months we have made laser damage measurements at pulse lengths of 10, 1, 0.6 and 0.45 picoseconds, which have verified the higher damage resistance of the new coatings and provided data on the scaling of damage threshold with pulse length in a regime not previously studied.

The results presented in [1] suggest that the best high-index materials are gadolinium fluoride and lanthanum fluoride. Because of difficulties experienced with depositing good films of lanthanum fluoride, we concentrated on gadolinium fluoride and dysprosium fluoride, in combination with cryolite and aluminium fluoride as the low-index materials. Material combinations for which damage test data are presented here are as follows (the sample designations E, F, etc are arbitrary):

E, K	Gadolinium fluoride/cryolite
F	Dysprosium fluoride/Aluminium fluoride
M	Gadolinium fluoride/Aluminium fluoride
N	Dysprosium fluoride/cryolite
Q, V	Hafnium oxide/silica.

The hafnium oxide/silica combination is now used by most commercial manufacturers of UV dielectric mirrors, and samples were obtained from two different suppliers for comparison with the fluoride multilayers. The fluoride multilayers were conventional quarter-wave stacks designed for high reflectivity at wavelengths between 248 and 260 nm at normal incidence, and were deposited on silica substrates by electron-beam evaporation.

These samples were damage-tested at three different laboratories, using closely similar procedures. The measurements at 25 ns were made at Loughborough University of Technology, those at 10 ps, 1 ps and 450 fs at the Rutherford Appleton Laboratory and those at 600 fs at the Max-Planck Institut für Biophysikalische Chemie in Göttingen, Germany. The samples were exposed to the damaging laser beam at or near the focus of a lens, and viewed by dark-field schlieren imaging to detect the onset of damage, as illustrated in Figure 1. The dark-field image of the sample surface is very sensitive to the increase in scatter from sites where damage has occurred, and indeed our criterion for damage was the first observation of a permanent (and usually increasing) level of scatter from a previously non-scattering site. The measurements at 20 ns, 10 ps, 1 ps and 600 fs were made using this technique, while for the 450 fs measurements the illuminated surface was viewed by eye against a dark background. Undamaged sites were exposed to pulses from the laser, at repetition rates between 1 and 4 Hz, until either damage occurred at the site or more than 100 shots had been delivered without evidence of damage. This procedure was repeated for a range of laser fluences around the damage threshold. At each pulse length and fluence the number of shots required to cause damage was recorded for up to 5 different sites on the sample. These data allowed us to determine both the 100% damage fluence, i.e. that fluence which will invariably damage the sample in a single shot, and the maximum fluence at which the sample will survive undamaged for a large number of shots.

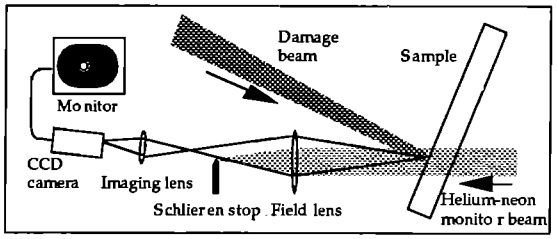

Figure 1. Arrangement used for the damage tests.

The average fluence incident on the sample was recorded for each set of measurements. However, diffraction effects and non-uniformities in the beams produced significant intensity variations at or near the focus, with peak intensities several times greater than the average. To account for these effects, beam profiles were recorded at the sample plane using CCD cameras with video or frame storage. The integrated grey level over the spot area in the stored image was assumed proportional to the average fluence, and the value of the highest grey level then yielded the peak fluence, which was typically from 1.6 to 2.8 times the average. This technique was used for all except the 450 fs data, which were corrected using the peak-to-average ratios measured for corresponding spot diameters with 10 ps pulses; the focusing lens and the beam diameter were the same, and the B-integral for the 450 fs pulses was estimated to be 2.5, so self-focusing effects would not cause much degradation of the beam profile.

Uncertainties in the damage fluences are associated mainly with fluctuations in laser energy, which were typically ±15% for the picosecond and subpicosecond pulses, and ±10% for the 25 ns pulses. Each peak-to-average ratio was measured

from several recorded spot profiles, and the values found were consistent to ±5%. Uncertainties in the damage fluence at 450 fs are estimated at ±30%, because the peak fluence values were less reliable and also because the sample viewing technique used was probably less sensitive to the onset of damage. Uncertainties in pulse length are relatively small: all the lasers used are well-characterised, and their pulse lengths are believed accurate to within 10% of the quoted values.

The results obtained for the multilayers listed are presented in Table 1 and Figure 2 below.

Sample	Pulse length				
	450 fs	600 fs	1 ps	10 ps	25 ns
GdF_3/cryolite (E)	1.0	0.70	0.95	3.5	13.5
GdF_3/cryolite (K)	-	1.03	0.95	2.5	10.5
GdF_3/AlF_3	-	1.18	0.95	2.2	10.5
DyF_3/cryolite	-	0.92	0.95	2.5	10.5
DyF_3/AlF_3	-	-	-	-	11.0
HfO_2/SiO_2 (Q)	0.3	0.29	0.56	1.3	6.0
HfO_2/SiO_2 (V)	-	-	0.56	1.1	3.2

Table 1. Fluences in Joules cm^{-2} giving 100% probability of damage in a single shot.

It is clear that all the fluoride samples have greater resistance to damage than the hafnia/silica comparison samples. For the long-term survival fluences plotted in Figure 2, this difference is a factor of between 2.5 and 3, and is maintained over the range of pulse lengths investigated. This implies that if the damage thresholds of two coatings are compared using 25 ns pulses, they will have the same relative resistance to damage at, say, 10 ps. There is little difference between the various material combinations in the fluoride coatings, though sample E consistently had the highest damage resistance of those tested. This may reflect the difference in the type of pumping used in the coating plants. The vacuum chamber used for sample E was cryopumped, while the other samples were deposited in a chamber pumped by a conventional oil diffusion-pump, and may be contaminated with traces of oil.

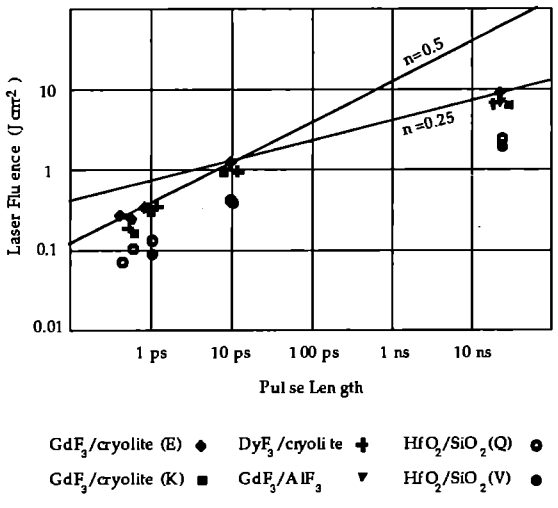

Figure 2. A plot showing the laser fluences at which the samples survived many shots without damage, as a function of pulse length. Some of the plotted symbols have been shifted laterally to avoid overlap. Solid lines are drawn for two values of the scaling exponent n in Equation 1.

The variation of damage threshold with pulse length typically follows a scaling law of the form

$$\text{LDT} \propto (\text{pulse length})^n, \qquad (1)$$

where other workers [3] have obtained exponents in the range 0.25 to 0.4 in the nanosecond pulse regime, consistent with the present results. The change between pulse lengths of 25 ns and 10 ps corresponds to an exponent n = 0.25 in equation (1), while for shorter pulses an exponent of 0.5 fits the data fairly well. For some of the fluoride samples the exponent appears to increase again at shorter pulse lengths, becoming closer to 1 between 1 ps and 600 fs. This may arise from nonlinear effects in the coating leading to increased absorption. We intend if possible to measure the LDTs of these samples with 100 fs pulses to see whether this trend continues.

We conclude that while the fluoride multilayers have significantly higher damage resistance than conventional oxide-based multilayers, the scaling of damage threshold with pulse length is very similar, and consistent with scaling laws obtained for longer pulses and other UV wavelengths. We are confident that damage measurements made at 25 ns can now be used to predict the performance of mirror coatings in the picosecond regime. These results will prove useful in the design of the multiplexing optics for the Titania system, and in the further development of chirped-pulse amplification schemes for Sprite.

The authors are grateful to Ian Edmond and Gary Fletcher of Technical Optics Ltd for their work on the design and deposition of the fluoride coatings, and to Dr Klaus Mann at the Max Planck Institut für Biophysikalische Chemie in Göttingen for his assistance with the 600 femtosecond measurements.

REFERENCES

1. T Izawa et al, Proceedings of the 22nd Conference on Laser Induced Damage in Optical Materials, Boulder, Colorado, SPIE Vol 1441, p 339, (1990)

2. D T Sheerin and D C Emmony, Central Laser Facility Annual Report 1992, pp 130-131

3. K Mann, H Gerhardt, G Pfeifer and R Wolf, Proceedings of the 23rd Conference on Laser Induced Damage in Optical Materials, Boulder, Colorado, SPIE Vol 1624, p 436, (1991)

DEMONSTRATION OF RAMAN PULSE COMPRESSION

C J Hooker, G J Hirst, M H Key, K Osvay, J M D Lister and M J Shaw
Rutherford Appleton Laboratory

G H C New, K E Hill and D C Wilson
Imperial College, London

INTRODUCTION

The possibility of using Raman amplification in lightguides as a means of pulse compression was first put forward in 1988 [1]. A considerable amount of computer modelling was done to confirm the basic principle involved, and to predict the performance of an amplifier used in this way [1, 2], but the technique was never tried experimentally. We report here the first experiments on Raman pulse compression carried out with the Sprite Raman system.

The idea of Raman pulse compression is shown schematically in Figure 1. Compression occurs because the energy of a number of relatively long KrF pump pulses is extracted by a short Stokes pulse, thus leading to a greater increase in power than would occur if the pump pulses were simply combined together. The velocities of the pump and the Stokes along the guide are different because the pump beams are inclined to the axis at an angle of a few degrees, so the Stokes gradually overtakes the pump and thus gains access to all the pump energy.

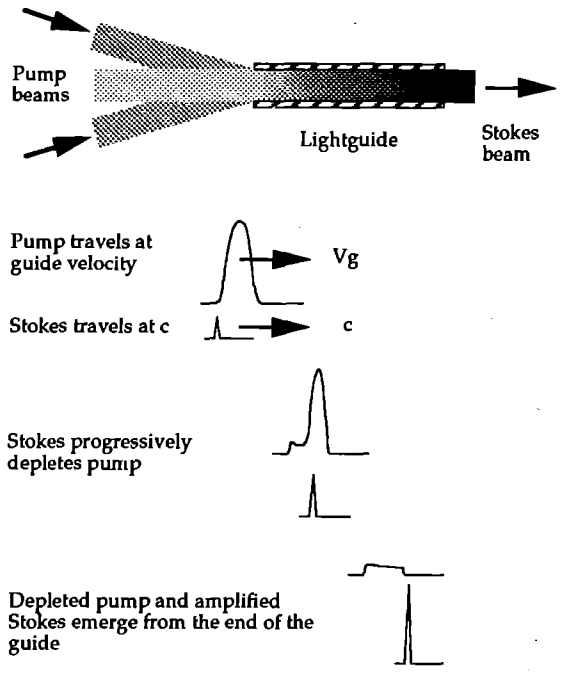

Figure 1. Schematic of Raman pulse compression.

THEORY

Computer modelling of Raman pulse compression indicates that the amplified Stokes pulse will vary in length depending on the degree of saturation in the amplifier. With small inputs, the pulse tends to stretch slightly, but when the input is large, the output Stokes pulse can be shorter than the input by about 20%. The other factor which significantly affects the output pulse length is the relative timing of the pump and Stokes pulses. If the Stokes pulse enters the lightguide just behind the pump, it can overtake the pump pulse and extract the pump energy without being stretched. If the Stokes is at the head of the pump, the phonon wave established in the Raman medium scatters the pump energy into a new Stokes pulse whose length is the same as that of the pump pulse, and pulse compression does not occur. Depending on the exact timing of the two pulses, post-pulses of varying amplitude and length are also present. Figure 2 shows the effect of relative timing on the Stokes output for one set of experimental conditions similar to those actually used.

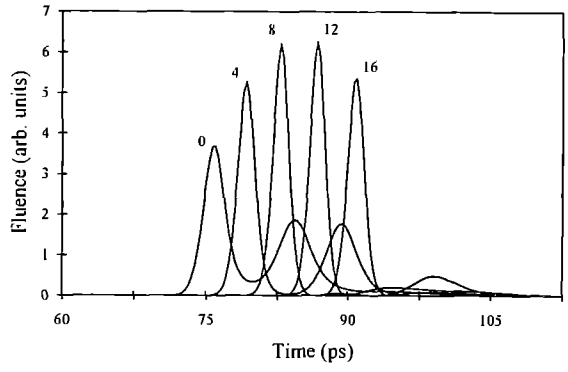

Figure 2. Predicted output pulse shapes for different relative timing of pump and Stokes. Pulse lengths and energies: Pump 20ps, 190 mJ; Stokes 2.6 ps, 1.1 mJ. Guide length: 200 cm. Methane pressure: 3 bar. The number above each curve is the Stokes delay (in ps) relative to the peak of the pump pulse.

The computational model of the Raman interaction process used for these calculations involves a one-dimensional treatment in which the pump and Stokes beams travel collinearly at slightly different speeds through the interaction region. This speed differential provides a crude representation of the three-dimensional geometry of the amplifier, in which as many as seven pump beams propagate at small angles to the axially-directed Stokes beam. There are, however, certain geometrical effects which cannot be represented in this simplistic way, and it is possible that the predictions of the model are in error as a result.

A more sophisticated two-dimensional code is therefore being developed, in which two co-planar pump beams propagate at small angles $\pm\vartheta$ to the axis; pump beam reflections are also taken into account. While this will still be an imperfect representation of the true situation, it includes all the key geometrical features present in the actual amplifier, and should provide a greatly enhanced theoretical tool for understanding and predicting the behaviour of Raman amplifiers.

EXPERIMENTS

Our experiments were performed using the smaller light-guided amplifier in the Sprite system, RA2, which has a 2.5 cm square lightguide. This amplifier was used rather than RA3 because it is possible to vary the distance between the segmented pump mirror array and the amplifier entrance, thus

changing the angle of the pump beams within the guide. The oscillator was set up to produce short pulses, initially of 4 picoseconds, in order to generate short Stokes pulses. The oscillator pulse length was later reduced to 2.5 picoseconds, and the best data were obtained at this pulse length. The short KrF pulse was stretched to approximately 16 picoseconds by spectral filtering in the multiplexer room, in order to provide the longer pump pulses necessary for the observation of pulse compression.

In designing the experiment, we had intended to ensure saturating inputs to RA2 by preamplification of the short Stokes pulse in RA1 with an unstretched pump pulse. However, the near-field profile of the beam became severely distorted in RA1, due to imprinting of hot-spots in the pump beam. Increasing the angle of the pump beam at RA1, and employing an expander lens to increase the degree of spatial averaging failed to cure the problem, so it was decided to omit RA1. We were able to increase the length of RA2 to 2 metres using a second section of lightguide, and this, together with thicker windows to allow operation at pressures up to 4 bar, gave enough gain-length to achieve saturation. However, the initial stages of amplification were under conditions of small-signal gain rather than saturation, which would be expected to give larger amplitude post-pulses, as undepleted pump energy is scattered into the tail of the Stokes pulse.

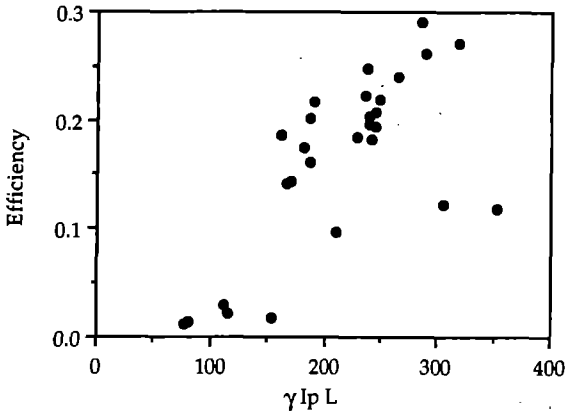

Figure 3. Raman amplifier efficiency.

Measurements of pulse length were made after the output of RA2, using a single-shot UV autocorrelator based on a design by Szabó et al [3]. This device, which has the capability for interferometric operation, is described in more detail in the paper on Sprite CPA, in Section B2 of this report. One of the main difficulties experienced with the autocorrelator was that it required a very uniform near-field beam profile to obtain accurate results. Even after RA1 had been abandoned, the near-field of the amplified beam from RA2 was not very uniform, again due to non-uniformities in the pump beams imprinting themselves onto the Stokes while the gain was still in the small-signal regime. This problem was finally solved by introducing a diffuser into the pump beam before the segmented mirror. The available pump energy was reduced by about 50%, but the gain was restored by increasing the methane pressure. The remaining pump beam was very uniform and gave an acceptable near-field in the Stokes output, permitting reasonably accurate pulse length measurements to be made.

Our aim was to scan the parameter space of Stokes timing and amplifier gain (by varying the methane pressure), in order to see whether short Stokes pulses could be amplified at reasonable efficiency by long pump pulses without stretching to the same length as the pump. The results are summarized in Figures 3 and 4, which show respectively the amplifier efficiency as a function of gain coefficient, γIpL, and the pulse compression factor as a function of Stokes delay. Efficiency here is defined as the ratio

Stokes output/(Pump input x Guide transmission)

in order to take into account the pump energy lost to reflections in the lightguide. The maximum efficiency achieved was about 30%, which is comparable with the performance of RA2 under normal operating conditions (i.e. without any attempt at pulse compression. The pulse compression factor is defined as the ratio of the pulse length of the pump to that of the output Stokes, and its' behaviour is less straightforward, as can be seen from Figure 4.

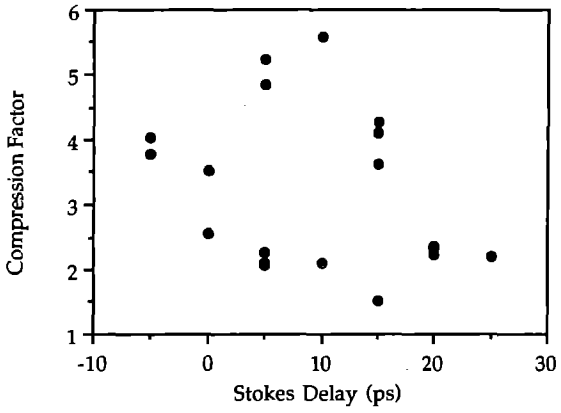

Figure 4. Pulse compression factor as a function of Stokes delay. Pump pulse length 16 ps; Stokes (input) pulse 2.5 ps.

The maximum pulse compression achieved was about 5.5, corresponding to a Stokes pulse of length 2.9 ps. However, at the same delay setting, a different shot taken a few minutes later gave a pulse compression of only 2, which in fact represents a lengthening of the Stokes pulse from its original 2.5 ps to around 8 ps. The reason for this is not clear: there is no obvious difference between the two shots, which had similar energies, gains and efficiencies, and it is possible that the difference may lie in the spectrum of the pump beam, which was not recorded during the experiment. The data in Figure 4 have substantial scatter, and it is hard to draw any definite conclusions. It appears, however, that Raman pulse compression does work, in the sense that short Stokes pulses can be efficiently amplified by longer pump pulses, but that some effect can occur which stretches the Stokes pulse to several times its original length.

REFERENCES

1. J R M Barr et al, in Non-linear Optical Beam Manipulation, Beam Combining and Atmospheric Propagation, SPIE Proceedings 874 (1988) pp60-76.

2. K E Hill, G H C New, P A Rodgers and K Burnett, Optics Commun., 87,315-322, (1992)

3. G Szabó, Z. Bor and A Müller, Optics Letters 13, 746, (Sep 1988)

SECOND STOKES GENERATION

C J Hooker, G Bialolenker*, G J Hirst, J M D Lister and M J Shaw

Rutherford Appleton Laboratory
*Laser Department, NRCN, Beer'Sheva, Israel.

During the previous year's operations on Sprite there were indications that radiation was being generated in the Raman amplifiers at frequencies other than the Stokes [1]. There were two main pieces of evidence for this. The first was a discrepancy between energies measured immediately after the laser and those measured in the target area after transmission through the chamber. It appeared that there were losses of between 10 and 20 percent on some of the mirrors. The second piece of evidence was the appearance on the far-field monitor of 'snow': a speckle pattern covering the entire field of view of the monitor. This was not present on every shot, but appeared most consistently on shots with high energy. Integrated over the field of view, there seemed to be far more energy in the speckle pattern than in the Stokes beam itself, whose far-field was still visible as a small spot at the centre of the screen.

One interpretation of these effects, consistent with all the observations, was that second Stokes radiation with a wavelength of 290 nm was being generated in RA3. This light would be transmitted through the mirrors en route to the target chamber, resulting in the observed losses. A second possible reason for losses would be if some of the second Stokes were emitted at an angle to the main Stokes beam axis. The nitrogen dioxide used as a variable attenuator for the far-field camera has much lower absorption for the second Stokes, so the signal at that wavelength would be larger, accounting for the large amount of energy apparently present in the 'snow'. The far-field camera is not achromatic, so the second Stokes would not be brought to a focus and would appear to cover the entire field of view.

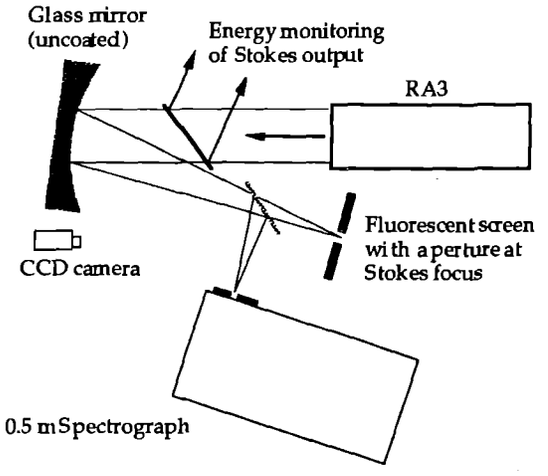

Figure 1. Diagnostics for investigation of second Stokes generation in RA3.

To investigate the conditions for second Stokes generation, with a view to controlling or eliminating it as a source of loss, some measurements were made at the output of RA3. The diagnostic arrangement is shown in Figure 1. The energy in the Stokes beam was monitored by a calorimeter in a portion of the beam split off by a silica plate close to the exit window of RA3. The calorimeter was placed far enough away that all the residual KrF pump beams were excluded. The first Stokes input energy was also routinely monitored.

An uncoated glass spherical mirror placed behind the splitter collected the light emerging from the amplifier. In order to minimise aberrations, the mirror was used at the smallest possible off-axis angle, and it was placed close to the amplifier exit window in order to collect off-axis radiation. A mirror was placed in the converging focal cone to divert the light into a 0.5 metre spectrograph to examine the spectrum, using the fourth order of the grating to obtain sufficient dispersion. Spectra were recorded using Polaroid film at first, but the amount of light available was not sufficient to obtain well-exposed negatives. Accordingly, a second CCD camera was used, with a framestore system, to obtain measurements of the energy in the second Stokes line. Later in the investigation, the spectrometer input mirror was removed, and a fluorescent Perspex screen placed in the focal plane of the spherical mirror. The screen was viewed by a CCD camera, in an arrangement which served as a form of wide-angle far-field monitor for the amplifier output. A hole drilled in the screen transmitted the focus of the Stokes beam, the fluorescence from which would otherwise have saturated the camera.

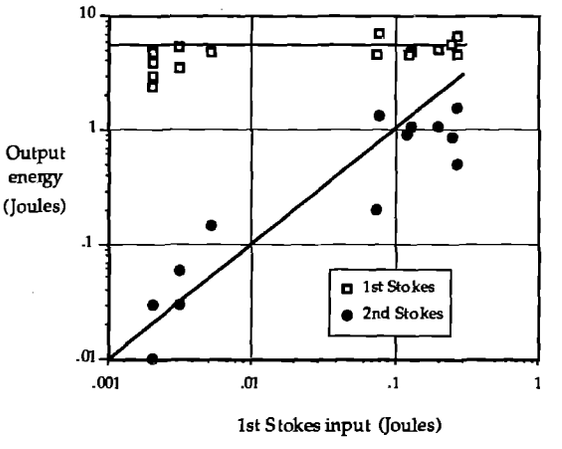

Figure 2. Output energies of first and second Stokes, showing dependence on Stokes input to RA3.

The intensity of the second Stokes line was recorded by the CCD camera attached to the spectrometer, and the data analysed on the framestore system. It was found that the amount of second Stokes correlated well with the first Stokes input to RA3, although the first Stokes output remained practically constant over a wide range of input energies, indicating that the amplifier was heavily saturated. Approximate energies were obtained from the uncalibrated CCD data by scaling them so that the maximum energy in the second Stokes was 20% of the first Stokes output energy, as observed. The data are plotted in Figure 2, where it can be seen that the energy in the second Stokes is proportional to the first Stokes input. Qualitatively, the explanation for this

is that when the Stokes input is larger, the amplifier saturates earlier, leaving a longer gain length for the second Stokes to grow from noise. It can be shown that a linear dependence on Stokes input is to be expected when there is saturation in the amplifier.

The results from the far-field imaging using the fluorescent screen were unexpected. In the far field, the second Stokes appears as a set of radial lines, each of which extends a few degrees on either side of the axis of the amplifier. A typical example is shown in negative form in Figure 3. When the input Stokes was blocked, the rays disappeared, as shown in Figure 4. In both of these images the spots due to the pump beams are visible. To confirm that the lines were second Stokes, some spectra were recorded on Polaroid using the spectrometer without a slit. The radial structure was present in the second Stokes line but absent in the first.

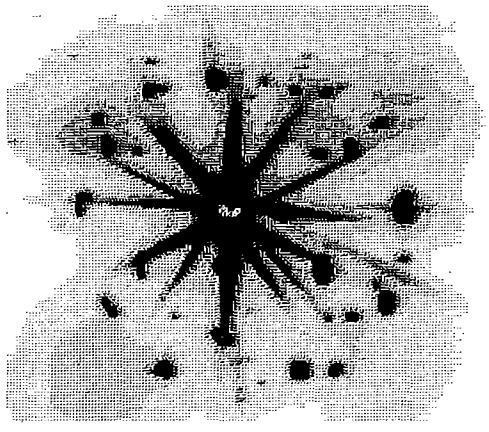

Figure 3. Radial lines at the second Stokes wavelength in the far-field of RA3. Spots due to the pump beams are visible both here and in Figure 4.

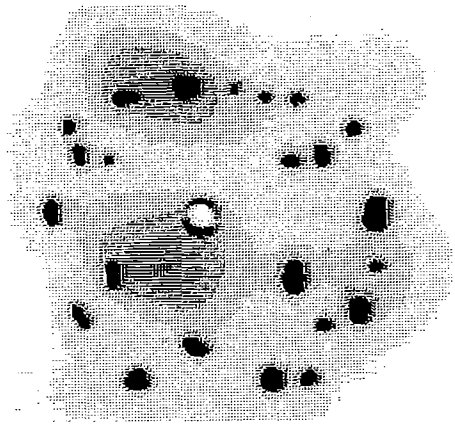

Figure 4. Far-field image showing the absence of second Stokes rays when the first Stokes input is blocked.

More detailed examination of the far-field pattern revealed that there were seven rays, whose directions corresponded with the positions of the seven KrF pump beams entering the amplifer. In fact, each ray lies in a plane defined by the Stokes axis and one of the pump beams.

Our explanation for this effect is as follows. Hot-spots in the pump beams, which are known to be present from near-field profiles, are converted into 'hot lines' on the Stokes beam profile by the transverse motion of the pump beam across the Stokes during their passage down the lightguide, as in Figure 5(a). As the beam travels down the amplifier, each of these lines defines a plane whose orientation depends on the direction of the pump beam. Self-generated second Stokes photons are preferentially amplified along any direction lying in the plane, because the integrated intensity in the first Stokes, and hence the gain, is greatest along such directions. In the far-field, therefore, the second Stokes emission appears as a set of narrow fans at orientations matching those of the pump beams. Figure 5(b) shows this schematically.

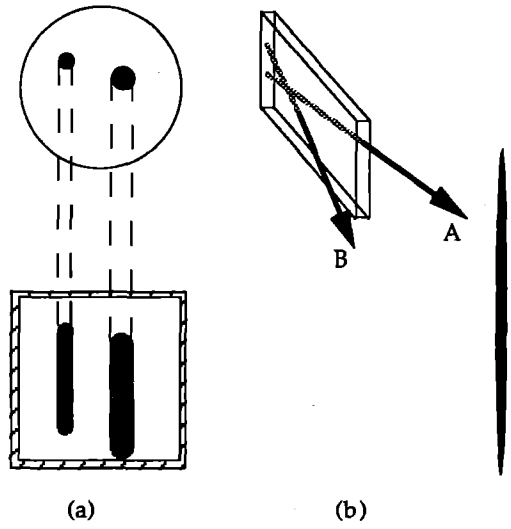

Figure 5. The generation of second Stokes rays by pump beam hot-spots: (a) The formation of 'hot lines' on the Stokes beam, and (b) preferential amplification within particular planes. Ray A experiences higher gain than ray B.

Our conclusion from the above results is that second Stokes generation is indeed the cause of the various phenomena seen in previous work with the Raman system. However, it is clear that the amount of energy lost to second Stokes can easily be reduced to around 1% by operating RA3 at moderately high gain with a small input energy. In this regime, saturation occurs only towards the output end of the lightguide, leaving insufficient gain length for the second Stokes to cause significant depletion.

REFERENCE

1. J M D Lister and G Bialolenker, Central Laser Facility Annual Report 1992, RAL-92-020, p142.

ENHANCED RAMAN BEAMS ON SPRITE

D C Wilson[1], S Hancock, C J Hooker, G H C New[1] and M J Shaw

Rutherford Appleton Laboratory
[1]Imperial College, London

INTRODUCTION

Work began this year on the design and implementation of the first phase of the upgrade to the Sprite Raman system. (The proposed two phase programme to improve the capabilities of the Raman system was outlined in last year's annual report[1].) The first phase of the programme involves making only relatively minor changes to the current system set-up. The aims of this phase are to improve the quality of the Raman beam to target, to improve the efficiency with which energy is extracted from the Sprite KrF amplifier, and to increase (by a factor of three) the amount of energy available at the target. This phase of the programme will be implemented in two stages, the first of which is the subject of this report.

IMPROVING THE BEAM QUALITY TO TARGET

One of the principal aims of this stage of the upgrade programme is to improve the quality of the Raman beam at target. This will be achieved through improved spatial filtering of the beam between the Raman amplifiers RA2 and RA3, and by a reduction in the total B integral between RA3 and target. The changes to be made to the current set-up in order to achieve these improvements are detailed below. (Depending on the results of the CPA experiment currently being performed on Sprite, these changes will be implemented either on their own, as an intermediate step in this first stage of the upgrade, or they will be implemented later together with the changes, discussed later on, to enhance the energy of the Raman beam.)

In order to improve the spatial filtering of the beam, the current 2m long vacuum spatial filter (VSF) between RA2 and RA3 is to be replaced with a new, longer VSF which, in addition to improving the beam quality, has been designed to minimise the amount of spherical aberration in the Raman beam arriving at RA3. The layout of the new VSF is shown in figure 1, which depicts the modified layout of the multiplexer room in R2, after completion of phase 1 of the Raman upgrade programme.

The lenses L1 and L2 will act as the input and output windows of a new 4m long vacuum pipe. The current set-up employs separate lenses and windows, so this will reduce the amount of material through which the beam must pass. The 60 μm pinhole will be one of an array of pinholes in a tantalum sheet, and will be positioned remotely using electric stepper motors. The longer vacuum pipe requires a longer focal length focusing lens (f=2.3m) and this will lead to a less intense focus at the pinhole. This in turn should lead to reduced pinhole damage and hence better, and more reproducible beam quality beyond the pinhole. The diverging beam emerging from the VSF will be turned through 180 degrees via two 45 degree mirrors and then recollimated by lens L3 to produce a 10 cm diameter collimated beam at the entrance aperture to RA3. The telephoto arrangement of the lenses L2 and L3, allows us to fit a VSF of effective length 9.2m into a distance of 7.25m. This length can be easily accommodated by moving RA2 back to the current position of RA1. The surface curvatures of lenses L2 and L3 have been designed, with the aid of a ray-tracing routine, to reduce spherical aberration to a minimum. Results from the ray-tracing routine suggest that the ray divergence due to spherical aberration, after lens L3, is 3000 times less than the far field angular divergence of a diffraction limited beam -- so diffraction limited beam quality at the entrance to RA3 should be achievable.

The B integral between RA3 and target is currently 5.0 (assuming 0.5 TW Stokes output) of which 2.1 is due to air and 2.9 to calcium fluoride. The B integral will be reduced by two measures. Firstly, collimation of the Raman beam before RA3 will allow us to replace the calcium fluoride lens currently employed at the output of RA3, with a thin (.75 mm) fused silica window (Hoya plate), thus reducing the calcium fluoride contribution to the B integral significantly. In addition, the aperture of RA3 is to be increased from 8cm to 10 cm, and, in order to produce 10 cm diameter pump beams at the entrance to RA3, the Sprite lens plate is to be moved back so that the beams leaving the Sprite beam pipe are slightly diverging. The increase in beam aperture will reduce the beam intensity, and hence the B

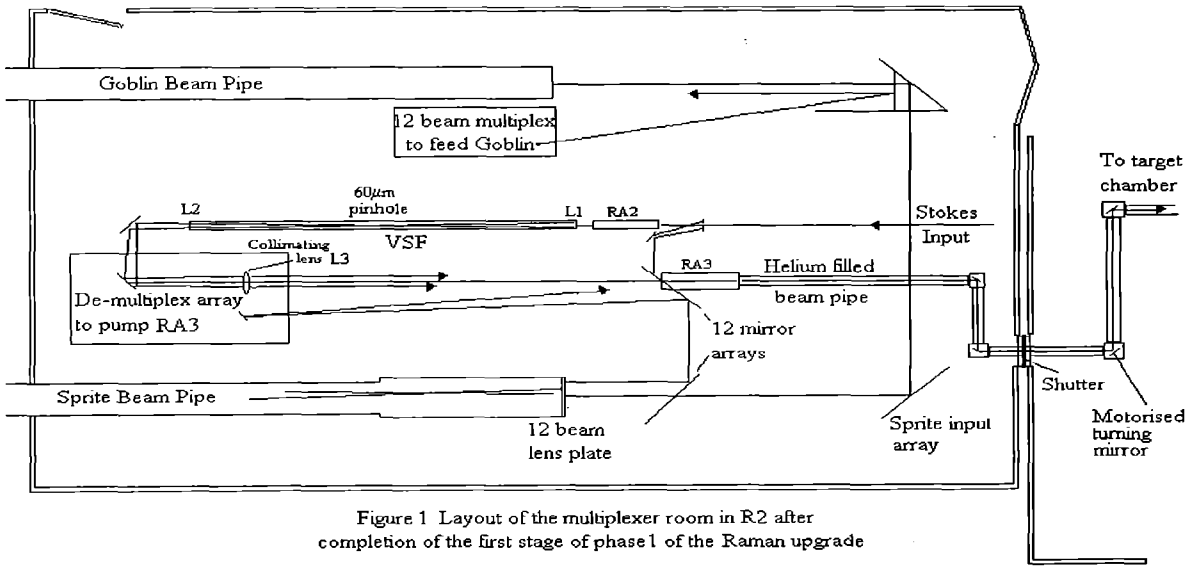

Figure 1 Layout of the multiplexer room in R2 after completion of the first stage of phase1 of the Raman upgrade

integral beyond RA3, to 64% of its current value. Overall, the B integral will be reduced to 2.5, half its current value. The increase in beam aperture necessitates the building of a new light guide for RA3 and a new pipe to accommodate it. The method of assembly and the design of the new light guide differ somewhat from those of the current light guide. The new design is shown in cross-section in figure 2.

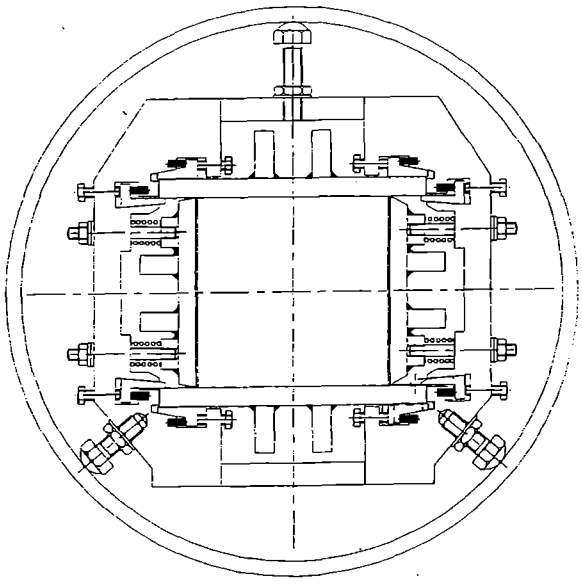

Figure 2 Cross-section of new RA3 Raman amplifier

One problem that has been encountered with the present design is that a significant amount of energy appears to be lost if gaps are present at the corners between the reflecting surfaces of the horizontal and vertical glass plates. These gaps may arise if high points occur on any of the contacting surfaces. To reduce the probability of such high points being present, the vertical plates of the new light guide will have their horizontal edges bevelled back (see fig. 2), reducing the area in contact with the horizontal plates to just a 1mm wide strip along the length of the guide. In addition, the new light guide will not be glued together but will be assembled and held in an adjustable mount (fig. 2), with the glass plates being glued separately to the mount, but not to each other. This should produce a better contact between the glass plates along the length of the guide and it has the added advantage of making the light guide aperture adjustable. This will allow us to experiment with a rectangular aperture light guide (horizontal dimension 100 to 120 mm).

The measures described above are expected to lead to greatly improved Raman beam quality beyond RA3. They are quite straightforward to implement and could be introduced quickly without too much disturbance to the current set-up. If they are performed on their own, as an intermediate step, these changes could be made at the beginning of Period III of this year's operating schedule.

ENHANCED ENERGY

The changes to be made in order to enhance the energy in the Raman beam are somewhat more drastic than those discussed so far. The plan is to increase the number of beams multiplexing the KrF system from eight to twelve. This will lead to a 57% increase in the amount of energy pumping RA3 and the power in the Raman beam is expected to rise from about 0.5 TW to about 0.8 TW. While the overall layout of the system will remain very similar to the present layout, several large scale modifications to the equipment in the multiplexer area do need to be made in order to enable twelve beam multiplexing of the KrF amplifiers. On Sprite the input mirror array, the lens plate, the beam pipe and the back mirror will all need to be replaced with components designed to accommodate twelve 10 cm diameter beams and the current input and output lenses will also need replacing. Two new mirror arrays, each consisting of twelve 15 cm diameter, 45 degree mirrors, will be used to turn the Sprite output beams through 180 degrees and on to the array of demultiplexing mirrors which feeds the pump beams into RA3. These two new arrays will replace the current Sprite output mirror array. The final arrangement of the KrF and Raman system in the multiplexer area following this stage of the Raman upgrade is shown in figure 1.

In order to avoid the problem of increased B integral, due to the increase in the Raman beam intensity beyond RA3, it is proposed that the Raman beam should be piped between RA3 and the target chamber through helium gas. This will involve the construction of a beam pipe between RA3 and the target chamber and the introduction of four motor driven turning mirrors to steer the beam to target (see figure 1).

Evidently, the energy enhancement part of the upgrade programme involves a considerable amount of engineering and the purchase or manufacture of several new components. However, as well as the obvious advantage of producing a higher energy Raman beam, several other improvements are expected to result from its implementation. Firstly, it is predicted that the near field of the Raman beam out of RA3 will be improved due to image relaying between Goblin and Sprite and due also to improved averaging resulting from the increase in the number of pump beams. The increase in the number of pump beams and the new arrangement for pumping RA3 will lead to more uniform pumping of that amplifier. Furthermore, the average B integral for each of the pump beams will be reduced from 3.0 to 1.6. With the Raman beam being piped through helium, the only contribution to the B integral beyond RA3 will be the target chamber window, so this B integral will be reduced to approximately 1, giving further improved beam quality at target. Finally, this part of the upgrade is entirely compatible with stage 2 of the Enhanced Raman Beams programme, which involves double pulsing the KrF beams to produce two Raman beams on target, and as such represents a necessary and useful first step towards the completion of this programme.

REFERENCE

1. S Hancock et al CLF Annual Report, p. 121, 1992

MEASUREMENT OF THE NON LINEAR REFRACTIVE INDEX OF VARIOUS GASES AT 248 NM

D C Wilson* C J Hooker and M J Shaw

Rutherford Appleton Laboratory

*Imperial College, London

INTRODUCTION

One of the major limits to the short pulse performance of Sprite is the B-integral in the long air paths used in the system. This gives rise to beam break-up and self-phase modulation which affects both the Raman and CPA operation of the system (see section B6). The non-linear index of air has been recently measured[1] at 308 nm where a value of 2.9 x 10^{-16} esu was obtained. At 248 nm a somewhat higher figure might be expected due to the near UV resonance in O_2 as pointed out by Hellwarth[2]. This latter paper also shows that very much lower values of non-linear index would be expected in Ar or He.

In the initial designs for the Titania upgrade for Sprite, the B-integral for air propagation presents an even bigger problem and so the replacement of air by other gases in the high intensity parts of the system is under active consideration. This work describes measurements of the non-linear index at 248 nm in the gases Air, N_2, (and by subtraction, O_2) Ar, Ne, He and CH_4 which provides a useful data set for the Titania design

EXPERIMENTAL

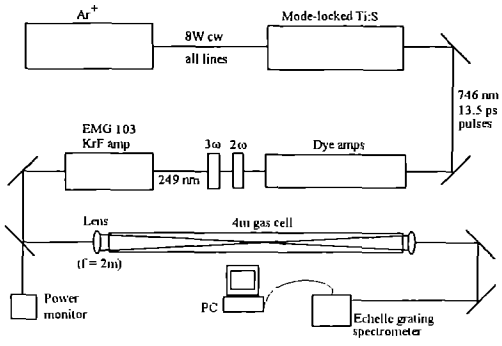

Fig. 1. Experimental set up

The experimental set up is shown in Fig. 1 which used the Sprite front end operating at 12 ps with no modifications. The 248 nm KrF beam has an energy of about 2 mJ after the second pass of the EMG 103 and was focussed into a 4m long pressure cell (RA0) with a 2m focal length lens. The transmitted beam (after suitable attenuation) was focussed onto the slit of an Exitech™ echelle grating spectrometer having a resolution of 0.2 cm^{-1}. Spectra were recorded as a function of gas pressure in the cell for each of the gases under study. During the pressure scan the average power of the laser was continuously monitored and the laser gain adjusted to keep it constant (to within about 10%). Scans were made with increasing and decreasing pressures.

RESULTS AND ANALYSIS

Spectral broadening in air, N_2, and CH_4 was readily and reproducibly observed at sub-atmospheric pressure. The maximum pressure employed was limited to that which gave a modest broadening (corresponding to a B of less than 3 or so). This was in order to keep the intensity-length product more or less constant and avoid spatial beam break up. For the rare gases, much higher pressures were necessary. Broadening in Ar was easy to observe with pressures up to 4.5 bar but at the maximum pressure we could use (9 bar) broadening in Ne was only just observable and for He no broadening could be produced at all.

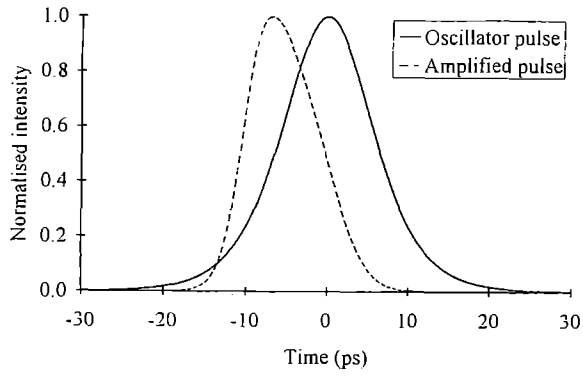

Fig. 2. Sech^2 oscillator pulse and the third harmonic amplified and saturated pulse used in the simulations.

In all cases the broadening was much greater to the long wavelength side of the peak indicating a laser pulse having a faster rise time than fall time. The general features of the broadening were the same in all gases with the exception of CH_4. In this case the red shifted broadening was observed up to about 250 Torr but at higher pressures strong blue shifted broadening was seen. The onset of the blue shift was coincident with the observation of stimulated Raman scattering from the cell and could be explained by pump pulse depletion due to the SRS.

The analysis involved choosing a pulse shape P(t) such that the non-linear phase shift B(t) = - B_0 P(t) where B_0 is given by

$$B_0 = \Gamma k \int_0^l I_0 \, dl$$

where Γ = 4.2 x 10^{-3} n_2(esu) and I_0 is the peak intensity of the laser pulse. The spectrum was then simulated by taking the Fourier transform of the pulse including the non-linear phase shift. The value of B_0 at each pressure was obtained by least squares fitting the simulated spectrum to the actual spectrum with B_0 as a parameter

The main problem with the analysis involved choosing the pulse shape which best fitted the data over the full pressure range. The only pulse shape information was the autocorrelation trace of the Ti-Sapphire oscillator output which was consistant with a $sech^2$ pulse of 12 ps FWHM and a streak camera measurement of the KrF pulse which showed a fast rise and slow fall time pulse of approximately 10 ps duration but with insufficient dynamic range to be useful as an input for the simulation. Assymetric Gaussian and assymetric $sech^2$ pulses were initially tried but gave poor fits to the data. Eventually it was found that the best fits to the data were obtained by operating on the assumed oscillator pulses as follows. $Sech^2$ pulses of 13 ps FWHM were cubed to simulate the third harmonic stage and then amplified in a saturating amplifier to a level of 6.5 E_{sat}. The pulse width and saturation level were used as variable parameters but are entirely consistant with the measured pulse length and KrF laser output energy. Fig. 2 shows the 746 nm oscillator pulse shape and that of the amplified third harmonic.

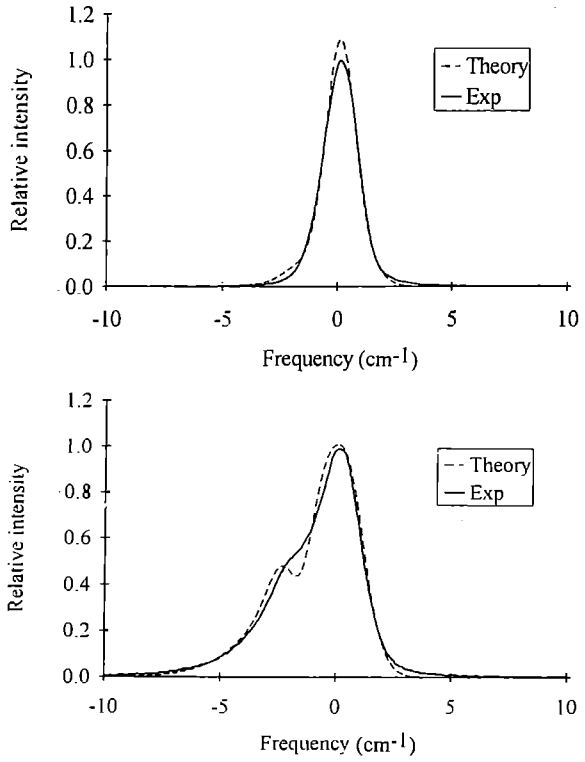

Fig. 3. Upper: Experimental and simulated specra for zero pressure in the gas cell. Lower: Experimental and simulated spectra for a 3000 Torr pressure of Ar in the gas cell.

Using this pulse shape, an initial degree of self phase modulation was applied to fit the spectrum with no gas in the cell. Fig. 3a shows a typical zero pressure fit. The simulated spectrum was normalised to have the same total energy as the experimental data (areas normalised). The typical zero pressure B-integral was 1.3 which is not inconsistant with what might be expected from the total thickness of window and lens material in the system.

Fig. 3b shows a typical fit to the experimental data at 3000 Torr pressure of Ar giving a B-integral of about 3. The smearing out of the dip seen in the simulated spectrum is not unexpected since the experimental data will contain a range of intensity-length products due to spatial variations whereas the simulated spectrum is based on a single value. Insufficient information on the spatial profile was available in order to simulate this effect.

Fig. 4 shows the values of B-integral obtained from the fitting routine as a function of pressure for the gases studied. The points plotted are averages of typically 5 fitted spectra at each pressure with the exception of Ne and He which are the averages of 25 fittings. The SRS onset in CH_4 is easily seen and the non-linear index is obtained from the lower slope. The relative values of n_2 come from the slopes of the curves and are given relative to air in Table 1.

Table 1. Relative values of non-linear index at 248 nm.

Gas	Relative n_2
Air	1.0
N_2	0.62
O_2	2.5
Ar	0.23
Ne	0.005
He	<0.002
CH_4	0.94

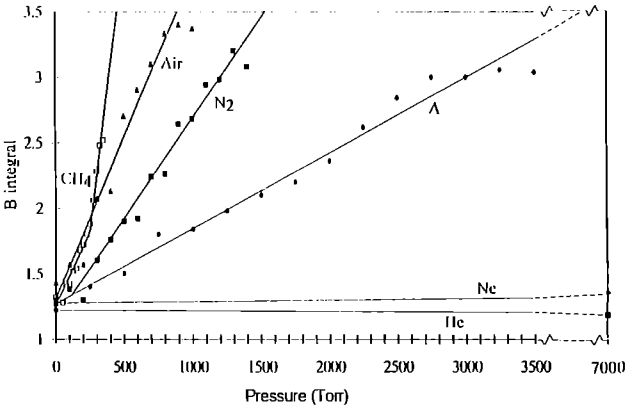

Fig. 4. Calculated B-integral as a function of absolute gas pressure for the gases studied.

The absolute vale of n_2 depends upon the value of the intensity-length product through the focus in the gas cell. The peak power, obtained from the pulse energy and pulse shape was 180 MW at the entrance to the cell. The near field was 5 mm in dia and the far field was estimated by measuring the transmission through a 200 μm pinhole which was found to be 50%. From this data a minimum value for the intensity-length product of 4.5 TW/cm is obtained. Assuming a Gaussian focus gives 7.6 TW/cm and assuming the 50% transmitted via the pinhole was diffraction limited gives 9.2 TW/cm. A value of 6.8 ± 2.4 TW/cm covers the range and gives an absolute value of n_2 for air at 248 nm, 760 Torr and 300K of 2.9 ± 1.0 x 10^{-16} esu.

REFERENCES

1. Y Shimoji et al J Opt Soc Amer B, **6**, 1994 (1989)

2. R W Hellwarth Phys Rev A, **41**, 2766 (1990)

PERFORMANCE OF THE OBERON AND TITANIA DIODES

A K Kidd, R Bailly-Salins[1], P S Carr[2], G J Hirst and M J Shaw

Rutherford Appleton Laboratory
[1]CEA, Is-sur-Tille, France
[2]University of Portsmouth

INTRODUCTION

During the past twelve months, a total of 187 diode shots have been fired on the pulsed power test module in R7. Two diode designs have been successfully tested, namely the Oberon diode (124 shots) and the Titania diode (63 shots). This report summarises the results obtained.

OBERON AND TITANIA DIODE IMPEDANCE

The design parameters for the Oberon and Titania diodes are listed in Table 1.

	Oberon	Titania
Diode voltage (kV)	850	600
Diode impedance (Ω)	5.5	4.0
Pulse length (ns)	250	168

Table 1 Diode parameters

Figure 1 shows the experimental voltage and current traces obtained for a voltage on the Oberon diode of 745kV. The voltage trace (Figure 1a) shows oscillations on the leading edge of the pulse which relaxes to a reasonably constant magnitude.

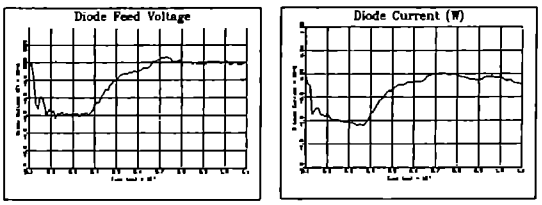

(a) (b)

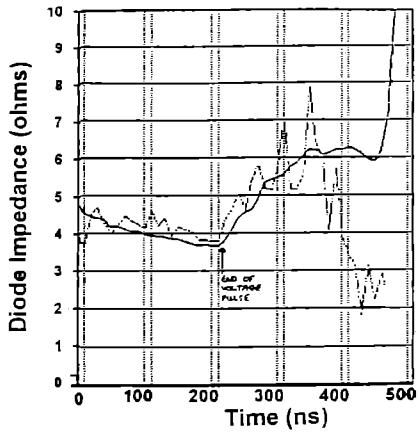

(c)

Figure 1 Experimental waveforms of (a) diode feed voltage, (b) diode current (West) and (c) comparison of experimental and theoretical variation of diode impedance with time for a diode voltage of 745kV

However, the magnitude of the current pulse continues to increase indicating a decreasing diode impedance. The behaviour of the Oberon diode impedance is investigated over a range of diode voltages from 550 to 745kV. The diode impedance is calculated from the digitised voltage and current waveforms and is found to decrease with increasing charging voltage (Figure 1c). Furthermore, the impedance is a function of time within the diode voltage pulse as the diode closes due to cathode plasma.

The simulation code BERTHA is used to model the behaviour of the Oberon pulsed power system; the circuit is described elsewhere[1]. A Child-Langmuir law dependence is assumed to model the diode impedance behaviour[2]:

$$\frac{433}{\sqrt{V}}\frac{(d_{ak}-vt)^2}{A} \qquad (1)$$

where V is the diode voltage (MV), d_{ak} is the anode-cathode spacing (5.0cm), v is the diode closure velocity ($cm\mu s^{-1}$), t is the time from plasma formation (μs) and A is the area of the diode ($2700cm^2$).

The experimental variation of diode impedance with time for a diode voltage of 600kV is compared with the code simulations in Figure 1c. The initial oscillation is due to inductive effects associated with the rapidly changing currents on the leading edges of the pulses. The Oberon diode has been designed to have an impedance of 5.5Ω for an anode-cathode spacing of 5.0cm. At 745kV, the impedance settles down to 4.6Ω 100ns after the start of the diode voltage pulse (t=50ns in Figure 1c) and decreases steadily to 3.8Ω at 250ns due to cathode plasma drifting towards the anode. This period corresponds to the region of constant diode voltage (Figure 1a). Over the period 250 to 550ns, the voltage falls to zero and this dominates over the closing effect serving to increase diode impedance to 6.5Ω at 400ns. There is close agreement between theory and experiment up to this point. After this time, the diode shorts out and the impedance collapses. This effect is not included in the model of the diode and the theory and experiment deviate. The oscillations on the trailing edge of the impedance trace are due to the combined effect of rapidly falling current and increasing error due to the small magnitude of voltage and current.

Although the design pulse length for Titania is 168ns, the diode was tested at a pulse length of 250ns. The Titania diode impedance is described by Child-Langmuir physics, ie a purely cathode plasma with a closure velocity of 3.5-4.0$cm\mu s^{-1}$. The Titania diode has been designed to have an impedance of 4.0Ω for an anode-cathode spacing of 4.0cm. At 500kV, the impedance decreases from 4.6Ω to 4.2Ω over the latter part of the voltage pulse. The diode behaviour at 600kV is similar qualitatively; the diode impedance is, however, lower with a decrease from 4.2Ω to 3.8Ω.

The Oberon impedance is consistent with the code simulations if we assume an expansion of the electron emitting area from the

cathode of 10-20% over the duration of the voltage pulse. This last point is confirmed by the following:

(a) **Quartz Gauge Diagnostics**

Computer modelling and the analysis of thermoelastic pressure induced in a quartz gauge[3,4] indicate that the cathode emitting area is wider than the cotton velvet strip. This viewpoint is enhanced by the good agreement obtained between voltage and current density profiles deduced from numerical simulations using the simulation code Thepied[3], based on data obtained from the quartz gauges, and the experimental waveforms (Figure 2b).

(b) **Computer Modelling**

Computer modelling using the electron optics code, EGUN[5], indicates an expansion of the emitting area of 10-20% over the duration of the voltage pulse (Figure 2a).

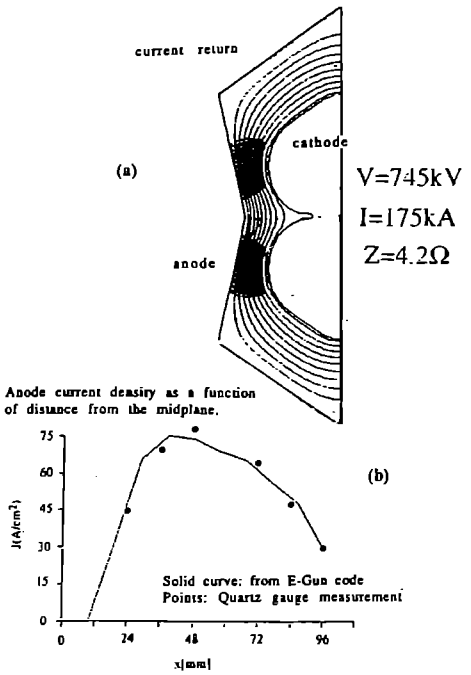

Figure 2 (a) Electron beam trajectories calculated from EGUN, (b) Anode current density deduced from quartz gauge measurements

The EGUN code predicts that the two electron beams exhibit pinching (Figure 2a). In order to reduce the pinch effect, aswell as the diode inductance, the Titania diode is designed to provide a current return path located between, and effectively isolating, the two sections of cathode (Figure 3). This return is cut away in the region of the two diode feeds.

The electron trajectories within the diode chamber are monitored by placing chlorostyrene film on the anode plates. The film is sensitive to electron bombardment and becomes opaque on exposure. The film is analysed using a densitometer.

Bars are placed along the length of the velvet emitting area which inhibit electron emission. These bars define a width of emission on the cathode of 7cm. The experimental results obtained with the Titania diode indicate that with a 7cm wide emitting velvet area without electron emission inhibitors, the electron beam width recorded at the anode is 13-15cm. With the incorporation of electron-emission inhibiting bars along the edges of the velvet, this was reduced to 7.6-9.0cm.

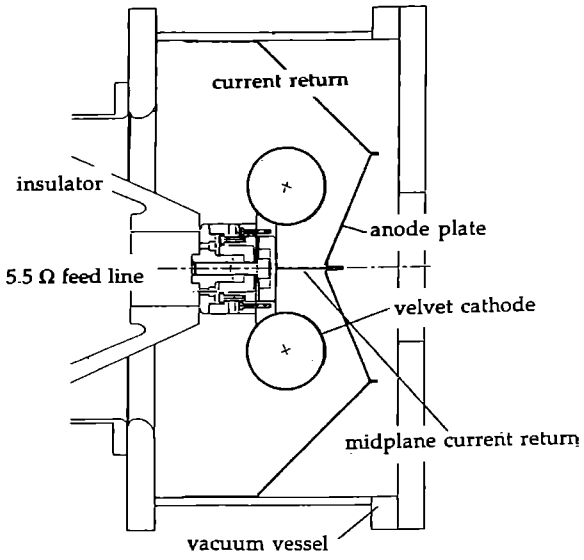

Figure 3 The Titania diode chamber

The equipotential distribution in the vacuum region between the cathode and anode is shown in Figures 4a and 4b for electron emission with and without inhibiting bars. These results are obtained with the EGUN electromagnetic field code[5] for the design diode voltage of 600kV.

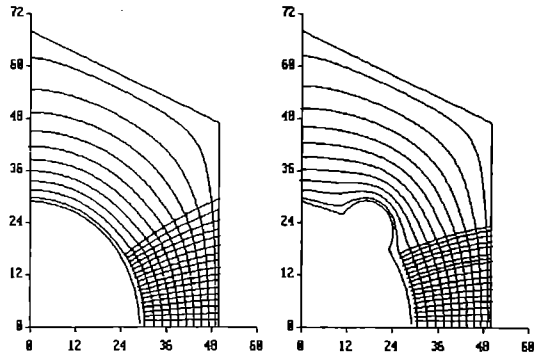

Figure 4 Equipotential plot and electron beam trajectories in the cathode-anode region
(a) without and (b) with emission inhibitors

For the case of no emission inhibitors, the simulated beam width at the anode is 11.5cm compared with the experimental value of 13-15cm. This discrepancy is possibly due to the fact that the width of the emitting area is believed to be some 10-20% greater than the design value of 7cm. With the inhibitors in place, the simulations agree reasonably well with experiment - the code indicates the beam width to be 8.6cm, compared with the experimental value of 7.6-9.0cm.

The effect of replacing the velvet emitter with a cheese grater on diode impedance is investigated. The anode-cathode spacing is kept constant at 40mm, as is the width of the emitting area (70mm). Figure 5 shows the diode impedance behaviour for a voltage on the diode of 555kV.

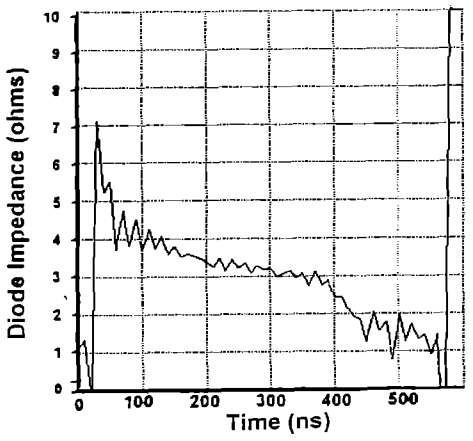

Figure 5 Experimental waveform of diode impedance: width of cheese grater emitter = 70mm; anode-cathode separation = 40mm; diode voltage = 555kV

The diode impedance falls by about 25% over the latter part of the voltage pulse and there is no diode recovery on the trailing edge of the voltage pulse. The result is a decrease in diode impedance from 4.0Ω to 3.0Ω over the duration of the diode voltage pulse.

References

1. A K Kidd.
Comparison of experimental results and simulated waveforms of voltage and current in the Oberon pulsed power system.
RAL internal report No. KrFDev\17\92\R, Sept.1992.

2. C W vonRosenberg, Jr. and D A Reilly.
Design trade-off studies for diodes', final report of 'Review of vacuum breakdown limits in the presence of high current relativistic electron beams and design trade-off studies for diodes.
Avco Research Laboratory Contract No. 9-XT9-E9580-1, August 1990.

3. R Bailly-Salins.
Thermoelastic pressure induced by electron deposition.
RAL internal report No. KrFDev\18\92\R, Sept.1992.

4. R Bailly-Salins, A K Kidd, M J Shaw and G J Hirst.
Oberon's diode: Electron beam kinetic energy, current density and emitting area modelling from the thermoelastic pressure induced in a thick Al anode.
Paper PP9, IIIrd Workshop on KrF Laser Technology, Abingdon, UK, 3-5 November, 1992.

5. R Bailly-Salins.
Electron optics program.
RAL internal report (1989).

ELECTRON BEAM ENERGY DEPOSITION WITH THE OBERON PULSED POWER SYSTEM

A K Kidd, R Bailly-Salins[1], P S Carr[2], G J Hirst and M J Shaw

Rutherford Appleton Laboratory
[1]CEA, Is-sur-Tille, France
[2]University of Portsmouth

ELECTRON BEAM ENERGY DEPOSITION WITHIN A TARGET GAS VESSEL

The Oberon diode is designed to generate an 850keV electron beam. A spatial diagnostic of electron trajectories is to monitor the path taken by the electron beam through a target gas. The target cell is 3m in length and 1m diameter, and contains pure nitrogen at a pressure of 1 bar. The nominal pumped length is 2m. In order that the e-beam enters the gas, one-quarter of the solid anode plate is removed and replaced with a 12μm anode foil and a 35μm pressure foil (titanium). The pumped volume is $0.39 \times 10^6 cm^3$. The path of the e-beam is monitored through one end of the vessel by means of a CCD camera and is shown in Figure 1 for an Oberon diode voltage of 700kV.

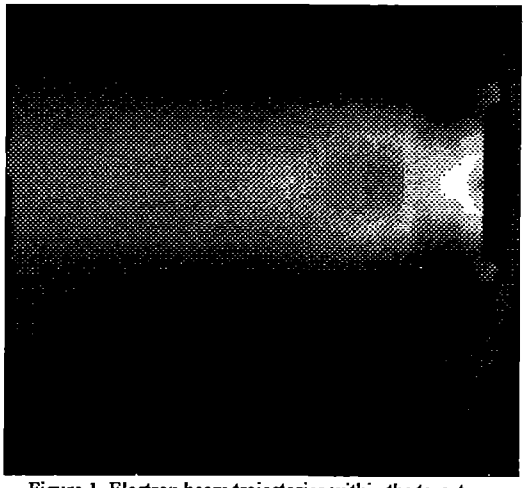

Figure 1 Electron beam trajectories within the target gas vessel for a diode voltage of 700kV

The two beams from the two sections of the cathode exhibit pinching, as predicted by the electron optics code, EGUN[1], and in fact cross over within the target vessel. Figure 2 shows a three-dimensional plot of the energy deposition within the gas for a diode voltage of 700kV.

The amount of energy deposited in the vessel manifests itself as a rise in pressure of the target gas. This pressure jump, ΔP, is related to the magnitude of the deposited energy, E, by:

$$E_{gas} = \frac{1}{\gamma - 1} \Delta P V_c \qquad (1)$$

and is recorded by means of a baratron. The energy in the diode, E_{diode}, is determined by the computer code EXPTZ[2] from the digitised traces of diode voltage and total current according to:

$$E_{diode} = 1/4 \int_0^{\infty} i(t)v(t)dt. \qquad (2)$$

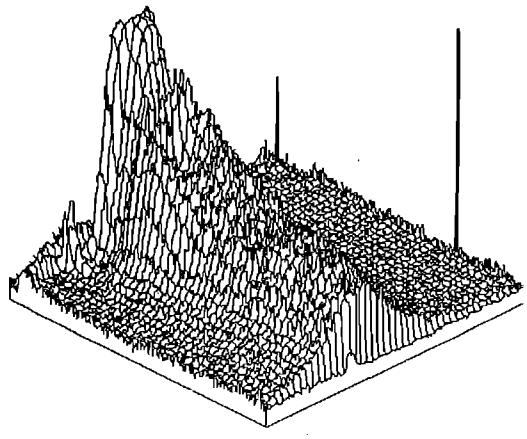

Figure 2 Electron beam deposition at a diode voltage of 700kV in N_2 : 3D distribution

since only one quarter of the beam is extracted. The foil transmission efficiency, η, is defined as:

$$\eta = \frac{E_{gas}}{E_{diode}} \qquad (3)$$

where E_{gas} is the energy deposited in the gas. Figure 3 shows the foil transmission efficiency as a function of energy in the diode for voltages on the diode of between 550 and 745kV. The efficiency is 50% at the lowest energy and falls to 40% as the electrons are lost to the far wall at higher voltage.

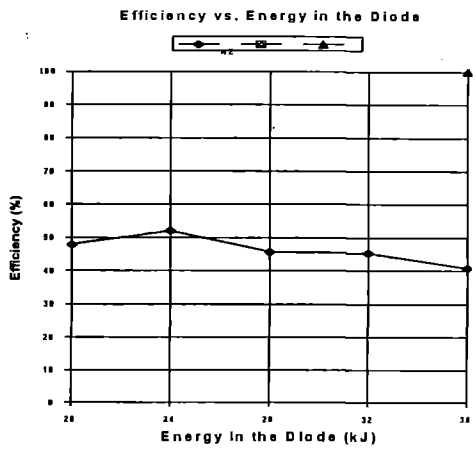

Figure 3 Efficiency vs. energy in the diode

In order to increase the stopping power of the target gas, a quantity of SF_6 was added to the nitrogen in a roughly 50/50 mix whilst maintaining a total pressure of 1 bar. Figure 4

shows a three-dimensional plot of the energy deposition within the gas for a diode voltage of 700kV.

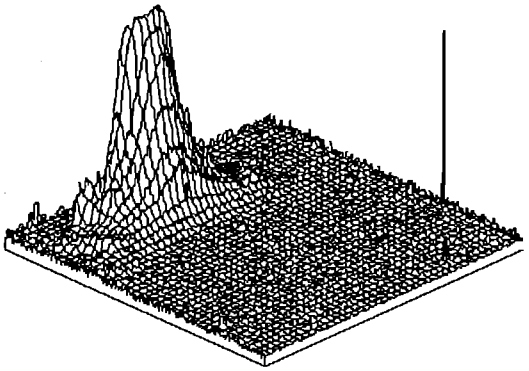

Figure 4 Electron beam deposition at a diode voltage of 700kV in N_2/SF_6: 3D distribution

A foil transmission efficiency of 52-58% was estimated although the precise value was uncertain due to the uncertainty in the precise ratio of constituents in the target gas.

References

1. A K Kidd, R Bailly-Salins, P S Carr, G J Hirst and M J Shaw
Performance of the Oberon and Titania Diodes.
Annual Report to the Laser Facility Committee (1993).

2. A K Kidd.
Comparison of experimental results and simulated waveforms of voltage and current in the Oberon pulsed power system.
RAL internal report (1992).

PROGRESS ON THE TITANIA AMPLIFIER MODULE

S Angood, J Govens, G J Hirst, A K Kidd, H T Medhurst, M J Shaw and B Wyborn
Rutherford Appleton Laboratory

INTRODUCTION

The outline design of the TITANIA amplifier module was presented in last year's annual report. In this paper we report on the progress in construction and on some of the details of the final design. Prior to beginning the stripdown of the old pulsed power test facility the diode test chamber was modified to accept a diode of the type proposed for TITANIA. The results are reported elsewhere in this section. The conclusions as far as the TITANIA design was concerned were that a) velvet was a better choice of electron emitter than the tantalum cheese grater, b) field profilers were necessary to control the edge emission from the velvet and c) it was possible to use a midplane current return between the two halves of the cathode.

CONSTRUCTION

Construction of the new module began in January this year. The Marx generator was modified by the removal of 8 capacitors. The opportunity was taken to renew the copper sulphate resistors and to clean the spark gaps. The new transfer tank and the 4 PFLs have been fitted and the assembly of the PFL switches is well advanced. The first phase of construction ends with the switch outputs being terminated in 4 dummy loads. This will allow testing and characterization of the switches prior to the installation of the diodes.

DIODE AND LASER VESSEL DESIGN

The bulk of the design is complete and several long delivery items are being manufactured. The most significant item being the diode vacuum vessel which is being constructed from a 3" thick steel forging. The choice of such a thick vessel avoids the need for any welding and more importantly provides a very significant degree of shielding from X-rays produced by the electron beam. Approximately two orders of magnitude reduction of dose is expected from the 3.5 Tonne vessel.

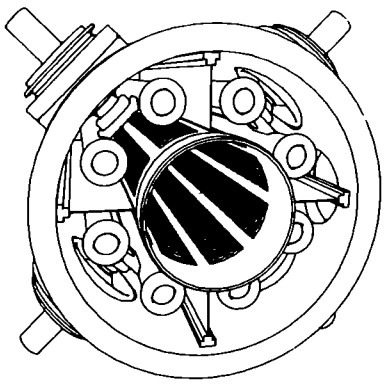

Fig. 1. Cut away view of the Titania diode vessel. Midplane current returns removed for clarity.

The laser cell is also being manufactured. The Hibachi structure will be cut from a flat stainless steel sheet before rolling to its final shape. The clear laser aperture is 420 mm. Fig 1. shows a cut away view of the diode and laser vessels.

Further electric field calculations and the test diode results have been incorporated into the insulator and cathode design shown in Fig. 2. The use of the field shaper at the feedthrough keeps the electric field angle to the vacuum surface very close to the optimum 45° and the field distribution is very nearly uniform with a mean field of 40 kV/cm. The midplane current returns effectively divide the vessel into 8 magnetically isolated compartments. These current returns are fixed to the outer vessel and slide in contact rails fixed to the laser gas vessel. The other current returns do the opposite. For servicing, the gas vessel and interdiode current returns extract along the axis on rails. The vessel is then transferred to a trolley which allows the whole laser vessel to be rotated for foiling

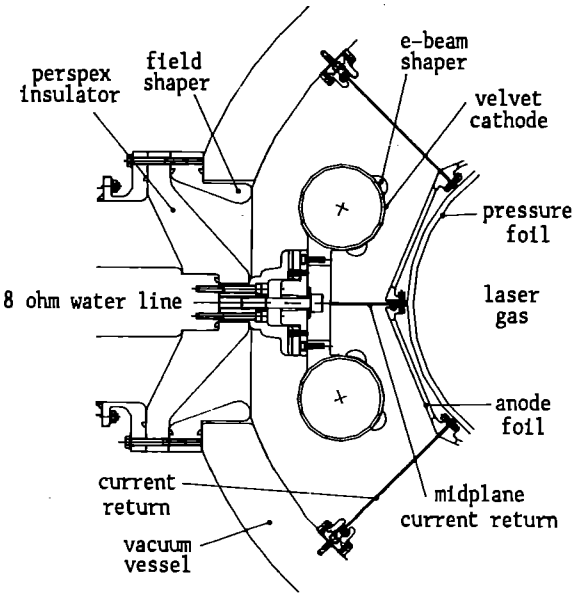

Fig. 2. Section through diode compartment.

The cathode support structure will be constructed from nickel-plated aluminium as will the "bumps" which define the edge of the emitting area. In the test diode these bumps were found effective in reducing edge emission from the velvet cathode and focused the electron beam in the direction of the foil window.

PROGRAMME

The testing of the switches was due to commence on 1st April but late delivery of the switch insulating diaphragms have delayed this phase. This testing is now scheduled to start in May. The diode construction phase is ahead of schedule and plans for the first diode shots for November appear feasible. The first laser shots (as a long pulse oscillator) should be obtained by the end of the year.

FOCAL SPOT SMOOTHING USING SPECTRAL DISPERSION

C N Danson, D A Pepler, and C E Ollman
Rutherford Appleton Laboratory (UK)

INTRODUCTION

The smoothing of focal plane distributions of high-power lasers is of particular importance to laser-plasma interaction studies. There are many techniques used to achieve smoothing. In this report we present results of experiments on the VULCAN high power Nd:glass laser to implement Smoothing by Spectral Dispersion (SSD)[1]. This technique involves dispersing a broad bandwidth oscillator output which is then incident on a standard Random Phase Plate (RPP)[2]. The speckle pattern normally associated with the RPP is smeared out in the dispersed direction.

SSD TECHNIQUE

Smoothing in this method is obtained by the insertion of a spectrally dispersive element into a broad bandwidth laser beam which causes a wavelength dependent divergence, which when focused smears or smoothes the beam in the direction of the divergence. In these experiments a reflective diffraction grating was used.

The effect of placing the grating in the beam is to increase the beam divergence in one direction only, and so, at the focus of a lens the original spot becomes a line. However, in the SSD technique the grating is used in conjunction with a RPP, and in this case each individual speckle is smeared, thereby smoothing the whole spot. A schematic of the SSD technique is shown in figure 1.

The bandwidth of the laser source and the dispersion controls the degree of smoothing. The divergence is given by

$$\delta\beta = \frac{(\sin\alpha + \sin\beta)\delta\lambda}{\lambda\cos\beta} \qquad \text{where} \quad \sin\beta = (NK\lambda) - \sin\alpha$$

and N is the diffraction order, K the grating density, $\delta\lambda$ the bandwidth, λ the wavelength, α and β are the incident and diffracted angles. Given the bandwidth of the laser source, the divergence is chosen according to the focal spot size generated by the RPP, resulting in a smoothed focal spot, but with no significant increase in its size.

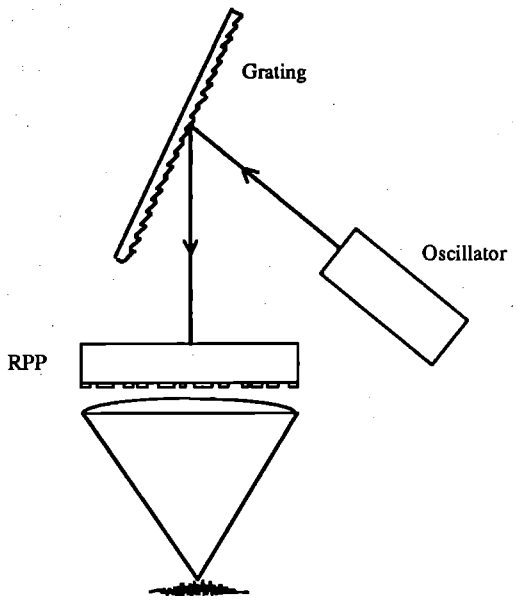

Figure 1 Schematic of the SSD technique

In the SSD operations on VULCAN the grating chosen had 300 lines/mm, was operated with a 9 degree angle of incidence, which, when used with a laser source of 1.4 nm bandwidth produced an angular dispersion of 0.170 mRad at the system output. Using a RPP with 1 mm elements and a 1 m focal length lens (typical operating parameters on VULCAN), the focal spot size was 1 mm. The dispersion will contribute a further 0.17 mm, producing an elongation of 17 % in the overall spot size in the plane of the dispersion.

Figures 2 and 3 show the focal spots generated by a RPP and for the SSD configuration. Figure 2(b) and 2(c) show cross-sections of the RPP focal spot taken in the horizontal and vertical planes. Figure 3(b) and 3(c) similarly show the cross-sections of the focal spot of the SSD. These clearly demonstrate the difference in smoothing between the horizontal and vertical planes. The majority of the smoothing in this case is in the horizontal plane, but since the dispersion of the grating is uni-directional it is possible to change the direction of the smoothing on the target simply by rotating the grating.

Spectral dispersion however has a possible further advantage in enhancing the conversion efficiency of harmonic generation[3,4]. Although the normally broader bandwidth laser source used with SSD would lose efficiency due to a miss-match of phase-angles in the conversion crystal, the induced dispersion can compensate for this so that each frequency component is tuned to its phase-matching angle thereby increasing the overall conversion efficiency.

CONCLUSIONS

Focal spot smoothing techniques have been used in a range of scheduled laser-plasma interaction experiments on the VULCAN Nd:glass laser facility. Using spectral dispersion we have demonstrated good one-dimensional smoothing. Introducing the SSD grating improves on the smoothing produced by RPP, greatly enhancing an already successful technique. The technique also has the advantage that it does not suffer from the poor near-field quality introduced when using Induced Spatial Incoherence (ISI).

ACKNOWLEDGEMENTS

The authors would like to acknowledge the assistance of R M Stevenson of the Atomic Weapons Establishment PLC, Aldermaston (UK) in processing the far-field images.

REFERENCES

1. S Skupsky et al, *Journal of Applied Physics*, Vol. 66, No. 8, pp3456-3462 (1989)
2. Y Kato et al, *Physical Review Letters*, Vol. 53, No. 11, pp 1057-1060 (1984)
3. RW Short and S Skupsky, *IEEE Journal of Quantum Electronics*. Vol. 26, No 3. pp 580-588. March 1990.
4. MD Skeldon et al, *IEEE Journal of Quantum Electronics*. Vol. 28, No 5. pp1389, May 1992.

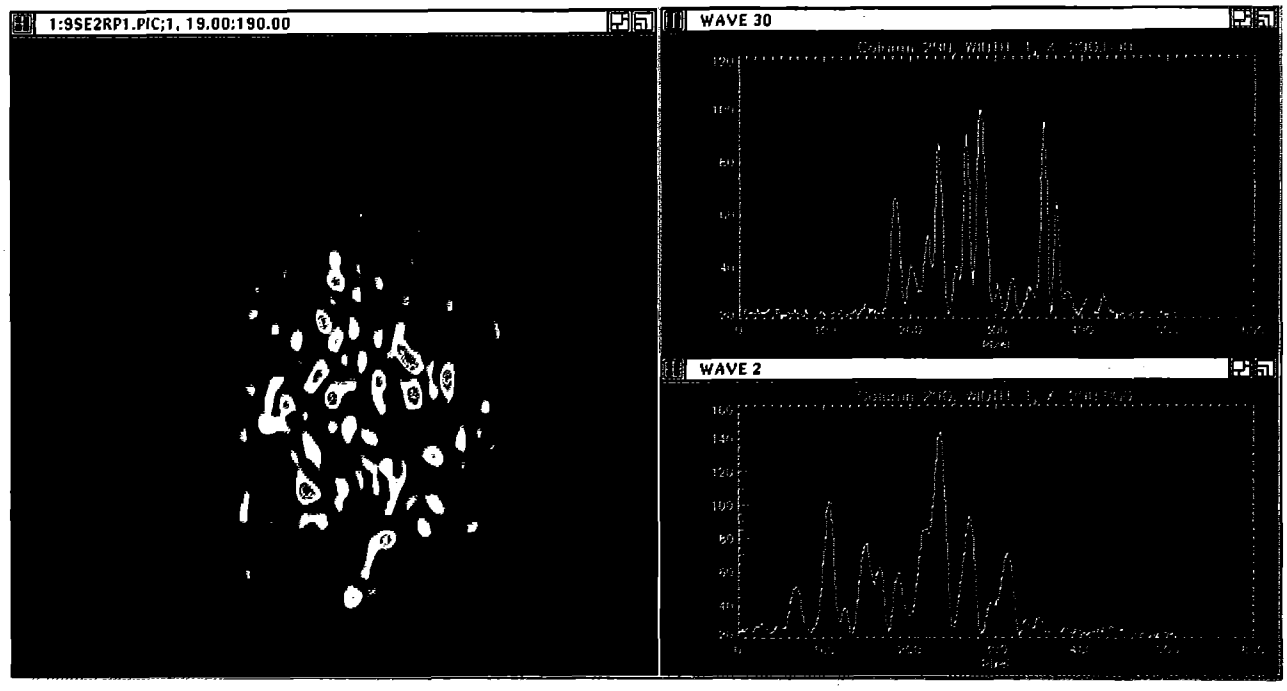

Figure 2 RPP focal profiles
(a) Far-field image
(b) Horizontal cross-section
(c) Vertical cross-section

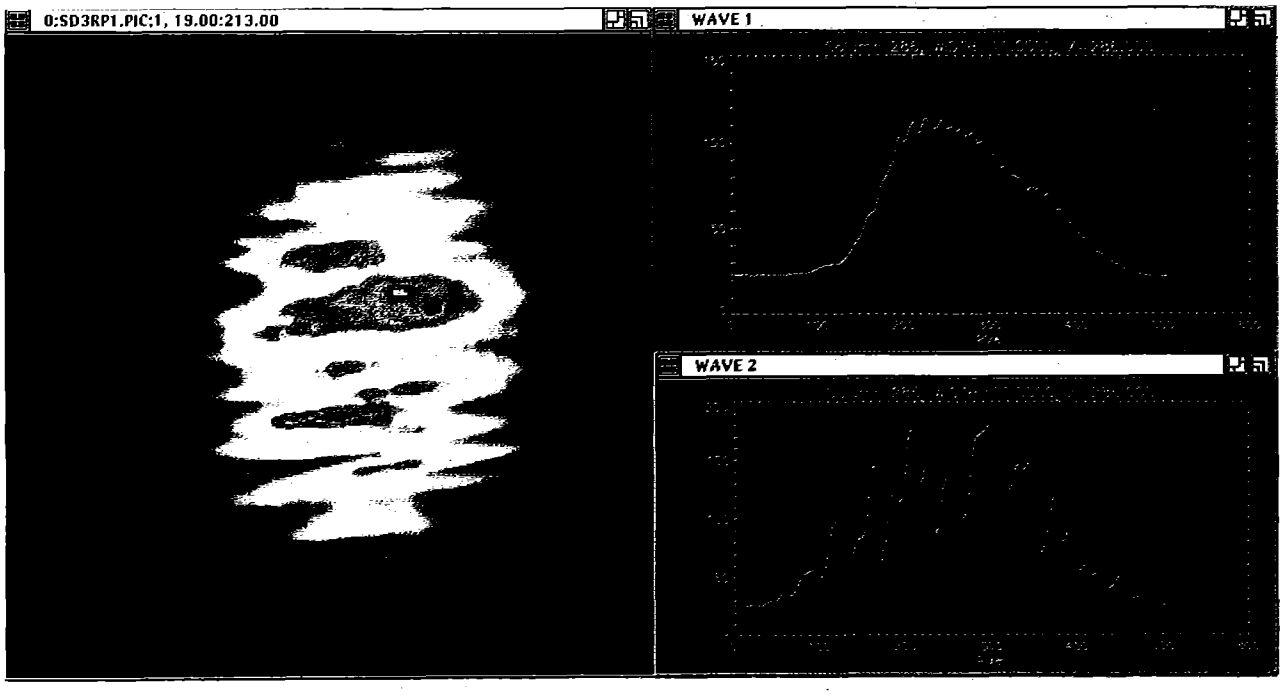

Figure 3 SSD focal profiles
(a) Far-field image
(b) Horizontal cross-section
(c) Vertical cross-section

COMPARISON OF RANDOM PHASE PLATES FOR FOCAL SPOT SMOOTHING

R M Stevenson[1], D A Pepler[2], M J Norman[1] and C N Danson[2]

[1]Atomic Weapons Establishment PLC, Aldermaston (UK)
[2]Rutherford Appleton Laboratory (UK)

INTRODUCTION

A random phase plate (RPP) is a binary diffractive optic formed by the tessellation of some basic element shape. Each element acts as a diffracting aperture and the resulting focal profile is the superposition of diffracted light from all the apertures. The focal spot consists of a high spatial frequency speckle pattern. The RPP distribution is randomly formed with half of the elements producing a zero phase shift and the other half, a π radian phase shift. The equal areas of 0 and π destructively interfere exactly on axis. The small scale speckle contains mainly high spatial frequencies which in many laser-plasma interaction experiments will be smoothed by energy transportation in the plasma. It is possible to find a number of element shapes which can be used to form the RPP pattern. In this report we compare four different shapes, looking at the far-field profiles and the growth of modulation in the near-field of the beam.

BASIC MASK DESIGNS

Two mask types using square[1] and hexagonal array[2] structures have been generally used in the manufacture of RPPs. Typical mask structures and the resulting shape of the focal profiles are shown in figure 1a and 1b. The square elements result in a square-like focus but with the overall intensity profile following a sinc^2 envelope in the two axis. The mask structure for a hexagonal array produces a better focal distribution than the square, being symmetric on three axis and having an almost circular central spot.

A method of producing truly circularly symmetric focal profiles is to use the mask structure shown in figure 1c, with it's resulting focal profile. The distribution is achieved by generating concentric circles of the required element spacing and then filling each annuli with an integral number of sub-elements calculated by dividing the area of the annuli by the area of each 'square' sub-element. Here the central region is more circular, and has much less subsidiary structure surrounding the central spot than that produced by the square. This is because the subsidiary spots have been swept into a full 2π thereby reducing their intensity. It is interesting to note, that with this RPP, the further one moves away from the central point, the greater is the similarity to that of a square distribution.

An alternative shape to produce a regular tessellation is a triangle, so this too was used to produce a RPP. Figure 1d shows the triangular RPP mask and the resultant focal spot. This simple distribution

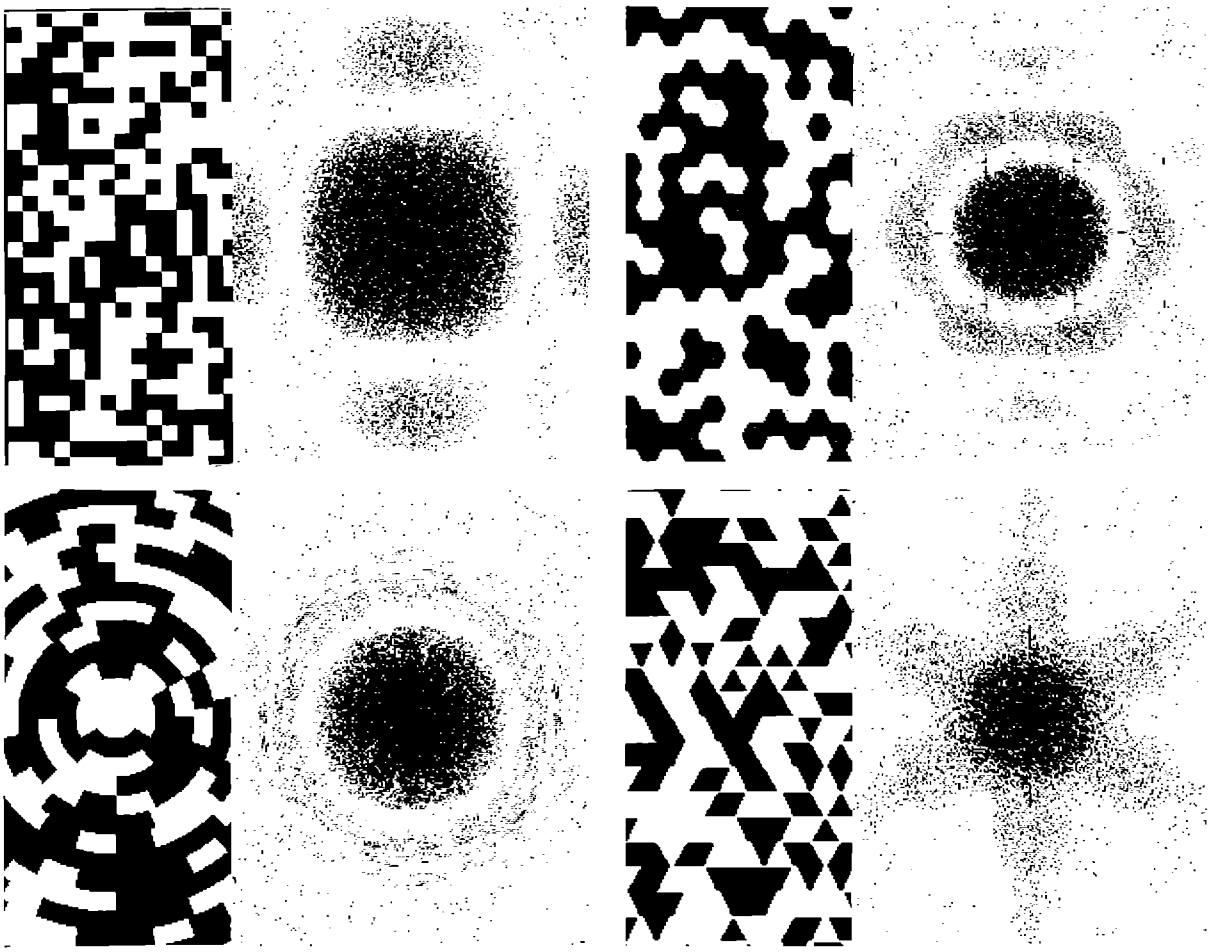

Figure 1 Random phase plate mask patterns and associated focal profiles
(a) Square structure (b) Hexagonal structure
(c) Circular structure (d) Triangular structure

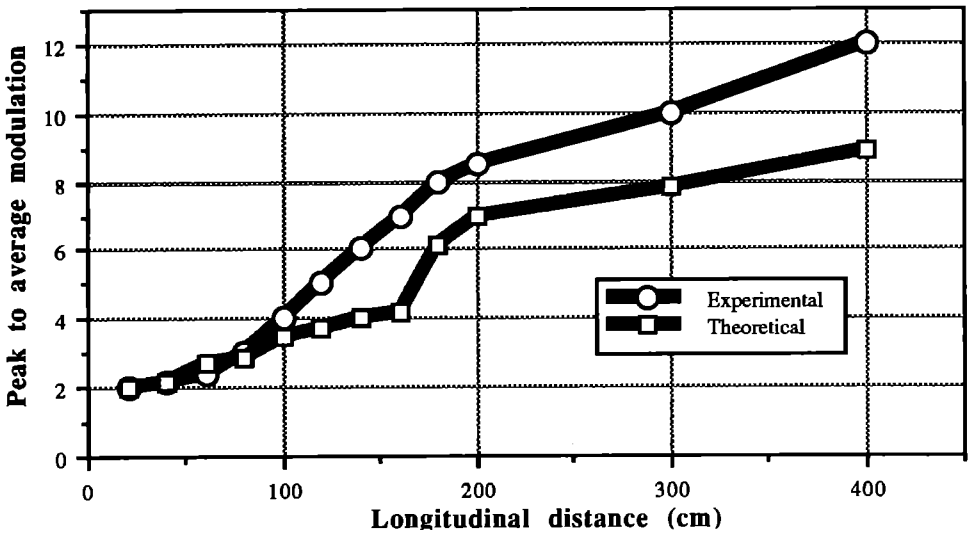

Figure 2 Graph showing the near-field beam modulation after a square RPP

produces an almost circular central spot, and like the hexagon has a three-fold symmetry, but instead of a ring around the center, it has six triangular tails streaming away from the center. These residual structures can be reduced by randomly imposing a distortion on the triangles to sweep the tails into a greater arc, as obtained with the circular structure.

NEAR-FIELD INTENSITY MODULATIONS FROM RPPs

The RPPs are designed to modify the focus of the laser beam but due to the diffraction from each aperture the near-field after the RPP will also be modulated[3]. There are resulting problems when propagating the beam in the near-field through any optical component as the modulations can be severe and through non-linear self-focusing lead to optical damage. Figures 3a through to 3d show the experimental near-field modulation that occurs in the beam after a 2 mm square RPP, and show an increasing depth of modulation with distance from the RPP. At 120 cm, a 5:1 intensity modulation can easily be achieved. Computer modelling of the near-field distribution has also been used to analyse this process, with the comparison of these results shown in figure 2.

Each edge or transition from one phase to the other will cause a diffracted wave to be propagated. The combination of these diffracted waves will be an interference pattern with constructive interference generating high intensity peaks within the acute angled sections. The obtuse angled sections are better protected against the near-field modulation due to destructive interference. The intensity modulation is dependent on the distance from the phase plate and in theory should reach a maximum at the Fresnel distance, approximately given by[4]

$$L = R^2 / \lambda$$

where λ is the wavelength, R is the radius of the diffracting object and L is the distance from it. In practice the modulation increases past this point, but this can be resolved by noting that in the randomness of the phase pattern, there will be sections of the mask that are sized as a multiple of the standard element size, with a correspondingly greater amount of energy and requiring a greater Fresnel distance. It should also be noted that in the analysis, a 64 by 64 array size was used and this results in an under-estimate of the intensity modulation for large longitudinal displacements due to the lack of contributions from the structure outside the array bounds.

Table I shows the relative intensities to be expected when using each of the four element shapes described in section 2.3. This data was taken calculating the modulations that each plate produces at distances from 20 cm to 400 cm.

Table I. Comparison of modulation ratios in the same focal plane

RPP design	Relative modulation ratio
Triangle	1.00
Square	1.11
Hexagon	1.15
Circle	1.20

The comparison shows that the fewer the number of vertices in any element the lower is the near-field intensity modulation for any given image plane. The lowest number of vertices in a regular tessellation is three, produced from the triangular structure. Therefore in terms of the near-field modulation it is beneficial to use the triangular structure RPP.

CONCLUSIONS

We have compared different mask structures and demonstrated good smoothing from all of the RPPs. Each RPP produces a slightly different far-field image and there is some advantage in using the circular structure as the subsidiary peaks have the lowest intensity. When comparing the propagation after the RPP the triangular structure produces the smallest peak to average modulations, which may be an issue if the RPP is used before the final focusing lens.

REFERENCES

1. Y Kato et al, *Physical Review Letters*, Vol. 53, No. 11, pp 1057-1060 (1984)
2. J Kelly (Editor), LLE Review Quarterly Report, DOE/DP40200-65, Vol 33, Oct-Dec 1987.
3. L G Seppala et al., LLNL - Poster paper CWF41. CLEO '91
4. Lipson and Lipson, Optical Physics . Cambridge University Press - Second Edition.

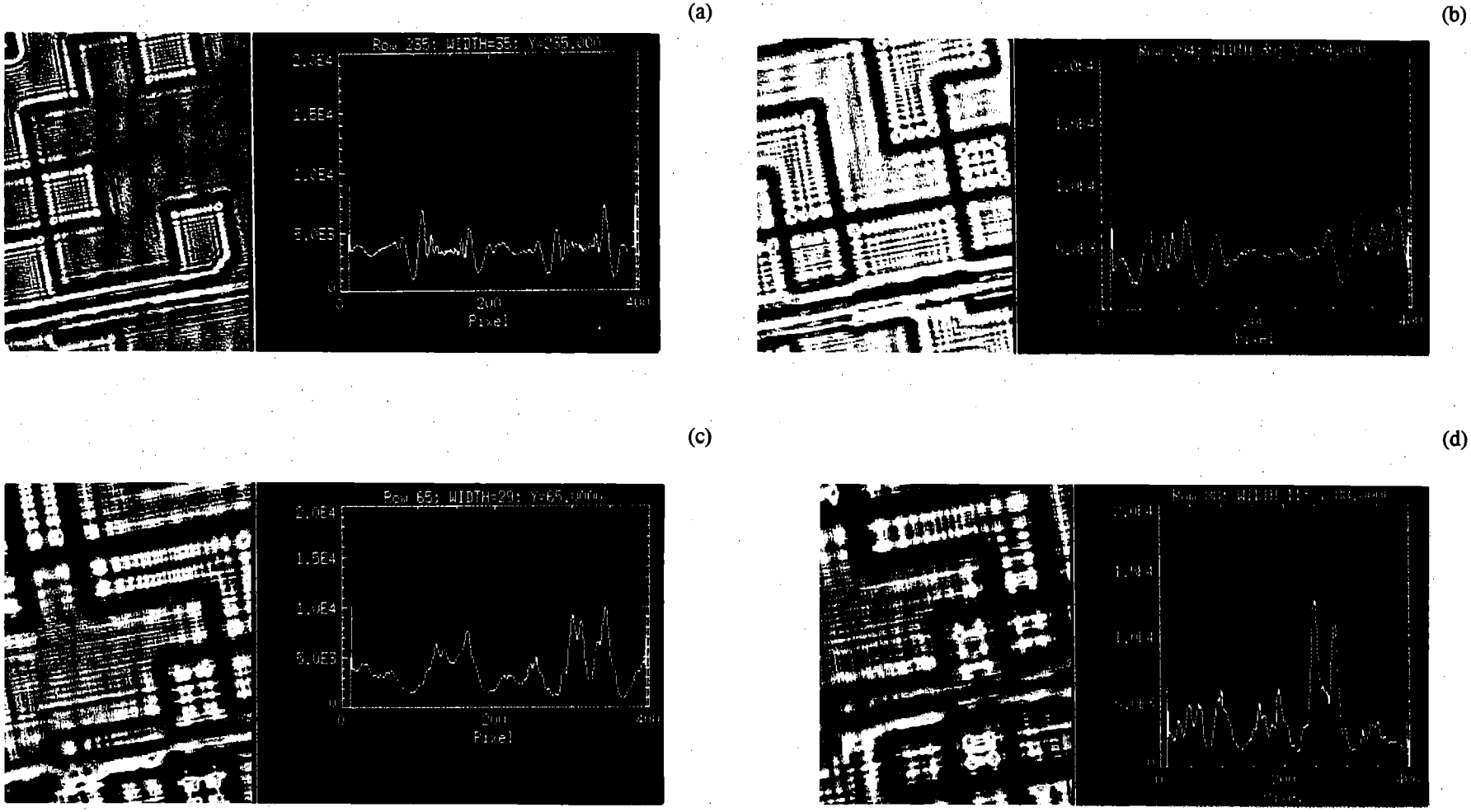

Figure 3 Experimental near-field modulation that occurs in a laser beam after passing through a 2 mm RPP
(a) 20 cm (b) 40 cm (c) 80 cm (d) 120 cm beyond the RPP

GENERATION OF UNIFORM INTENSITY OPTICAL AND X-RAY PROFILES USING BINARY PHASE ZONE PLATE ARRAYS *

R M Stevenson, M J Norman and T H Bett
Atomic Weapons Establishment PLC, Aldermaston, Berkshire,UK

D A Pepler, C N Danson and I N Ross
SERC Rutherford Appleton Laboratory, Chilton, Didcot, Oxon, UK

The generation of uniform focal intensity profiles is important for a number of applications including laser / plasma interaction experiments. We report on a technique utilising a binary-optic focusing system capable of producing uniform intensity optical and X-ray profiles.

Kato et al[1] developed the random phase plate to scramble the phase of the beam with the resulting improvement in the intensity profile due to the superposition of many small beamlets. These have been utilised successfully for a number of years at several labs in high power laser systems. However, these techniques are inefficient at producing top hat intensity profiles. Deng et al[2] has extended the work by using an array of refracting lenses to provide uniform illumination more effectively.

We report on the design, development and use of several novel binary phase plates for the generation of a range of focal profiles used to produce relatively flat top intensity distributions from a non-uniform input beam. This technique uses a phase zone plate array[3] (PZP), the design of which is based on the Fresnel zone plate, and a principal focusing lens. The twin lens combination gives a resultant focal spot size (FWHM) of

$$W_S = W_Z F_P / (R_m^2 / m\lambda - m\lambda / 4)$$

where: W_z is the diameter of the individual Fresnel zones; F_p is the focal length of the principal optic; R_m the radius of the Fresnel zone of order m; and λ the wavelength of light.

The phase plate is fabricated using conventional photo-lithographic techniques to give phase delays of 0 or π radians in the even or odd orders of the zone plates. Figure 1 shows a typical mask design used to generate the phase distributions of two PZPs. The black and white areas represent 0 or π phase shifts respectively. Each individual cell is randomly phased across the plate to minimise any zeroth order coherence spike. The PZP of this mask design produces a circularly symmetric focal spot with 94% of the incident beam energy contained in the focal region.

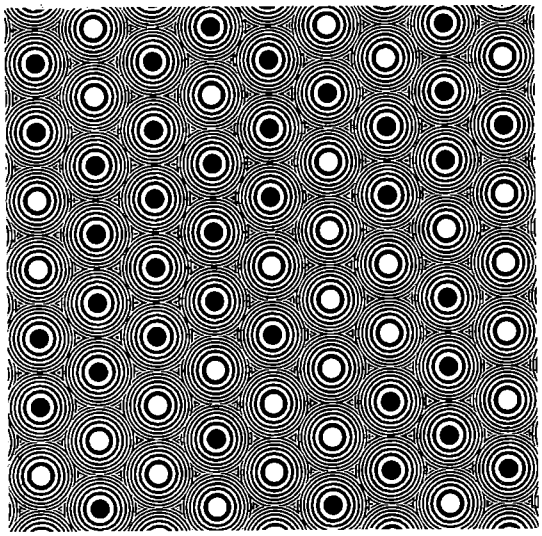

Figure 1 Typical mask design used for PZPs

The uniform intensity profiles obtained from these devices are a result of the overlapping images produced by de-focusing the principal lens / phase plate combination. Due to the averaging of many beamlets this technique is largely independent of the cross-sectional geometry of the input beam. The mask type shown above, with zones of 20 mm diameter and 17 m focal length is designed to be used with a 200 mm principal focusing lens and with a 0.527 µm laser beam and produces a 235 µm spot in the far-field. A line scan of the focal spot in the focal plane of the principal lens is shown in figure 2(a). A central spike is clearly present, but if the target plane is moved slightly beyond focus, the central spike can be defocused relative to the spot. For this particular PZP and focal length of the principal focusing lens the optimal focal plane is 300 µm after focus. The far-field image in this plane is shown in figure 2(b) where there is still a relatively flat topped focal spot but with a slight degradation in the edge definition. If the lens is further defocused the spot becomes more gaussian, as shown in figure 2(c). A comparison of the standard RPP alongside the PZP images is shown in figure 2(d). This image was taken using the same system as described above and also defocused by 300 µm.

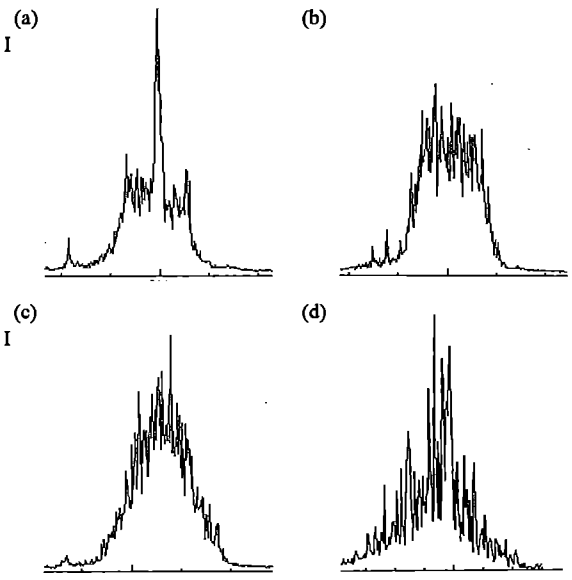

Figure 2 Focal spot profiles
(a) In focal plane (FP) (b) 300 µm beyond FP
(c) 500 µm beyond FP (d) RPP far-field

The range of focal spots that can be generated using this technique is limited by: the focal length of the principal focusing element; the size of the smallest elements of the zone plates which can be manufactured using the photo-lithographic process; and that the zone plate must contain a minimum number of elements. The graph in figure 3 demonstrates the range of focal spot sizes available for a 1 m focal length lens at 1.053 µm. The manufacturing boundary conditions of the PZP masks are given by the heavy lines. The solid line is where each Fresnel cell has only four zones, and the dotted line where the minimum structure size is 40 µm. The thin lines on the graph are lines of constant focal spot size, calculated from the Fresnel cell diameters and the focal length of the zone plate.

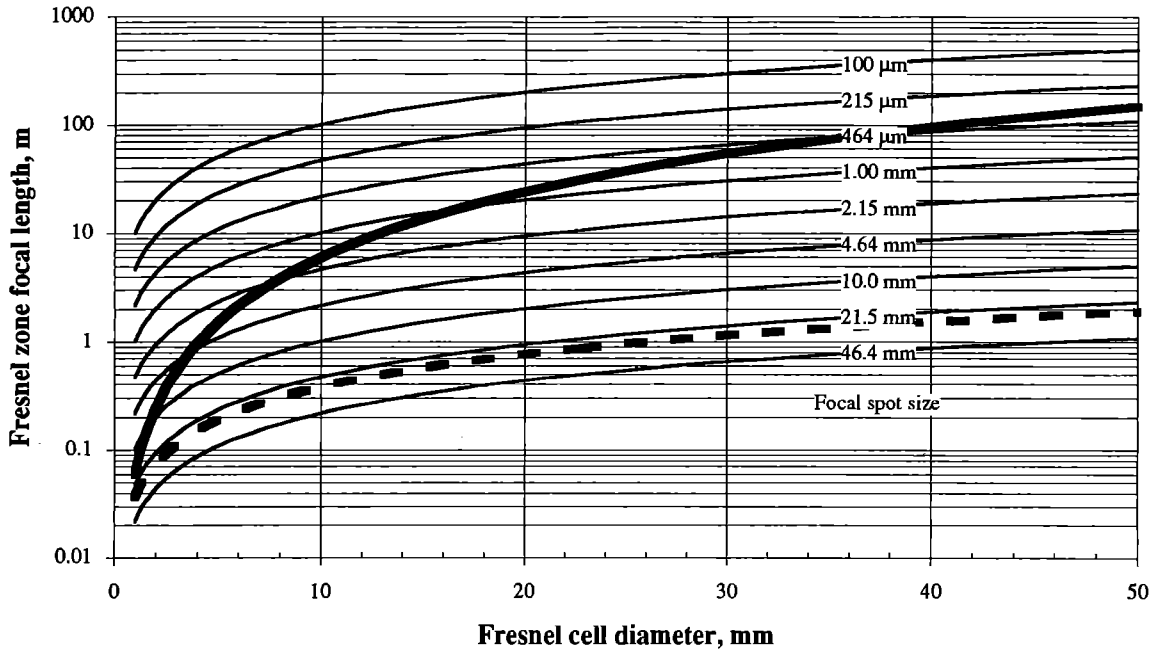

Figure 3 Graph showing the range of focal spots available using PZPs

The graph can also be used with focal lengths other than 1 m, and with different wavelengths. This is achieved by scaling the focal spot sizes by the focal length in meters and by the ratio of the operating wavelength to 1 µm.

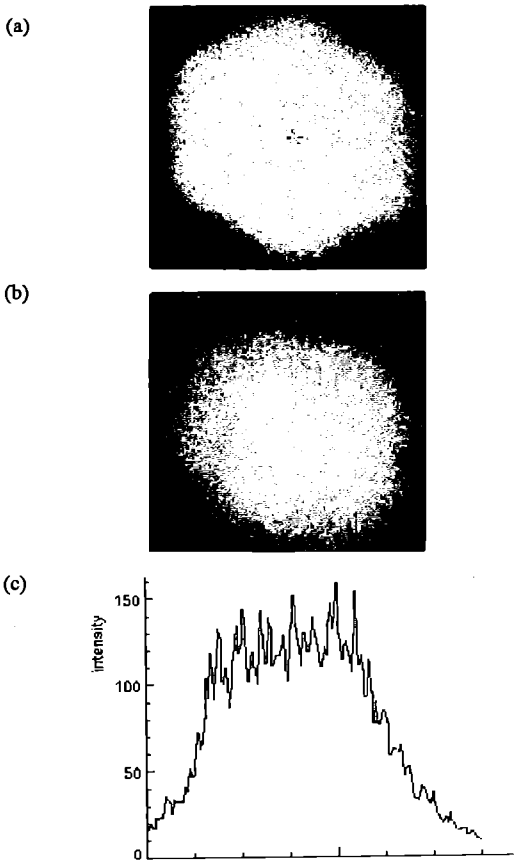

Figure 4 X-ray emission from gold foil
(a) Pinhole image in principal focal plane
(b) Pinhole image in optimum focal plane
(c) Line-scan through image

A laser / plasma experiment was conducted to monitor the effectiveness of the smoothing. The target was 100 µm thick gold foil, illuminated at normal incidence using a 300 ps pulse with ~15 J energy and of 527 nm wavelength. The optimum target plane was found to be ~200 µm from the principal focal plane. This is different from the optical measurements because the separation of the principal focusing lens and the PZP could only be controlled to within a few millimeters, enough to change the focusing conditions.

The X-ray emission produced from this target was detected with a pinhole camera filtered with beryllium. A pinhole image of the X-rays produced in the principal focal plane is shown in figure 4(a). This reproduces the optical images quite closely showing the bright central spot and the hexagonal structure. An image in the optimum plane is shown in figure 4(b) with a corresponding line-scan through the centre of the image in figure 4(c). The scan shows an extremely uniform X-ray image with a flat-topped profile.

CONCLUSION

We have used a novel focusing technique consisting of a principal lens and a PZP array. We have demonstrated the ability to produce flat topped optical and X-ray focal profiles. These are significantly more uniform and efficient than the profiles produced from a standard random phase plate. The new PZP arrays have been used in a number of laser / plasma interaction experiments and preliminary results indicate a significant improvement in the data obtained.

REFERENCES

(1) Y. Kato et al. Phys. Rev. Letters No. 53 p1057 (1984)
(2) X. Deng et al. Appl. Optics Vol.25, No.3 p377 (1986)
(3) L A Hornak. Appl Optics Vol 26, No 17 p 3649 (1987)

* Subject to provisional patent

MANIPULATION OF FOCAL PROFILES USING PHASE PLATES: DESIGN, SIMULATION AND USE

V.Biancalana[1], P.Chessa[1], C.Danson[2] and D.Pepler[2]

[1] IFAM (CNR) via del Giardino, 7 - Pisa - (Italy)
[2]CLF-RAL Chilton - Didcot - (UK)

INTRODUCTION.

Phase plates with randomly distributed phase areas (random phase plates, RPP) have been used for several years [1] to smooth the laser spots in ICF and related laser-plasma experiments. In spite of the invention of other very effective smoothing methods as induced spatial incoherence (ISI [2]) and smoothing by spectral dispersion (SSD [3]) RPP are still the most employed smoothing technique thanks to their simple and versatile use. Special RPP having high aspect ratio cells have also been used to make elongated focal spots in X-ray lasers experiments [4,5]. The physical effect of phase plate devices can be described in the far field region in terms of multi-beam interference and it can account for high contrast patterns with high spatial frequency distribution. The intensity distribution in the focal spot can be effectively controlled by the use of non-random PP [6]. The effect of both random and non-random phase devices can be evaluated numerically thus allowing accurate design of phase plates. Here we briefly report on the main features of a code [7], developed to simulate PP behaviour with realistic beams, then some results will be presented of the code together with simple physical descriptions of the analyzed devices. Some comparison with the experimental tests of the PP are then shown.

THE CODE

A code was developed to evaluate the e.m. field distribution on a cross-section of a laser beam which is focused by suitable lenses. Here we briefly describe the main features of the code, a detailed description being reported in Ref.7. The starting point of the code is given by the Kirchhoff theorem, which gives the e.m. field value in the point $\mathbf{r}=(x, y, z)$ related to a monochromatic field assigned on a plane covered by $\mathbf{r}'=(x', y', 0)$

$$E(\mathbf{r}) = \frac{k}{2\pi i}\int_{-\infty}^{\infty}\int_{-\infty}^{\infty} E(\mathbf{r}')\,\frac{e^{ikR}}{R}\,\frac{z}{R}\left(1+\frac{i}{kR}\right)dx'dy' \qquad (1)$$

where $k = 2\pi/\lambda$ is the wave-vector and $R = |\mathbf{r}-\mathbf{r}'|$. This formula can be reduced to standard Fourier integral under very weak conditions which are essentially given by the paraxial condition (small transverse size with respect to R) and "optical" approximation (small wavelength with respect to both transverse and longitudinal sizes). Eq.1 can therefore be written as

$$E(r)\,e^{-i\frac{\pi(x^2+y^2)}{\lambda z}} = \frac{k}{2\pi i}\frac{e^{ikz}}{z}\int_{-\infty}^{\infty}\int_{-\infty}^{\infty} E(r')\,e^{i\frac{\pi(x'^2+y'^2)}{\lambda z}}\,e^{-i2\pi\frac{xx'}{\lambda z}}\,e^{-i2\pi\frac{yy'}{\lambda z}}\,dx'dy'$$

where we see that apart from the dependence on z expressed by the term outside the integral, the values $E(r)\,e^{\frac{-i\pi(x^2+y^2)}{\lambda z}}$ and $E(r')\,e^{\frac{i\pi(x'^2+y'^2)}{\lambda z}}$ are linked by a 2D Fourier transform. Thus effective routines could be used to evaluate the Fresnel-Kirchhoff integral. Usually Gaussian distributions were used for the amplitude profile $|E(r)|$ of the field in the input plane. A phase term $\psi(r')$ was considered, and the complex value was in turn sampled in a 2D array. The real and imaginary parts $|E(r)|\cos(\psi(r'))$ and $|E(r)|\sin(\psi(r'))$ were then treated with FFT routines. Suitable phase distributions $\psi(\mathbf{r}')$ were assigned to this boundary condition $E(\mathbf{r})$ in order to take in account either spherical or cylindrical optics used to focus the beam. A term taking a discrete set of values as a function of transverse coordinates x , y was then added to the input phase in order to simulate phase plates, in this way several devices were simulated including squared and circular random phase plates, stripe phase plates, and other phase devices described below. A second term could also be added to the phase values in the input plane where the boundary condition is given. This term was a "regular" function of the transverse coordinates obtained by smoothing a random function generated by the computer. The average quadratical amplitude (variance) of the function was simply controlled by adjusting a multiplicative factor, while its "regularity" was set by recursive numerical smoothing of the function itself. These two parameters allowed us to use this term to simulate both aberration and reduced spatial incoherence of the beam, thus giving a "realistic" beam quality. The code output consists of both graphical files reproducing the laser spot with gray-scale pictures and numerical data reporting statistical properties of the intensity distribution in the spot. Input parameters can be easily scanned in a given range in order to point out the output dependence on some physical condition of the focused beam. For instance the spatial evolution of the focal pattern can be analyzed along the beam axis in given intervals around the focus.

RESULTS OF THE CODE AND EXPERIMENTAL FOCAL PATTERNS.

In Fig.1 focal patterns of ideal Gaussian beam are simulated passing through a squared element RPP (a), a "conventional" circular RPP (b), and a special RPP having a circular distribution of elongated cells (c), which gives a centrally peaked average intensity distribution. Portions of the respective RPPs are also reproduced. In Fig.2 three focal spots are shown from simulations of realistic beams; increasing phase disturbs were considered in 2a, 2b and 2c cases.
In Fig.3 the same realistic beam of Fig.2b is considered, passing through circular RPP. The phase difference introduced by the RPP was $\phi=\pi$ (as usually required) in the case of Fig.3a and $\phi=\pi/2$ in the case of Fig.3b. In the latter case the spot is given by the superimposition of a standard RPP pattern and the unsmoothed pattern. The theoretical weights of the two intensity patterns can be

easily evaluated to be $\sin^2(\phi/2)$ and $\cos^2(\phi/2)$ respectively.
The equivalent plane images shown in Fig.4 have been recorded by focusing an IR beam of Vulcan with different lenses. The beam was passed through a circular RPP. Both overall shape and internal structures can be compared to simulations. Differences in size are related just to different focusing condition. The RPP patterns are quite insensitive to the beam quality, in fact both simulation of Figs. 1b and 3a show features which are comparable to the experimental ones.
Stretching of focal spots have been studied and simulated with the use of either high aspect ratio RPP or cylindrical elements: related simulations are shown in Fig.5a and 5b respectively, while Fig.5c shows an experimental image of the spot obtained by lighting a scatter plate with the CW Nd beam focused by a tilted lens. A CCD was used to take the picture from an axis which was different from the laser one, the external frame reproduces a 1mm square observed by the same CCD and it is reported as a reference.
Special PPs have also been considered to produce multi-spot distributions. Phase gratings with very low dispersion are made up of stripe phase plates, both two or three maxima can be obtained in the focal spot, corresponding to ±1 and 0 diffraction orders. A device producing a triple spot in the focal plane was built and used in an experiment at CLF [8]: results of simulation, equivalent plane images and effects in laser plasma interaction are also reported elsewhere in this report [9].
A simulation for $\phi=\pi/2$, which gives three not exactly balanced maxima, is shown in Fig.6. The stripe phase plate is considered in conjunction with a stretching device which is a high aspect ratio RPP in the case of Fig.6a and a cylindrical element in the case of Fig.6b. The image shown Fig.6c was obtained with such a stripe phase plate having $\phi=\pi/2$ in conjunction with a tilted lens. The same CCD was used as for Fig.5c.

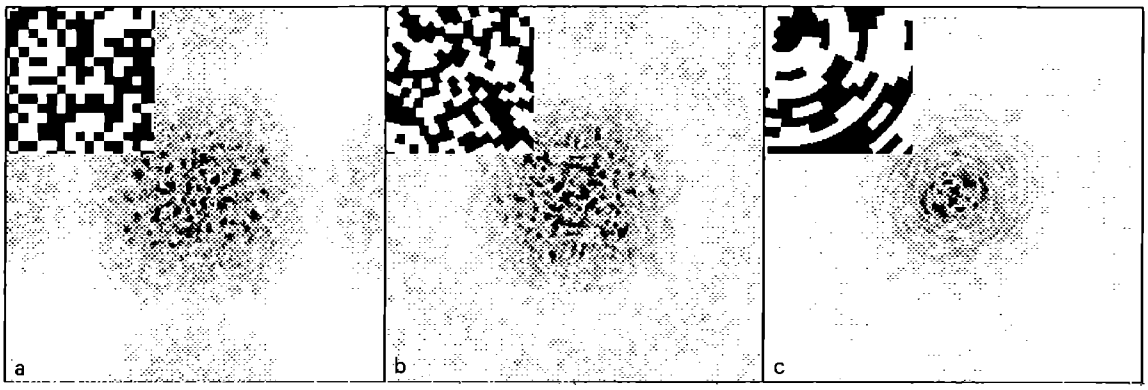

Fig.1: Simulation of squared (a), circular (b), and special (c) random phase plates with Gaussian beam. Portions of the respective plates are also reproduced.

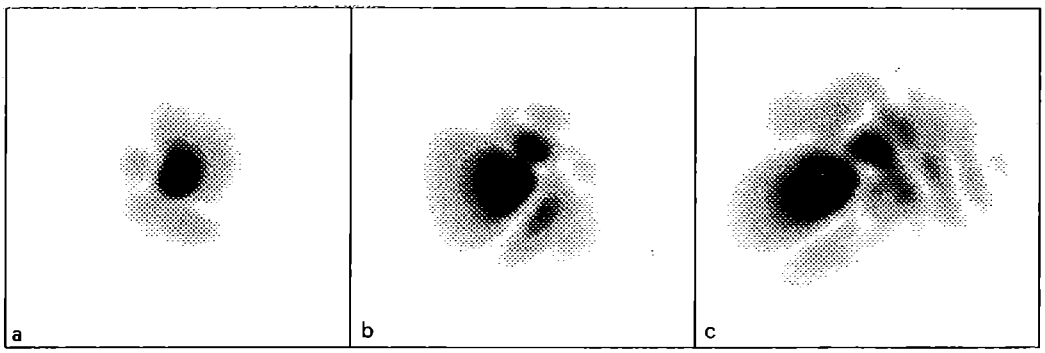

Fig.2: Simulation of realistic beams, the amplitude of the phase "disturb" increases from (a) to (c).

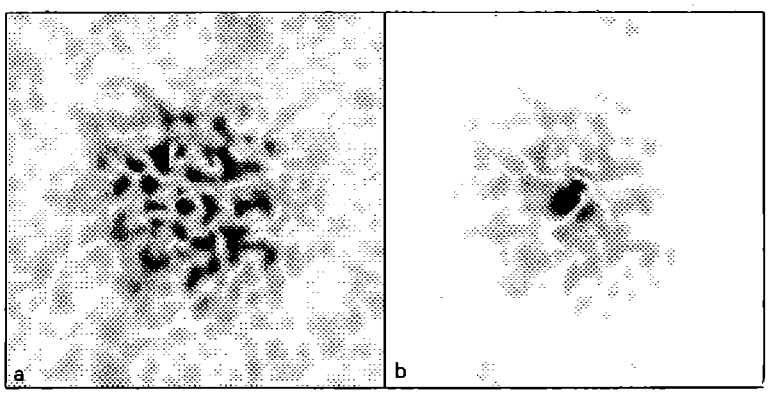

Fig.3: The same beam of Fig.2b is simulated after passing a circular RPP. The RPP dephasing is π in the case (a) and $\pi/2$ in the case (b). In the latter case a superimposition of patterns of Fig.2b and Fig.3a can be observed.

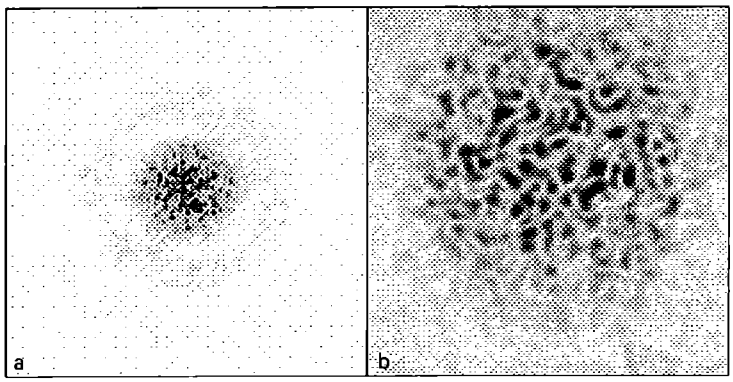

Fig.4: Experimental tests of circular RPP (dephasing $\pi/2$), 2 and 10 meters lenses respectively were used to focus a Vulcan IR beam. The secondary ring and the internal features can be observed in detail in (a) and (b) respectively.

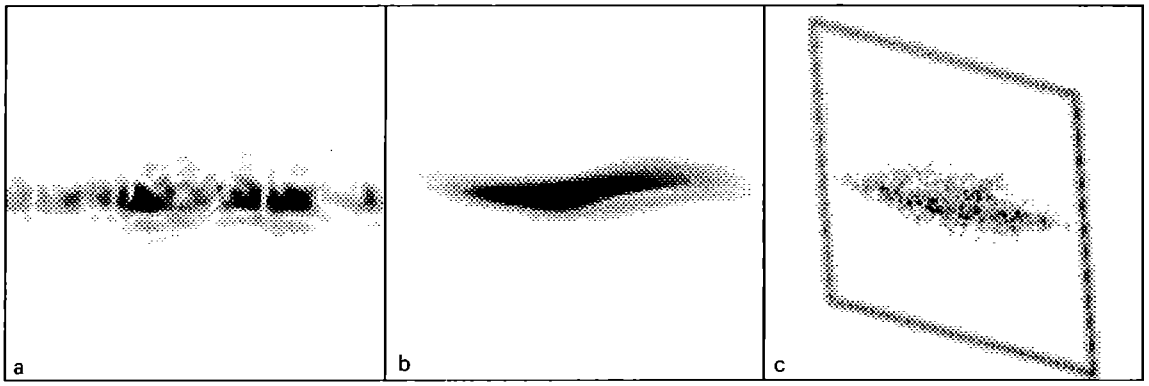

Fig.5: Stretching of focal spots. The effect of a high aspect ratio (10:1) RPP and of a cylindrical element was simulated in (a) and in (b) respectively. The experimental spot shown in (c) was observed by a CCD microscope looking at a diffuser lighted with a CW laser focused by a tilted lens. The reference frame is a square 1 mm in size.

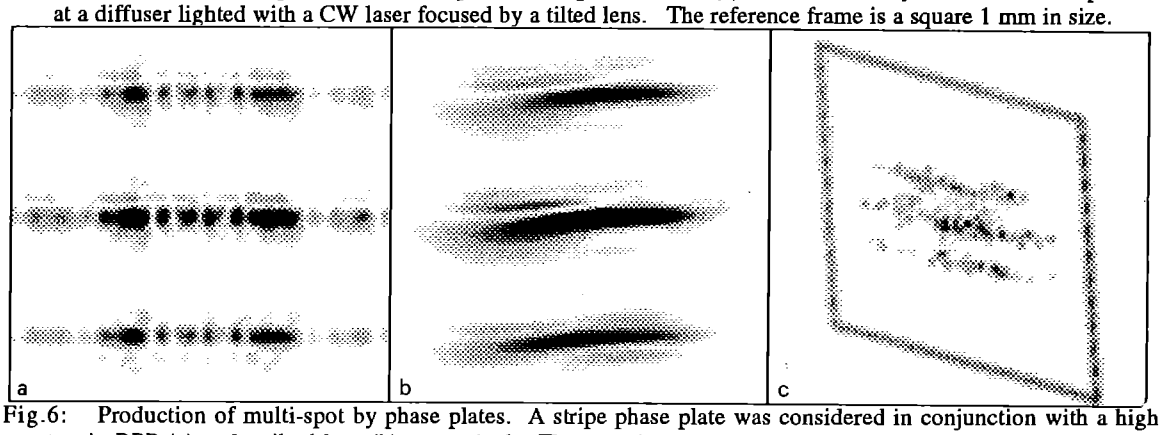

Fig.6: Production of multi-spot by phase plates. A stripe phase plate was considered in conjunction with a high aspect ratio RPP (a) and a tilted lens (b) respectively. The experimental spot shown in (c) was obtained as for Fig.5c.

In conclusion, it has been demonstrated that the effects of phase devices on laser beams can be effectively evaluated using a FFT code. We developed a code taking into account "realistic" beams, which were simulated by adding smooth random functions to the phase of Gaussian beams. By this code the effects of several phase plates were successfully simulated. Shape and overall size of the focal intensity distribution as well as statistical features of the pattern inhomogeneities can be accurately studied in simulation. Comparison with experimental tests showed very good matching between real and simulated spots.

REFERENCES

1. Y.Kato, K.Mima, N.Miyanaga, S.Arinaga, Y.Kitagawa, M.Nakatsuka and C.Yamanaka; Phys.Rev.Lett. vol.53 p.1057 (1984).
2. R.H.Lehmberg and S.P.Obenschain; Opt.Comm. vol.46 p.27-31 (1983).
3. S.Skupsky, R.W.Short, T.Kessler, R.S.Craxton, S.Letzering and J.M.Soures; J.Appl.Phys. vol.66 p.3456-3462 (1989).
4. C.Danson, R.Bann, J.Exley, D.Pepler, I.Ross, and I.Watson; Inst.Phys.Conf.Ser. n°116 (1990, IOP Publishing Ltd.)
5. M.Desselberger, L.A.Gizzi, V.Barrow, J.Edwards, F.Khattak, S.M.Viana, O.Willi and C.N.Danson; Appl.Opt. vol.31 p.3759 (1992).
6. H.Dammann and K.Gortler; Opt.Comm. vol.3 p.312-315 (1971).
7. V.Biancalana and P.Chessa; to be published in Appl.Optics (1993)
8. L.A.Gizzi, T.Afshar-Rad, V.Biancalana, P.Chessa, C.Danson, A.Giulietti, D.Giulietti, E.Schifano, S.M.Viana and O.Willi; 22nd Anomalous Absorption Conference, Lake Placid NY USA (1992).
9. A.Giulietti, T.Afshar-Rad, V.Biancalana, P.Chessa, C.Danson, D.Giulietti, L.A.Gizzi, E.Schifano, S.M.Viana and O.Willi; SERC-CLF internal rep. (1993).

ULTRA FAST LASER PULSE CHOPPING OF A 1.053μm LASER BEAM

A.K.L. Dymoke-Bradshaw[1], P.A. Kellett[1], C.N. Danson[2] and D.A. Pepler[2]
[1]Kentech Instruments Ltd. [2]Rutherford Appleton Laboratory

INTRODUCTION

A 25ns long 1.053μm laser beam has been successfully chopped with a Pockels cell driven by a solid state pulse generator to give pulse widths of ~100ps. Using this technique it should be possible to provide any pulse length from 100ps to several nanoseconds. A computer controlled pulse generator able to provide a range of pulse lengths is under construction. More recent developments in pulse generator technology may enable significantly shorter pulses to be chopped.

EXPERIMENTS

A Pockels cells, type 1112, made by Fast Pulse Technology Inc. driven by a newly developed pulse generator, has been tested on the Vulcan laser system with the aim of chopping a short pulse from the 25ns "Q" switched long pulse oscillator.

The Pockels cell uses two DKDP (KD_2PO_4) crystals and is "V" coated for use at 1.053μm. The optional "C" type connectors were used to try to improve the electrical bandwidth of the cell. In this configuration the quoted optical rise time of the cell is 85ps. The electrical performance of the cell was measured with a Tektronix sampling system looking at the transmitted and reflected electrical pulse from a S52 pulse generator (rise time of the measuring system is about 30ps). The results are shown in figure 1. These indicate that the Pockels cell electrical rise time is about 150ps.

The pulse generators used to drive the cell were two made by Kentech Instruments Ltd. The first was a 150ps 2.2kV pulser and the second a 65ps 3.8kV pulser that has recently been developed. Waveforms from these pulse generators are shown in figure 2. These pulsers use avalanche transistor technology to produce pulses with good reliability and low jitter (approximately 10ps rms).

The Pockels cell is placed between two "V" coated polarisers. The half wave voltage is expected to be about 3.2kV on these double crystal cells at 1.053μm. By operating below the half wave voltage one can expect to obtain somewhat faster optical than electrical speed due to the Sin^2 transmission coefficient. The second higher voltage pulse generator is probably too narrow to obtain efficient switching and much of the 3.8kV will be lost due to the relatively slow electrical performance of the cell.

The transmitted pulse was passed through an etalon, with a round trip spacing equivalent to 333ps, and then detected with a Hadland 675 S1 streak camera. Some typical results of the streaks are shown in figure 3.

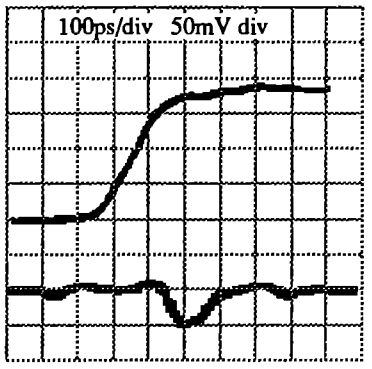

Figure 2 The transmitted (upper) and reflected (lower) pulses of a 200mV 30ps rising pulse into a 1112 Pockels cell

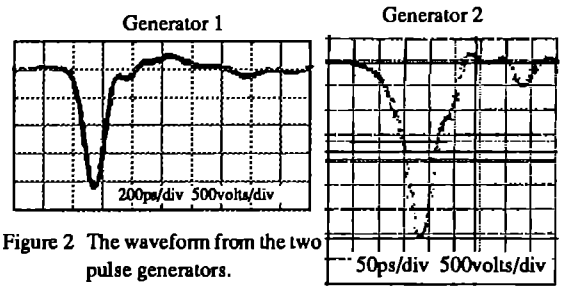

Figure 2 The waveform from the two pulse generators.

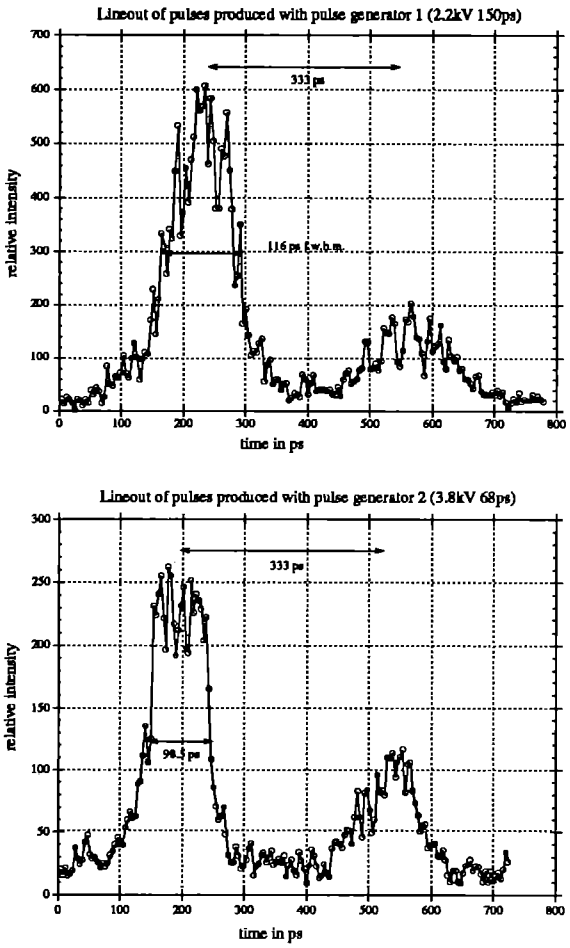

Figure 3 Lineouts of typical images obtained of the laser pulse after chopping, showing pulse widths down to around 100ps.

DISCUSSION

This technique shows that pulse lengths of the order of 100ps are obtainable. In order to improve on this several options are available. Firstly, a type 1111 cell may be used. This has a single crystal and consequently twice the half wave voltage. This would require 4 generators like the second one used here to achieve efficient switching. This cell is likely to be faster than the pulse generators.

An alternative would be to use the Pockels cell nonlinearity further and so obtain increased optical bandwidth for the same electrical bandwidth by pulsing the cell though a full wavelength of rotation. Pulse generators to do this are available and are capable of about 7kV in 75ps and consequently fairly fast optical response ought to be obtainable. The disadvantage of this technique is that the pulse generators can only produce pulses of few nanoseconds long and consequently a second slower pulse would follow the first unless some additional method of holding the chopping off is used.

NEW X-RAY LASER TARGET CHAMBER GEOMETRY

G.F.Cairns[1], D.M.O'Neill[1], C.L.S.Lewis[1], D.Neely[1], A.G.MacPhee[1]
C.Danson[2], A.Damerell[2], M.H.Key[2], D.Rodkiss[2], R.Wyatt[2]

[1]Dept. of Pure and Applied Physics, Queens University of Belfast, BT7 1N
[2]Rutherford Appleton Laboratory, Chilton, Didcot, Oxon

INTRODUCTION

The acquisition of a new cylindrical chamber represents a further major development in the X-ray laser programme. Funding from the X-ray laser rolling grant has provided a facility which can utilise the two 150mm backlighter beams available from the Vulcan laser, along with the standard six 110mm beams which have been used up to this point. The new chamber can be attached to the current spherical one or it can be used as a stand-alone chamber.

The current thrust of the X-ray laser programme is a) to enhance the Germanium and Yttrium x-ray lasing beams for application purposes such as X-ray microscopy and holography, where beam coherence is of particular importance, and b) to develop shorter wavelength lasers approaching the water window. The new Vulcan facility described here addresses the first of these issues and represents the first phase of providing a user beam-line for 15-25nm lasers.

CHAMBER HARDWARE

A schematic diagram of the new chamber geometry is shown in figure 1 and a photograph of the actual facility is shown later. It shows the new chamber bolted to the spherical one, with the two 150mm beams coming in from opposite sides in the horizontal plane. The beams are brought to line foci along the main axis using a combination of two cylindrical lenses and an aspheric/spheric doublet on each side. In the first experiment using this setup, the new target geometry was used in an 'amplifier' mode, where its plasma was effectively seeded by the x-ray laser signal from the standard double target configuration in the 'old' spherical chamber, now acting as an 'injector'. Coupling was achieved using an imaging concave x-ray mirror (fig.1). A number of options are available for feeding the 150mm beams into the new chamber.

These options include, as illustrated in figure 2:

1)Opposing beamlines,

a) Offset from common axis: this allows for the standard opposing slab geometry as illustrated in figure 1, (2a).

b)Centred on a common axis: this is particularly appropriate for the shooting of foil targets symmetrically from both sides, (2b).

2)Same side angled in vertical plane: this should allow for shooting at higher intensities by overlapping beams or for shooting longer line foci, (2c).

3)Stand alone configuration: this provides for all eight beams(6*110mm and 2*150mm) going into the new chamber. This is illustrated in (2c) by the inserted broken lines. Two rings of ports around the chamber allow

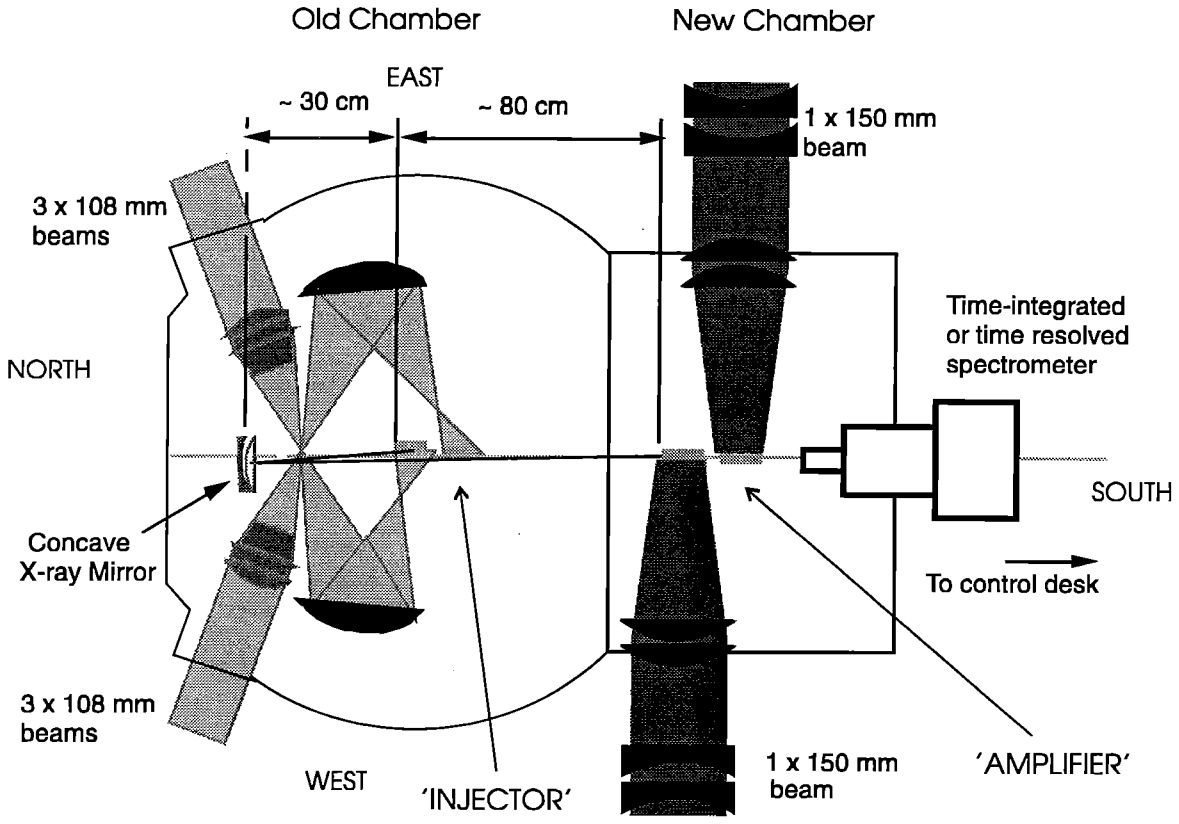

Figure 1 New Chamber Geometry

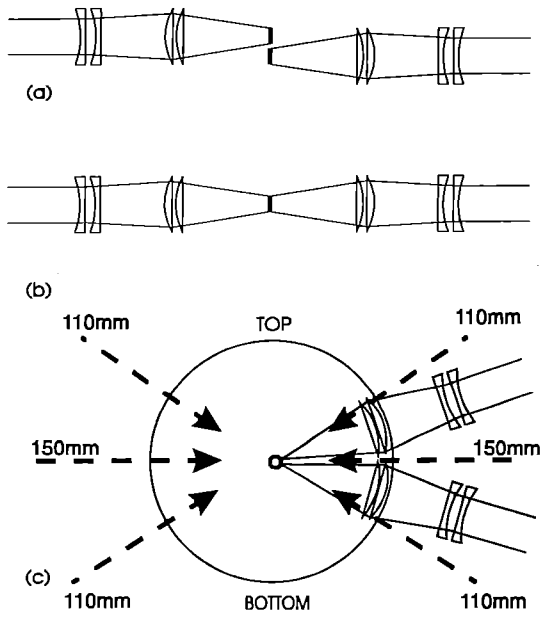

Figure 2 Beam Configurations

the 2*150mm beams plus 4*110mm beams to enter on one ring whilst the other two beams enter further along the chamber. A number of other permutations of this setup are possible.

Both possibilities in option(1) were used in the first experiment with foil targets being shot with the opposing centred beamlines.

LINE FOCUS OPTICS

The optics for producing the horizontal line focus from the 150mm beams consisted of an aspheric/spheric focusing lens doublet and a pair of cylindrical diverging lenses, (fig.3). Their specifications are given in table 1. By varying the angle between the crossed axes of the cylindrical lenses, the degree of divergence in the horizontal plane can be changed, which in turn modifies the length of the line focus. With the axes perpendicular to each other (90degrees), a spot focus is produced and when the axes are parallel (0 degrees), the maximum divergence is produced. In fact two line foci are produced which are perpendicular and displaced relative to each other. As the angle between the axes is increased, the line foci move towards each other and get shorter. The length of line focus not only depends on the angle of rotation but also on the separation of the cylindrical pair and the doublet.

Extensive ray tracing analysis using the Beam4 Stellar software package was carried out during the lens design phase. It was possible to estimate the intensity distribution in the line focus plane. Taking multiple reflections into account, the optical component separations, including the window and pellicle, were optimised for given focal length ranges. It is not possible to access all focal lengths from 0mm-40mm using one setup. Instead several different spacers are required to set limits on the cylindrical-spherical lens separation for different focal length ranges. Spacer flanges which hold the window and cylindricals in a fixed position relative to the chamber achieve this end. The line focus closest to the spherical lenses was used in the first experiment with typical lengths ranging from 10mm to 25mm for the given 25cm spacer flange.

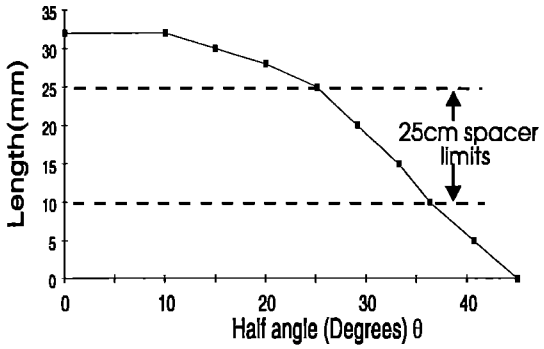

Figure 4 Line focus length versus rotation angle

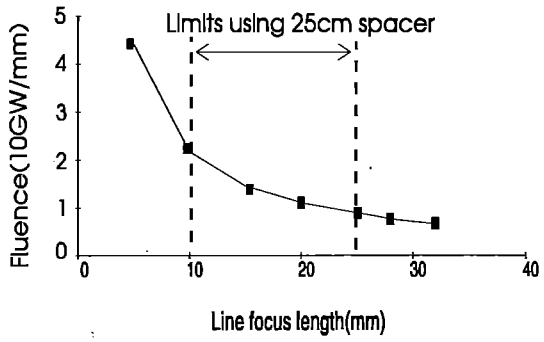

Figure 5 Estimated fluence/mm for different lengths

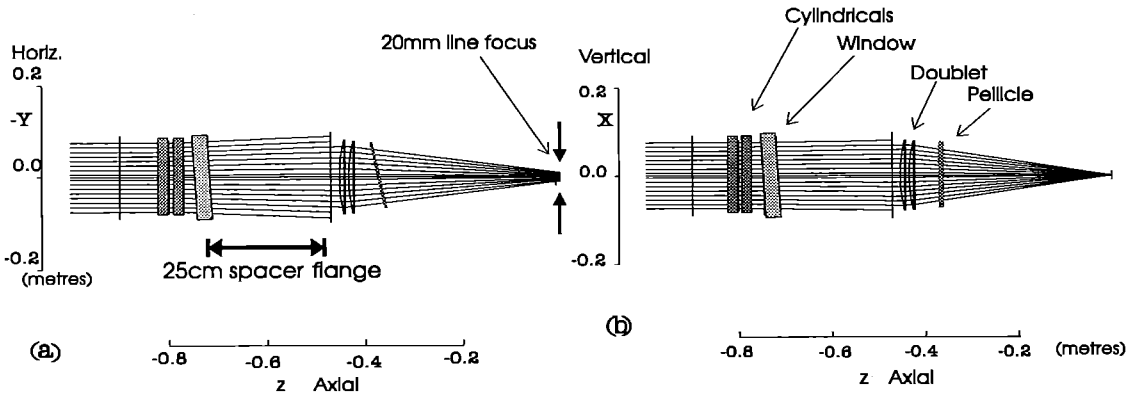

Figure 3 Schematic view of optics for a 20mm line focus

Lens Type	Plano-convex spherical	Plano-convex aspherical	Plano-concave cylindrical
Material	Spectrsil 'B' fused quartz	Spectrsil 'B' fused quartz	BK-7 glass
Diameter	156mm	160mm	160mm
Centre thickness	12mm	11mm	15mm
Radius of curv. Surf.#1	350.8mm	373.8mm	1345.3mm
Radius of curv. Surf.#2	Flat	Flat	Flat
Focal length	780.1	831.3	-2991.5mm
Refractive index (1054nm)	1.4497	1.4497	1.5067

Table 1 Optics specification

In practice, the cylindricals are adjusted relative to each other to give a desired length, and then the composite is rotated to align the line focus horizontally. The doublet lens has to be moved along its optics axis in order to keep the line focus on the main chamber axis; in general as the line focus length is increased ,the doublet has to move closer to the main chamber axis.

The effect of beam energy leaking past a target into the opposite beam optics and possibly back again was also minimised by modelling using the ray trace software. This was particularly important when the beamlines were centred opposite each other for shooting foil targets.

Figure 4 shows the variation of the line focus length with the angle of rotation for a 25cm spacer case. The angle of rotation θ, is defined as the angle each cylindrical lens is rotated /counter rotated from the case where both cylindrical axes are parallel and vertical. Beyond a length of 25mm the end of the line gets clipped due to the spherical lens housing being smaller than the expanded beam. Consequently the longer lengths use a smaller portion of the input beam. The limits of the usable lengths are also shown.

An estimate of the fluence per unit length for different lengths of line focus is shown in figure 5.

ALIGNMENT OF NEW TARGET

The new target was aligned along the main axis using two telescopes, a collimated HeNe beam and an illumination source. By reflecting the HeNe beam off the surface of the target substrate, and projecting it onto a precalibrated screen, it was possible to set the target in angle relative to the main axis in the horizontal plane. Using the transverse axial telescope, #2 in fig.6, a magnified image of the end of the target allowed alignment in the x-direction, i.e. along the E/W axis; its crosswires had been prealigned on the main axis.

A strong halogen lamp was projected into the chamber and by means of a mirror and colliminating lens, made to illuminate the full length of the target. This allowed a telescope (#1 in fig.6), to project a magnified image onto a screen, which had been pre-referenced to an aligned dummy target. It was then possible to set the target's position in the vertical(y), and in the axial(z) i.e. N/S direction, as well as aligning it in the horizontal plane. The projection telescope resided in the horizontal plane of the target.

When using the opposing double target configuration, the two targets were aligned relative to each other off-line as for the standard targets.

ALIGNMENT OF THE COUPLING X-RAY MIRROR

In the first experiment using the new setup, the output x-ray laser beam was coupled from the 'injector' into the new target plasma, to act as a seed, using a multilayer Mo/Si mirror of focal length 0.25m (fig.1). The concave mirror was optimised to select the 23.6 and 23.2nm Germanium lasing lines. It had the advantage over direct coupling of selecting the wavelength range of interest and of imaging the beam into the amplifying plasma thus providing some control over the degree of coupling.

Alignment of the XRM was achieved using an optical fibre dummy target in the usual injector target position. A HeNe laser was coupled into it. A CCD camera with a graticule was placed at the 'amplifier' input face position and the XRM adjusted to image visible light from the 'injector'/(fibre) output face to the reference graticule. A highly magnified image was produced by using a microscope objective extended out from the front of the CCD camera. The camera and graticule were mounted on a base plate which could be placed on the new target mount for each alignment procedure. Initially the drop in mirror was inserted and the tranverse axial reference HeNe beam focused onto the graticule, using the transverse telescope. The graticule was located along the main axis (N/S) where the end of the 'amplifier' target would be located. By

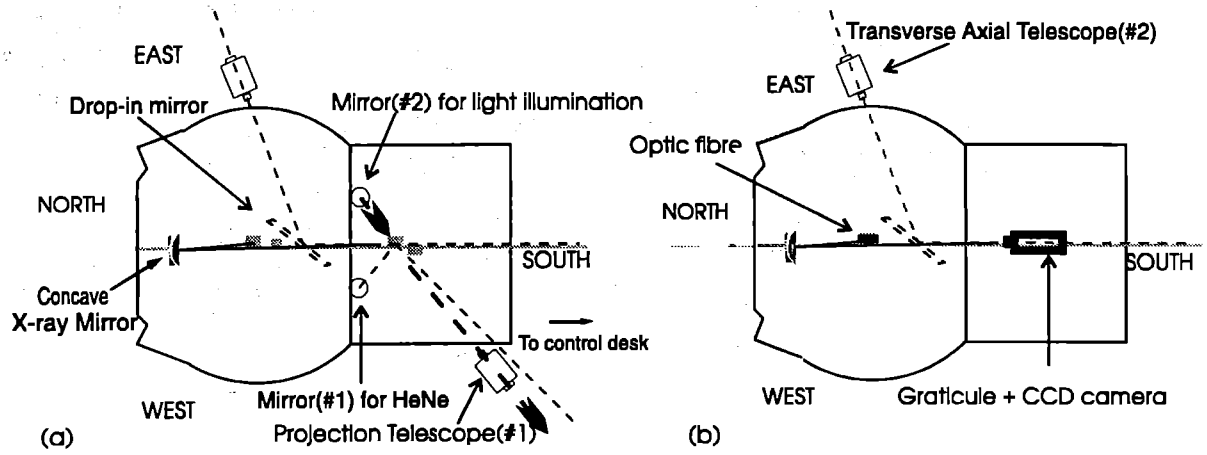

Figure 6 Alignment Arrangement

adjusting the target mount drives, the reference HeNe spot was centred on the graticule whilst its image was observed on the TV screen.

Having referenced the 'end of target' position on the screen, the drop-in mirror was removed and the fibre mount aligned in the 'injector' position. The light from the fibre end corresponded to the lasing beam output from the north end. Adjustment of the XRM allowed the output from the fibre to be imaged onto the centre of the graticule, the referenced position. An offset of the imaged spot had to be introduced to correct for two things, i) the fact that the fibre was cylindrical and of cladding diameter 110microns; therefore its output did not coincide exactly with the output lasing beam, ii) the optimum position of coupling into the second plasma i.e. for the optimum gain region, was located at some distance (~100um), from the target surface. The lateral displacement of the focused spot was achieved by driving the XRM sideways(E/W direction), whilst observing the spot moving on the TV screen. Settings could be made to better than 50μm.

Offset from common axis: this allows for the standard opposing slab geometry as illustrated in figure 1, (2b).
Offset from common axis: this allows for the standard opposing slab geometry as illustrated in figure 1, (2b).In order to align the end of the amplifier in the N/S direction an aperture with two holes to either side was placed in front of the XRM. This gave two beams which were brought to a focus at the graticule. By moving the focusing point i.e. by moving the XRM along the main axis, two spots were observable. On the TV screen these spots appeared to come together and move apart as the focused point was scanned along the axis. This allowed estimation of the axial(N/S) position to better than 3mm.

SUMMARY

An account has been given of the new X-ray laser chamber geometry as used in the current series of experiments on the Vulcan laser. The cylindrical optics have been shown to give good line foci, the lengths of which can be varied by varying the angle between the cylindricals' axes. Depending on the spacer flange used, a number of ranges of foci lengths are available; the size of the spacers have been determined by detailed modelling to reduce the effects of ghost reflections.

The alignment system for the 'injector'-'amplifier' configuration allows for settings to better than 50μm in the transverse direction and to better than 3mm along the main axis, for the coupling of the 'injector' plasma output into the end of 'amplifier' by the XRM.

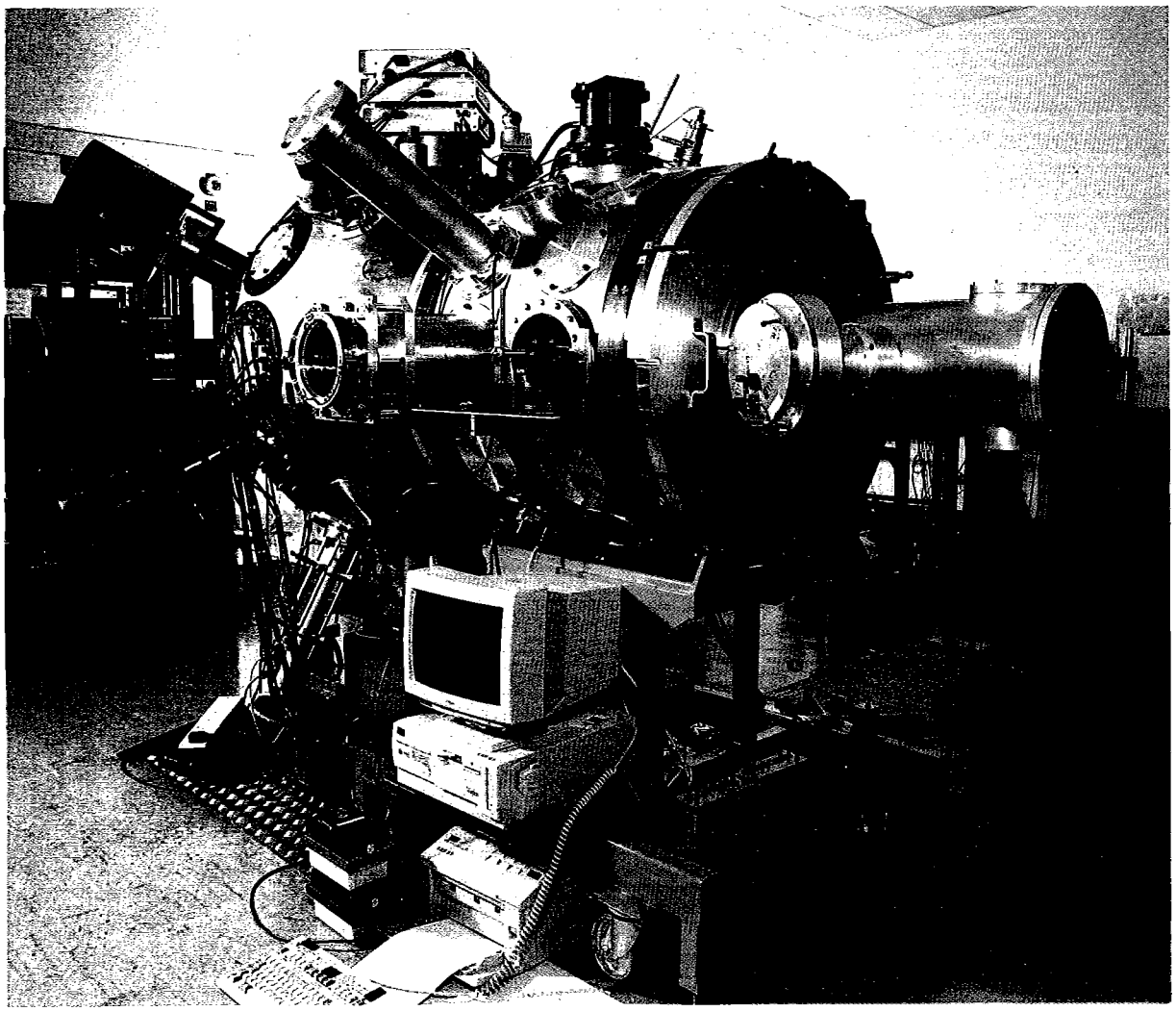

CCD IMAGING FROM 0·7keV TO 8keV WITH MULTI-PINNED PHASE TECHNOLOGY.

A. G. MacPhee and C. L. S. Lewis

Department of Pure and Applied Physics
Queens University of Belfast
BT7 1NN

INTRODUCTION

A ccd based imaging system, from Andor Technology LTD, has been used for x-ray detection from 4·2Å-10·05Å (1·238keV-2·95keV). The detector head incorporates an EEV 15-11 series, ultra-low dark current, inverted mode device, (table 1):

No. of Pixels	1024x256
Pixel size	27μm square
Image area	27·6mm×6·9mm
Full well capacity (image)	250 000 electrons
Full well capacity (readout)	$>10^6$ electrons
Charge transfer efficiency	0·999999
Dark signal @ 20°C inverted mode	400 electrons/element/s
Dark signal @ -20°C inverted mode	5 electrons/element/s
Dark signal @ 20°C standard mode	$3.5x10^4$ electrons/element/s
Dark signal @ -20°C standard mode	650 electrons/element/s
Output amplifier sensitivity	3.6μV/e
Output amplifier gain	0.54 into 32KΩ

Table 1

The reduction in generation-recombination current inherent in these devices is achieved by maintaining the silicon surface at the oxide interface in complete inversion during integration and partial inversion during readout: Throughout operation, the p-type substrate is biased to the potential present at the interface between the n-type buried channel and the gate insulating oxide layer when the clocks are low. Holes flow into this interface region from the p-type channel stops between adjacent pixel columns, *totally* quenching thermal carrier generation. An asymmetric potential well structure in the three phase charge transfer register provides a potential barrier between pixels whilst all clock phases are low and hence their oxide interfaces in inversion. This is achieved by implanting a low concentration of a p-type impurity (Boron) into the upper region of the buried channel under one of the electrodes, soaking up the n-type buried channel charge there, thus reducing its associated channel potential. During readout, the *high phase* of the gate clock duty cycle (i.e. the time when the interface is *no longer* in inversion and hence reverts to the conventional level of leakage) is sustained only so long that the charge transfer efficiency of the device is not compromised. A net reduction in dark current of approximately two orders of magnitude results over conventional devices operating at the same temperature.

DETECTOR SENSITIVITY

The polysilicon gate structure and insulating silicon oxide/nitride layers of EEV CCDs are roughly 1·5μm thick. Hence below 1keV, where photon absorption lengths are less than 2μm, sensitivity drops off and is ultimately limited to about 0.7keV with DQE~14%. The depletion region is approximately 15μm thick, so that above 8keV, where the absorption length is greater than 20 μm, DQE drops below 24%. Maximum DQE, ~80%, is reached at about 2·5keV, (fig.1)[1].

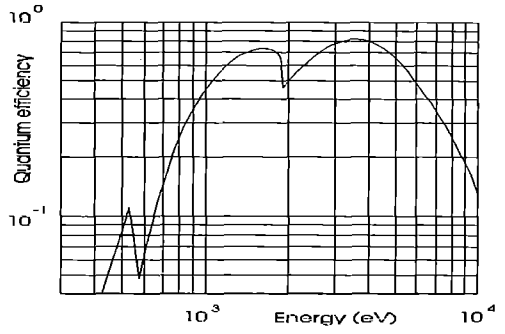

Fig.1 X-Ray QE of EEV 15-11 series CCD[1]

SYSTEM PERFORMANCE

The RMS noise of the system at -20°C is equivalent to approximately 15 electrons per read cycle. 16-bit digitisation is therefore set at 1 count = 12·5 photo-electrons, for 1·2 counts RMS noise. From 1·15eV to 3·5eV, electron hole pairs are generated by the inner photo-electric effect with an internal quantum efficiency of 1, with excitation of electrons across the silicon valence-conduction band gap (1·1eV). Secondaries are not generated until the threshold for impact ionisation, ~3·5eV, which tends to a mean 3·65eV required per electron hole pair generated by about 10eV incident photon energy. The excess energy above that of the band gap is lost to the lattice through phonon excitation at the Raman vibration energy (0·063eV): The number of phonons excited between electron-hole pair production events is equal to the ratio of the mean free path for impact ionisation to that for Raman scattering, ~17·5. The residual energy deficit is due to the distribution in final charge carrier energies below the impact ionisation threshold. Hence for one incident 2·5keV photon, 44 counts are recorded.

Software control of the clock phases on the image and readout registers and the reset gate at the output amplifier, allow for horizontal and vertical binning of pixel data prior to digitisation, for enhanced signal to noise and dynamic range. Reset noise at the output FET is eliminated by correlated double sampling. Data acquisition occurs at a pixel rate of 77 kHz, for a frame rate of 0·29 Hz with no binning and 75 Hz with all pixels binned in the short dimension. The system can be set to trigger automatically on detection of a signal variation across the device, or externally with a 13μs pre-trigger. A calibrated temperature controller circuit regulates the current delivered to a peltier cooler to maintain the CCD at a pre-set temperature, down to -40°C.

APPLICATIONS

Through analysis of the ionisation balance obtained from spatially resolved measurements of resonance line emissions from a high aspect ratio laser-plasma, the relative temperature along the column can be estimated. In

conjunction with a suitable detector, geometries of Bragg crystal spectrometers incorporating various crystals and a space resolving entrance slit have been demonstrated to spectrally resolve such emission with sufficient dynamic range to permit this analysis. The CCD head has been customised to interface with such an instrument utilising a single curved (300mm radius convex) KAP crystal (fig.2). This increases spectral range and angular tolerance, whilst reducing source broadening (figs.3):

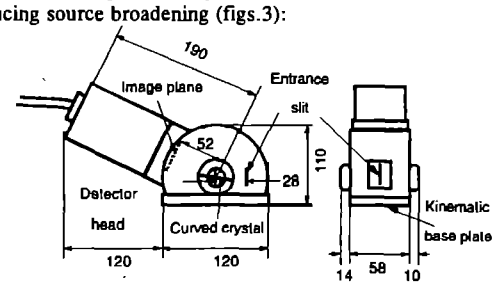

Fig.2 CCD crystal spectrometer schematic (mm).

The system has been used to monitor the uniformity of irradiation of targets in X-ray laser experiments at RAL[2,3] (July '92-Aug. '92: Ne and F-like spectra from Y plasmas; 300μm spatial resolution over 30mm; 4·23-5·88Å spectral range; 10mÅ crystal limited linewidths, Nov. '92-Jan. '93: Ne and F-like spectra from Ge plasmas; 300μm spatial resolution over 30mm; 7-10·05Å spectral range; 10mÅ crystal limited linewidths, fig.4 and at the ILE Osaka[4] (Oct. 92'-Nov. 92': Ne and F-like spectra from Ge plasmas; 720 μm spatial resolution over 50mm; 7-10·05Å spectral range; 10mÅ crystal limited linewidths). During the experiment in Japan, spectral data were reduced using PV-WAVE on a DEC5000 workstation at Queen's Belfast via internet; the results being available for presentation at both sites within twenty minutes of a laser shot.

Alternative front ends for the detector under development include single slits with step-wedge x-ray filters for 1D imaging with multiple energy transmission bands; differential magnification crossed slits and pinhole arrays for 2D plasma imaging.

By replicating the process for 1024×256 pixel device production in the short direction, whilst omitting the readout register from the long dimension, large arrays with 1024×(n×256) pixels of the same series are also available for pinned mode operation. In addition, arrays with active imaging areas distributed across a large wafer are available to permit small areas of interest to be interrogated over a large image area at reduced readout time. Hence cooling requirements are relaxed and data file size reduced, along with the obvious reduction in price compared to very large area imagers.

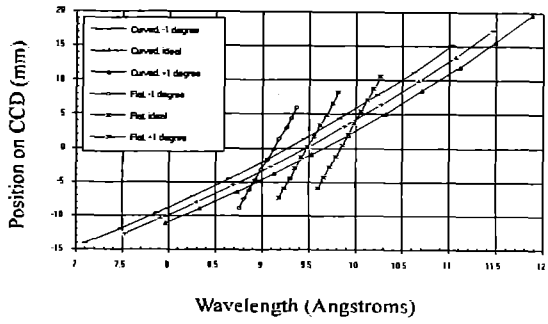

Fig.3 Dispersion curves for KAP (2d=26·64Å): 550mm from source; 80mm to detector; 300mm radius convex and flat crystals; ideal and ± 1° incidence.

With single kilovolt photons producing hundreds of electron hole pairs in the substrate, keV X-ray downconverting phosphors are being investigated in order to both reduce and linearise the overall sensitivity of the system above 700eV, enhancing the dynamic range of the system for these energies by greater than an order of magnitude.

For the UV-XUV region from 10eV-1keV; a system with the potential for photon counting with 27μm² resolution and > 13 bit dynamic range is being developed, using rare earth phosphors to be coupled to the chip via a fibre optic window, ultimately to be coated onto the chip directly and overcoated with 1000Å Al for a light tight shield, completing the spectral range accessible to CCDs for laser plasma diagnostics.

REFERENCES

[1]. C. Castelli, et al, 'Soft X-ray Response of Charge Coupled Devices', NIM **A310**, 240-243 (1991)

[2] CLS Lewis et al, 'Collision pumped soft X-ray lasers: progress at RAL', Proceedings of the 3rd International Colloquium on X-ray Lasers, pp23-30, (1992).

[3] C.L.S. Lewis et al, 'Soft X-ray laser coupling between independent plasmas via a concave relay mirror',SERC Central Laser Facility, Ann. Rept., (1993)

[4] H. Daido et al, 'Germanium Soft X-Ray Laser in a Wall Confined Laser Produced Plasma', OSA Short Wavelength V: Proceedings of the Second Topical Meeting, Physics with Intense Laser Pulses, March 29-31, (1993)

ACKNOWLEDGEMENTS

The author wishes to recognise the assistance provided by Andor Technology LTD (10 Malone Rd., Belfast, BT9 5BN), through their provision of the imaging system and many useful discussions.

Fig.4 Typical kilovolt spectrum from Ge plasma.

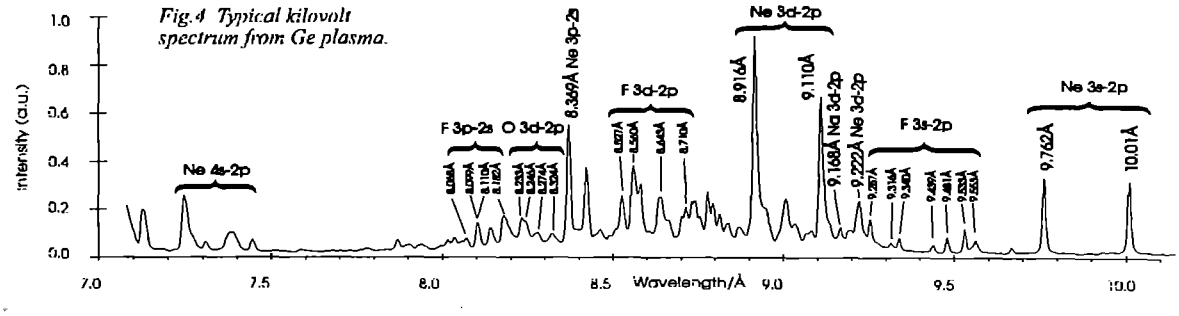

SYNCHRONISATION OF THE OUTPUTS OF A CW MODELOCKED OSCILLATOR AND A Q-SWITCHED LONG PULSE OSCILLATOR

CN Danson, L Barzanti, DA Pepler and RWW Wyatt

Rutherford Appleton Laboratory

INTRODUCTION

This report describes a technique for synchronising the output of a cw modelocked oscillator to actively Q-switched and / or actively modelocked oscillators. We present results of experiments to synchronise a cw diode pumped Nd:YLF additive pulse modelocked (APM) oscillator to a single longitudinal mode Q-switched long pulse oscillator to better than 50 ps. Several oscillators, producing either short (70 ps - 200 ps) or long (600 ps - 4.5 ns) pulses and either narrow-band or broad-band outputs are available for use on VULCAN. In normal operation two of these oscillators are operated side-by-side, injecting their respective pulses into two separate amplifier chains. These two pulses are required to be synchronised to better than 50 ps.

To increase the range of pulsewidths available a cw APM oscillator was installed, which produces a train of 2 ps pulses. These are produced at a rate of 134 MHz, and the requirement was to synchronise one of the 2 ps pulses with one of the other more standard long pulse oscillators.

For initial experiments the need for absolute synchronisation was not important, only one amplifier chain was being required on alternate shots and timing jitter of the order of several hundred picoseconds could be tolerated. However, the dual pulse operation was also being requested for future operation with the short pulse to be used as a probe for longer pulse experiments.

SYNCHRONISATION SYSTEM

Figure 1 shows a schematic of the system to synchronise the pulses from the APM oscillator and the long pulse oscillator. The long pulse oscillator cavity is kept in a low-Q state by means of a negative feedback circuit. This establishes a pre-lase by clamping the first relaxation oscillation generated following the firing of the flashlamp. The pre-lase level can be maintained for tens of microseconds which allows the cavity to stabilise prior to Q-switching, and provides time for the synchronising of the system trigger with the APM oscillator frequency-generated RF signal. The rising edge of the first relaxation oscillation is detected using a photodiode to trigger a pulse generator. This in turn, is used to trigger the sync circuit and produce a pulse which is synchronous to the RF generated from the APM oscillator.

The RF is derived directly from the APM oscillator output by means of a photodiode which is fed into an RF amplifier. The amplifier, with a 150 MHz roll-off followed by a low frequency filter, is effective in keeping the signal free of noise, and allows for a truly synchronous signal to the optical pulse train of the oscillator to be introduced to the synchronising circuits. The synchronising circuit 'sync box' is triggered by a pulse derived from the long pulse oscillator, and produces an output signal synchronous to the phase of the APM oscillator, which is used as the VULCAN system master trigger.

The master trigger is then fed into a pulse distribution system

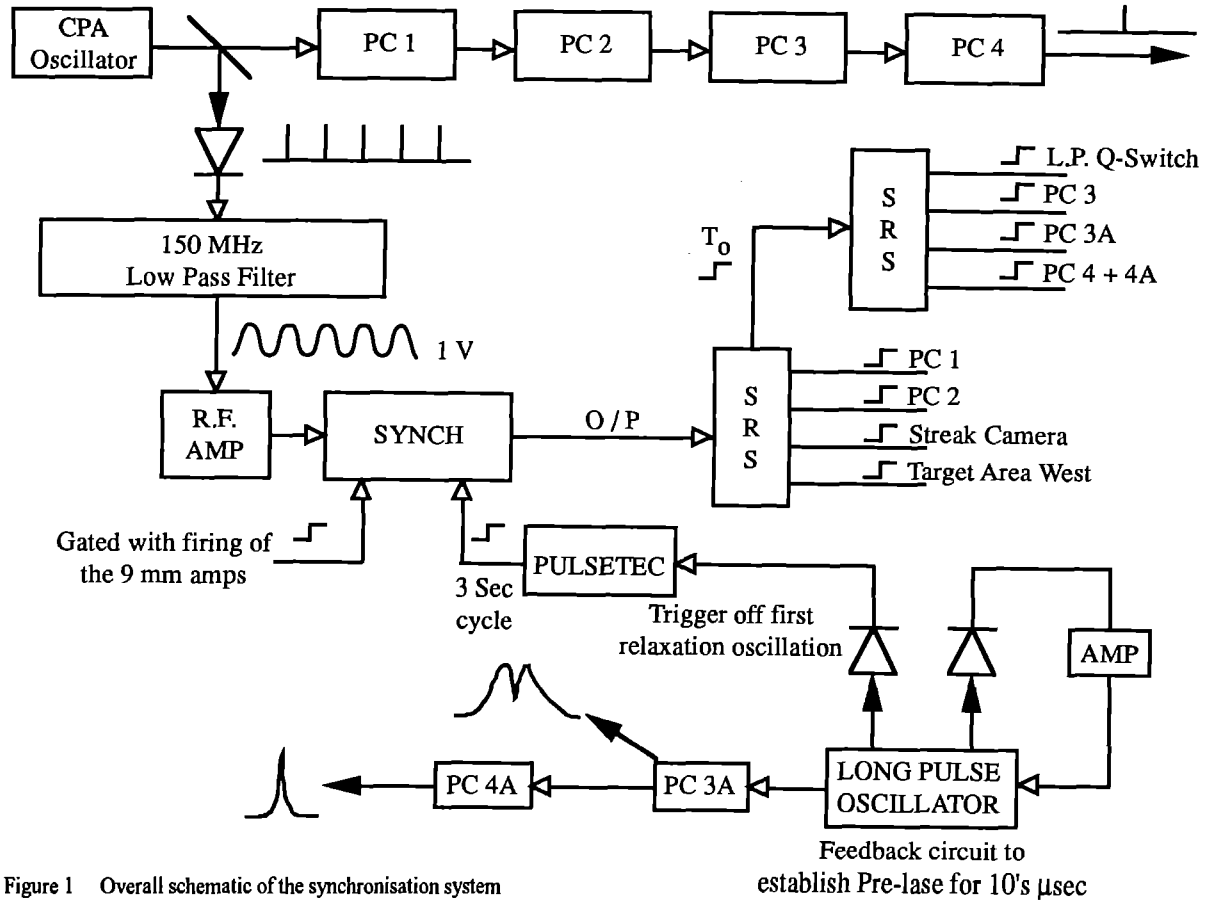

Figure 1 Overall schematic of the synchronisation system

consisting of two multi-channel digital delay generators which provide the triggers for various Pockel cells, including: the long pulse oscillator Q-switch which generates an approximately gaussian optical envelope of ~20 ns FWHM; and the switchout system, which takes a 0.6 - 4.5 ns slice from this envelope. Other pulses to be generated include streak camera triggers and a master trigger for target area diagnostics. The long pulse Q-switch is timed to open ~10 μs after the commencement of the pre-lase.

RF SYNCHRONISATION CIRCUIT

A schematic of the RF synchronisation circuit is shown in figure 2. The 134 MHz sinusoidal RF signal is initially squared off and scaled down by a factor of ten in frequency to allow the use of TTL circuitry. The pulse train is then NAND gated with the output of a set / reset flip-flop, set by the trigger derived from the long-pulse oscillator, and will remain 'high' until it is reset by a negative going edge of the reset input.

The divide by 100 chip starts counting on the first negative transition of the 13.4 MHz signal input. This allows the synchronisation of the pulse to the RF, because, irrespective of where the 'set' level goes

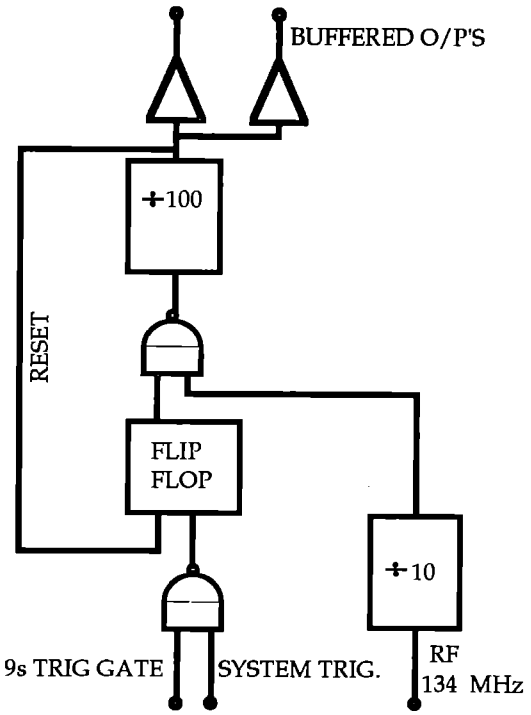

Figure 2 RF sync box synchronisation circuit

'high' in relation to the pulse period, the NAND gate output will only go from a 'low' to a 'high' state on the next transition of the pulse train. The divider counts 50 pulses before changing state and remains 'high' for a further 50 pulses. The falling edge of this pulse resets the flip-flop to zero, shutting off the RF until the next 'set' pulse. Thus only one pulse of 3.7 μs duration and delay is output from the circuit. This pulse is amplified and buffered with discrete transistor circuits and is then output as the main system trigger.

PERFORMANCE

The trigger signal derived above is used to trigger the pulse selection Pockel cell drivers (Kentech Instruments) in both amplifier chains. These Pockel cell drivers have outputs of the order of 600 ps and 1.4 ns and in the short pulse line, the pulse selection process acts as an optical gate, allowing the transmission of just one of the 2 ps pulses within the 600 ps time window. In the long pulse line, the pulse selection is of a 1.4 ns slice out of the 25 ns envelope of the oscillator output.

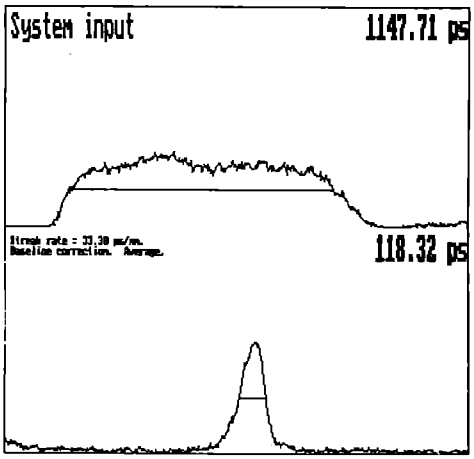

Figure 3 Streak camera image of the synchronised CPA and long-pulse oscillator outputs

The synchronisation of these gates is sufficient that the 2 ps pulse can be centered in the 600 ps window and the relative jitter between this pulse and the long pulse kept to better than 50 ps. An optical streak camera image of the long pulse together with the CPA short pulse is shown in figure 3. The shot to shot jitter on these shots was measured at +/- 150 ps but this was limited by the pulse generated from the Stanford digital delay generator. This has now been replaced with cable based delay system which has demonstrated jitters of the pulses of +/- 50 ps.

DISCUSSION

It has been demonstrated that a long pulse Q-switched oscillator can be synchronised with a cw mode-locked oscillator. For future experiments it will be necessary to synchronise the cw output with a standard Kuizenga actively mode-locked oscillator. Experiments are underway to use the RF signal generated from the cw oscillator to drive the mode-locker in the Kuizenga oscillator. This should allow synchronisation of a full range of pulse generators for injection into the VULCAN system.

ACKNOWLEDGEMENTS

The authors wish to acknowledge discussions with Prof Hutchinson of Imperial College, London.

VULCAN OPERATIONAL STATISTICS

CN Danson and DA Pepler

Rutherford Appleton Laboratory

VULCAN was again very active during the year 1992 / 1993 with a total of 5593 shots being fired. All four target areas have been operational for scheduled experiments during this year with a total of 3214 shots, including 1388 full disc shots being delivered to the main target areas and 809 target shots to TA 4. The shot failure rate continued to be very low at < 3 %.

The experiments scheduled were of a wide range and from many different groups, including a group from the Istituto di Fisica Atomica e'Molecolare [IFAM(CNR)], Pisa, Italy.

We have demonstrated that the chirped pulse amplification (CPA) operation can be provided as a facility, and laser / plasma experiments have successfully been completed using this technique. The CPA oscillator and pre-amplifier system is more complex than the normal oscillator injection but has shown itself to be sufficiently reliable that other types of experiments have been scheduled for the coming year alongside CPA experiments.

A further major facility enhancement was the new X-ray laser chamber extension in TA East, commissioned in November / December '92. This was used for the world's first demonstration of an X-ray laser produced using an injector / amplifier configuration.

EXPERIMENTAL PERIOD	EXPERIMENT (Number of disc shots)			
	TA WEST	TA EAST	TA 2	TA 4
22 Mar - 5 Apr	High resolution spectroscopy (126)	Thermal smoothing (60)		X-ray microscopy
13 Apr - 2 May		CEC experiment (189)		
3 May - 23 May				X-ray microscopy
7 Jun - 20 Jun	Non - LTE opacity (84)	Soft X-ray ASE laser (105)		
21 Jun - 11 Jul				X-ray microscopy
19 Jul - 29 Aug		RT instabilities (97)	Equation of state & opacity (160)	
7 Sept - 20 Sept		Soft X-ray de-coupling (185)		
21 Sept - 11 Oct	Facility development			X-ray microscopy
12 Oct - 25 Oct	CPA set - up			
26 Oct - 15 Nov	CPA experiment (61)	X-ray facility development		
30 Nov - 27 Dec		X-ray laser (172)		X-ray spectroscopy
11 Jan 31 Jan				Biological imaging
1 Feb - 14 Feb	CPA set - up			
15 Feb - 28 Feb	CPA interaction with hydrogen (149)			
1 Mar - 21 Mar				Biological imaging
TOTAL No. OF SHOTS	420	808	160	809

Table I. VULCAN statistics for the year to March 1993

SPRITE OPERATIONS

G J Hirst, E J Divall, S W Downes and J M D Lister

Rutherford Appleton Laboratory

INTRODUCTION

This reporting year has been a particularly busy one for Sprite, with a number of operational and performance records being broken. This section summarises the scheduled programme, with more detailed reports of individual experiments appearing elsewhere.

SHOT STATISTICS

One measure of the level of activity on Sprite is the total number of system shots, defined as ones in which either or both of the e-beam machines is fired. There were 3171 system shots this year, exceeding the previous record by more than 45%. Of these 1973 were "target" shots (i.e. were delivered to the target area in periods allocated to external-user experiments). Again this is a record and, for the first time, exceeds the number of "test" shots (those used by CLF staff for laser development and for machine testing and optimisation). Figure 1 shows the figures for the last 5 years and reveals the steadily increasing use of Sprite as a target-shooting facility.

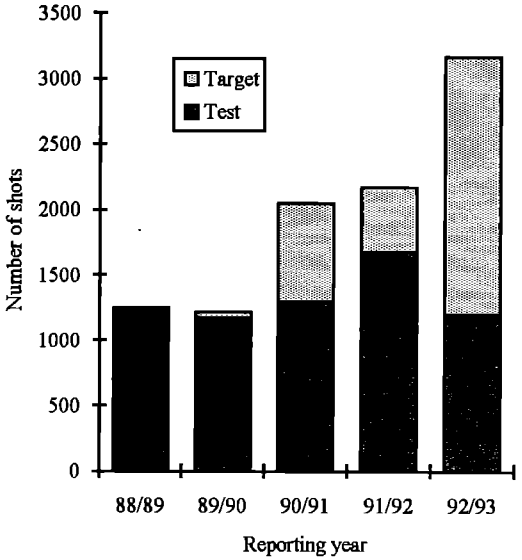

Figure 1 Annual numbers of Sprite test shots and target shots

SCHEDULED OPERATIONS

This year 27½ weeks were allocated to external users, 13½ weeks to laser development and the remaining 11 weeks were used for changes to the laser configuration, engineering upgrades, maintenance and planned shutdowns.

A brief account of the external-user experiments is given in Table 1. Further details can be found in Section A of this Report. The dates shown in the table include the standard two-week set-up period, in which target shots are not usually fired. One of the factors responsible for the large increase in the number of target shots this year is the type of target being used. The first and fourth experiments involved solid targets whereas the remainder used gas-jets. The major operational difference is that the gas-jets do not need attention from the experimenters between shots, allowing better use to be made of Sprite's relatively high repetition rate. This is particularly true if the diagnostic suite is also fully automated. During the last (gas-jet) run another new record of 65 target shots in a single day was set.

Four periods of laser development were scheduled this year. These covered studies of Raman beam stability, sub-picosecond amplification in the Sprite KrF system, Raman pulse compression and chirped-pulse amplification in Sprite. They are again described more fully elsewhere in this Section. The Raman stability experiment took two weeks in June and 181 system shots were fired. The subpicosecond tests used 92 shots in three weeks during July. The Raman compression study ran for five weeks (including a week of set-up) in August and September and accounted for 352 shots. The CPA experiment has been allocated eight weeks, beginning early in March, but the first phase has concentrated on oscillator development and no system shots were fired before the end of the reporting year.

Infrastructure improvements in 1992/93 have included the installation of a turbomolecular pump on the target chamber and the provision of new electrical and cooling-water supplies to the Oscillator Room. Plans to upgrade the rest of the cooling system are well in hand. Other notable events included the firing of the 15,000th system shot (in January), the 5,900th system shot with the current Sprite anode-foil (in March) and last, but not least, the recruitment of one of us (EJD) to the Sprite Operations staff in February.

ACKNOWLEDGEMENTS

It is a pleasure to acknowledge the support of the CLF Engineering staff, in particular John Govans, Harry Medhurst and Dave Wood.

Experiment	Institution(s)	Dates (inc. Set-up)	Laser Configuration	Pulse Duration	Typical Energy	Target Shots
Picosecond plasmas	Imperial College	16.3.92 - 24.4.92	KrF	3 ps	1.3 - 1.4 J	380
Harmonic generation / Multiphoton ionisation	Imperial College / Oxford-Essex-Göttingen	4.5.92 - 12.6.92	Raman	12 ps	2.5 - 5.5 J	435
Multiphoton ionisation	Oxford-Imperial College-Essex-Göttingen-Alberta	29.9.92 - 6.11.92	Raman	12 ps	2.5 - 3.5 J	535
Heated-foil EXAFS	Essex-RAL	16.11.92 - 23.12.92	Raman	12 ps	2.5 - 4.0 J	157
Thermal conduction	Imperial College	4.1.93 - 12.2.93	Raman	12 ps	3.0 - 4.5 J	519

Table 1 Summary of external-user experiments

SPRITE SYSTEM PERFORMANCE

J M D Lister, G J Hirst, E J Divall and S W Downes

Rutherford Appleton Laboratory

INTRODUCTION

During the year ending March '93, work has continued towards achieving higher performance from the Sprite KrF laser system. A new Ti:Sapphire oscillator has been installed, new pre-amplifier configurations implemented and experiments conducted to demonstrate shorter pulse operation, both in Raman mode and in single pulse KrF mode.

FRONT-END DEVELOPMENT

In July a Spectra-Physics "Tsunami" mode-locked Ti:Sapphire oscillator was installed (replacing the sync-pumped dye laser system) to provide greater flexibility in terms of pulse duration, and to make operation easier. Relatively minor changes to the optics allow near transform-limited pulses of between 100fs and 60ps to be generated.

The new oscillator performed very well in terms of stability and ease of operation in the femtosecond regime. However, some problems were experienced in generating stable 12ps pulses for the Raman system. In order to obtain the best performance from the Raman amplifiers it is essential that the pulses generated by the oscillator are very close to the transform limit at 12ps. Since the installation of the new oscillator, the output energy of the Raman system has been reduced by 20 - 25%. Measurements have indicated that the problem is probably due to spectral broadening of the amplified KrF pump beams. Previous experiments have suggested that this broadening is strongly dependant on the width of the spectrum from the oscillator.

As part of the Chirped Pulse Amplification (CPA) experiment on Sprite, a new Ti:Sapphire amplifier stage has been installed after the existing dye amplifier stages. A previous attempt to use a Ti:S amplifier[1] was not entirely successful, mainly due to non-uniform end-pumping of the amplifier rod and to non-linear effects in the transmissive optics of the short-pulse beam line. The new amplifier rod is side pumped in a Bethune cell arrangement. This system is easier to set up, and gives better performance.

Modifications to the discharge pumped KrF pre-amplifier (EMG103) carried out earlier in the year have allowed it to be used in an off-axis mode for the first time[2]. In this configuration, energy extraction is increased for a saturating amplifier (at the expense of lower gain) and the level of amplified spontaneous emission (ASE) at the start of the KrF amplifier chain is reduced.

KrF SYSTEM

In April '92, the Sprite system was used to deliver 3ps pulses to target (the shortest available from the sync-pumped dye laser oscillator then in use). The maximum energy was 1.6J at the output of Sprite, giving a brightness of over 10^{18} W cm^{-2} st^{-1} and a contrast ratio between the short pulse and the ASE of 3 x 10^7. This level of ASE has caused some problems for solid target experiments.

More recently, the installation of the Ti:S oscillator has enabled us to produce sub-picosecond pulses. An experiment was carried out to amplify 300fs pulses directly in the KrF chain. This confirmed that the limit for this mode of operation is probably 1-2ps, due to nonlinear absorption in the silica laser windows and B-integral effects in the air and in optics after the final amplifier. It is now believed that any attempt to deliver sub-picosecond pulses to target will require a CPA based system.

A significant increase in brightness can also be achieved by improving the beam quality. Until recently, aberrations in the KrF beam line have limited the focussability to about 20 times the diffraction limit. Little effort had been made to improve this since the Raman system could produce near diffraction limited beams from poor quality pump beams. Staged improvements to the optics have now produced a system with static aberrations of less than 2 times the diffraction limit. The most significant changes were the replacement of the Goblin amplifier back mirror and the sealing of the Sprite beam pipe to allow it to be filled with helium. A few very recent results suggest that the beam is not significantly degraded in amplification to energies of 1.5J. Figure 1 shows far-field images of the KrF oscillator beam before and after the improvements.
Details of the KrF CPA experiment currently in progress (April '93) are reported in section B2.

Figure 1 KrF far-field images, (a) before and (b) after optics improvements

RAMAN SYSTEM

Most of the Sprite target experiments this year have used the 12ps high brightness Raman system. Design work for the enhanced Raman system is well advanced and is reported in section B3. The performance of the present Raman system is detailed in Table 1.

	Maximum	Typical
Pump energy (J)	11	9
Input energy (mJ)	200	80
Output energy (J)	5.6	3.5
Gain	1000	40
External efficiency (%)	60	45
Divergence (μrad)	5.0 (minimum)	7.0
Brightness (W cm^{-2} sterad^{-1})	> 10^{20}	5 x 10^{19}

Table 1 Raman system performance (RA3)

As mentioned above, the Raman system is presently performing below the level achieved last year in terms of output energy, although improvements in beam quality have kept the brightness of the beam above 10^{20} W cm^{-2} st^{-1}. Earlier this year the final Raman amplifier RA3 gave typical output energies of 5J, with a maximum of nearly 7J, although the far-field beam quality was found to be degraded significantly for the higher energy shots. This is believed to be due to second Stokes generation in the final amplifier and in the air, and to B-integral effects in the air path and the optics to the target chamber. These problems will be addressed in the Raman upgrade by increasing the beam diameter, minimising the path in air and in transmissive optics between RA3 and the target chamber, and by improving the near-field uniformity of the pump beams.

In recent experiments, the typical output energy from the system has been reduced to 3.5 - 4.0J. This is believed to be due to broadening of the pump spectrum after amplification. Although the spectrum of the generated pulses is close to the transform limit for 12ps pulses, it is thought that energy at a low level in the wings of the spectrum may be seeding broadening in the air at lower intensities than might otherwise be expected. Figure 2 shows the spectra of the 12ps KrF pulses before and after amplification in the e-beam amplifiers. It is possible that although the width of the spectra from the current and the previous oscillators appears the same at the 50% level, the sync-pumped oscillator in fact produced a cleaner spectrum in the wings. If this is the case, then it should be possible to spectrally filter the output of the Ti:S oscillator without significant loss of energy, and hence return to the high efficiencies previously obtained from the Raman system.

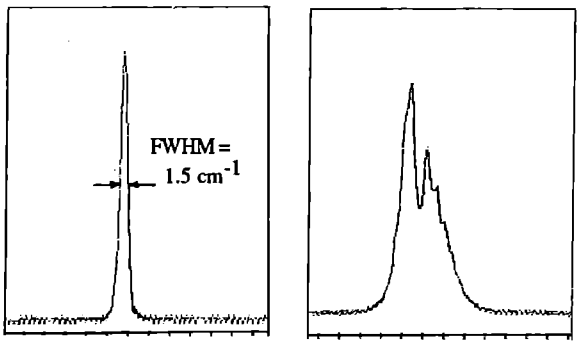

Figure 2 Spectra of the KrF pump pulses (a) before and (b) after amplification

During the target experiment in Jan/Feb, the far-field beam profiles were of a consistently high quality. Figure 3 shows both near-field and far-field images (with line profiles) of the Raman beam for one target shot during this experiment. The FWHM divergence is 5.6μrad (1.5 times diffraction limit), giving a value for the brightness of the beam of greater than 10^{20} W cm^{-2} st^{-1}. It is, however, difficult to calculate this figure precisely, since the CCD camera used for the far-field images does not have a high enough dynamic range to enable us to measure accurately the fraction of the total energy contained within the central spot. There is also some evidence of degredation of the beam quality in the path between the laser area (where the far-field diagnostic is located) and the target chamber.

The pulse contrast ratio (prepulse level) of the Raman beam has previously been shown[3] to be greater than 10^{10}:1 for 40ps pulses and no change in this value is expected at 12ps.

In a preliminary experiment we have also demonstrated Raman pulse compression in the penultimate amplifier of the Raman system (RA2). Stokes pulses of 2.5ps duration were amplified by pump pulses of about 20ps duration in a 2m long lightguide amplifier. Output pulses of less than 3ps duration were obtained with gains of around 500 and conversion efficiencies approaching 30% (see section B3). At this time there is no plan to test Raman pulse compression in the final Raman amplifier RA3.

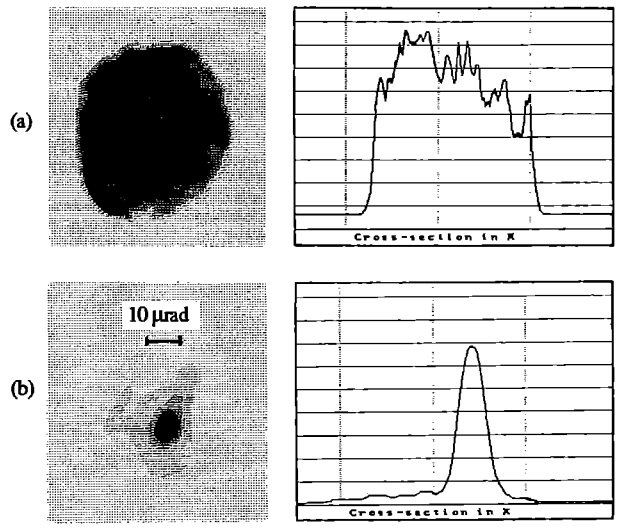

Figure 3 (a) Near-field and (b) far-field of amplified Raman beam

CONCLUSIONS

Many aspects of the performance of the Sprite laser system have been improved over the last year. The limit of the present 12ps Raman system has probably been reached, and further significant increases in beam brightness will require the upgrade described in section B3. The KrF beam quality has been improved and sub-picosecond pulses should soon be available via CPA.

The number of shots to target each year is continuing to increase dramatically, partly due to the increased use of gas-jet targets. The maximum shot rate of the system (>15 shots/hour) is still rarely demanded by users. Hardware modifications are continuing to improve the reliability of the system. In May 1993 changes to the optics in the Sprite pulse forming lines (successfully tested on Goblin last year) should eliminate one of the few remaining weak points in the pulsed power system.

REFERENCES

1. M Amit, J M D Lister, I N Ross, Annual Report to the LFC (1991) RAL-91-025, Section B1.6

2. S. Szatmari et al, Appl. Phys. B 53, p82 (1991)

3. I N Ross et al, Optics Comm, 78, 263 (1990)

RADIATION DAMAGE TO GOBLIN WINDOWS

E J Divall and G J Hirst

Rutherford Appleton Laboratory

INTRODUCTION

The e-beam pumped KrF amplifier, Goblin, uses an argon/krypton/helium/fluorine mixture contained in a chamber with calcium fluoride windows (Fig.1). Calcium fluoride is chosen because it has high resistance to fluorine damage and low two-photon absorption at the 248.6 nm laser wavelength. After several months on the machine, however, the windows develop a significant absorption peak in the UV. In the two samples measured the 248.6 nm transmission was reduced from >90% to 68.2% and 80.4%. (Fig.2). Further examination in a KrF probe beam showed that the windows had become fluorescent, both in the yellow and the blue/green, the latter with a lifetime of a fraction of a second. The fluorescence was noticeably brighter from those parts of the windows which had *not* been exposed to the main laser beam, and it tended to decrease slightly with increased exposure to the probing UV.

Previous work by King and Nestor[1] on the properties of calcium fluoride found that typical laser grade material has atomic impurities of 50-100 ppm. These are capable of forming colour centres when exposed to high energy radiation i.e. both the UV beam and bremsstrahlung X-rays generated from the e-beams. These radiations have sufficient energy to free electrons by the photoelectric effect and by Compton scattering, some of which become trapped at the crystal imperfections, hence activating the colour centres and introducing new absorption bands.

In our case the whole crystal is affected - suggesting that the major damage is X-ray based. However the central area, exposed to the laser beam, shows less damage which implies that the UV is partially restoring the transmission.

THE EFFECTS OF ANNEALING

The colour centres were relieved by annealing the window at 400°C for 2 hours. Care must be taken during this process as the crystal may shatter if heated or cooled at a rate greater than 100°C/hour. Measurements of the transmission after annealing showed that it had been restored to within 5% of its original value (Fig.2). Preliminary experiments using 253.7 nm mercury light to bleach the colour centres showed some increase in the transmission, but at the low exposures which were used this process was not as effective as the thermal one.

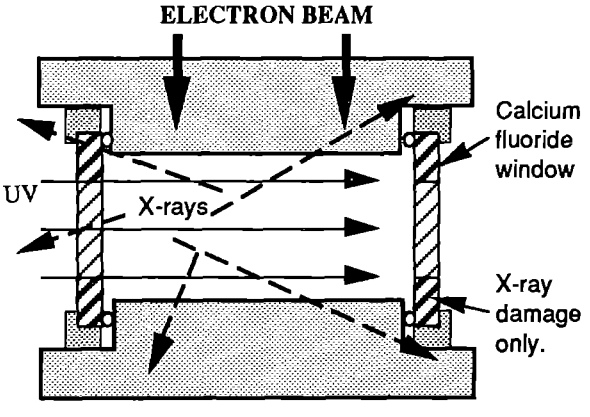

Figure 1 Diagrammatic section through Goblin

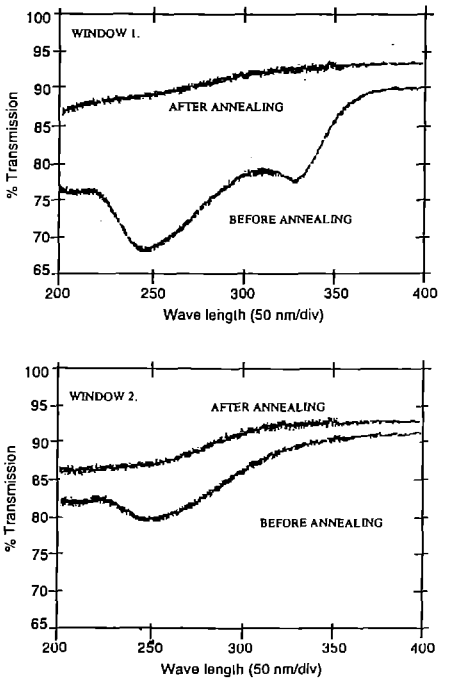

Figure 2 Transmission of two calcium fluoride windows before and after annealing

HYPOTHESIZED BEHAVIOUR

In a new calcium fluoride crystal the colour centres are unoccupied and hence no UV absorption peaks are observed. When the window is exposed to X-rays Compton scattering occurs. This acts equally on all electrons and leads to activation of the colour centres. Eventually an equilibrium between activation and deactivation (heavily biased in favour of activation) will be reached.

Previous observations show that the colour centres in our particular samples of calcium fluoride are only slowly activated by UV light. However once activated they have a strong absorption in the UV, so deactivation by the UV beam is much more likely than activation. Hence under X-ray *and* laser irradiation the equilibrium position is shifted, with fewer colour centres being occupied by electrons than in the X-rays-only case. The window's UV absorption coefficient will therefore be lower.

This is consistent with the observed results. The outer section of the window fluoresces (and presumably absorbs) more strongly as it is only exposed to X-rays. The central area is also subject to laser irradiation, which may initially cause the window to damage more quickly but which eventually limits the level of absorption.

REFERENCES

(1) C W King and O H Nestor, "Calcium fluoride: New properties for an old material", SPIE Los Angeles Jan1989

LASER SUPPORT FACILITY PROGRAMME

W T Toner

INTRODUCTION

This section contains reports from some 30 user groups of whom six were first time users. In total 56 experiments and loans were carried out, fully saturating the capacity of the facility. The publications recorded show a further increase (13%) on last year and cover a remarkable breadth of scientific fields. The list of highlights from the work of both Loan-Pool and RAL-based facility users given below is inevitably partial.

In Chemistry, a partially CEC supported programme of work by the Birmingham group at Rennes has taken gas phase chemical kinetics into a new temperature range and has shown that radical-radical and radical-molecular reactions remain quite fast at ultra low temperatures. At Bristol, novel measurements have been made of the spectra of cold radicals in a supersonic jet. New results have been obtained in the study of the picosecond transient Raman spectrum of photoexcited S_1 *trans*-stilbene including, for the first time, the observation of a late time mode-specific solvent and temperature dependent broadening and shifting of a group of lines. In nanosecond time resolved Raman spectroscopy it has been observed for the first time that the structures of the triplet states of some porphyrins are modified on binding to the protein BSA. Novel work is reported on the interaction of triplet states of napthalene derivatives with oxygen, observed by picosecond transient absorption of solutions under 50 to 80 atmosphere pressures of oxygen.

In Biology, it has been shown for the first time that the vitamin E radical is located at the cell-membrane-water interface to enable its recycling to vitamin E by vitamin C. The unique programme of work on the repair of DNA damaged by UV and X-rays has shown that while the repair of UV damage can be described by a simple kinetic model, the repair of X-ray damage involves additional steps, possibly reflecting the greater number of damage mechanisms in action.

In Physics, pulsed laser tagging of laser cooled ions in a Penning trap at Imperial College has made it possible for the first time to measure the ion cloud rotation frequency directly. At Southampton specially doped crystalline materials have been used to achieve, for the first time, highly efficient internal geometry self-pumped phase conjugation at wavelengths exceeding 1μm, and with record reflectivities of 76%.

Significant advances in technique are also reported. A record 200 mWatt average soft X-ray power at 1nm wavelength was obtained from the 50 Hz laser point source X-ray generator giving 2krad/s dose rates for DNA damage experiments. With 5 x 10^{12} photons/mm^2/mrad^2/0.1% bandwidth at 3.37 nm, this source is only beaten by the world's most powerful synchrotrons and has considerable potential for X-ray lithography. A femtosecond Ti-Sapphire laser was commissioned and a chirped pulse dye amplifier utilising Bethune cells was developed to produce 350 mJ, 110 fs pulses in a near diffraction limited beam (Strehl ratio 0.52) with a brighness of 3.2 x 10^{17} W cm^{-2} sterad^{-1}. Enhanced infrared detection sensitivity is now available from a singlet oxygen detector and also from a back-illuminated liquid N_2 cooled CCD detector. In a REMPI experiment remarkable sensitivity at 4x signal to noise ratio of 4 x 10^4 NO cm^{-3} per quantum state was demonstrated.

PICOSECOND TIME-RESOLVED RESONANCE RAMAN STUDIES OF TRANS-STILBENE

R. E. Hester[1], P. Matousek[2], J. N. Moore[1], A. W. Parker[2], W. T. Toner[2], and M. Towrie[2]

[1]Chemistry Department, University of York

[2]Rutherford Appleton Laboratory

INTRODUCTION

The photophysics of *trans*-stilbene (tS) has been studied using several techniques of ultrafast spectroscopy, and the principal features of the process are established [1]. Photolysis populates the S_1 excited state which has a low barrier to rotation about the olefinic C=C bond. S_1 tS in n-hexane at room temperature undergoes this rotation with a time constant of c. 90 ps to produce a twisted intermediate which then relaxes rapidly onto the S_0 surface to produce either *cis*- or *trans*-stilbene in the ground electronic state. While this overall mechanism is established, recent studies indicate that the detailed nature of these intramolecular processes and the rôle of the solvent require further clarification.

Picosecond time-resolved resonance Raman spectroscopy (ps-TR^{3}S) has been applied successfully to the study of S_1 tS and recent studies [2,3] have revealed the existence of mode-specific solvent-dependent changes occurring on a *c.* 10 ps timescale following photoexcitation. Other studies have shown that the bandwidth of the S_1 tS visible absorption spectrum narrows on a similar timescale on photoexcitation at wavelengths significantly shorter than the origin of the $S_0 \rightarrow S_1$ transition [4]. In this study, ps-TR^{3}S has been used to probe S_1 tS using several pump and probe wavelengths and a range of temperatures in order to reveal further details of this mechanism.

EXPERIMENTAL

The ps-TR^{3}S apparatus has been described [5]. A train of 6 ps pulses from a cavity-dumped dye laser is amplified by a copper vapour laser-pumped dye amplifier operating at 4.46 kHz to produce stabilized pump and probe pulses of energies 0.2 - 2.5 μJ and 1 - 12 μJ , respectively. The pump beam is generated by frequency doubling the probe beam in a BBO crystal. The pump and probe wavelengths are decoupled by stimulated Raman shifting when required. After passing the probe beam through a variable optical delay, the pump and probe beams are focused together into the sample collinearly, and Raman scattering is collected at 90° for analysis by a spectrograph with CCD detection. The sample solution is flowed through a 0.5 mm open jet and sample temperatures varied through immersion of the solution flow tube in a bath placed after the circulating pump. Accumulation times of typically 5 min were used. The concentration of tS in all solutions was 1 x 10^{-3} mol dm^{-3}.

RESULTS

We have obtained ps TR^3 spectra of excellent quality from S_1 tS in the solvents n-hexane and hexadecane, and in aqueous micelles of the neutral (non-ionic) surfactant Triton X100R. The spectra have been measured over the range 200-1700 cm^{-1}, with pump wavelengths from 275 - 310 nm and solution temperatures from - 50 to + 50 °C. Lorentzian profiles gave the best fit to the observed Raman bands. The peak positions, bandwidths, and relative intensities have been measured as functions of the delay time between the pump and probe pulses, of the pump and probe wavelengths, and of the temperature. Perdeutero-tS (d-tS) spectra also have been obtained.

Fig. 1(a) shows a part of the ps-TR^3 spectrum of S_1 tS obtained from an n-hexane solution using a 10 ps delay between pump (285 nm) and probe (570 nm) pulses. Solvent peaks have been subtracted and the bands fitted by Lorentzians. Fig. 1(b) shows the changes resulting from an increase in the delay time from 10 to 80 ps and the difference between the two spectra in 1(b) is shown in 1(c). The largest changes are seen for the *c.* 1570 cm^{-1} band, but changes also are evident in the *c.* 1180 cm^{-1} band and possibly in the *c.* 1240 cm^{-1} band. Both peak wavenumber shifts and bandwidth changes contribute to these effects. Fig. 2 shows that changes in peak position and bandwidth for the *c.* 1570 cm^{-1} band display similar kinetics with both short (*c.* 4 ps) and long (*c.* 10 ps) components. These changes show similar kinetics but different magnitudes with shorter wavelength pulses, as shown in Fig. 3. Pumping at 285 nm and probing at 570 nm or 605 nm reveals that the effects shown in Fig. 3 result primarily from changes in the pump wavelength.

In spite of the excellent signal-to-noise ratios we were unable to observe anti-Stokes bands in the 1100-1600 cm^{-1} region. Only the *c.* 285 cm^{-1} band was distinguishable, and this gave the expected Stokes/anti-Stokes intensity ratio of 4/1. We were, however, able to measure four weak bands in the transient Stokes Raman spectrum at *c.* 1850, 1810, 1755 and 1705 cm^{-1}. Interestingly, these correspond to combinations of the *c.* 285 cm^{-1} mode with those at *c.* 1570, 1530, 1465 and 1420 cm^{-1}.

All the results this far were obtained for S_1 tS in n-hexane at a temperature of *c.* 18 °C. By changing the sample temperature from this value we found that, with fixed pump and probe wavelengths (305 and 610 nm, respectively, chosen so as to minimize the changes to the *c.* 1570 cm^{-1} band arising from excitation above the electronic origin), mode-specific changes

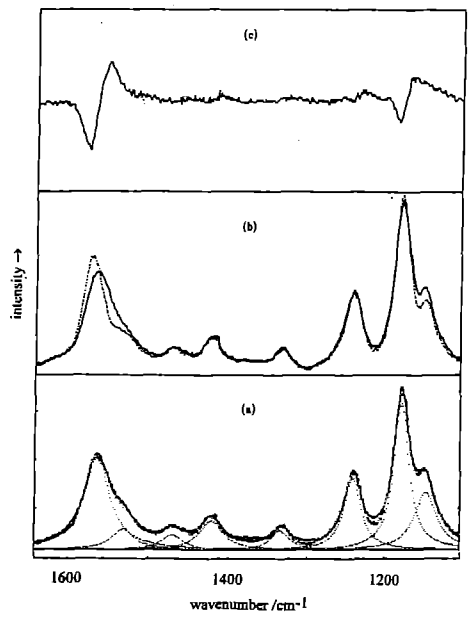

Fig. 1. S_1 tS resonance Raman spectrum, obtained from tS in n-hexane at 18 °C using 285 /570 nm pump/probe pulses with delays of (a) 10 ps and (b) 10 and 80 ps. The difference between the spectra shown in (b) is shown in (c). Solvent bands have been subtracted and the band shapes fitted by Lorentzians in (a).

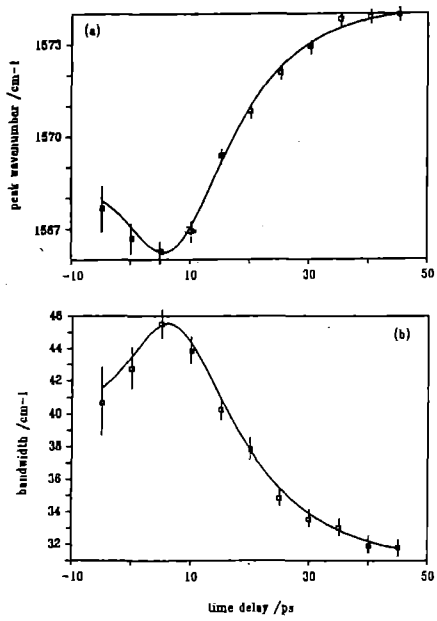

Fig. 2. Peak wavenumbers (a) and bandwidths (b) of the band at *c.* 1570 cm^{-1} at various time delays between pump/probe pulses at 275/550 nm. Data from S_1 tS in n-hexane at 18 °C. The fitted curves are based on the convolution of the instrument response with a double exponential (growth and decay).

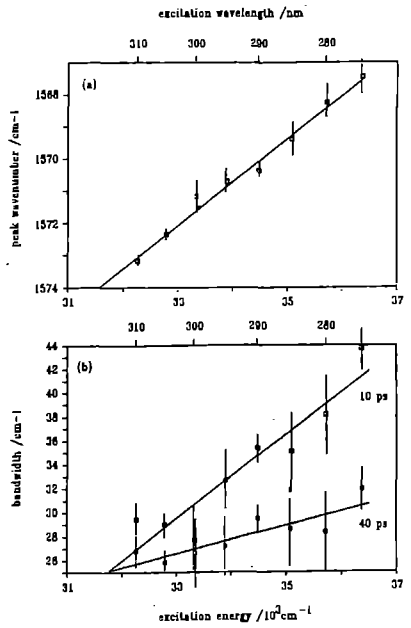

Fig. 3. Peak wavenumbers (a) and bandwidths (b) of the *c.* 1570 cm^{-1} band at various excitation energies (wavelengths) of the pump (shown) and probe (2 x pump wavelength) pulses. The data in (a) were obtained at 10 ps delay time and those in (b) at 10 and 40 ps. Data from S_1 tS in n-hexane at 18 °C.

were obtained for a fixed pump/probe delay time of 20 ps, i.e. temperature-induced mode-specific changes. By far the largest effects in the 1100 - 1600 cm^{-1} region again were apparent in the *c.* 1570 cm^{-1} band. With increasing sample temperature, the peak shifted to lower wavenumbers and broadened, as shown in Figs. 4 and 5. Kinetic measurements made at -33, 20, and 40 °C, with 285/570 nm pump/probe wavelengths, showed the peak wavenumber changes with delay to be temperature independent.

The S_1 tS lifetime was found to vary with temperature in both n-hexane and hexadecane. From Arrhenius plots of ln k (the rate constant for S_1 tS decay) versus inverse temperature, activation energies of (14.1 ± 2.1) and (14.6 ± 1.0) kJ mol^{-1}, respectively, were determined for S_1 tS in these two solvents in agreement with earlier literature [6].

Changing the solvent from n-hexane to hexadecane gave a closely similar set of results for the temperature dependence and also for both the pump/probe wavelength dependence and the *c.* 1570 cm^{-1} peak shifts with pump/probe delay time. However, the S_1 tS lifetime was significantly increased in hexadecane at 20 °C and at this temperature the Raman spectra in n-hexane and in hexadecane were different. The spectra of S_1 tS in n-hexane at - 15 °C and in hexadecane at + 40 °C were closely similar. For S_1 tS entrained in aqueous Triton X100R micelles at 20 °C, marked differences were observed in band positions and kinetic behaviour. For the 285/570 nm pump/probe condition the *c.* 1570 cm^{-1} (in n-hexane) band shifted down by 4.6 cm^{-1} and broadened from c. 29 to 35 cm^{-1} at 20 °C. In the variable pump/probe time-delay experiments in Triton X100R, this band showed an early time peak shift to lower wavenumber over the period 0 - 10 ps but the size of the subsequent (10 - 40 ps) shift to higher wavenumber was only about half (2.2 cm^{-1}) that observed for the n-hexane solution. The bandwidth changes with delay time in the micellar data were similar in form but of smaller size than those obtained from hexane solution. Moreover, the *c.* 1570, 1240 and 1180 cm^{-1} bands were narrower at the very shortest than at all longer time delays. The S_1 tS lifetime again was significantly increased in the micellar system as compared with n-hexane solutions.

The behaviour of d-tS in n-hexane was found to be qualitatively similar to that of tS, except that no initial decrease in band

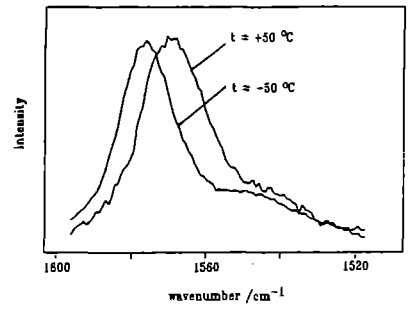

Fig. 4. Effects of changing temperature on the *c.* 1570 cm^{-1} band from S_1 tS in n-hexane at 20 ps delay time between pump (305 nm) and probe (610 nm) pulses.

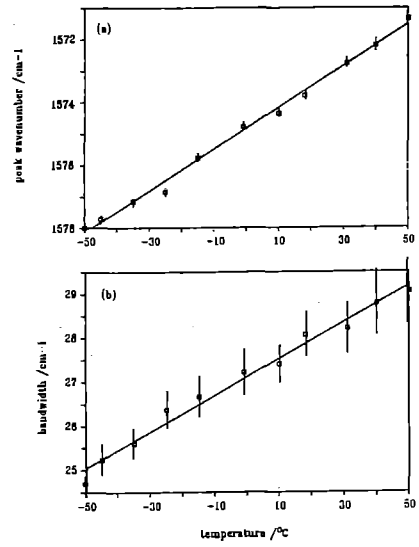

Fig. 5. Peak wavenumbers (a) and bandwidths (b) of the *c.* 1570 cm^{-1} band at various temperatures. The data were obtained at 20 ps delay time between pump (305 nm) and probe (610 nm) pulses. Data from S_1 tS in n-hexane.

wavenumber in the 0 - 10 ps range of pump/probe delay times was observed. The *c.* 1570 cm^{-1} peak shifted directly and progressively to higher wavenumbers and the band became narrower over the *c.* 0 - 50 ps range of pump/probe delay times, but the kinetics yielded a time constant some 1.8 times slower than for tS itself.

DISCUSSION

Our vibrational mode selectivity data are supportive of the pioneering work of Gustafson *et al.* [2] and Hamaguchi *et al.* [3] but go considerably beyond these studies and enable us to gain further insights into the early time behaviour of photoexcited tS in solution. In particular, the mode-specific temperature dependence of S_1 tS and the effects of inclusion of S_1 tS in aqueous micelles are reported here for the first time.

The S_1 tS Raman band at c. 1570 cm^{-1} is associated with a vibrational mode which is of mainly olefinic C_o=C_o bond stretching character in S_0 tS [7]. This shows by far the greatest sensitivity to mode-selective effects associated with changes in solvent, pump-probe delay time, pump wavelength, and temperature. A few other modes show smaller effects, as is illustrated in Fig. 1 for the *c.* 1180 cm^{-1} band which corresponds to a mode involving mainly C_o-C_p (olefinic carbon to phenyl carbon bond) stretching in S_0 tS. The wavelength range shown in Fig. 3 corresponds to an excess energy range from *c.* 1000 - 5000 cm^{-1} (310 - 275 nm). The mode-selective effects were found to be proportional to the excess photoexcitation energy given to the S_1 tS.

From more recent studies of mode-specific, solvent-dependent dynamics in S_1 *trans*-4,4'-diphenyl- stilbene [8] it appears that for this effect the dielectric properties of the solvent are more important than the viscosity. Certainly our own data support this latter claim in that we find very similar dynamics for the mode-specific changes in the spectra of S_1 tS in both n-hexane and hexadecane, despite the large difference in their bulk viscosities (0.31 mPa s for n-hexane and 3.34 mPa s for hexadecane at 20 °C), and in n-hexane at widely different temperatures (from -33 to +40 °C) where the viscosity changes are large. The aqueous Triton X100R micellar environment, which induces different behaviour from that of either of the other solvents, differs from them not only in viscosity but also in polarity. We may anticipate that the effective dielectric constant within the Stern layer of the micelle will be relatively large (*c.* 40, *cf.* n-hexane *c.* 1.9). Thus our data are consistent with microdielectric stabilization of S_1 tS being a major factor.

Our temperature-induced mode-specific effects are strikingly similar in form and in magnitude to those changes associated with excess energy effects, although there are quantitative differences between the peak position and bandwidth effects, as may be seen from a comparison of Figs. 3 and 5. It seems reasonable, then, to attribute these to thermal activation of S_1 tS in its local solvent cage. The lack of high wavenumber anti-Stokes Raman band intensity enhancement in our spectra indicates that intramolecular vibrational relaxation processes eliminate any "hot" olefin modes on a timescale which is faster than our measurements. But anharmonic coupling of the olefinic "doorway" modes to low wavenumber "exchange" modes [9], through which process energy is transferred out to the solvent environment, certainly could result in the generation of low wavenumber "hot" modes. Such low energy "hot" modes may alternatively be generated by direct heating of the sample and it seems that the *c.* 10 ps process observed through the high wavenumber bands may correspond to relaxation of the "hot" low-wavenumber modes. The strong coupling of the C_o=C_o stretch with the C_o-C_p-C_p deformation at *c.* 285 cm^{-1} [7], indicated by our observation of combination bands in the *c.* 1700 - 1850 cm^{-1} region, may point to a special rôle for this particular deformation as an "exchange" mode.

The temperature dependence of the overall S_1 tS lifetime was found to yield similar values for the size of the intrinsic barrier to internal rotation and isomerization to those reported previously. This is consistent with the earlier reported conclusion that the barrier is independent of alkane solvent.

Taking all the available evidence together, we may visualise a possible mechanism for the observed mode-selective dynamics as follows. Photoexcitation of S_0 tS creates S_1 tS in an initially 'hot' state, with vibrational excitation of a wide range of modes, dependent on the excess energy provided, i.e. on the photoexcitation wavelength. Ultrafast intramolecular vibrational energy redistribution occurs, resulting in an essentially impulsive creation of vibrationally 'hot', highly anharmonic, low frequency (deformation) modes which distort the molecular geometry [10]. The observed early-time (0 - 5 ps) exponential decrease in the *c.* 1570 cm^{-1} peak wavenumber and increase in bandwidth both are consistent with such distortions, these being damped by coupling to the local solvent cage. Superimposed on these initial IVR effects is a longer-timescale (0 - 40 ps) 'cooling' process, involving energy transfer from these low frequency modes to the reorientating solvent environment which also provides progressively increasing microdielectric stabilization of the S_1 tS [8,11]. The proposed rôle of vibrationally 'hot' low frequency modes is consistent with the fact that raising the temperature produces similar results to those observed at 10 ps on increasing the excess energy in the photoexcitation pulse. However, our measurements of the excess energy and temperature dependence of the *c.* 1570 cm^{-1} peak wavenumber and bandwidth show the increase in width with excess energy to be different from the corresponding increase with temperature. This indicates that at delay times less than *c.* 40 ps S_1 tS is not in true equilibrium either internally or with the solvent.

ACKNOWLEDGEMENTS

We are grateful to S. Umapathy for his assistance in the early stages of this work, to V. Kamalov, I. Lednev and D. Phillips for helpful discussions, to M. Russell and A. P. Tilley for experimental assistance, and to T. L. Gustafson for preprints of his work.

REFERENCES

1. D. H. Waldeck, Chem. Rev. 91, 415 (1991).
2. W. L. Weaver, L. A. Huston, K. Iwata and T. L. Gustafson, J. Phys. Chem. 96, 8956 (1992).
3. K. Iwata and H. Hamaguchi, Chem. Phys. Lett. 196, 462 (1992).
4. B. I. Greene, R. M. Hochstrasser and R. B. Weisman, Chem. Phys. Lett. 62, 427 (1979) ; F. E. Doany, B. I. Greene and R. M. Hochstrasser, Chem. Phys. Lett. 75, 206 (1980).
5. P. Matousek, R. E. Hester, J. N. Moore, A. W. Parker, D. Phillips, W. T. Toner, M. Towrie, I. C. E. Turcu and S. Umapathy, Rev. Sci. Instr., submitted.
6. P. M. Felker and A. H. Zewail, J. Phys. Chem. 89, 5402 (1985); J. Schroeder and J. Troe, J. Phys. Chem. 90, 4216 (1986).
7. M. Tasumi, T. Urano and H. Hamaguchi in : Time-Resolved Vibrational Spectroscopy, ed. G. H. Atkinson (Gordon and Breach, New York, 252 (1987).
8. R. M. Butler, M. A. Lynn and T. L. Gustafson, J. Phys. Chem., in press.
9. R. M. Shelby, C. B. Harris and P. A Cornelius, J. Chem. Phys. 70, 34 (1979).
10. S. A. Asher and J. Murtaugh, J. Am. Chem. Soc. 105, 7244 (1983).
11. K. Yoshihara, A. Nmiki, M. Sumitani and N. Nakashima, J. Chem. Phys. 71, 2892 (1983).

DEVELOPMENTS TO THE PICOSECOND TR^3 SYSTEM FOR THE STUDY OF METAL-CENTRED TRANSIENTS.

A H R Al-Obaidi[1], S E J Bell[1], J J McGarvey[1], R A McNicholl[1], M Hegarty[1], D I C Martin[1], S J Rigby[1] and P Matousek[2]

[1]School of Chemistry, Queen's University of Belfast.

[2]Laser Support Facility, Rutherford Appleton Laboratory.

INTRODUCTION

The picosecond time-resolved resonance Raman (TR^3) system at RAL is at a well developed stage with regard to temporal characterization of pulses and generation of reproducible pulse-to-pulse delays. A pair of pulses of 6 ps duration is produced, the first being generated by pumping a dye at 532 nm which lases in the region 550-650 nm. The second pulse is produced by frequency doubling the first[1]. In practice, there are still a number of difficulties in using lines other than 610 and 305 nm, especially since the laser energy falls off markedly at other wavelengths. Furthermore, wavelengths less than 300 nm tend to create unwelcome decomposition products and many organic solvents begin to absorb strongly in this region.

In its present form the set-up is ideal for studying a small number of systems such as the excited states of stilbenes, which have received a great deal of attention and are well documented. However, TR^3 studies of many species of organic and biological interest, as well as metal complexes, need pairs of pulses tuneable over the range 300-600 nm, pointing to the need for significant additional development of the system in order to cover that range adequately.

Among the systems of interest to us are the excited states of polypyridyl complexes of Cu^I, $[Cu(L)_2^+]$, (L= (2,2' biquinoline [BIQ] or L = 6,7-dihydro-5,8-dimethyldibenzo-1,10-phenanthroline [DMCH]). We have already extensive data for these complexes including transient absorption spectra, excited state Raman spectra obtained with single colour 10 ns pulses from a Nd-YAG laser[2] and Raman spectra of the electrochemically-reduced species[3]. The most stable excited states of these complexes are ^{3}MLCT (metal to ligand charge transfer). These may be formulated as $[(L)Cu^{II}(L^{\cdot-})]^+$ in which a Cu^{II} centre is coordinated by a neutral and a reduced (radical-anion) ligand. The lifetimes of these states of the two complexes is *ca* 1ns[4]. The ligand radical anions $BIQ^{\cdot-}$ and $DMCH^{\cdot-}$ absorb at *ca* 500 nm[3].

RESULTS AND DISCUSSION

The set-up which was used in these experiments is illustrated in Figure1. Raman shifting in DMSO generated 746 nm radiation from the 610 nm laser line. It was found that circulating the DMSO (using a dye laser circulator), rather than simply stirring the solvent, increased the beam quality and long-term stability of the system. The energies of the laser pulses that were obtained are summarised in Table 1. Since the laser energies ultimately available at the sample (Table 1) are too low to enable complete conversion to the excited state, obtaining the smallest possible spot diameter becomes crucial.

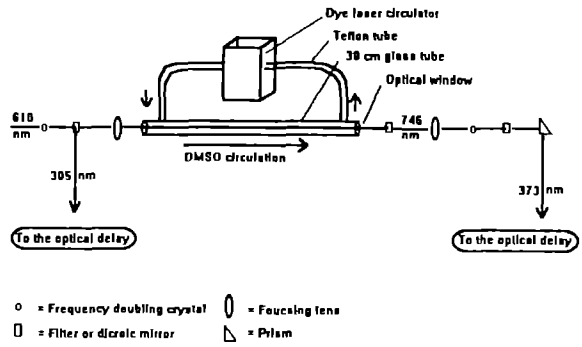

Fig. 1 Schematic layout showing the Raman shifter in the TR^3 system.

Table 1 Wavelengths and the typical energies which were used in TR^3S experiments.

Pump/probe wavelength (nm)	Output (μJ)	At the sample (μJ)
610	60.0	6.7
305	6.0	1.7
746	17.0	1.0
373	1.7	0.4
610	35.0	4.0
373	0.25	0.1
305	6.0	1.7
373	0.25	0.1

A normal (chromatic) lens focuses the pump and probe beams in different focal planes so that maximum overlap of these beams can only be achieved at the expense of spot size, giving less excited state. We have found that using a concave mirror to focus the pump & probe beams (at 305 & 610 nm) allows overlap to be achieved without compromising spot size. In comparative tests with stilbene samples we found that this arrangement gave signals with three times more excited state than in comparable experiments using a focussing lens.

In our initial time-resolved Resonance Raman (TR^3) experiments on $Cu(DMCH)_2BF_6$ and $Cu(BIQ)_2BF_6$ the most easily generated laser wavelengths at 610/305 nm were used. The sample was pumped at 305 nm and probed at 610 nm or vice-versa. Depopulation of the ground state was readily attained using either the 305 or 610 nm laser line as the pump wavelength. This depopulation was characterized by loss of ground-state features with respect to solvent bands when the spectra were probed by pulses at the other wavelength. However, only weak excited-state Raman bands could be observed, presumably because the excited-state absorption is weak at both these probe wavelengths and the degree of resonance enhancement is correspondingly low (Figure 2).

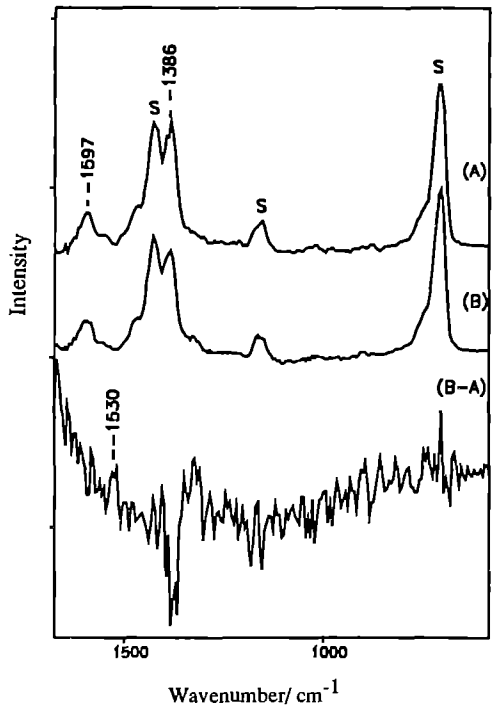

Fig. 2 TR[3] S of $[Cu(BIQ)_2]BF_6$ in CH_2Cl_2 (10^4M), probing at 305 nm (1 μJ) and pumping at 610 nm (5 μJ), delay time for (A) -100 and for (B) +100 ps, The bottom trace is the difference spectrum .

Ground state depletion could also be observed using a single laser pulse at various energies in either dichloromethane or methanol as solvents (Figure 3).

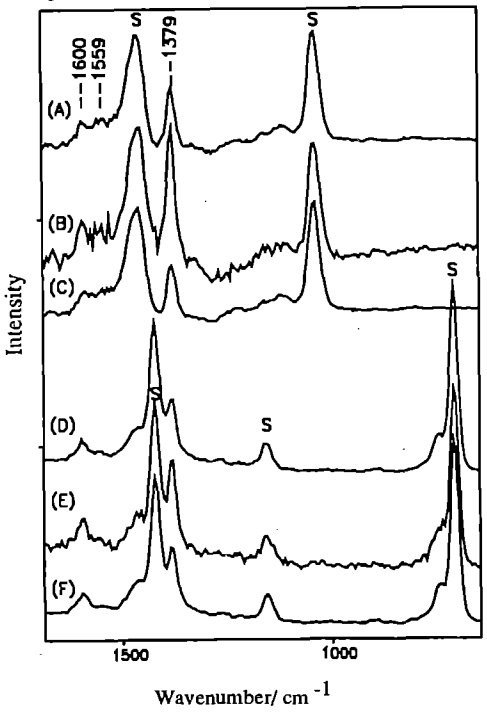

Fig 3 The RRS of $[Cu(BIQ)_2]^+$ at various laser energies using 305 nm excitation . Traces (A), (B), and (C) in MeOH solution and (D), (E) and (F) in CH_2Cl_2 solution. Laser energies for (A) and (D) were 2.5 μJ, (B) and (E) 0.5 μJ and (C) and (E) 2.5 μJ.

In order to achieve better resonance with the excited-state absorption we generated a laser line at 373 nm using the Raman shifter described above. Since a high quality beam profile was achieved we were able to record ground state Raman spectra of a range of samples with good signal-to-noise ratio (Figure 4).

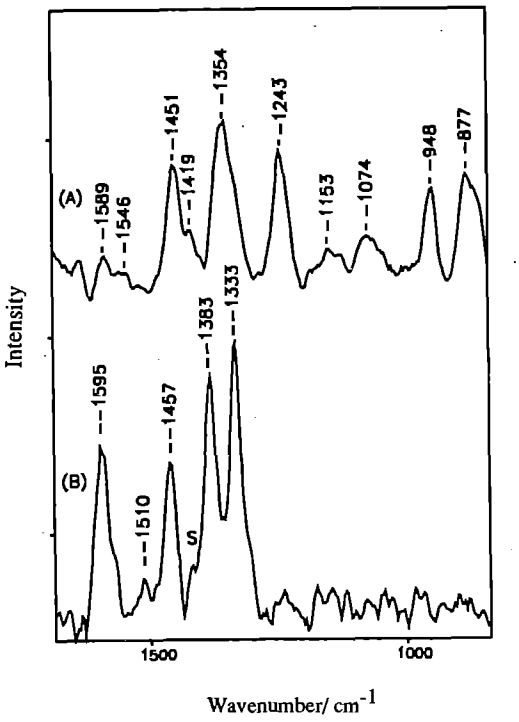

Fig 4 RRS of (A) ZnTPPC (zinc tetra 4-carboxyphenyl porphyrin) in water (10^{-4}M) and (B) $[Cu(BIQ)_2]^+$ in CH_2Cl_2 (10^{-3}M) recorded using 373 nm excitation (0.4 μJ).

Unfortunately, when the solution of $Cu^I(L)_2$ was pumped at 305 nm to generate the excited state, a very large background luminescence was observed. This background, which is not a problem when using either longer (610 nm) or shorter (305 nm) probe wavelengths, lies in the spectral window used with the 375 nm probe and swamps the Raman signals. This emission was observed for several other organic solvents but does not occur with water. This means that the system could now be used to study aqueous samples at this new probe wavelength.

REFERENCES

1. P Matousek, A J Langley, A W Parker, W T Toner, M Towrie, C E Turcu, M Wise, D Phillips, R E Hester, J N Moore and S Umapathy. Annual Report to the Laser Facility Committee, Rutherford Appleton Laboratory Report RAL-92-020 219, (1992).

2. K C Gordon and J J McGarvey . Chem . Phys. Lett., 162, 117 (1989).

3. A H R Al-Obaidi, K C Gordon, J J McGarvey and S E J Bell to be submitted to J Phys Chem. 1993.

4. D I C Martin, S J Rigby, S E J Bell, J J McGarvey, J-M Lehn, A Marquis-Rigault, A Langley and W Shaikh. Annual Report to the Laser Facility Committee Rutherford Appleton Laboratory Report RAL-92-020 153, (1992).

ACKNOWLEDGEMENTS

We wish to thank Dr A W Parker and Dr A J Langley for assistance with some of the experiments.

We are grateful to SERC for support (GR/F 42980).

TIME-RESOLVED RESONANCE RAMAN STUDIES OF WATER-SOLUBLE PORPHYRINS AND THEIR PROTEIN COMPLEXES IN THE EXCITED TRIPLET STATE

C. R. Lefley, J. N. Moore and R. E. Hester

Department of Chemistry, University of York.

INTRODUCTION

The nature of electronically excited porphyrins is of considerable interest because of their involvement in the primary photochemical reactions of systems ranging from photosynthetic reaction centres to solar energy conversion catalysts. Our specific interest in these molecules arises from their role in photodynamic therapy (PDT) [1]. It has been demonstrated that on injection into the body many water-soluble porphyrins are selectively retained in cancerous cells and that subsequent illumination with visible light can cause destruction of these cells. This destruction may be related to the production of singlet molecular oxygen, which is generated on quenching of the triplet excited states by oxygen [2], as observed *in vitro* both for free and protein-bound porphyrins.

The excited states of porphyrins have been investigated mainly using transient uv/visible absorption spectroscopy [3]. While this technique is able to provide excellent kinetic and mechanistic information it is unable to give the detailed structural information on these systems which is needed for their complete characterization. In contrast, time-resolved resonance Raman (TR^3) spectroscopy yields a rich vibrational spectrum which, on assignment, can reveal in detail the changes in structure and bonding occurring between ground and excited states. It is only recently that TR^3 spectroscopy has been applied to the study of porphyrins in the excited triplet state (T_1), and spectra have been reported for tetraphenylporphyrin systems in non-aqueous solution [4]. To date there have been no reports on the triplet states of the water-soluble derivatives, although it is important that an understanding of the excited states and photochemistry of these molecules is developed because of their use in PDT treatment. In particular, it is desirable to elucidate the effect which biological material such as protein has on the excited states in order to understand their action in the body.

In this report we describe our studies of the triplet state Raman spectra of *tetrameso*(4-sulphonatophenyl)porphyrin (TPPS) and its zinc complex (ZnTPPS) in aqueous solution. We also report the first Raman studies of these systems in the triplet state when bound to the protein Bovine Serum Albumin (BSA). Our extensive range of studies on other porphyrins is described briefly.

EXPERIMENTAL

TR^3 spectra were obtained using the pump/probe technique. Two pulsed XeCl excimer lasers were used to pump two dye lasers in order to allow independent tuning of both photolysis and probe wavelengths. The pump beam was used at a wavelength of either 420 nm or 425 nm and the probe at 460 nm (repetition rate 10 Hz, pulsewidth *ca.* 7 ns). The energies at the sample were maintained at *ca.* 1 mJ/pulse for both lasers, and the delay time between the pump and probe pulses was controlled by an electronic delay circuit.

All samples were prepared to a concentration of 2.5×10^{-4} mol dm^{-3} in phosphate buffer at pH7 (Fisons), and BSA (Sigma) was added in an equimolar ratio where used. The sample solution was flowed through a quartz capillary tube under air-equilibrated conditions.

RESULTS AND DISCUSSION

Fig. 1 shows the ground state uv/visible absorption spectra of ZnTPPS in aqueous solution both in the absence and presence of BSA. The change in the spectrum on addition of BSA indicates that binding occurs and also enables the selection of 425 nm as an appropriate photolysis wavelength for the TR^3 studies because this allows excitation of either free or protein-bound porphyrin. A similar study showed 420 nm to be appropriate for excitation of the free base TPPS. The probe wavelength was selected to coincide with the T_1-T_n electronic transition at 460 nm, as known from the literature [5], in order to obtain resonance enhancement of the Raman spectra.

Initial experiments were performed which reproduced the triplet state spectra of ZnTPP reported in the literature [4]. Fig. 2a shows the TR^3 spectrum obtained for the water-soluble porphyrin complex ZnTPPS using a time delay of 50 ns between pump and probe laser pulses, and Fig. 2b a spectrum of this system in the presence of BSA taken at the same time delay under similar conditions. The results of a parallel study on free TPPS are shown in Fig. 3.

It is known from time-resolved uv/visible absorption studies that in air-saturated solutions TPPS and ZnTPPS display excited state lifetimes on the order of 1-15 ns for the singlet and 1-2 μs for the triplet states, respectively. In these studies we observe the Raman spectrum at a time delay of 50 ns after photolysis, and therefore the spectra may be assigned to the triplet states.

The triplet state spectra of these porphyrins show a characteristic dominance of the substituted phenyl ring modes at *ca.* 1595, 1235 and 1190 cm^{-1}, as reported for ZnTPP [4]. Indeed the Raman spectrum of triplet ZnTPPS is very similar to that reported for ZnTPP. There are some small differences in band positions, but the similarity of the spectra suggest that there is only a small perturbation of the T_1 state upon *para* sulphonation of the *meso*-phenyl rings.

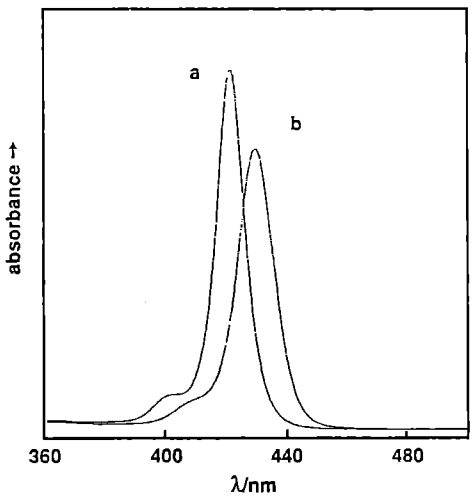

Fig. 1. UV/vis absorption spectra of ZnTPPS (7×10^{-5} mol dm^{-3} in buffer at pH7), a) unbound and b) bound to BSA.

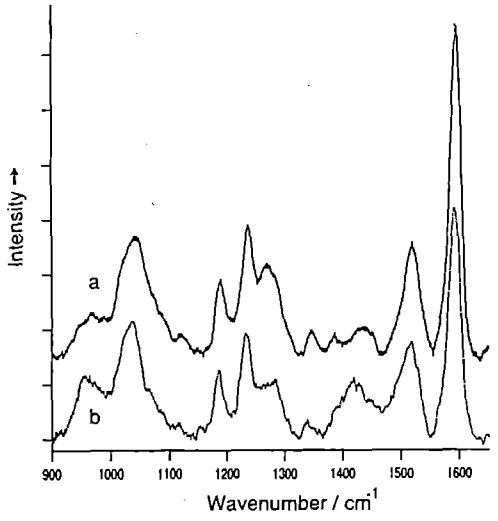

Fig. 2. TR^3 spectra of ZnTPPS in phosphate buffer at pH7, a) unbound and b) bound to BSA. Spectra obtained using a delay of 50 ns between pump (1 mJ, 425 nm) and probe (1 mJ, 460 nm) pulses.

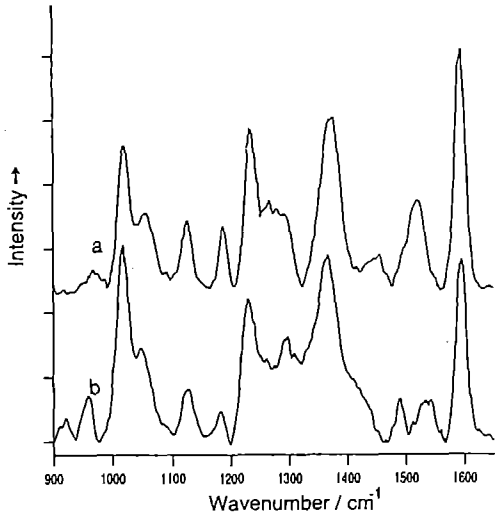

Fig. 3. TR^3 spectra of TPPS in phosphate buffer at pH7. a) unbound and b) bound to BSA. Spectra obtained using a delay of 50 ns between pump (1 mJ, 420 nm) and probe (1 mJ, 460 nm) pulses.

Although the triplet state spectra of ZnTPPS and TPPS are similar in general, there are a number of distinct differences, such as the TPPS bands found at 1376, 1126 and 1059 cm^{-1} which are absent in the ZnTPPS spectra. This can be explained in part by the lowering of the symmetry from D_{4h} (ZnTPPS) to D_{2h} (TPPS). The a_g modes of TPPS which correlate with the a_{1g} and b_{1g} modes of the metalloporphyrin are Raman active whereas only the a_{1g} modes are active for ZnTPPS. Hence the triplet state spectrum of TPPS consists of many more bands than are seen in that of ZnTPPS. A detailed discussion of the triplet state spectrum of TPP has been given in the literature [6].

It is known from time-resolved uv/visible absorption studies that on binding to protein the porphyrin triplet state lifetime increases significantly [7]. This has been suggested to occur due to the restriction of oxygen from the site of binding, thus limiting the degree of quenching. Hence, TR^3 spectra observed at 50 ns time delay for protein-bound systems also are attributable to the triplet state. It is clear from a comparison of the data presented in Fig. 2a and 3a with those in Fig. 2b and 3b that the triplet state vibrational spectra are different and therefore that the structures of both ZnTPPS and TPPS in their triplet states change on binding to BSA. Steady-state Raman studies carried out in York have shown that the ground electronic states also change on binding.

The changes in the triplet spectra on binding are relatively small for ZnTPPS, as can be seen from Fig. 2. Principally, the band at 1448 cm^{-1}, assigned as a $\nu(C_\beta\text{-}C_\beta)$ mode, shifts down by *ca.* 25 cm^{-1}. The band at 1042 cm^{-1}, which may consist of two components, decreases in bandwidth. Greater changes are observed in the triplet state spectra of TPPS on binding to BSA, as shown in Fig. 3. Specifically, in the spectral region 1400-1550 cm^{-1}, two bands are identified in the unbound porphyrin spectrum, at 1452 cm^{-1} (a depolarized band, unassigned) and at 1524 cm^{-1} (a broad band assigned to a mode arising from mainly $\nu(C_\beta\text{-}C_\beta)$ stretching). On binding, these bands are no longer present and two new features at 1490 cm^{-1} and 1534 cm^{-1} appear. Other bands undergo significant changes on binding, such as those occurring at 1376, 1295 and 1059 cm^{-1}.

In addition to the studies described above we have obtained an extensive set of results on the polarizations of the Raman bands, which aid in band assignments, on the spectra observed at different time delays, which confirm that T_1 is probed, and on the spectra observed at different porphyrin/protein ratios, which allow us to probe the possible occupancy of different binding sites. We have made preliminary observations of the copper analogue, CuTPPS, for the triplet state in both free and protein-bound forms. A different class of porphyrin, *tetrameso* (4-N-methylpyridyl)porphyrin (TMPyP) and derivatives, which show binding to DNA but not protein [8], has also been studied. We have obtained triplet state spectra of the free base, acidified and Zn - metallated forms free in solution. These systems display quite different and distinct triplet state spectra due to the different structure and charge of the ring substituents.

CONCLUSION

We have obtained excellent TR^3 spectra for a wide range of triplet excited state porphyrins which allow us to probe the structural changes occurring on photoexcitation. These spectra have been obtained under a variety of conditions, and in particular we have observed for the first time that the structures of the triplet states of TPPS and ZnTPPS are modified when these porphyrins are bound to the protein BSA. We have obtained excited state spectra of a number of other porphyrins. The full assignment of these spectra and interpretation of our results is underway in combination with steady-state Raman studies of these systems in York.

ACKNOWLEDGEMENTS

We acknowledge the technical assistance of the staff of the LSF, in particular Sue Tavender.

REFERENCES

1. B. W. Henderson and T. J. Dougherty, Photochem. Photobiol. 55, 145 (1992).
2. I. Rosenthal, C. M. Krishna, P. Riesz and E. Ben-Hur, Rad. Res. 107, 136 (1986).
3. D. Kim and D. Holten, Chem. Phys. Lett., 98, 584 (1983).
4. D. Kim, J. Terner, and T. G. Spiro, J. Am. Chem. Soc., 108, 2097 (1986).
5. K. Kalyanasundaram and M. N. Spallart, J. Phys. Chem. 86, 5163 (1982).
6. J. C. de Paula, V. A. Walters, C. Nutaitis, J. Linel, and K. Hall, J. Phys. Chem., 96, 10591 (1992).
7. J. Davila and A. Harriman, Photochem. Photobiol., 51, 9 (1990).
8. G. R. Parr, and R. F. Pasternack, Bioinorganic Chem., 7, 277 (1977).

SURFACE-ENHANCED RAMAN SPECTRA OF PORPHYRINS ON GOLD MELLFS AND RESONANCE RAMAN STUDIES OF BINUCLEAR COPPER COMPLEXES WITH AZACRYPTAND LIGANDS

A H R Al-Obaidi[1], S E J Bell[1], S J Rigby[1], Lu Qin[1], J Nelson[1,2] and J J McGarvey[1]

[1]School of Chemistry , The Queen's University of Belfast, Belfast BT9 5AG, Northern Ireland.

[2]The Open University, (Northern Ireland)

INTRODUCTION

This report describes the results obtained for two rather different types of systems investigated by means of the Ti-sapphire laser, on loan to us during Period II.

(i) Surface-enhanced Raman studies of porphyrins on gold MELLFs

Recently we reported[1] a reversible photo-induced demetallation of the silver porphyrin AgTMPyP to the free base form, H_2TMPyP (TMPyP = *meso*-tetrakis-(4-N-methylpyridyl)porphyrin). The reaction occurred at the surface of the metal liquid-like film (MELLF[2]) which forms when an aqueous silver sol is shaken with a solution of the porphyrin in dichloromethane :

$$Ag^{II}(TMPyP) \underset{\text{dark}}{\overset{h\upsilon}{\rightleftharpoons}} H_2(TMPyP)$$

We describe here a study of the Raman scattering from the porphyrin on the surface of a gold MELLF. The formation of these novel gold films was reported by us in an earlier paper.[3]

RESULTS AND DISCUSSION

The free base porphyrin H_2TMPyP can incorporate silver on either Ag sol or MELLF surfaces with considerable ease. We have found that this is not the case for either gold sol or MELLF surfaces. As Figure 1 shows , there is no indication of gold incorporation into the free base porphyrin, H_2TMPyP even in samples which had been left standing for more than 48 hours. (It is already known[1] for silver MELLFs and sols that the time required for complete metal incorporation may vary from seconds to hours or days).

We can offer no simple explanation for the absence of gold incorporation. The oxidation state of Ag in the metal porphyrin is +2 and we would expect gold to be present as Au^{3+} if incorporation did occur. The ionic radius of Au^{3+} is somewhat smaller than that of Ag^{2+} but the oxidation of Au^0 to Au^{3+} requires a higher potential than for Ag^0 to Ag^{2+}.

The surface-enhanced Raman (SER) spectra of the free base porphyrin on either Au sol or MELLF surfaces are significantly weaker than those recorded on the corresponding silver surfaces. This is mainly attributable to (i) lack of resonance enhancement (RRS) at wavelengths in the region of 700 nm (trace B, Figure 1) and (ii) the fact that the shortest available wavelength from the Ti-sapphire laser (consistent with maintaining sufficient power for generation of acceptable Raman spectra), barley coincided with the red edge of the gold surface plasmon. Nevertheless the spectra in traces A and D are clear and the bands are well-defined.

To our knowledge these are the first reported SER spectra of a porphyrin at gold surfaces.

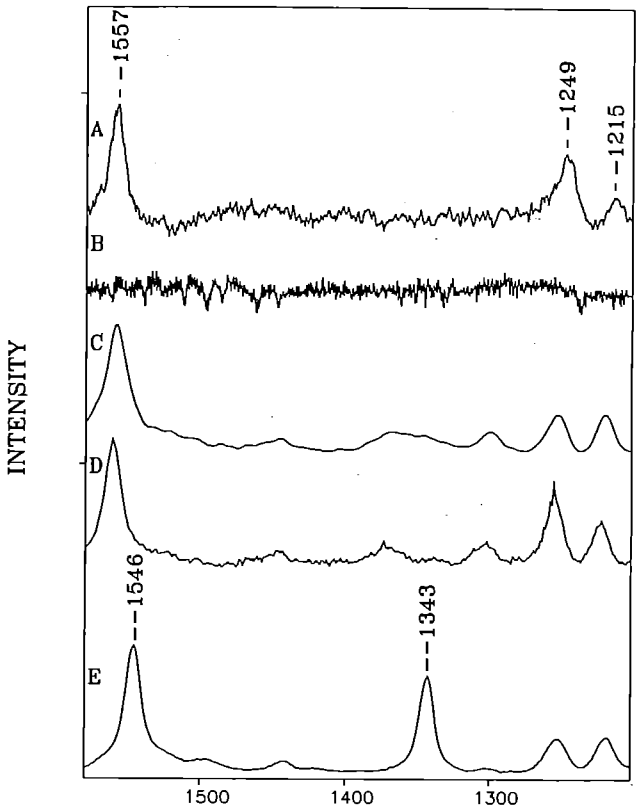

Fig. 1 SERS and RRS of H_2TMPyP (A) on gold MeLLF, (B) in an aqueous solution , (C) on silver MeLLF, (D) aqueous solution and (E) as in (C) but left until the silver metal had fully incorporated. Traces (A) and (B) recorded at λ_{ex}= 720nm and the others at 457.9nm. The laser powers were 40 mW for (A), (B) and (C) and ~1 mW for (D) and (E). H_2TMPyP concentrations ~10^{-7}M for (A), (C) and (D) and 10^{-3}M for (B) and (E). Spectral accumulation times; 60 s for (A), (C) and (E) and 300 s for both (B) and (D).

(ii) Resonance Raman spectra of binuclear copper complexes with azacryptand ligands.

The newly developed facile[4] route to azacrpytands furnishes a relatively small hexaimine ligand, L^1 (Figure 2a). This ligand normally functions[5] as a homonulceating host but on treatment with excess Cu(I) or Cu(II), dinuclear complexes are obtained. The copper ions, sited[6] on the C_3 axis in approximate D_{3h} symmetry, are *ca*.2.4 A^o apart (Figure 2c). The product isolated on treatment with Cu(II) turns out to be a *mixed-* (or better, *average-*) valence $[Cu^{1.5}\cdots\cdots Cu^{1.5}]^{3+}$ species. The octaamine cryptand, L^2, (= L^1 + 12H) (Figure 2b), obtained by reduction of L^1 likewise gives an average-valence $[Cu_2L^2]^{3+}$ cation. Electronic spectra of both cations show several absorption features, with intense bands near 750 and 320nm and associated shoulders around 600 and 1100 nm.

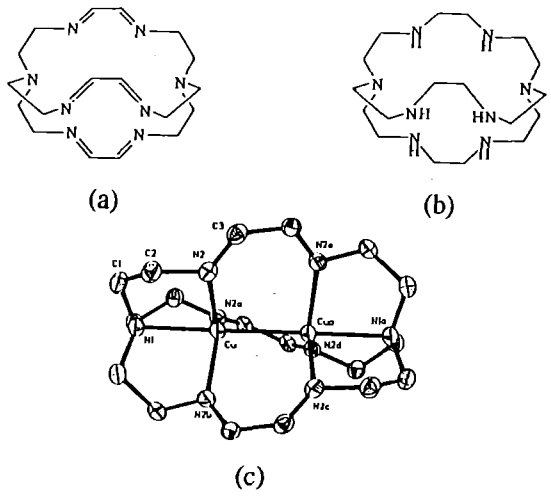

Fig.2 Structures of (a) L'; (b) L^2 ; and (c) X-ray structure of $[Cu_2L^1]^{3+}$.

These absorptions presumably derive from transitions of the $[Cu_2]^{3+}$ cation. Resonance Raman (RR) studies of the 750 nm band using the Ti-sapphire laser as excitation source have been explored to help elucidate the transitions. In the case of L^2 the complex with two different counterions has been examined. The spectra are shown in Figure 3 for the complexes with both the reduced and unreduced ligands. Both complexes with the reduced ligand exhibit three bands at 290, 275 and 240 cm^{-1} and as might be expected the counterion has no effect. The 290 cm^{-1} feature is common to all three complexes but it is impossible to draw any firm conclusions about band assignments at this early stage. A Cu····Cu stretching mode would be expected to occur at frequencies significantly below 300 cm^{-1}. A possible candidate for the 290 cm^{-1} band could be the 'axial' Cu-N_{Br} mode (Figure 2c, Br denotes bridgehead nitrogen) but any such conclusions must be regarded as extremely tentative at this stage. Further studies are obviously required. We hope to extend RR investigations to the 1100 nm band. A study by magnetic circular dischroism spectroscopy currently in progress[7] should further assist in the assignment of these absorptions.

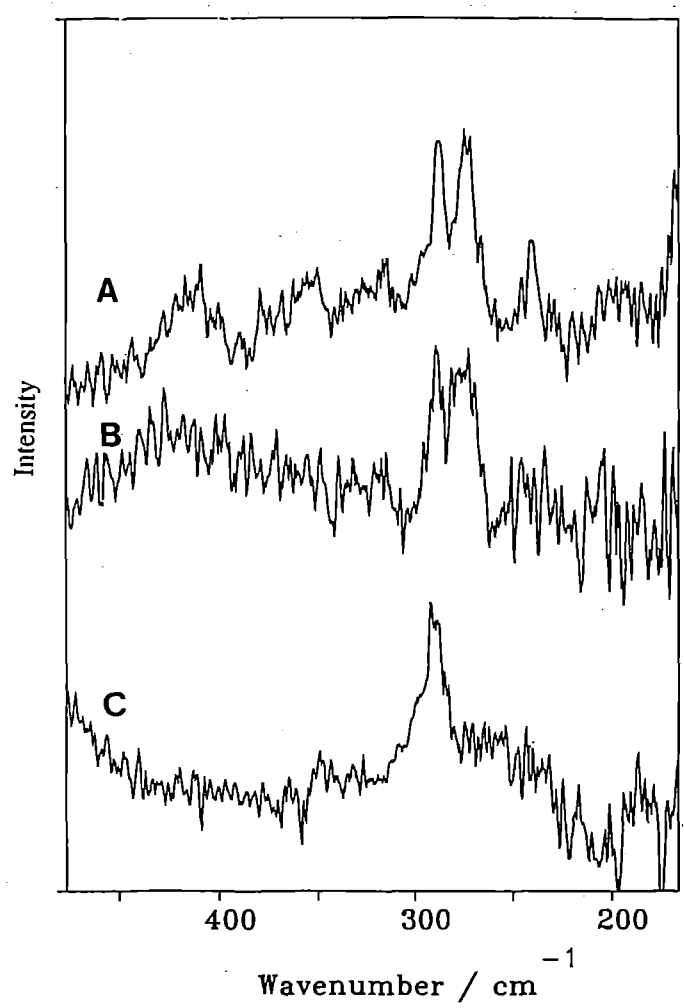

Fig. 3 RRS of (A) $Cu_2(L^2)(ClO_4)_3$, (B)$Cu_2(L^2)_3$ and (C) $Cu_2(L^1)(ClO_4)_3$ recorded at 750 nm, laser power 100 mW, accumulation times were 60 min. for (A) and 5 min. for (B) and (C). Concentrations *ca* 10^{-4}M in water in all cases.

REFERENCES

1. A H R Al-Obaidi, S J Rigby, S E J Bell and J J McGarvey. J.Phys. Chem., 96, 10960 (1992).
2. D Yogev and S Efrima. J. Phys. Chem., 89, 5754 (1988).
3. S E J Bell, J J McGarvey, S J Rigby and D G Walmsley. J. Raman Spectroscopy, 22, 763 (1991).
4. D McDowell and J Nelson. Tetrahedron Letters, 385 (1988) .
5. J Hunter, J Nelson, C Harding, M McCann and V McKee. J. Chem. Soc., Chem. Commun., 1148 (1990).
6. C Harding, V McKee and J Nelson. J. Am. Chem. Soc., 113, 9684 (1991).
7. A J Thompson and J Nelson. Work in progress.

ACKNOWLEDGEMENTS

We are grateful to the SERC for support (GR/F 82672 and GR/G00310) and the award of an earmarked studentship to SJR.

PICOSECOND PUMP-PROBE INVESTIGATIONS OF HYDROCARBON-MOLECULAR OXYGEN COMPLEXES AND PHOTOCHROMIC DYE SYSTEMS

F. Wilkinson[1], D.J. McGarvey[1], J. Hobley[1] and D.R. Worrall[1]

A. Langley[2], W. Shaikh[2] and W. Noad[2]

[1]University of Technology, Loughborough, Leicestershire LE11 3TU

[2]Rutherford-Appleton Laboratory, Chilton, Oxfordshire

HYDROCARBON-MOLECULAR OXYGEN COMPLEXES

INTRODUCTION

We are interested in understanding the interactions between the excited states of organic molecules (M^*) and molecular oxygen (O_2) which lead to excited state quenching and singlet oxygen ($O_2, {}^1\Delta_g$) production (see ref 1). The well known fact that molecular oxygen is a potent quencher of the excited states of organic molecules has implications for a diverse range of chemical systems of commercial, industrial and biological importance. The mechanism of excited state quenching by oxygen is not well understood and is potentially very complex. It is believed that quenching proceeds through excited state complexes, $(M..O_2)^*$, of the excited organic molecule with O_2. Numerous hydrocarbon-O_2 complexes may be postulated from the combination of M with O_2 in a variety of initial electronic states in which M or O_2 (or both M and O_2) are excited. In addition to these excited state complexes excited charge transfer (CT) states, $(M^+..O_2^-)^*$ which can significantly influence excited state quenching rates, are also possible. A detailed discussion of these complexes has been given by Birks (2).

In 1953 Evans (3) reported the observation of additional absorption features in the UV/visible absorption spectra of oxygenated solutions of organic molecules. These additional absorption bands arise from oxygen perturbation of ground state ($^1M_0$) --> triplet state ($^3M^*$) and charge transfer (CT) transitions (eq.1) within a contact complex, $^3(M..O_2)$, of the organic molecule (M) with molecular oxygen (O_2).

$$^1M_0 + O_2\ {}^3\Sigma_g^- \leftrightarrow {}^3(M..O_2) \xrightarrow{h\nu} {}^3(M^+..O_2^-)^* \quad (1)$$

Thus in principle it is possible to directly populate the excited state complexes and CT states which are actually formed during diffusional quenching of excited states by O_2. Selective preparation of excited state complexes by the use of pulsed lasers combined with appropriate detection methods may then lead to an enhanced understanding of the photophysical processes operating within these complexes and thus to a detailed description of excitation quenching by oxygen. This is the objective of our work in this area which has resulted in two recent publications (4,5) to which the reader is referred to for additional information.

RESULTS AND DISCUSSION

The hydrocarbons used predominantly in this work have been naphthalene derivatives substituted at the -1 position. In reference 1 we reported picosecond pump-probe data for 1-ethylnaphthalene-O_2 complexes in acetonitrile and cyclohexane at maximum oxygen pressures of ~4 atmospheres. In this report we describe some of our results for 1-methoxynaphthalene-O_2 complexes in acetonitrile and cyclohexane at oxygen pressures ranging from 2 atmospheres to 80 atmospheres.

During the last year we have made use of two laser systems, namely the Spectron actively mode-locked picosecond Nd:YAG synchronously pumping a model 375B dye laser (Spectra Physics) and the Tsunami femtosecond titanium-sapphire laser pumped by a Spectra Physics 171 Argon-ion laser. With the spectron system the pump wavelength was 353nm (~7ps, ~4uJ) and the probe wavelength was 424nm. With the Tsunami laser system the pump wavelength was 373nm (~ 800fs at the sample due to pulse stretching, 2uJ) and the probe wavelength was 436nm.

Excitation into the CT bands of oxygenated methoxynaphthalene solutions at either 353nm or 373nm gives rise to a prompt and relatively long-lived absorption at 424nm and 436nm. We attribute this absorption to the lowest excited triplet state (singlet state population is precluded on energy grounds) of 1-methoxynaphthalene formed rapidly from the initially populated Franck-Condon CT state.

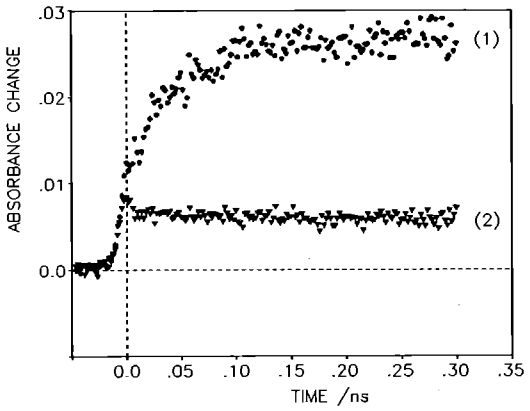

Figure 1. Subnanosecond absorption traces obtained following 7ps, 353nm excitation of (1) 1M 1-methoxynaphthalene in air-equilibrated acetonitrile containing an aromatic ketone as a sensitiser, (2) 1M 1-methoxynaphthalene in acetonitrile equilibrated with three atmospheres of oxygen. Solutions were optically matched at 353nm.

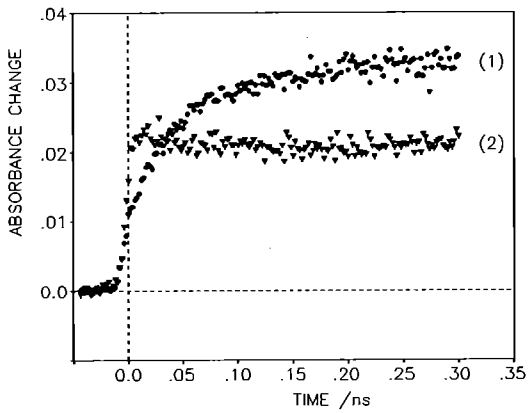

Figure 2. Subnanosecond absorption traces obtained following 7ps, 353nm excitation of (1) 1M 1-methoxynaphthalene in air-equilibrated cyclohexane containing an aromatic ketone as a sensitiser, (2) 1M 1-methoxynaphthalene in cyclohexane equilibrated with three atmospheres of oxygen. Solutions were optically matched at 353nm.

This identification is supported by recent picosecond pump-probe measurements carried out at high oxygen pressures (50-80 atm) in which it was possible to observe the diffusional quenching of the triplet state by oxygen over one or two nanoseconds. The yield of 1-methoxynaphthalene triplet state produced following CT excitation was determined in a polar solvent (acetonitrile) and a non-polar solvent (cyclohexane) by comparison with the triplet absorption observed when sensitised by an aromatic ketone in an optically matched solution. The two solvents exhibit quite different behavior as shown by the absorption traces in figures 1 and 2. It is apparent that the triplet yield following CT excitation in acetonitrile is low (~25%) while in cyclohexane it is relatively high (~70%). This behavior is similar to that which we observed for 1-ethylnaphthalene previously (5) where it appears that the polar solvent facilitates efficient internal conversion to the ground state. However for 1-methoxynaphthalene in acetonitrile the triplet state yield from the CT state is considerably less than in the case of 1-ethylnaphthalene in acetonitrile. The lower oxidation potential of 1-methoxynaphthalene relative to 1-ethylnaphthalene probably accounts for the lower probability of triplet formation from the CT complex.

PHOTOCHROMIC DYE SYSTEMS

Substituted spiro-indolino-naphthoxazines undergo a rapid isomerisation when irradiated in the ultra violet region of the spectrum (6). The primary photochemical step occurs on the femtosecond timescale, and is followed by a series of intermediate stages resulting in the formation of the coloured merocyanine form of the molecule. Previously work has been carried out on cyclohexane solutions of a spiro-indolino-naphthoxazine, SINO1. This compound has an iso-butyl group on the indoline nitrogen (R_1) and an indoline group at the 6' position of the naphthoxazine ring (R_2). The results of this work led to the proposition of the following reaction scheme,

$$A \rightarrow A^{*} \overset{k_1}{\rightarrow} B \overset{k_2}{\rightarrow} C$$

where $k_1 = 1.1 \times 10^{11}$ and $k_2 = 2.1 \times 10^{10}$.

The work reported here has been undertaken on the same photochromic compound in both cyclohexane and 1-butanol using sub picosecond laser pulses from the Tsunami titanium-sapphire system pumping at 373nm and probing at 436nm (see above). Also two other compounds have been studied; SINO2 on which R_1 is a methyl group and R_2 is an indoline and SINO3 on which R_1 is a methyl group and R_2 is a hydrogen.

RESULTS AND DISCUSSION

The most significant result of this work was the discovery of a transient state in the colouration reaction of SINO1 and SINO2 in 1-butanol, having a lifetime of around one nanosecond. It is interesting to note that the lifetime of this state is unaltered by the substituent R_1, see figure 3.

Another interesting result of this work is the similarity of the kinetic traces observed for SINO1 and SINO2 over the first 20 picoseconds of the reaction (see figure 4) and although SINO3 shows a depletion just after the pump pulse the subsequent kinetics are very similar to those seen for the other two compounds.

Masuhara (7) observed spectral shifts in the time resolved spectra of SINO3 which he attributed to a re-equilibration of various merocyanine isomers after their initial formation. The lack of effect of R_1 upon SINO1 and SINO2 would suggest that this one nanosecond transient is not due to isomerisation of the open merocyanine forms susequent to their initial production.

It is, however, not unreasonable that the nanosecond transient observed for SINO1 and SINO2 is due to a triplet state intermediate in the isomerisation process and without the availability, to date, of spectral resolution it has been difficult to assign the observed state to either merocyanine isomerisation processes or to the presence of a triplet state in the isomerisation reaction scheme.

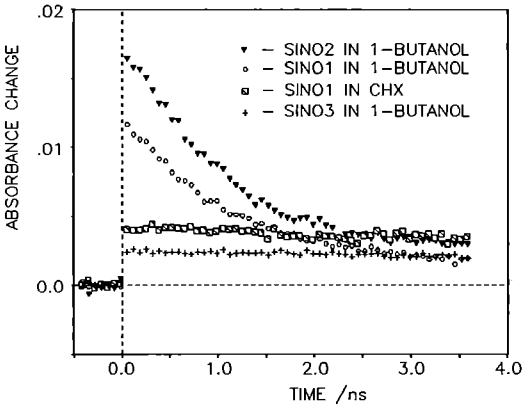

Figure 3. Kinetic traces for several spiro-indolino-naphthoxazines in cyclohexane (CHX) and 1-butanol.

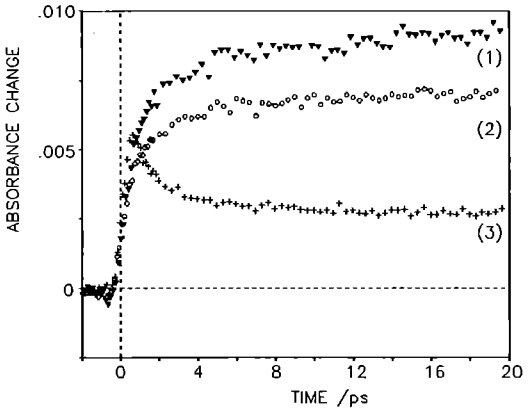

Figure 4. Rise kinetics for three photochromics in 1-butanol; (1) SINO2, (2) SINO1, (3) SINO3.

REFERENCES

(1) Wilkinson F., D.J. McGarvey, D.R. Worrall, A. Goodwin, J. Hobley, A. Langley and W. Shaikh, Annual Report to the Laser Facility Committee, Rutherford Appleton Laboratory Report RAL-92-020,159, (1992).

(2) Birks J.B., Photophysics of Aromatic Molecules, Chpt.10, p492, Wiley (1970).

(3) Evans D.F., J. Chem. Soc., 345 (1953).

(4) McGarvey D.J., P.G. Szekeres and F. Wilkinson, Chem. Phys. Letters, 199, 314, (1992).

(5) McGarvey D.J., F. Wilkinson, D.R. Worrall, J. Hobley, and W. Shaikh, Chem. Phys. Letters, 202, 528, (1993).

(6) Wilkinson F., D.R. Worrall, M. Naftaly, J. Hobley, D.J. McGarvey, A. Goodwin, A.J. Langley and W. Shaikh, Annual Report to the Laser Facility Committee, Rutherford Appleton Laboratory Report RAL-91-025,163, (1991).

(7) Tamai N. and H. Masuhara, Chem. Phys. Letters, 191, 189, (1992).

TRIPLET STATE PHOTOPHYSICS OF PHTHALOCYANINE PHOTOSENSITISERS

A. Beeby[1], S.M. Bishop[2], M.S.C. Simpson[2], H. Meunier[3], A.W. Parker[4] and D. Phillips[2]

[1] Department of Chemistry, University of Durham, South Road, Durham, DH1 3LE
[2] Department of Chemistry, Imperial College, London, SW7 2AY
[3] Department of Chemistry, Assumption College, Massachusetts, USA,
[4] Laser Support Facility, Rutherford Appleton Laboratory, Didcot, Oxon, OX11 0QX

INTRODUCTION

Phthalocyanines are well established as second generation photosensitisers for photodynamic therapy (PDT) of tumours and other diseases. The activity of these sensitisers is generally accepted to be mediated by the formation of singlet molecular oxygen, $^1\Delta_g$ O_2, which is produced by energy transfer from the triplet state of the dye. Disulphonated aluminium phthalocyanine has been identified as a compound with optimum photobiological activity[1] and is a promising drug candidate. Clearly an understanding of the fundamental photophysical properties and how environment can affect the activity of this drug are essential if we are to understand the primary mechanisms of photodynamic action. As reported previously[2] our group has studied the singlet and triplet state photophysics of $AlPcS_2$ in a variety of solvent and model biological systems. A particularly interesting observation was that changing the solvent from H_2O to D_2O significantly increases both the lifetime and quantum yield of the triplet state. We have attributed to the replacement of the axial -OH ligand to -OD on the central metal ion. Following this observation alternate ligands that preferentially bind to the central metal ion were sought and the changes to the molecules photophysics determined. This work coincided with reports of fluoride ions, which are known to form a complex with Al^{3+}(aq), inhibited the photobiological activity of aluminium phthalocyanines[3].

In parallel to this a fully deuterated zinc phthalocyanine was prepared and the photophysical parameters determined in order to investigate the effects of isotopic substitution on the periphery of the macrocycle.

EXPERIMENTAL

Triplet state studies were carried out using the ns-laser flash photolysis apparatus based at the Laser Support Facility, as detailed in previous reports[4]. Samples were prepared to have an absorbance of 0.05- 0.5 at the excitation wavelength and were pumped at 355nm for quantum yield, kinetic and time resolved absorption measurements and also at 660-680nm for kinetic measurements. Laser energies in the range 10 - 1000μJ per pulse were employed. Triplet extinction coefficients were calculated from the bleach of the ground state using time gated spectra acquired on the OMA. Triplet quantum yields were determined by absolute and relative methods. Zinc tetraphenyl porphyrin was used as a standard material, Φ_t = 0.84, ε_t = 74,000 $mol^{-1}dm^3cm^{-1}$ at 470nm[5].

RESULTS AND DISCUSSION

(i) Triplet extinction coefficient and quantum yield of $AlPcS_2$.

The triplet quantum yield of $AlPcS_2$ in H_2O (PBS, pH 7.4) has been determined to be 0.17±0.03, in D_2O this increases to 0.22±0.04. The value in H_2O is somewhat lower than those reported by Harriman *et al.*[6] and Kier *et al.*[7], (Φ_t = 0.42), however it is believed that this is due to the earlier workers using inaccurate values for the extinction coefficient for the triplet absorption band at 490nm. Harriman *et al.* reported a value of 18,000 $mol^{-1}dm^3cm^{-1}$, much less than that determined in this work using the time resolved spectrometer at the LSF. Using the bleach of the Q-band at 670nm (ε = 1.8 x 10^5 $mol^{-1}dm^3cm^{-1}$) we have determined, ε_t (490) = 36000±6000 $mol^{-1}dm^3cm^{-1}$. Similar values have been obtained for $AlPcS_2$ in methanol, $ZnPcS_2$ in methanol and ZnPc in toluene/pyridine, and these correspond well with the values reported by Darwent *et al.*[8]. Braun *et al.*[9] have reported that the triplet extinction coefficient for AlPcCl in chloronaphthalene was dependent upon the laser power used. We have shown that in the range 50-2000μJ per pulse, absorbed in a volume of 0.25cm^3, the extinction coefficient is independent of laser energy.

(ii) Effects of added fluoride

The addition of 10mM sodium fluoride to aqueous $AlPcS_2$ brings about a 6nm blue shift in the Q-band, indicating the formation of a fluoro-aluminium complex in which the axial -OH ligand has been exchanged for -F. A similar 4nm shift was seen for this species in methanol solutions on addition of 10mM tetrabutylammonium fluoride (TBAF). The triplet quantum yields in H_2O and D_2O are markedly increased by the addition of fluoride, Φ_t = 0.25±0.04 and 0.37±0.06 respectively. A summary of the triplet state and singlet state data is shown in Table 1. From this data we can calculate the rate coefficients of the deactivation processes of the singlet state and observe the effects of the modified ligand and solvation. The triplet quantum yield of $ZnPcS_2$ in methanol has also been determined, Φ_t = 0.50±0.06, and the value agrees well with those of similar compounds, ($ZnPcS_4$), Φ_t = 0.56).[10] Addition of fluoride caused no change in the triplet yield nor in the triplet lifetime; unlike Al^{3+}(aq), Zn^{2+}(aq) does not form a strong complex with F^-. Further, the triplet quantum yield of $GaPcS_2$ in methanol has also been measured and this too unchanged by addition of 10mM TBAF (Φ_t = 0.37±0.04), although a 3nm blue shift of the Q-band was observed. This suggests that the complex formed between $GaPcS_2$ and F^- does not alter the triplet state photophysics. Preliminary spectroscopic and photochemical data has indicated that the quantum yields of singlet oxygen formation follows the same pattern, and the yield from $AlPcS_2$ is increased by the addition of fluoride.

(iii) Photophysics of ZnPc-d_0 & d_{16}

It is know that the isotopic substitution of D for H on the periphery of porphyrins leads to a change in their photophysics.[11] In order to examine the possible role of the C-H vibrational modes on the deactivation of the excited electronic states of phthalocyanines a deuterated compound, ZnPc-d_{16} was prepared[12] and its photophysics in toluene/1% pyridine compared to the protiated species. Interestingly, the triplet state lifetime, quantum yield and the quantum yield of singlet oxygen formation (τ_t = 330±30μs in a 2μM solution, Φ_t = 0.59±0.07, Φ_Δ = 0.52±0.06) were unaffected by the isotopic exchange, indicating that the peripheral substituents play a minor part in the deactivation of the excited electronic states.

Table 1 Summary of Photophysical Parameters of $AlPcS_2$ in Phosphate Buffered Saline and Effects of Added Fluoride

Solvent	τ_f/ns	Φ_f	Φ_t	Φ_{ic}	$10^7 k_f/s^{-1}$	$10^7 k_{isc}/s^{-1}$	$10^7 k_{ic}/s^{-1}$
H_2O	5.2	0.40±0.04	0.17±0.03	0.43±0.07	7.7±0.8	3.3±0.6	8.3±1.2
H_2O + F^-	4.4	0.35±0.03	0.25±0.04	0.40±0.07	7.6±0.5	4.8±0.4	9.1±1.5
D_2O	6.8	0.52±0.05	0.22±0.04	0.26±0.09	7.9±0.8	3.2±0.3	3.8±1.4
D_2O + F^-	5.4	0.44±0.04	0.37±0.04	0.19±0.08	8.1±0.8	5.4±0.4	3.5±1.5

This work shows that the axial ligand and co-ordinated solvent of aluminium phthalocyanine compounds play an important role in the mechanism for excited state deactivation. Using the data in Table 1 we can calculate the rate coefficients for the three deactivation pathways open to the singlet state; fluorescence, k_f, internal conversion, k_{ic}, and intersystem crossing to the triplet, k_{isc}. These values are included in Table 1.

The data presented above shows clearly that the rate of the deactivation of the singlet state by fluorescence is not significantly affected by the solvent type, nor the exchange of -OH/D for -F. Isotopic exchange brings about a reduction in the rate of $S_1 \rightarrow S_0$ internal conversion, but does not affect the rate of the intersystem crossing process. Exchange of the ligand to the fluoro-complex reverses this observation; the internal conversion process is not affected by the ligand exchange but the rate of intersystem crossing is increased by ca. 50%. The addition of fluoride does not prevent the isotopic composition of the solvent influencing the system. It is known that in the aluminium phthalocyanine the central metal ion is 6-co-ordinate; 4-bonds to the nitrogens of the macrocycle, one to the axial ligand and one to a solvent molecule. The results presented indicate that the co-ordinated solvent molecule also plays an important part in the deactivation of the excited states.

CONCLUSIONS

The triplet state photophysics of $AlPcS_2$ (ε_t, Φ_t and τ_t) have been accurately determined. The lower Φ_t of our results compared values reported by earlier workers is attributed to the value of ε_t used in calculations.

Addition of F^- to $AlPcS_2$ forms a complex in which there is an axial fluoride ligand and this has different photophysical properties to that with the -OH ligand. An important consequence of this ligand is that Φ_t is increased, which in principle also increases its potential as a PDT photosensitiser. Similar experiments with $ZnPcS_2$ and $GaPcS_2$ resulted in no change in excited state photophysics.

Solvent deuteration is known to enhance PDT efficiency of sensitisers; it is well established that the exchange of D for H within the solvent reduces the rate at which singlet oxygen is deactivated by non-radiative pathways. During the course of this study we have also demonstrated that the photophysics of the phthalocyanine sensitiser are modified by isotopic exchange of the solvent, and that the observed increase in photooxidation of a substrate in D_2O compared to H_2O occurs for two reasons, (i) the longer lifetime of singlet oxygen in D_2O and (ii) the increased triplet quantum yield of the sensitiser in D_2O.

REFERENCES

1. WS Chan, JF Marshall, RK Svenson, J Bedwell and I Hart *Canc Res* (1990) 50 4533
2. A Beeby, SM Bishop, AJ MacRobert, AW Parker, MSC Simpson and D Phillips *SERC CLF Annual Report* (1992) RAL-92-020 147
3. E Ben Hur, TMAR Dubbleman and J van Steveninck *Photochem Photobiol* (1991) 54 703
4. A Beeby, AW Parker and D Phillips *SERC CLF Annual Report* (1991) RAL-91-025 193
5. I Carmichael and GL Hug *J Phys Chem Ref Data* (1986) 15 1
6. J Davila and A Harriman *Photochem Photobiol* (1990) 51 9
7. WF Keir, EJ Land, AH MacLennon, DJ McGarvey and TG Truscott *Photochem Photobiol* (1987) 46 587
8. J Darwent, I McCubbin and D Phillips *JCS Farad II* (1982) 78 347
9. P Jaques and AM Braun *Helv Chim Acta* (1981) 64(6) 1800
10. A Harriman, G Porter and M-C Richoux *JCS Farad II* (1980) 76 1618
11. R P Burgner and A M Ponte-Goncalves *Chem Phys Lett* (1977) 46 275
12. S Bishop, A Beeby, AW Parker and D Phillips Paper in preparation.

A FLASH PHOTOLYSIS STUDY OF DIBENZOYLMETHANE

Andrew Beeby

Department of Chemistry, University of Durham, South Road, Durham DH1 3LE

INTRODUCTION

In solution dibenzoylmethane exists as a cyclic hydrogen bonded enol (I). It has been suggested in the literature that following excitation an excited electronic state of (I) isomerises to a non-hydrogen bonded form (IIa or IIb) which thermally isomerises back to either the starting material (I) or to the keto form, (III). Alternatively (I) may convert directly to (III) by a photochemically induced [1,3]-H-transfer. Finally it is possible for (I) to undergo a [1,5]-hydrogen shift to generate (I); this step would be undetectable for this system. The keto form, which is present as a minor component in the equilibrated solution isomerises to the thermodynamically favoured enol (I), [1,2,3]. It has also been reported that irradiation of (I) does not form singlet oxygen, [4].

Laser flash photolysis was used to investigate the species fromed on irradiation of (I) and also of the intermediates. The flash photolysis apparatus at RAL allows the acquisition of transients in the range 300 - 800nm; due to experimental difficulties (failure of Xe lamp, coupled with the poor throughput and sensitivity of the probe optics in the UV it was not possible to record data below 300nm. The H-bonded enol (I) has a broad absorption band centred at 340nm and extending to almost 400nm, whereas the diketo form is reported to have a maximum at 250nm. The spectrum of the E-enol (IIb) has not been yet been identified although by analogy with a model compound which is locked into the enol form by O-methylation, it expected to have a maximum around 290nm.

The preliminary experiments presented here concern the transients generated following the irradiation of dibenzoylmethane in aerated and degassed cyclohexane and ethanol.

RESULTS AND DISCUSSION

A degassed solution of dibenzoylmethane in cyclohexane was irradiated at 350nm. Time resolved absorption measurements at 340-380nm showed a rapid bleaching of the ground state (τ_r < 1μs) followed by a slow decay to a weakly absorbing transient, (τ = 3.5ms). This transient decayed back to the baseline and had a lifetime of 10-15ms. Monitoring the solution at 300nm showed the rapid formation of a transient (τ_r < 1μs) which decayed back to the starting point with a lifetime of 3.5ms. No transient absorptions could be detected in the range 400-800nm. Interestingly aeration of the solution caused only a small reduction, (≈20%), in the lifetimes of the observed transients. It is known that the photolysis of enoliseable 2-alkyl benzophenones produces isomeric enols, and that the process that forms these is not quenched by molecular oxygen, [5].

Time resolved measurements do indicate that in aerated cyclohexane singlet oxygen is formed in low yield, $\Phi_\Delta \approx 0.03$. The rise time of the singlet oxygen luminescence is ca. 1μs, consistent with the diffusion limited quenching of an excited state formed rapidly after the excitation pulse by oxygen.

Flash photolysis studies of an aerated ethanol solution of (I) showed a rapid bleach of the ground state in the region 340 - 380nm, (τ_r < 1μs), which decayed back to the baseline with a lifetime of ca. 3ms. No new absorbing species could be detected in the range 340 - 800nm.

Degassing the solution brought about a significant change in the photophysics of this compound. Monitoring the ground state at 360nm showed a bleach with a rise-time of < 1μs. This recovered back to the baseline by a complex decay; the data may be fitted to a double exponential function with lifetimes of 70μs and ca. 1.5ms.

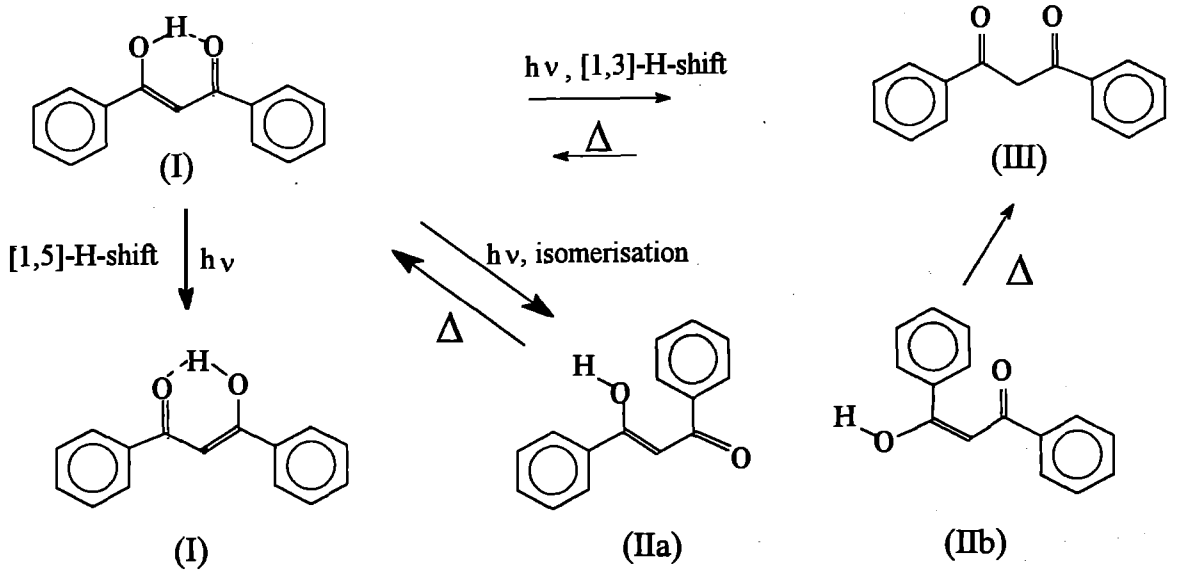

Possible Pathways of Reaction for Dibenzoylmethane Following Irradiation

At longer wavelengths (380 - 420nm) a transient absorption was measured which grew in with an exponential function with a lifetime of 70μs and then decayed back to $\Delta A = 0$ with a single exponential and a lifetime of 1.5ms. No other transients were detected in the range 440 - 800nm. Monitoring the absorbance at 300nm there was evident for a short lived absorption superimposed upon the bleach of the ground state. The poor signal to noise ratio at wavelengths <300nm prevented measurements in this region. Early and late time gated difference spectra calculated from the transient decays at 10nm intervals are shown in Figure 1 along with the absorption spectrum of (I). A kinetic scheme to explain the observed kinetics is outlined below.

$$(I) + h\nu \rightarrow A$$

$$A \rightarrow B \quad k_a$$

$$A \rightarrow (I) \quad k_b$$

$$B \rightarrow (I) \quad k_c$$

Where $^1/(k_a + k_b) = 1.5 \times 10^{-3}$ s and $^1/k_c = 7 \times 10^{-5}$ s

The absorption profile of species B (370 - 420nm), corresponding to spectrum 3 in figure 1, suggests that it is not due to the ground electronic states of the enols (II) or of the keto form (III), and as yet is unidentified. Species A could be either one of the enol forms or the keto form; as yet there is insufficient experimental data to unambiguously assign the spectrum. The time resolved spectral data reported above was confirmed by a brief experiment using the time-gated OMA.

Future work will enable the characterisation of the products and intermediate species formed upon irradiation of this important class of compound. The studies will investigate the roles of solvent type and oxygen.

REFERENCES

1 D. Veierov *et al, J. Amer. Chem. Soc.* **99** (1977) 2723-29

2 P. Yankov *et al. Bulg. J. Phys.* (1985) 629-32

3 P. Yankov *et al, J. Photochem. Photobiol. B* **41** (1988) 205-14

4 D. Guangson *et al, Youji Huaxue* **2** (1987) 115-18

5 G. Porter *et al, J. Chem. Soc.* (1971) 3772-77

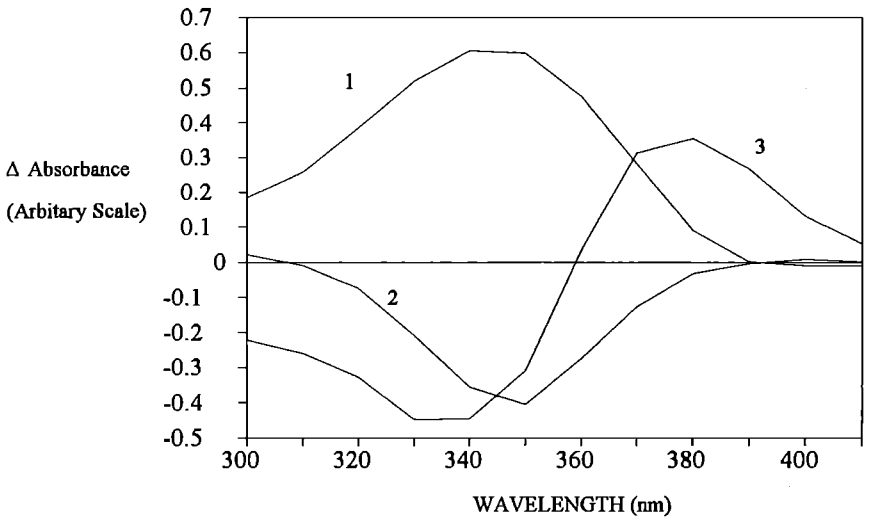

Figure 1 (1) absorption spectrum of (I) in ethanol, (2) time gated difference spectrum at short time delay (Δt = 1 μs) and (3) time gated difference spectrum at long time delay (Δt = 1ms).

SINGLET OXYGEN SENSITISATION BY DNA

S.M. Bishop[1] M. Malone[2] M.C.R. Symons[2] A.W. Parker[3] and D. Phillips[1]

[1]Department of Chemistry, Imperial College, London
[2]Department of Chemistry, Leicester University
[3]Rutherford Appleton Laboratory

INTRODUCTION

The accepted molecular level theory for the photoinduced damage of DNA is described in the charge sequestration model of Adams and Cooke[1]. Briefly the $DNA^{+\cdot}$ radical (the positive charge residing on guanine base residues) is produced when ionising radiation interacts with DNA. Such ionising radiation produces positive holes (electron loss centres) and negative charge centres. Charge migration occurs and the subsequent charge recombination process is arrested by electron affinic molecules, such as O_2 and radiosensitising drugs, removing the negative charge and leaving the radical cation. An alternative mechanism for producing this radical has been proposed whereby triplet electronically excited state DNA bases transfer an electron to electroaffinic molecules according to the Rehm-Weller equation[2]. If O_2 acts as the electron acceptor then superoxide would be produced as shown by equation 1 below:-

$$^3Base + O_2 \rightarrow Base^{+\cdot} + O_2^{-\cdot} \qquad (1)$$

$$^3Base + O_2 \rightarrow Base + O_2(^1\Delta_g) \qquad (2)$$

Alternatively, though, the triplet base could transfer its energy to ground state O_2 via a type II photodynamic mechanism resulting in the production of singlet oxygen ($O_2(^1\Delta_g)$) as shown in equation 2. This is a highly reactive excited state of oxygen that is believed to be an important intermediate in the photooxidation of biological and other systems. It may be generated by energy transfer from electronically excited compounds (usually in the triplet state) and can be detected directly from its characteristic $^1\Delta_g \rightarrow {}^3\Sigma_g^-$ phosphorescence at 1270nm.

The yield of singlet oxygen (Φ_Δ) is given by equation (3)

$$\Phi_\Delta = S_\Delta \Phi_t \qquad (3)$$

where Φ_t is the triplet quantum yield and S_Δ is the fraction of oxygen quenchings of T_1 leading to $O_2(^1\Delta_g)$ formation. In order for $O_2(^1\Delta_g)$ to be formed via energy transfer, the $S_1 \rightarrow T_1$ gap of the molecule must exceed 94.5 kJ mol^{-1}, the energy of $O_2(^1\Delta_g)$, a property that all of the DNA bases possess.[3] The Φ_t of the DNA bases and nucleosides in condensed phase are not insignificant[4] and so it is therefore possible that they could photosensitise the production of singlet oxygen. In this study we have determined the Φ_Δ for the bases, nucleotides, dinucleotides and DNA in either acetonitrile or D_2O. In addition we have performed a number of preliminary experiments in an attempt to elucidate the mechanisms of photoinduced DNA damage.

EXPERIMENTAL

Solutions of DNA, nucleotides, nucleosides, dinucleosides and bases in either acetonitrile or D_2O (10^{-4}-10^{-5}M) were irradiated with 248nm attenuated light from the KrF Questek excimer laser (10ns, 0-1.5mJ/pulse). The 1269nm singlet oxygen luminescence from the excited samples was detected at right angles to the laser beam, using a North Coast EO-817P liquid nitrogen cooled germanium photodiode, after passing through a 1270nm silicon filter (30nm bandpass). Φ_Δ of thymine, adenine, cytosine and uracil in acetonitrile were determined via comparison of laser power/$^1O_2$ signal graphs with two standards anthracene ($\Phi_\Delta^{MeCN} = 0.66$) and acridine ($\Phi_\Delta^{MeCN} = 0.88$). Prior to this experiment the Φ_Δ^{MeCN} of these two standard compounds was determined in an analogous manner to that described above using benzophenone as standard ($\Phi_\Delta^{MeCN} = 0.37$)[5] and irradiating with the 351nm attenuated output of a XeF excimer laser (10ns, 0-1.5mJ/pulse).

The set-up for the UV laser flash photolysis experiments is described in a previous RAL report.[6] A KrF excimer laser (248nm) was used as the pump and a xenon lamp as the analysing light.

RESULTS AND DISCUSSION

The Φ_Δ^{MeCN} of four of the DNA bases are shown in the table below (all results are quoted within a ± 15% error). For comparison Φ_t^{MeCN} are also reported.[4]

DNA base	Φ_Δ^{MeCN}	Φ_t^{MeCN}
Thymine	0.07	0.06
Uracil	0.13	0.20
Adenine	0.03	---
Cytosine	0.02	---

For the pyrimidine bases thymine and uracil, singlet oxygen is produced with near 100% efficiency from the triplet state suggesting that a Type II photodynamic mechanism predominates.

Solutions of guanine, 2'-deoxyguanosine 5'-monophosphate (GMP), thymidylyl(3'→5')-2'-deoxyguanosine (T-G) and DNA in D_2O showed no detectable singlet oxygen signal, whilst those of thymine, 2'-thymidine 5'-monophosphate (TMP) and thymidylyl(3'→5')-2'-deoxyadenosine (T-A) in D_2O did. The figure below shows the singlet oxygen decay traces for GMP and TMP in D_2O.

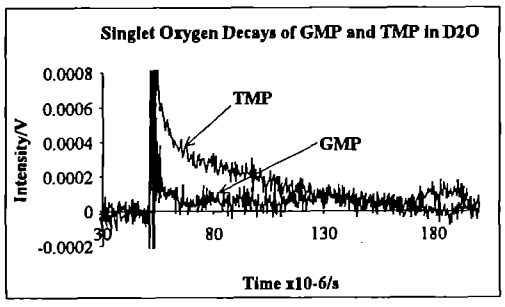

Further evidence that GMP does not generate $O_2(^1\Delta_g)$ was obtained by adding azide (10^{-2}M) which is an efficient $O_2(^1\Delta_g)$ quencher. The resultant decay trace for GMP was exactly the same as the GMP only curves. The Φ_Δ for TMP in D_2O was estimated to be 0.009 which is comparable with the Φ_t result obtained for this species in H_2O.[7]

The presence of a guanine residue in the base pair gives a system which does not generate singlet oxygen. This result is rather surprising - for example, in the T-G dinucleoside the triplet T has the lowest energy triplet state (^{3}TMP = 315 kJ mol^{-1}; ^{3}GMP = 325 kJ mol^{-1})[3]. Thus if ^{3}G is formed, triplet-triplet energy transfer would be expected to occur to give only ^{3}T - a species that we know can sensitise the formation of $O_2(^1\Delta_g)$. However, another possible reaction of ^{3}G is to generate $O_2^{-\cdot}$ by electron transfer producing $G^{+\cdot}$. Recently, experiments by Lee and Rodgers[8] have shown that of the five bases only guanosine (ground state) quenches singlet oxygen. The results above can also be explained if the molecule does generate singlet oxygen by Type II photodynamic action on excitation, but it is rapidly quenched by the guanine residues present. If this latter hypothesis is correct another mechanism for the photodamage of DNA is possible where singlet oxygen produced by a Type II photodynamic mechanism from the DNA triplet state is quenched by close proximity of a guanine residue, leading to oxidative damage to the DNA chain.

It is also feasible that guanine and GMP do not generate singlet oxygen at all. However, little is known about the triplet state parameters of such molecules and therefore it is not understood whether they are able to participate in photodynamic Type II energy transfer. The triplet states of these species could quite conceivably enter into electron transfer reactions with O_2 to give the radical cation as reported previously[2]. A series of preliminary UV Laser Flash Photolysis experiments were performed in an attempt to verify this hypothesis. A solution of GMP in D_2O (10^{-4}M) was irradiated with 248nm attenuated laser (130mJ/pulse) in degassed, aerated and oxygen saturated environments. The amount of $GMP^{+\cdot}$ was determined by probing the solution at 320nm[9] after the flash and measuring the intensity at t_o from the decay profile. A signal was seen in degassed solution indicating that there was some photoionisation at the pulse power used. In aerated solution this signal was seen to increase by 50% suggesting that electron transfer to O_2 from triplet GMP is indeed taking place, but contrarily, with a saturated O_2 solution the $GMP^{+\cdot}$ signal was seen to be less than that for both aerated and degassed. This situation can be explained if, as Cadet and co-workers recently reported[10], guanine radicals (formed on rapid deprotonation of $G^{+\cdot}$) react with molecular oxygen generating oxygenated products. The mechanism of formation and nature of the major photoproducts for singlet oxygen oxidation of guanine residues is reported not to involve a cation radical.[10] It could therefore be inferred that excited guanine residues produce electron transfer photoproducts whilst singlet oxygen generated from the other DNA base moieties produces Type II photooxidation products on being quenched by ground state guanine residues.

CONCLUSIONS

Φ_Δ for thymine, adenine, cytosine and uracil in MeCN have been determined for the first time. Triplet excited DNA may generate $O_2(^1\Delta_g)$ via a Type II photodynamic mechanism. However, whilst individually the triplet states of T, U, A and C are capable of sensitising the production of $O_2(^1\Delta_g)$, the ability of DNA to do so remains unclear. This is because the presence of guanine residues quenches $O_2(^1\Delta_g)$, possibly forming oxidised moieties and potentially DNA damage. The fate of triplet excited guanine residues is still open to debate though the work of this report suggests that an energy transfer reaction to oxygen producing the characteristic molecular DNA photoproduct $DNA^{+\cdot}$ is more likely than a Type II mechanism.

ACKNOWLEDGEMENT

We thank Peter O'Neill for providing us with details of the $G^{+\cdot}$ UV absorption spectrum.

REFERENCES

1. GE Adams and MS Cooke *Int J Radiat Biol* (1969) 15 457.

2. TJ Kemp, AW Parker and P Wardman *J Chem Soc Perkin Trans II* (1987) 397.

3. SY Wang (Ed) 'Photochemistry and Photobiology of Nucleic Acids' (1976) Vol.1 Acad Press New York.

4. C Salet and RV Bensasson*Photochem Photobiol* (1975) 22 231.

5. SK Chattopadhyay, CV Kumar and PK Das *J Photochem* (1984) 18 293.

6. A Beeby, AW Parker and D Phillips *SERC LSF Ann Rep* (1991) 193.

7. C Salet, RV Bensasson and RS Becker *Photochem Photobiol* (1979) 30 325.

8. PCC Lee and MAJ Rodgers *Photochem Photobiol* (1987) 45 79.

9. LP Candeias, P O"Neill, GDD Jones and S Steeken *Int J Rad Biol* (1992) 61 15.

10. J Cadet, M Berger, G Buchko, J-L Ravanat and H Kasai 'Frontiers of Photobiology' (1993) ICS Vol. 1021 pp49 Elsevier Sci. Publ. Amsterdam.

LASER SPECTROSCOPY OF OPEN-SHELL METALLOCENES

Jeremy N. Hill, Robin N. Perutz and A. Denise Rooney

Department of Chemistry, University of York, York YO1 5DD

INTRODUCTION

Knowledge of the photophysics of organo-transition metal complexes is often lamentably weak when set against their rich photochemistry. The intense laser-induced fluorescence (LIF) of open-shell metallocenes isolated in low-temperature matrices has enabled us[1,2] to obtain a detailed description of the lowest energy ligand-to-metal charge-transfer excited states of $(\eta^5\text{-}C_5H_5)_2Re$, $(\eta^5\text{-}C_5H_5)_2Mo$, $(\eta^5\text{-}C_5H_5)_2W$ and $(\eta^5\text{-}C_5Me_5)_2Re$. The use of matrix isolation methods allows high quality spectra to be obtained of molecules which are extremely labile in fluid phases: the first three molecules above are known only as reactive intermediates in solution. However, it is important to know to what extent the measurements are influenced by the effects of the matrix. For this reason, we require data for each sample in both nitrogen and argon matrices. The first goal of this year's work was to obtain emission and excitation spectra for $(\eta^5\text{-}C_5H_5)_2Re$ in argon matrices. In addition, we attempted to measure its quantum yield for emission in a nitrogen matrix. Armed with a detailed set of Franck-Condon profiles and frequency data for ground and excited states, we have undertaken calculations designed to estimate the change in structure between ground and excited states.

The closely related bis(arene) metal complexes do not luminesce, but instead show resonance Raman spectra. The frequencies measured in the resonance Raman spectra for the bis(arene) metal complexes correspond to those measured by LIF for the metallocenes. Following measurements on matrix-isolated $(\eta^6\text{-}1,3,5\text{-}C_6H_3Me_3)_2V$ in York with fixed frequency cw lasers,[3] we recorded their resonance Raman spectra with pulsed tunable lasers at the RAL.

RESULTS

Rhenocene, $(\eta^5\text{-}C_5H_5)_2Re$, was generated by photolysis of the corresponding mono-hydride complex isolated in an argon matrix. Despite the poorly resolved absorption spectrum, it shows a highly resolved emission spectrum (Figure 1) with a series of vibrational progressions. Three of the four totally symmetric vibrational modes of the ground electronic state may be determined from this spectrum. An excitation spectrum may be determined from the variation in the intensity of peak A1 with laser excitation wavelength (Figure 2). As we have observed previously, the excitation spectrum is much sharper than the absorption spectrum (Figure 2) because of the site/conformer selectivity of the laser. The lifetime of the excited state was determined as 69.3 ± 1.4 ns. None of these features are affected significantly by the use of an argon matrix when compared to our earlier results with nitrogen. We attempted to measure the quantum yield for emission by collecting the total sample fluorescence and some laser emission on an optical multichannel analyser and comparing it to the fluorescence from a standard solution measured under similar conditions. Unfortunately, the signal-to-noise ratio was too low to obtain meaningful results.

The Franck-Condon intensity profiles observed in the emission and excitation spectra carry information about the change in the normal coordinates between ground and excited states. J. Zink (UCLA) has developed programs for simulating the spectra which employ Heller's wavepacket method based on the time-dependent Schroedinger equation.[4] In collaboration with Zink, we have successfully simulated the spectra of rhenocene. By making the further assumption that the normal and symmetry coordinates are identical, we have obtained a value for the compression of the rhenium to cyclopentadienyl-centroid distance in the excited state of 0.045 Å. We could also simulate the emission spectrum of $(\eta^5\text{-}C_5H_5)_2W$, but in this case the excitation spectrum could not be simulated with the same set of parameters, perhaps because of crossing to another excited state.

The bis(arene) metal complex, $(\eta^6\text{-}1,3,5\text{-}C_6H_3Me_3)_2V$, is a stable complex which could be cocondensed directly with nitrogen. Resonance Raman spectra were recorded with the same Spex Triplemate and OSMA detection system as for the LIF spectra described above. Satisfactory spectra were recorded both with pulsed and with cw excitation on the edge of the absorption band at 488 nm. The multi-channel detection system allowed us to record spectra far more rapidly than with the conventional photomultiplier used in York. However, attempts to measure an excitation profile were thwarted by laser damage to the matrix, which became apparent as the laser was tuned to shorter wavelength. The weakness of the resonance Raman signal when compared to the LIF also caused acute alignment problems.

REFERENCES

1. S E J Bell, J N Hill, A McCamley and R N Perutz.
J. Phys. Chem., 94, 3876 (1990).
2. R N Perutz, J N Hill and A McCamley.
Coord. Chem. Rev., 111, 111 (1991).
3. A McCamley and R N Perutz.
J Phys Chem., 95, 2738 (1991).
4. J I Zink and K S Kim Shin
Adv. Photochem., 16, 1 (1991).

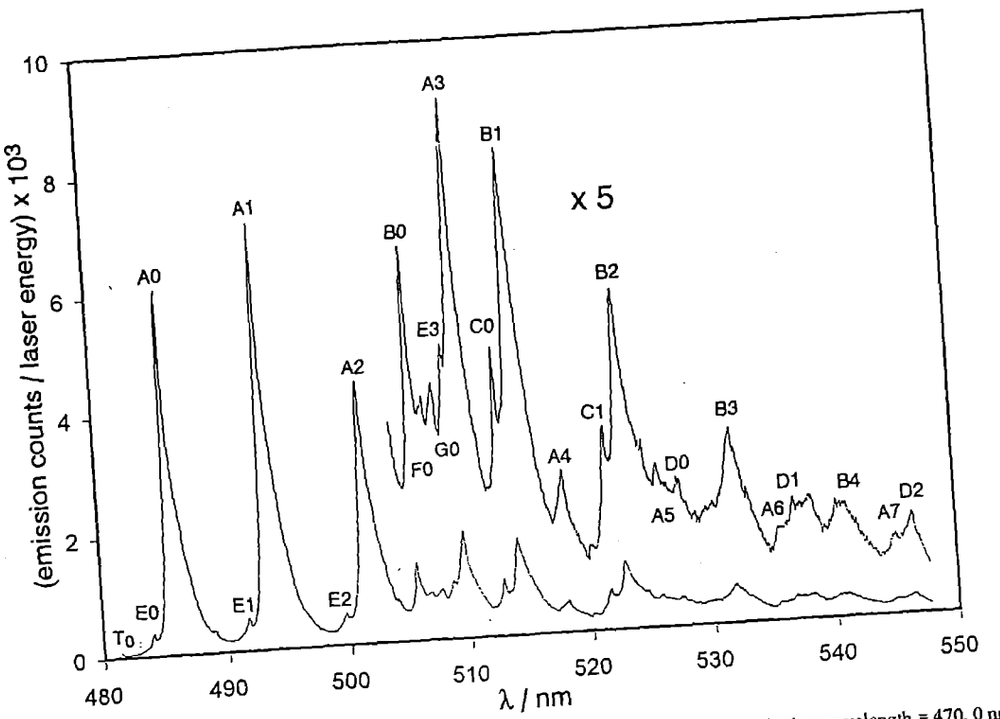

Figure 1. Emission spectrum of rhenocene, $(\eta^5\text{-}C_5H_5)_2Re$, recorded in an argon matrix (excitation wavelength = 470. 0 nm).

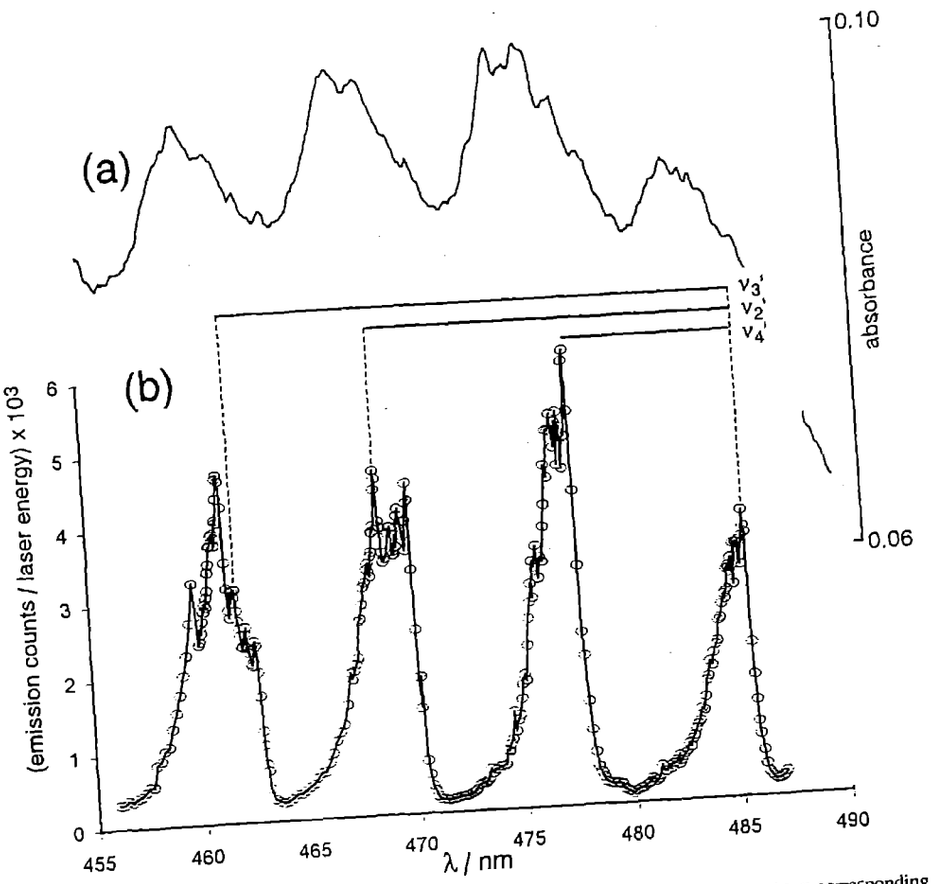

Figure 2. (a) Absorption spectrum of rhenocene, $(\eta^5\text{-}C_5H_5)_2Re$, in an argon matrix. (b) Excitation spectrum corresponding to the emission spectrum in figure 1 (calculated for the emission wavelength 493.8 nm). The frequency separations corresponding to the totally symmetric vibrations ν_4, ν_3, ν_2 are marked.

REMPI STUDIES OF THE DESORPTION DYNAMICS OF NO FROM DIELECTRIC SURFACES

C. J. S. M. Simpson[1] A. Takami[1], J. M. Curry[1], A. S. Solodukhin[1], A. W. Parker,[2] S. Bates[2] and M. Towrie[2]

[1]Physical Chemistry Laboratory, Oxford University
[2]Rutherford Appleton Laboratory

INTRODUCTION

Translational energy distributions, determined by TOF spectroscopy, have established that vibrational energy transfer following ultraviolet excitation can lead to non-thermal desorption of molecules which are not directly excited by the laser radiation[1]. These measurements do not, however, give information on the internal energy distributions of the desorbed molecules, which are expected to show rotational and vibrational excitation. An alternative state-specific technique is thus required, the most commonly used being Laser Induced Fluorescence (LIF) and Resonance Enhanced Multi-Photon Ionisation (REMPI) spectroscopy. Both techniques require a second laser to excite the desorbed molecules. In the LIF case, this results in the formation of electronically excited molecules, from which the fluorescence can be measured by a photo-multiplier tube. In the REMPI case, this results in the formation of molecular ions which can be deflected on to a suitable ion-counting device.

In LIF the molecules to be studied are pumped with a laser to an excited state, which then fluoresces back to the ground state. The spectra are obtained by monitoring the intensity of fluorescence as the excitation laser is tuned across the frequency range of interest. REMPI is a multiphoton process, in which the excited state produced by absorption of the first photon absorbs one or more further photons, which take the molecule to its ionisation limit. The ions thus formed are detected by a mass spectrometer or a multichannel plate. Again, the excitation laser is scanned to obtain the spectra.

REMPI enjoys several advantages over LIF for the analysis of desorbed NO. One of the major problems in the use of LIF in an apparatus such as that used here, is that of scattered light. The ultra high vacuum (UHV) chamber contains many polished metal surfaces which could readily scatter the laser radiation into the detector, causing saturation. This problem has been reported by Ertl[2]. Whilst scattered ultraviolet light will also cause saturation of a multichannel plate, the system is less sensitive to it and this was never a problem in this work. REMPI is also more sensitive than LIF, this is due to the almost unit efficiency with which ions can be detected and the fact that all the ions formed are deflected on to the detector. In contrast, the fluorescence produced in the LIF technique is given out in all directions and only a small amount of it is intercepted by the detector.

Gas phase, state to state analysis by REMPI has predominantly been limited to simple molecules such as H_2, NO, O_2, CO, NO_2, H_2S and NH_3[3]. In all cases, ionisation was achieved by means of resonant two- or three-photon excitation of high-lying electronic states. NO is a particularly attractive molecule for study due to the comparative ease of ionisation. The most frequently studied scheme is the 1 + 1 process using the $A\,^2\Sigma^+$-$X\,^2\Pi$ transition. This transition has the advantage that contributions from vibrational states greater than $v''=0$ are sufficiently displaced to allow rotational assignment for the different vibrational levels.

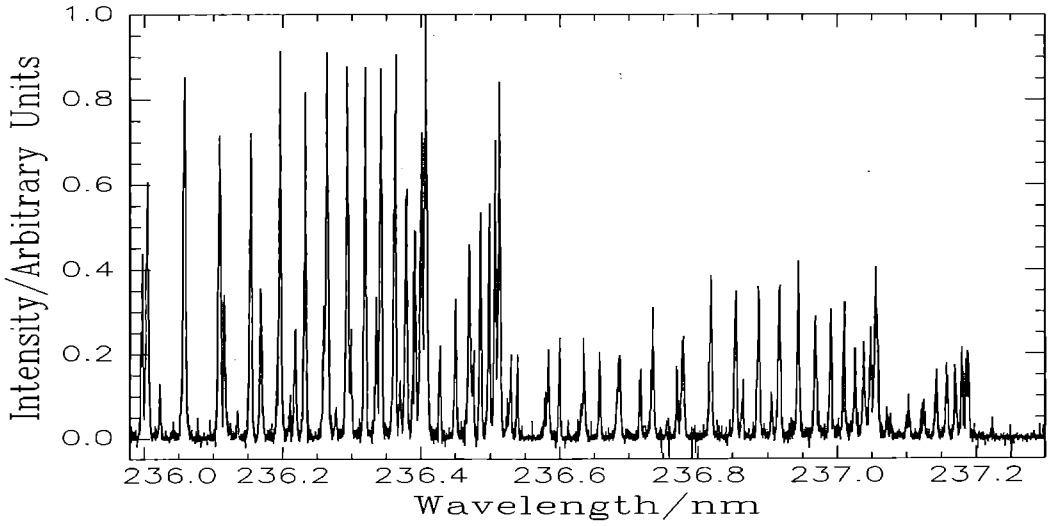

Figure 1 REMPI Spectrum for the (0,1) Band of NO

EXPERIMENTAL

The ion counting scheme incorporates a multi-channel plate and a grid and plate deflection cage. This was of a large enough construction to allow the REMPI laser to pass through without striking any surfaces. This set-up allowed the rotational characterisation of NO in $v''=1$ in the gas phase at room temperature at an effective concentration of 2×10^{-11} Torr. A major advance in this work was that the sensitivity of the detector allowed us to avoid the use of background dosing during the experiments, unlike the work of Sibener[4] or Ertl[2]. Saturation of the detector was avoided by using low desorption laser fluences and low laser fluences.

REMPI spectra for the (0,0), (0,1), (0,2), (1,3) and (0,4) bands were recorded. The ion signal dependence on the REMPI laser energy was measured for each band. If the electronic excitation process is saturated then analysis of the spectra will yield information on the ground state of the desorbed species. Assuming a linear dependence of the power, the spectra were normalised across the band for the variable dye laser energy, which was measured simultaneously to the ion signal. The spectra were taken over a range of conditions - the layer thickness was varied between 5 and one monolayers and the desorption laser fluence was varied between 0.4 and 1.7 mJ cm^{-2}. Spectra were also recorded for gas phase NO in both $v''=0$ and 1 at partial pressures of 2×10^{-9} and 4×10^{-7} Torr respectively.

TOF spectra were recorded for each band, both at high and low J values. These were obtained by altering the delay between firing the desorption and REMPI lasers.

Temperature Programmed Desorption (TPD) spectra were taken for the different layer thicknesses used. The multi-channel plate allowed accurate estimates of the yields to be made. The spectra have been used in previous work to calibrate the micro capillary array doser[5]. Spectra were recorded both before and after desorption laser shots, to investigate what percentage of the adsorbed molecules were desorbed during an experiment.

RESULTS AND DISCUSSION

A typical rotational spectrum is shown for the (0,1) band in Figure 1. The conditions used for this were 5 monolayers and a desorption laser fluence of 0.4 mJ cm^{-2}. Analysis of the rotational structure has shown that the degree of rotational excitation is low. The peak integrals were corrected for the Hönl-London line strength factors and then Boltzmann plots were produced in order to determine the rotational temperatures. For the gas phase measurements this gave a value of 290 $\pm$ 30 K for $v''=0$ and 300 $\pm$ 30 K for $v''=1$. For the desorption spectra the rotational temperature was independent of v'', the layer thickness used and the desorption laser fluence. Typically, these give 340 $\pm$ 60 K for the (0,0) band and 330 $\pm$ 40 K for the (0,2) band. A Boltzmann plot for the (0,1) band of a gas phase sample is shown in Figure 2. The best-fit lines for the different branches do not coincide. This is expected since partial saturation and intermediate state alignment effects were not taken into account during the analysis. A more thorough calculation has been performed by Zare[6], showing that if these effects are allowed for then the data can be fit by a single straight line. This degree of accuracy is not required in this work since the order of the result is more important than their exact values.

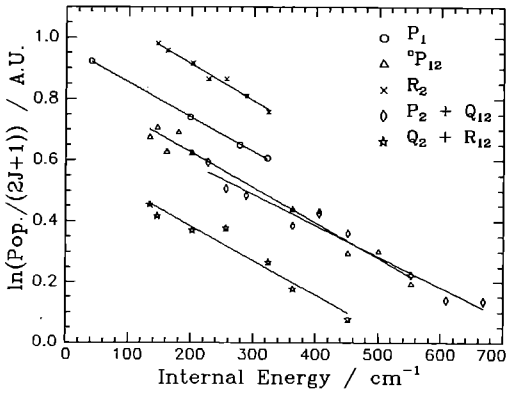

Figure 2 Boltzmann plot for the (0,1) band of $NO_{(\omega)}$

No estimation of the vibrational distribution has yet been made, as the analysis is still in progress. Unlike the work of Sibener, the low rotational temperatures prevent a direct comparison of the population of different vibrational levels by utilising overlapping high J lines. In this work there is significant population up to $v''=2$ above which it drops off.

The TOF spectra were fitted with a sum of two Maxwell-Boltzmann distributions allowing the calculation of characteristic translational temperatures. A spectrum for the (0,0) band, taken on the Q_1 (2½) line, is shown in Figure 3. It is important to note that the term "temperature" is artificial if the processes deviate significantly from thermodynamic equilibrium. Characteristic temperatures are only used here as a qualitative description of the pronounced differences found between various TOF spectra[4]. The faster of the peaks is ascribed to non-thermal desorption, and the slower to thermal desorption, due to local thermal heating.

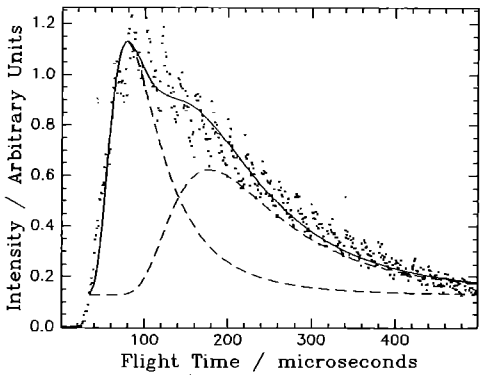

Figure 3 TOF spectrum for the (0,0) band

The TOF spectra show a dependence of the characteristic temperatures of both the thermal and non-thermal peaks on v'' and the layer thickness but not on the desorption laser fluence. The temperatures rise as v'' is increased, but decrease as the layer coverage is lowered from 5 to 2.5 to 1 monolayers. Increasing the laser fluence from 0.7 to 11.2 mJ cm^{-2} did not result in a significant change in the temperatures.

The results of the TPD analysis confirmed that very little

deformation of the surface coverage occurred at the low desorption laser fluences used. For a monolayer coverage, no change was observed in the TPD spectra after 5,000 laser shots at 0.7 mJ cm^{-2}, or after 10,000 shots at 0.4 mJ cm^{-2}. The binding energy of the adsorbed NO dimers was estimated to be 12 ± 0.2 $kJmol^{-1}$.

CO REMPI

A preliminary investigation was also made into the 2 + 1 REMPI of CO via the E $^1\Pi$-X $^1\Sigma^+$ transition previously studied by Zare[7]. A spectrum was measured for a gas phase sample, of pressure 3×10^{-7} Torr, between 215.0 and 215.6 nm. Since two photons are required in the first step, the power dependence is expected to follow a quadratic dependence if this step is saturated. From an experimental viewpoint this means that a much higher REMPI laser fluence is required than for the NO case to obtain a satisfactory signal. This was achieved by tightly focusing the beam before it entered the chamber. Signal averaging was also used to increase the signal to noise ratio. The spectrum obtained is shown in Figure 4, clearly showing the expected branch structure.

THESIS

K R Yoxall Part II Thesis, Oxford University, 1992.

REFERENCES

1. C J S M Simpson, K R Yoxall, A S Solodukhin, A Takami, J M Curry and A W Parker.
Energy Transfer between adsorbed molecules on a dielectric surface following ultraviolet excitation.
To be published.

2. E Hasselbrink, S Jakubith, S Nettersheim, M Wolf, A Cassuto and G Ertl.
Cross sections and NO product state distributions resulting from substrate mediated photodissociation of NO_2 adsorbed on Pd(111).
J. Chem. Phys., 92 3154 (1990).

3. D H Parker.
Laser ionization spectroscopy and mass spectrometry.
Ultrasensitive Laser Techniques (Academic, Orlando, 1983).

4. C Natzle, D Padowitz and S J Sibener.
Ultraviolet laser photodesorption of NO from condensed films: Translational and internal energy distributions.
J. Chem. Phys., 88, 7975 (1988).

5. S J Clemett, A W Parker, K v Puttkamer, A Takami and C J S M Simpson.
Non-dissociative laser induced desorption of molecules from dielectric surfaces.
J. Elect. Spectrosc. and Relat. Phenom., 54/55, 211 (1990).

6. M A Hines, H A Michelsen and R N Zare.
2 + 1 resonantly enhanced multi-photon ionisation of CO via the E $^1\Pi$-X $^1\Sigma^+$ transition: From measured ion signals to quantitative population distributions.
J. Chem. Phys., 93, 8557 (1990).

7. D C Jacobs, R J Madix and R N Zare.
Reduction of 1 + 1 resonance enhanced MPI spectra to population distributions: Application to the A $^2\Sigma^+$-X $^2\Pi$ system.
J. Chem. Phys., 85, 5469 (1986).

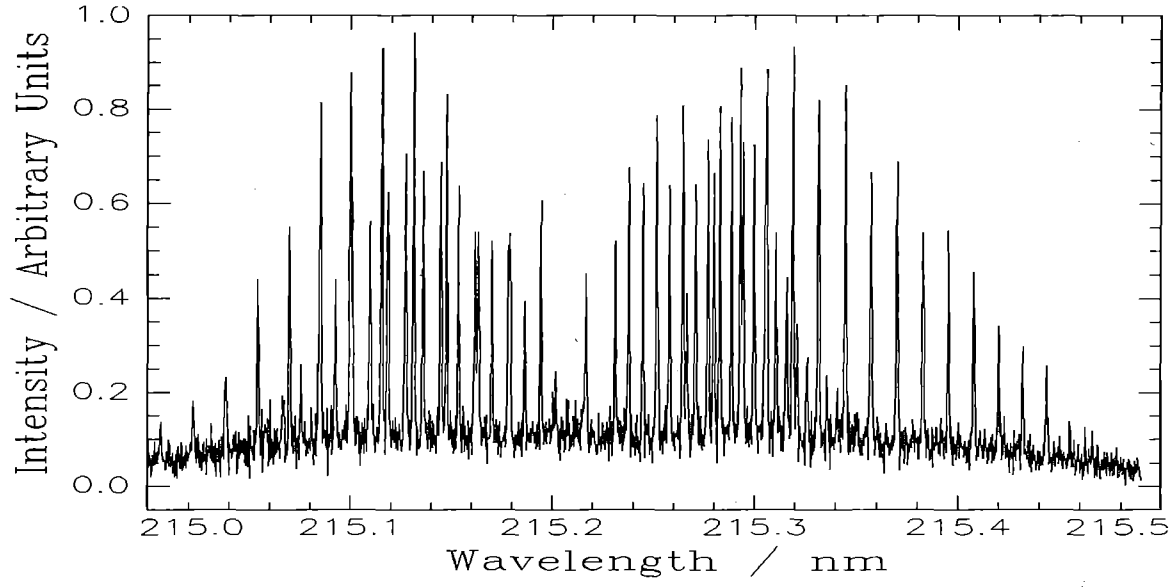

Figure 4 REMPI spectrum of CO

SURFACE PHOTOCHEMISTRY OF MOLECULAR SOLIDS

C Ning and J Pfab

Department of Chemistry
Heriot-Watt University
Edinburgh EH14 4AS

INTRODUCTION

One of the most exciting applications of lasers emerging in recent years is their use for initiating or probing surface chemistry and dynamics.[1,2] We have recently begun new experiments on studies of the surface photochemistry of molecular solids using photodesorption or surface photodissociation by pulsed laser light. As in much of our previous and continuing work on isolated gas phase molecules we use laser-induced fluorescence (LIF) to characterise the desorbate. The advantages of this approach utilising pulsed desorption in combination with delayed, pulsed laser spectroscopic probing of the desorbate have been outlined elsewhere.[2]

The work reported here summarises our first results with this new experiment obtained with the Questek LSF loan pool laser close to the end of our six month period before all our results could be evaluated. The system studied are films of 77 K cold frozen N_2O_4 and NOCl. We use LIF probing of desorbed nitric oxide (NO) on the well known γ-bands in the ultraviolet (220 to 280 nm).

$$N_2O_4\,(s) \xrightarrow{193\ nm} NO\,(v, J)\,(g)$$

$$NOCl\,(s) \xrightarrow{193\ nm} NO\,(v, J)\,(g)$$

EXPERIMENTAL

The octagonally shaped desorption chamber was made in-house from anodised aluminium. Eight ports in the horizontal plane permit several geometric configurations for laser desorption, laser probing of the desorbate, sample admission and for the mounting of the cooled sample holder. A telescope with photomultiplier for the observation of laser-induced fluorescence (LIF) can be mounted either vertically or in the horizontal plane. The chamber is evacuated vertically to a base pressure of 2 x 10^{-6} Torr.

A Nd:YAG pumped frequency doubled dye laser system (Lumonics HY 400, HD 500 and Hypertrak 1000) was employed for generating narrow bandwidth tunable laser light for probing NO in the UV. The laser desorption experiments were performed at 193 nm with the Questek ArF loan laser as shown schematically in Fig. 1:

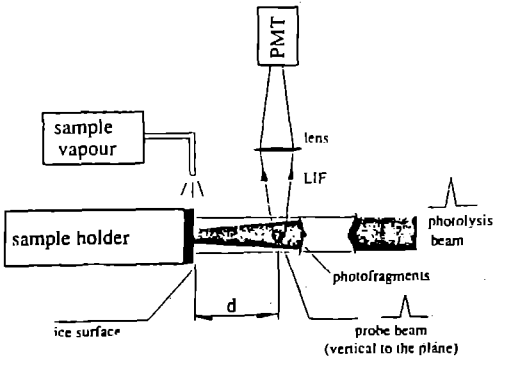

Figure 1 Experimental set up

Laser desorption of thick films of neat, frozen NO_2 and NOCl with 193 nm photons was studied using LIF of NO (v = 0). Samples of NO_2 and NOCl were purified by freeze-pump-thaw cycles and deposited by effusion from 1 to 10 Torr pressure through a 0.15 mm glass nozzle onto a stainless steel surface held at 160 K. When a thick film had formed deposition was stopped and the sample was cooled to 80 K. In this way contamination of the film by the NO impurity of the gaseous sample was reduced drastically. The beam of the ArF laser was directed along the surface normal using fluences of 50 $\mu J\ cm^{-2}$ to 10 $mJ\ cm^{-2}$. Desorbing NO was probed at a distance of 5 or 10 mm from the surface. The UV fluorescence was viewed by a GaAs photomultiplier through two solar blind filters to reduce scattered light. The PMT signal was processed by a boxcar integrator and recorded in digital form by a microcomputer.

RESULTS AND DISCUSSION

The UV laser photodissociation of N_2O_4/NO_2 on single crystal surfaces has been studied recently by Ertl, Polanyi and Rieley et al. who have characterized desorption channels by laser spectroscopy of the NO fragment[3]. Our experiment involves uncharacterized surfaces of porous or microcrystalline thick frozen films held at 80 K. For both the N_2O_4 and NOCl system we can readily observe NO(v=0) on 193nm photodesorption.

Fig.2 shows time-of-flight distributions of the desorbing NO(v=0, J=6.5) recorded at a distance of 10 mm from the surface. When transformed to velocity distributions the TOF data reveal Maxwellian distributions with a width corresponding a translational temperature T_t = 80±10 K and a maximum of 500 ms^{-1}.

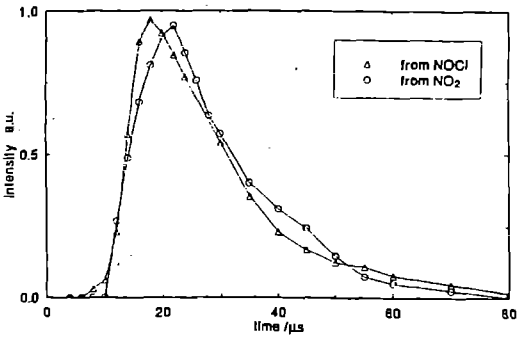

Figure 2 Optical time-of-flight distributions of NO(v=0, J=6.5) from the 193 nm desorption of N_2O_4/NO and NOCl

LIF spectra of NO(v=0) desorbed from 80 K cold NOCl films are shown in Fig.3. The spectra were recorded with 18 and 9 µs delays, respectively, between desorption and LIF probe pulses, using 193 nm desorption fluencies smaller than 300 $\mu J\ cm^{-2}$. NO(v=1) and very little NO(v=2) could also be seen.

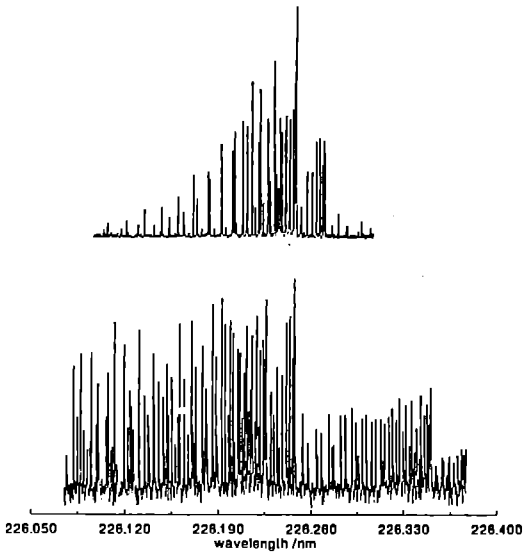

Figure 3 LIF spectra of NO(v=0) desorbed from NOCl, upper trace - slow and cold NO ($T_{rot} \sim T_s$); lower trace - fast and hot NO ($T_{rot} > T_s$)

Fig.4 shows the rotational distributions for NO(v=0) deduced from the LIF spectra of Fig.3 for NOCl and similar spectra recorded from the 193 nm desorption of N_2O_4 (ca 10 mJ cm^{-2}). Rotationally hot NO and cold NO from NOCl can be distinguished by their different flight times. No evidence for rotationally hot and fast NO was found for the desorption of N_2O_4 .

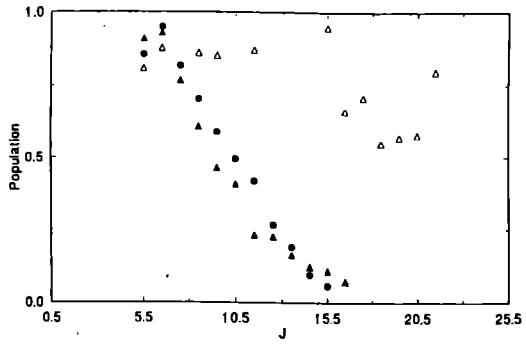

Figure 4 Rotational population distributions of NO (v=0) desorbed from frozen N_2O_4/NO_2 (filled circles) and NOCl (filled triangles - cold NO; open triangles - hot NO)

Both NO present as an impurity in the parent samples as well as NO photoproduct produced in the solid matrix can contribute to the observed desorption flux of cold, relaxed NO. Translational, rotational and electronic (spin-orbit) degrees of freedom appear to be equilibrated with the surface. N_2O_4 required higher laser fluencies to achieve the same desorption flux as for NOCl and did not reveal any evidence for hot NO. The fast and internally hot NO seen in the photodesorption of NOCl is taken as the first clear evidence for the formation of this fragment in the primary dissociation of solid NOCl at the surface.

REFERENCES

1. S.R.Meech.
Annu. Rep. Prog. Chem., Sect.C, 87, 235 (1990).
and J.Pfab, ibidem, 84, 105(1987).

2. E.Hasselbrink, G.Ertl et al.
J.Chem. Phys. 92, 3154 (1990).

3. St.J.Dixon-Warren, H.Rieley, J.C. Polanyi et.al.
J.Phys.Chem. 96, 10983 (1992).

ELECTRONIC SPECTROSCOPY OF INVOLATILE HEAVIER ELEMENT COMPOUNDS FORMED IN A FREE JET EXPANSION

J.M.Brown[1], I.R.Beattie[2], N.M.Lakin[1], S.P.Beaton[1] and M.P.Barnes[1]

[1]OxfordUniversity
[2]SouthamptonUniversity

i Introduction

With involatile solids, high temperatures are required to obtain adequate vapour pressures. This, however, causes problems with gas phase spectroscopy since the spectra obtained are broad and structureless and yield little information. In our experiment molecules formed in the heated region of an alumina nozzle are seeded into a high pressure inert gas stream (usually argon). They undergo a free expansion through a small orifice ($250\mu m$ diameter) into a rapidly pumped vacuum chamber. This causes the rotational, and to a lesser extent vibrational, energy to be converted into translational energy. In consequence, greatly simplified spectra which correspond to a rotational temperature of about 10K are obtained. The beam from a narrow band tunable dye laser is used to irradiate the jet and the resultant fluorescence is recorded (laser excitation spectroscopy). We have made use of the EMG 101E excimer and Lambda Physik FL3002 dye laser combination from the LSF loan pool to record the spectra of a number of interesting molecules.

During the loan period we have been able to extend our measurements of the spectra of InOH and $CuCl_2$, as well as making the first recording of the gas phase electronic spectrum of In_2O. We have also made some intriguing observations regarding the $Cd/H_2O/Ar$ system.

ii $In/In_2O_3/H_2/H_2O$

We have made several breakthroughs in the understanding of this complex system. The motivation for looking at reactions involving this set of compounds comes from their involvement in the chemistry of a degrading pressurised water reactor. In the event of a serious accident, control rods (composed mostly of an indium/cadmium alloy) are dropped into the hydrogen/steam environment of the reactor core. Identifying the principal vapour species formed is vital in assessing the effectiveness of present containment measures.

ii.1 InOH

Previous work undertaken in the RAL has centred on the reaction of indium with water vapour at about 850°C. The spectrum recorded consisted of a complex set of resolved and unresolved bands between 330-387nm. The resolved bands were attributed to indium(I) hydoxide (InOH).

It was found that by reducing indium(III) oxide using a 5% H_2/Ar mixture the InOH spectrum could be obtained selectively and at much greater intensity. This removed the problem of nozzle blockage which had plagued the experiment in the past. Consequently we were able to extend our measurements out to 400nm and confirmed that there were no bands to longer wavelength of those we had already seen. The spectra of InOH and its deuterated isotopomer were then recorded on a computer using the dye laser in burst scan mode. This has the advantage of allowing us to normalize the signals to the laser power and also calibrate the spectrum using the optogalvanic spectrum of a neon filled hollow cathode lamp. Figure 1 shows a portion of both spectra in this region.

The origin bands were also recorded at full rotational resolution on the computer. After considerable effort we have managed to install the intercavity etalon in the dye laser operating in the UV. This gave an improved linewidth of about $0.08cm^{-1}$ but no new structure was resolved in the line profiles of InOH signals. The Q branch of several perpendicular InOD bands were partially resolved. The improved accuracy with which the rotational separations are now known should allow us to determine the rotational constants of InOH and InOD to greater accuracy. Figure 2 contrasts the recording of a perpendicular InOH band made without the intercavity etalon with that made with it installed.

We also managed to repeat our measurements of the dispersed fluorescence of the strongest InOH bands but this time increased the delay on the detection gate in a systematic manner. We are hoping this will help in explaining the biexponential nature of the fluorescence decay curve which is not understood at the moment.

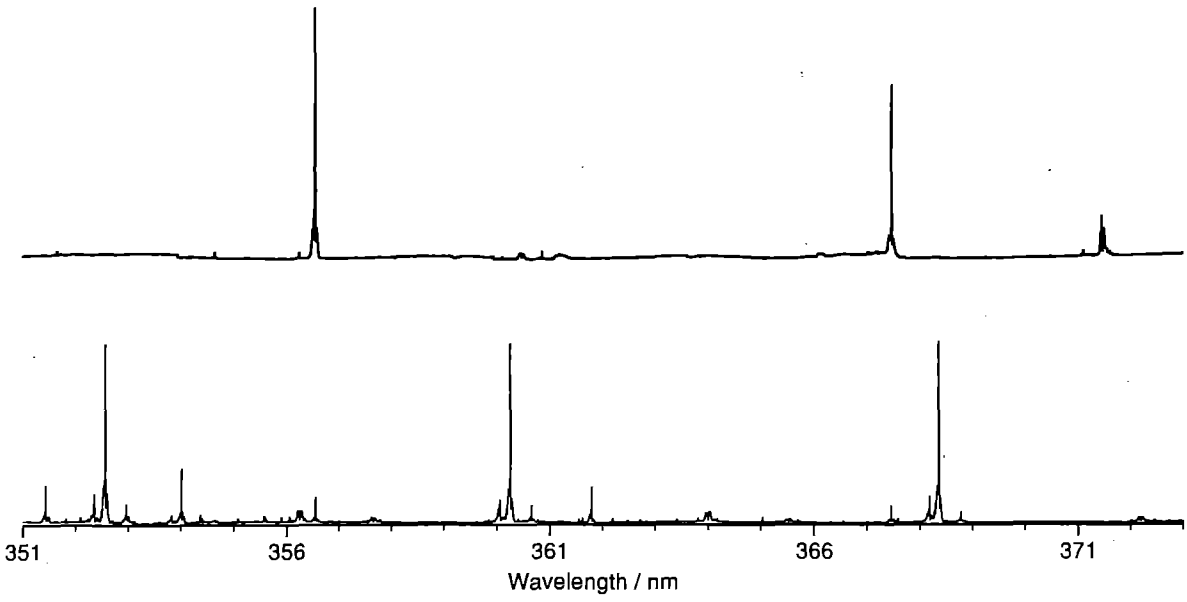

Figure 1. Electronic spectra of InOH (top) and InOD (bottom) from 351 nm to 373 nm.

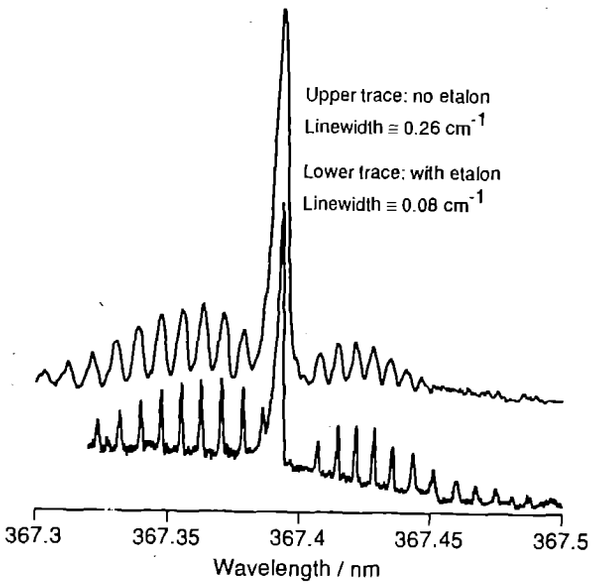

Figure 2. InOH band 2 recorded with and without intercavity etalon.

ii.2 In_2O

Our previous work has concentrated on the InOH bands from the In + H_2O reaction and largely ignored the unresolved bands which accompanied them. We have now discovered that these latter signals can be obtained selectively and at much greater intensity by reducing indium(III) oxide with indium at about 900°C. As a result we managed to record a new set of bands between 387-370nm which are shown in figure 3. There were no other bands to longer wavelength of those shown.

Although the rotational structure of these bands was unresolved the rotational constant of the carrier molecule can be estimated from the separation of the maxima of the P and R branches. This gave a B-value of approximately 0.02cm^{-1}. On this basis it seems likely that the carrier molecule is the suboxide (In_2O) but further work is needed to confirm this. We intend to record the same bands with the intercavity etalon installed since this should give a more accurate estimate for the rotational constant.

We also dispersed the fluorescence from the strongest band at 376nm; ground state separations of about 108 and 230cm^{-1} were measured. The larger value is close to that anticipated for the ground state bending frequency.

iii $Cd/H_2O/Ar$

We extended our study of reactor chemistry by looking at the reaction of metallic cadmium with water vapour at temperatures up to 750°C. In contrast to the indium work there was a decided lack of reactivity and those signals which were seen did not require water for their production.

Two strong signals were observed: the first at 371.098nm was identified as an atomic cadmium transition ($^1S_0 \leftarrow X^1S_0$) [1] and is the first two photon excitation observed using this equipment. A broader feature at 371.18nm appeared to be molecular in nature although dispersing the fluorescence gave rise to atomic cadmium signals only. This implies that we are looking at cadmium complexed with either argon or with another cadmium atom. Further work is needed to assign the carrier molecule fully.

iv $CuCl_2$

The yellow system of copper dichloride was recorded for the first time during a trip to the RAL two years ago. Since then the work has been continued in Oxford and will shortly be published [2]. The spectrum studied so far has a large number of overlapping vibronic bands which are difficult to interpret.

We are currently using the loan laser to record survey scans to longer wavelength in the hope of finding the origin band of the system. Dispersing the fluorescence for these bands should also help in their assignment.

References

[1] ATOMIC ENERGY LEVELS by Charlotte E.Moore, Circular of the National Bureau of Standards 467, III, 56 (1958).

[2] M.P.Barnes, R.T.Carter, N.M.Lakin and J.M.Brown. *Faraday Transactions*, to be published.

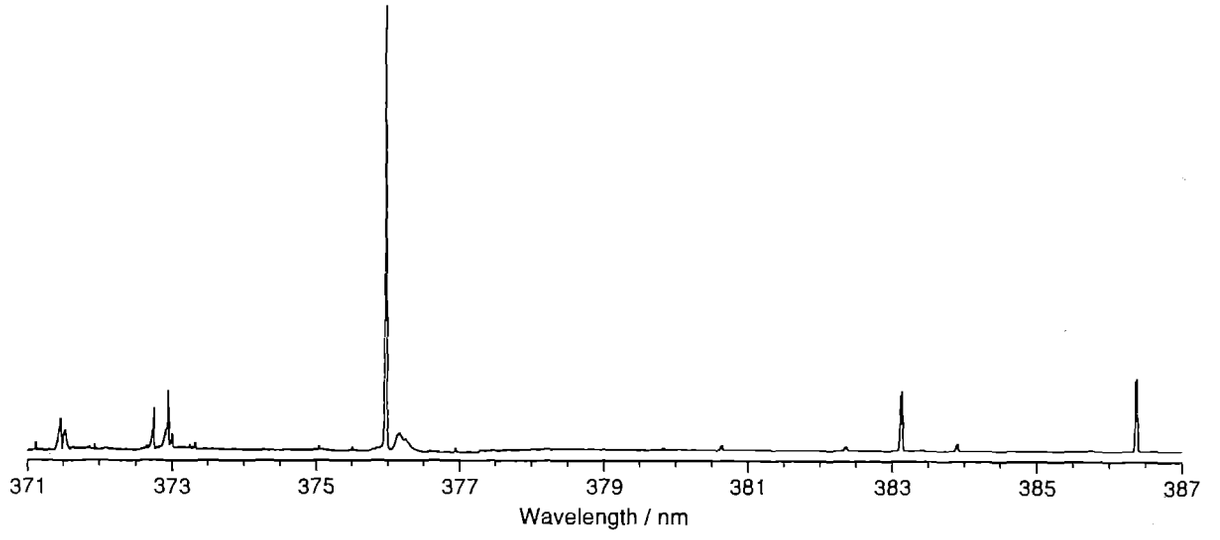

Figure 3. Electronic Spectrum of Indium suboxide (In_2O) from 371 nm to 387 nm.

STATE-TO-STATE CHEMICAL DYNAMICS

Graeme Maitland, Allister Watson and Kenneth G. McKendrick

Department of Chemistry, The University of Edinburgh

INTRODUCTION

These experiments comprised part of a programme of research into the dynamics of elementary gas phase chemical processes.[1] The general philosophy is to attempt to infer detailed information about the motions of individual atoms during the transient period of bond breaking and formation in a chemical reaction. This is achieved effectively by extrapolating either backwards from the experimentally observed motions of the asymptotically separated fragments (i.e. the distribution over product internal quantum states and translational energy), or forwards from the effect of particular forms of reagent energy (internal states, translational energy) on the outcome of the reaction.

Laser methods may be used for reagent preparation *and* product detection. The equipment borrowed from CLF was used in both these capacities, in two distinct experiments:

Experiment 1 'Hot Atom' Dynamics

This type of experiment may be represented schematically by a generic reaction scheme

$$AR \xrightarrow{h\nu} A + R \qquad (1)$$

$$A + BC \longrightarrow AB + C \qquad (2)$$

where a precursor molecule, AR, is photolysed to produce a reactive fragment, A, which then subsequently collides and reacts with a molecular reagent, BC. The AB product of the reaction is observed spectroscopically using an independent laser source.

Experiment 2 Stimulated Raman Pumping (SRP)

As a preliminary experiment towards future studies in which the molecular reagent in equation (2) will be prepared in a selected internal quantum state, we investigated the efficiency of SRP for the vibration-rotational excitation of diatomic molecules. In this method, two intense laser pulses with a frequency difference tuned to an allowed Raman transition coherently drive population between levels. The process may be monitored conveniently by detecting the Coherent Anti-Stokes Raman Scattering (CARS) signal simultaneously generated by four-wave mixing.

EXPERIMENTAL

The CLF provided a Nd:YAG laser-pumped dye laser system (Quanta-Ray GCR-11, PDL-3 and accessories).

In Experiment 1, the harmonics of the Nd:YAG laser were used as the photolysis source in conjunction with existing apparatus as shown in Fig. 1. Reactive fragments were generated in the presence of a molecular reagent in the source region of a time-of-flight (TOF) mass spectrometer. A second tunable dye laser system produced pulses which could be used to ionise reagent and/or product species selectively by resonance-enhanced multiphoton ionisation (REMPI). The characteristic REMPI excitation spectrum (ion yield of selected mass v. probe laser wavelength) is convertible to the distribution over quantum states of the molecule. In prinicple, spatial anisotropies may also be measured using polarised laser sources for photolysis and detection.

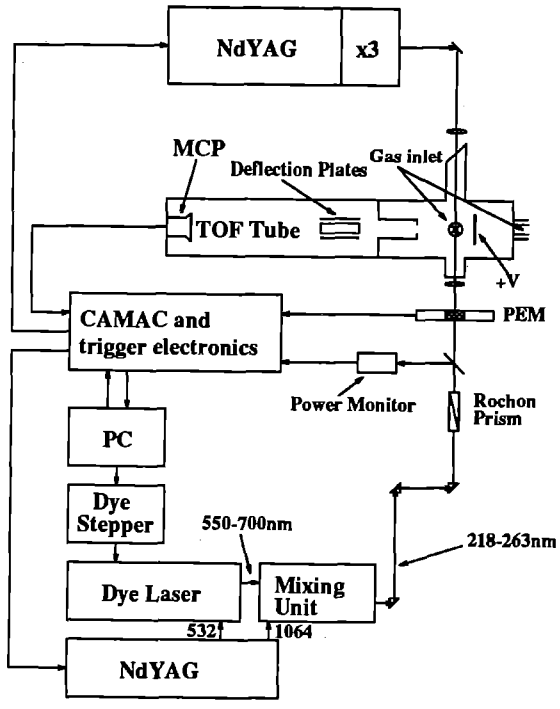

Figure 1 Schematic Apparatus for Experiment 1

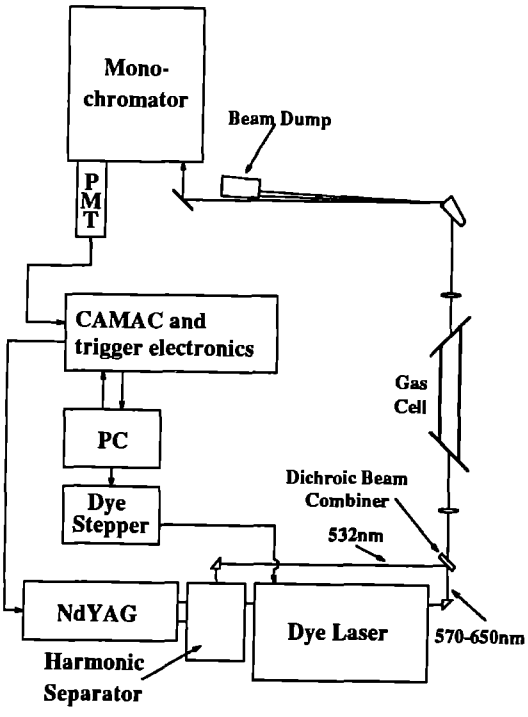

Figure 2 Schematic Apparatus for Experiment 2

In Experiment 2, fixed (Nd:YAG 532nm harmonic) and tunable (dye laser) pulses were combined and focussed into a gas cell, as shown in Fig.2. The blue-shifted CARS signal beam was spatially separated from the pump beams and directed onto a diffuse target at the entrance slits of a monochromator. The linear polarisation of the pump beams could be varied independently, and the polarisation of the CARS beam measured.

RESULTS

Experiment 1

Efforts were concentrated on the detection of HCl by [2+1] REMPI in the 220-250 nm region.[2] A typical REMPI excitation spectrum of a (thermalised) sample of HCl, obtained with the apparatus in Fig. 1, is shown in Fig. 3. The dominant vibronic transition in this region is the $F^1\Delta_2$-$X^1\Sigma^+$ (0-0) band.[2]

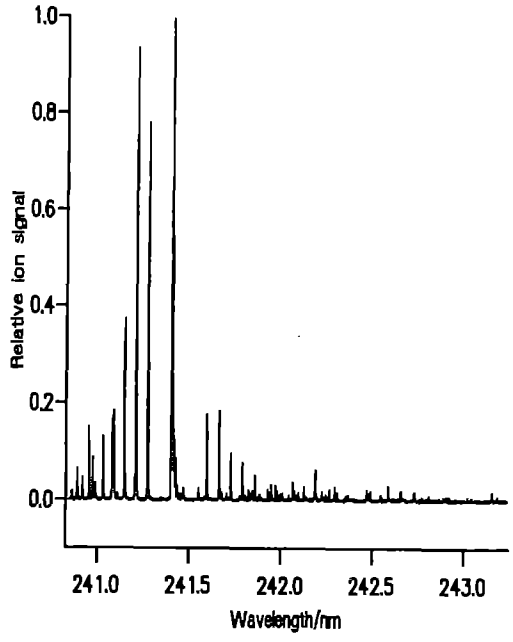

Figure 3 [2+1] REMPI excitation spectrum of HCl

Attempts were made to observe the nascent HCl product state distributions from reactions of Cl atoms with H-containing molecular reagents, and H atoms with Cl-containing reagents, respectively. The production of atomic fragments was monitored directly by REMPI when photolysing either Cl_2 at 355 nm or HI at 266 nm, respectively. In some cases, the density of the molecular reagent (e.g. HBr) in the probed volume could also be monitored directly by REMPI.

We were succesful in observing an increased density of HCl induced by the photolysis of the precursor. However, within the limited time available, we were not able to unambiguously resolve the nascent population from the thermalised background. The source of this background was traced to heterogeneous processes on the walls of the inlet gas injectors. These experiments were very useful in this respect for pointing the way to improved methods of precursor and reagent introduction (using pulsed valves) which have subsequently been implemented.

Experiment 2

HCl was also selected as the subject of the investigations of SRP. A typical CARS spectrum of the Q-branch of the fundamental 1-0 band is shown in Fig. 4.

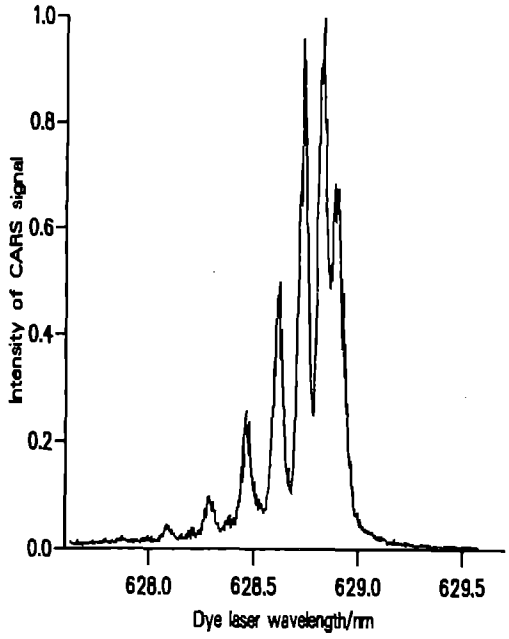

Figure 4 CARS spectrum of HCl

An important feature of the observations was the widely differing efficiencies of transfer on the strong Q- and weak S-branches, and the contrasting polarisation dependence of these branches, which influences the feasibility of using the SRP method for the preparation of spatially aligned reagent molecules. The quantitative data obtained are currently under analysis.[3]

REFERENCES

1. K. G. McKendrick
State-Specific Chemical Reaction Dynamics.
SERC Research Grant GR/E90199.

2. (a) S. Arepalli, N. Presser, D. Robie and R. J. Gordon.
Chem.Phys.Lett. 118, 88(1985);
R. Callaghan, S. Arepalli and R.J. Gordon.
J.Chem.Phys. 86, 5273(1987);
Y. Xie, P.T.A. Reilly, S. Chilukuri and R.J.Gordon.
J.Chem.Phys. 95, 854(1991).
(b) T.A. Spiglanin, D.W. Chandler and D.H. Parker.
Chem.Phys.Lett. 137, 414(1987);
E.A. Rohlfing, D.W. Chandler and D.H. Parker.
J.Chem.Phys. 87, 5229(1987).
(c) D.S. Green, G.A. Bickel and S.C. Wallace.
J.Mol.Spectrosc. 150, 303(1991);
ibid 150, 354(1991);
ibid 150, 388(1991);
D.S. Green and S.C. Wallace.
J.Chem.Phys. 96, 5857(1992).

3. G. Maitland,
Ph.D. Thesis, The University of Edinburgh (in preparation).

KINETICS OF REACTIONS OF THE CN RADICAL AT ULTRA-LOW TEMPERATURES

Bertrand Rowe,[1] Ian R Sims[1] and Ian W M Smith[2]

[1]The University of Rennes I
[2]The University of Birmingham

INTRODUCTION

The rates of elementary chemical reactions between neutral species at low temperatures are of great fundamental interest, as well as being important for an understanding of planetary atmospheres and chemistry in interstellar clouds. Until the present work there had been few measurements of rate constants below 200 K and very few indeed below 100 K.

In the present experiments, ultra-low temperatures are achieved by application of the CRESU (Cinétique de Réaction en Ecoulement Supersonique Uniforme) technique which has been developed by Rowe and co-workers and applied by them to measurements on ion-molecule reactions.[1] In essence, the method involves the creation of a uniform supersonic flow by means of an isentropic expansion of gas through a Laval nozzle. Thermal equilibrium is maintained, resulting in a meaningful temperature.

To determine rate constants for reactions of CN free radicals, laser pulse-probe experiments[2] have been performed in the ultra-low temperature environment provided by the CRESU expansion. In this way, kinetic data have been obtained on the reactions of CN with O_2, NH_3, C_2H_2, C_2H_4 and C_2H_6. For the reaction between CN and O_2 measurements have been made at temperatures as low as 13 K; in most other cases, the experiments have been carried out down to 26 K.

EXPERIMENTAL

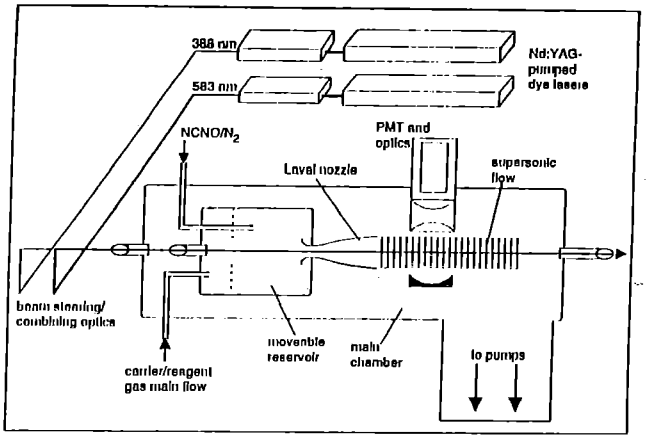

Figure 1 The apparatus used to study neutral-neutral reactions at ultra-low temperatures

Figure 1 shows a schematic diagram of the apparatus. The main chamber in which the Laval nozzle is mounted is approximately 4 m long and 0.5 m in diameter. It is evacuated by a powerful combination of Roots and rotary pumps. Two Nd:YAG laser pumped dye lasers from the RAL Loan pool provide radiation for

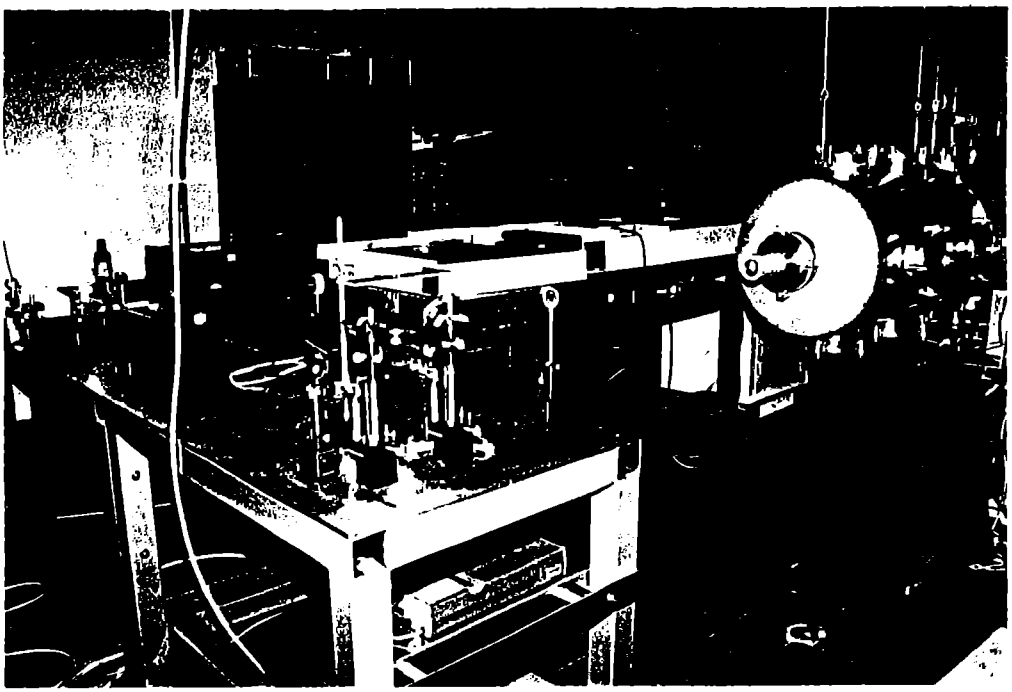

Figure 2 Photograph of the apparatus showing the laser beams entering the vacuum chamber behind the reservoir for the Laval nozzle

photolysis and observation of CN radicals. The beams from these lasers are combined and copropagate along the axis of the flow. The photograph in figure 2 shows the beams entering a window on the upstream end of the vacuum chamber. They then pass through the reservoir-nozzle assembly and along the full length of the gas flow.

The photolysis laser operates at 583 nm producing cold CN radicals by photolysis of NCNO just above the dissociation threshold. CN radicals are detected by observing laser-induced fluorescence (LIF) excited by radiation tuned to an absorption in the $B^2\Sigma^+$-$X^2\Sigma^+$ (0,0) band at 388 nm. Kinetic information is obtained by observing intensity of LIF signals as the delay between probe and pulse lasers is systematically varied.

RESULTS and DISCUSSION

Spectroscopic measurements on the (0,0) band of the CN $B^2\Sigma^+$-$X^2\Sigma^+$ system have been carried out by fixing the time delay between the photolysis and probe lasers and scanning the frequency of the probe lasers. The resultant LIF spectra can be compared with simulated spectra to obtain rotational temperatures. These are in excellent agreement with those estimated on the basis of the aerodynamic equation for given nozzles.

Kinetic information is obtained by fixing the probe laser frequency and scanning the time delay between pulse and probe. A typical LIF trace is given in the inset to figure 3 which displays the variation of first-order decay constants with concentration of O_2. The gradients of such plots yield the second-order rate constants (k) for reaction at a given temperature. The variation of k with temperature for the reaction of CN with O_2 is displayed in figure 4.

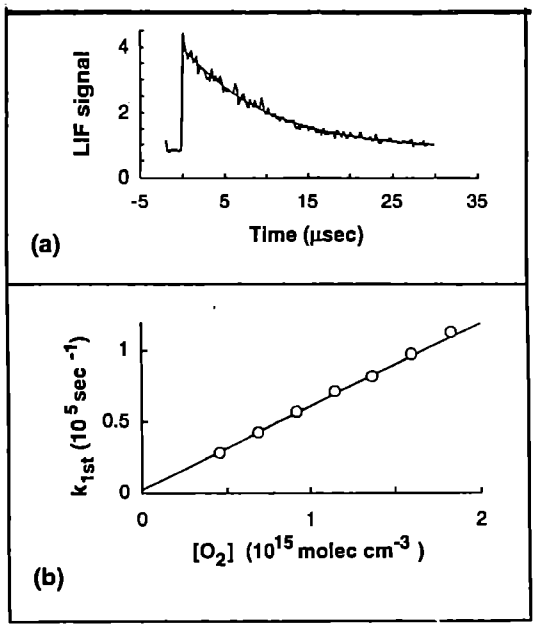

Figure 3 Kinetic data obtained at 75 K for the CN + O_2 reaction: (a) variation of LIF signal with time, yielding a pseudo-first-order rate constant, and (b) variation of first-order constants with concentration of O_2

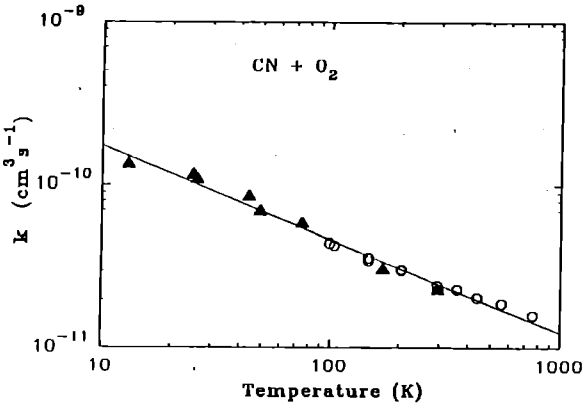

Figure 4 Variation of the rate constant for CN + O_2 with temperature. Results from the CRESU apparatus (●) are compared with those obtained earlier in cooled cell experiments in Birmingham (O)

Our experiments have taken gas-phase chemical kinetics into a quite new temperature range. Furthermore, it has been demonstrated that examples of radical-radical (CN + O_2), radical-unsaturated molecule (CN + C_2H_2, C_2H_4) and radical-saturated molecular (CN + C_2H_6, NH_3) reactions all remain quite fast at ultra-low temperatures. One paper, a Communication in the Journal of Chemical Physics, has been published[3] and two full-length papers are being prepared. During the next laser loan period, we hope to demonstrate the potential of our novel experiments for problems in reaction dynamics and for studying the formation of van der Waals and other weakly bound complexes.

REFERENCES

1. B R Rowe, J B Marquette and C Rebrion, J. Chem. Soc. Faraday Trans. 2, 85, 1631 (1989).
2. I R Sims and I W M Smith, J. Chem. Soc. Faraday Trans. 2, 84, 527 (1988).
3. I R Sims, J L Queffelec, A Defrance, C Rebrion-Rowe, D Travers, B R Rowe and I W M Smith, J. Chem. Phys., 97, 8798 (1992).

VIBRATIONAL STATE SPECIFICITY AND SELECTIVITY IN THE REACTIONS : N + OH ---> NO (v) + H and N + NO (v) ---> N_2 + O

Ian W M Smith, Richard P Tuckett and Christopher J Whitham

The University of Birmingham

INTRODUCTION

In our laboratory, we are investigating the product state distribution from bimolecular elementary reaction between two free radicals. Such reactions are characterised by no activation barrier, and rate constants which show zero or a negative temperature dependence. The potential energy surface over which the reaction proceeds can involve a deep minimum caused by the addition of the two radicals. Our programme aims to determine 'ground rules' for the factors that determine the product state distributions of such reactions; for example, the importance of the depth of the well compared to the exothermicity of the reaction. To date, there have been too few studies to establish such rules. In previous work we have studied the 4-atom reactions H + NO_2 → OH + NO, CN + O_2 → NCO + O, and O + NO_2 → NO + O_2 [1] but in each case one of the radicals is a stable molecule. Here we present results for the 3-atom reaction N + OH → NO + H [2] where both reactant radicals are unstable.

RESULTS AND DISCUSSION

The vibrational state distribution of NO formed in the radical-radical reaction N + OH ---> NO (v' < 9) + H [ΔH^o_0 = -204 kJ mol^{-1}] has been determined by a pulse and probe technique. OH radicals were generated by pulsed laser photolysis of H_2O_2 at 266 nm in a flow of N_2 which had been passed through a microwave discharge to produce N atoms. The N atoms are in excess, therefore the OH radicals are consumed under pseudo first order conditions. The vibrational state distribution of NO has been measured by laser-induced fluorescence spectroscopy from v'=0 up to the highest level that can be populated by the exothermicity of the reaction, v'=9. In these experiments, the probe laser is an excimer-pumped dye laser with appropriate doubling crystals provided by the RAL Laser Loan Facility, and this laser fires a fixed time delay (typically 15 μs) after the photolysis laser. At pressures of about 2 torr, this time delay is adequate to ensure complete rotational relaxation, but is low enough to observe nascent vibrational distributions. One of the peculiarities of this reaction is that the NO (v') is not destroyed by vibrational relaxation, but by the secondary reaction NO (v') + N ---> N_2 + O. This experiment can also be performed in the kinetics mode, in which the probe laser is fixed on a particular NO (v') band, and the time delay between the two lasers is scanned. The rise time is governed essentially by the rate of formation of NO (v'), the fall time by the rate at which NO (v') is consumed by the secondary reaction with N atoms. We have therefore determined the following data :

1. The vibrational state distribution of NO (v') from the N + OH ---> NO (v') + H reaction. The distribution decreases monotonically from a maximum at v'=0 to a minimum at v'=9, and corresponds to an average yield of ~31 % of the available energy. The experimental distribution is close to that predicted by phase space theory (Fig. 1). However this does not necessarily mean that the reaction proceeds via a long-lived NOH* complex in which complete energy randomisation occurs. Indeed, this is unlikely, and it seems much more likely that the constraints of angular momentum, which will be particularly severe in the N + OH reaction, are dominating the dynamics.

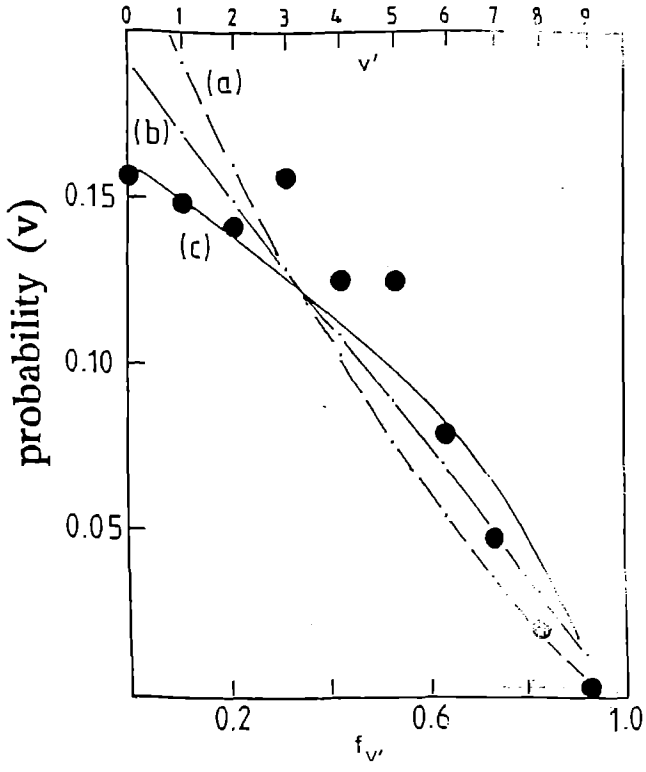

Figure 1 Comparison of the experimental vibrational distribution (●) of NO formed in the reaction betwen N atoms and OH with three calculated distributions: (a) the *prior* distribution according to the equations of Levine and Bernstein; (b) the *prior* distribution according to the model of Quack and Troe; and (c) a distribution based on the application of phase space theory

2. Rate constants for the reaction N + NO (v') --> N_2 + O as a function of v' from v'=0 to v'=9. The value increases by ~15 % from v'=0 to 4, with a slightly larger rise for v'>4. (The kinetics 'rise and fall' graphs are shown in figure 2.) The absolute value for v'=0 is 3.1E-11 cm^3 $molecule^{-1}s^{-1}$. The observation that the rate constant is almost independent of v' is not surprising. The cross section for this reaction is ~16 A^2, and therefore the transition state region is at a large N-NO distance, where motion orthogonal to the reaction coordinate (i.e. the NO vibration) is at a frequency scarcely perturbed from its value in the isolated NO molecule. Thus vibrationally adiabatic surfaces for N + NO (v') will be parallel up to the transition state region, and k(v') will essentially be a constant.

This work will be published in the 1 April 1993 volume of J. Chem. Phys.

REFERENCES

1. I W M Smith, R P Tuckett and C J Whitham
The vibrational state distribution of both products of the reaction
O + NO_2 ----> O_2 (v) + NO (v)
Chem. Phys. Lett . 200, 615-623 (1992)

2. I W M Smith, R P Tuckett and C J Whitham
Vibrational state specificity and selectivity in the reactions
N + OH ---> NO (v) + H and N + NO (v) ---> N_2 + O
J. Chem. Phys., 98, 000-000 (1993) [1 April 1993 volume]

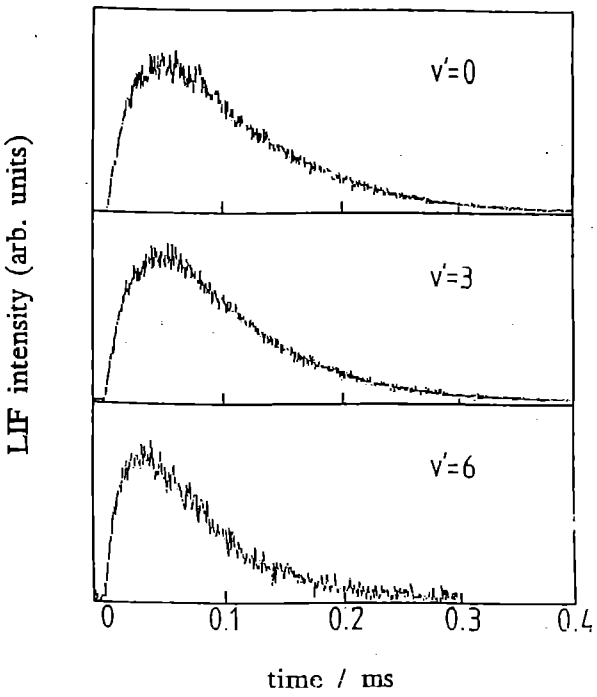

Figure 2 Traces of LIF signal against time showing the variation of NO populations in v'=0, v'=3 and v'=6

MPI SPECTROSCOPY OF RADICALS IN A SUPERSONIC JET - RYDBERG STATES OF SO

Keith Rosser, Qing-Yu Wang and Colin M. Western

School of Chemistry, University of Bristol

INTRODUCTION

Spectroscopy in a supersonic expansion has proved to be an invaluable addition to the arsenal of spectroscopic techniques by virtue of the very low temperatures achieved with this technique. Its use for the simplification of complex spectra and for taking spectra of van der Waals molecules is well documented. The use of a molecular beam with stable species is straightforward but taking spectra of radicals and other transient species presents some difficulties. This note describes development of a nozzle with an internal discharge for use with multiphoton spectroscopy with time of flight detection for the ions. This has required modification of both the nozzle and the time of flight mass spectrometer. To show the potential of the technique, MPI spectra of several Rydberg states of SO are presented. A more detailed description of this work is available elsewhere[1].

EXPERIMENTAL

The combined radical source and supersonic nozzle used here (see figure 1) is based on a design by Jouvet *et al*[2]. It consists of a pulsed molecular beam valve which is a modified solenoid operated fuel injection valve from a car. On the front of this is mounted a plastic (Delrin) piece with a ~1 mm diameter, 1 cm long channel for the gas. Half way down this channel a pair of tungsten electrodes (sharpened to points) project into the channel. The separation of these is adjustable, but is typically set so as to be as small as possible without touching. As the gas passes these electrodes (typically 1-2 ms after the solenoid is activated) a short (~5 ms) high voltage (<1 kV) pulse is applied to the electrodes, producing a spark. The voltage is usually set only slightly above the threshold for breakdown with the aim of producing a small spark; a wider electrode separation or a higher voltage gives an unstable discharge and more background ions or photons without increasing the signal of interest. The pressure within the channel is probably fairly close to the backing pressure (typically 1atm in these experiments) and so the hot gases produced by the spark can cool to room temperature before the start of the supersonic expansion. At the end of the channel we mount a pinhole (a 600 μm platinum electron microscope aperture for these experiments). This pinhole is held on by a metal plate which we bias positive (~200 V) to prevent ions generated in the spark from leaving the nozzle; without this precaution a large background is seen in the mass spectrometer. The probing laser is fired about 200 μs after the discharge (adjusted for best results). The operating pressure of the source region is up to 5×10^{-4} Torr with the nozzle operating.

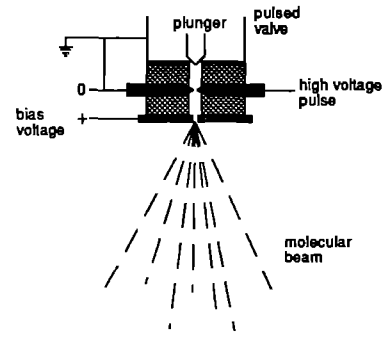

Figure 1 The discharge nozzle

We have found this nozzle to be a versatile source of free radicals and have taken cold LIF and MPI spectra of several species. For the current work SO was generated by discharging a mixture of 0.5% H_2S and 0.5% O_2 in Ar. SO signals (of similar strength) could also be produced by discharging SO_2/Ar or $SOCl_2$/Ar mixtures but gave a large background arising from one photon absorption in SO_2 which has a strong absorption in the mid UV.

SO is detected by multiphoton ionisation using a time of flight mass spectrometer for selectivity. The spectrometer is based on the standard design of Wiley and McLaren[3] and is shown in figure 2. To maximise the signal levels the supersonic nozzle is actually within the source region of the mass spectrometer with the molecular beam/laser beam interaction region approximately 1 cm from the nozzle. This requires a large source region (10 cm separation between the plates) so that the supersonic expansion is unhindered. This has the effect of degrading the resolution of the mass spectrometer as the important properties of the Wiley-McLaren design, insensitivity to initial position or velocity,

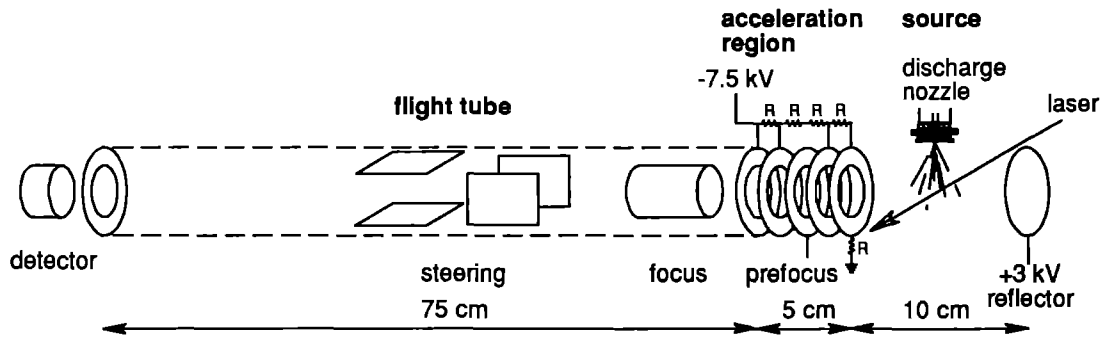

Figure 2 The time of flight mass spectrometer

requires a small source region—1cm is a more typical separation. The fields in the source region will also be non-uniform because of the presence of the nozzle. Trajectory calculations indicated that these effects can be partly compensated for by using higher fields and our drift tube in fact operates at –7.5 kV giving a measured resolution ~1 at m/e 80.

The acceleration region consists of four plates biased to give a uniform field with the exception of the third plate which is independently adjustable to give an extra degree of focusing. The drift tube has *x* and *y* steering plates and a focusing ring and at the end a focused mesh electron multiplier (Johnston Labs MM-1, active area 33 mm diameter) which can operate at the relatively high pressures (up to 10^{-5} Torr) present in our drift tube. The ion signal is amplified (EG&G PARC model 115 wide band preamplifier) and fed to a gated integrator (Stanford Research Systems SR250) and digital oscilloscope (LeCroy 9400A) and then to a computer.

RESULTS

In the current study we scanned the region 325 nm – 290 nm looking for two photon resonances. A typical set of spectra is shown in figure 3.

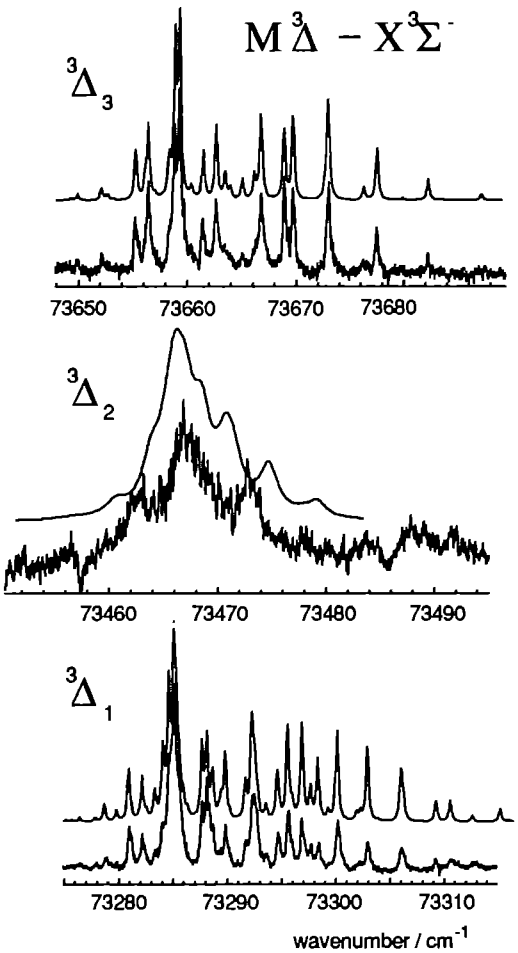

Figure 3 MPI spectrum of the $M^3\Delta$–$^3\Sigma^-$ 0–0 transition in SO.

We observed a series of $^3\Pi$ and $^3\Delta$ bands, each showing a spin-orbit splitting around 350 cm^{-1} and each showing rotational structure to a greater or lesser extent. The rotational constants measured are shown in table I. These values are broadly compatible with the earlier work of Barnes *et al.*[4], though our spectra were taken at a much lower temperature (6 K as opposed to 300K) and so reveal more states and make definitive assignments possible.

		T_0	A	λ	B
4pπ	$F^3\Delta$	62794.47	96.76	12.04	0.780
3dσ	$G^3\Pi$	66494.40	176.94	30.99	0.768
3dδ	$E^3\Pi$	67910.24	–178.05	8.85	0.765
5pπ?	$J^3\Delta$	70654.36	91.56	–	0.786
4dπ?	$M^3\Delta$	73469.84	93.16	7.48	0.772

Table 1 Rotational Constants

The low temperatures provide spectra free of rotational congestion and make possible measurement of linewidths. The band shown in figure 3 shows a very pronounced variation in linewidth with the Ω quantum number. This spin-orbit component dependent predissociation is also seen in the other bands observed, and implies that the predissociation is induced by singlet–triplet mixing. This singlet triplet mixing is also probably responsible for the wide variation in the values for the spin-spin constant λ seen in Table 1.

	Ω = Λ ± 1	Ω = Λ
$F^3\Delta$	1.3	2.5
$G^3\Pi$	1.3	1.8
$E^3\Pi$	1.3	1.6
$M^3\Delta$	<0.3	5

Table 2 Observed Linewidths / cm^{-1}

CONCLUSIONS

The supersonic nozzle with an internal discharge described here has proved to be an excellent method of taking cold spectra of free radicals with multiphoton ionisation. The simplification provided in a molecular beam is found to be invaluable in the analysis of the MPI spectra of the Rydberg states of SO presented here. The variation of lifetime with Ω suggests predissociation occurs via singlet states and the spin-spin constants also indicate a significant degree of singlet-triplet mixing in these states.

ACKNOWLEDGEMENTS

We are greatly indebted to Prof. R. N. Dixon for his help and advice during this project and to M. Green and A. Pugh for assistance with the development of the discharge nozzle. We would like to thank the Royal Society for a K. C. Wong fellowship for Q-YW and a 1983 University research fellowship for CMW.

REFERENCES

[1] K. N. Rosser, Q-Y. Wang and C. M. Western, J. Chem. Soc. Faraday Trans., 89, 391 (1993).

[2] C. Jouvet, C. Lavdeux-Dedonder and D. Solgadi, Chem. Phys. Lett., 156, 569 (1989).

[3] W. C. Wiley and I. H. McLaren, Rev. Sci. Instr., 26, 1150 (1955).

[4] M. Barnes, J. Baker, J. M. Dyke, M. Feher and A. Morris, Mol. Phys., 74, 689 (1991)

EXCITED STATE PROTON TRANSFER IN 3-HYDROXYFLAVONE AND RELATED MOLECULES.

Stuart Ormson[1], Robert G. Brown[1], Friedrich Vollmer[2] and Wolfgang Rettig[2]

[1] Chemistry Dept., University of Central Lancashire
[2] Iwan N Stranski Institüt, Technische Universität Berlin

INTRODUCTION

3-hydroxyflavone (I) is a well-studied example of a molecule which undergoes excited state intramolecular proton transfer (ESIPT) in room temperature solution [1-4]. In the excited state, the hydroxyl proton is more acidic than in the ground state and the carbonyl oxygen is sufficiently basic that it can accept the proton to yield a zwitterionic species. The latter is stabilized by the resonance form where the positive charge is localised on the heterocyclic oxygen thus producing a pyryllium ion. The consequence of the ESIPT reaction is a shift in the fluorescence from approximately 400 nm for the Franck-Condon excited state to 520-540 nm for the excited zwitterion. We have been investigating the ability of substituents in the 2-phenyl ring of I to modulate its absorption and fluorescence properties and we report here the results of our measurements on I, 3-methoxyflavone (Ia) and their derivatives with a 4'-N,N-dimethylamino group in the phenyl ring (II and IIa).

EXPERIMENTAL

Compounds I and II were prepared using the modified Algar-Flynn-Oyamada reaction reported by Smith et al [5]. The corresponding methoxyflavones (Ia and IIa) were prepared by methylation of the hydroxyflavone with dimethyl sulphate.

Absorption and fluorescence spectra and quantum yields were measured in spectroscopic or HPLC grade solvents which were checked for fluorescent impurities before use. Absorption spectra were measured on Hewlett-Packard 8452A and Perkin-Elmer Lambda 3 spectrophotometers and fluorescence spectra and quantum yields on a Perkin-Elmer LS5 fluorimeter with quinine sulphate as the quantum yield standard .

Fluorescence decay profiles were measured using the single photon counting technique [6] either at RAL (with picosecond laser excitation) or at the Daresbury Laboratory with the synchrotron in single bunch mode. The decay profiles were analysed by computer convolution and the "goodness of fit" evaluated on the basis of chi-square values and the distribution of residuals.

RESULTS AND DISCUSSION

3-hydroxyflavones with 4'-substituents such as CH_3, Cl, OCH_3 and CN behave essentially the same as I, but there are substantial differences when the 4'-substituent is an $N(CH_3)_2$ group (compound II). The absorption and fluorescence properties of I and II and their corresponding methoxy derivatives Ia and IIa (where proton transfer is blocked) are given in Tables 1 and 2 for two different solvent systems.

Table 1: Absorption and fluorescence properties of I, Ia, II and IIa in methylcyclohexane.

	Abs λ_{max}	Fluor λ_{max}	ϕ_f	τ_f ns
I	340	525	0.24	3.4
Ia	316	380	0.01	1.56
II	384	551	0.16	1.36
IIa	362	411	0.06	0.18

The introduction of the 4'-$N(CH_3)_2$ group causes a substantial red shift in the absorption of I and the absorption also becomes more intense. Our interpretation of these observations is that the $\pi-\pi^*$ excited state observed in absorption in I and Ia obtains a degree of charge transfer character upon substitution with the N,N-dimethylamino group. The fluorescence properties of the four compounds are in excellent agreement with literature values where these are available. In methylcyclohexane as solvent (Table 1 and Figure 1) the properties of II and IIa appear to parallel those of I and Ia in that a substantially greater Stokes shift is observed for the hydroxy compounds (I and II) than for their methoxy counterparts (Ia and IIa). The fluorescence quantum yields for the hydroxy compounds are much greater than for the methoxy compounds and their fluorescence lifetimes are longer. All the fluorescence observed here rises promptly and, for the most part, decays with single exponential kinetics. As would be expected, on the basis of the sub-picosecond lifetime of the Franck-Condon excited state in non-polar solvents [7], we do not observe this state as a precursor of the fluorescent state in I and II in methylcyclohexane.

Figure 1: Fluorescence spectra of the four compounds in methylcyclohexane.

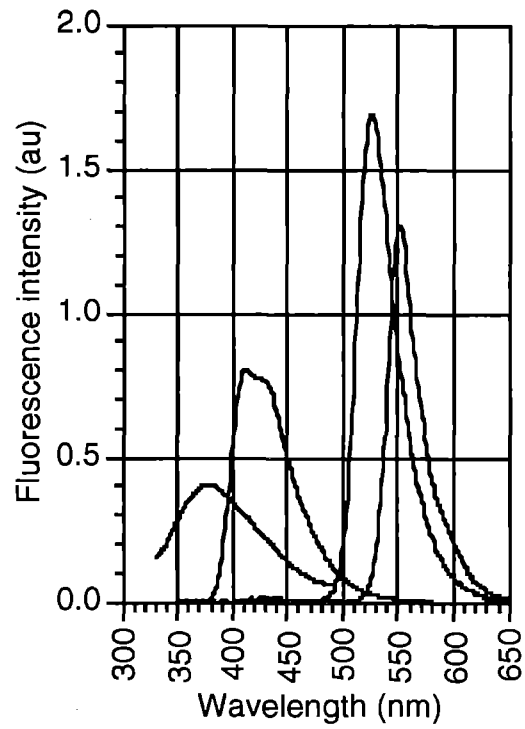

In the polar solvent (Table 2) there is clearly a substantial change in the photophysics upon N,N-dimethylamino substitution. The observed fluorescence yields for II and IIa (especially the latter) are enhanced by over an order of magnitude compared to I and Ia, both compounds fluoresce in approximately the same wavelength region and some of the fluorescence decay profiles exhibit double exponential behaviour (Figure 2). The biexponential fluorescence decays for II and IIa are wavelength dependent with the shorter of the two decays dominating the short wavelength side of the emission bands. At longer wavelengths this component disappears completely and the fluorescence decay becomes single exponential with a lifetime equal to that observed as the second component at the shorter wavelengths. This behaviour is consistent with the observed emission spectrum being composed of two strongly overlapping fluorescence bands (dual fluorescence).

Table 2: Absorption and fluorescence properties of I, Ia, II and IIa in acetonitrile.

	Abs λ_{max}	Fluor λ_{max}	ϕ_f	τ_f ns
I	340	389	0.006	
		526	0.04	0.75
Ia	313	420	0.02	0.03
II	398	507	0.07	0.37‡
IIa	380	486	0.48	2.43‡

‡ indicates double exponential decays

Figure 2: Fluorescence decay profiles for compound II in acetonitrile at 450 and 520 nm.

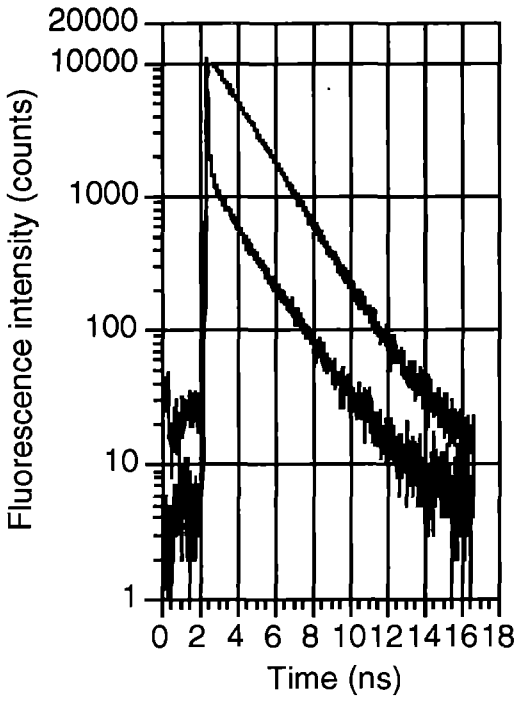

Our interpretation of these results is that there are three singlet excited state species contributing to the solution photophysics of II and IIa. In non-polar solvents they behave in the same way as I and Ia i.e. the initially populated Franck-Condon state immediately undergoes ESIPT in I and II to yield the proton transferred state which fluoresces with a large Stokes shift. ESIPT is not possible in the methoxy derivatives Ia and IIa and fluorescence is observed from the Franck-Condon excited state. In acetonitrile, both II and IIa fluoresce strongly with (apparently) a single band and a comparably large Stokes shift. As the red-shifted fluorescence from IIa cannot be due to ESIPT and is unlikely to all be due to emission from the Franck-Condon excited state, we suggest that the formation of a twisted intramolecular charge transfer (TICT) state [8] accounts for the high fluorescence yield for II and IIa in acetonitrile and for the unexpectedly large Stokes shift for IIa. We do not, however, rule out the possibility of contributions from Franck-Condon emission (dual fluorescence), especially in the light of the double exponential fluorescence decays that are observed.

The competition between TICT and ESIPT can be summarized as

$$A^* \overset{TICT}{\leftarrow} E^* \overset{ESIPT}{\rightarrow} K^*$$

where the initially excited enol (E*) can undergo ESIPT to produce the keto form (K*) or populate the TICT state (A*). Both solvent polarity, which accelerates TICT state formation, and hydrogen-bonding properties, which slow down ESIPT, affect this competition. In the case of II the adiabatically formed photoproduct changes from K* (ESIPT) in alkane solvents to A* (TICT) in alcohols, together with a possible contribution to the emission from the initially excited Franck-Condon state.

The unexpectedly high fluorescence quantum yields for II and IIa in acetonitrile compared to I and Ia also point to the fact that different states are producing the emission in the two cases. For the TICT interpretation presented above, this corresponds to an enhancement of the fluorescence quantum yield through TICT state formation which is rather uncommon especially in view of the intrinsicially forbidden nature of TICT states [9,10]. Vibronic coupling and mixing with allowed states, however, is a mechanism which can strongly enhance the TICT radiative rate, and there are other examples of highly emissive TICT molecules.

We are currently obtaining further data to confirm these conclusions by (a) extending the range of solvents used, (b) undertaking measurements at reduced temperature and (c) preparing model compounds.

REFERENCES

1. D. McMorrow and M. Kasha.
Proton transfer spectroscopy of 3-hydroxychromones. Extreme sensitivity to hydrogen-bonding perturbations.
J. Am. Chem. Soc., 105, 5133 (1983).
2. D. McMorrow and M. Kasha.
Intramolecular excited-state proton transfer. Hydrogen-bonding solvent perturbations.
J. Phys. Chem., 88 2235 (1984).
3. M. Itoh, Y. Fujiwara, M. Sumitani, and K. Yoshihara.
Mechanism of intramolecular excited-state proton transfer and relaxation processes in the ground and excited states of 3-hydroxyflavone and related compounds.
J. Phys. Chem., 90 5672 (1986).
4. D. McMorrow, T. P. Dzugan and T. J. Aartsma.
Excited state dynamics of the intramolecular proton transfer of 3-hydroxyflavone in the absence of external hydrogen-bonding interactions.
Chem. Phys. Letters, 103 492 (1984).
5. M. A. Smith, R. M. Neumann and R. A. Webb.
A modification of the Algar-Flynn-Oyamada preparation of flavonols.
J. Heterocyclic Chem., 5 425 (1968).
6. D. V. O'Connor and D. Phillips.
Time correlated single photon counting.
Academic Press, New York, 1984.
7. B. J. Schwartz, L. A. Peteanu and C. B. Harris.
Direct observation of fast proton transfer: Femtosecond photophysics of 3-hydroxyflavone.
J. Phys. Chem., 96 3591 (1992).
8. W. Rettig.
Charge separation in excited states of decoupled systems - TICT compounds and implications regarding the development of new laser dyes and the primary processes of vision and photosynthesis.
Angew. Chem. Internat. Ed., 25 971 (1986).
9. M. Van der Auweraer, Z. R. Grabowski and W. Rettig.
Molecular structure and temperature-dependent radiative rates in twisted intramolecular charge transfer and exciplex systems.
J. Phys. Chem., 95 2083 (1991).
10. W. Rettig, W. Majenz, R. Lapouyade and M. Vogel.
Adiabatic photochemistry with luminescent products.
J. Photochem. Photobiol. A: Chem., 62 415 (1992).

THE ORIGIN OF THE ANOMALOUS FLUORESCENCE FROM 4-N,N-DIMETHYLAMINOBENZOIC ACID AND ITS METHYL ESTER

John A. T. Revill and Robert G. Brown
Chemistry Dept., University of Central Lancashire

INTRODUCTION

Derivatives of 4-N,N-dimethylaminobenzoic acid (4DMABA) such as the nitrile and various esters have been known for a number of years to show anomalous fluorescence [se e.g. 1]. Two fluorescence bands are observed for these compounds in some solvents. The shorter-wavelength emission, with a Stokes shift of a few thousand wavenumbers, is identified as "normal" fluorescence from the locally-excited (i.e., Franck-Condon) singlet state to the ground state. In current terminology this is also referred to as a b* state. The anomalous, longer-wavelength emission (from a state labelled a*) has a number of possible origins.

The suggestion that the a* emission results from a twisted intramolecular charge transfer (TICT) state has met with quite wide acceptance [2,3]. However, Varma and co-workers, at an early stage in the studies of these molecules, proposed that the a* emission was due to a solute/solvent exciplex and have maintained this belief in a series of later papers. More recently, Phillips' group has presented evidence that the a* emission of 4-N,N-dimethylaminobenzonitrile and the methyl esters of 4-N,N-dimethylamino- and 4-N,N-diethylamino-benzoic acid in a supersonic jet is due to dimer formation [4,5].

We have studied the solution photophysics of all of the amino- and N,N-dimethylamino-benzoic acids and their methyl esters [6] and are able to contribute to the current debate about the origin of the anomalous fluorescence from 4DMABA and its methyl ester (M4DMAB). As part of these studies we have measured the fluorescence decay profiles of these two compounds in a range of solvents and the results of some of these measurements are summarised here.

RESULTS AND DISCUSSION

In our hands, the anomalous fluorescence from both 4DMABA and M4DMAB is concentration dependent [6-8]. Coupled with the observation of different excitation spectra for the two emission bands, this evidence points towards the presence of two ground state species as accounting for the observed behaviour. Unfortunately, we do not observe any change in the absorption spectra over the relevant concentration range so we have been unable to use this to confirm our proposals. The measurement of fluorescence decay profiles can provide powerful evidence for testing alternative kinetic mechanisms in a situation such as that present here. Mechanisms such as excimer, exciplex or TICT state formation require a parent-daughter relationship between the b* and a* states whereas two different ground state species will be kinetically isolated.

Table 1: Fluorescence decay characteristics of 4DMABA in acetonitrile.

Emission (nm)	Concentration (micromolar)	Lifetime (ns)
350	10.0	1.66
480	10.0	2.30
350	1.0	1.29/2.74‡
480	1.0	2.23
350	0.1	0.2/1.85‡
480	0.1	2.27

‡ double exponential decay profiles observed.

Although 4DMABA and M4DMAB exhibit anomalous fluorescence in a range of solvents [6-8], we report here the fluorescence decay behaviour of these compounds in acetonitrile as being typical. The decay properties of 4DMABA are given in Table 1. In acetonitrile, the a* fluorescence decays by a single exponential, whereas the b* fluorescence sometimes requires two exponentials for an adequate fit. The lifetime of the a* band is independent of concentration and excitation wavelength. A lifetime in a range of 2.1-2.3 ns is always obtained and there is no evidence of a rise time indicative of an excited state precursor. It is possible that there is a third excited species which is very short-lived and which is the precursor of both emitting states but there appears to be no other obvious kinetic relationship between the two emitting states.

Similar results are obtained for M4DMAB in acetonitrile (Table 2). Here, the fluorescence decay of the a* state is always double exponential and the range of lifetimes for the b* decay are rather wider than for 4DMABA but once again, there is no evidence of a rise component in the profiles or of a kinetic relationship between the two emitting states.

Table 2: Fluorescence decay characteristics of M4DMAB in acetonitrile.

Emission (nm)	Concentration (micromolar)	Lifetime (ns)
355	5.0	1.70/2.21‡
480	5.0	2.36
355	0.5	1.65/2.45‡
480	0.5	2.49
355	0.05	1.69/2.49‡
480	0.05	2.71

‡ double exponential decay profiles observed.

We interpret these observations as confirming our earlier conclusion about the presence of a second ground state species as the source of the a* fluorescence. They also imply that this is the only source of the a* species - the b* state does not appear to be a precursor of a*, although the reverse may possibly be true given the more complex decay profiles observed for the b* fluorescence band.

REFERENCES

1. G. Wermuth, W. Rettig and E. Lippert.
The dual fluorescence of p-substituted dialkylanilines: the twist mechanism occurs even in inert solvents.
Ber. Bunsenges. Phys. Chem., 85 64 (1981).

2. W. Rettig.
Charge separation in excited states of decoupled systems - TICT compounds and implications regarding the development of new laser dyes and the primary processes of vision and photosynthesis.
Angew. Chem. Internat. Ed., 25 971 (1986).

3. M. Van der Auweraer, Z. R. Grabowski and W. Rettig.
Molecular structure and temperature-dependent radiative rates in twisted intramolecular charge transfer and exciplex systems.
J. Phys. Chem., 95 2083 (1991).

4. R. Howell, H. Petek, D. Phillips and K. Yoshihara.
An investigation of the fluorescence behaviour of 4-(N,N-dimethylamino)benzonitrile cooled in a supersonic jet.
Chem. Phys. Lett., 183 249 (1991).

5. R. Howell, A. C. Jones, A. G. Taylor and D. Phillips.
Laser-induced fluorescence of dimethylaminobenzoic esters in solution and supersonic jet.
Chem. Phys. Lett., 163 282 (1989).

6. J. A. T. Revill.
Photophysics of the amino- and dimethylamino-benzoic acids and their methyl esters.
PhD thesis, University of Central Lancashire (1993).

7. J. A. T. Revill and R. G. Brown.
Excimer versus TICT state formation in polar solutions of methyl 4-(N,N-dimethylamino)benzoate.
Chem. Phys. Lett., 188 433 (1992).

8. J. A. T. Revill and R. G. Brown.
Anomalous fluorescence properties of 4-N,N-dimethylaminobenzoic acid in polar solvents.
J. Fluorescence, 2 107 (1992).

STRUCTURAL INVESTIGATIONS OF α-TOCOPHEROXYL AND RELATED RADICALS IN SOLVENT, MICELLAR AND MEMBRANE SYSTEMS USING TIME-RESOLVED RESONANCE RAMAN SPECTROSCOPY

Roger H Bisby* and Anthony W Parker#
*Department of Biological Sciences, Salford University, #Laser Support Facility, RAL

Introduction

Vitamin E (α-tocopherol) is the most important chain breaking antioxidant of cellular membranes and lipoproteins[1]. Its high efficiency in this role is due to stereoelectronic factors which result in it being a good reductant of lipid peroxyl radicals, and which stabilise the resulting α-tocopheroxyl radical. The comparatively long lifetime of the radical allows it to be recycled by a reductant which may be ascorbate (vitamin C), ubiquinol or a thiol. In the case of ascorbate or a water soluble thiol the aqueous phase reductant must have some degree of access to the α-tocopheroxyl radical in the membrane or lipoprotein particle. The location of the α-tocopheroxyl radical in such structures is therefore of interest. In our previous Annual Report[2] we had begun to extend our laser flash photolysis studies on α-tocopheroxyl to structural investigations using TR^3 spectroscopy. Over the past year we have continued this study[3].

Results and Discussion

a) TR^3 Spectra of Tocopheroxyl Radicals.

Laser photolysis (308 nm) of α-tocopherol produces the α-tocopheroxyl radical by monophotonic photoionisation[4]. Using photolysis at this wavelength and probing within the long wavelength absorption band of the radical at 425 nm[4] TR^3 spectra of α, β and δ-tocopheroxyl radicals in methanol have been obtained (Figure 1). The Raman spectrum of α-tocopheroxyl radical contains two peaks at 1504 and 1595 cm^{-1}. By analogy with the TR^3 spectrum of 4-methoxyphenoxyl radical[5] these are assigned to the C-O stretch (Wilson ν_{7a}) and ring C=C stretch (Wilson ν_{8a}) respectively. In the β and δ-tocopheroxyl radical spectra these two bands are present but there is an additional feature at *ca.*1200 cm^{-1}. We assign this band to the C-H bending (Wilson ν_{9a}) mode which occurs at 1163 cm^{-1} in 4-methoxyphenol[5]. This band is absent in α-tocopheroxyl because of the presence of the methyl substituents which are replaced by hydrogen at ring position 7 in β-tocopherol and ring positions 5 and 7 in δ-tocopherol. For α-tocopheroxyl in *n*-hexane other, much weaker spectral features were observable, see Figure 3.

The TR^3 spectrum of the α-tocopheroxyl radicals are indicative

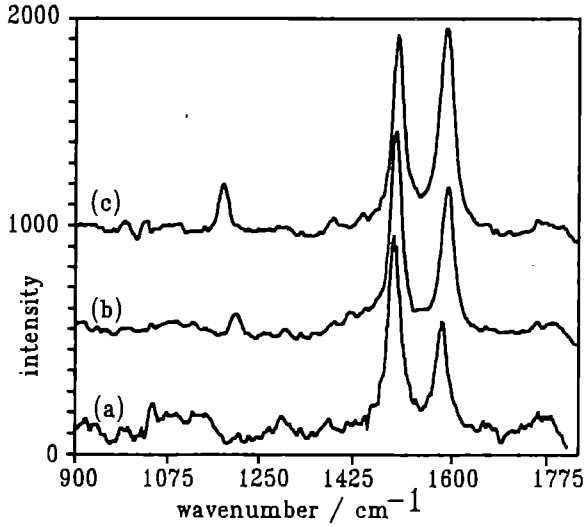

Figure 1: Resonance Raman spectra of (a) α-tocopheroxyl; (b) β-tocopheroxyl and (c) δ-tocopheroxyl radicals obtained by photolysis (308 nm) of the respective tocopherols (5 x 10^{-3} mol dm^{-3}) in methanol. The probe pulse was 425 nm, delayed 2μs after pump pulse.

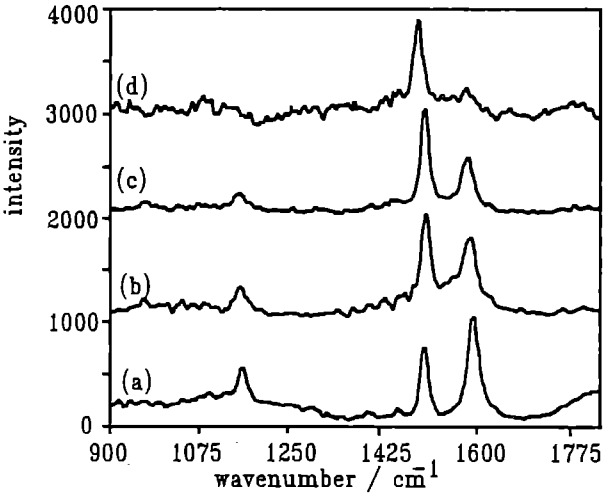

Figure 2: Resonance Raman spectra of the 4-methoxyphenoxyl radical in:- (a) aqueous phosphate buffer (50 x 10^{-3}mol dm^{-3} at pH 7.5; (b) in methanol and (c) in octanol. The spectrum of the 4-methoxy-2,3,5,6-tetramethylphenoxyl radical in ethanol is shown in (d). Spectra were obtained from 5 x 10^{-3} mol dm^{-3} solutions of the parent phenol with a 308 nm pump pulse, except (d) which used 270 nm, and a 425 nm, 2 μs delayed probe pulse.

of the delocalisation of the unpaired electron which leads to radical stabilisation as discussed by Ingold and co-workers[6-8]. The high frequency of the C-O stretching vibration indicates that this bond has nearly double bond character and the high intensity of the C=C stretch (*ca.* 1590 cm^{-1}) band shows a strong interaction of the *para* oxygen atom 2p orbital with the phenoxyl π-system. This interaction is dependent on the *para* substituted group. X-ray structure studies on pentamethyl-6-hydroxylchromanol (used because α-tocopherol is a liquid) shows the *para* oxygen atom 2p orbital is almost perpendicular to the plane of the aromatic ring. In contrast the 2p orbital in 4-methoxy-2,3,5,6-tetramethylphenol lies almost parallel to the plane of the ring due to steric interactions between the 4-methoxy group and the 3- and 5-methyl substituents. This lack of delocalisation in the latter compound has been suggested as the reason for its poor activity as an antioxidant[6-8]. Since the resonance Raman spectra of the substituted phenols reflects the extent of electron delocalisation a comparison was made between the resonance Raman spectra of 4-methoxy-2,3,5,6-tetramethylphenoxyl and 4-methoxyphenoxyl radicals. The spectra are shown in Figure 2 with assignments given in Table 2. The spectrum of 4-methoxyphenoxyl radical is in agreement with earlier results[5]. In the 4-methoxy-2,3,5,6-tetramethylphenoxyl spectrum the *ca.* 1600 cm^{-1} band is very weak in comparison to this band in 4-methoxyphenoxyl radical. This is caused by the predicted lack of resonance enhancement for this mode because of the poor electronic interaction of the methoxy-substituent with the aromatic system and the phenoxyl radical site. This effect is also responsible for the 40 nm blue shift in the ground state absorption spectrum which made it necessary to use 270 nm pump wavelength.

b) Solvent Dependence of the TR^3 Spectra.

The TR^3 of α-tocopheroxyl radical in solvents of varying polarity and H-bonding capacity are summarised in Table 1.

Table 1-Resonance Raman bands (cm^{-1}) of tocopheroxyl radicals in solvents, micelles and membranes

RADICAL	SOLVENT	DIELECTRIC CONSTANT (20 °C)	C-O STRETCH (ν_{7a})	C=C STRETCH (ν_{8a})	C-H BEND (ν_{9a})	INTENSITY RATIO[a] (ν_{8a}/ν_{7a})
α-tocopheroxyl	methanol	32.6	1504	1595		0.70
	ethanol	24.5	1504	1586		0.62
	propan-2-ol	18.3	1504	1590		0.52
	octan-1-ol	10.3	1505	1589		0.38
	dimethylsulphoxide	46.6	1497	1583		0.38
	acetonitrile	37.5	1502	1586		0.36
	acetone[c]	20.7	*ca.*1502	*ca.*1595		0.34
	tetra-hydrofuran	7.6	1501	1581		0.22
	n-hexane	1.9	1504	1581		0.18
	SDS micelles		1500	1593		0.81
	HTAC micelles		1500	1590		0.48
	Triton micelles		1498	1586		0.36
	DMPC bilayers		1500	1587		0.45
β-tocopheroxyl	methanol	32.6	1507	1605	1205	0.85 (0.11[b])
δ-tocopheroxyl	methanol	32.6	1511	1603	1181	1.26 (0.20[b])

[a]Ratios are ± 0.03. [b]Values in brackets are intensity ratio of ν_{9a}/ν_{7a}. [c]Raman spectra in acetone were weak

The C-O stretch (ν_{7a}) occurs at 1504 cm^{-1} in most of the solvents and is strong in all instances, whereas Figure 3 shows that the intensity, and to some extent peak position, of the higher frequency C=C stretch (ν_{8a}) varies with solvent. At first it is unexpected that a change in solvent polarity (dielectric constant) and the ability of the solvent to act as a hydrogen donor should influence the position of the C=C stretch. Indeed, H-bonding normally reduces the double bond character of C=O groups and as such one would expect this mode to be influenced most, if this is the case then our initial assignments are incorrect. However, Tripathi and Schuler[5] have shown that in a series of substituted phenols the intensity of the C=C, ν_{8a}, band is increased by electron delocalisation involving the *para* oxygen. The effect of our solvent band intensities, summarised in Figure 4, may therefore be taken as an indication that increasing solvent polarity assists in electron delocalisation for the α-tocopheroxyl radical. According to Figure 4 the solvents fall into two groups, those able to act as hydrogen bond donors, giving structure I, and those which cannot and stabilise the radical by promoting the formation of the zwitterionic type structure II. The results show that the hydrogen bonding effect is the stronger and the ν_{8a} band position shift is rationalised by noting that whilst H-bonding causes a decrease in electron density in the C-O bond, it is compensated by an equal donation of electron density from the *para* oxygen atom as illustrated in Structure (II). The overall effect of H-bonding results in a lowering of conjugation

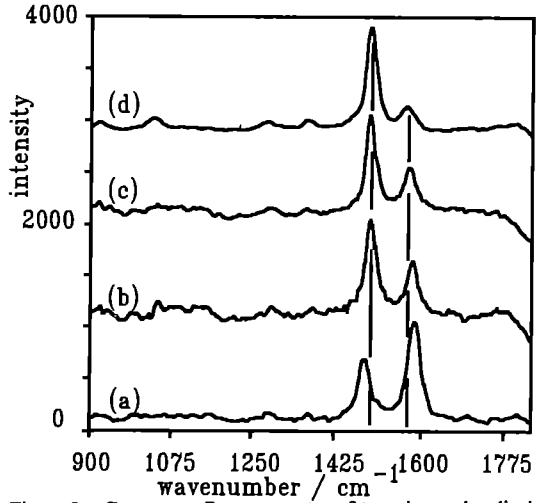

Figure 3: Resonance Raman spectra of tocopheroxyl radicals from (a) Trolox C in aqueous phosphate buffer (50 x10^{-3} mol dm^{-3}, pH 7.0); (b) α-tocopherol in methanol; (c) α-tocopherol in *n*-hexane. The concentrations of α-tocopherol or Trolox C were *ca.* 5 x 10^{-3} mol dm^{-3}. Spectra were obtained using a 308 nm pump pulse and a 425 nm probe pulse with 2 μs delay.

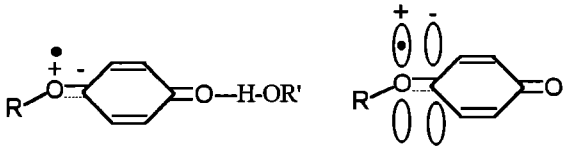

Stucture (I) Structure (II)

as the molecule adopts the quinoid structure. This causes a tightening of the ring C=C bonds and leads to the observed increase in the ν_{8a} stretching frequency. Figure 3 also contains the TR^3 spectrum of Trolox C radical in water which when compared with the spectrum of α-tocopheroxyl in methanol shows the intensity of the ν_{8a} band is enhanced and is more intense than the ν_{7a} band. The results discussed above for the solvent effect on the ν_{8a}/ν_{7a} intensity ratio and ν_{8a} band position are also evident in the spectra of 4-methoxyphenoxyl radical, see Figure 2 and Table 2. In addition, the Wilson ν_{9a} band at 1161 cm^{-1} in water is shifted to lower wavenumbers in less polar solvents and diminishes in intensity relative to the ν_{7a} band.

c) TR^3 Spectra of α-tocopheroxyl Radical in Micellar and Membrane Systems.

The Raman band positions and relative intensities for α-tocopheroxyl radical in micellar and bilayer membranes are summarised in Table 1. Based on the evidence of solvent effects above the position of the C=C (ν_{8a}) stretch at 1593 and 1590 cm^{-1} in SDS and HTAC micelles respectively are indicative of relatively polar environments, comparable with the free radical in ethanol or methanol. The frequencies in Triton X-100R-S micelles (1586 cm^{-1}) and DMPC bilayers (1587 cm^{-1}) indicate less polar environments, but still substantially more polar than a hydrocarbon-like medium such as hexane. The interpretation of the band ratio (ν_{8a}/ν_{7a}) is complicated by the division of solvents into the groups in Figure 4. However, the ratio in SDS (0.81) very clearly indicates a polar environment in contact with a H-bonding molecule (water). The high micropolarity of the α-tocopheroxyl radical site in SDS is not surprising considering the known penetration of water molecules into the SDS micelle. The lower dielectric constants reported by the Raman spectra for α-tocopheroxyl in HTAC and Triton X-100R-S micelles may reflect the longer apolar chains of these detergents. The effective dielectric constant in the Stern layer of a number of micelles has been estimated to be in the range 36-46. Less polar environments than this are reported for the α-tocopheroxyl radical in HTAC and Triton X-100R-S micelles based on the Raman intensities. If the line corresponding to H-bonding solvents is used for comparison with the situation in DMPC bilayers, then the intensity ratio of the Raman spectrum (0.45) reflects a fairly low effective dielectric constant in the region of 12-15. Previous estimates[9] of the dielectric constant experienced by the phenolic group of α-tocopheroxyl itself in

Table 2-Resonance Raman bands (cm^{-1}) of tocopheroxyl radical analogues

RADICAL	SOLVENT	C-O STRETCH (ν_{7A})	C=C STRETCH (ν_{8A})	C-H BEND (ν_{9A})	INTENSITY RATIO (ν_{7A}/ν_{8A}) [ν_{9A}/ν_{7A}]
	water, pH 7.5[a]	1514 (1518)	1609 (1607)	1161	2.15 [0.48]
4-methoxyphenoxyl	methanol	1516	1602	1157	1.28 [0.52]
	ethanol	1514	1598	1156	0.92 [0.23]
	octan-1-ol	1514	1597	1154	0.62 [0.18]
4-methoxy-2,3,5,6-tetramethylphenoxyl	ethanol	1501	*ca.*1593[b]		<0.15
Trolox C	water, pH 7.0	1492	1600		1.62
	methanol	1504	1588		0.73
MDL 73404	water, pH 7.0	1490	1595		1.12
MDL 73404 Radical cation	HCl solution (10 mol dm^{-3})		1620		

[a]Values in parenthesis for 4-methoxyphenoxyl are from reference 21. [b] very weak

bilayer membranes are in the range 26-36 and are in accord with the orientation of α-tocopherol in the membrane. The lower dielectric constant for the α-tocopheroxyl radical reflects its less polar nature which may allow it to become more buried in the bilayer than α-tocopherol itself. Further studies using bilayers prepared without ethanol and containing a range of lipid molecules are clearly required.

d) Water Soluble Analogues

Two synthetic water soluble analogues of α-tocopheroxyl, Trolox C and MDL 73404 have been used to investigate protonation of the tocopheroxyl radical. From laser flash photolysis studies the absorption maximum for MDL 73404 was found to be 440 nm in water, pH 7.0. This is shifted to 465 nm in concentrated HCl due to formation of the radical cation. The resonance Raman spectra of both these species was investigated by photolysing solutions of MDL 73404 with 308 nm and probing at 425 nm. At pH 7.5 the spectrum was similar to that of α-tocopheroxyl in methanol with peaks at 1490 cm^{-1} (ν_{7a}) and 1595 cm^{-1} (ν_{8a}) and we assign these peaks to the MDL 73404 neutral phenoxyl radical. However, in concentrated HCl the Raman spectrum changes to a single strong band at 1620 cm^{-1}. This feature is similar to the TR^3 spectrum of hydroquinone radical cation and we assign this band to the ring C=C (ν_{8a}) mode. The pK_a of the MDL 73404 radical cation was obtained by 'titration' of the transient absorption at 465 nm against HCl concentration. By use of the Hammett acidity function (H_o) and a plot of H_o versus $\log\{[TOH^{+\cdot}]/[TO^{\cdot}]\}$ which was linear a value of the thermodynamic acid dissociation constant, pK_a, -1.4 ± 0.1 was obtained for the MDL radical cation. This value is considerably lower than the pK_a value of Trolox C, pK_a=2.3 determined by Thomas and Bielski[10]. TR^3 measurements on Trolox C were hindered by low solubility in very acidic solutions but a rather

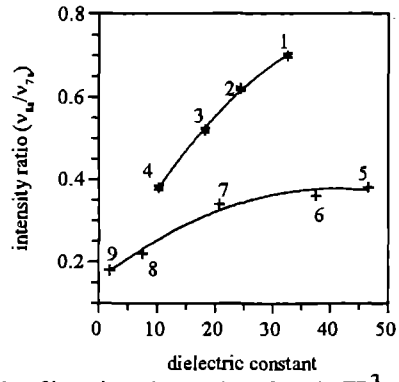

Figure 4: Plot of intensity ratios, ν_{8a}/ν_{7a}, from the TR^3 spectra of the α-tocopheroxyl radical in solvents as a function of their dielectric constant. The solvents are:- methanol (1); ethanol (2); propan-2-ol (3); octan-1-ol (4); dimethylsulphoxide (5); acetonitrile (6); acetone (7); tetrahydrofuran (8); *n*-hexane (9).

noisy Raman spectrum of the in 0.2 mol dm^{-3} HCl was similar to that for the neutral radical. We conclude the reported value is in error. Our pK_a value of -1.4 for the radical cation lies between the pK_a of hydroquinone radical cation (-0.8) and phenoxyl and cresoxyl radicals (between -2.0 and -1.6), as would be expected for a radical which has intermediate valence properties. Finally, attempts to observe the α-tocopheroxyl radical cation in any solvent system at neutral pH were unsuccessful. This infers that the deprotonation process takes place faster than the time resolution of our nanosecond TR^3 apparatus. Assuming that the neutral radical protonates with a second order rate constant of the order of 10^{10} dm^3 mol^{-1} s^{-1}, the pK_a value for the radical cation indicates that deprotonation should occur on the picosecond timescale

Acknowledgements

The authors are grateful to Dr F.Bolenius (Merrel Dow) for the gift of the cationic tocopherol analogue MDL 73404, to Dr E. W. Thomas (University of Salford) for synthesis of 4-methoxy-2,3,5,6-tetramethylphenol and to Henkel Corporation for the gift of β- and δ-tocopherols. We also thank Sue Tavender for her help with the experimental setup.

1) See for example G. W. Burton and K. U. Ingold, *Ann. N.Y. Acad. Sci.*, (1989) **570**, 7 and H. Esterbauer, J. Gebicki, H. Puhl and G. Jurgens, *Free Rad. Biol. Med.*, (1992) **13**, 341.

2) R. H. Bisby and A. W. Parker, *CLF Annual Report, RAL-92-020*, (1992) 149.

3) A. W. Parker and R. H. Bisby, Accepted *J. Chem. Soc. Faraday Trans.*, (1993).

4) R. H. Bisby and A. W. Parker, *FEBS Lett.*, (1991), **290**, 205.

5) G. N. R. Tripathi and R. H. Schuler, *J. Phys. Chem.*,(1988), **92**, 5129.

6) G. W. Burton and K. U. Ingold, *J. Am. Chem. Soc.*, (1981) **103**, 6472.

7) G. W. Burton, T. Doba, E. J. Gabe, L. Hughes, F. L. Lee, L.Prasad and G. W. Ingold, *J. Am. Chem. Soc.*, (1985) **107**, 7053.

8) G. W. Burton and K. U. Ingold, *Acc. Chem. Res.*, (1986) **19**, 194

9) J. G. Lesard and M. Fragata. *J. Phys. Chem.*, (1986) **90**, 811

10) M. J. Thomas and B. H. J. Bielski, *J. Am. Chem Soc.*, (1989) **111**, 3315

INITIAL EVENTS IN LUCIFERASE LIGHT EMISSION

Chittock, R.S.†, Lidzey, D.G.‡, Tavender, S.❁, Parker, A.❁, Berovic, N.‡, Wharton,C.W.†, Beynon, T.D.‡, Jackson, J.B.†

†School of Biochemistry ‡School of Physics and Space Research, The University of Birmingham, Edgbaston, Birmingham, B15 2TT.

❁Laser Support Facility, Rutherford Appleton Laboratory, Chilton, Didcot, Oxon, OX11 OQX

INTRODUCTION

The substrates of luciferase, the light-producing enzyme of the firefly *Photinus pyralis*, are ATP, oxygen and the heterocyclic co-factor luciferin (1). Our research aims to investigate the properties of this complex system, with the aim of incorporating it into molecular electronic devices for pattern recognition, image storage and molecular switching (2). The system is held in an *'Off'* (non-reacting) state by replacing ATP with caged ATP (c-ATP), a photolysable analogue (3). A UV pulse from an excimer laser uncages the ATP, converting the enzyme to the *'On'* (light-emitting) state. This report describes a series of experiments performed at the LSF to characterise this system.

EXPERIMENTAL DETAILS

Bioluminescence was measured using a sensitive photomultiplier operated in photon-counting mode (Fig. 1). The PMT could not be allowed to see the laser flash or the bright fluorescence from luciferin, even though most of the former was removed by an interference filter placed between the sample and the detector. A MOSFET based circuit was used to ground the first dynode in the PMT chain in response to an external pulse that also triggered the laser and initiated data collection, thus removing HT from the photocathode during the laser pulse. Photoelectrons were still produced , appearing as a noise spike when the HT was re-applied, limiting the time resolution of the system. In future runs it may be possible to replace the MOSFET gate with a fast mechanical shutter.

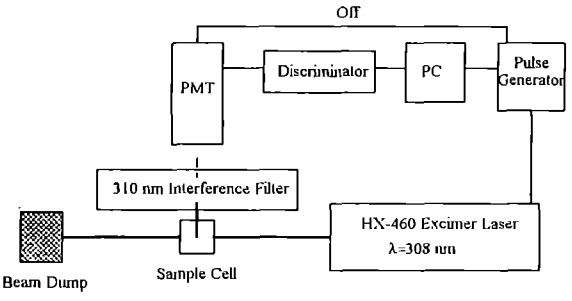

Figure 1. Schematic Diagram of Apparatus

RESPONSE TIME OF UV-INDUCED BIOLUMINESCENCE

When luciferase was mixed with luciferin and c-ATP a low background luminescence was observed due to ATP impurity in the c-ATP. Final concentrations were: Luciferase = 425 nm; luciferin = 50 μM; c-ATP = 85 μM. The solution was illuminated with a single UV pulse at 308 nm from a Lumonics HE-460 excimer laser (50 mJ / 10 ns pulse). Bioluminescence was measured as the number of photons emitted in 50 ms time bins. To correct for the artefactual fluorescence transient the experiment was repeated from a sample in which c-ATP had been omitted. Subtraction gave a corrected response time of UV-induced bioluminescence with a rise-time of approximately 0.2 s. (Figure 2, solid line).

Figure 2. Kinetics of Laser-Induced Bioluminescence

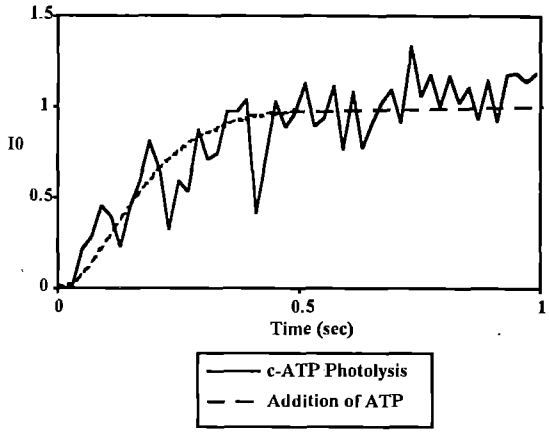

Results agree well with the onset of bioluminescence when ATP is mixed rapidly with luciferase + luciferin using a stopped-flow machine (Figure 2, dashed line). This demonstrated that photolysis of c-ATP will not be rate-limiting in any proposed device.

EFFECT OF OXYGEN

Luciferase was mixed with luciferin and c-ATP. Final concentrations were luciferase = 425 nM; luciferin = 50 μM; c-ATP = 85 μM. When oxygen concentration was reduced by lowering the pressure in the cuvette to 100 mm. Hg , the background level of bioluminescence fell to zero. Illumination of the sample with six laser pulses at 308 nm to uncage c-ATP gave no observable bioluminescence. Restoration of the cell to atmospheric pressure produced a slow rise in bioluminescence to approximately four times its initial value. The slow response was caused by slow re-equilibration of oxygen in the sample. Any prototype device would use a thin layer of enzyme, so the recovery of bioluminescence is expected to be in the order of msec. Since the rate-limiting step of the luciferase reaction occurs before the oxygen step this may provide a mechanism to decrease the overall response time of the system.

This result demonstrates that oxygen deprivation can be used as a means to store information in this system. On the basis of this experiment we have used the enzyme system immobilised in thin agarose gels to store images for up to one hour.

SELF ABSORPTION EFFECTS

The peak uncaging wavelength of luciferase is approximately 310 nm. Luciferin also has a significant absorption at this wavelength. At low luciferin concentrations, the observed bioluminescence induced by a given number of laser shots increases linearly with luciferin concentration. If luciferin concentration is increased above its K_m for luciferase the increase in bioluminescence caused by the extra luciferin does not compensate for the decrease in the amount of c-ATP photolysed due to the increased absorbance by the luciferin.

Figure 3
Effect of [Luciferin] on Laser-Induced Bioluminescence

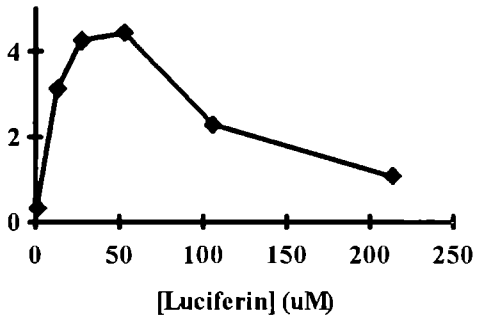

Figure 3 shows the effect of increasing luciferin concentration on observed bioluminescence. Luciferase concentration was 425 nM; c-ATP concentration was 85 μM. Bioluminescence was measured as the peak activity observed. Optimum bioluminescence was observed at around 50 μM luciferin. This is an important result, demonstrating the optimum luciferin concentration to be used in these experiments. It is hoped that this effect can be avoided in future experiments by synthesising a new caged ATP derivative with an uncaging action spectrum that does not overlap that of luciferin.

CONCLUSIONS

These experiments have demonstrated several important properties of our luciferase-based system which have proved useful in the construction of prototype molecular electronics devices. These immobilise the components in a thin agarose gel, allowing 2D patterns to be written and stored at the microscopic level. It is hoped to extend this work to enzyme immobilised in monolayers on surfaces. In future work at the LSF we hope to use the methods described here to characterise these immobilised systems and compare them with the same components in solution.

REFERENCES

1) M. De Luca and W.D. McElroy (1978) Meth. Enzymol. **57**, 3-16

2) N. Berovic, R.S. Chittock, D.G. Lidzey, C.W. Wharton, T.D. Beynon, J.B. Jackson (1993) Molecular Crystals and Liquid Crystals, *in press*

3) J.A. McCray and D.R. Trentham (1989) Ann. Rev. Biophysics and Biophysical Chemistry **18** 239-270

KINETICS AND MECHANISM OF DNA REPAIR: THE NATURE OF THE UV-LASER DAMAGE-INDUCED 'PANIC' PHASE DNA SYNTHESIS

W.Meaking,R.A.Meldrum,J.Edgerton,S.Ward and C.W.Wharton

School of Biochemistry,University of Birmingham
Edgbaston,Birmingham B15 2TT.

INTRODUCTION

Since every cell in an organism can be damaged up to 10^4 times a day,DNA repair forms a vital part of the life sustaining system. In recent Annual Reports we have described extensive experiments that have been designed to elucidate the nature and role of the 'panic' phase DNA synthesis that we have observed shortly after both UV and X-irradiation of mammalian cells. Thus use of DNA polymerase inhibitors has pointed to the involvement of polymerases delta and epsilon,both of which carry exonuclease enzymes which can edit DNA of low fidelity to restore the correct genetic code. The introduction of excess nucleotides,which distort the natural balance of the pools of dATP,dTTP,dCTP and dGTP required to drive DNA synthesis has indicated that the DNA synthesis during the panic phase may be of low fidelity. We have shown that the panic phase is seen at doses as low as $10J/m^2$,which is biologically relevant but,of course,delivered at a much higher (laser) intensity than would occur either in nature or as a result of Hg lamp illumination as has been traditional in DNA repair experiments. It seems likely that the power density of the illumination used to inflict damage on the DNA may have an effect on the type of damage induced. The panic phase is progressively attenuated as the power density per laser shot is decreased but we have not been able to show conclusively whether the response is entirely dependent upon laser intensities. This factor requires further careful study.

Electroporation has played a central role in our methodology in that it has been used to load impermeant cells with the break trapping reagent we use to label breaks which occur during the course of the DNA repair process. Although it has been difficult in the case of UV irradiation of HL60 cells,which replicate rapidly and continuously,we have now been able to show in all cases that electroporation is not responsible for the observation of the panic phase. Cells can be loaded with ^{3}H-thymidine, which can diffuse into cells and subsequently be phosphorylated to TTP,the active form for DNA synthesis. In all these experiments a transient such as that seen in experiments which use electroporation was observed. The disadvantage of such experiments is that the pool size of TTP may be depleted during the early repair response and so lead to difficulty in the detailed kinetic interpretation of the panic phase.

In this report we describe kinetic modelling of the panic phase,experiments designed to address the nature of the UV laser-induced danmage in cellular DNA and studies of the effect of the mushroom toxin α-amanatin on the DNA repair process.

RESULTS AND DISCUSSION

Fig. 1 shows a typical example of the UV-induced panic phase behaviour,measured by the incorporation of the chain termination inhibitor *α-32P-ddATP.*

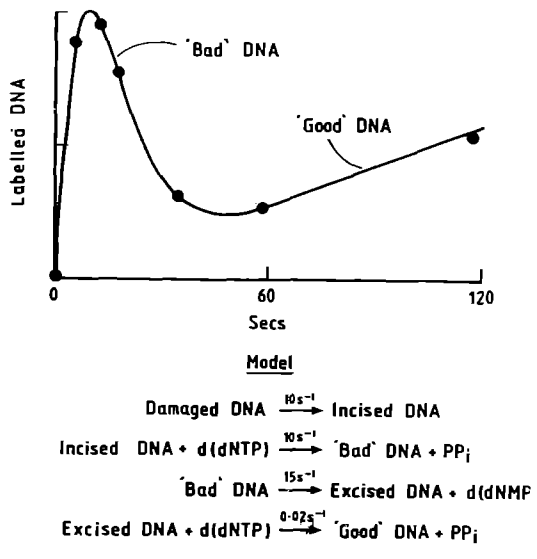

Fig. 1. Model of the time-dependence of the incorporation of α-^{32}P dideoxyadenosine triphosphate into DNA following 100 J/m^2 248 nm UV irradiation.

The rapidly synthesised '*bad*' DNA has repair patches terminated with ^{32}P-ddAMP but not necessarily opposite thymidine as in correctly base paired DNA. The '*good*' DNA thus represents ddA correctly paired with T but this is still lethal to the cell and is removed on a much slower time scale. In experiments with thymidine,a 'normal' nucleotide the repair patches are also proposed to be of low fidelity but the '*good*' DNA will be correct DNA. The kinetic model is shown in the lower portion of the fig. and with some additions broadly follows conventional ideas concerning the mechanism of the repair of UV damage in eucaryotes. The second step,namely a polymerisation that gives incorrect DNA,is the one that would normally be expected to give 'good' DNA i.e. the repair would be complete at this stage. The 'bad' DNA so produced has to be cleaned up in the subsequent stage followed by a repolymerisation to give high fidelity DNA. The step in which initially damaged DNA is excised has not been explictly included in the model since it is kinetically redundant in

that no change in labelling of the DNA ocurs,but must,of course,happen. It is clear that this model fits the data well and also shows that,as generally proposed,the incision/polymerisation steps are rate limiting. The model allows predictions to be made regarding the behaviour of all the other components of the system and is to be use in the future to design experiments which will allow further validation and analysis of the panic phase. The fit to the data was initially obtained manually using a simulation program 'MODEL' written by R.S.Chittock. That the fit is the best one has recently been shown by an extension of this program that allows numerical optimisation of the fit by using the Marquardt algorithm;this gave an identical answer.

Are direct UV laser-induced breaks responsible for the panic phase?

It has previously been found that UV lasers can induce *direct single strand* breaks in DNA *in vitro*,albeit with a quantum yield of only ca. 10^{-6} [1]. In view of the similar panic phase response we have observed for both UV and X-irradiation and the fact that the latter is known to produce direct single and double strand breaks,we resolved that it was important to look for laser induced breaks in our *in vivo* sytem. We have used two methods for this,fluorescent assays of unwinding FADU and alkaline elution [2]. Both methods measure the rate at which the double helical structure of DNA unwinds and this is dependent on the number of breaks in the DNA. In FADU the amount of double stranded DNA remaining after a fixed unwinding time is determined by the enhanced fluorescence of ethidium bromide intercalated into double stranded DNA. In alkaline elution the DNA is placed on a filter at high pH,where the DNA will unwind. The rate at which the unwound molecules pass through the filter is a measure of the rate of unwinding. The method was calibrated using gamma rays and some elution curves are shown in Fig. 2.

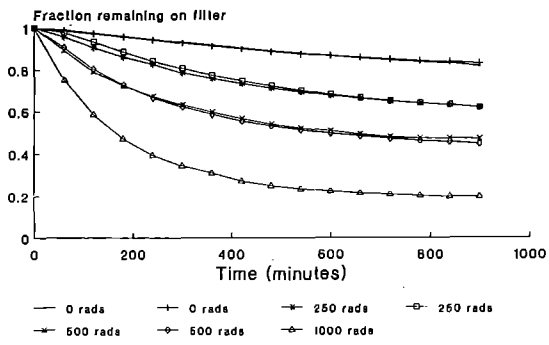

Fig. 2. Alkaline elution of DNA extracted from gamma irradiated HL60 cells. The eluted pieces of DNA were assayed by measurement of the amount of 3H-thymidine label with which the DNA was labelled for one cell cycle (ca. 24 h.) prior to irradiation. For further details see the text.

It can be seen that both the rate and extent of elution are dose dependent. Fig. 3 shows the calibration line for both the FADU and alkaline elution methods.

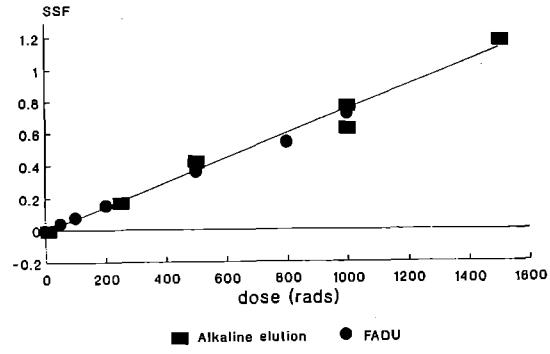

Fig. 3. Calibration of alkaline elution and FADU as a measure of gamma radiation induced breaks in HL60 cellular DNA. The strand scission factor (SSF) ia a measure of the rate of elution and hence the number of breaks.

Fig. 4 shows elution curves for 248 nm UV-irradiation applied to the cells exactly as in DNA repair experiments,while

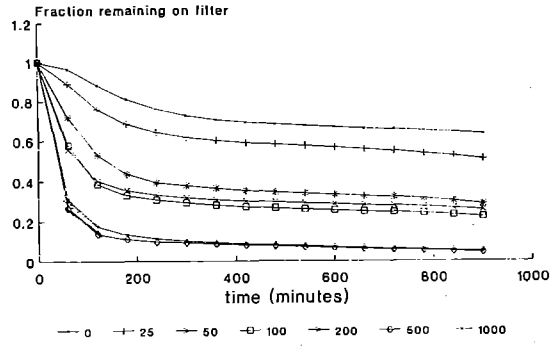

Fig. 4. Alkaline elution of 248 nm irradiated HL60 DNA,doses are in J/m^2. it is apparent that direct breaks are induced by doses as low as 25 J/m^2.

Fig. 5 shows the dose response. It is clear that direct breaks are induced in cellular DNA by UV and therefore it is a strong possibility that the common response between UV and X-rays results from the repair of a common form of damage.

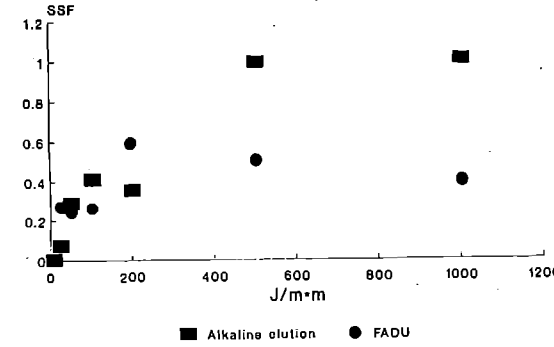

Fig. 5. The relationship between the strand scission factor and the UV dose,see legend to Fig. 3 and the text.

In order to verify this interpretation it will be necessary to perform time-resolved experiments to determine if these breaks are being 'repaired' during the panic phase. Although both the FADU and alkaline elution methods gave a good calibration line with gamma radiation it is clear that the response to UV is different. The FADU method is apparently saturated by low levels of UV while alkaline elution shows a classical 'saturation' curve. It is difficult to believe that the damage itself saturates so we assume that it is the detection method that does so. It appears that the breaks caused in the DNA by UV are different as compared with Gamma ray induced breaks and are caused by multiphoton absorption (see below). The maximum UV dose we have used in DNA repair experiments is 100 J/m^2 and this is in an approximately linear region of the dose response curve prior to the onset of saturation.

We have also studied the effect of UV power density upon the formation of direct breaks and Fig. 6 shows a plot of the dose per shot against the SSF. There is a strong positive peak power dependence at a constant dose so it seems that break induction is a nonlinear optical phenomenon as perhaps might be expected. At this wavelength two photon absorption will provide sufficient excitation energy to cause direct breaks in the DNA.

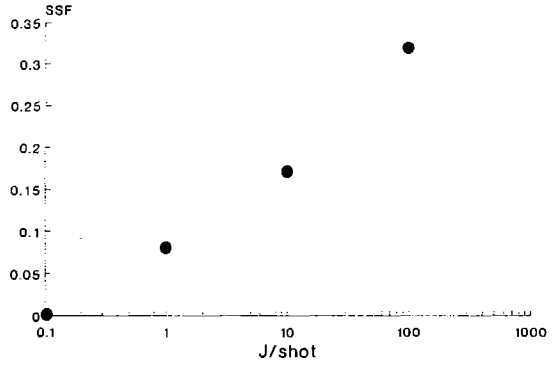

Fig.6.The power dependence of the SSF in alkaline elution for UV irradiation.

Is RNA polymerase involved as a marker protein in DNA repair?

Hanawalt [3] has shown that active transcribing genes have priority in repair;they are needed to make proteins for the cell if it is to survive. Also only the transcribed strand of the DNA is repaired rapidly,since this is the one being copied to RNA [4]. On this basis it has been proposed that RNA polymerase II,the enzyme which copies RNA to DNA,and which will stall at damage sites might be the protein which marks damage sites and guides in the repair proteins. If α-amanatin,the toxin from Amanita *Phalloides* is used to stall the RNA polymerase molecules prior to a repair experiment,i.e. at undamaged sites,they would not be able to act as guides for damage repair.

Fig. 7 shows the results of one such experiment. α-amanatin apparently strongly attenuates the burst phase of DNA synthesis but enhances the second phase which in this case with ddATP will be terminated repair patches,not fully correct DNA.

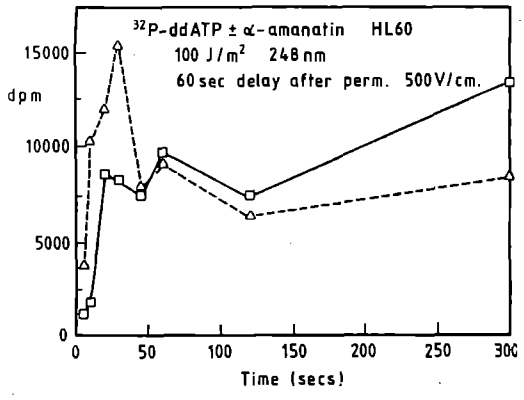

Fig. 7. The effect of the RNA polymerase inhibitor α-amanatin on the early repair of UV damage. triangles - no inhibitor; squares 1μM α-amanatin. A 60 second delay after electroporation at the lower voltage of 500V/cm is allowed to permit ingress of the break trapping α-^{32}P ddATP. This lower EP voltage causes little DNA damage and gives 60 % long term viability of the cells.

There is thus some evidence for the involvement of RNA polymerase in the panic phase but more work will be required to resolve its role. It seems not to incorporate ddATP molecules which need to be removed rapidly before a final elimination of chain terminating molecules which occurs much later in the overall repair process.

REFERENCES

1. Schulte-Frohlinde,D.,Simic,M. & Gorner,H. (1990) Photochem. Photobiol. 52,1137.

2. Kohn,K.W.,Ewig,R.A.G.,Erickson,L.C. & Zwelling,L.A. (1981)
in DNA Repair,A Laboratory Manual,Eds. Freidberg,E.C. & Hanawalt,P.C.,Dekker,New York,pp. 379-402.

3. Madhani,H.D.,Bohr,V.A. & Hanawalt,P.C. (1986) Cell 45,417.

4. Mellon,I.,Spivak,G. & Hanawalt, P.C. (1987) Cell 51,241.

PHOTOIONISATION OF NUCLEIC ACIDS USING 193NM LIGHT

S Botchway[1], P O'Neill[1], A W Parker[2] and M C R Symons[3]

[1]MRC Radiobiology Unit, Chilton
[2]LSF, Rutherford Appleton Laboratory
[3]University of Leicester

INTRODUCTION

The lethal and mutagenic effects of ionising radiation are thought to be due to damage induced in DNA. Of the many types of lesion induced in DNA, the DNA double strand breaks has been implicated in the processes leading to cell inactivation. One of the major processes resulting from ionising radiation is the formation of an ion pair. It has been shown from epr studies on DNA irradiated at 77K[1], that the resulting electron becomes localised on the pyrimidine bases and the electron loss centre localised on guanine. This latter radical has been suggested to lead to a strand break, a process which would involve transfer of the damage from the base moiety to the sugar-phosphate backbone. It is important to gain information on the radical cations/deprotonated forms in order to enhance our understanding of the pathways leading to DNA damage induced by ionising radiation.

Several recent studies have shown that the base moieties of DNA undergo photoionisation with 193 nm light[2,3,4]. Due to the importance of ionisation events in the early pathways leading to the biological effects of radiation, it therefore seems appropriate to use 193 nm light to generate one-electron oxidised bases of DNA so that the properties of these radicals could be assessed. The use of 193 nm light was thought to provide a "clean" method of producing the radical cations of purine and pyrimidine nucleosides in aqueous solution at pH 7. Alternative approaches using pulse radiolysis to generate the radical cation in aqueous environment have involved the use of the powerful oxidant $SO_4^{\cdot-}$, which generally interacts by one-electron oxidation. However recent findings on the interaction of $SO_4^{\cdot-}$ with pyrimidines have indicated that the reaction proceeds through adduct formation without generation of the pyrimidine radical cations[4]. This report presents the preliminary findings on the photoionisation of DNA model compounds by 193 nm. The usefulness of this method has been demonstrated for probing the reactivities of the resulting one electron oxidised radicals and may provide a valuable method for investigation of charge migration in mixed systems.

METHOD

Briefly, aqueous solutions containing the purine and pyrimidine at pH ~7 have been photolysed with a pulse of 193 nm from an excimer laser. The concentrations of the solutes were such that the optical density of the solutions at 193 nm is about unity. The optical absorption changes with time following the laser pulse were monitored spectrophotometrically. Typical power per pulse was in the range 1.2-30 mJ. The quantum yields for photoionisation were determined from a comparison of the concentration of electrons produced (absorbance at 650 nm) upon photolysis of the nucleosides with the concentration of electrons produced upon photoionisation of NaCl and assuming $\phi_e = 0.46$[2]. The optical absorption spectra of the radicals produced upon photoionisation of the purines and pyrimidines were determined in aerated solution so that the electrons are removed by reaction with oxygen ($k \sim 10^{10}$ dm^3 mol^{-1} s^{-1}). It has been assumed that the DNA base radicals are not particularly reactive with oxygen, allowing the determination of their optical properties.

RESULTS AND DISCUSSION

Photolysis of 2'-deoxyguanosine, adenosine, cytidine monophosphate (CMP) and thymidine in aqueous solution with 193 nm light under anaerobic conditions results in the formation on solvated electrons with an absorption maximum centred around 650 nm. The observation of solvated electrons is consistent with photoionisation of the base moiety. Photolysis of the cuvette containing water does not produce e^-. Figure 1 shows the dependence of the absorbance at 650 nm on the energy of the laser pulse.

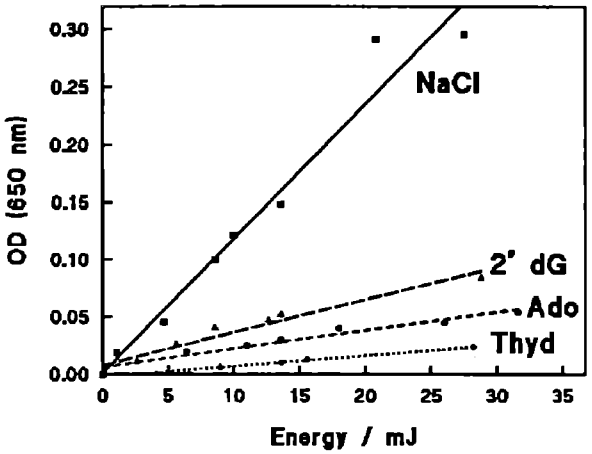

Figure 1. Dependence of OD at 650 nm on laser energy

These dependences are linear with the except of that with thymidine and are indicative of monophotonic processes. With thymidine, the dependence has a major quadratic component. The quantum yields for photoionisation of DNA bases with 193 nm light is shown in Table 1. These yields are consistent with guanine having the lowest ionisation potential.

Compound	Quantum Yield for Photoionisation
2'-deoxyguanosine	0.084
Adenosine	0.046
CMP	0.024
Thymidine	0.033

Table 1. Quantum yields for photoionisation by 193 nm light.

The optical absorption spectra determined ~ 10μs after flesh photolysis of aerated solutions of the purines and pyrimidines are shown in Figure 2. Under these conditions, the electrons are scavenged by oxygen to yield superoxide which is transparent at λ > 300 nm. It is also assumed that the majority of the excited states have relaxed within 10 μs. The optical spectra determined with 2'-deoxyguanosine and adenosine are consistent with those determined by one-electron oxidation of these purines using other methods[4].

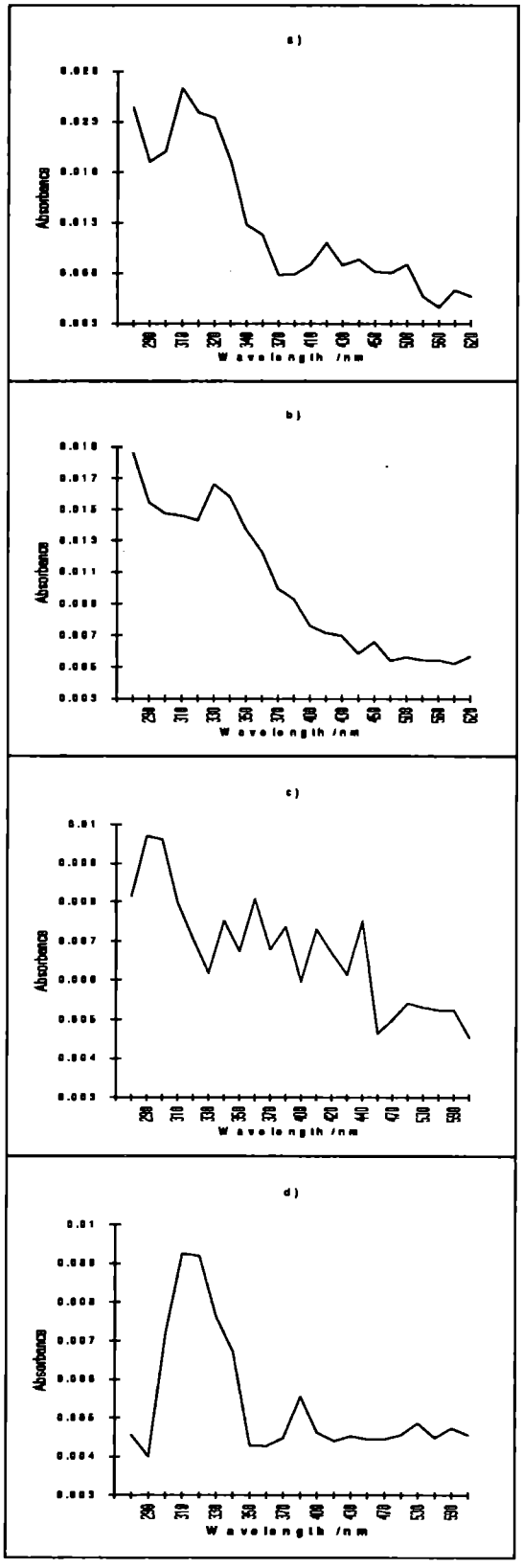

Figure 2. Optical absorption spectra of species produced upon photoionisation of a) 2'-deoxyguanosine, b) adenosine, c) thymidine and d) CMP.

The following reaction scheme is proposed to account for the formation of the deprotonated radical cations of these purines upon photoionisation.

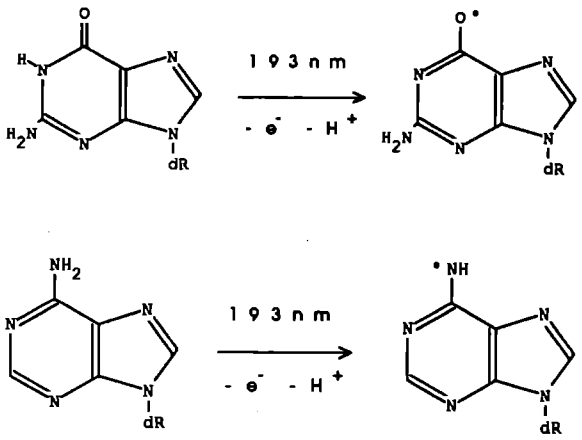

The pK_a value[5] of the radical cation of 2'-deoxyguanosine is 3.9. With thymidine and CMP, it is assumed that the optical absorption spectra shown in Figure 2 represent the radical cations or their deprotonated forms. The assignment of these radicals is tentative in the absence of benchmark spectra of the radical cations from these pyrimidine compounds.

SUMMARY

It has been confirmed that 193 nm light photoionised DNA model compounds monophotonically with the formation of the radical cation. Thymine is the only exception, involving a biphotonic component. The optical absorption spectra of the resulting pyrimidine and purine radicals have been determined and are in agreement with earlier work. These preliminary experiments demonstrate that we will be able to use 193 nm photoionisation to investigate the properties of one electron oxidized DNA model compounds. The usefulness of this approach will be important in studies aimed at gaining information on the redox properties of these radicals with specific reference to charge migration. Future studies will also aim at improving the quality of the cationic radical spectra.

REFERENCES

1. P J Boon, P M Cullis, M C R Symons and B W Wren. J. Chem. Soc., *Perkin Transactions II*, 1393-1399 (1984).

2. L P Candeias, P O'Neill, G D D Jones and S Steenken. Int. J. Radiat. Biol., 61, 15-20 (1992).

3. H Görner, M Wala and D Schulte-Frohlinde. Photochem. Photobiol., 55, 173-184 (1992).

4. P Wolf, G D D Jones, L P Candeias and P O'Neill. Int. J. Radiat. Biol., In Press (1993).

5. K-D Asmus, D J Deeble, A Garner, K M Ali Idriss and G Scholes. Br. J. Cancer, 37 (Suppl. III), 46-49 (1978).

THE KINETICS OF REPAIR OF SOFT X-RAY DNA DAMAGE IN MAMMALIAN CELLS.

W.Meaking*,R.Meldrum*,J.Edgerton*,E.Turcu+ and C.Wharton*.

* School of Biochemistry,University of Birmingham.
+ Rutherford Appleton Laboratory.

X-rays are known to produce at least 7 or more forms of damage in mammalian cell DNA. These consist of single strand breaks, double strand breaks, base damage, base loss, intramolecular crosslinks, DNA protein crosslinks or denatured zones in the DNA. The latter three types of damage are more likely to occur at significantly high doses of x-rays.

Since the damage produced by x-rays is complex it is not surprising that we have found the the profiles of the DNA repair kinetics following soft x-ray damage are complex. The production of 1.2keV x-rays and the automated machinery and methods for gathering DNA repair kinetics data has been described previously (1,2) as has the 'caged' DNA break-trapping agent (3).

Figure 1 shows rate profiles of incorporation of photolysed ^{3}H-TTP into DNA of V79 confluent fibroblasts following damage by 500 rads of soft x-rays. Unlike the profiles of rates of polymerization after 248nm UV laser damage which shows one transient between 0 and 60 seconds after damage, there appears to be two transients in the early stages of repair of x-ray damage to DNA. The first occurs between approximately 0 and 30 seconds and the second between approximately 60 and 150 seconds after damage. The control time course which is measured in cells which have not received x-rays but have been permeabilised by electroporation to allow entry of the 'caged' molecule and then subjected to the 351nm UV photolysing pulse, is almost entirely flat. DNA replication synthesis inhibited in these confluent cells by contact inhibition, therefore background incorporation of radiolabelled nucleotide by replication synthesis is negligible. The flatness of the time profile of radiolabel incorporation by the control cells also indicates that electroporation has no significant effect upon DNA repair activity in this time domain. The cells are electroporated by a series of parallel platinum plates which are set 2mm apart and lowered onto the surface grown cells. A voltage of 500 volts/cm is discharged to permeabilise the cells. Viabilty of the cells after this voltage is 85 to 95%.

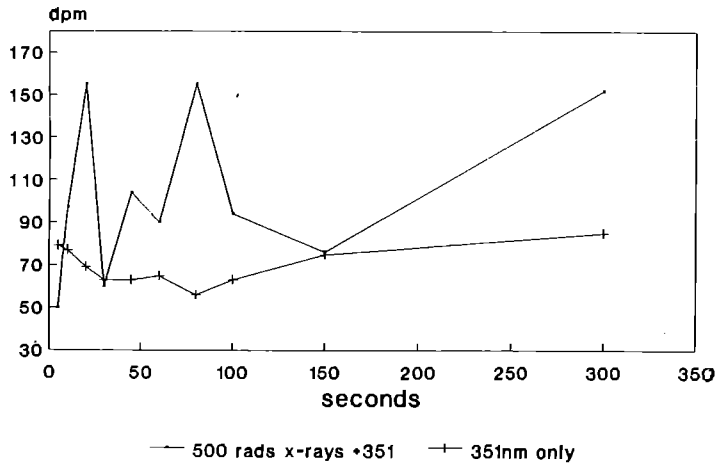

Figure 1. The incorporation of ^{3}H-TTP into the DNA of surface permeabilised V76 cells following DNA damage by soft x-rays.

Cells were permeabilised by 500 volts/cm to allow entry of the caged molecule. An interval of 60 seconds was allowed before x-ray damage was applied. The caged molecule was then activated by a 351nm UV laser pulse of 1kJ/m^2 at the times shown on the x-axis after x-ray damage. After a further interval of 10 seconds the reactions were quenched.

Squares and solid line cells irradiated with 500 rads x-rays

Diamonds and dotted line cells received no x-rays.

THE DETECTION OF SOFT X-RAY INDUCED BREAKS IN DNA.

The alkaline elution technique which detects breaks in mammalian cell DNA is described in some detail in the report on our experiments on UV induced DNA damage.
Figure 2 shows that there is a clear dose response relationship of formation of DNA breaks after damage by soft x-rays.

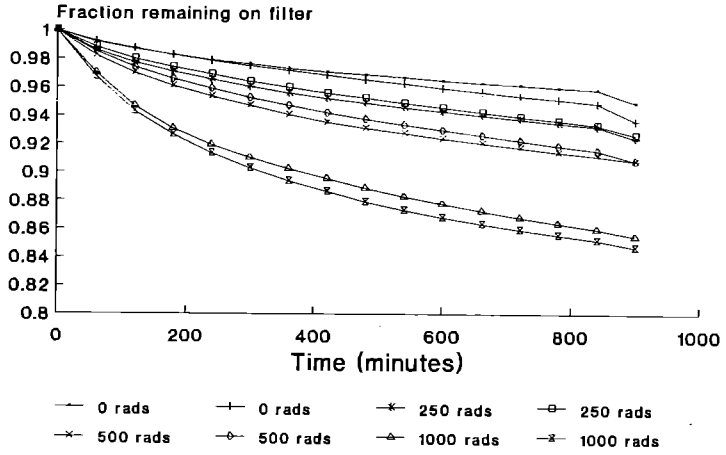

Figure 2. Alkaline elution of DNA extracted from soft x-irradiated V76 surface growing fibroblasts. The eluted pieces of DNA were assayed by measurement of the amount of ^{3}H-thymidine label in the DNA in each fraction The DNA was prelabelled with ^{3}H-thymidine for 24 hours before irradiation. Details of the method can be found in the report on repair on UV-induced DNA damage.

REFERENCES

1. Meldrum et al, SERC Central Laser Facility Annual Report 1992
2. Turcu et al, SERC Central Laser Facility Annual Report 1992 p232
3. Meldrum et al, Biochem J. 1990, 266,pp885-890

INVESTIGATION OF THE USE OF COHERENT 3.37 nm X-RAYS FOR MUSCLE DIFFRACTION

N.Berovic[1], R. A Thornhill[2], N. Thomas[1], I.C.E.Turcu[3], I.N. Ross[3]

1 School of Physics and Space Research, University of Birmingham
2 School of Biological Sciences, University of Birmingham
3 Rutherford Appleton Laboratory

INTRODUCTION

X-ray diffraction from intracellular protein is a well developed technique. It relies on the fact that protein is polymerised into ordered structures so that Bragg diffraction can take place. The wavelength of X-rays has uniformly been 0.15 nm. This choice, originally determined by the Cu-anode of the X-ray set was retained on synchrotron sources in order to meet the criteria for sample transparency, low radiation damage and high diffraction efficiency. Investigations with a longer wavelength, which would be of the same order of magnitude as the repeat distance of protein arrays, would add considerably more information and help in the interpretation of structural changes which are observed with 0.15 nm.

DESIGN

The target chamber of the KrF picosecond plasma X-ray source has a 250μm exit window for X-rays. A secondary chamber was made to attach at this point so that the target specimen can be positioned in the X-ray beam . The target could be rotated with respect to the beam axis so that Bragg angles could be set for different lattice spacings. It had a provision for a film plate detector and an intensified CCD detector. The chamber was air tight in order to keep the absorption of X-rays down by filling it with He. The target, which would typically be a fibrous material, had to be enclosed in a thin sealed container so that it could be kept moist to avoid drying.

TEST RUN

Problems were encountered during commissioning of the new equipment. Very thin specimens required long exposure times during which equipment failures occurred. These have been rectified so that it was possible to expose continuously for one hour. Tests were done with two target materials : 0.1 μm diameter latex spheres and insect flight muscle fibres. The muscle fibres were sectioned either transversely into 0.2 μm thick targets or longitudinally into 5 μm diameter bundles of myofibrils. There was no time to test the wet specimens.
X-rays were detected on film mainly, since the CCD cooling was not available.
Fresnel diffraction due to the external shape of the fibres was observed but no evidence was found for diffraction from the internal structures.

CONCLUSIONS

Further development work is required to provide higher detection efficiency of weak X-ray reflections from thin specimens. To preserve the internal structures, wet specimens will have to be used which will add to the absorption losses.

INVESTIGATION OF ION DYNAMICS IN A PENNING TRAP USING A PULSE-PROBE TECHNIQUE

K. Dholakia, G.Zs.K. Horvath, W. Power, D.M. Segal
and R.C. Thompson.

Blackett Laboratory, Imperial College, Prince Consort Road, London, U.K.

INTRODUCTION

In a Penning trap atomic ions are confined by static electric and magnetic fields. The motion of ions in such a trap is characterised by three oscillation frequencies. One of these, the magnetron frequency ω_m, corresponds to a relatively slow circular drift of an ion about the centre of the trap. For a cloud of ions the magnetron motion manifests itself as a rotation of the cloud. The magnetron frequency is given by

$$\omega_m = \frac{\omega_c}{2} - \left(\frac{\omega_c^2}{4} - \frac{\omega_z^2}{2}\right)^{1/2} \qquad (1)$$

where $\omega_z = \sqrt{4eV_{DC}/[M(r_0^2 + 2z_0^2)]}$ is the axial oscillation frequency, $\omega_c = eB/M$ is the cyclotron frequency, V_{DC} is the applied potential and $2r_0$ and $2z_0$ are the diameter of the ring and separation of the endcaps respectively. For our experimental conditions a typical value for ω_m is 50 kHz. Under the influence of laser cooling the ions in a Penning trap can form into ordered structures and images of such structures have been obtained. However, the inherent rotation of the ions around the magnetic field axis in the Penning trap means such images are inevitably in the form of concentric rings[1].

Computer simulations have been performed for large numbers of ions in a Penning trap and show that, at low temperatures, these systems should condense into a series of concentric shells[2]. This has already been observed for trapped beryllium ions[1]. The ions are predicted to diffuse relatively rapidly within a shell but the diffusion of ions between shells is predicted to be much slower[2].

Using a loan pool pulsed laser (Datachrom YAG pumped dye laser) we have demonstrated a new method for studying the motion of ions within the cloud. We have used the pulsed laser to 'tag' a portion of the ion cloud by putting the ions into a metastable state. Since the tagged ions do not scatter light from the cooling laser, their motion from one part of the cloud to another can inferred. Bollinger *et al.*[3] have reported preliminary results using a similar 'tagging' method that uses two cw lasers. The essential difference in our technique is that the tagging pulse is short compared to the magnetron period. We show that our method can be used to measure accurately the ion cloud rotation frequency. It should also be possible to obtain information on diffusion rates in the cloud.

EXPERIMENT

The experiment is done using a cloud of Mg^+ ions and the level scheme for the relevant transitions in Mg^+ is shown in figure 1(a). The magnetic field responsible for the radial confinement in the Penning ~ 1 T trap causes the Zeeman splitting shown in the figure. The linearly polarised cw cooling laser is tuned to the closed cycle (A on the figure). The pulsed laser is tuned to cover the Raman transition (B) depositing ions into the $M_J = +1/2$ level of the ground state manifold. This state is highly metastable with respect to direct spontaneous decay to the $M_J = -1/2$ ground state.

The experimental technique is shown schematically in figure 1(b). The pulsed laser beam can be spatially offset from the cw cooling laser. The pulsed laser tags a section of the ion cloud and as the cloud rotates at the magnetron frequency the tagged section moves in and out of the cw laser beam. As a result the fluorescence level as a function of time after the laser pulse is expected to show dips at twice the magnetron frequency (for the laser beam positions shown in the figure). The frequency of the dips can be used as a measure of the cloud rotation frequency.

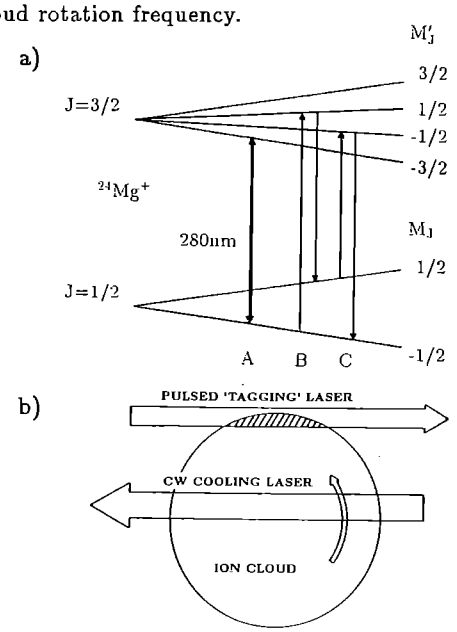

Figure 1. a) Mg^+ level scheme showing Zeeman splitting. b) Experimental method.

The trap and cw laser system used for this work have been described elsewhere[4]. The pulsed laser radiation near 280 nm is generated by frequency doubling the output of a multimode pulsed dye laser. The dye laser has a bandwidth of $\sim$ 20 GHz at 560 nm. It is pumped by the second harmonic of a flashlamp pumped Q-Switched YAG laser. The pulsed laser system typically produced $\sim 100\mu$J pulses of UV light at a repetition rate of 10 Hz. The non-TEM_{00} output of the pulsed laser beam is cleaned up using a spatial filter and an aperture. Even a rather weak source of light is sufficient to saturate the UV transition; in fact the $\sim 75\mu$W of cw power is adequate for this purpose. This places very small demands on the efficiency of the pulsed laser system and as a result we are free to waste a large amount of the pulsed UV light in producing spatially clean pulses. Throughout the experiment UV pulses of ~ 1—10μJ were used. The UV pulses counterpropagate with the cooling laser through the trap.

The laser does not have a sufficiently narrow bandwidth to allow us to tune rigorously to only transition B

in figure 1(a). The pulsed laser can therefore cause transitions A and C as well. Furthermore, even for transition B there is a branching ratio back to the ground state. As a result the laser pulses only put ~30% of the population into the metastable state. This means that the expected modulation of the detected fluorescence (dips) will not be 100%.

A photon count TTL pulse train is generated form a photomultiplier and is fed into a multichannel scaler (MCS). The minimum dwell time (bin length) of the MCS is 2 μs and the maximum pass length (number of bins) is 4096. The pulsed laser produces a timing pulse 200 μs before the firing of the Pockels cell which initiates the pump laser pulse. We use this pulse to trigger the MCS. In this way we get a picture of the fluorescence before and after the arrival of the laser pulse.

RESULTS AND DISCUSSION

The cloud rotation frequency is a function of the applied voltage V_{DC} and is typically $\sim$ 50 kHz. We therefore need to run the MCS with its minimum dwell time ($2\mu s$) to have a reasonable number of bins per rotation period. The minimum dwell time therefore places a practical limit on the applied voltage of $V_{DC} < 10$ V. Our signal level is such that we collect on average about one photon per rotation period. This means that we need to average over a large number of laser shots to produce a meaningful fluorescence trace. In practice we take 1—5×10^3 pulses per trace. It therefore takes 2–10 minutes to record a trace. The need to keep the experimental parameters constant over this timescale imposes stringent stability requirements. Figure 2 shows an MCS trace taken with a 2 μs dwell time. The trace shows no modulation during the period before the arrival of the laser pulse. The large spike corresponds to background scatter from the laser pulse. Immediately after this pulse, dips appear in the trace as expected. A Fourier transform of the MCS trace is also shown in figure 2. It gives three peaks: the largest peak gives the cloud rotation frequency. The higher frequency peaks are harmonics which merely appear in the Fourier transform because the peaks in the MCS trace are non-sinusoidal.

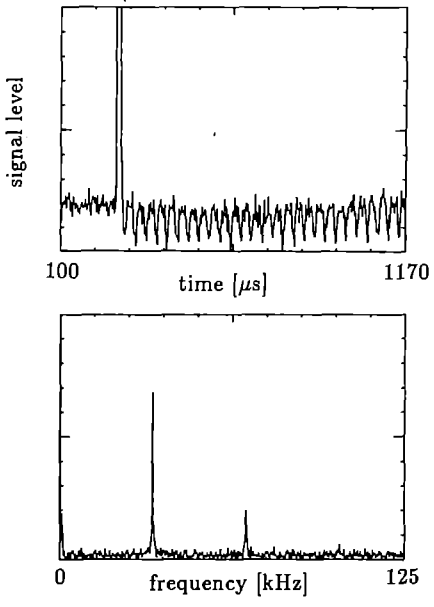

Figure 2. A typical MCS trace and its Fourier transform.

We have used the pulse–probe method to measure the cloud rotation frequency as a function of V_{DC} and results for a particular ion cloud are shown in figure 3. The solid line corresponds to the value for the frequency obtained using equation (1). The fundamental frequency measured for this particular cloud was actually $2\omega_m$. The data has been plotted as ω_m for a clear comparison with the predicted curve. There is clearly good agreement between the calculated values for ω_m and the experimentally derived values over the range tested.

With very cold clouds space charge effects become important. The primary effect of space charge is to shift the oscillation frequencies. We have shown the pulsed laser method to be capable of measuring much greater degrees of space charge shift than the photon correlation method[5].

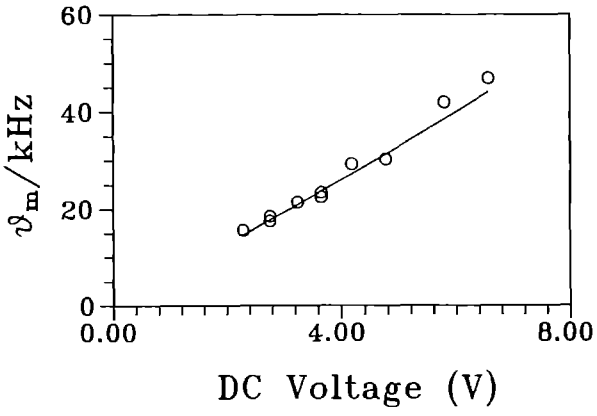

Figure 3. The cloud rotation frequency $\nu_m = \omega_m/2\pi$ versus V_{DC}.

CONCLUSIONS

We have demonstrated a method for obtaining information about the motion of clouds of ions in a Penning trap. The method has allowed us to measure the cloud rotation frequency in a Penning trap over a range of parameters not accessible to the photon correlation method of ref. 4 and is as such complementary to that method. In particular the pulse-probe method works for larger clouds than the photon correlation method. We are currently performing further analysis of the data obtained and we hope to be able to recover information relating to diffusion rates in the ion cloud.

ACKNOWLEDGEMENTS

We thank SERC and the LSF at RAL for the loan of the pulsed laser used in this work. One of us (G.H.) thanks the Swiss National Science Foundation for support and the CVCP for an ORS award. This work was supported by SERC.

REFERENCES

[1] S.L. Gilbert, J.J. Bollinger and D.J. Wineland, Phys. Rev. Lett **60**, 2022 (1988).

[2] eg. D. Dubin and T. O'Neil, Phys. Rev. Lett. **60** 511 (1988).

[3] J.J. Bollinger and D.J. Wineland, "Microplasmas" Scientific American Jan. 1990.

[4] K. Dholakia *et al.*, Phys. Rev. A **47** 441 (1993).

[5] K. Dholakia *et al.* (in preparation).

DISSOCIATIVE IONIZATION OF N_2 AND CO USING INTENSE LASERS AT 248 AND 305 NM

K Codling [1], G M Cross[1], L J Frasinski[1], P A Hatherly[1], A J Langley[2], W Shaikh[2] and M Stankiewicz[1].

[1]J J Thomson Physical Laboratory, University of Reading.

[2]RutherfordAppletonLaboratory.

ABSTRACT

Analysis of conventional ion time-of-flight spectra of N_2 and CO at laser wavelengths of 248 and 305 nm suggests that fragmentation is predominantly charge-asymmetric. In a recent publication we describe the use of covariance mapping to prove that charge-symmetric fragmentation is, in fact, the dominant mechanism at 305 nm. This present contribution shows that the same is true at 248 nm. Moreover, the dissociation energies associated with specific fragmentation channels are the same, within experimental error, for both molecules and at both wavelengths.

INTRODUCTION

The ability to generate laser pulses of short duration has meant that laser E fields can now be produced with strengths that are comparable with the internal fields binding electrons in diatomic molecules. Under the action of such fields, sequential or step-wise removal of the outer valence electrons occurs, followed by a rapid separation of the fragment atomic ions in what is often termed a Coulomb explosion. This terminology tends to be used even though the energies of the fragment ions are rarely explicable in such simple terms, see Codling and Frasinski (1992) and references therein.

An exception is the case where a heavy molecule such as I_2 (vibrational period 155 fs) is multiply ionized by a laser of very short duration (<100 fs). The molecule is effectively 'inertially confined', see Strickland et al (1992). Here, the Coulomb explosion model is appropriate and the experimentally observed maximum dissociation energies of the various fragment ion pairs (charge q_1 and q_2) are given, to a good approximation, by the formula $U(eV) = 14.4\ q_1q_2/r(Å)$, where r is the neutral molecule internuclear separation of 2.66Å. In other words, one can assume a rapid 'vertical' transition to repulsive Coulomb states.

In the case of lighter molecules such as N_2 and CO and longer laser pulses, this simple picture breaks down in that the kinetic energies of the fragment ions are always considerably less than that given by the above formula. For example, Cornaggia et al (1991, 1992) found in certain cases a factor of 2 reduction, independent of fragmentation channel. When Frasinski et al (1987) first studied N_2 at 600 nm using a 0.6 ps laser of focused intensity of 3×10^{13} W/cm^2, they suggested that these low energies might be explained in terms of a simple dynamical model. Once double ionization has occurred, the N^+ ions start to move apart. As the laser E field rises the N^+ ions are further ionized, but since the inter-ion separation is now increased, the kinetic energies are proportionally less; the processes of ionization and dissociation are interspersed, see also Codling et al (1989). This so-called 'non-vertical' model is expected to be particularly poor at low ionization stages, because the potential energy curves are far from Coulomb-like. Nevertheless, Normand et al (1991) studied N_2, CO and O_2 at 610 nm and found that their results could be explained using such an approach.

At 600 nm Frasinski et al (1989b) observed that fragmentation was predominantly charge-symmetric. (One must include in this category those channels where the two fragment ions differ by no more than one unit of elementary charge). Cornaggia et al (1991) found similar behaviour at 615 nm. They also found, quite surprisingly, that the dissociation energies of the various fragment ion pairs is independent of laser pulse rise time, over a range from 0.1 to 2 ps. Cornaggia et al (1992) also showed that the branching ratios for the various channels are the same for N_2, CO and C_2H_2 but different for C_2H_4, indicating the importance of the molecular bond (triple versus double).

At shorter wavelengths the situation was quite different. Normand et al (1991) found that for lasers of approximately equal focused intensities ($\approx 10^{15}$ W/cm^2), the stage of ionization reached at 305 nm is much less than at 610 nm and that the kinetic energies of the fragment ions are considerably reduced. In fact in both N_2 and CO the highest atomic ion stage created was two. But more importantly, they were unable to find correlations between N^+ and N^{2+} in the case of N_2 or between C^{2+} and O^+ (or C^+ and O^{2+}) in the case of CO. They were therefore obliged to explain their results in terms of *asymmetric* fragmentations, $[N_2^{2+}] \rightarrow N + N^{2+}$ and $[CO^{2+}] \rightarrow C^{2+} + O$; $C + O^{2+}$. This was in stark contrast to the situation at 610 nm, where the charge-symmetric process $[N_2^{6+}] \rightarrow N^{3+} + N^{3+}$ was reached.

This contrasting behaviour was explained by Normand et al (1991) in terms of the different states of the molecular double-ion accessed at the two wavelengths. At 610 nm the lifetime of the $[N_2^{2+}]$ ion was assumed to be short relative to the laser pulse rise time and the sequence was therefore able to proceed to high stages of ionization, as suggested earlier. At 305 nm, on the other hand, the lifetime of the $[N_2^{2+}]$ was assumed long, the inter-ion separation did not increase, insufficient energy was now available to reach the $N^+ - N^{2+}$ repulsive curve and the dissociative ionization sequence aborted at this point. The molecular double ion fragmented via charge-symmetric and charge-asymmetric processes, leaving the N^+ and N^{2+} ions with low kinetic energies.

Somewhat earlier, Boyer et al (1989) had studied N_2 at 248 nm using a laser of pulse length 0.6 ps and focused intensity $\approx 10^{16}$ W/cm^2. They noted the similarities between their ion time-of-flight (TOF) spectra and the 'single photon' spectra of Eberhardt et al (1989). They assumed vertical transitions at the neutral

molecule internuclear separation of 1.10Å to purely repulsive Coulomb states. In this simple picture, they could only explain the relatively low energies of the N^{2+} and N^{3+} ions if *asymmetric* fragmentation were invoked. That is, they found the dominant channels to be $[N_2^{2+}] \rightarrow N + N^{2+}$ and $[N_2^{4+}] \rightarrow N^+ + N^{3+}$. The N^{3+} ions with 20 eV kinetic energy had to be associated with N^+ ions rather than N^{2+} or N^{3+} ions, since U $\approx$ 40 eV in this case. Moreover, the symmetric dissociation $[N_2^{4+}] \rightarrow N^{2+} + N^{2+}$ could not be countenanced because U $\approx$ 52 eV and no N^{2+} fragments were observed in their TOF spectra with an appropriate energy.

The experimental facts therefore appeared to indicate that symmetric fragmentation occurs at the higher wavelengths and asymmetric fragmentation at the lower wavelengths. This conclusion is in conflict with the result of a Thomas-Fermi-Dirac field-ionization model. Using this approach Brewczyk and Frasinski (1991) determined the maximum charge a diatomic molecule can retain when exposed to an axial, static electric field, as a function of field strength and internuclear separation. They then considered a simple dynamic situation whereby the molecule is exposed to a laser E field of finite rise time. They tracked the evolution of the system as the E field and ion separation increased up to the point where the ions were so far apart that the inner potential barrier inhibited charge transfer between the two ions (wells). At this point they found that the remaining charge had been shared almost equally between the two ions, through the action of the oscillating laser E field. In other words charge-symmetric fragmentation is favoured.

It should perhaps be emphasised at this juncture that the analysis of conventional, one-dimensional TOF spectra of homonuclear molecules can be at best ambiguous and at worst in error. This is because such spectra cannot differentiate the asymmetric process $[N_2^{2+}] \rightarrow N + N^{2+}$ from the symmetric one $[N_2^{4+}] \rightarrow N^{2+} + N^{2+}$; the technique is insensitive to neutral particles. However, Frasinski et al (1989a) devised a procedure called covariance mapping that allows unequivocal correlation of the various fragment ion pairs with their parent molecular ion precursors. In a recent publication Codling et al (1991) used this technique to study more definitively than had been possible previously, the fragmentation processes in N_2 and CO at 305 nm. Their conclusions were that the fragmentation channels were in fact predominantly charge-symmetric in both molecules.

The question remained as to whether the same is true at 248 nm. Gibson et al (1989) appeared to confirm the importance of the asymmetric channel $[N_2^{2+}] \rightarrow N + N^{2+}$ by observing a new, laser-induced fluorescence channel at a wavelength of 55.8 nm. Nevertheless it seemed worthwhile to apply the covariance technique at 248 nm and attempt to determine the real facts. This paper presents the results of the investigation and discusses their implications.

EXPERIMENTAL PROCEDURE

The basic experimental set-up consisted of a laser and an ultra high vacuum system housing a TOF mass spectrometer. Pulses delivered by a synchronously-pumped dye laser were amplified through a three-stage dye amplifier pumped by a Nd:YAG laser operating at 10 Hz. The laser light was frequency doubled in a KDP* crystal and subsequently mixed with the fundamental in a BBO crystal to produce 248 nm radiation. This was amplified by tandem KrF amplifiers. The 0.1 mJ, 1.2 ps (FWHM) pulses were focused down by an f/4 lens system to produce an intensity of about 10^{15} W/cm^2.

The drift tube of the TOF spectrometer was 25 mm in length, with no restricting apertures, and incorporated microchannel plate ion detectors. The gas was admitted at right angles to both the laser beam and the drift tube axis, see Hatherly et al (1990). Voltages +U and -U applied across the interaction region ensured 100% collection efficiency for both forward and backward ions, regardless of their kinetic energy or charge state. The design of the drift tube was such that the TOF, t, of a particular ion of mass m and charge q is given by the expression

$$t = A(m/qU)^{1/2} + B(mv_{\parallel}/qU).....$$

$$\text{valid for } mv_{\parallel}^2/2 \leq 0.1\ qU$$

Here $mv_{\parallel}$ is the initial momentum component along the drift tube axis and A and B are instrumental constants. This results in the separation of the forward ions ($mv_{\parallel} < 0$) and backward ions ($mv_{\parallel} > 0$) into two peaks. An example can be seen in the TOF spectrum, figure 1, the peaks being labelled N_f^+ and N_b^+.

The covariance mapping technique has been described at length by Frasinski et al (1989a) and will not be discussed here. As mentioned earlier, this statistical approach allows unambiguous correlation of all charged fragments resulting from the multielectron dissociative ionization process. A cursory glance at the above equation shows that the covariance map is, in essence, a momentum correlation map. By comparing the covariance map (which contains only ion-ion correlations) with the concurrently accumulated one-dimensional TOF spectrum (which contains, in addition, those ions from ion-neutral fragmentations), one can learn about ion-neutral fragmentations.

RESULTS AND DISCUSSIONS

Figure 1 shows a covariance map of N_2 obtained at 248 nm. The diagonal, vertical and horizontal stripes are due to ringing following detection of a large scattered light pulse; the microchannel plates are sensitive to radiation of 248 nm wavelength. This scattered light is seen also in the conventional TOF spectrum displayed, for convenience, along the x and y axes. The bottom spectra of figures 1 and 2 show the scattered light in the absence of gas and emphasise the extent of the problem. Nevertheless, by careful adjustment of parameters it was possible to produce covariance maps that were relatively free from unwanted background in those regions where features were expected to occur. Unfortunately the black-and-white versions of the two maps do not bring out the weaker features with such clarity as the false-colour originals.

One can see quite clearly three fragmentation channels, namely $[N_2^{2+}] \rightarrow N^+ + N^+$, $[N_2^{3+}] \rightarrow N^+ + N^{2+}$ and $[N_2^{4+}] \rightarrow N^{2+} + N^{2+}$. It is a simple matter to determine where the two features associated with the asymmetric fragmentation of the $[N_2^{4+}]$ ion (namely $N_b^+ + N_f^{3+}$ and $N_b^{3+} + N_f^+$) should lie. There are no signs of such features. We conclude that the fragmentation of N_2 at 248 nm is predominantly *charge-*

symmetric. The 'peak' (not maximum) dissociation energies of the three channels are shown in Table 1. One notes that the energies associated with each channel rise steadily with ionization stage - the error bars are absolute errors but the relative errors are considerably less. Also shown, for comparison, are the dissociation energies associated with the equivalent channels at 305 nm. An earlier publication by Codling et al (1991) concentrated on the symmetry of fragmentation. Here, one sees that the kinetic energies at 248 nm and 305 nm are the same, within experimental error.

In the previous publications we commented upon the difficulties of analysing one-dimensional TOF spectra and stated that the N^{2+} ions observed earlier by Cornaggia et al (1990) at 305 nm should be associated with the process $[N_2^{3+}] \rightarrow N^+ + N^{2+}$ rather than $[N^{2+}] \rightarrow N + N^{2+}$. It now seems likely that a considerable number of the N^{2+} ions seen in the earlier TOF spectra should be associated with the channel $[N_2^{4+}] \rightarrow N^{2+} + N^{2+}$ as suggested in Table 1. The energy of the $N^+ + N^+$ channel given by Cornaggia et al (5.4 eV) is somewhat higher than observed at 248 nm. However, the N^+ energies at 248 nm range from zero to at least 6 eV.

There appears to be no agreement between the fragmentation energies observed here and the earlier 248 nm data of Boyer et al (1989). Their N^+ kinetic energies peaked at about 4.5 eV (dissociation energy 9 eV), the N^{2+} spectrum showed two peaks at 6.5 and 12.5 eV and there was a broad spectrum of N^{3+} energies centred at about 20 eV. We have no explanation for this disagreement, except to point to the differences in laser rise time (0.6 ps instead of 1.2 ps) and focused intensity (10^{16} W/cm^2 instead of 10^{15} W/cm^2).

Figure 2 shows a covariance map of CO taken at 248 nm. As in N_2, one can see three channels, namely $[CO^{2+}] \rightarrow C^+ + O^+$, $[CO^{3+}] \rightarrow C^{2+} + O^+$ and $[CO^{4+}] \rightarrow C^{2+} + O^{2+}$. The last of these is rather hard to see on this black-and-white figure. Once again, there are no signs of the asymmetric channel $[CO^{4+}] \rightarrow C^{3+} + O^+$. This confirms the predominance of charge-symmetric fragmentation. The energies of the channels obtained at 305 nm shown in Table 1 are very similar to those at 248 nm. The $C^{2+} + O^{2+}$ channel was not observed at 305 nm; this is probably because the intensity used at 305 nm was somewhat less (5×10^{14} W/cm^2). Shown, for completeness, are the energies obtained by Lavancier et al (1991) from their one-dimensional TOF spectra. The C^{2+} ions were initially associated with O atoms ie $[CO^{2+}] \rightarrow C^{2+} + O$, and the O^{2+} ions with C atoms ie $[CO^{2+}] \rightarrow C + O^{2+}$. If two reassignments are made, the agreement between the two sets of 305 nm data is good.

In summary, one sees that the covariance mapping technique has demonstrated that fragmentation in N_2 and CO is predominantly charge-symmetric at wavelengths of 610 nm, 600 nm, 305 nm and 248 nm. (Recent work at 740 nm also shows symmetric fragmentation). We now wish to comment briefly upon a limitation of the technique; it is incapable of determining whether two correlated ions are created almost instantaneously (termed 'nascent' ions by Hill et al (1992)) or whether the initial process is fundamentally asymmetric, for example $N + N^{3+}$, and that the final symmetry is achieved by subsequent ionization of the neutral atom at large internuclear separation ('post-dissociation ionization'). Hill suggests a criterion for the occurrence of the latter process, that the laser pulse length should exceed 500 fs.

Hill et al (1992) have studied the multielectron dissociative ionization of N_2 at 193 nm using pulses of 10-15 ps duration and focused intensities of about 5×10^{14} W/cm^2, a regime that should be dominated by post-dissociation ionization. They explain the low energy N^{2+} and N^{3+} ions in their conventional TOF spectra in terms of asymmetric processes $N + N^{2+}$ and $N + N^{3+}$. Clearly such processes are more accessible, energetically, than the symmetric ones $N^{2+} + N^{2+}$ and $N^{3+} + N^{3+}$. These asymmetric processes are assumed to be precursors to a symmetric outcome. However, if nascent N^{3+} ions are produced, then it is likely that the accompanying neutral atoms will be singly ionized at some point in the focal volume, leading to the charge-asymmetric outcome $N^+ + N^{3+}$. No such channel is observed at 248 or 305 nm. Whether this channel is present at 193 nm will not be known until covariance mapping is employed.

Furthermore, if this post-dissociation ionization occurs at large internuclear separations, the $N + N^{3+}$, $N^+ + N^{3+}$, $N^{2+} + N^{3+}$ and $N^{3+} + N^{3+}$ channels should have roughly the same dissociation energy. Cornaggia et al (1992), using a 1.2 ps laser pulse, found the following sequence at 600 nm: $N^+ + N^+ + 5$ eV; $N^+ + N^{2+} + 12$ eV; $N^{2+} + N^{2+} + 24$ eV; $N^{2+} + N^{3+} + 35$ eV; $N^{3+} + N^{3+} + 51$ eV. This sequence can hardly be explained in terms of post-dissociation ionization. Of course, what constitute large distances becomes a matter of semantics but if 'atomic' ionization does occur at large distances, the photoelectron spectrum should reflect this. One should therefore perform electron-ion covariance mapping experiments to ascertain the real facts, see Frasinski et al (1992).

The validity of the Hill et al approach rests on the reality of asymmetric fragmentation and it was felt that the recent observations by Strickland et al (1992) on I_2 provided the required evidence. Using sub-100 fs laser pulses at a wavelength of 630 nm, Strickland et al claimed to see the $I^+ + I^{3+}$ channel quite strongly. They also observed the $I^{2+} + I^{4+}$ channel. Hatherly et al (1993) have just completed experiments on I_2 at 740 nm using a Ti-sapphire laser with a pulse length of about 150 fs. Their covariance maps showed *no signs* of asymmetric channels but all symmetric channels up to $I^{5+} + I^{5+}$ were observed, with maximum dissociation energies ranging from 5 eV ($I^+ + I^+$) to 95 eV ($I^{5+} + I^{5+}$). It seems unlikely that this disagreement can be explained in terms of the different wavelengths used but there remains the possibility that the different pulse rise times could provide the answer.

The large differences in the TOF spectra of N_2 and CO at the two wavelengths, 600 and 248 nm, is not understood at the present time. The much lower kinetic energies at 248 nm cannot, of course, be explained in terms of a field-ionization, Coulomb explosion model. Although the tunnelling approach may be valid for low frequency, high intensity fields, it is not so appropriate at the higher frequencies; at 248 nm the multiphoton approach should have greater validity. The fact that at 600 nm the kinetic energies of the fragment ions are independent of laser rise times, at least in the range 0.1 to 2 ps, is surprising (Normand et al, 1992). We find a similar behaviour at 248 nm;

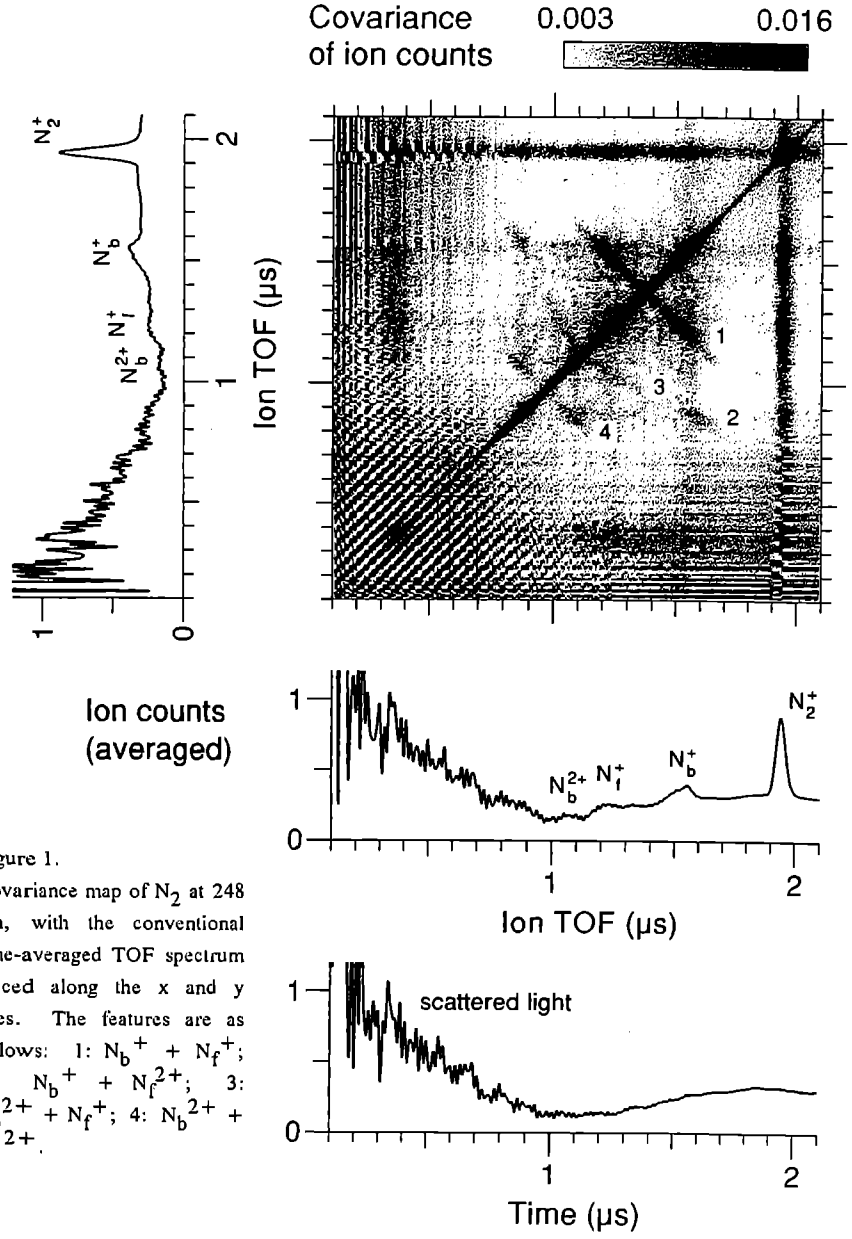

Figure 1.
Covariance map of N_2 at 248 nm, with the conventional time-averaged TOF spectrum placed along the x and y axes. The features are as follows: 1: $N_b^+ + N_f^+$; 2: $N_b^+ + N_f^{2+}$; 3: $N_b^{2+} + N_f^+$; 4: $N_b^{2+} + N_f^{2+}$.

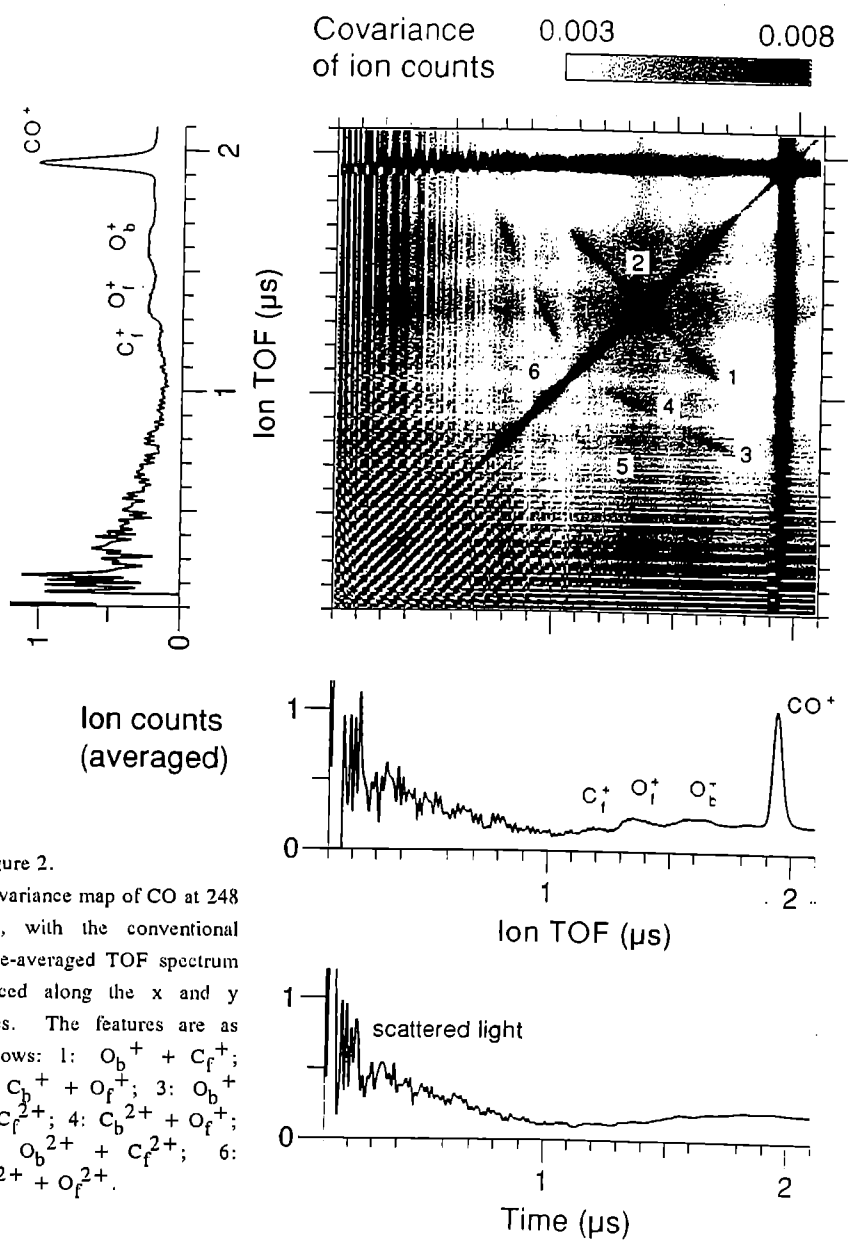

Figure 2.
Covariance map of CO at 248 nm, with the conventional time-averaged TOF spectrum placed along the x and y axes. The features are as follows: 1: $O_b^+ + C_f^+$; 2: $C_b^+ + O_f^+$; 3: $O_b^+ + C_f^{2+}$; 4: $C_b^{2+} + O_f^+$; 5: $O_b^{2+} + C_f^{2+}$; 6: $C_b^{2+} + O_f^{2+}$.

the kinetic energies are independent of pulse rise time in the range 1 to 4 ps. This implies the existence of laser-induced intermediate states that may couple in some way to the Coulomb states, see Normand et al (1991).

Some progress has been made in understanding the low proton kinetic energies observed in H_2 in terms of a bond softening mechanism (Zavriyev et al, 1990). Perhaps such an approach may find application in more complex molecules.

Table 1. 'Peak' dissociation energies of ion pairs in N_2 and CO

	248 nm	305 nm	305 nm[a]
$N^+ + N+$	4.5 (± 1.0) eV	4.2 (± 1.0) eV	5.4 (± 0.7) eV
$N^+ + N^{2+}$	8.0 (± 1.5) eV	8.5 (± 1.5) eV	-
$N^{2+} + N^{2+}$	10.0 (± 2.0) eV	9.5 (± 2.0) eV	10.3 (± 1.2) eV[b]
$C^+ + O^+$	4.5 (± 1.0) eV	4.0 (± 1.0) eV	4.2 (± 0.45) eV
$C^{2+} + O^+$	6.5 (± 1.5) eV	6.5 (± 1.5) eV	6.55 (± 0.70) eV[c]
$C^{2+} + O^{2+}$	9.5 (± 2.0) eV	-	8.75 (± 0.95) eV[d]

[a]Data on N_2 from Cornaggia et al (1990); on CO from Lavancier et al (1991)
[b]Assumed to be $N^{2+} + N$
[c]Assumed to be $C^{2+} + O$
[d]Assumed to be $C + O^{2+}$

ACKNOWLEDGEMENTS

We are pleased to acknowledge the Science and Engineering Council (UK) for their support and the use of the Laser Support Facility of Rutherford Appleton Laboratory.

REFERENCES

Boyer, K., Luk, T.S., Solem, J.C. and Rhodes, C.K. 1989 Phys. Rev. A39 1186.

Brewczyk, M. and Frasinski, L.J. 1991 J. Phys. B: At. Mol. Opt. Phys. **24** L307.

Codling, K., Frasinski, L.J. and Hatherly, P.A. 1989 J. Phys. B: At. Mol. Opt. Phys. **22** L321.

Codling, K., Cornaggia, C., Frasinski, L.J., Hatherly, P.A., Morellec, J. and Normand, D. 1991 J. Phys. B.: At. Mol. Opt. Phys. **24** L593.

Codling, K. and Frasinski, L.J. 1993 J. Phys. B: At. Mol. Opt. Phys. to be published

Cornaggia, C., Lavancier, J., Normand, D., Morellec, J. and Liu H.X. 1990 Phys. Rev. A **42** 5464.

Cornaggia, C., Lavancier, J., Normand, D., Morellec, J., Agostini, P., Chambaret, J.P. and Antonetti, A. 1991 Phys. Rev. A**44** 4499.

Cornaggia, C., Normand, D. and Morellec, J. 1992 J. Phys. B: At. Mol. Opt. Phys. **25** L415.

Eberhardt, W., Plummer, E.W., Lyo, I-W., Carr, R. and Ford, W.K. 1987 Phys. Rev. Lett. **58** 207.

Frasinski, L.J., Codling, K., Hatherly, P.A., Barr, J., Ross, I.N. and Toner, W.T. 1987 Phys. Rev. Lett. **58** 2424.

Frasinski, L.J., Codling, K. and Hatherly, P.A. 1989a Science **246** 1029.

Frasinski, L.J., Codling, K. and Hatherly, P.A. 1989b Phys. Lett. A**142** 499.

Gibson, G., Luk, T.S., McPherson, A., Boyer, K. and Rhodes, C.K. 1989 Phys. Rev. A**40** 2378.

Hatherly, P.A., Frasinski, L.J., Codling, K., Langley, A.J. and Shaikh, W. 1990 J. Phys. B: Atom. Mol. Opt. Phys. **22** L291.

Hatherly, P.A., Cross, G.M. Frasinski, L.J., Stankiewicz, M. and Codling, K. 1993 to be published.

Hill, W.T., Zhu, J., Hatten, D.L., Cui, Y., Goldhar, J. and Yang, S. 1992 Phys. Rev. Lett. **69** 2646.

Lavancier, J., Normand, D., Cornaggia, C., Morellec, J. and Liu, H.X. 1991 Phys. Rev. A43 1461.

Normand, D., Cornaggia, C., Lavancier, J. and Morellec, J. 1991 In "Multiphoton Processes" ed. G. Mainfray and P. Agostini (Saclay: Commissariat a l'Energie Atomique) p.191.

Normand, D., Cornaggia, C and Morellec, J. 1992 In "Coherence Phenomena in Atoms and Molecules in Laser Fields" Ed. A.D. Bandrauk and S.C. Wallace (Plenum: New York) p.133.

Strickland, D.T., Beaudoin, Y., Dietrich, P. and Corkum, P.B. 1992 Phys. Rev. Lett. **68** 2755.

Zavriyev, A., Bucksbaum, P.H., Muller, H.G. and Schumacher, D.W. 1990 Phys. Rev. A**42** 5500.

PHOTOREFRACTIVE PROCESSES AT NEAR INFRARED WAVELENGTHS

Graeme W. Ross, Petr Hribek and Robert W. Eason

Optoelectronics Research Centre and Department of Physics,
University of Southampton, Southampton, SO9 5NH, UK.

I Photorefractive Phase Conjugation

Phase conjugation using photorefractive crystals has found many applications in areas such as optical processing and distortion correction. The simplest and most elegant configuration (self-pumped phase conjugation, SPPC) allows phase conjugation without the need for additional optics - a single laser beam incident upon a cut, polished crystal induces a refractive index grating which in turn diffracts light to generate the precise phase conjugate of the incident beam. Observation of the effect has been carried out mainly in the visible part of the spectrum where crystal response has tended to be most efficient. However, with the availability of diode lasers operating at near infrared wavelengths, recent attention has been drawn to the possibility of extending the crystal response to allow observation of SPPC and other photorefractive processes at diode compatible wavelengths. Efficient SPPC has already been observed with reflectivities as high as 72% at 800nm, using a nominally undoped crystal of photorefractive $BaTiO_3$, and there has been a concerted effort to extend and enhance the response in the near infrared region via the addition of different dopants.

Experiments to assess phase conjugation at near infrared wavelengths were carried out on a crystal supplied by Sandoz Huningue S.A., France, and a comparison was made with a nominally undoped sample of $BaTiO_3$[1].

The Sandoz $BaTiO_3$ crystal used was grown by the top-seeded solution growth technique from 99.999% purity starting materials, annealed and electrically poled. An unknown accidental impurity produced an enhanced absorption in the red and near infrared with an absorption peak at about 640nm that gave the crystal a blue colour. The absorption spectrum measurement (Fig. 1) for this crystal was performed with a Perkin-Elmer Lambda 9 spectrometer using randomly polarized light perpendicular to the c-axis.

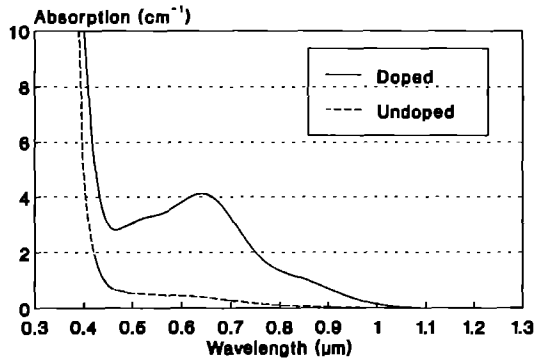

Fig 1 Absorption spectra of doped and undoped $BaTiO_3$ using randomly polarised light

With the crystal mounted in air on a combined rotation-translation stage, a systematic study was undertaken to assess the phase conjugate reflectivity with respect to wavelength, horizontal beam position on the entrance face, external angle of incidence and input power. A Ti:sapphire laser pumped using a 5W argon laser, and calibrated using an Anritsu optical spectrum analyser, was used to provide a tunable source of infrared radiation.

Phase conjugation was optimised by rotating the crystal to Brewster's angle (~ 67°, as in Ref. 1) to both minimise the Fresnel reflection and also maximise access to the largest electro-optic coefficient. Fig. 2 compares the wavelength response of the doped and undoped samples.

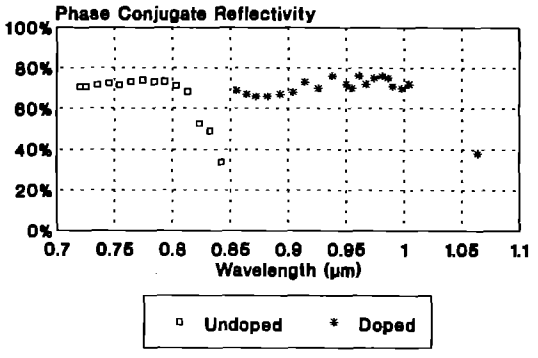

Fig 2 Phase conjugate reflectivity against wavelength

The response time of the process in the blue crystal was measured over the range 7mW to 70mW at 800nm, where we define response time as the time taken for the phase conjugate signal to rise from 10% to 90% of its saturated value. Typical response times at intensities of ~1Wcm^{-2} were ~100s. After each measurement the crystal was uniformly illuminated for 2 minutes using a 75W white light source to ensure that all gratings were erased. Data suggested that the response time is proportional to I_{in}^{-x} where x = 0.75 - a sublinear relationship indicating, perhaps, the presence of shallow traps in the photorefractive mechanism.[2]

The unexpectedly high infrared reflectivity of the blue crystal (given the high absorption) raises questions regarding the photorefractive mechanism responsible. If we assume that the beam is totally internally back reflected from the crystal faces to form transmission refractive index gratings, the crystal absorption and the round-trip path length, in fact, imply a maximum reflectivity of up to a factor of four less than that observed. This inconsistency implies that, in the absence of significant light induced transparency, reflection gratings near the entrance face of the crystal may perhaps be responsible for the high reflectivities by a backward scattering mechanism[3].

During the course of the experiments, it also was found that instabilities in the phase conjugate reflectivity could be removed by vibrating the crystal slightly. Further investigations are currently under way, as are investigations into the instability suppression, and the species responsible for the enhanced infrared response.

Summary I :

- Phase conjugation (possibly due to stimulated backscattering) at near infrared wavelengths
- Reflectivities of up to 76% at 1μm and 38% at 1.064μm
- Laser diode compatibility
- Vibration stabilisation

II Incoherent Beam Coupling

Beam coupling using the class of mutually pumped phase conjugators in photorefractive materials has recently become a subject of great interest as a method of forming a holographic link between two mutually incoherent, even independent, laser sources. The beam coupling interaction within the photorefractive crystal may be explained by the sharing of fanning gratings, with automatic Bragg matching allowing a self-reinforcing, self-aligning interconnect to form between the two sources. In this way, phase conjugates of both beams are generated simultaneously : diffracted light from source 1 forms the phase conjugate of beam 2 (hence the source of photons for the phase conjugate of beam 2 is beam 1, and vice versa) permitting the exchange of spatial information without cross-talk. Several geometries exist for incoherent beam coupling, however, an interesting feature of the Double Phase Conjugate Mirror (DPCM) geometry[4] (Fig. 3) is the possibility of gain as previously demonstrated at 488nm by Fischer et al.[3] In this section, we examine gain using the DPCM at near infrared wavelengths, and utilise the wavelength tolerance of the DPCM geometry (the Double Colour Pumped Oscillator - DCPO[5]) to aid coupling between two separate lasers.

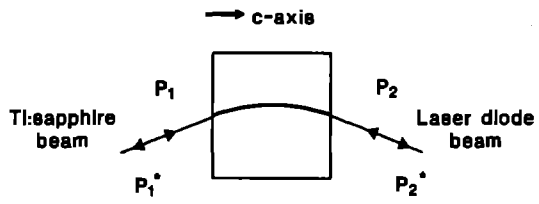

Fig 3 Incoherent beam coupling

The crystal used in our experiment was a 6mm cube of nominally undoped $BaTiO_3$ which has been shown previously to exhibit favourable response[1] at near infrared wavelengths. The lower absorption compared to that of the doped sample (Fig. 1) consequently means that the undoped crystal has a higher transmission which is advantageous here : a high transmission means efficient coupling of the two sources.

In our experiment[6], a laser diode and a Ti:sapphire laser were used to provide the mutually incoherent beams. The laser diode was a SHARP LTO17 AlGaAs device operating single longitudinal mode at around 808nm. The laser diode beam (~5.8mW) was incident on the +c face of the photorefractive crystal (Fig. 3) and light from the Ti:sapphire laser (tuned to approximately the same nominal wavelength as the laser diode) was incident on the -c face of the crystal. A variable neutral density filter placed in the path of the Ti:sapphire beam allowed the incident power ratio of Ti:sapphire to laser diode at the crystal ($r = P_1 / P_2$) to be adjusted. Fig. 4 shows the effective laser diode reflectivity ($R = P_2^* / P_2$) of the crystal for different incident power ratios (r). It can be seen from Fig. 4 that $R > 1$ for the range $\sim 3 < r < \sim 80$, and the curve exhibits the characteristic shape predicted theoretically and observed experimentally by Fischer et al.[3] in their DPCM experiments. The maximum reflectivity of ≥ 6, which to our knowledge is the highest reported to date at near infrared wavelengths, occurs with an incident power ratio of $r \sim 23$.

The wavelength of the DCPO configuration was then examined by measuring the transmission ($T = P_2^* / P_1$) as a function of Ti:sapphire wavelength. The results demonstrate that transmission is greatest (~0.3) for a range of wavelengths spanning ~15nm around the nominal diode wavelength. This maximum transmission would intuitively occur when both sources are of the same wavelength (allowing precise Bragg matching) and implies that perhaps the wavelengths of the two sources are matched over this region.

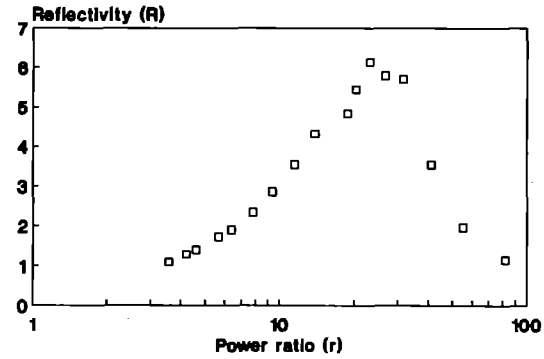

Fig 4 Graph of phase conjugate reflectivity against incident power ratio

This would in turn imply that light channelled from the Ti:sapphire laser into the laser diode facet by the DCPO influences the lasing characteristics of the laser diode by forcing it to lase at the Ti:sapphire wavelength. In order to confirm this, and also to assess the effects of feedback into the diode, an Anritsu optical spectrum analyser was used to monitor the laser diode wavelength as a function of Ti:sapphire wavelength. In the range 800nm to 814nm, it was found that when the injected Ti:sapphire wavelength corresponded to a longitudinal mode of the laser diode, the diode lased single mode at the injected Ti:sapphire wavelength, and the diode mode spacing was confirmed to be 0.33nm. Fig. 5 shows the diode wavelength for a selection of such injected Ti:sapphire wavelengths.

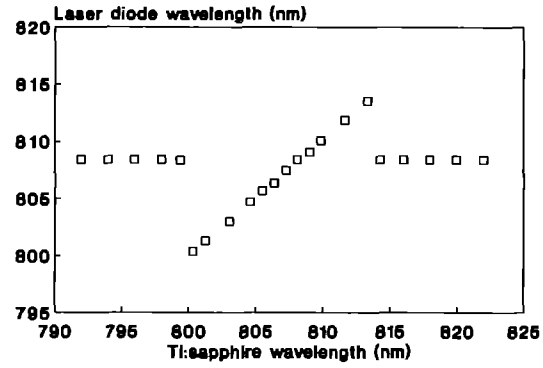

Fig 5 Laser diode wavelength against Ti:sapphire wavelength

At wavelengths outside the range 800nm to 814nm, the laser diode was unaffected by the Ti:sapphire. The region in which the laser diode wavelength follows closely that of the Ti:sapphire, corresponds to the region of maximum ~0.3 transmission. It would seem that the main factor influencing the width of this region is the laser diode gain bandwidth : outside this region, the laser diode cannot support the lasing wavelength imposed by the Ti:sapphire and instead relaxes to its nominal wavelength, at which point the fraction of Ti:sapphire signal injected into the diode facet is reduced by the angular offset due to the DCPO Bragg selection.

Summary II :

- Phase conjugation with gain : reflectivity of 600%
- Infrared operation (laser diode compatibility)
- No coherence requirement
- Wavelength tolerance
- Laser diode tuning

III Phase conjugate fibre laser

Phase conjugate optics have also been used as external mirrors providing feedback for systems such as dye and Argon ion lasers[7] by photorefractive four-wave mixing. Once initiated, the phase conjugate process may become self-sustaining by the lasing action. In this section we report feedback into a multimode optical fibre amplifier to demonstrate lasing[8]. Work was initially motivated by the idea of forming a double-pass amplifier using phase conjugate feedback. Correction of polarisation and modal scrambling in passive multimode fibre has already been demonstrated using phase conjugation[9]. It was found in our earlier work, however, that the expected gain observed in the fluorozirconate fibre used was too low for efficient brightness enhancement due to signal saturation. However, during the course of the investigation, it was found that it was possible to form a laser cavity with the fibre as the amplifying medium and a passive phase conjugate mirror acting as one of the reflectors.

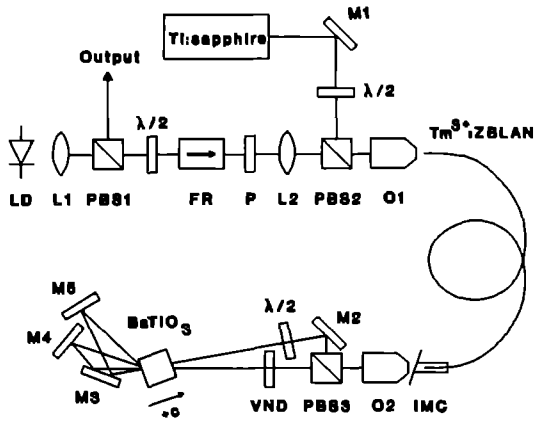

Fig 6 Experimental arrangement. LD laser diode; L's lenses; PBS's polarising beam splitters; FR Faraday rotator; P polariser; O's microscope objectives; IMC index-matching cell; VND variable neutral density filter; M's mirrors

Our experimental arrangement is shown in Fig. 6. The injected signal was provided by a SHARP LT017 single stripe AlGaAs laser diode operating single longitudinal mode at ~808nm at room temperature and isolated using a Faraday rotator and polariser. The amplifying medium was a 6m length of fluorozirconate fibre of the standard ZBLAN composition doped with 500ppm by weight of Tm^{3+} ions. It has been demonstrated by Carter et. al.[10], that efficient laser action and high small-signal amplification between 805nm and 830nm can be achieved by pumping this system at 785nm, with a possible single pass gain at 806nm of ~20dB for a 6m length of fibre. This amplification range ensured the compatibility of the AlGaAs laser diode, the ZBLAN fibre and the $BaTiO_3$ crystal. The pump wavelength was also chosen because of its compatibility with AlGaAs semiconductor diode lasers, although for our initial experiment the pump power was provided by a Ti:sapphire laser. Phase conjugation was achieved using the undoped 6mm cube of photorefractive $BaTiO_3$ in a ring configuration - an arrangement useful for phase conjugating small signals. Reflectivities of up to 22% (uncorrected for Fresnel reflection) have been measured with this particular crystal in the ring configuration using e-polarised light at 808nm.

Initially, with no grating present in the crystal and with only pump light incident on the fibre, no lasing was observed as the fluorescent output from the fibre was insufficient for grating formation due to its large spectral bandwidth. With the laser diode signal injected, however, the ring conjugator was established after a few seconds and lasing in the fibre was observed. The lasing wavelength was determined using an Anritsu optical spectrum analyser and found to match that of the laser diode to within the 0.1nm resolution of the analyser.

When the laser diode signal was then blocked, the photorefractive grating persisted and the fibre continued to lase. Blocking the phase conjugate feedback ring prevented lasing and confirmed that the photorefractive grating was indeed providing the feedback mechanism into the fibre. The 4% Fresnel reflection at the un-matched end of the fibre completed the laser resonator. Lasing occurred only when the incident pump light was greater than ~600mW. The lasing wavelength (808.1nm) was closely matched to that of the laser diode, but appeared to be at a wavelength corresponding to a mode adjacent to the fundamental operating wavelength of the diode (807.7nm) within the resolution limits of the spectrum analyser. The wavelength tended to be unstable, however, as lasing was also observed at wavelengths corresponding to the fundamental diode wavelength and at shorter wavelengths. The timescale of these changes (a few seconds) would suggest a grating competition process within the photorefractive crystal and implies perhaps that gratings are written by the diode not only by the fundamental diode wavelength, but also by the adjacent modes amplified on a single pass through the fibre.

A simple analysis using the Kogelnik model[11] - regarding the bandwidth of a single sinusoidal transmission grating of period 1.6μm and length 6mm - indicates a FWHM diffraction bandwidth of ~2nm centred on the Bragg-matched wavelength. This would confirm that one single grating would be capable of providing feedback of fluorescent emission from the fibre over this range of wavelengths. Reasons as to why laser operation does not remain at the fundamental diode wavelength (which would be expected to yield the strongest grating which would be reinforced in turn by the lasing action) have not, as yet, been determined. Methods of achieving stable single frequency operation are under further investigation as are experiments on tunability by crystal rotation and externally-applied electric field.

Summary III :

- Self-sustaining phase conjugate feedback into a fluorozirconate fibre amplifier allowing laser action in the near infrared

REFERENCES

1. G.W.Ross and R.W.Eason, Opt. Lett. **17**, 1104 (1992)
2. D.Mahgerefteh and J.Feinberg, Phys. Rev. Lett. **64**, 2195 (1990)
3. R.A.Mullen, D.J.Vickers, L.West and D.M.Pepper, J. Opt. Soc. Am. B **9**, 1726 (1992)
4. S.Sternklar, S.Weiss, M.Segev and B.Fischer, Opt. Lett. **11**, 528 (1986)
5. B.Fischer, S.Sernklar and S.Weiss, IEEE J. Quantum Electron. **25**, 550 (1989)
6. G.W.Ross and R.W.Eason, Opt. Lett. **18**, 15 Apr (1993)
7. M.Cronin-Golomb, B.Fischer, J.Nilsen, J.O.White and A.Yariv, Appl. Phys. Lett. **41** 219 (1982)
8. G.W.Ross, J.N.Carter, S.W.James, R.W.Eason, R.Kashyap, S.Davey and D.Szebesta, Opt. Lett. **17**, 1676 (1992)
9. I.McMichael, P.Yeh and P.Beckwith, Opt. Lett. **12**, 507 (1987)
10. J.N.Carter, R.G.Smart, A.C.Tropper, D.C.Hanna, S.F.Carter and D.Szebesta, IEEE J. Lightwave Technol. **9** 1548 (1991)
11. H.Kogelnik, Bell Syst. Tech. J. **48**, 2909 (1969)

PARTICLE IMAGE VELOCIMETRY (PIV) TO PRODUCE VELOCITY MAPS IN HYDRAULIC SYSTEMS

C. Greated[1] and I.Shepherd[2]

[1] Physics Department, The University of Edinburgh
[2] Hydraulics Research, Wallingford.

INTRODUCTION

This project is concerned with the development of a fibre-optic delivery system for Particle Image Velocimetry (PIV). It involves the use of PIV in situations without specially designed flumes and facilities. Flows to be investigated include the pick up of sand from river beds and the flow around sea-wall armour blocks, in collaboration with Hydraulics Research, Wallingford.

EXPERIMENTAL WORK

The prototype PIV system was tested at Hydraulics Research, Wallingford. The aim of this work was to assess the problems involved in using the apparatus in an environment unsuitable for optics requiring frequent, sensitive adjustments. The hazards encountered at Wallingford include concrete dust, high humidity, working in unenclosed areas, vibration from other equipment and restricted optical access to the wave flume. The safety of the other workers in the building is the highest priority.

EXPERIMENTAL APPARATUS

The overall experimental layout is shown in Fig. 1. The 5W cw laser (used at 2W max) was situated in an office near to the flume. A fibre optic link was made to the scanning beam optics adjacent to the measuring area. The PIV box contains an octagonal rotating mirror (used at rotation speeds of 30 to 85 rps) to scan the beam through 90 degrees, and a parabolic mirror to collimate the pseudo light sheet to a width of 500 mm. A front silvered mirror (treated by baking at high temperature to withstand water damage), 600 mm x 30 mm, was fixed to the flume base 1000 mm from the glass wall at 45 degrees to the horizontal to bring the light sheet parallel to the glass. The camera used was a Nikon F801 with flat focus micronikkor lens and Tmax 400 black and white film. This was mounted at 500 mm from the flume window with its base horizontal. The wavemaker was set to produce random waves with some breaking occurring in the measuring area, approximately 0.5 m from the start of a sloping pebble beach.

Three films were taken using a range of camera settings and varying scanning speeds.

Two fibres were tested for the link:
50 μm - the small size of the core requires the incident laser beam to be highly focused, giving the possibility of thermal breakdown at the fibre ends. Light launched into cladding modes causes loss of intensity. The small core and low numerical aperture (N.A.) give a narrow beam at the output.

600 μm - the large core size enables easy light launching with very low losses. The material of the fibre (doped silica) is designed for low attenuation at argon wavelengths. The large core and relatively large (N.A.) give a wider beam at the output.

The 600 μm fibre was used in the prototype system to give greater safety until the system was finalised.

RESULTS

Analysis of the PIV photographs produced shows that Young's fringes are visible in some areas. However the overall illumination is too low due to a combination of factors;

* the laser was not able to work at its full power

* the glass wall of the flume was badly scratched.

* the beam diameter in the light sheet was too large.

OPTIMISING THE ILLUMINATION

To increase illumination for PIV measurements a small diameter beam is required for the scanning light sheet, so a small core, low N.A. fibre should be chosen for the link from the laser to the PIV box. Improved fibre preparing techniques have shown that a 50 μm fibre may be used to carry the required laser power. This is the smallest available multimode fibre; the next smallest fibre, at = 10 μm, being incapable of transmitting high power beams without thermal breakdown occurring.

Current work includes a more thorough investigation of the properties of the fibre to evaluate light losses and reduce them where possible.

Some light is lost by launching into cladding modes from where it escapes through the fibre jacket instead of propagating along the core. These cladding modes can be removed by stripping a length of the fibre jacket and immersing the bare fibre in an index-matched fluid. Attenuation then occurring in a straight length of fibre is due to absorption in the fibre material, usually by impurities. Light is also lost by bending the fibre so that total internal reflection no longer occurs for all rays in the core. The minimum bending radius for no light loss is determined by removing cladding modes and then measuring output power with a variable radius loop introduced into an other wise straight fibre.

The accuracy of the focusing of the light onto the fibre end is checked by replacing the fibre end with a 50 μm pinhole. If the full laser power is still detected it can be assumed that the beam is focused to less than 50 μm and can be adjusted to be completely incident on the fibre core. The distance from the objective lens of the micropositioner to the fibre endface, and the incident beamwidth must be measured to ensure that the N.A. of the fibre is not exceeded.

To avoid the possibility of thermal breakdown occurring the focus must be outside the fibre so that light is spreading out into the fibre rather than coming to a focus inside the core.

FUTURE WORK

The theory shows that a small diameter beam is not possible over the required collimation distances (≈2 m) with the current experimental arrangement. This means that only small areas or low speed flows may be measured as the illumination is increased for a longer scanning time and a smaller light sheet width.

The system will be used in its current form to investigate the flow around model sea-wall armour blocks. In this application the beam length, and hence the beam diameter, can be reduced as the measuring area is close to the flume base and the blocks are 50 mm cubic structures (approximately 1/40 scale models).

To look at larger areas or faster flows the apparatus needs to be altered to reduce the illumination difficulties.

The proposed system consists of an underwater PIV box, to be placed inside the flume. The parabolic mirror will be removed and the octagonal rotating mirror replaced by a 24-sided rotating mirror. The light sheet will now be fan shaped, scanning through an angle of 30 degrees. The illumination in the sheet can be kept nearly constant by using a wide beam at the PIV box focusing to the top of the measuring area. The shape and size of the PIV box must be such as to create minimal disturbance in the flow under investigation.

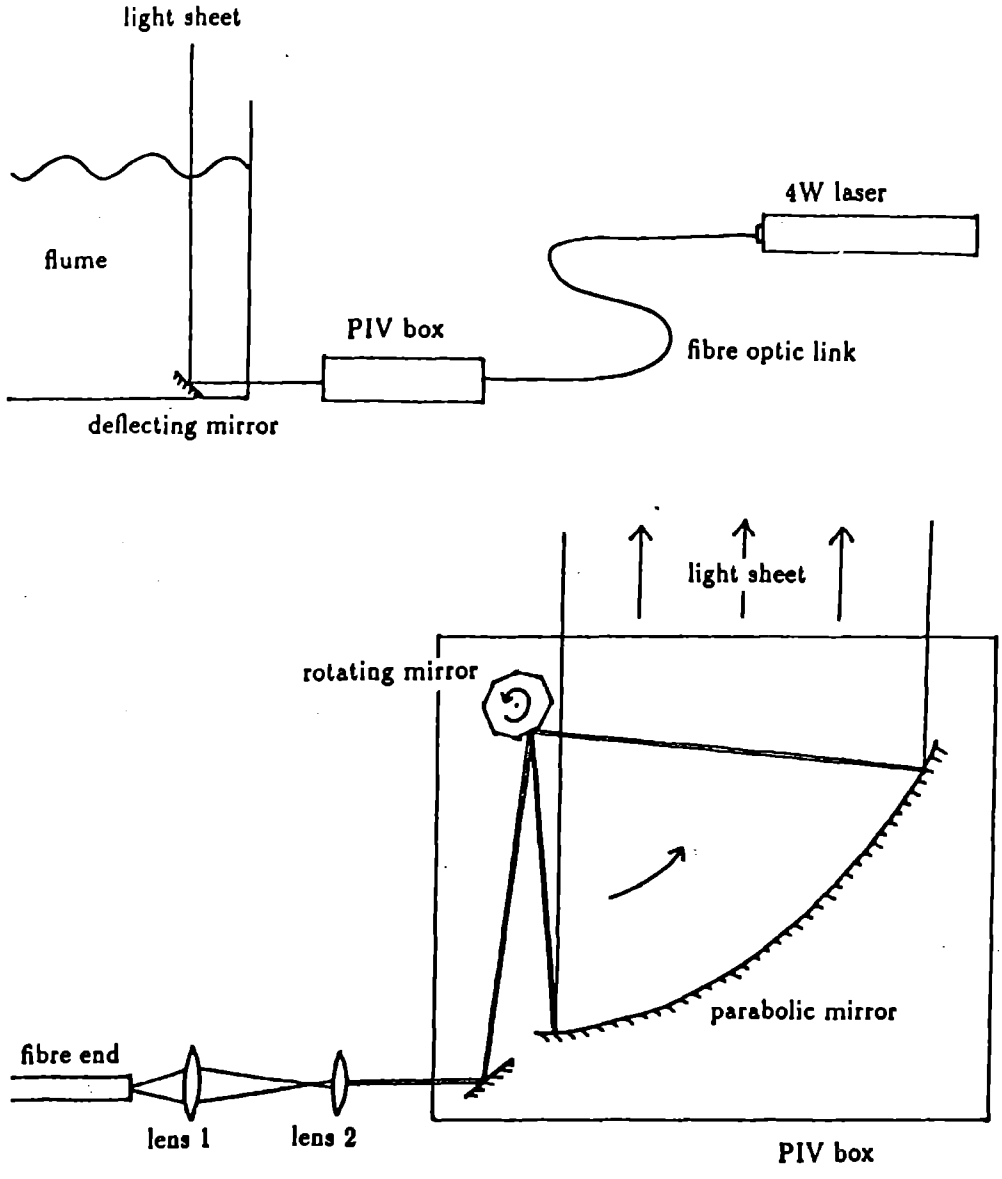

figure 1: Experimental apparatus

X-RAY HOLOGRAPHIC IMAGING AT 3.37 nm

I C E Turcu[1], I N Ross[1], G J Tallents[2], J Krishnan[2], L Dwivedi[2], A Hening[3]

[1] Rutherford Appleton Laboratory
[2] Dept of Physics, University of Essex, Colchester CO4 3SQ
[3] Institute of Atomic Physics, PO Box MG-21, Bucharest, Romania

In last year's Annual Report and in Ref 1 we have reported first measurements on lateral coherence length of 3.37 nm X-rays (in the "water window" spectral region) obtained from the high repetition rate, high average power KrF laser-plasma X-ray source. A lateral coherence length of ~ 20 μm was measured at a distance of 31.7 cm from the plasma source.

In the present paper we report an experiment using these coherent X-rays to record a simple "in line" Gabor hologram with an exposure time of 2 min at 10 Hz laser repetition rate (equivalent to 1.2 s at maximum laser repetition rate of 100 Hz). The hologram was reconstructed in a He Ne laser beam.

Figure 1 shows a schematic of the laser-plasma X-ray source and the beam line for coherent X-rays, containing: X-ray window, specimen holder, holographic plate and atmospheric pressure gas mixture of helium:nitrogen (9:1) to monochromatise the emission from the mylar ($C_{10}H_8O_4$) tape target[(1)] on the 3.37 nm C VI spectral line. The object consisted of two carbon fibres of 1 μm and 10 μm diameter respectively shown in Figure 2a, mounted in the proximity of the X-ray windows (X-ray aperture). The distance between X-ray source and object is 27 cm and between object and holographic plate 2 cm. These distances satisfy, in the case of the 1 μm fibre, the conditions for reducing interference between the virtual and real image in a Gabor hologram.

The recorded hologram is shown in Figure 2b, with clearly visible fringes, and the microdensitometer trace is shown in Figure 3. The fringes produced by the 1 μm fibre have been compared with a calculation based on the Rayleigh-Sommerfield theory[(2)] and good agreement was obtained.

An attempt was made to reconstruct the hologram by inserting the original Agfa plate in a He Ne laser beam as shown in Figure 4. When focusing the microscope objective on to the plate we can see clearly the fringes of the 1 μm fibre hologram, Figure 5b. By moving the objective axially (~ 100 μm) we brought in focus the hologram plane which results in the reconstructed image, Figure 5a.

In conclusion we have demonstrated experimentally the use of the High Average Power Laser Plasma X-ray Source for holographic microscopy in the "water window" spectral region with the potential of exposure times as short as 1 second. This compares favourably with holographic exposure times obtained with synchrotron sources[(3)]. A more detailed description of the experiments can be found in Reference 4.

REFERENCES

1. H Daido, I C E Turcu, I N Ross, J G Watson, M Steyer, R Kaur, M S Schulz and M Amit, Appl Phys Lett 60, 1155 (1992).

2. G B Parrent and B J Thompson, Opt Acta 11, 183 (1964).

3. C Jacobsen, S Lindaas and M Howells, X-ray Microscopy III, Springer 244 (1992).

4. I C E Turcu, I N Ross, M S Schulz, H Daido, G J Tallents, J Krishnan, L Dwivedi, A Hening, J App Phys, In print for 15 Jun 1993.

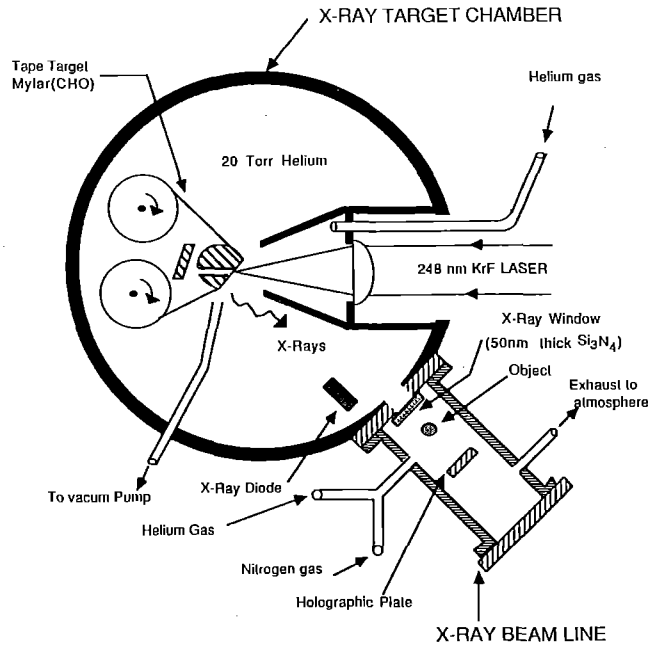

Figure 1 Beamline for coherent 3.37 nm X-rays on the High Aerage P:ower KrF Laser-Plasma Source

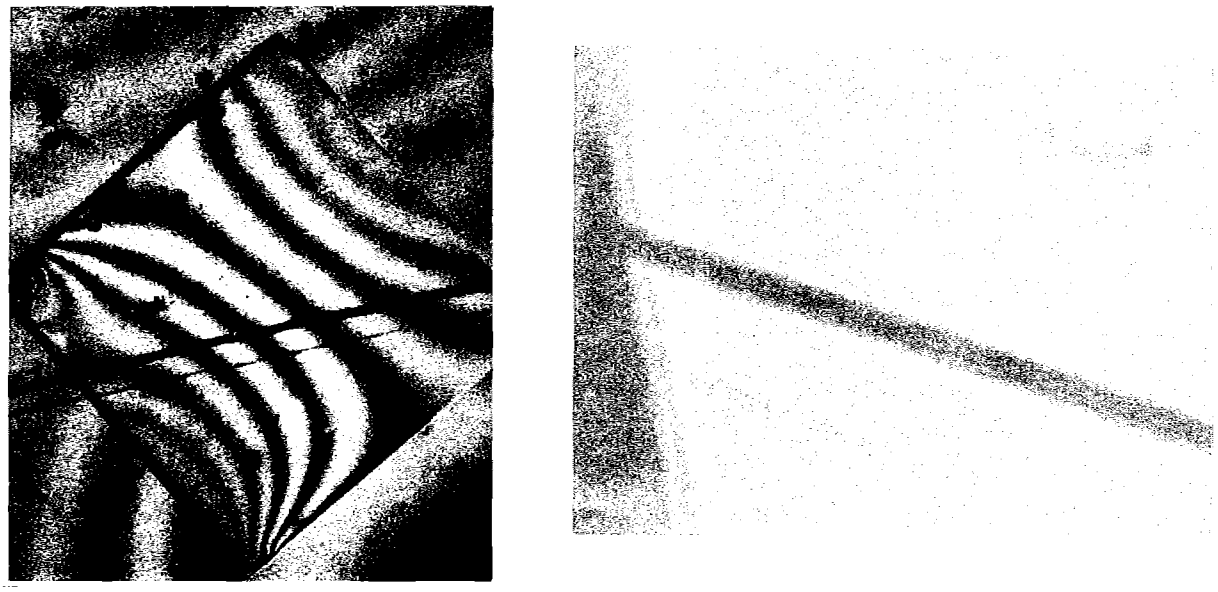

Figure 2 Recording of X-ray Hologram at 3.37 nm.
(a) X-ray Window on which carbon fibre is mounted.
The silicon-nitride window has dimensions of 0.5 mm*0.5 mm*50 nm and is coated with 100 nm aluminium UV filter.
(b) Magnified X-ray Hologram of Carbon Fibre.
Hologram is recorded on Agfa 10E56 holographic plate. The plate to object distance is 20 mm. The beamline is at atmospheric pressure with a flow of helium and nitrogen gas mixture (9:1).

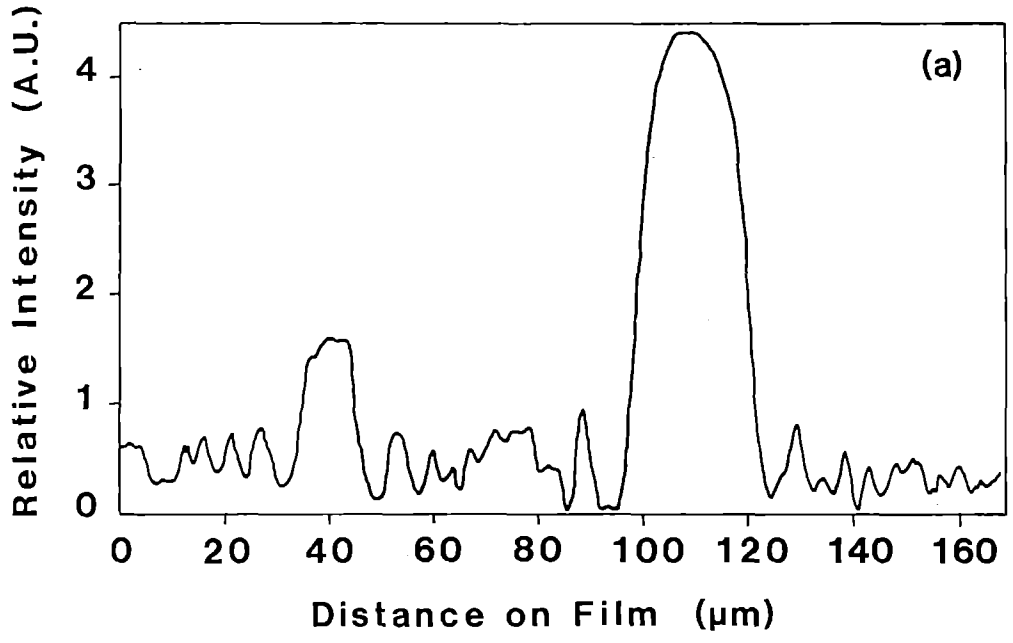

Figure 3 Densitometer trace corresponding to 2(b).

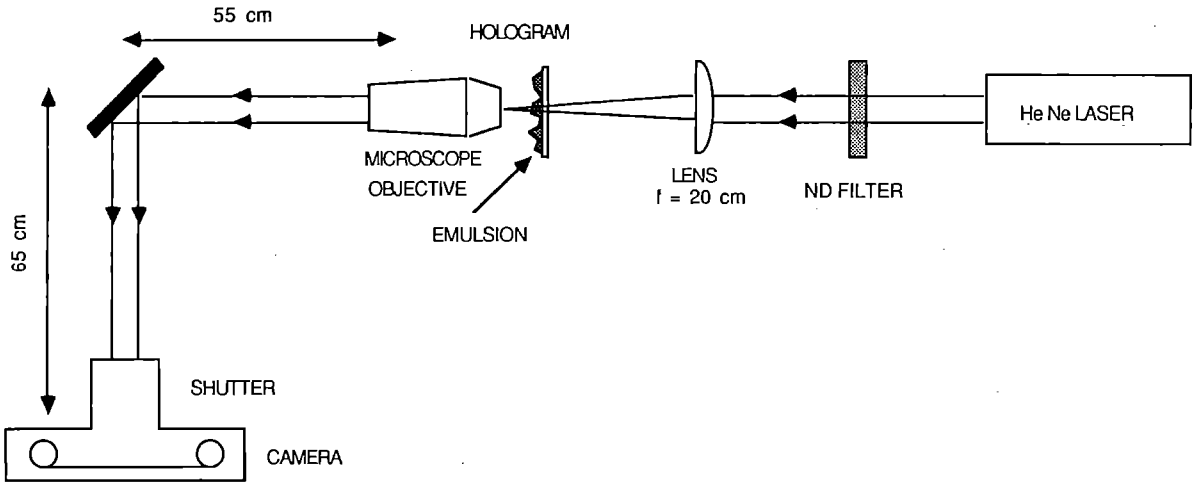

Figure 4 Experimental Arrangement for the reconstruction of X-ray Holograms using a He Ne Laser .

Figure 5 Reconstruction of X-ray Hologram with He-Ne laser.
The reconstruction is performed with a microscope objective of magnification: X45/0.65. The objective is brought to best focus on:
(a) the hologram, showing clear edges on the fibres;
(b) the substrate (plate), showing fringes around the fibre edges.

CALIBRATION OF AN EXCIMER LASER-PLASMA SOURCE FOR X-RAY LITHOGRAPHY

I C E Turcu[1], J R Maldonado[2], I N Ross[1], H Shields[3], P Trenda[4], P Fluck[5] and H Goodson[1]

[1]Rutherford Appleton Laboratory
[2]IBM FSC Manassas Va, Rt 52, Zip 399, Hopewell Jct, NY, USA
[3]Jamar Technology Co, 3956 Sorrento Valley Blid, San Diego, CA92121, USA
[4]Institute of Physics, Czech Academy of Sciences, Prague, The Czech Republic
[5]King's College, Strand, London WC2R 2LS

INTRODUCTION

Soft X-rays of 1 nm wavelength are a strong contender for the production of 256 MBit and 1GBit DRAMs. Compact synchrotrons, generating tens of watts of X-ray power per beam, into ten beams or more, will constitute the main source for large production of microchips. Nevertheless, such machines require a relatively large initial investment and occupy extensive factory space. Therefore smaller, laboratory size, X-ray sources will be needed to generate the power of only one synchrotron beam to be used either by large companies for R&D work, or by small companies which cannot afford a synchrotron and have a limited production.

The High Power Excimer Laser-Plasma X-ray Source at Rutherford Appleton Laboratory has been successfully used for X-ray lithography at 1 nm wavelength (Ref 1). The source was upgraded to run on 7 picosecond KrF pulse-trains and the X-ray average power was increased from 40 mW to 200 mW. Because this is only an order of magnitude below the X-ray average power required for reasonable wafer throughput, an extensive calibration experiment was carried out in collaboration between Rutherford Appleton Laboratory, IBM and Jamar. The following measurements were performed:-

(a) absolute X-ray emission measurements from Copper and Iron targets: (1) using calibrated, filtered PIN X-ray diodes,
(2) calibrated photochromic film.
(b) spectral an spatial measurements on the X-ray source using a crystal spectrometer and a pinhole camera respectively.
(c) lithographic exposures on IBM proprietary mask and resist (Fig 1)
(d) comparisons, showing very good agreement between the different measuring techniques used (see Table 1).

TABLE 1

	Be (12.5 um) Flux (mJ/cm2)	Sl (3.8 um) Flux (mJ/cm2)	Be/Sl Flux (mJ/cm2)	Be/Sl/Resist Flux (mJ/cm2)	% Efficiency Cosine Dist	Effective Wavelength Angstrom
IBM	43.8	48.	23.4	18.6	2.2	9.3
RUTHERFORD'S	52.4	55.4	24.7		2.9	10.0

Effective Wavelength on Resist
Laser Power 4W, 40 Hz (40 W KrF laser)
8 minute exposure at 11.5 cm

Following our other experimental results:-

(1) hv~1.2keV (1 nm wavelength) X-rays were generated from Cu tape targets. The efficiency of converting KrF laser energy (trains of picosecond pulse) into Cu L-shell X-rays was on average 2.9% into 2 pi steradians.

(2) 115 mW (37 mW/sr) was the average X-ray power generated when the laser system was run at 40 Hz. The maximum X-ray power measured was 153 mW (49 mW/sr). All the exposures were performed at 40 Hz, although 80 Hz operation was demonstrated.

(3) The exposures were performed in the target chamber in ambient helium gas at atmospheric pressure.

(4) No damage (due to target debris) was seen on the 2 micron silicon membranes exposed directly at 100 mm from the source, ie, no protective beryllium foil between X-ray source and membrane.

(5) Lithographic exposures were carried out with the mask placed at 135 mm from the X-ray source, behind a 12.5 micron beryllium foil. The X-ray power density delivered at the surface of the Be foil was 0.18 mW/cm^2.

(6) Pinhole camera pictures of the X-ray source size show the typical dimensions to be 10 micron.

(7) X-ray spectra of the source, taken through beryllium and silicon filters confirmed previous published data; the spectral lines extend from 0.8 nm to 1.3 nm centred around 1 nm.

In conclusion good agreement ±20% was obtained between measurements performed by RAL and IBM, also confirming the High Average Power Excimer Laser-Plasma X-ray source as a front runner source for lithography among the alternatives to synchrotron sources.

REFERENCES

1. I C E Turcu, I N Ross, A Hening, J G Watson and P Herman
Present RAL report.

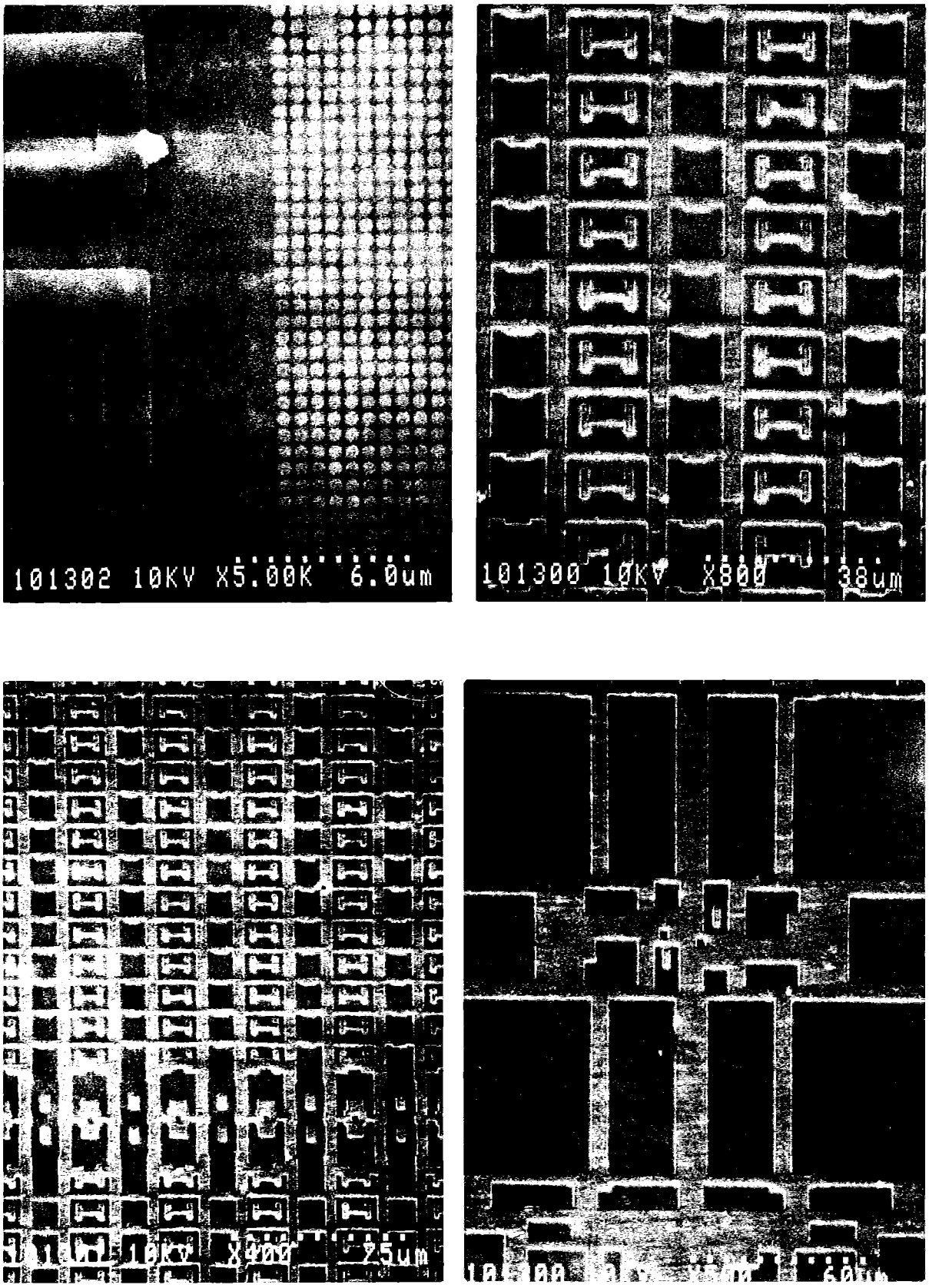

Figure 1 SEM images of the replica of an IBM proprietary mask obtained by X-ray lithography in photoresist, using RAL high average power KrF laser-plasma source.

X-RAY LITHOGRAPHY AT 1 nm WITH 200 ps KrF LASER-PLASMA SOURCE

I C E Turcu[1], I N Ross[1], A Hening[2], J G Watson[1] and P Herman[1]

[1]Rutherford Appleton Laboratory
[2]Institute of Atomic Physics, PO Box Mg-21, Bucharest, Romania

INTRODUCTION

In last year's Annual Report[1] we have presented a novel 200 ps KrF excimer pulse-train bus system for X-ray generation with improved conversion efficiency for 1 nm Cu L-shell/emission. We have used this laser system for X-ray lithographic printing of microstructures, with exposure times of only 5 min which represents up to an order of magnitude improvement on previous exposure times with X-rays generated by 20 ns excimer laser pulses. Other improvements result from:

(a) 1 nm X-ray wavelength have increased transmission through X-ray masks, as well as being the preferred wavelength for X-ray lithography with synchrotron sources.

(b) the 200 ps generate much less target debris in comparison to 20 ns pulses, allowing thinner filter to be used to protect the X-ray mask (or in this experiment no filter at all).

A simple lithographic exposure cell was placed at 10 cm from the plasma X-ray source (Fig 1), along the target normal. The mask to wafer gap was 25 micron. A trial mask was written in house, using a focussed gallium ion-beam microfabrication machine, in 300 nm of gold on a 400 nm silicon-nitride substrate coated with 100 nm aluminium uv filter on the opposite side (Fig 2). The substrates were manufactured by Dr P Anastase in King's College, London. The photoresist, Hoechst ZA114, 700 nm thick was developed after X-ray exposure, 7 min in AZ400K developer (1:4).

The X-ray exposure was carried out at a laser repetition rate of 40 Hz, and an average X-ray power of 0.12 mW/sq.cm was delivered at the mask (0.1 mW/sq.cm at photoresist) for 5 minutes. Figure 4 shows an SEM image of the photoresist in which the mask features (0.7 micron lines and 1.2 micron spaces) are replicated with high resolution. In particular the defect a the end of the slot cut by the ion-beam in the mask (Figure 3) appears to be reproduced as a feature ~100 nm wide, 500 nm long and 700 nm tall.

In conclusion a novel excimer-dye picosecond laser system was designed and implemented for generating a laser plasma X-ray source for lithography. 1 nm X-rays of 40 mW average power were obtained. X-ray lithography was performed with high resolution and exposure times of 5 min. A further order of magnitude improvement in X-ray conversion efficiency measured with 4 ps pulses (Ref 2) and a 2.5 times increase in repetition rate (100 Hz) could reduce the exposure time to 12 seconds.

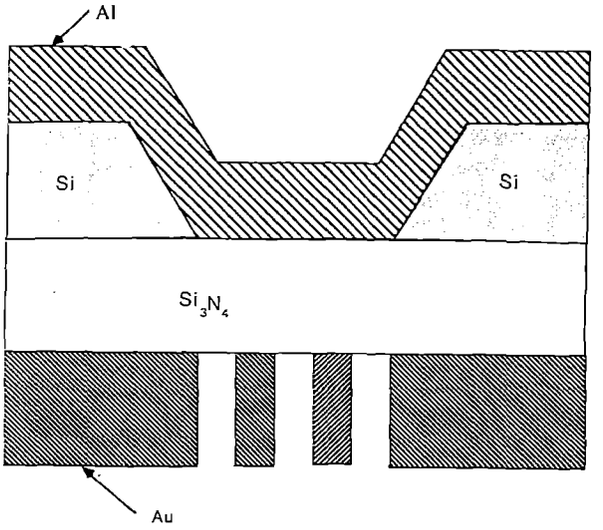

Figure 2 X-ray mask consisting of:
400 nm Si_3 My substrate,
300 nm of Au as X-ray absorber,
and 100 nm Al as uv filter.

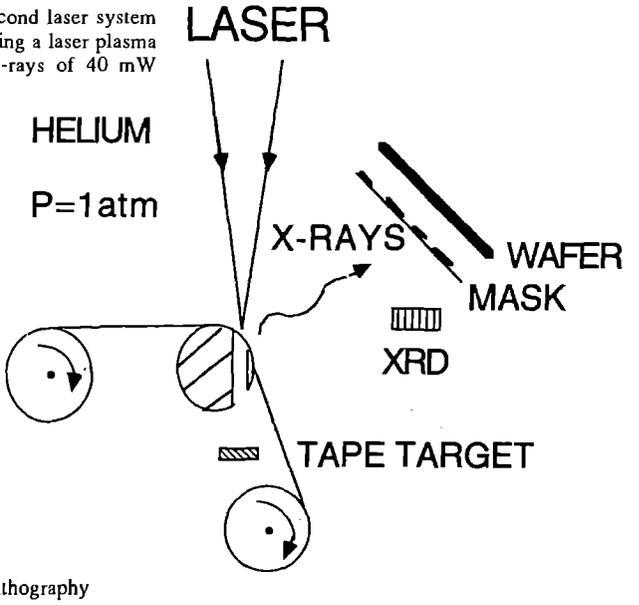

Figure 1. Schematic of proximity X-ray lithography

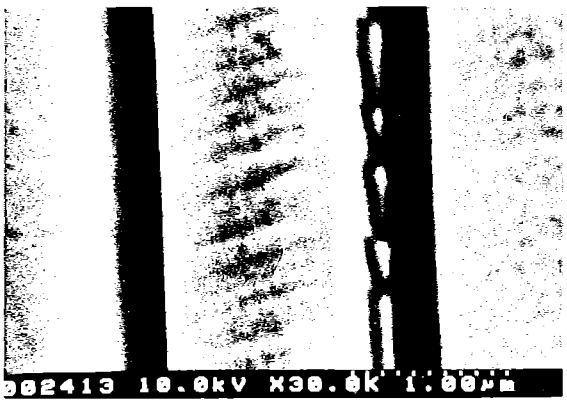

(a)

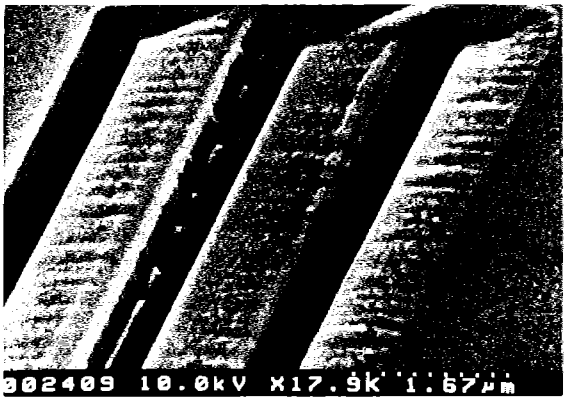

(b)

Figure 3. SEM images of X-ray mask showing 1.2 micron lines and 0.7 micron spaces as well as imperfections. (a) along the walls of the gold lines (b) at the end of the gold lines.

Figure 4 SEM images of the replica of the mask obtained by X-ray lithography in photoresist. Note good reproduction of mask imperfections over the features of ~100 nm.

REFERENCES

1. I C E Turcu, I N Ross, M Steyer, M Amit, B Soom, K Osvay, A Hening, R Kaur and S Quayum
Rutherford Appleton Laboratory Report RAL-92-020, 229, (1992).

2. I C E Turcu, I N Ross and G J Tallents
Rutherford Appleton Laboratory Report RAL-92-020, 223, (1992).

FURTHER INVESTIGATION OF LASER-GENERATED PLASMAS AS SOURCES FOR X-RAY MICROSCOPY

Alan Michette,[1], Edmond Turcu,[2], Paul Fluck[1] and Ian Ross[2]

[1]King's College London
[2]Rutherford Appleton Laboratory

INTRODUCTION

The use of laser generated plasmas (LGPs) as an alternative x-ray source for scanning transmission x-ray microscopy (STXM) has been documented previously and preliminary experiments have produced images.[1] The spatial resolution was approximately five times worse than in images taken using the same microscope at the SRS at Daresbury. This was primarily due to a low signal to noise ratio caused by electrical noise in the detector because of insufficient shielding.

PICOSECOND PULSE TRAINS

Previous microscopy work has been carried out using 22 ns, 248 nm pulses, for which the x-ray pulse lasts approximately 4 ns, the remainder of the 22 ns pulse being reflected. Using picosecond pulses eliminates this problem because of the short time scales involved. By decreasing the pulse length, the irradiance and, hence, the conversion efficiency may also be increased. In addition there is very little debris compared to that associated with the plasma produced with the 22 ns pulse. To further increase the x-ray output, a train of picosecond pulses within the 22 ns envelope may be used.

To produce the picosecond pulse train a mode-locked YAG laser, producing 500 ps pulses, was frequency doubled via a BBO crystal to $\lambda = 532$ nm. The beam was used to pump a DODCI dye laser, producing $5 - 15$ ps pulses at $\lambda = 746$ nm. The resultant beam was amplified in three further dye cells pumped by a Q-switched frequency-doubled YAG laser and frequency-tripled to $\lambda = 248$ nm.

A pulse stacker consisting of 50% beam splitters was used to create two beams, each with 4 pulses separated by 2 ns intervals. The two UV beams, of diameter 7 mm and separation 20 mm, entered a preamplifying laser and then were made to meet in a second amplifier via a telescope arrangement of lenses and mirrors. The amplifying lasers were commercial Questek 2440 excimer lasers operated with a krypton fluoride fill. The amplified beams contained 4 pulses each with each pulse having energy $8 - 10$ mJ. The pulses were superimposed on the amplified spontaneous emission from the amplifiers. The timing of the amplifiers was adjusted to ensure that all of the pulse train was amplified. The ASE for this experiment was measured to be 40-50%, but further tuning of the system could feasibly reduce this value to $\approx$10%.

The beams were focused by an $f = 7$ cm fused silica lens which was 80% transmitting at the laser wavelength. Two spots of diameter approximately 10 μm were formed, with separation 20 μm, such that the irradiance on target was $\approx 7 \times 10^{15}$ W cm^{-2}.

SPECTRA

The target used was mylar; standard audio tape with the reverse side exposed. The tape was pulled between two reels over a spindle with a hole to allow propagation of debris particles. The chamber was evacuated and allowed to 20 torr helium pressure; the helium entered the chamber at 5 l min^{-1} via a hose adjacent to the lens and was pumped out along with target debris. The helium retarded large debris particles whilst being 98% transparent to soft x-rays.

To give a quasi-monochromatic spectrum 10 torr of nitrogen was used in the chamber. This removed all lines and continua due to the carbon and oxygen in the mylar at wavelengths shorter than the nitrogen K edge and differentially attenuated all lines at longer wavelengths, leaving the L_α line at 3.37 nm dominant. A calibrated PIN diode was used to measure the x-ray flux.

To investigate the effect of nitrogen filtering, transmission grating spectra were taken with and without nitrogen. A metallised transmission grating, made at King's College, was used. The grating consisted of gold lines on a 100 nm carbon substrate with 200 nm of aluminium evaporated onto the reverse side to act as a filter for visible and ultraviolet radiation. The grating area was $50 \times 40 \mu$m and the line spacing was 126 nm, giving approximately 7900 lines mm^{-1}. The grating was 0.7% efficient in the first order at 3.37 nm.

The spectra confirmed that the use of 10 torr nitrogen eliminated radiation for $\lambda < 3.06$ nm, whilst the L_α line was attenuated to approximately 50% of its strength in an atmosphere of only helium. The He$_\alpha$ at 4.02 nm is attenuated more than the L_α line and is barely visible in the filtered spectrum.

COMPARISON OF NANOSECOND AND PICOSECOND PULSES

The L_β, L_γ and He$_\beta$ lines, which from previous work[2] would be expected, are absent. A possible, and plausible, explanation of this is the combined effects of continuum lowering[3] and line merging,[4] brought about by the hot, dense nature of the plasma. Similar work carried out using a Raman amplified KrF laser[5] with 12 ps pulses and an aluminium target shows the same effect. The spectra are beneficial to microscopy applications since the He$_\beta$ line at 3.5 nm is absent. Due to its proximity to the L_α line this line is extremely difficult to remove by filtering and its absence enhances the monochromaticity of the source.

Thus quasi-monochromatic output is obtained which is suitable for use with a zone plate microscope.

The x-ray conversion efficiency into the L_α line was measured to be 1.5% sr^{-1} and 5.4$\pm$0.2% in total, to be compared to 0.2% sr^{-1} for single 22 ns pulses. The reason behind this is straightforward. Using nanosecond pulses, a large 'plume' of plasma is produced, through which the laser beam has to propagate. The critical density is established very quickly,

sured to be 1.5% sr^{-1} and 5.4±0.2% in total, to be compared to 0.2% sr^{-1} for single 22 ns pulses. The reason behind this is straightforward. Using nanosecond pulses, a large 'plume' of plasma is produced, through which the laser beam has to propagate. The critical density is established very quickly, a large fraction of the incident laser radiation is reflected, and x-rays produced within the plasma are absorbed. Using picosecond pulses, a large fraction of the incident laser radiation is absorbed, whilst the plasma expands very little due to the very short time scales involved.

REFERENCES

1 A G Michette, I C E Turcu, M S Schulz, M T Browne, G R Morrison, P Fluck, C J Buckley and G F Foster *Rev. Sci. Instr.* **64** (to be published in June 1993).

2 I C E Turcu, M C Gower, C J Reason, P Huntington, M Schulz, A G Michette, F Bijkerk, E Louis, G J Tallents, Y Al-Hadithi, D Batani *Proc. SPIE* **1503** 391 (1991).

3 J Stewart and K Pyatt *Astrophys. J.* **144** 1203 (1966).

4 D R Inglis and E Teller *Astrophys. J.* **90** 439 (1939).

5 D Riley, L A Gizzi, F Y Khattak, A J Mackinnon, S M Viana and O Willi *Phys. Rev. Lett.* **69**, 3739 (1992).

MUONIUM 1S - 2S EXPERIMENT

P E G Baird[1], J R M Barr[2], D Berkeland[3], M G Boshier[3], B Braun[4], G H Eaton[5], A I Ferguson[6], H Geerds[4], V W Hughes[3], K Jungmann[4], F Maas[4], P Matousek[5], B Matthias[4], M Persaud[6], G zu Putlitz[4], I Reinhard[4], P G H Sandars[1], W Schwarz[4], W T Toner[5], M Towrie[5], L Willmann[4], K A Woodle[7], G Woodman[1], L Zhang[4]

[1]Department of Physics, University of Oxford, Oxford
[2]Department of Physics, University of Southampton, Southampton
[3]Physics Department, Yale University, New Haven, CT
[4]Physikalisches Institut, Universität Heidelberg, Heidelberg
[5]Rutherford Appleton Laboratory
[6]Department of Physics and Applied Physics, University of Strathclyde, Glasgow
[7]Brookhaven National Laboratory, Upton, NY

INTRODUCTION

The purely leptonic muonium atom (μ^+e^-) consists of two "pointlike" particles[1]. The system is free from the limitations due to the finite nuclear size which are imposed on the theoretical description of natural atomic hydrogen isotopes and all exotic hydrogen-like systems which have hadronic constituents. Experiments measuring the hyperfine structure splitting in the ground state and the 1S-2S energy interval of atomic hydrogen have reached and accuracy which is beyond or close to the precision of the theory. The calculations are limited by the knowledge of the charge distribution within the proton and the dynamics of the charge constituents of the proton. In the muonium the theory of the ground state hyperfine structure is more than an order of magnitude more accurate and agrees at the 36 ppb level with the latest experiment.

MUONIUM 1S-2S EXPERIMENT

Presently the best opportunity worldwide for an optical excitation of the 1S-2S transition in muonium by Doppler-free optical two-photon laser spectroscopy in muonium is offered at the pulsed muon channel of the ISIS facility at the Rutherford Appleton Laboratory.

The RAL experiment which aims for a precise determination of the frequency separation between the $1^2S_{1/2}$,F = 1 and the $2^2S_{1/2}$,F = 1 energy levels, took two weeks of beam time in summer 1991. The muonium measurements were preceded by three month of setup for the laser system and systematic tests of the experiment using 1S-2S two-photon signals from atomic hydrogen and deuterium.

The concept of the experiment uses a pulsed intensive laser light at λ = 244 nm for the excitation of the weak transition. The pulsed light is generated by pulsed amplification of a cw laser beam at λ = 488 nm in an excimer laser pumped dye laser amplifier. The frequency of the cw laser is known to 0.5 MHz. The d_4 line of molecular $^{130}Te_2$ serves as a frequency reference. It has been calibrated by the NPL in London.

The blue light is frequency doubled in a BBO crystal. The 2S state is photo-ionized by a third photon from the same laser field with high probability. The positive muon (μ^+) released by the photoinization is accelerated to 2 keV, transported through an energy and momentum selective path and focused onto a microchannel plate detector. Counts are accepted in a well defined 100 ns narrow time-of-flight window.

RESULTS

• Muonium $1^2S_{1/2}$ - $2^2S_{1/2}$ centroid transition frequency:
$\Delta\nu_{m,exp}$ = 2 455 529 000.8(32.8)(32.4) MHz
$\Delta\nu_{m,theor}$ = 2 455 528 934.3(3.6) MHz

For the experimental value the first error is statistical, the second one is due to systematic effects. The theoretical uncertainty arises from the knowledge of the muonium mass. There is agreement between theory and experiment within two standard deviations.

•Lamb shift contribution to Muonium 1S-2S:
$\Delta\nu_{LS,exp}$ = 6 990.5(32.8)(32.4) MHz
$\Delta\nu_{LS,theor}$ = 7 056.2 MHz

•Hydrogen-Muonium isotope shift:
$\Delta\nu_{HM,exp}$ = 10 532 415.5(33)(34) MHz
$\Delta\nu_{HM,theor}$ = 10 532 478.8(3.6) MHz

•Deuterium-Muonium isotope shift:
$\Delta\nu_{DM,exp}$ = 11 203 448.4(37)(34) MHz
$\Delta\nu_{DM,theor}$ = 11 203 473.1(3.6) MHz

•Muon Mass extracted from the isotope shift measurements:
m_μ = 105.658 95(29)(31) MeV/c

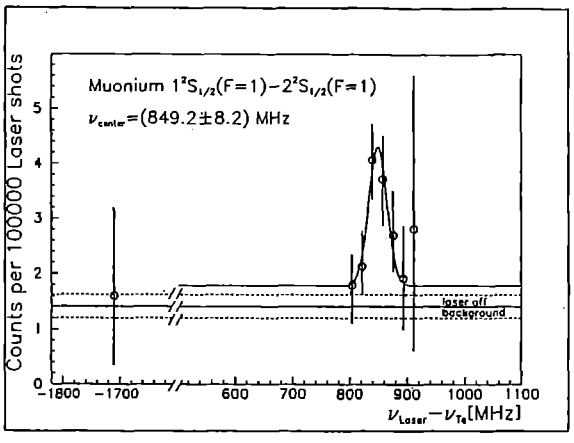

Fig 1 The 1S-2S transition signal in muonium is displayed normalized to 10^5 laser shots. The error bars denote a 68.3 % confidence level of the raw data poisson distribution normalised to 10^5 laser shots. The straight lines give the background level during laser off normalized to 10^5 laser shots together with error limits corresponding to a confidence level of 68.3 %.

REFERENCE

1. V.W.Hughes, in: "The Future of Muon Physics", K.Jungmann, G. zu Putlitz, and V.W.Hughes (eds.), Springer, Heidelberg (1992).

PICOSECOND TIME-RESOLVED RESONANCE RAMAN SPECTROSCOPY APPARATUS

R E Hester[1], A.J.Langley[2], P Matousek[2], J N Moore[1], A W Parker[2], D Phillips[3], A P Tilley[2], W T Toner[2], M Towrie[2], I C E Turcu[2] and S Umapathy[1]

[1]Department of Chemistry, University of York
[2]Rutherford Appleton Laboratory
[3]Department of Chemistry, Imperial College

INTRODUCTION

This report describes the picosecond time-resolved resonance Raman spectroscopy apparatus developed recently[1,2,3,4,5].

APPARATUS DESCRIPTION

The layout of the apparatus is shown in Fig. 1. A 5-20 nJ, 6 ps linearly polarised seed pulse generated from a cavity-dumped dye laser (Spectra Physics 3500) synchronously pumped by a frequency-doubled Spectron mode-locked Nd:YAG laser (82 MHz, 0.6 W) is amplified by injection into a 6-stage butterfly configuration dye amplifier which is synchronously pumped by a copper vapour laser (Oxford Lasers Cu40) operating at 4.46 kHz with an average power of about 30 W (511 nm and 578 nm) and pulse width of 40-50 ns. A Bethune cell[6], as illustrated in Fig. 1, is used in the amplifier.

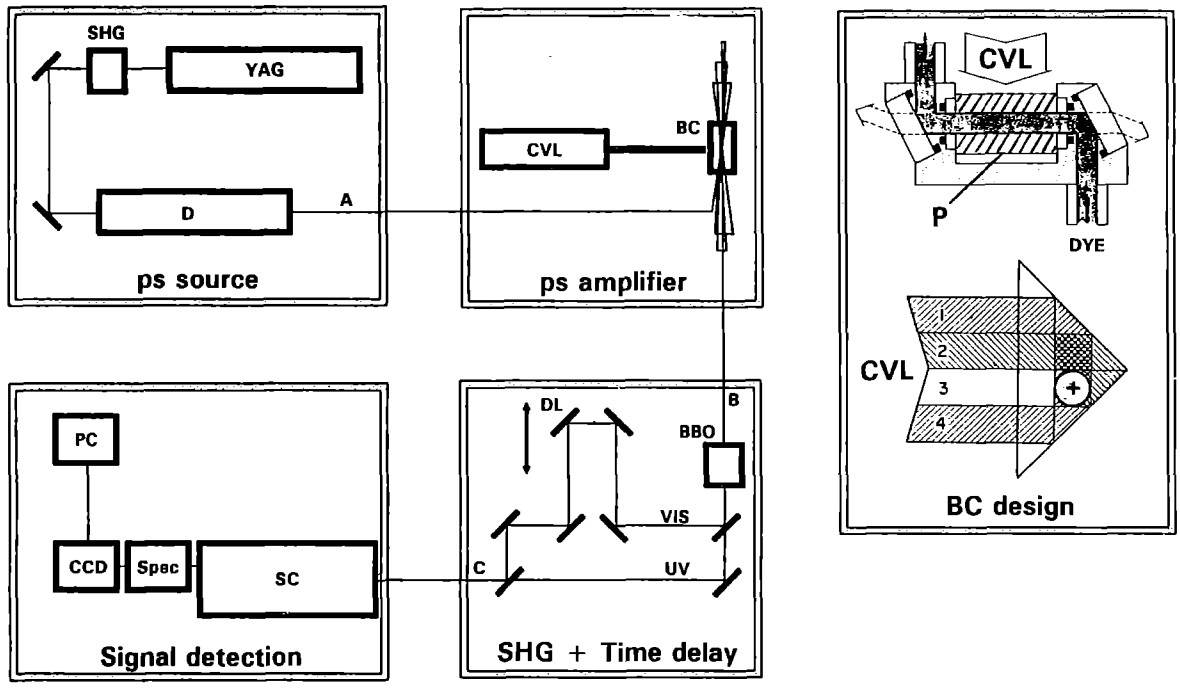

Fig 1 The layout of the picosecond TR[3] apparatus
Key: YAG, mode-locked Nd:YAG laser; SHG, second harmonic generator; D, cavity dumped dye laser; CVL, copper vapour laser; BC, Bethune cell; P, prism with offset dye channel; BBO, β-barium borate crystal; DL, delay line; SC, sample compartment; Spec, spectrometer; A - 610 nm, 4.46 kHz, 20 nJ, 6 ps; B - 610 nm, 4.46 kHz, 55 μJ, 6 ps; C - 610 nm and 305 nm, 10 and 2.5 μJ, respectively.

In total six dye mixtures are used in the amplifier and three in the dye laser to give wavelength coverage from 550 nm to 655 nm. The fundamental output of the dye amplifier has an energy exceeding 4 μJ per pulse over the whole tunable range with a peak of 55 μJ per pulse at 610 nm. The values stated were obtained using fresh dyes. Typical long term operational values (> 5 hours) are about 50 % lower. The amplified pulse is frequency-doubled using a β-barium borate (BBO) crystal (type I) with conversion efficiency of 10-12 %.

A feedback arrangement consisting of a large area photodiode monitoring the dye amplifier output coupled to a motor-driven spiral iris which partially blocks the copper vapour laser beam is used to stabilise pump and probe power. If the iris is set to block some 10 % of the beam initially, the amplifier output power can be held stable to within ± 2 % over a 3 hour run.

The UV and visible beams are separated using dichroic mirrors. A grating can be used in the probe beam path to suppress amplified spontaneous emission from the dye amplifier. Usually the UV beam is used to initiate (pump) photochemical reactions and the resonance Raman spectrum of the transient species is obtained from the delayed, visible (probe) pulse. The time delay between the pump and probe pulses can be varied up to 1000 ps using an optical delay line fitted with a calibrated time-per-distance encoder.

During data collection a filter blocks the residual probe beam from entering the pump beam path. The zero-delay time position of the

delay line is set by removing this filter and using the pattern of interference between probe light propagating via the probe path and residual probe light propagating via the pump beam path. The interference is easily detectable using a photodiode. Differential time delay between pump and probe introduced after this point is estimated to be < 2 ps.

The transmission efficiencies from the amplifier/BBO crystal into the sample region are 25 % for the probe beam and 50 % for the pump beam. Both pump and probe beams are focused into the sample from below using a 5 cm (or 2.5 cm) focal length fused silica lens. A CCD camera (Heimann KH 92) with a microscope objective is used to monitor the spatial overlap of the pump and probe beams within the sample. Transient Raman spectra of *trans*-stilbene, obtained after initial alignment by this means, are usually good but can be improved by up to 50 % if the pump and probe overlap is further optimised while monitoring the observed TR^3 signal. Clearly resolved transient signals from the excited singlet (S_1) state of *trans*-stilbene are obtained with short (1 - 2 s) accumulation times.

The sample solution is flowed horizontally either through an open jet or a fused quartz cuvette. Raman scattered light is collected at 90° and imaged onto the spectrometer slit through a filter. The polarization of the probe beam is fixed in the horizontal plane along the axis defined by the flowing sample solution (oriented at 90° to the spectrometer entrance slit). A polarization rotator (two Fresnel rhombs in series) can be placed in the path of the pump beam in order that any desired relative polarization of the pump and probe beams can be achieved whilst maintaining the correct polarization of the probe beam with respect to the spectrometer slit. Typically, this relative polarization angle is set at the "magic angle", 54.7 °, in order that the observed kinetics are free from effects arising from rotational reorientation. A single grating (600 or 1200 l/mm) spectrometer (Jobin Yvon HR 640) with a liquid nitrogen cooled CCD camera (Wright Instruments) is used. The spectral resolution of the spectrometer with the CCD camera using the 600 l/mm grating is 3.8 ± 0.3 cm^{-1}. The readout of the CCD is performed by a Tandon 286 PC computer which also can be used for analysis of the spectrum.

EXTENDED WAVELENGTH GENERATION BY STIMULATED STOKES RAMAN SCATTERING

Efficient stimulated Stokes Raman scattering was obtained using dimethyl sulfoxide (DMSO, BDH 99.5 % purity) and provides the means of extending the tunable range of the apparatus.

A 10 cm focal length lens was used to focus the amplified laser pulses (611 nm, 55 μJ/pulse) into a glass cuvette of 18 cm diameter containing DMSO. The liquid was stirred to avoid local overheating within the laser beam waist. The pulse energy of the first stimulated Raman line was measured to be 19 μJ, i.e. 35 % energy conversion efficiency. The wavenumber shift was 2923 cm^{-1} resulting in a line at 744 nm when using a fundamental laser wavelength of 611 nm. The bandwidth of 1st Stokes Raman line at 744 nm was measured to be 13 ± 2 cm^{-1} (FWHM).

A 5 cm focal length lens was used to focus the 1st stimulated Stokes Raman line into a second cuvette with static DMSO. This produced a stimulated Stokes emission at 951 nm which is the second Stokes Raman line with respect to the fundamental beam at 611 nm. The shifted beam had a pulse energy of 4 μJ. This corresponds to an energy conversion efficiency of 21 % from the first stimulated Raman line and 7.3 % from the original fundamental beam at 611 nm. The measured bandwidth of the second stimulated Raman line was 12 ± 2 cm^{-1}.

Stimulated Stokes emission was also obtained in benzene, 992 cm^{-1} wavenumber shift (Aldrich, spectrophotometric grade, 99 % purity) with an energy conversion efficiency of 5 %.. The fundamental laser beam at 570 nm had a pulse energy of 7 μJ.

PERFORMANCE

The apparatus has been used recently in study of the early relaxation processes of singlet excited state *trans*-stilbene having approximately 100 ps lifetime in n-hexane (20°C). The results are presented in the Chemistry section of this Report and in paper[7].

CONCLUSIONS

We have demonstrated an apparatus with a moderately high repetition rate which is capable of yielding good quality picosecond TR^3 spectra. The current set-up is tunable from 550 nm to 655 nm with the pump (or probe) being generated through frequency doubling of the fundamental. Stabilised pulse energies at the sample are >1 μJ/pulse (probe) and >0.2 μJ/pulse (pump).

Further tuning is possible using stimulated Stokes Raman generation in dimethyl sulfoxide (2923 cm^{-1}) which gives up to 35 % energy conversion in the first and up to 7 % energy conversion in the second Stokes Raman line.

ACKNOWLEDGEMENTS

It is a pleasure to thank S.E.J.Bell, J.Diggins, A.Jaweed, P. Miller, F.O'Neill, I.N.Ross, W.Shaikh, S.Tavender, R.Williams and M.Wise for contributions to this work.

REFERENCES

1. I C E Turcu, J Diggins, M Hannah, F O'Neill, I N Ross, S Bell, R E Hester, S Umapathy, J M Barr, Central Laser Facility Annual Report, RAL-89-045, 1989.

2. S Umapathy, E Turcu, J N Moore, S E J Bell, R E Hester, Central Laser Facility Annual Report, RAL-90-026, 1990.

3. G J Hirst, P Matousek, P Mawson, W T Toner, M Towrie, A W Parker, R Williams, Central Laser Facility Annual Report, RAL-91-025, 1991.

4. P Matousek, A J Langley, A W Parker, W T Toner, M Towrie, I C E Turcu, M Wise, D Phillips, R E Hester, J N Moore, S Umapathy, Central Laser Facility Annual Report, RAL-92-020, 1992.

5. P Matousek, R E Hester, J N Moore, A W Parker, D Phillips, W T Toner, M Towrie, I C E Turcu, S Umapathy, submitted for publication in Rev. Sci.Instrum., 1993.

6. D.S.Bethune, Appl.Opt. **20**, 1897 (1981).

7. R.E.Hester, P.Matousek, J.N.Moore, A.W.Parker, D.Phillips, W.T.Toner, M.Towrie, submitted for publication in Chem.Phys.Lett., 1993.

NUMERICAL ANALYSIS OF RAMAN SPECTRA

P Matousek, A W Parker, W T Toner, M Towrie

Rutherford Appleton Laboratory

INTRODUCTION

A numerical code has been developed for the accurate analysis of picosecond transient Raman spectra obtained from the picosecond time-resolved resonance Raman apparatus (described elsewhere in this Section). In particular, we wish to resolve very subtle transient changes in the Raman spectra induced by the redistribution of excess excitation energy within photoexcited molecules. The program was written in Borland Turbo Pascal 6.0 and uses the Levenberg-Marquardt method[1]. The code fits Lorentzian and/or Gaussian peaks to the entire transient Raman spectrum while fitting the background to a polynomial function of a specified order. Cosmic ray signals are automatically located at the beginning of the fitting process and rejected.

PROGRAM DESCRIPTION

The program first crudely estimates the average standard deviation of a single data point in the spectrum in order to recognise and reject the signals due to cosmic rays. This is made by taking each data point and measuring its distance from the average value taken from the two neighbouring points, $\Delta = y_n - (y_{n-1} + y_{n+1})/2$. It assumes that the change of the Raman intensity across three adjacent data points are small compared to fluctuations due to random noise. Then fluctuations of the parameter Δ from point to point will represent the noise signal and one can then estimate the average standard deviation of single data points by approximating them to the average standard deviation of the Δ. The program disregards all data points having Δ higher than 5 x the average standard deviation by assigning them zero weight.

The code then determines the standard deviation of each data point more precisely, ignoring all data points recognised earlier as cosmic ray signals. A fast fourier transform with a low frequency pass filter is used to smooth the Raman spectrum. The smoothed spectrum is subtracted from the raw data in order to extract the pure noise signal. The standard deviation is measured from the extracted noise signal.

The program searches for the best solution through an iteration process. It begins with initial guess parameters of the fitted function (1) supplied by the operator. The fitting stops when convergence is achieved and there is no further decrease in the total chi^2 parameter.

$$y(x) = \sum_{k=1}^{m} A_k / (1+(2(x+C_k)/B_k)^2) + \sum_{k=1}^{n} D_k \exp(-(x+E_k)^2/F_k) + \sum_{k=1}^{l} G_k x^{k-1} \qquad (1)$$

A graphical display of each iterative step allows the operator to examine the progress of the fit. Any number of parameters can be fixed before calling the fitting routines. Finally, a full numerical summary of the fit is displayed. The program gives amplitude, area, bandwidth and position for each peak fitted as well as standard error of each fitted parameter and the total chi^2 value of the fit. The analysis shown on Fig. 1 was carried out on a Viglen 4DX266 PC (66 MHz) and took about 20 s which is at least two orders of magnitude faster and an order of magnitude more accurate than our commercial packages. The program has been successfully applied to analysis of more than 300 spectra of the *trans*-stilbene S_1 state where vibrational mode-specific effects show up as small perturbations of Raman bands. The results of the analysis are presented in the Chemistry Section.

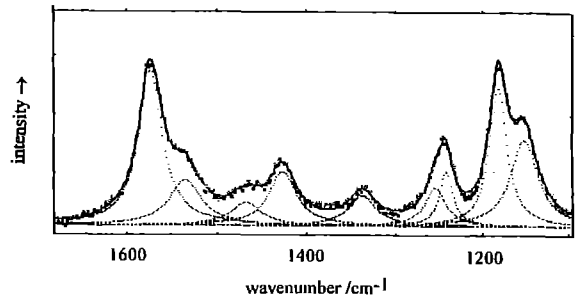

Fig 1 Results of numerical fitting of 8 Lorentzian peaks to a Raman spectrum of the excited state of *trans*-stilbene (1 x 10^{-3} mol dm^{-3}) in n-hexane obtained with pump/probe wavelengths of 275/550 nm at 40 ps delay time. The broken lines are the fitted single Lorentzian peaks and the solid line is their superposition.

VOIGT FUNCTION

A modification of the program has been written in order to fit the Voigt function (convolution of Gaussian and Lorentzian functions) to a Raman band. Such analysis can give an answer to what degree a Raman band is non uniformly broadened or distorted by instrumental effects. The code fits a range of Lorentzian functions (typically n = 50) with equal widths, separated by a small, fixed step δ and amplitudes varying with a Gaussian distribution,

$$y(x) = \sum_{k=-n/2}^{k=+n/2} A \exp(-(k\delta/B)^2 / (1+(2(x+C+k\delta)/D)^2) + \sum_{k=1}^{l} E_k x^{k-1} \qquad (2)$$

The following parameters are fitted: width of Lorentzian peaks D and width B, position C and amplitude A of the Gaussian envelope as well as parameters E_k of polynomial background.

REFERENCE

1. W.H.Press et al, Numerical recipes in Pascal, Cambridge University Press, Cambridge, 1989.

A HIGH BRIGHTNESS LASER USING TITANIUM SAPPHIRE AND DYE TECHNOLOGY

Andrew J Langley, William J Noad, Ian N Ross and Waseem Shaikh

Rutherford Appleton Laboratory

INTRODUCTION

The increasing demands for short pulse and high power tuneable lasers have led to a rapidly increasing number of systems. Perhaps the most popular are those using titanium sapphire oscillators together with solid state multipass or regenerative amplifiers and using chirped pulse amplification to achieve up to terawatt performance for pulses as short as 100 fs. These systems are complex and expensive[1-3] and may not be essential for many applications. The work described here set out to optimise the performance of a short pulse titanium sapphire oscillator coupled to a conventional dye amplifier[4] to generate high power diffraction and transform-limited pulses.

PRINCIPLES

The amplification of picosecond pulses from a synchronously pumped dye laser with this system has allowed us to achieve pulse energies of several hundred micro-Joules, with little or no pulse distortion[5]. However, this was not the case when we attempted to amplify 100fs pulses from a titanium sapphire oscillator. Figure 1 shows that the spectra of amplified 100fs pulses were broadened by self-phase-modulation for output powers in excess of ~ 1GW up to the maximum achievable pulse output of 4GW.

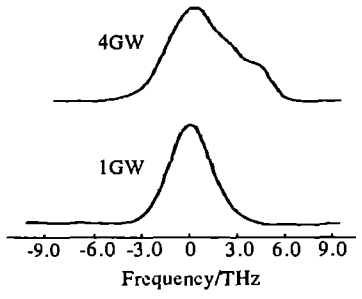

Figure 1

In addition, the presence of group velocity dispersion resulted in a pulse stretch in the dye amplifier from input to output of 100 fs to 150 fs respectively. To eliminate these effects a chirped pulse amplification (CPA) and recompression scheme is implemented and since the pulse need only be stretched by a factor < 10 , a novel scheme which is both simple and efficient can be used .

We also changed the final dye amplifier to a Bethune cell which enabled the pulses to be amplified to high power with very good beam uniformity and low wavefront distortion.

DESCRIPTION

A diagram of the experimental arrangement is shown in Figure 2. The short pulse source comprised a titanium sapphire oscillator (Spectra-Physics Tsunami) pumped by 5 Watts all lines from an argon-ion laser (Spectra-Physics 171). This readily produced an 82 MHz train of pulses tuneable from 100 fs to 300 fs pulselength and from 730 nm to > 800 nm wavelength. Before amplification these pulses were stretched to a pulse duration > 650 fs using the negative GVD in a prism pair (SF10) in double pass with a separation of approximately 2 m. To maintain good pulse quality with freedom from spatial dispersion in the output beam the beam waist should be close to the rear mirror of the stretcher and this was accomplished using a 2 m focal length lens.

The pulses were amplified using a modified three stage dye amplifier system (Spectra-Physics PDA1) in which the final axially pumped amplifier is replaced by a 6 mm aperture Bethune cell amplifier. Unlike the axially pumped amplifier, the gain distribution across the beam in the Bethune cell can be made quite uniform and does not imprint onto the beam the doughnut-shaped intensity profile of the pump beam. Best performance of the dye amplifier system at 750 nm was achieved using rhodamine 700 dye which has a peak gain wavelength (in ethanol) of approximately 720 nm. The strong amplified spontaneous emission at this peak wavelength was eliminated by inserting a narrow band filter ($\Delta\lambda$ ~10 nm) before the final amplifier.

Recompression of the amplified stretched pulse was achieved very simply, using the positive GVD in a block of SF10 glass of thickness 145 mm. The beam was expanded to 20 mm diameter through the block to keep the intensity length product down below the threshold for self phase modulation and self focusing.

A diagnostic package was set up to measure the near and far field intensity distributions of the amplified beam and the spectrum and autocorrelation of the recompressed output pulses. The diagnostics providing stored images via a CCD and frame

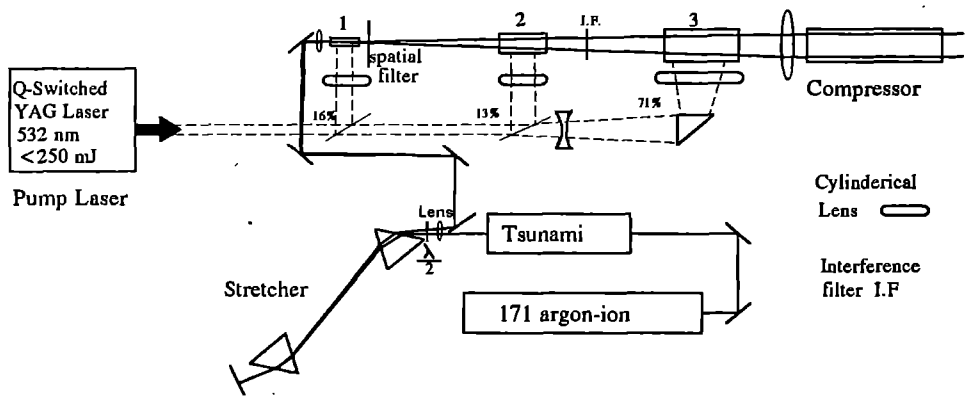

Figure 2 Plan of 100fs Pulse Amplifier

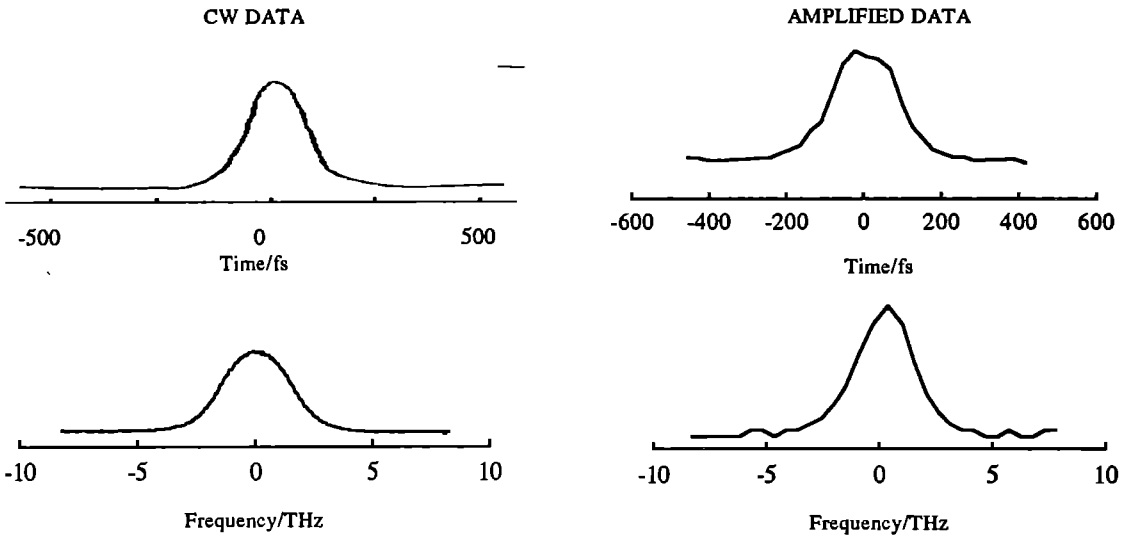

Figure 4 CW and Amplified Pulse Autocorrelations and Spectra

grabber[5]. The autocorrelation and spectrum were recorded simultaneously using a single shot autocorrelator and spectrometer[6]. A secondary test was necessary to enable accurate calibration of the far field profile in terms of absolute intensities which could then be compared to those obtainable with a 'diffraction limited' beam. This test used a linear photodiode to measure the fraction of pulse energy transmitted through a pinhole of known size in the focal plane.

MEASUREMENTS

The oscillator was set up to deliver pulses close to 100 fs. Wavelength was set at ~750 nm which gave good oscillator performance and enabled use of an efficient and stable dye in the amplifiers. Pulse energy was 2 nJ and spectral width close to transform limit ($\Delta\nu\Delta t \approx 0.315$) for sech² profiles[7].

The amplifier system was optimised with respect to beam geometry, dye concentrations and pump energy distribution to give uniform output beam profile, low beam divergence and high energy. Using pump energies of 250 mJ in 8 ns @ 532 nm, maximum output energies > 350 μJ were obtained with low levels of ASE (<5%). Thus a maximum power at the amplifier output of 0.5 GW is well below the threshold for nonlinear processes. A near field distribution is shown in Figure 3 demonstrating good uniformity over an approximately flat top profile. Following recompression through the SF10 block the beam was sent into the diagnostic package.

Figure 4 shows autocorrelation traces and spectra for oscillator pulses (pulse durations recorded using a scanning autocorrelator) together with the autocorrelation trace and spectrum of the amplified recompressed pulse. In the latter case the single shot autocorrelator was used. Recompression was optimised by adjusting the length of the pulse stretcher. Typical pulse durations achieved were 120±10fs. for input pulses of 100 fs. The amplified pulse in figure 4 had a duration of 111fs while the corresponding spectral widths were 2.88 THz and 3.21 THz, giving $\Delta\nu\Delta t \approx 0.34$ and 0.32, for the amplified and unamplified pulses respectively. The small increase in pulse width and $\Delta\nu\Delta t$ is not very significant considering the measurement inaccuracies and small changes that can be expected as a result of strong gain saturation in the dye amplifiers which changes both the spectral and temporal width and shape of the amplified pulses[8].

Figure 3 Averaged near field distribution

Figure 5 shows a far field distribution of the amplified and recompressed pulses. By also measuring the fraction of total pulse energy transmitted by a pinhole in the far field (20% was transmitted through a pinhole of size = 0.83 x FWHM of the true Airy distribution) absolute far field intensities could be determined. Shown in Figure 6 is the corresponding Airy distribution with respect to the Fraunhofer diffraction of a circular aperture demonstrating a Strehl ratio[9-10] (fraction of Airy intensity at peak) of 0.52 or a FWHM of 1.33 x diffraction limit.

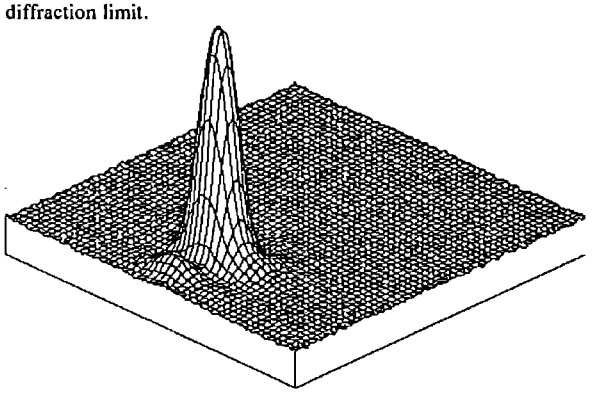

Figure 5 Far field distribution

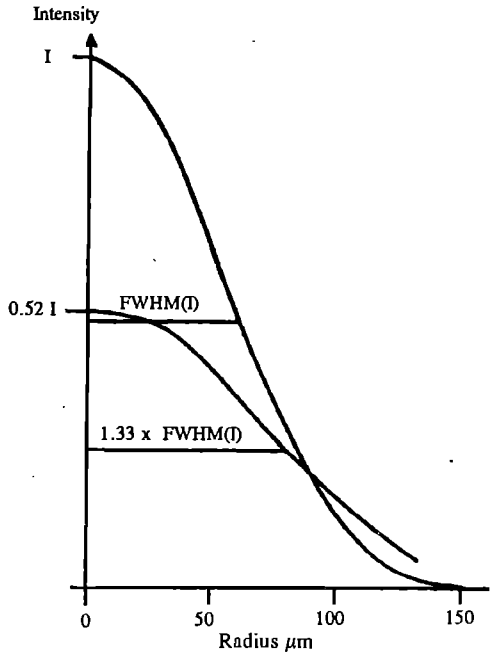

Figure 6 Airy distribution

The measurements can be combined to give a peak brightness (B) for the system of 3.1 x10 ^{17}W/cm^2/steradian. This enables a calculation of the focused intensity using an optic of focal ratio F using the relation:

$$I = \pi B/4F^2$$

Thus for F = 1, the potential peak intensity on a target is 2.4 x 10^{17}W/cm^2.

CONCLUSION

A short pulse system using conventional dye amplifiers and an unconventional chirped pulse amplification scheme has been shown to be capable of generating intensities > 10^{17} W/cm^2 and is within a factor of 2 of the theoretical limit set by the energy and pulse duration. Since titanium sapphire oscillators are now capable of generating pulses down to < 20 fs relatively easily[11] and there is spare bandwidth in the dye used in the amplifiers it should be possible to further increase the peak power of the recompressed pulse by perhaps as much as a factor of 4.

REFERENCES

1. D.Strickland and G.Morou. Optics Comm. 56 219(1985).
2 P.Maine, D.Strickland, P.Bado, M.Pessot and G.Mourou. IEEE J.Quantum Electronics QE-24 398(1988)
3 P.Maine and G.Mourou. Optics Lett. 13 467(1988)
4. CLF Annual Report 226(1992).
5. CLF Annual Report 223(1992).
6. CLF Annual Report (1993).
7. K L Sala, G A Kenny-Wallace and G E Hall. IEEE Journal of Quantum Electronics QE-16 909 (1980).
8. Y.H Chuang, L.Zheng and D.D. Meyerhofer. IEEE Journal of Quantum Electronics 29 270(1993).
9. Born and Wolf. Principles of Optics. pp 462 (6th Edition).
10. K.Strehl Z.F. Instrumkde 22 213 (1902).
11. B.E.Lemoff and C.P.J.Barty. Optics Letters 17 1367(1992).

SINGLE-PULSE AUTOCORRELATOR AND SPECTROMETER SYSTEM FOR THE MEASUREMENT OF SUBPICOSECOND LASER PULSES

Andrew J Langley, William J Noad, Ian Ross and Waseem Shaikh

Rutherford Appleton Laboratory

The development, at RAL, of a 10Hz system[1] to amplify 10nJ 100fs pulses, from a mode-locked titanium-sapphire oscillator, to several hundred microjoules resulted in the need for single-pulse diagnostics both for laser system development and applications based experiments. The single-pulse autocorrelator and spectrometer constructed for this purpose is shown in figure 1. The beam from the laser was collimated by lens L1 and, on entering the autocorrelator, was divided by a 1mm thick 50:50 beam splitter BS. In one of the two beams a corner-cube retro-reflector was used as an optical delay line for set-up and callibration purposes. A 10cm cylindrical lens L2 was used to focus the combined beams in the horizontal plane at the type I, 1mm thick, BBO crystal. The small angle ($\approx 10^{o}$) between the beams, and thus between the pulse fronts, served to introduce a temporal variation across the overlapping beams at the crystal. The UV beam generated at the crystal was imaged by lens L3 onto a Pulnix TM 765 CCD camera. The autocorrelator gave an adequate signal with input pulse energies of only 5 to 10μJ.

The simple spectrometer consisted of a focussing lens L4, slit S, collimating lens L5, an 1800 lines/mm diffraction grating G, and a cylindrical lens L6 which imaged the spectrum onto another Pulnix TM 765 CCD camera. The practical resolution of the spectrometer was ≈0.1 THz and was adequate for the purposes of measuring the linewidth of our pulses. The autocorrelation and spectral images resulting from a single laser pulse were transfered from the CCD cameras sequentially to a framestore (Oxford Framestores Applications Ltd) in a Viglen III/LS personal computer[2] for display and analysis.

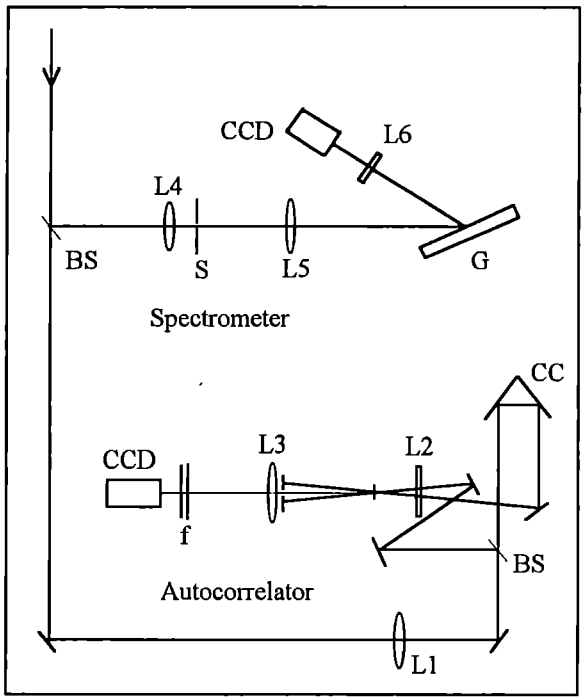

Figure 1 Single-pulse autocorrelator and spectrometer

One of the difficultes associated with all single-shot autocorrelators is the non-uniformity of intensity across the input beam and the effect this has upon measurement. This problem was reduced in our system by selecting a large diameter (2cm) input beam so that the intensity varied little over the 4mm active width of the crystal. This was confirmed during alignment of the system by varying the position of the corner cube, and thus the optical delay, to ensure that the width and shape of the measured autocorrelations did not change significantly within the ≈1.5ps time window of the device. This method also provided a callibration. Our other main concern in the design of the autocorrelator was pulse broadening due to group velocity dispersion in optical components. We estimate[3] that the total effect of all the components used would stretch a 100fs pulse to ≈105fs duration which we believe is acceptable for the experiments envisaged.

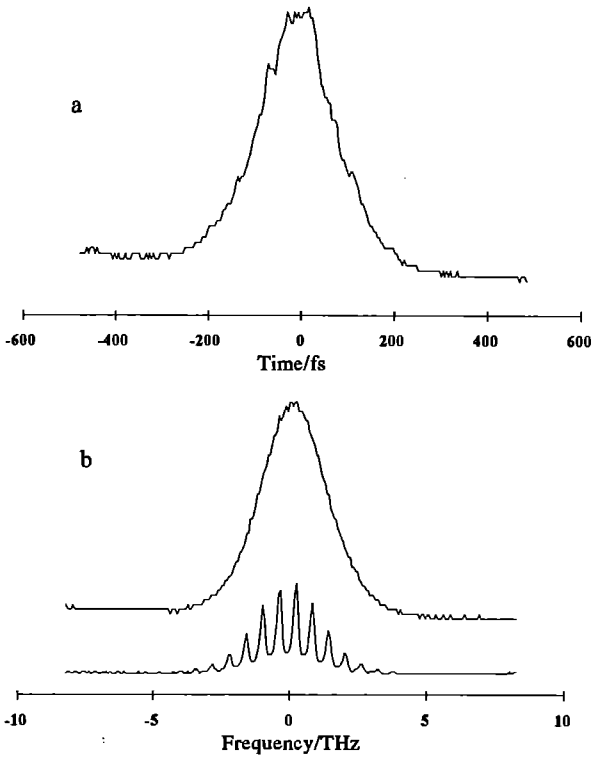

Figure 2

Figure 2a shows an autocorrelation measurement of an amplified pulse of 350μJ energy at 746nm. The FWHM of the autocorrelation is 180fs which would result from a pulse of duration 118fs FWHM assumed to have a $sech^2$ pulse shape. In figure 2b is shown the spectrum corresponding to the pulse measured in the autocorrelation. The lower trace is simply for callibration and was obtained by placing a $20cm^{-1}$ free spectral range Fabry-Perot etalon in the beam before the spectrometer. The FWHM of the spectrum is 2.88THz which gives a time-bandwidth product of 0.34 close to the 0.31 expected for transform limited $sech^2$ pulses.

1. CLF Annual Report (1993)

2. CLF Annual Report 223, (1992)

3. Z Bor. J. Modern Optics, 35, 1907, (1988)

CONSTRUCTION OF A THIRD-ORDER CORRELATOR FOR THE MEASUREMENT OF PICOSECOND PULSES

Lawrence H Edwards[1] and Andrew J Langley[2]

[1]University of St. Andrews
[2]Rutherford Appleton Laboratory

The measurement of pulse shape can be important in some laser experiments and much effort has been devoted to developing methods[1,2] for pulse analysis. Unfortunately, one of the only simple, and therefore widely used, methods is second-order autocorrelation[3]. This provides an indication of pulse duration but because of the symmetric nature of the autocorrelation function, all pulse-shape information is lost. A technique which can provide more information is third-order correlation[4]. This works on the principle that a frequency doubled light pulse will be shorter than the fundamental pulse because the doubled intensity is quadratically dependent upon the intensity of the fundamental. A cross-correlation of the a light pulse with its second-harmonic pulse will show asymmetry if the pulse is asymmetric. The object of the current work, which formed the basis of a short MSc project for one of us (LHE), was to design and build a third-order correlator and to assess its application to pulse analysis.

EXPERIMENTAL

The laser used in these experiments consisted of a mode-locked, synchronously-pumped, picosecond dye-laser SPDL operating at around 750nm and amplified to 400μJ at a repetition rate of 10Hz. The SPDL pulses could be stabilised using an external "feedback" cavity[5] to produce Fourier transform-limited pulses of ≈5ps in duration. Without feedback the laser was less stable.

A diagram of the correlator constructed is shown in figure 1. Beam-splitter BS was designed to optimise the efficient generation of second and third-harmonic radiation. The input side was uncoated to allow most of the 746nm radiation to reach the thin (1mm), type I, KDP doubling-crystal. The other side of the beam-splitter was coated for efficient reflection of 373nm. A half-wave plate for 746nm in the doubling arm, and therefore full-wave plate at 373nm, served to rotate the polarisation of the incoming light by 90°, ensuring that the doubled light reached the tripling crystal with the same polarisation as the fundamental.

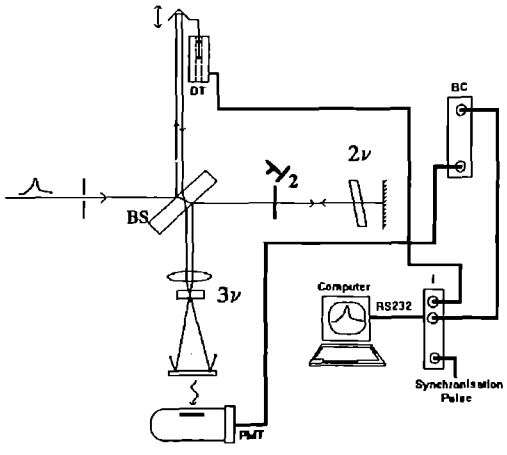

Figure 1

In the other arm of the correlator was the scanning arrangement which consisted of a corner-cube retro-reflector on a slide attached via a cam and wheel to a motor. In the measurement of delay in third-order correlation it is vital to avoid the systematic introduction of asymmetry to the data. This was overcome in our system by using a differential transformer (Schlumberger DFg2.5) DT, attached to the slider, and which gave a voltage output proportional to position and so, for example, the position of data points was not convolved with the sinusoidal motion of the delay. The signal from the DT was transferred, via a digital to analogue converter, to a Viglen 33MHz 386 PC. Upon reflection at the corner-cube, and passage back through the beam-splitter, the fundamental light was focused, together with the 373nm, by an achromatic doublet at the type I, BBO mixing crystal. The mixed radiation at 246nm was detected by a photomultiplier PMT the signal from which was transferred via a Stanford Research Systems SR250 Gated Integrator to the PC.

RESULTS AND ANALYSIS

An example of a third-order correlation showing that the technique is sensitive to pulse asymmetry is presented in figure 2. The SPDL was set up to produce a satellite pulse in addition to the main pulse. A second-order autocorrelation, being symmetrical, can only show the presence of a satellite pulse as a bump either side of the main correlation. The third-order data shows the satellite on one side of time-zero only and indicates that the satellite follows the main pulse.

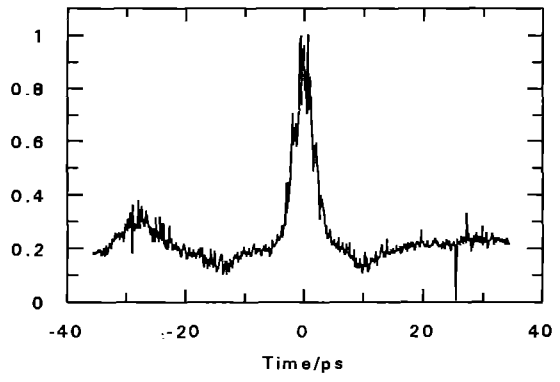

Figure 2

The Analysis of third-order correlation data might ideally consist of finding the function with the best fit to the data from amongst a set of selected functions with varying degrees of asymmetry. Unfortunately, this option was not available to us within the time constraints of the project and so we opted for the alternative approach of semi-quantifying the degree of asymmetry present in the data. This involved plotting the residuals obtained when the correlation data, rotated about the position of its maximum, was subtracted from the unrotated data.

To illustrate this figure 3 shows three simulated third-order correlations of three Gaussian pulses with fall-time to rise-time ratios of 1.4, 2.0 and 2.5 in curves 1,2 and 3 respectively. The plot of their residuals in figure 4 shows clearly the effects of increasing asymmetry. Sech^2 pulse shapes gave very similar data. When trying to do the same thing with real and most probably noisy data, however, the problem becomes one of identifying the

maximum about which to rotate the data. An effective method in which to achieve this is to convolve the raw data with a symmetric function which smoothes the data and most effectively allows the maximum to be identified. In simulation trials we found that a Gaussian, somewhat narrower than the simulated autocorrelations, worked most effectively.

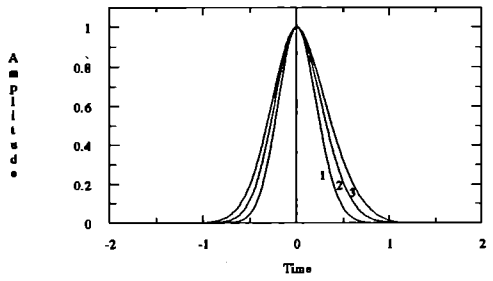

Figure 3

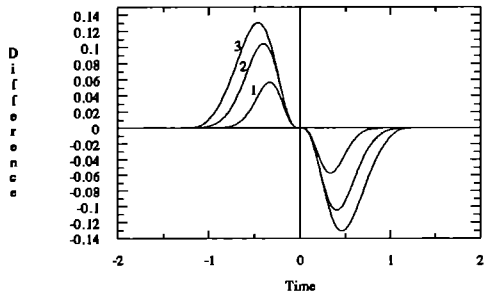

Figure 4

A third-order correlation of pulses derived from the SPDL, with feed-back applied to the laser, is shown in Figure 5. The data was centred, using the convolution technique mentioned, and the residuals are plotted in figure 6.

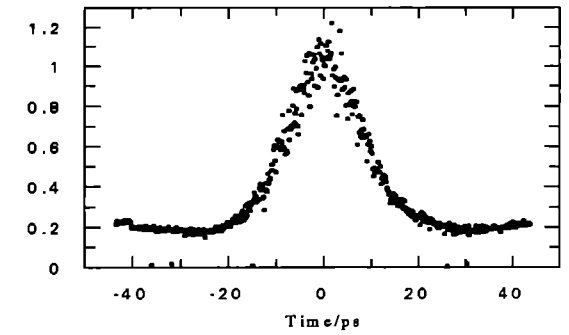

Figure 5

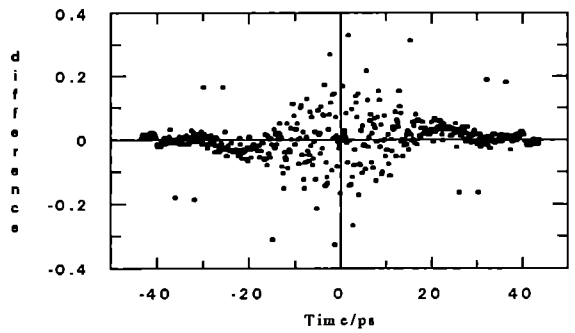

Figure 6

The residuals are randomly scattered over most of the data but have a tendency to deviate by a few percent from zero in the wings of the correlation. We tentatively suggest that this indicates that these pulses were symmetric or at worst only slightly asymmetric.

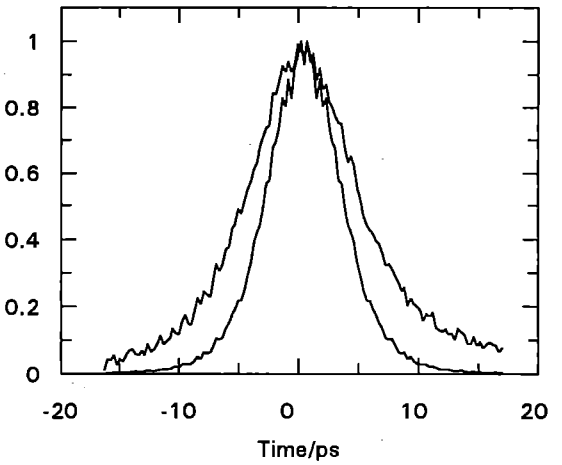

Figure 7

Pulse symmetry represents a special case in which the shape of the original pulse can be calculated uniquely from the second-order autocorrelation data using Fourier transformations[6]. Figure 7 shows the pulse shape (inner curve) obtained from the second-order autocorrelation (outer curve) measured simultaneously with the third-order data presented above. The ratio of the pulse FWHM (7ps) to the autocorrelation FWHM was 0.652 close to the expected value of 0.648 for $sech^2$ pulses. (The ratio for Gaussian pulses is 0.707). This corresponds with the widely accepted view that SPD lasers produce $sech^2$ shaped pulses[7]. Interestingly, the symmetry of third-order correlations of pulses derived from the SPDL running without feedback indicated that such pulses, or noise bursts, were also symmetric about time-zero.

In conclusion we believe that, with due care, the data obtained can be interpreted. The correlator was relatively easy to use but is restricted to laser wavelengths longer than about 600nm because of tripling-crystal limitations. The measurements would be improved considerably by normalisation accounting for laser-pulse intensity fluctuations.

We acknowledge the University of St. Andrews for the provision of an MSc studentship to LHE.

REFERENCES

1. D Bradley and G New. Proceedings of the IEEE. 52(3), 313 (1974).
2. J C Diels, J J Fontaine, I C McMichael, F Simoni. Applied Optics. 24(9), 1270 (1985)
3. K L Sala, G A Kenney-Wallace, G E Hall. J. Quant. Elec. IEEE. 16(9), 990 (1980)
4. J Etchepare, G Grillon, A Orszag. J. Quant. Elec. IEEE. 19(5), 775 (1983)
5. P Beaud, J Q Bi, W Hodel, H P Weber. Optics Comm. 80, 31 (1990)
6. The Fourier Transform and its Applications 2nd Edition. R N Bracewell. McGraw-Hill. (1986)
7. C J Hooker, J M D Lister, I N Ross. Optics Comm. 80, 375 (1991)

NOVEL ROTATIONAL DYNAMICS IN ANISOTROPIC FLUID MEDIA STUDIED BY POLARISATION RESOLVED PICOSECOND TCSPC

Pamela Chandna[1], Angus Bain[1], Andrew J Langley[2], Mike Towrie[2] and Pavel Matousek[2]

[1]Department of Physics, University of Essex, Colchester, CO4 3SQ
[2]Rutherford Appleton Laboratory

INTRODUCTION

Conventional time resolved fluorescence anisotropy experiments involve the photoselection of an anisotropic array of molecular orientations in an isotropic fluid medium by an ultrashort light pulse. Collisions with the isotropic background lead to the randomisation of this distribution and the consequent decay of the fluorescence anisotropy R with time. R(t) decay curves yield the second order orientational correlation functions for isotropic rotational diffusion, whose correlation times, τ_{or}, can be used to extract information on the orientationally averaged nature of microscopic frictional forces[1][2][3].

In contrast, the study of orientational dynamics in anisotropic media affords the possibility of observing collisional dynamics in a wholly new light. In particular, the interaction of polarised laser radiation with an already anisotropic molecular array leads to the preparation and subsequent evolution of additional (higher order) correlation functions for molecular motion[4]. Furthermore, since the dynamics are no longer averaged over an isotropic background, the conventional selection rules governing isotropic relaxation no longer hold and a radically different collisional modification of the initial distribution may result[4][5]. It should be noted that chemical reactivity and energy exchange processes, such as Förster transfer, can be expected to be substantially modified under such conditions[6] and that orientationally sensitive spectroscopic techniques should be particularly revealing in this context.

Recent developments in sapphire jet technology now afford the routine production of thin high optical quality fluid jets. In such environments the highly directional nature of molecular collisions is predicted to lead to significant molecular alignment[4]. The sign and magnitude of this alignment is a sensitive probe of the anisotropy of the collisional processes and the directional nature of frictional forces operating at the molecular level[8].

Steady state fluorescence measurements of R6G in ethylene glycol jets show evidence of significant molecular alignment and/or anisotropic orientational relaxation with the flow[7]. Steady state measurements invariably convolve the initial anisotropy of the system, its interaction with polarised laser radiation and its subsequent evolution[5]. Picosecond time resolved fluorescence anisotropy measurements are crucial to unravel the complex dynamics of such systems. This report describes novel picosecond time correlated single photon counting (TCSPC) studies of R6G in ethylene glycol and polyethylene glycol flows together with a comparison of R6G dynamics in identical but isotropic fluid environments.

The differences between isotropic and anisotropic R6G dynamics are marked, illustrating the presence of an initial alignment along the jet axis, together with highly anisotropic orientational motion of the array following excitation.

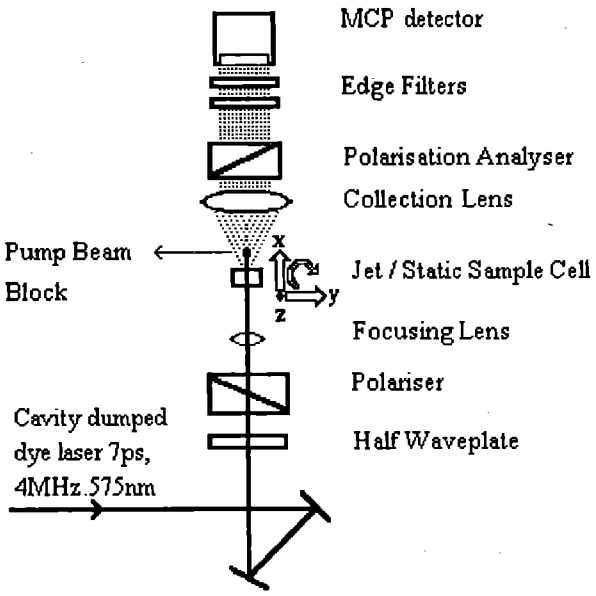

Figure1 optical layout.

EXPERIMENTAL

The optical arrangement is shown in Figure 1. We have successfully employed a colinear fluorescence collection geometry, which is essential for polarisation dependent studies of thin samples in that the additional complication of angle dependent Fresnel factors is removed from the analysis. Direct and scattered pump radiation is prevented from reaching the MCP detector by a combination of edge filters and a small beam block. The system has non-preferential detection of any particular polariastion (a g factor of unity). This is demonstrated in Figure 2, which shows $I_V(t)$ and $I_H(t)$ curves for an isotropic sample of R6G excited with 45° polarisation at 575 nm. Both curves are identical at all times, as should be the result for an isotropic system under these excitation conditions [9]. The sapphire nozzle was mounted on a precision stage allowing xyz positioning and rotation about the jet axis.

Fluorescence decay curves for emission polarised parallel and perpendicular to the jet axis were recorded as a function of excitation polarisation angle θ (relative to the jet axis). Similar measurements were performed with the isotropic cell to provide a reference. The instrument response function (105 ps) was determined by light scattering from a suspension of "Coffee-mate" (a non-fluorescent scatterer).

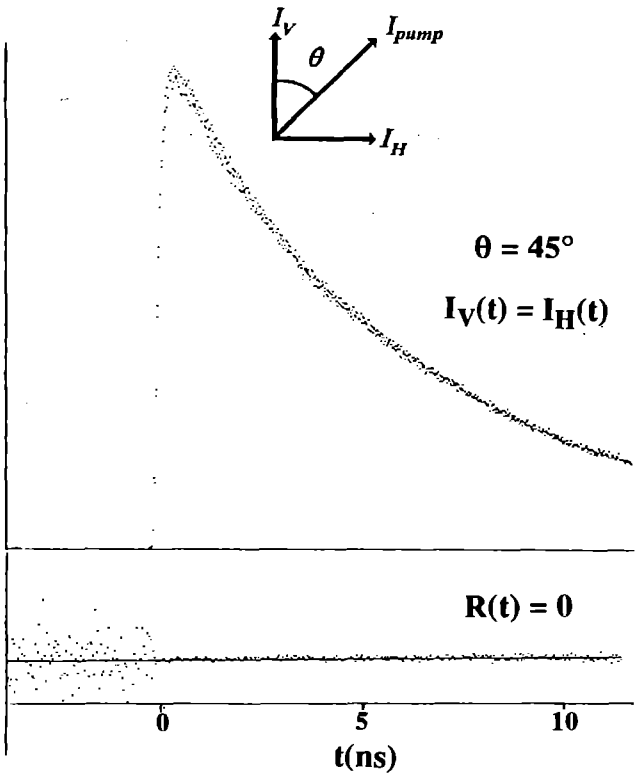

Figure 2 g factor assessment.

RESULTS AND DISCUSSION

Figure 3 shows $I_{||}(t)$, $I_{\perp}(t)$ and R(t) curves for a 0.9 gl^{-1} solution of R6G in an ethylene glycol / polyethylene glycol jet (viscosity 38 cP), excited on axis (spot size 50 μm), 5.5 mm downstream from a 500 μm sapphire nozzle with a backing pressure of 8 psi. The corresponding data for the reference (isotropic) sample of the same solution, in a 500 μm strain-free quartz cuvette is displayed in Figure 3a. Figures 3b and 3c correspond to excitation polarisations parallel (θ = 0°) and perpendicular (θ = 90°) to the flow axis respectively. The R(t) curves are defined (conventionally) relative to the excitation polarisation vector in each case.

The differences between the jet and isotropic fluorescence profiles are striking. It is immediately apparent that the initial anisotropy R(0) is a strong function of excitation polarisation relative to the jet axis. For parallel excitation R(0) is 0.40±0.015, significantly higher than the isotropic cell (R(0) = 0.36±0.015), whilst perpendicular excitation results in considerably reduced R(0) of 0.30±0.015. These observations are consistent with the interaction of polarised laser radiation with an initially aligned array of R6G molecules about the flow axis. The variation of R(0) with θ can be used to extract information on the moments of the ground distribution function [4][5][9] and will be discussed elsewhere[9].

The subsequent orientational dynamics of molecules photoselected with orientations parallel and perpendicular to the flow axis are equally distinct. In isotropic systems R(t) will always decay exponentially to zero due to the isotropic nature of solvent-solute collisions, as can be seen by reference to the isotropic cell. For a photoselected array of R6G molecules, aligned parallel to the jet axis, the anisotropy decays non-exponentially to a constant value. The orientational dynamics for excitation at 90° are most marked:, the $I_{||}(t)$ and $I_{\perp}(t)$ curves meet at $\tau = 4.2$ ns, the system behaving as if it were isotropic, before reaching a final negative value corresponding to alignment along the jet axis. Neither R(t) curve is consistent with isotropic rotational diffusion. The passage of R(t) from positive to negative for 90° excitation is unequivocal evidence of cross relaxation between moments of the excited state orientational distribution functions, a process forbidden in isotropic systems[4].

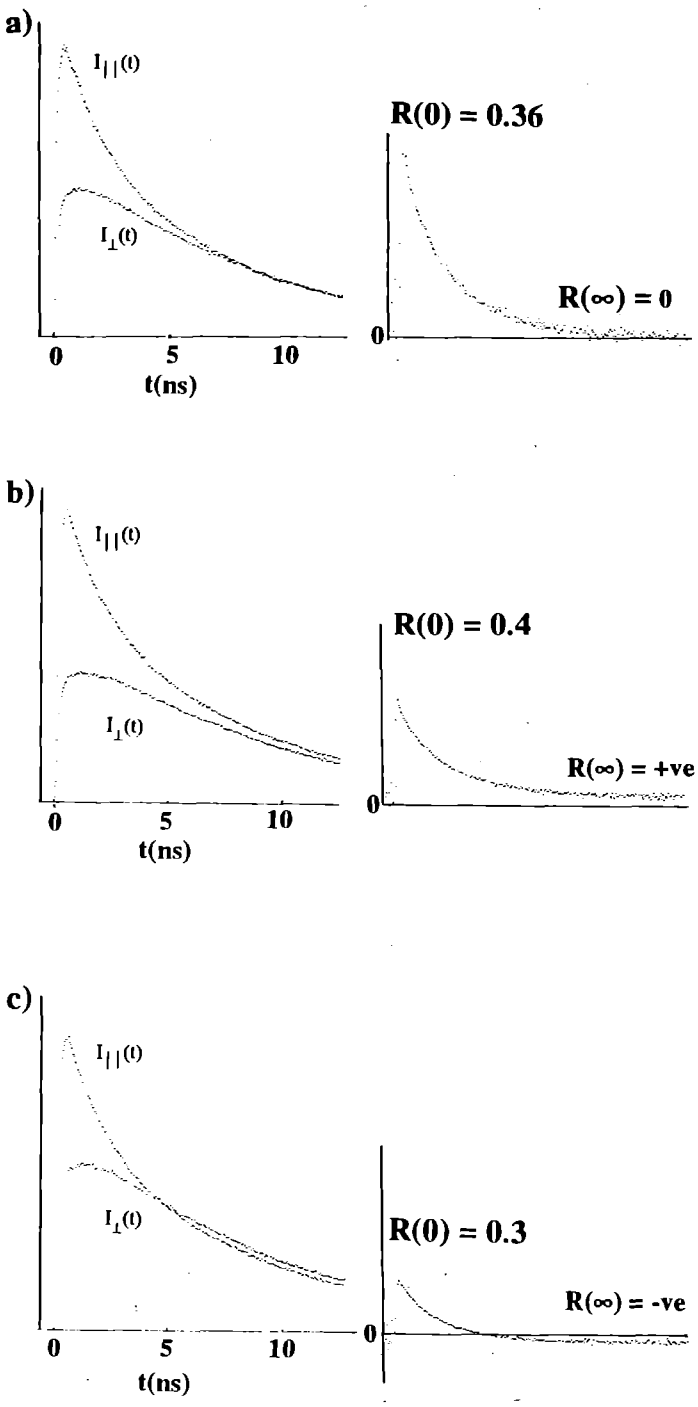

Figure 3
$I_{||}(t)$, $I_{\perp}(t)$ and R(t) curves as a function of excitation polarisation angle θ a) isotropic cell, $I_{||}(t)$, $I_{\perp}(t)$ and R(t) are independent of θ b) jet with excitaion polarisation parallel to the jet axis θ = 0° c) jet with excitation polarisation perpendicular to the jet axis θ = 90°

The long time anisotropy of the system in both cases corresponds to a residual alignment parallel to the jet axis and if the fluorescence observables are defined in terms of the jet axis system (I_V, I_H), this yields an identical residual anisotropy (to within experimental error) of approximately 3% for both θ = 0° and θ = 90°.

Subsequent investigations of R6G jet dynamics have focused on the variation of $I_V(t)$ and $I_H(t)$ as a function of excitation polarisation. In all cases the system is seen to return to a constant final anisotropy (within experimental error), independent of the

to final orientation distribution is, however, a complex function of the excitation polarisation relative to the jet axis, and significant departures from isotropic fluorescence observables, measured with the same polarisation geometry, are seen. Figure 4 shows the results for excitation polarised at 45° to the jet axis. In an isotropic system this produces identical $I_V(t)$ and $I_H(t)$ curves, as shown in Figure 2. The jet dynamics in this situation are quite distinct, with R(t) remaining constant at ~ 3%. It was not possible to obtain identical $I_V(t)$ and $I_H(t)$ curves under any excitation polarisation conditions.

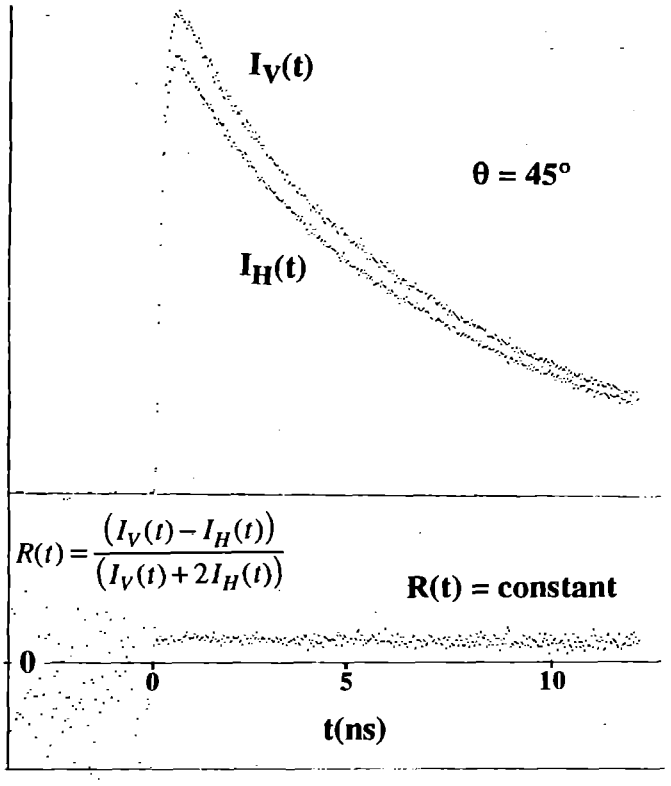

Figure 4 jet with excitation polarisation at 45° to the jet axis.

The coupling between the ground and initial excited state orientational distribution functions is, however, sensitive to the excitation polarisation [4] [5] [9] and it is possible to find a "magic angle" excitation polarisation for a given ground state orientational distribution which gives rise to, an initially isotropic excited state [9] (in terms of the polarisation observables allowed in single photon electric dipole transitions). It is then possible to observe the evolution of this isotropic array of molecules under the anisotropic collisional conditions of the jet. For the R6G ethylene glycol / polyethylene glycol system studied, the magic excitation angle was found to be at θ = 49° from the jet axis; the $I_V(t)$, $I_H(t)$ and R(t) curves are shown in figure 5. The anisotropy is seen to reach its equilibrium value with an exponential grow in time of τ = 1.25 ns.

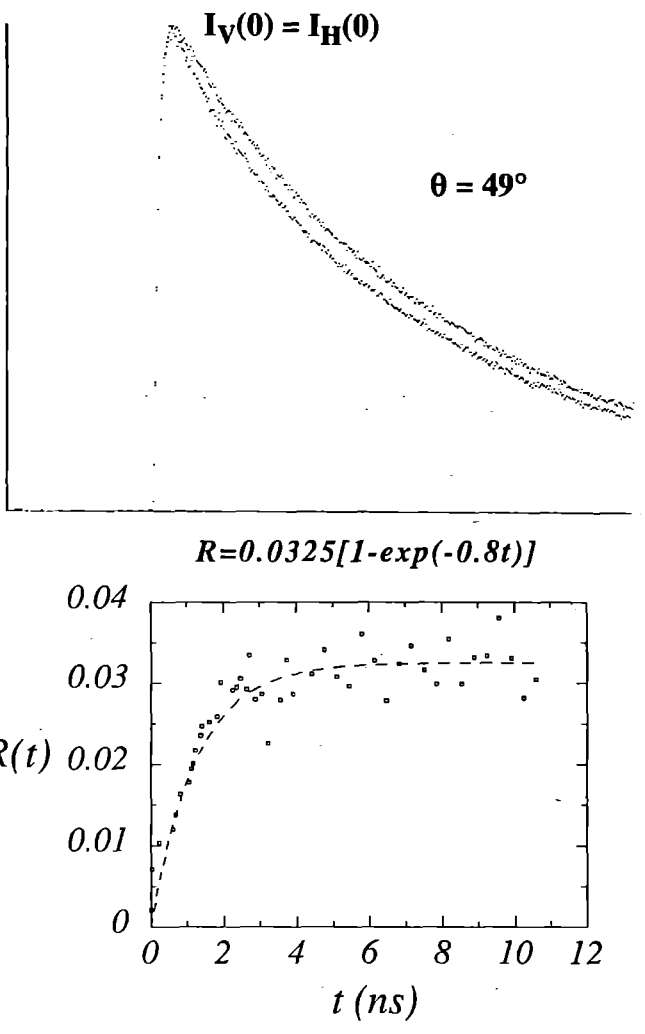

Figure 5 magic angle excitation at θ = 49° to the jet axis. The R(t) curve shows the growth of collisional induced alignment with an exponential rise time of 1.25 ns

These results clearly indicate the presence of dynamic molecular ordering mechanisms within the jet. We believe that these are the first real-time measurements of such processes. Further polarised TCSPC experiments at RAL are planned, to investigate these new and intriguing phenomena.

REFERENCES

1. M.Lee, A.J.Bain et al., J. Chem. Phys. **85** 4341 (1986), P. S.Hubbard, Phys. Rev. **131** 115 (1963)
2. L.A.Philips, S.P.Webb and J.H.Clark, J. Chem. Phys. **83** 5810 (1985)
3. D.Ben-Amotz and T.W.Scott, J. Chem. Phys. **87** 3739 (1987)
4. A.J.Bain, D. Phil Thesis, University of Sussex (1984)
5. A.J.Bain, A.J.McCaffery, J.Chem. Phys.**83** 2627 (1985), ibid **83** 2632 (1985)
6. G.A.Kenney-Wallace, J.H.Flint and S.C.Wallace, Chem. Phys. Lett, **32** 71 (1975), P.A.Anfirud, Ph.D Thesis Iowa State University (1987)
7. A.J.Kenyon, A.J.McCaffery and C.M.Quintella, Mol. Phys. **72** 965 (1991), A.J.Kenyon, A.J.McCaffery, C.M.Quintella and J.F.Winkel, Mol. Phys.**74** 871 (1991)
8. D.F.Calef and P.G.Wolynes, J. Chem. Phys. **72** 535 (1980)
9. A.J.Bain and P.Chandna, manuscript in preparation.

HIGH AVERAGE POWER, 7 PICOSECOND, KrF LASER SYSTEM FOR X-RAY GENERATION

I C E Turcu, I N Ross, A J Langley, P Trenda[1], W Shaikh, S Quayum and H Goodson

Rutherford Appleton Laboratory
[1]Institute of Physics, Czech Academy of Sciences, Prague, Czech Republic

INTRODUCTION

We report on major development work on the excimer based laser-plasma X-ray source, which resulted in generation of X-ray average powers of 200 mW, for University and commercial users.

Last year we reported a breakthrough in the efficiency of converting laser energy to X-rays. 11% X-ray conversion efficiencies[(1)] to 1 nm X-rays were achieved by using 4 ps KrF laser pulses focused to power densities of 10^{15}W/cm^2. We therefore modified the picosecond front end of laser-plasma X-ray source[(2)] to generate 4-10 ps pulses instead of 200 ps used last year.

The new laser system is shown schematically in Fig 1. We introduced several novel features:-

(a) Diffraction limited, 4 -10 ps pulses produced by a synchronously pumped dye laser,

(b) The front end operates at 746 nm wavelength which improves the ratio of pulse intensity to background to better than 10^4,

(c) Use of a Bethune Cell (BC) as the final dye amplifier for good beam quality,

(d) 10% efficient frequency conversion (746 nm to 248 nm) system based on two BBO crystals,

(e) Efficient use of the multiplexer by angularly multiplexing the two pulse-train beams it generates, and amplifying both in the KrF system. The two beams diverge only 0.2 mrad after expansion in the telescope, and product X-ray sources (plasmas) each of 10 μm diameter and spaced by 20 μm. This is a new concept of "spatially distributed X-ray sources" which is useful in scaling the average power of the laser (and X-ray source) and may find other applications.

(f) The trains of picosecond pulses were amplified in two different configurations for the KrF amplifier(s):

(i) the double pass amplifier configuration[(2)] is used routinely, with the second excimer operated in XeF as pump for the picosecond front end dye amplifiers,

(ii) the use of two single pass KrF amplifiers(1) and Fig. 1, with a Q-switched YAG as pump for the dye amplifiers. This system allows better energy extraction from the KrF amplifier: 140-160 mJ in 8 pulses as compared to 100-120 mJ in configuration (1) system (1) is scalable in KrF laser power by using a number (3-10) of KrF final amplifiers in parallel by splitting the KrF pre-amplifier output beam. Such a system could provide an X-ray average power of 1W - 10 W for a commercial lithographic exposure too. System (2) also reduces losses in beam energy which appear in system (1) due to the overfilling of the focusing lens (in the X-ray chamber) by the large dimensions of the amplified KrF beam. The main limitation of system (2) when the YAG pump is used, consists in the 10 Hz repetition rate. This can be easily improved by using another excimer (as shown in Fig 1) with high repetition rate.

The main specifications of the X-ray source area described in Table 1. A maximum X-ray average power of 200 mW at 50 Hz was generated using System (1), for 1.2 keV X-rays. This corresponds to 3.3% average (over many shots) X-ray conversion efficiency into 2π steradians (or 1%/Steradian). When using System (2), the X-ray conversion efficiency obtained with a single 20 mJ, 4 ps KrF laser pulse, which is 1.75%/sr.

Table 1

REPETITION RATE	50 HZ
EXCIMER AVERAGE POWER	20 W
PULSE DURATION	4-10 ps
X-RAY SOURCE SIZE	10-20 μm
X-RAY AVERAGE POWER	200 mW
1.2 keV PHOTONS	
"WATER WINDOW" PHOTONS	200 mW
1.5 keV PHOTONS	10 mW
3.37 nm LINE	5 x 10^{12} (PHOTONS/S/ mm^2/mr^2/0,1% BANDWDITH)
0.78 nm LINE	2 x 10^{11}
SHORTEST WAVELENGTH	0.7 nm (1.7 keV)
COHERENT X-RAYS	3.37 nm
FOCUSED X-RAYS	30 μm LATERAL COHERENCE AT 30 cm
FOCUS 50 NM DIA	1000 photons/shot
FOCUS 1mm DIA	10^{10} photons/shot (future)
He PRESSURE IN X-RAY CHAMBER	0 - ATMOSPHERIC
LONG TERM OPERATION WITHOUT LENS CLEANING	>10^6 SHOTS
X-RAY CHAMBER FOR UNIVERSITY AND COMMERCIAL USERS	- keV: X-DNA (2 krad/sec) -keV: X-LITHOGRAPHY (1 min exposure) -WW: MICROSCOPY (50 pixel/sec) HOLOGRAPHIC MICROSCOPY (5 sec exposure) - WHOLE SPECTRUM: SPECTROSCOPY (K and L-shell) CALIBRATION (Spectrometers, streak cameras, detectors)

Table 1 also shows the high spectral brightness for the 3.37 nm spectral line of Carbon VI, which at 5 x 10^{12} is comparable with medium sized synchrotrons. Nevertheless, synchrotrons generate such a brightness over a continuum spectrum, whereas our source has a discrete, line spectrum. Also, while synchrotron radiation is a collimated beam, the plasma source is a point source. This has advantages for the coherent properties of the source and therefore microscopy including holographic X-ray microscopy in the water window spectral region.

As can be seen from Table 1 the high average X-ray power translates in very short exposures for biochemistry (DNA experiment) and lithography.

In conclusion we have demonstrated and implemented at RAL, the most powerful soft X-ray source besides synchrotrons. The source can be scaled to the 1 W X-ray power level by using a larger, 80-100 W KrF excimer final amplifier. This will make even more interesting for University and commercial users, and will open a number of new applications. As is shown in the Physics and Biology sections of the present Annual Report, we have also developed a number of beamlines (many being world first) for different user experiments, therefore insuring the versatility of this state-of-the-art facility.

REFERENCES

1. I C E Turcu, I N Ross and G J Tallents
   Report RAL-92-020, 233, (1992).

2. I C E Turcu, I N Ross, M Steyer, M Amit, B Soom, K Osvay, A Hening, R Kaur and S Quayum
   Report RAL-92-020, 229, (1992).

HIGH POWER LASER-PLASMA X-RAY SOURCE

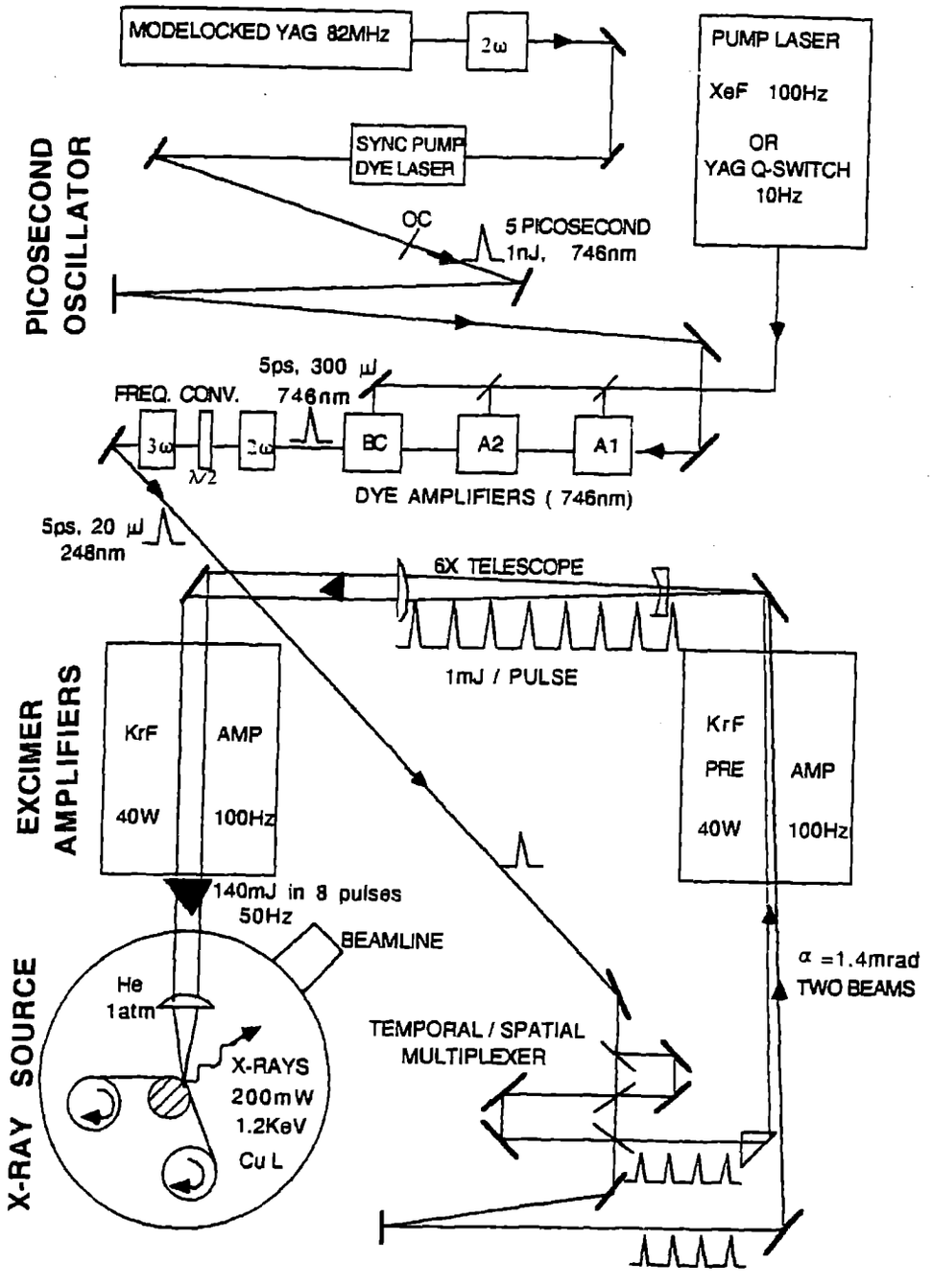

LASER SUPPORT FACILITY: OPERATIONS AND DEVELOPMENT

A total of 41 user experiments were scheduled at RAL and 15 experiments using loan lasers were completed during the year. There were 71 user proposals for laser experiments and these exceeded the number of experiments approved by the Panel and scheduled by a factor of 1.2. The distribution by subject area is given in table 1.

Table 1

	Physics	Chemistry	Biology
Applications %	20	60	20

THE PICOSECOND LABORATORY

Andrew Langley, Pavel Matousek and Waseem Shaikh

A total of 13 scheduled experiments and several off-line development projects were carried out using the picosecond facility. Once again these have ranged widely across the scientific disciplines with much of this work appearing in this years CLF Annual Report.

We have succeeded in running scheduled experiments continuously throughout the year despite a considerable amount of reorganisation in the laboratory. There had been problems with the layout of the picosecond laboratories for some time, and this year we have reorganised the laboratories so that the transient absorption apparatus can be set up permanently and single-photon counting and the TR^3 experiments have more space.

The other main development has been the transfer to titanium-sapphire TiS technology for the source of 100 fs pulses for the 10 Hz amplified system. This has, at least in part, addressed the needs of some users for shorter pulses and we have successfully carried out both pump/probe and multi-photon ionisation experiments with the new system. This change has motivated much development work (described elsewhere in this CLF report) to optimise the performance of the laser; notably by the use of CPA techniques and a Bethune cell for an improved intensity-profile of the beam.

In summary the new system currently performs as follows. The 171 argon- ion pumped titanium-sapphire oscillator (Spectra-Physics Tsunami) produces pulses which can be varied between 80 and 400 fs, at a repetition rate of 82 MHz, with pulses energies of about 2 nJ at 750 nm. (We currently have optics to cover the range 740-820 nm). On amplification, typical minimum pulse durations are 120 fs with 400μJ/pulse at 750 nm. At 370 nm energies of 30μJ/pulse are achieved by SHG in BBO.

The improved beam-quality and shorter pulse-length enabled us to obtain accurate and detailed transient absorption kinetics, on the sub-picosecond timescale, on samples with Δ absorption changes as small as $5x10^{-3}$ with a noise level of $\approx 2x10^{-4}$ peak-to-peak.

This change from dye-based systems, and the switch in wavelength to the near IR (750-850 nm), has interested physicists working with semiconductors and chemists or biologists wishing to excite in the 400-500 nm region i.e. double the fundamental TiS range. Next year we will obtain a 10W pumped TiS system and will then be able to access the full 740-1000 nm range available from these lasers. There is much work to do in 1993/94 to produce shorter amplified pulses and to extend the wavelengths available.

Much development work has been successfully invested in the picosecond time-resolved resonance Raman, TR^3, spectroscopy apparatus which is now fully operational. Raman spectra and lifetimes can be measured for transients with lifetimes from 10 to 1000 picoseconds. The wavelength coverage for the apparatus is between 550 - 655 nm and its frequency doubled line (275 - 327.5 nm). The spectral resolution is 10 cm^{-1}.

The time-correlated single-photon counting apparatus is now also fully operational. Three user groups have used the apparatus this year and invested their own efforts during off-line time to develop the system to suit their needs.

THE NANOSECOND LABORATORIES

Anthony Parker, Susan Tavender and Edmond Turcu

This year has seen the nanosecond lasers put to a wide variety of uses and a total of 30 experiments were scheduled. The reliability remained very good with time lost due to faults at *ca.* 2%. Both Raman/time-resolved Raman and laser flash photolysis have featured highly. A new experimental technique was introduced, Resonant Enhanced Multi-Photon Ionisation (REMPI) to study the dynamics of laser induced desorption. This collaborative project required diverse expertise with Oxford University concentrating on the ultra-high vacuum chamber and RAL staff on the lasers and detection side. The system boasts a sensitivity of detecting 4×10^{4} NO molecules cm^{-3} per quantum state with a signal/noise ratio of 4.

The laser generated plasma X-ray source (partly funded through the Eureka programme) has continued to be developed. The purchase of the titanium sapphire laser for the picosecond laboratory allowed the Spectra-Physics mode locked YAG laser to be used to generate trains of 248 nm picosecond pulses. The current set-up extracts 120 mJ from the KrF excimer laser amplifier using a train of 8 pulses each 7 ps long. Focusing this output onto a copper target (*ca.* 1 nm X-rays) has produced a record 200 mW (64 mW/sr) average X-ray power at 50 Hz repetition rate and this intensity (5×10^{12} photons/s/mm^2/$mrad^2$/0.1% bandwidth at 3.37 nm) is only beaten by the worlds most powerful synchrotrons. These improvements have been passed onto users (eg 2 krad/s dose rate for DNA damage experiments) and a company purchased time on the source to test the system for themselves.

A new state of the art back illuminated liquid nitrogen cooled CCD camera and single grating spectrograph has been purchased from a recently funded grant (Truscott/Land/Parker) for TR^3 investigations on carotenoid radicals. A one year post-doctoral fellow (based at Keele University) has been appointed to help develop the system.

An outside of hours experiment performed by the Institute For Animal Health (Edinburgh) used an excimer laser (248 nm) to induce mutations in a strain of scrapie. However, the infectivity of the irradiated samples will not be known until next year when the bioassay has been completed.

THE LASER LOAN POOL Michael Towrie

In 1992 the six month loan periods were retained leading to a total of 10 chemistry and 5 physics based loans. During this time most of the lasers proved reliable with the exception of the now very old EMG101 excimer laser and a also number of weeks lost in Edinburgh due failure of the Spectron Nd:YAG.

The Quanta-Ray Nd:YAG pumped dye system and the Questek fluoride excimer have been well received by the Users. The Questek has been used predominantly at 193 nm as a photolysis source and the Quanta-Ray system for spectroscopy of gas phase molecules.

The remaining Nd:YAG laser systems were used to obtain the spectra of jet cooled molecules or laser cooled ions in an ion trap and also in an attempt to obtain time resolved Raman spectra from semiconductor materials. Based on the success of the first experiments using the custom built CRESU apparatus in Renne, Smith and Rowe were again allocated two lasers early in 1993 for the continuation of their highly rated work on the kinetics and dynamics of reactions between radicals at very low temperatures.

The CW lasers have seen use in Edinburgh and Queen's where the argon ion was used by as an intense light source for velocity mapping hydraulic systems by particle image velocimetry and the titanium sapphire system to study novel metal liquid like films by surface enhanced Raman scattering.

The demand for loan pool lasers remains high despite the concern that several of the lasers, through advanced age, are now running below specification and do not offer Users state of the art technology. In

particular EMG101 and Datachrom lasers are no longer economical to maintain and the EMG101 will be retired after September 1993 although the Datachrom may still be used for less demanding experiments.

Table 2: Major Laser Support Facility Equipment

	Laser (wavelength range/max pulse energy/ pulse length/max rep rate)	main uses
RAL B	two excimer pumped dye laser (200-950 nm/20 mJ/30 Hz)	ns-TR^3, Raman, fluorescence, laser flash photolysis. REMPI. Delays from ms to ns.
	fluoride excimer laser (157, 193, 222, 248 nm/400 mJ/20 ns or 4 ps for 248 nm using YAG laser seed pulse 100Hz)	DNA damage/repair, laser desorption, laser generated plasma X-ray source, X-ray lithography, scanning microscopy.
	argon ion (525, 514, 488, 457 364, 353 nm/cw source)	Raman spectroscopy
EDL	cw argon ion (all lines) pumped mode-locked titanium sapphire laser (100 fs, 10 nJ, 720-820 nm)seeding a Q-switched Nd:YAG pumped dye amplifier (740-800 nm/400 μJ 370-445 nm/30 μJ)	transient absorption spectroscopy (using continum generation), multiphoton-ionisation (10^{16} Wcm^{-2})
ASER	copper vapour pumped amplifier system (550-655 nm/55 μJ/6 ps/4.5 kHz)	ps-TR^3
	mode locked Nd:YAG pumped cavity dumped dye laser (560-640 nm/20 nJ/4 ps/4 MHz)	single photon counting
LASER LOAN POOL	Quanta Ray GCR-11 (1064 nm/320 mJ, 532 nm/155 mJ, 355 nm/70 mJ, 266 nm/30 mJ/10 Hz) with PDL-3 dye laser (400-900 nm/45 mJ/<0.08 cm^{-1} bandwidth)	transient spectroscopy, photolysis and reaction kinetics
	Quantal Datachrom 5000 (1064 nm/650 mJ, 532 nm/200 mJ, 355 nm 70 mJ/20 Hz) with dye laser (420-700 nm/40 mJ/<0.08 cm^{-1} bandwidth). Frequency doubling with autotracking, mixing manual control.	transient spectroscopy, photolysis and reaction kinetics
	JK Hyperyag 750 (1064 nm/700 mJ, 532 nm/200 mJ, 355 nm/40 mJ, 266 nm/10 mJ/20 Hz) with PDL-2 dye laser (400-900 nm/45 mJ/<0.1 cm^{-1} bandwidth)	transient spectroscopy, photolysis and reaction kinetics
	Spectron (1064 nm/580 mJ, 532 nm/180 mJ, 355 nm/35 mJ, 266 nm/10 mJ/10 Hz) with PDL-2 dye laser (400-900 nm/40 mJ/0.1 cm^{-1} bandwidth)	transient spectroscopy, photolysis and reaction kinetics
	FI3002 dye laser (350-950 nm + doubling (N.B. no pump laser)	transient spectroscopy, photolysis and reaction kinetics
	Spectra Physics 2025 argon ion (5 W visible/0.4 W UV single line)	gas phase kinetics, particle image velocimetry and semiconductor science
	Spectra-Physics titanium sapphire system (680-1040 nm/500 mW)	IR Raman studies, fibre amplifier and waveguide studies
	Fluorine excimer laser (157 nm/10 mJ, 193 nm/400 mJ, 249 nm/600 mJ, 351 nm/300 mJ)	photolysis source and laser ionisation